Processing strategies and limitations of continuous Wurster coating with product classification

Dissertation
zur Erlangung des akademischen Grades

Doktoringenieur
(Dr.-Ing.)

von **M.Sc. Daniel Müller**
geb. am 16.12.1987 in Schönebeck (Elbe)

genehmigt durch die Fakultät für Verfahrens- und Systemtechnik
der Otto-von-Guericke-Universität Magdeburg

Promotionskommission:	Prof. Dr.-Ing. habil. Ulrich Krause (Vorsitz)
	Prof. Dr.-Ing. habil. Evangelos Tsotsas (Gutachter)
	Prof. Dr.-Ing. Andreas Bück (Gutachter)
	Prof. Dr.-Ing. Robert Dürr (Gutachter)

eingereicht am: 24.03.2022

Promotionskolloquium am: 15.08.2022

Your time is limited, so don't waste it living someone else's life. Don't be trapped by dogma – which is living with the results of other people's thinking.

Steve Jobs

Abstract

The applications of layerwise spray granulation include the so called layering for the transfer of non-volatile substances from solutions, suspensions or melts into disperse solid products made of dry, compact, and mostly round particles as well as the so called coating for bringing functional materials onto core particles. The granular product form is characterized by precise dosing, storability, longer shelf life, high specific surface area, and low specific weight. A certain range of grain size or layer thickness is often required in order to either obtain a dust-free and free-flowing product, to control the redissolving behavior, to guarantee the functionality of coating layers, or to generate necessary properties for further processing of bulk solids. Fluidized bed spray process is a possible technology for implementation of layerwise particle formulation, which offers good conditions for uniform particle growth with energy-efficient drying of sprayed liquids due to intensive mixing and fast heat and mass transfer. The transition from the widely applied discontinuous mode of fluidized bed spray granulation to continuous mode requires complex operation concepts for ensuring process stability, controlling fluidized bed mass and product characteristics, identifying process limits, and designing the equipment properly. In case of layerwise granulation, a distinction can be made between slight-growth and large-growth processes. Slight-growth processes are characterized by product particles that are not much larger than before the spraying treatment, such as for taste masking or controlled release of active substances. A discontinuous mode of operation should be used for such processes, because product requirements such as homogeneous coating can hardly be met by continuous processing for the reason of broad residence time distributions in fluidized beds and insufficient separation properties between product and starting material. In large-scale granulation, products are much larger than primary particles, which is the case when layering and coating with thick functional layers. Continuous operation can be implemented in such processes by air classification. For the agglomeration-free granulation of small core particles the Wurster-spray configuration, and for larger starting materials the top-spray version is recommended.

In previous work by Hampel, a successful process concept for continuous layerwise fluidized bed spray granulation with external product classification could be implemented, in which product is classified by an upward gas flow and bed mass is controlled by manipulating the classifier gas velocity. Based on Hampel's reference case, on the one hand, processing strategies for stable fluidization and spraying conditions with adjustable product mean size and short startup times were aimed to be designed in the present dissertation. On the other hand, different process limits should be formulated, which specify a range of permissible process parameters and are included in overall operation concepts.

Three models have been created in the theoretical part of this thesis. The first is the so-called ideal continuous layerwise granulation model, or in short the ICLG-model. It is a purely analytical model of continuous layerwise granulation under ideal conditions, from which the essential relationships between process parameters and desired product characteristics arise. The second is a modified version of Hampel's population balance model, which is divided into three functional compartments for spraying, drying, and classification, and is therefore referred to as the three-compartment population balance model here. With the help of this PB-model, several startup processes of continuous granulation with external product classification were simulated for three different processing strategies and various parameter conditions. In these simulations, one of the strategies was able to keep the bed mass in a stable range and control the product mean size very precisely for the different desired particle size enlargement ratios. It has been shown that the ratio of the solids spray rate to the feed rate of external nuclei (cores) is the key element for controlling product mean diameter, and that adequate control deviations in bed mass are obtained when a proportional (linear) control structure is used. The offset value of it, the so-called set separation gas velocity, is adapted to the terminal sinking velocity of the desired product. The third model is a two-zone continuum model of circulating Wurster fluidization without particle growth, which is abbreviated here as the TZC-model. Based on this model, fluid flow and particle transport dynamics in the process chamber are described; diverse dimensionless characteristics and three process limits of Wurster granulation are defined. Most important are the dimensionless inlet gas velocity, the dimensionless water spray rate, and the dimensionless bed mass. They allow to compare Wurster granulation for different chamber sizes and can be used for setting parameters in scale-up strategies. The presented process limits cover minimal Wurster-fluidization, process-gas satu-

ration, and Wurster-tube exceedance by the expanded bed. Approximate solutions have been derived for these process limits, which presuppose some simplifications such as an isothermal system, adiabatic walls, or negligible evaporation in the Wurster tube. The three process limits span a parameter range that must not be left for stable process control. The operation points of Hampel's continuous granulation experiments were within this range.

The experimental part of this thesis contains a study with several discontinuous multi-stage granulation experiments for different process parameters, analyses of the conveying behavior of the double-pinch valve for the feed of external nuclei and the double-pinch valve for bed discharge and classifier input, as well as measurements of the inlet gas temperature drop by heat losses across the inflow plate and of process gas temperature decrease by evaporation cooling within the Wurster tube. The discontinuous granulation study enables to optimize the inlet gas and spray parameters in regard of stable process conditions, validate the inline detection system of bed masses from Hampel's work, and determine spray fluctuations, spray losses, effective coating densities, necessary growth times, and possible particle growth limits of pneumatic conveyability through the Wurster tube. By conveying behavior analyses, the accuracy of nuclei feed rate and classifier entry rate can be improved and underlying effects of dosing can be better understood. On this basis, various methods for setting arbitrary nuclei feed rates are defined and discussed. The findings of model studies and experimental preliminary investigations are taken into account in process strategy development and employed in continuous granulation experiments. The successful process strategy from the PB-simulation study forms the basis for this. The granulation experiments are carried out on laboratory scale with small core materials in a ProCell LabSystem with Wurster inserts. The results are remarkably good in regard of controlled product mean size at steady state, but there is also need for improvement in the startup strategies, since the product size distribution may significantly exceed the target values and damped PSD-oscillations of the bed and product can occur.

Kurzzusammenfassung

Zu den Anwendungen der schichtartigen Sprühgranulation gehört das Layering zur Überführung nichtflüchtiger Substanzen aus Lösungen, Suspensionen oder Schmelzen in disperse Feststoffprodukte mit trockenen, kompakten und meist runden Partikeln sowie das Coating zur Beschichtung von Kernpartikeln mit artfremden funktionalen Materialien. Die granulare Produktform zeichnet sich durch gute Dosierbarkeit, Lagerfähigkeit, Haltbarkeit, einer hohen spezifischen Oberfläche und geringem spezifischen Gewicht aus. Häufig ist ein bestimmtes Spektrum der Korngröße beziehungsweise der Schichtdicke gewünscht, um entweder ein staubfreies und rieselfähiges Produkt zu erhalten, das Wiederauflösungsverhalten zu steuern, die Funktionalität von Coatingschichten zu gewährleisten oder notwendige Eigenschaften für die Weiterverarbeitung der Schüttgüter zu generieren. Das Wirbelschicht-Sprühverfahren ist eine Technologie für die Umsetzung der schichtartigen Partikelformulierung, die durch intensive Durchmischung und schnellen Wärme- und Stofftransport gute Voraussetzungen für eine gleichmäßige Partikelbeschichtung und energieeffiziente Trocknung des eingesprühten Flüssigkeitsanteils bietet. Der Übergang von der weit verbreiteten diskontinuierlichen Fahrweise der Wirbelschicht-Sprühgranulation hin zu einer kontinuierlichen Fahrweise verlangt jedoch komplexe Betriebskonzepte zur Beibehaltung der Prozessstabilität, Regelung der Wirbelschicht-Bettmasse, Steuerung von Produkteigenschaften, Darstellung von Prozessgrenzen, sowie einer guten apparativen Gestaltung.

Bei der schichtartigen Granulation kann zwischen Geringwachstums- und Großwachstumsprozessen unterschieden werden. Geringwachstumsprozesse sind durch Produktpartikel gekennzeichnet, die nur wenig größer sind als vor der Sprühbehandlung, beispielsweise für Geschmacksmaskierung oder zur kontrollierten Freisetzung aktiver Substanzen. Eine homogene Beschichtung kann jedoch mit kontinuierlicher Prozessführung aufgrund von breiten Verweilzeitverteilungen in Wirbelschichten und unzureichenden Trenneigenschaften zwischen Produkt und Ausgangsmaterial kaum erzielt werden. Deshalb sollten Geringwachstumsprozesse eher diskontinuierlich ausgeführt werden. In Großwachstumsprozessen sind die Produktpartikel viel größer als die Kerne, was bei dicken funktionalen Schichten der Fall ist. Die kontinuierliche Betriebsweise kann in solchen Prozessen wegen des Partikelgrößenunterschiedes mithilfe einer Gegenstromklassierung realisiert werden. Zur Vermeidung von Agglomeration ist für die schichtartige Granulation kleinerer Kernpartikel eher die Wurster-Konfiguration und für größere Ausgangsmaterialen die Top-Spray-Variante zu empfehlen.

In einer vorherigen Arbeit von Hampel wurde bereits ein Prozesskonzept für die kontinuierliche schichtartige Wirbelschicht-Sprühgranulation mit externer Produktklassierung und Bettmassenregelung umgesetzt, in dem das Produkt durch Aufwärtsgasströmung klassiert und die Bettmasse durch Manipulation der Klassiergasgeschwindigkeit geregelt wird. Ausgehend von diesem Referenzfall, sollen in der vorliegenden Dissertation einerseits Prozessstrategien zur Gewährleistung stabiler Fluidizations- und Sprühbedingungen mit beliebiger Steuerung der mittleren Produktkorngröße und kurzen Anfahrzeiten entworfen werden. Andererseits sollen Prozessgrenzen formuliert werden, die Bereiche zulässiger Prozessparameter beschreiben und in die Betriebskonzepte dieser Arbeit eingehen.

Im theoretischen Teil der Dissertation wurden drei Modelle erstellt. Das Erste ist das sogenannte ideal continuous layerwise granulation model oder ICLG-Modell. Es ist das rein analytische Modell einer kontinuierlichen schichtartigen Granulation unter idealen Bedingungen, woraus wesentliche Beziehungen zwischen Prozessparametern und gewünschten Produkteigenschaften für die Prozessstrategien hervorgehen. Das Zweite ist eine modifizierte Version des Populationsbilanzmodells von Hampel, welches sich in drei funktionale Bereiche - Sprühen, Trocknen und Klassieren - gliedert und hier als three-compartment population balance model bezeichnet wird. Mithilfe dieses PB-Modells werden Anfahrprozesse der kontinuierlichen Granulation mit externer Produktklassierung für verschiedene Prozessstrategien und -bedingungen simuliert. Eine der Strategien konnte die Bettmasse stets stabil halten und die mittlere Produktkorngröße für verschiedene geforderte Kornvergrößerungsverhältnisse exakt steuern. Dabei hat sich das Verhältnis von Feststoffsprührate zur Kernpartikel-Zugaberate als Schlüsselelement für die Steuerung der Produktkorngröße erwiesen. Adäquate Regelabweichungen der Bettmasse werden erhalten, wenn eine proportionale Regelstruktur verwendet und dessen Offsetwert, die Soll-Trenngasgeschwindigkeit, an die stationäre Sinkgeschwindigkeit des gewünschten Produktkorns gekoppelt wird. Das dritte Modell ist ein Zwei-Zonen-Kontinuumsmodell der zirkulierenden Wurster-Fluidization ohne Partikelwachstum (TZC-Modell). Auf dessen Basis werden Fluiddynamik und

Feststoffbewegung in der Prozesskammer beschrieben und dimensionslose Kenngrößen sowie Prozessgrenzen zur Charakterisierung der Wurster-Granulation definiert. Die wichtigsten Parameter sind die dimensionslose Eintrittsgasgeschwindigkeit, die dimensionslose Wassersprührate und die dimensionslose Bettmasse. Sie erlauben eine Vergleichbarkeit der Wurster-Granulation für unterschiedliche Kammergrößen und können für das Scale-up genutzt werden. Zu den hier aufgestellten Prozessgrenzen gehören die minimale Wurster-Fluidisation, die Prozessgassättigung und die Bettexpansion über das Wurster-Rohr. Es wurden Näherungslösungen für diese Prozessgrenzen hergeleitet, die auf vereinfachenden Annahmen wie zum Beispiel ein isothermes System, adiabate Wände oder Vernachlässigung der Verdunstung innerhalb des Wurster-Rohres beruhen. Diese drei Prozessgrenzen spannen einen Parameterbereich auf, der für eine stabile Prozessführung nicht verlassen werden darf. Die Betriebspunkte der Arbeit von Hampel liegen innerhalb dieser Prozessgrenzen.

Der experimentelle Teil dieser Arbeit enthält eine Studie mit mehreren diskontinuierlichen mehrstufigen Granulationsexperimenten bei unterschiedlichen Prozessparametern, Analysen des Förderverhaltens von Doppel-Quetschventilen für die Primärpartikelzugabe und den Austrag aus dem Bett in das Klassierrohr, sowie Messungen des Eintrittsgastemperaturabfalls durch Wärmeverluste über die Gasverteilerplatte und der Prozessgastemperaturabnahme durch Verdunstungskühlung innerhalb des Wurster-Rohres. Die diskontinuierliche Granulationsstudie dient der Optimierung der Eintrittsgas- und Sprühparameter hinsichtlich stabiler Prozessbedingungen, der Validierung des Inline-Detektionssystems für die Bettmasse nach Hampel, und der Bestimmung von Sprühschwankungen, Sprühverlusten, effektiven Coatingdichten, notwendigen Wachstumszeiten, und eventuellen Partikelwachstumsgrenzen der pneumatischen Förderbarkeit durch das Wurster-Rohr. Durch die Untersuchungen des Förderverhaltens der Doppel-Quetschventile sollen die Genauigkeit der Primärpartikel- und Klassierrohr-Zugabe optimiert und Teileffekte der Förderdynamik besser verstanden werden. Zudem werden hieraus verschiedene Methoden zur Einstellung beliebiger Kernpartikel-Zugaberaten definiert und diskutiert. Die Erkenntnisse der Modellstudien und der experimentellen Voruntersuchungen fließen in die Prozessstrategieentwicklung ein und finden in mehreren kontinuierlichen Granulationsexperimenten Anwendung. Die erfolgreiche Prozessstrategie aus der PB-Simulationsstudie bildet hierbei die Grundlage. Die Granulationsexperimente werden mit recht kleinen Kernmaterialien in einem Apparat des Typs ProCell LabSystem mit Wurster-Einbau durchgeführt. Es zeigen sich bemerkenswert gute Ergebnisse hinsichtlich der gesteuerten Produktkorngröße. Bei den Strategien zur Verkürzung der Anfahrzeiten besteht allerdings noch Verbesserungsbedarf, da hier Zielüberschreitungen der Produktkorngrößenverteilung und gedämpfte Oszillationen in mehreren Fällen beobachtet wurden.

Nomenclature

Roman symbols

A	cross-sectional area or surface area	[m^2]
Ar	Archimedes number	[−]
Bo_{ax}	Bodenstein number of axial dispersion	[−]
c_d	drag coefficient of sinking particles	[−]
c_{dis}	drag coefficient of gas distributor plate	[−]
D	diameter of mechanical component, plate section, or tube	[m]
D_{ax}	axial dispersion coefficient	[m^2/s]
D_{mix}	mixing coefficient of axial dispersion	[m^2/s]
d	sphere diameter; sphere-equivalent diameter of a particle	[m]
d_{dis}	diameter of holes in perforated bottom plate	[m]
F	force	[N]
f	fluidization number	[−]
G_d	growth rate	[m/s]
g	acceleration constant of earth gravity	[m/s^2]
H	height	[m]
I	electric current signal	[A]
i	counter variable in iterations; single element of a set of values or variables	[−]
j	counter variable in iterations; single element of a set of values or variables	[−]
K	dimensionless substituent; dimensionless constant	[−]
K_m	gain factor	[m/s/kg]
K_{dis}	pressure drop coefficient after McAllister et al.	[−]
k	counter variable in iterations; single element of a set	[−]
k_{pul}	pulsation factor	[−]
k_{sep}	separation frequency factor	[1/s]
k_{sw}	swarm sinking correction factor	[−]
k_{tur}	turbulence constant	[−]
k_{wa}	correction factor of wall effect on sinking velocity	[−]
L	length of multiple particles in series; length of an apparatus component	[m]
M	absolute mass	[kg]
M_{bed}	bed mass	[kg]
M_{dos}	dosage mass	[kg]
M_{set}	set bed mass	[kg]
$\tilde{M}$	molar mass	[g/mol]
$\dot{M}$	mass flow rate	[kg/s]
$\dot{M}_f$	nuclei feed rate	[kg/s]
$\dot{M}_{dpv}$	conveying rate of a double-pinch valve	[kg/s]
$\dot{M}_{p,hit}$	bed outlet hit rate	[kg/s]
$\dot{M}_{sep}$	separator entry rate; bed discharge rate	[kg/s]
$\dot{M}_{spr}$	total spray rate	[kg/s]
$\dot{M}_{spr,s}$	solids spray rate	[kg/s]
$\dot{M}_w$	water spray rate	[kg/s]
$m_{k,r}$	k'th raw moment of an r-based particle size distribution with $r \in \{0, 1, 2, 3\}$	[m^k]
m_{sw}	Richardson-Zaki exponent	[−]
m_{pul}	exponent of pulsation factor	[−]
$\dot{m}_f$	bed-mass-specific feed rate	[1/s]

$\dot{m}_{spr,s}$	bed-mass-specific solids spray rate	[1/s]
$\dot{m}_w$	area-specific water spray rate	[kg/s/m^2]
N	number of particles in a system; number of holes	[−]
$N_{f,step}$	number of steps of a normalized feed rate step function	[−]
N_{man}	number of reflux-discharge cycles within a manual bed mass control period	[−]
$\dot{N}$	total number flow rate	[1/s]
n_{pum}	pump rotation speed	[rpm]
P_j	generalized controlled process variable with $j \in \{m, u, d\}$	[kg; m/s; m]
p	absolute pressure; excess pressure; vapor pressure	[Pa, bar]
Re	Reynolds number	[−]
$\tilde{R}$	ideal gas constant	[J/mol/K]
T	temperature	[°C, K]
T_{sep}	separation function	[−]
t	time	[s]
t_{dpv}	double-switch time, single dosage time step, or dosing cycle time	[s]
$t_{gr,set}$	required growth time	[s]
t_{V1}	opening time of the upper valve in a double-pinch valve sluice	[s]
t_{V2}	opening time of the lower valve in a double-pinch valve sluice	[s]
u	superficial flow velocity in general	[m/s]
u_g	separation gas velocity	[m/s]
$u_{g,set}$	set separation gas velocity	[m/s]
u_s	terminal sinking velocity	[m/s]
S	state property vector (units: see $\dot{M}$, T, Y, and ε)	
s	thickness	[m]
V	volume of a disperse or spatial system	[m^3]
$V_{dpv,sl}$	sluice volume of a double-pinch valve	[m^3]
$\dot{V}$	volume flow rate	[m^3/s]
x_s	mass fraction of solids in spray solution	[−, %]
Y	moisture content of air	[−, g/kg]
$\tilde{y}$	molar fraction of a component in gas mixture	[−, %]
z	vertical coordinate	[m]

Greek symbols

α	spray zone proportion factor	[−]
γ	angle of inclination	[°]
γ	skewness of a particle size distribution	[−]
ϵ	permissible iteration error	[−]
ε	relative void volume or porosity	[−]
ζ	relative deviation from a certain central value	[−, %]
ρ	effective mass density	[kg/m^3]
ν	kinematic viscosity	[m^2/s]
ξ_ρ	normalized particle density	[−]
σ	standard deviation of a number-based particle size distribution	[m]
τ	residence time; duration	[s]
Φ	dimensionless ratio of two quantities	[−]
Φ_ρ	coating-to-core density ratio	[−]
Ω	mass flow rate ratio	[−]
ω	flow velocity ratio	[−]

Mixed and compound symbols

$M_{dos,f}$	prepared dosage mass	[kg]
m_ε	Brötz-exponent	[−]
$n(d)$	non-normalized number density distribution	[1/m]
$\dot{n}(d)$	non-normalized number density distribution flow rate	[1/m/s]
$Q_r(d)$	normalized cumulative particle size distribution of the dimensioning type $r \in \{0,1,2,3\}$	[−]
$q_r(d)$, $q_z(d)$	normalized particle size distribution density of the dimensioning type $r, z \in \{0,1,2,3\}$	[1/m]
u_ε	interstitial flow velocity in general	[m/s]
α_m	bed mass fraction of spray zone	[−]
ΔM_{sam}	discharged bed mass of a sampling unit	[kg]
Δp	pressure difference; pressure drop; pressure loss	[Pa, bar]
$\Delta t_{dos,f}$	dosing time gap of feeding a nuclei package	[s]
$\Delta t_{f,step}$	step time of a normalized feed rate step function	[s]
Δt_{man}	duration of reflux-discharge cycles within a manual bed mass control period	[s]
Δt_{sam}	duration of a sampling unit	[s]
δ_{bl}	dimensionless boundary layer thickness	[−]
ε_s	solids volume fraction	[−]
ζ_d	relative control deviation of product mean size	[−, %]
ζ_{dos}	relative standard deviation of single dosage masses	[−, %]
ζ_j	generalized relative control deviation with $j \in \{m,u,d\}$	[−, %]
ζ_m	relative control deviation of bed mass	[−, %]
ζ_{q_r}	relative standard deviation of an r-based particle size distribution with $r \in \{0,1,2,3\}$	[−, %]
ζ_u	relative control deviation of separation gas velocity	[−, %]
η_{dry}	drying potential	[−]
Θ_{loss}	relative temperature drop	[−]
$\Theta_{Y,dis}$	drying capacity reduction factor of heat losses	[−]
$\Theta_{Y,noz}$	drying capacity reduction factor of nozzle gas injection	[−]
κ_{sep}	separation sharpness	[−]
λ_{tor}	outflow coefficient of modified Torricelli approach from Burgschweiger a. Tsotsas	[−, %]
μ_{bed}	dimensionless bed mass	[−, %]
$\dot{\mu}_{g,noz}$	dimensionless nozzle air rate	[−, %]
$\dot{\mu}_w$	dimensionless water spray rate	[−, %]
ξ_{exc}	dimensionless inlet gas velocity of the Wurster-tube-exceedance limit	[−, %]
ξ_{in}	dimensionless inlet gas velocity	[−, %]
ξ_{mwf}	dimensionless inlet gas velocity of the minimal-Wurster-fluidization limit	[−, %]
ξ_{sat}	dimensionless inlet gas velocity of the process-gas-saturation limit	[−, %]
σ_{q_r}	standard deviation of an r-based particle size distribution with $r \in \{0,1,2,3\}$	[m]
$\tau_{f,step}$	overall duration of step-wise increase of feed rates	[s]
$\tau_{gr,set}$	model-based required growth time	[s]
τ_{man}	overall duration of a manual bed mass control period	[s]
τ_{sep}	separation time constant for PB-modeling	[s]
$\Phi_{a,exc}$	cross-sectional expansion factor of the Wurster-tube-exceedance limit	[−]
Φ_{bu}	gas-to-nuclei density ratio	[−]
Φ_d	obtained particle growth ratio based on mean values of q_0	[−]
$\Phi_d(d_{m,q_0})$	obtained particle growth ratio based on mean values of q_0	[−]
$\Phi_d(d_{m,q_1})$	obtained particle growth ratio based on mean values of q_1	[−]
$\Phi_d(d^*_{3,0})$	obtained particle growth ratio based on mean-volume-equivalent diameters	[−]
$\Phi_{d,set}$	desired particle growth ratio or desired particle size enlargement ratio	[−]
$\Phi_{d,cr}$	minimum required particle growth ratio	[−]
$\Phi_{dpv,i}$	single dosage fluctuation factor	[−]

$\Phi_{f,loss}$	mass fraction of nuclei losses	$[-,\%]$
$\Phi_{f,step}$	normalized feed rate step function	$[-]$
$\Phi_{fill,i}$	single dosage correction factor of reduced fill-in time	$[-]$
$\Phi_{flush,i}$	single dosage correction factor of reduced flush-out time	$[-]$
$\Phi_{h,1-\alpha}$	dimensionless bed height	$[-]$
Φ_m	spray-to-feed rate ratio	$[-]$
$\Phi_{spr,loss}$	mass fraction of spray losses	$[-,\%]$
$\Phi_{a,exc}$	cross-sectional expansion factor of the Wurster-tube-exceedance limit	$[-]$
$\Phi_{u,eva}$	overall gas velocity correction factor of evaporation	$[-]$
$\Phi_{u,T,dis}$	gas velocity reduction factor of heat losses	$[-]$
$\Phi_{u,T,eva}$	gas velocity reduction factor of evaporation cooling	$[-]$
$\Phi_{u,Y,eva}$	gas velocity enhancement factor of released water vapor	$[-]$
$\Phi_{u_{s,pr}}$	relative product sinking velocity	$[-]$
Φ_d^{-3}	core-to-particle volume fraction of a coated single particle	$[-]$
$\Phi_d^{-3}(d^*_{3,0})$	average core-to-particle volume fraction of a coated bulk material	$[-]$
$\phi_{f,step}$	step width of a normalized feed rate step function	$[-]$
ϕ_{sh}	shape factor	$[-]$
$\varphi_{dis,i}$	cross-sectional area fraction of distributor plate section i	$[-]$
$\Psi_{dis,i}$	opening ratio of distributor plate section i	$[-]$
Ψ_{sph}	overall sphericity of particle system	$[-]$
$\Psi_{sph,p}$	sphericity of single particle	$[-]$
$\Omega_r(d)$	non-normalized cumulative particle size distribution of the dimensioning type $r \in \{0,1,2,3\}$	$[\mathrm{m}^r]$
$\omega_r(d)$	non-normalized particle size distribution density of the dimensioning type $r \in \{0,1,2,3\}$	$[\mathrm{m}^{r-1}]$

Subscripts

Ar	argon
act	actual
ad	adiabatic system
amb	ambient
app	apparatus; process chamber
air	dry air
b	bulk
bed	packed bed; fluidized bed
bl	boundary layer
bot	bottom of spray zone and drying zone
bu	buoyancy
c	coating
ch	characteristic
chan	channel
conv	convection along coordinate
core	core
cr	critical
d	drag; related to particle size
dis	gas distributor plate or inflow plate
dpv	double-pinch valve
dry	dry content of humid air; drying potential; drying time
eff	effective
elu	elutriation point
emp	empirical function
emp	empty process chamber
end	end; final state; terminal simulation point; final iteration loop

eva	evaporation
exc	Wurster-tube-exceedance limit
exp	experimental
f	feed; nuclei; core particle
$fill$	filling level; filling a sluice volume
fl	fluid
$flush$	flushed particles
g	gas
gr	growth
gra	gravity
hit	hitting the bed outlet channel
i	counter variable in iterations; single element of a set of values; index of distributor plate section
in	inlet gas
inv	inverse
iso	isothermal system
j	counter variable in iterations; single element of a set of values; stage number
k	counter variable in iterations; single element of a set of values; index of experimental subsection
$loss$	heat losses; material losses
log	logarithmic
m	mean; mass-specific; ratio of mass flow rates; related to bed mass
man	manual bed mass control
max	maximal
mf	isothermal homogeneous minimal fluidization conditions
mid	middle; unweighted central value
min	minimal
mix	mixing
mod	modal value of a particle size distribution
mon	monodisperse
mwf	minimal-Wurster-fluidization limit
new	new start value of an iteration loop
N_2	molecular nitrogen
noz	nozzle
O_2	molecular oxygen
off	total discharge mode (offset) of a classifier
$open$	opening
out	outlet
PA	equivalence of projected area between particle and sphere
p	single particle; arbitrary particle; constant pressure
pn	pneumatic transport
pol	polydisperse
pul	pulsation
pum	pump
pr	product
$proj$	projected area
q_r	related to symbol $q_r(d)$
qu	quadratic flow regime
$quad$	quadratic approximation
r	dimension type (basis) of particle size distributions
rec	recycle
ref	reference characteristics
$refl$	total reflux mode of a classifier
rn	fluidization range number
S	equivalence of surface area between particle and sphere
SV, p	equivalence of volume-specific area between particle and sphere

SV	effective Sauter diameter
s	solid phase; dissolved solids; sinking
sat	saturation conditions in general; isenthalpic saturation point; process-gas-saturation limit
sep	separation; separator; separator inlet; classifier; bed granule discharge
set	set value; desired value; required value
sh	shape
smp	smallest possible
sph	sphericity; sphere
spr	spraying; spray solution
$step$	step function
stp	standard temperature and pressure
sur	surroundings
sys	system
sw	swarm
T	related to temperature change
top	top of spray or drying zone
tor	Torricelli
tot	total; all particles
tur	turbulence
u	related to separation gas velocity or process gas velocity
V	equivalence of volume between particle and sphere
$V1$	upper pinch valve
$V2$	lower pinch valve
vap	water vapor
$void$	voids; solid-free phase
w	water
wa	wall
wt	Wurster tube
Y	related to change in moisture content
z	dimension type (basis) of particle size distribution
0	number-based; initial conditions; zero-growth conditions; offset of a control function; process chamber bottom; zero degrees Celsius; stage zero; core material
25	product discharge probability of 25 %
32	ratio of third raw moment to second raw moment of particle size distribution; Sauter diameter of spherical particle system
50	median value of a particle size distribution
75	product discharge probability of 75 %
α	spray zone
$1-\alpha$	drying zone
$1+Y$	dry-air-specific
ε	void volume; void area
ρ	material density
*	power mean; generalized mean; Hölder mean; approximate solution of a quantity; free variable
**	particle size average from the ratio of two raw moments

Abbreviations and acronyms

a.	and
CM	control method (processing strategy)
CMFL	calculation method of fluidization limits
CV	coefficient of variation
EB	experiment for discontinuous (batch) granulation
EBD	experiment for bed discharging
EC	experiment for continuous granulation
EF	experiment for feeding external nuclei
F	feed rate control method
GAS	growth acceleration strategy
ICLG	ideal continuous layerwise granulation (model)
IM	initial material (raw bulk material)
MFC	mass flow controller
MS	Microsoft
P	proportional controller
PB	population balance
PC	personnel computer
PD	proportional–derivative controller
PI	proportional–integral controller
PID	proportional–integral–derivative controller
PSD	particle size distribution
RSD	relative standard deviation
SD	standard deviation
SFF	separation frequency factor
SFM	spray-to-feed rate setting method
TZC	two-zone continuum (model)
TZCM	two-zone continuum model (parameter variation series)
V	valve

Operators, functions, and relation symbols

d	total differential
∂	partial differential
Δ	difference
$\frac{\partial}{\partial x}(...)$	partial derivative of the term in parentheses with respect to a variable (here x)
$\frac{\mathrm{d}}{\mathrm{d}x}(...)$	first derivative of the term in parentheses with respect to a variable (here x)
$'$	first derivative; state of air after humidification
$''$	state of air after further humidification
f(...)	function of symbols in parentheses
$\mathrm{f}_{\mathrm{emp}}(...)$	empirical correlation to symbols in parentheses
$\mathrm{find}_{\max,x}\big(y(x)\big)$	arbitrary search method for value of a abscissa x with maximal value of a function y
$\mathrm{find}_{\min,x}\big(y(x)\big)$	arbitrary search method for value of a abscissa x with minimal value of a function y
floor(...)	floor function
$\bar{x}$	mean value of a random variable x
(...)	function of symbols in parentheses; compound factor; vector of elements
[...]	unit bracket; compound factor
{...}	set of variables or numbers
$\in$	element of

Contents

1 Introduction

Many substances in the chemical, pharmaceutical, and food industry are produced in liquids. These can be starting materials for further chemical synthesis reactions, auxiliary materials, pharmaceutical coatings, or functional additives such as preservatives, flavorings, or binders. But also waste materials such as landfill leachate and liquid manure contain valuable ingredients for the fertilizer industry. The dissolving media (e.g., water) are often of no use for further processing or end-use of product, require waterproof packaging or container materials for storage and delivery, possibly reduce the shelf life of biodegradable ingredients, and increase energy consumption as well the cost of transportation. Spray drying can remove the solvent and convert the solute into particulate solid state. Such disperse solids are very small in particle size and referred to as powders. Due to their fine dispersity, they have unfavorable properties for transport, storage, and further processing. The dustiness of powders is one them, which is associated with material losses, health risks from inhalation, risk of explosion in air, environmental pollution, or increased wear and tear of mechanical components from fouling. The cohesiveness of powders is another undesired property, since it worsens their flow behavior and dosability, redissolubility in liquids, and can lead to bridging and clogging in conveyors, silos, and other types of containers. In order to improve these product quality aspects, powder particles have to be enlarged. This can be achieved for instance through wet granulation, as in twin-screw, high-shear (agitated beds), or fluidized bed granulators, where the primary powder particles are aggregated by applying binder droplets, and are formed to larger bulk solids with more porous intraparticle structures. This type of particle formulation is recommended for instant for beverage granules or other product with quality requirements of rapid dissolution behavior. However, those granules lack in breaking resistance, whereby dusty fragments can arise again in post-processing and during transport. A possibility for particle size enlargement without use of binders is provided by dry granulation processes such as compaction or tableting. Additionally, binder materials are also dispensed with in layering processes, in which primary particles are coated with the same material. The porosity of such products is usually lower than of those created by aggregation-based particle growth. The benefit of smaller porosity is an increase in bulk density, reduction of transport costs, and saving storage space. Another application of converting valuable substances from liquids into solids is coating. Here, core particles are covered with other materials, commonly by thin layers, for functional reasons, as for example taste masking, controlled release of active substances (e.g., drugs or agricultural agents), sealing and protection against external influences (oxidation, radiation, or humidification), or modification of surface structure (smoothing and roughening). Production of thick coatings on primary particles of different material is rare in industry, but it is also a process of granulation. An example for this are multiple unit pellet systems (short: MUPS) from the pharmaceutical industry, where drug-containing layers are built on inert cores and coated with polymers. Coating and layering belong to layerwise granulation processes, which is the subject of this work, and where agglomeration is attempted to be avoided.

Background and objectives

Layerwise granulation can be implemented in top-spray, bottom-spray, or Wurster fluidized beds. Agglomeration tendency is larger with top-spray than with bottom-spray or Wurster configuration, but for bigger primary particles (cores) top-spray is also a good alternative for layer-by-layer formulation. Layering or coating on fine raw bulk materials should be rather operated with bottom-spray or with Wurster equipment, since higher shear forces occur in such processes. Fluidization offers the combination of intense mixing and efficient heat and mass transfer for drying solvents off wetted particles by hot process gas (often air). Compared to spray agglomeration in fluidized beds, layerwise particle growth is much slower. Large-growth layerwise granulation, where product mean size is a multiple of core mean size, is hard to realize in batch mode, or even impossible, because of strong increase in bed mass. Especially, Wurster granulation must be operated with holdups in a small margin to guarantee proper circulating Wurster fluidization conditions. The granulation batches must be therefore interrupted and continued with smaller holdups in consecutive stages to gain high overall size enlargement ratios by layerwise growth mechanisms. Those process stops are accompanied by long production downtimes and an immense effort in cleaning and preparation of the

granulator system. This gives a motivation to switch from the frequently employed discontinuous mode of operation to a continuous mode. The challenge here is to selectively and efficiently remove the coarse product from the bed and to control both bed mass and product mean size (or average coating layer thickness).

Size-selective product discharge can be realized by internal or external classification. In former work by Hampel [1, 2], a processing strategy was developed with continuous feeding of external nuclei (cores), external product separation in a straight-duct air classifier, fine-fraction recycle, and feed-back control of bed mass by manipulation of the average separation gas velocity. This operation concept has proved to be feasible in various experiments of several hours. However, product size control was missing and large-growth granulation was not part of the objectives of Hampel's case study. Additionally, continuous granulation with external product classification is not a suitable process for classical thin coating due to imperfections of the classifier and size variety of external nuclei. For this reason, large-growth granulation, where sinking velocities of product granules is clearly larger than those of external nuclei, should be one focus when continuous operation is generated through air classification.

In the present work, development of a processing strategy for continuous layerwise granulation with external product classification, stable bed mass control, adjustable product size, and short startup times is the major aim. Describing and finding various process limits such as product separability of air classifiers, adequate fluidization and spraying conditions, maximal spray rates and process-gas saturation, particle growth beyond stable Wurster fluidization, and particle flow rates of practical conveyors make up the second focus of this thesis.

Outline

The present dissertation comprises a discussion of fundamentals, three model analyses (theoretical part), several experimental preliminary investigations of sub-processes of the continuous granulation system used, and the results of several continuous granulation experiments. In the fundamentals, methods for characterizing bulk solids and calculating fluid-particle dynamics are brought together. These should strengthen process understanding and provide basics for developing models, describing process limits, and analyzing properties of experimental products. In addition, the experimental process of Hampel's case study and the associated population balance model is recapitulated.

The theoretical part includes an analytical model of ideal continuous layerwise granulation, a numerical three-compartment population balance model of continuous granulation with straight-duct air classification, and the two-zone continuum model of circulating Wurster fluidization without particle growth, where fluid dynamics are calculated analytically and fluid-particle interactions iteratively. The ideal continuous layerwise granulation model is intended to answer how the process parameters would have to be set under the most ideal conditions of continuous granulation, how the bed granule characteristics are distributed, whether bed mass and product grain size are dependent on each other under stationary conditions or independent, how long it takes to achieve certain particle size enlargement ratios (product growth time), what product properties ensue, whether and under what conditions the terminal sinking velocity of product granules is smaller than that of external nuclei. The three-compartment population balance model is a modification of Hampel's PB-model, wherewith continuous granulation with air classification was simulated for different processing strategies and parameter conditions. Findings from the ideal granulation model for controlling product mean size are incorporated into the simulation processing strategies. In the PB-simulations, dynamics of bed mass and bed and product granule size distributions of the transient phase as well as the control accuracy in bed mass and product mean size of the stationary states are examined. The best processing strategy is used in the experiments of this thesis, but with some adaptations to practical detail problems that are not considered in the PB-model. The two-zone continuum model was created for describing flow separation through a gas distributor plate (perforated metal plate), circulating fluidization in the Wurster chamber, and limits of minimal Wurster fluidization, process-gas saturation, and Wurster-tube exceedance, for which some analytical approximation solutions are derived. In addition, the process parameters of Hampel's continuous granulation experiments were characterized by the two-zone continuum model to take it into account for the choice of inlet gas parameters of the experiments of this work.

The practical partial studies of the present thesis include discontinuous multi-stage granulation experiments, two analyses of dosing or conveying behavior of a double-pinch valve for feeding external nuclei (nuclei feeder) and a double-pinch valve for discharging bed granules (bed discharger) and feeding the classifier tube (classifier entry rates), and several continuous granulation experiments. Furthermore, temperature drop measurements are carried out to quantify the effect of heat losses around the utilized inflow plate

and of evaporation within the installed Wurster tube, which play rather a minor role in this work. The multi-stage batch granulation experiments were conducted to find better parameter conditions with more process stability and maximum particle growth limits of pneumatic conveyability through the Wurster tube, to check error of the inline bed mass detection method implemented by Hampel and the accuracy of spray rates, to estimate proportions of spray losses, and to derive effective coating densities and growth times for large-growth granulation conditions. In the dosing analysis of the nuclei feeder, individual dosage masses, short-term mean values (minutes) and long-term mean values (hours) of conveying rates, and dosing fluctuations were determined depending on the operation parameters (switching times and nuclei filling level) and for different materials types (size and density). On the basis of these results, various feed rate control methods have been designed, and their applicability for the continuous experiments is discussed. The analysis of the bed discharger examines the influence of inlet gas parameters and the switching times of the double-pinch valve on bed discharge rates or classifier entry rates. The study should show which transport phenomenon dominates the overall bed discharge dynamics, if bed discharge rate can be manipulated, and under which parameter conditions the fluctuations in conveying rate are low, and the average bed discharge rate is maximal. The results of all partial studies of the present dissertation find application in the design of overall operation concepts for the continuous granulation experiments. This includes relationships from the ideal granulation model, one processing strategy from the PB-study, parameter settings with regard to the inlet gas, the nozzle gas, and the spray rate, two feed rate control methods, and a few startup strategies that shall accelerate transient particle growth and shorten the time to reach steady states. Attention is paid to the oscillating behavior and control deviations of bed mass and product mean size.

2 Fundamentals

2.1 Characterization of disperse materials

2.1.1 Types of particle size distributions

In general, the individual particles of bulk materials from granulation processes vary in size. Granule size variety is quantitatively described by so-called particle size distributions (short: PSD), e.g., by $q(d)$ representing a normalized density distribution or by $Q(d)$ for a normalized cumulative distribution, where d can be defined by different types of particle size coordinate. The attribute "normalized" is often left out when referring to q- and Q-distributions.

Definition of particle size coordinate

For spherical particles, only one measure of length is used to define the particle size coordinate d of PSDs, which is the sphere diameter. In case of non-spherical particles, the following single particle characteristics are commonly used to describe d:

$$d = \begin{cases} d_{SV,p} = \frac{6V_p}{A_p} & \text{, specific-area-equivalent sphere diameter} \\ d_{V,p} = \left(\frac{6V_p}{\pi}\right)^{1/3} & \text{, volume-equivalent sphere diameter} \\ d_{S,p} = \left(\frac{A_p}{\pi}\right)^{1/2} & \text{, surface-equivalent sphere diameter} \\ d_{PA,p} = \left(\frac{4A_{proj}}{\pi}\right)^{1/2} & \text{, circle-equivalent diameter of projected area} \end{cases} . \tag{2.1}$$

Here, $d_{SV,p}$ denotes the diameter of a sphere with same volume-specific surface area, V_p the actual volume of a single particle, A_p the actual surface area of a particle, $d_{S,p}$ the diameter of a sphere with same surface area, and $d_{PA,p}$ the diameter of a circle with area that equals the projected particle surface area A_{proj} for a certain angle of view. The specific-area-equivalent diameter $d_{SV,p}$ can be expressed by the diameters of the volume-equivalent and surface-equivalent spheres according to:

$$d_{SV,p} = \frac{d_{V,p}^3}{d_{S,p}^2}. \tag{2.2}$$

In case that the *sphericity after Wadell* [3], given with

$$\Psi_{sph,p} = \frac{\pi d_{V,p}^2}{A_p} = \frac{\text{surface area of volume-equivalent sphere}}{\text{actual surface area of particle}} \leq 1, \tag{2.3}$$

is uniform for all individuals of a particulate system, the coordinates of $d_{S,p}$, $d_{V,p}$, and $d_{SV,p}$ are convertible into each other via this relationship:

$$\Psi_{sph,p} = \frac{d_{V,p}^2}{d_{S,p}^2} = \frac{d_{SV,p}}{d_{V,p}}. \tag{2.4}$$

Through Eqs. 2.3 and 2.4, it becomes evident that the specific-area equivalent diameter is always lower or equal to the volume-equivalent diameter, and the latter is always lower or equal to the surface-equivalent diameter:

$$d_{SV,p} \leq d_{V,p} \leq d_{d,S}. \tag{2.5}$$

The specific-area-equivalent diameter $d_{SV,p}$ is not to be confused with the Sauter diameter of spherical particles d_{32} (Eq. 2.46) or with the effective Sauter diameter for bulk solids with other particle shapes d_{SV} (Eq. 2.48). Only for systems that consist of mono-sized spheres, $d_{SV,p}$ confirms with d_{32} and with d_{SV}; for monodisperse systems of same-shape non-spherical particles, $d_{SV,p}$ is equal to d_{SV}, but not to d_{32}. The volume-equivalent diameter $d_{V,p}$ is often used as the characteristic distributed property of bulk solids in

particle technology for the reason that it lies in the middle range of Eq. 2.5 and can be calculated by particle masses (e.g., sieve analyses) and densities (e.g., pycnometric methods). The circle-equivalent diameter of the projected area $d_{PA,p}$ can be determined for instance by static or dynamic image analyses. Due to the angle of view, measurements of this parameter can vary even for the same particle. However, $d_{PA,p}$ serves as good approximation for the volume-equivalent particle diameter $d_{V,p}$ for nearly-spherical objects. It is therefore applied for characterizing the raw materials and granules produced by the experiments of this thesis. Other types of single particle characteristics are mentioned for instance by Geldart [4] or by Allen [5].

Types of dimensioning the classes of particle size - bases of PSDs

Diverse methods for sampling, defining characteristic lengths (diameter) of single particles, and measuring particle size distributions are described in [6]. There are four main types for dimensioning particle size distributions, also named as bases, which are differentiated by a generalized index $r \in \{0, 1, 2, 3\}$. Particle size distributions are measured on the basis of numbers for $r = 0$, of lengths for $r = 1$, of surface areas for $r = 2$, and of volumes of particles for $r = 3$. This way, q_0 and Q_0 are referred to as the number-based, q_1 and Q_1 the length-based, q_2 and Q_2 the area-based, and q_3 and Q_3 the volume-based PSDs. The fundamentals of particle characteristics calculated from these PSD-types can be found in many literature sources, such as in [7–12]. The non-normalized particle size distributions of the four dimensioning types are the number density distribution $n(d)$, the length density distribution $l(d)$, the area density distribution $a(d)$, and the volume density distributions $v(d)$. The normalized and non-normalized types of particle density distributions are related to each other by the total number $N_{p,tot}$, total length $L_{p,tot}$, total surface area $A_{p,tot}$, and total volume $V_{p,tot}$ of the individuals in a certain particulate system. These relations can be generalized by the r-dimensional non-normalized density distribution of single particles $\omega_r(d)$ and the r-dimensional total volume of population $\Omega_{r,tot}$ according to:

$$q_r(d) = \frac{\omega_r(d)}{\Omega_{r,tot}}, \tag{2.6}$$

with $\omega_0(d) = n(d)$ and $\Omega_{0,tot} = N_{p,tot}$ for the number basis, $\omega_1(d) = l(d)$ and $\Omega_{1,tot} = L_{p,tot}$ for the length basis, $\omega_2(d) = a(d)$ and $\Omega_{2,tot} = A_{p,tot}$ for the area basis, and $\omega_3(d) = v(d)$ and $\Omega_{3,tot} = V_{p,tot}$ for the volume basis. Thereby, the different measurement properties (number, length, area, and volume) are unified under the designation *generalized volume* of the type r. Especially the term *generalized* shall indicate here that r is optional within $\{0, 1, 2, 3\}$.

The overall integral of the normalized particle size distribution above the d-coordinate is unity for each of the dimensioning types:

$$\int_0^\infty q_r(d)\mathrm{d}d = 1 \qquad \text{, for } r \in \{0, 1, 2, 3\}. \tag{2.7}$$

The normalized cumulative particle size distribution of an arbitrary basis $Q_r(d)$ ensues from the integral of $q_r(d)$ from zero to the variable d:

$$Q_r(d) = \int_0^d q_r(d)\mathrm{d}d. \tag{2.8}$$

The corresponding non-normalized cumulative particle size distribution, symbolized by $\Omega_r(d)$, is obtained by multiplying $Q_r(d)$ with the generalized total volume $\Omega_{r,tot}$:

$$\Omega_r(d) = Q_r(d)\Omega_{r,tot} = \int_0^d \omega_r(d)\mathrm{d}d. \tag{2.9}$$

The differential increment of the normalized cumulative PSD (symbolized by $\mathrm{d}Q_r$) represents the percentage in terms of the generalized volume of r that can be measured in particle size range from d to $d + \mathrm{d}d$. The infinitesimal $\mathrm{d}Q_r$ can be expressed by

$$\mathrm{d}Q_r(d) = q_r(d)\mathrm{d}d = \frac{\omega_r(d)}{\Omega_{r,tot}}\mathrm{d}d \tag{2.10}$$

in accordance to Eqs. 2.6 and 2.8. The differential increment of the non-normalized cumulative PSD (symbolized by $\mathrm{d}\Omega_r$) contains the absolute amount in terms of the generalized volume of r that can be measured in particle size range from d to $d + \mathrm{d}d$:

$$\mathrm{d}\Omega_r(d) = \omega_r(d)\mathrm{d}d. \tag{2.11}$$

Interrelationship between PSDs and moments of different dimensioning types

The generalized non-normalized particle size distribution $\omega_r(d)$ can be expressed by the product of a generalized shape factor $\phi_{sh,r}$, the r'th power of d, and the number density distribution $n(d)$. For spherical particles, it follows to:

$$\omega_r(d) = \phi_{sh,r} d^r n(d) \qquad \text{, for } r \in \{0,1,2,3\}. \tag{2.12}$$

The zero-dimensional shape factor always equals unity regardless of the shape of the particles: $\phi_{sh,0} = 1$. The one-, two-, and three-dimensional shape factors of spheres are given with $\phi_{sh,1} = 1$, $\phi_{sh,2} = \pi$, and $\phi_{sh,3} = \pi/6$, which is used in this work. The total generalized volume of the four dimensioning types is defined by the following integrals, or by the r'th moment of the number-based PSD $m_{r,0}$ from Eq. 2.27:

$$\Omega_{r,tot} = \int_0^\infty \omega_r(d)\mathrm{d}d = \int_0^\infty \phi_{sh,r} d^r n(d)\mathrm{d}d = N_{p,tot}\phi_{sh,r}\int_0^\infty d^r q_0(d)\mathrm{d}d = N_{p,tot}\phi_{sh,r} m_{r,0}. \tag{2.13}$$

Equation 2.12 can be solved for the non-normalized number density distribution resulting in

$$n(d) = \frac{\omega_r(d)}{\phi_{sh,r} d^r} \qquad \text{, for } r \in \{0,1,2,3\},$$

whereby, two different dimensioning types, indicated by z and r, can be related with one another by the following rational equation:

$$\frac{\omega_z(d)}{\phi_{sh,z} d^z} = \frac{\omega_r(d)}{\phi_{sh,r} d^r} \qquad \text{, for } z,r \in \{0,1,2,3\}. \tag{2.14}$$

By putting Eq. 2.12 with $n(d) = N_{p,tot} q_0(d)$ and Eq. 2.13 in Eq. 2.6, an expression is derived to calculate the $q_r(d)$-distribution from the number-based density distribution $q_0(d)$:

$$q_r(d) = \frac{d^r q_0(d)}{\int_0^\infty d^r q_0(d)\mathrm{d}} = \frac{d^r q_0(d)}{m_{r,0}} \qquad \text{, for } r \in \{0,1,2,3\}. \tag{2.15}$$

A general equation for transforming a certain PSD-function $q_r(d)$ of the basis r into another PSD-function $q_z(d)$ of the basis z can be derived from Eqs. 2.6, 2.14, and 2.15 via

$$q_z(d) = \frac{d^z}{d^r}\frac{m_{r,0}}{m_{z,0}} q_r(d) = \frac{d^{z-r} q_r(d)}{\int_0^\infty d^z \frac{q_0(d)}{m_{r,0}}\mathrm{d}d} = \frac{d^{z-r} q_r(d)}{\int_0^\infty d^{z-r}\frac{d^r q_0(d)}{m_{r,0}}\mathrm{d}d} = \frac{d^{z-r} q_r(d)}{\int_0^\infty d^{z-r} q_r(d)\mathrm{d}d}$$

to

$$q_z(d) = \frac{d^{z-r} q_r(d)}{m_{z-r,r}} \qquad \text{, for } z,r \in \{0,1,2,3\}. \tag{2.16}$$

Multiplying d^k on both sides of Eq. 2.16 and integrating this over the entire d-coordinate (negative domain excluded) lead to the subsequent relationship between three different moments out of two PSD-densities of the bases r and z:

$$m_{k,z} = \int_0^\infty d^k q_z(d)\mathrm{d}d = \frac{\int_0^\infty d^{k+z-r} q_r(d)\mathrm{d}d}{m_{z-r,r}} = \frac{m_{k+z-r,r}}{m_{z-r,r}} \qquad \text{, for } z,r \in \{0,1,2,3\}. \tag{2.17}$$

The transformations of Eqs. 2.16 and 2.17 which are possible with $z \in \{0,1,2,3\}$ and $r \in \{0,1,2,3\}$ are summarized in Table 2.1.

Numerical description particle size distribution

As mentioned above, particle size distributions are often given in form of a finite list with measured properties (represented by $\Delta\Omega_{r,i}$) for different size classes (indicated here by i or j). Therefore, PSDs need to be

$r:$	0	1	2	3
$q_{z=0}(d)$	$= q_0(d)$	$= \frac{d^{-1}q_1(d)}{m_{-1,1}}$	$= \frac{d^{-2}q_2(d)}{m_{-2,2}}$	$= \frac{d^{-3}q_3(d)}{m_{-3,3}};$
$q_{z=1}(d)$	$= \frac{d^{1}q_0(d)}{m_{1,0}}$	$= q_1(d)$	$= \frac{d^{-1}q_2(d)}{m_{-1,2}}$	$= \frac{d^{-2}q_3(d)}{m_{-2,3}};$
$q_{z=2}(d)$	$= \frac{d^{2}q_0(d)}{m_{2,0}}$	$= \frac{d^{1}q_1(d)}{m_{1,1}}$	$= q_2(d)$	$= \frac{d^{-1}q_3(d)}{m_{-1,3}};$
$q_{z=3}(d)$	$= \frac{d^{3}q_0(d)}{m_{3,0}}$	$= \frac{d^{2}q_0(d)}{m_{2,1}}$	$= \frac{d^{1}q_0(d)}{m_{1,2}}$	$= q_3(d);$
$m_{k,z=0}$	$= m_{k,0}$	$= \frac{m_{k-1,1}}{m_{-1,1}}$	$= \frac{m_{k-2,2}}{m_{-2,2}}$	$= \frac{m_{k-3,3}}{m_{-3,3}};$
$m_{k,z=1}$	$= \frac{m_{k+1,0}}{m_{1,0}}$	$= m_{k,1}$	$= \frac{m_{k-1,2}}{m_{-1,2}}$	$= \frac{m_{k-2,3}}{m_{-2,3}};$
$m_{k,z=2}$	$= \frac{m_{k+2,0}}{m_{2,0}}$	$= \frac{m_{k+1,1}}{m_{1,1}}$	$= m_{k,2}$	$= \frac{m_{k-1,3}}{m_{-1,3}};$
$m_{k,z=3}$	$= \frac{m_{k+3,0}}{m_{3,0}}$	$= \frac{m_{k+2,1}}{m_{2,1}}$	$= \frac{m_{k+1,2}}{m_{1,2}}$	$= m_{k,3};$

Table 2.1: Upper part: overview on possible transformations of a particle size distribution $q_r(d)$ of a certain basis $r \in \{0,1,2,3\}$ into a particle size distribution $q_z(d)$ of a certain basis $z \in \{0,1,2,3\}$; lower part: overview on possible transformations of k'th moments of z-based particle size distributions into ratios of moments of different r-based particle size distributions with $z, r \in \{0,1,2,3\}$.

described numerically over a discretized size coordinate, as for example in the following way:

$$d_{i=0} = d_{min} \tag{2.18}$$

$$d_{i=i_{max}} = d_{max}, \tag{2.19}$$

$$\Delta d_i = \frac{d_{max} - d_{min}}{i_{max}}, \tag{2.20}$$

$$d_i = d_{i=0} + i\Delta d_i \quad , \text{for } i \in \{0,1,2,...,i_{max}\}, \tag{2.21}$$

$$d_{i,mid} = \frac{1}{2}(d_i + d_{i-1}) \quad , \text{for } i \in \{1,2,...,i_{max}\}, \tag{2.22}$$

$$\Delta Q_{r,i}(d_i) = \frac{\Delta\Omega_{r,i}(d_i)}{\Omega_{r,tot}} \quad , \text{for } i \in \{1,2,...,i_{max}\}, \tag{2.23}$$

$$Q_{r,i=0} = Q_{r,i}(d_{i=0}) = 0, \tag{2.24}$$

$$Q_{r,i}(d_i) = \sum_{j=1}^{i} \Delta Q_{r,j}(d_j) \quad , \text{for } i \in \{1,2,...,i_{max}\}, \tag{2.25}$$

$$q_{r,i}(d_{i,mid}) = \frac{\Delta Q_{r,i}(d_i)}{\Delta d_i} \quad , \text{for } i \in \{1,2,...,i_{max}\}. \tag{2.26}$$

Therein, the d-coordinate is divided into a predefined number of size classes (i_{max}) between a lower bound (indicated with $i = 0$) at the overall minimum diameter d_{min} and an upper bound (indicated with $i = i_{max}$) at the overall maximum diameter d_{max}. The index i refers to a certain size class of the discretized coordinate. The single values of the cumulative PSD-vector Q_i are associated to the upper bound of the corresponding class i; whereas the values of the density distribution q_i are referred to the middle size of the classes $d_{i,mid}$.

2.1.2 Scalar average characteristics of particle size distributions

Raw moments of particle size distributions

Raw moments (short: moments) of the four main types of particle size density distributions q_r are defined by the following integral

$$m_{k,r} = \int_0^\infty d^k q_r(d)\mathrm{d}d \quad , \text{for } r \in \{0,1,2,3\}, \tag{2.27}$$

where the exponent k can have integer numbers: $k \in \{..., -3, -2, -1, 0, 1, 2, 3, ...\}$. In case that $k = 0$, all of these moments are unity: $m_{0,r} = 1$ for $r \in \{0, 1, 2, 3\}$. Moments are useful for describing the interrelationship between the different PSD-types, as shown before, and diverse average characteristics of PSDs, outlined in the following.

Arithmetic means of characteristic length, surface area, and volume

The arithmetic mean of the generalized volume is defined as ratio of the total generalized volume to the total number of particles: $\bar{\Omega}_r = \Omega_{r,tot}/\Omega_{0,tot}$. Applying this for the one-, two-, and three-dimensional PSD-basis, the arithmetic means of the characteristic particle length $\bar{L}_{p,0}$, of the particle surface area $\bar{A}_{p,0}$, and of the particle volume $\bar{V}_{p,0}$ are obtained from:

$$\bar{L}_{p,0} \coloneqq \frac{L_{p,tot}}{N_{p,tot}} = \frac{\Omega_{1,tot}}{\Omega_{0,tot}} = \int_0^\infty \phi_{sh,1} dq_0(d)\mathrm{d}d, = \phi_{sh,1} m_{1,0}, \tag{2.28}$$

$$\bar{A}_{p,0} \coloneqq \frac{A_{p,tot}}{N_{p,tot}} = \frac{\Omega_{2,tot}}{\Omega_{0,tot}} = \int_0^\infty \phi_{sh,2} d^2 q_0(d)\mathrm{d}d = \phi_{sh,2} m_{2,0}, \tag{2.29}$$

$$\bar{V}_{p,0} \coloneqq \frac{V_{p,tot}}{N_{p,tot}} = \frac{\Omega_{3,tot}}{\Omega_{0,tot}} = \int_0^\infty \phi_{sh,3} d^3 q_0(d)\mathrm{d}d = \phi_{sh,3} m_{3,0}. \tag{2.30}$$

These number-based mean values are also related to other average size characteristics, as given below.

Types of average diameter

The general mean diameter d_{m,q_r} of a polydisperse system is defined by the first moment of the general particle size distribution $q_r(d)$:

$$d_{m,q_r} \coloneqq m_{1,r} = \int_0^\infty dq_r(d)\mathrm{d}d \qquad \text{, for } r \in \{0, 1, 2, 3\}. \tag{2.31}$$

The commonly used mean diameter, sometimes called the *mean size* or just the *mean*, corresponds to the definition in Eq. 2.31 for the number-based PSD ($r = 0$). It is symbolized here by d_m, conforms with the first moment of the number-based PSD $m_{1,0}$, and is related to the arithmetic mean of the particle length $\bar{L}_{p,0}$:

$$d_m \coloneqq d_{m,q_0} = m_{1,0} = \int_0^\infty dq_0(d)\mathrm{d}d = \frac{1}{\phi_{sh,1}} \bar{L}_{p,0}. \tag{2.32}$$

Another concept of particle size average characteristic follows from the so-called *power mean* (see for instance in [13]), which is also known as *generalized mean* (not to be confused with d_{m,q_r}) or *Hölder mean* in literature, and is calculated by the k'th root of the k'th moment. According to this, various average diameters (symbolized by $d^*_{k,r}$) can be formulated for different values of k and for the different dimensioning types r:

$$d^*_{k,r} \coloneqq (m_{k,r})^{1/k} \qquad \text{, for } k \neq 0 \text{ and } r \in \{0, 1, 2, 3\}. \tag{2.33}$$

However, k must be non-zero in this formula in order to avoid division by zero. The common mean diameter d_m matches with the power mean of Eq. 2.33 for $k = 1$ and $r = 0$:

$$d^*_{1,0} \coloneqq (m_{1,0})^{1/1} = d_m. \tag{2.34}$$

In addition, the number-based power means of Eq. 2.33 ($r = 0$) are congruent to the mean-area-equivalent diameter (symbolized by $d^*_{2,0}$) for $k = 2$ and to the mean-volume-equivalent diameter (symbolized by $d^*_{3,0}$) for $k = 3$:

$$d^*_{2,0} = (m_{2,0})^{1/2} = \left(\frac{\bar{A}_{p,0}}{\phi_{sh,2}}\right)^{1/2}, \tag{2.35}$$

$$d^*_{3,0} = (m_{3,0})^{1/3} = \left(\frac{\bar{V}_{p,0}}{\phi_{sh,3}}\right)^{1/3}. \tag{2.36}$$

The power mean of $k = -3$ and $r = 0$, which is given with

$$d^*_{-3,0} = (m_{-3,0})^{-1/3}, \tag{2.37}$$

is useful to calculate the number-based average effective particle density ($\bar{\rho}_{p,q_0}$, see Eqs. 3.50 to 3.52) in the context of the ideal continuous layerwise granulation model, as shown later in Chapters 3 and 4.

Moreover, the ratio of the $(k+1)$'th to the k'th moment of a certain q_r-function also provides average characteristics of particle size. It is symbolized here by $d^{**}_{k+1,k,r}$ and defined according to:

$$d^{**}_{k+1,k,r} = \frac{m_{k+1,r}}{m_{k,r}} \qquad \text{, for } r \in \{0,1,2,3\}. \tag{2.38}$$

Exchanging r with z in Eq. 2.38 provides an equivalent expression with $d^{**}_{k+1,k,z} = m_{k+1,z}/m_{k,z}$ of the basis $z \in \{0,1,2,3\}$. On this, the moment-transformation equation (Eq. 2.17) can then be applied, wherewith $d^{**}_{k+1,k,z}$ can be expressed by moments of PSDs of a different basis $r \in \{0,1,2,3\}$:

$$d^{**}_{k+1,k,z} = \frac{m_{k+1,z}}{m_{k,z}} = \frac{\frac{m_{k+1+z-r,r}}{m_{z-r,r}}}{\frac{m_{k+z-r,r}}{m_{z-r,r}}} = \frac{m_{k+1+z-r,r}}{m_{k+z-r,r}} \qquad \text{, for } z,r \in \{0,1,2,3\}. \tag{2.39}$$

This transformation is useful for identifying the different meanings of the Sauter diameter, see below in Eq. 2.46.

The *median values* (symbolized by d_{50,q_r}) of the particle size distributions q_r of the four dimensioning bases may also be used. They are associated with the 50th percentile of the corresponding PSD

$$Q_r(d_{50,q_r}) = \int_0^{d_{50,q_r}} q_r(d)\mathrm{d}d \coloneqq 0.5, \tag{2.40}$$

and must often be determined by numerical methods due to unknown inverse function of $Q_r(d)$ or complex and rough shapes of measured PSD-curves.

The *modal values* (symbolized by d_{mod,q_r}) of the $q_r(d)$-functions are further quantities for the characterization of bulk solids. They can be determined with search methods (e.g., "max"-function in MATLAB or MS Excel), which find the location of the maximal function value in a data list, according to:

$$d_{mod,q_r} = \mathrm{find}_{\max,d}\big(q_r(d)\big). \tag{2.41}$$

The modal diameter is a local characteristic of PSDs, and therefore independent from the PSD-moments of Eq. 2.27.

A $q_r(d)$-independent average size characteristic is the *unweighted central value* (symbolized by d_{mid}) of a polydisperse system. It is defined by

$$d_{mid} = \frac{1}{2}(d_{min} + d_{max}), \tag{2.42}$$

and can be used when q_r is unknown, but the overall minimum and maximum diameters of the bulk material are given, as for instance, in the product flow from continuous granulation with external sieve-milling circuit, [14, 15]. This type of mean is the easiest to determine, but it has no physically rational meaning.

Particle size variety

Particle size variety can be quantified by several scalar properties derived from the PSD. The following examples are used in the present thesis. One is the (*general*) *standard deviation* (short: SD, symbolized with σ_{q_r}) of a particle size distribution, which is calculated according to:

$$\sigma_{q_r} = \left(\int_0^\infty (d - d_{m,q_r})^2 q_r(d)\mathrm{d}d\right)^{1/2} = \left(m_{2,r} - m_{1,r}^2\right)^{1/2} \qquad \text{, for } r \in \{0,1,2,3\}. \tag{2.43}$$

The square of this standard deviation ($\sigma^2_{q_r}$) is called the *variance* of the particle size distribution. In the present work, standard deviations of the number-based particle size distributions q_0 are only symbolized by σ. Another PSD-spread parameter is the (*general*) *relative standard deviation* (short: RSD, symbolized here with ζ_{q_r}), which is also named as *coefficient of variation* (short: CV or CoV). It is defined as the ratio of the standard deviation to the mean diameter:

$$\zeta_{q_r} = \frac{\sigma_{q_r}}{d_{m,q_r}} = \left(\int_0^\infty \left(\frac{d}{d_{m,q_r}} - 1\right)^2 q_r(d)\mathrm{d}d\right)^{1/2} = \left(\frac{m_{2,r}}{m_{1,r}^2} - 1\right)^{1/2} \qquad \text{, for } r \in \{0,1,2,3\}. \tag{2.44}$$

Such coefficients of variation (ζ_{q_r}) have been used for example by Rumpf a. Gupte [16] as characteristic property (referred to as dispersion parameter) for describing the influence of particle size variety on flow resistance in packed beds. The values of σ_{q_r} and ζ_{q_r} are equal to zero for monodisperse and larger than zero for polydisperse systems.

Skewness of particle size distributions

The skewness γ_{q_r} is a scalar quantity that describes the asymmetry of particle size distribution q_r around its mean diameter d_{m,q_r}. It is defined as the third central moment of the PSD divided by the third power of the standard deviation σ_{q_r}:

$$\gamma_{q_r} = \frac{\int_0^\infty (d - d_{m,q_r})^3 q_r(d) \mathrm{d}d}{\sigma_{q_r}^3} \qquad \text{, for } r \in \{0,1,2,3\}. \tag{2.45}$$

Skewness values less zero ($\gamma_{q_r} < 0$) indicate that the area below the tail left from the mean value is larger than the area rightwards from it. Those PSDs have a *negative skew*, and are denoted as *left-skewed* or *left-tailed*. In the opposite way, particles size distributions, whose skewness values are larger than zero ($\gamma_{q_r} > 0$), have a *positive skew* and are called as *right-skewed* or *right-tailed*. The skewness of symmetric distributions is zero; but, this does not imply that asymmetric distributions always possess a non-zero skewness. They can have zero too; but, it occurs in very rare cases.

Sauter diameter and volume-specific surface area of polydisperse systems with spherical particles

The Sauter diameter of polydisperse systems with spherical particles is symbolized here with d_{32} to distinguish it from the effective Sauter diameter of any particle shape, which is represented by d_{SV}. The Sauter diameter of spheres was firstly introduced by Sauter [17] for determination of particle size of fuel fog in combustion engines. It is defined by the ratio of the third to the second raw moment of the number density distribution (to which the index "32" is referred), as shown in the first line on the right-hand side of Eq. 2.46. Via Eqs. 2.38 and 2.39, the Sauter diameter of spheres can also be converted to moment ratios of the length-based PSD $d^{**}_{2,1,r=1}$, the area-based PSD $d^{**}_{1,0,r=2}$, and the volume-based PSD $d^{**}_{0,-1,r=3}$, which are listed in the second to the fourth line of Eq. 2.46:

$$\begin{aligned} d_{32} \coloneqq d^{**}_{3,2,0} &= \frac{m_{3,0}}{m_{2,0}} \\ &= d^{**}_{2,1,1} = \frac{m_{2,1}}{m_{1,1}} \\ &= d^{**}_{1,0,2} = \frac{m_{1,2}}{m_{0,2}} = m_{1,2} = d_{m,q_2} \\ &= d^{**}_{0,-1,3} = \frac{m_{0,3}}{m_{-1,3}} = \frac{1}{m_{-1,3}} = d^{*}_{-1,3}. \end{aligned} \tag{2.46}$$

The second line of this equation is of less use in the literature. The third line reveals that Sauter diameter conforms with mean diameter of the area-based PSD: $d_{32} = d_{m,q_2}$. The definition of the Sauter diameter by $m_{1,2}$ can be found in DIN ISO 9276-2, [18]. Additionally to this, it turns out from the last line of Eq. 2.46 that d_{32} represents also the power mean of the volume-based PSD q_3 according to Eq. 2.33 with $k = -1$. This notation is advantageous for gravimetrically determined size distributions of particles with a uniform apparent density. Numerical formulas of the Sauter diameter in the form of $d_{32} = m_{-1,3}^{-1}$ are given for instance by Wirth in [19] and by Tsotsas in [20].

The relationship between the Sauter diameter and the volume-specific surface area of the disperse system $a_{v,tot}$ (not to be confused with A_p/V_p volume-specific surface area of a single particle) can be derived from Eqs. 2.29 and 2.30, which ensues to

$$d_{32} = \frac{6V_{p,tot}}{A_{p,tot}} = \frac{6}{a_{v,tot}} \qquad \text{, for spheres.} \tag{2.47}$$

The various possibilities of deriving the Sauter diameter from measurement data and Eq. 2.46, but also the physical meaning behind d_{32}, given in Eq. 2.47, are the reasons for its frequent use. Strictly speaking however, Eqs. 2.46 and 2.47 are only valid for the special case of perfect spheres, and are therefore better suited for disperse fluid-fluid systems, such as sprayed liquids in gases.

Effective Sauter diameter and volume-specific surface area of polydisperse systems with arbitrary particle shape

Bulk solids deviate more or less from the shape of perfect spheres. As described before with Eq. 2.1, there are different ways of characterizing size of non-spherical particles, and hence, of defining the d-coordinate. The moments according to Eq. 2.27 also depend on the meaning of d, which leads to different d_{32}-values between the described coordinates: specific-area equivalent diameter $d_{SV,p}$, volume-equivalent diameter $d_{V,p}$, and surface-equivalent diameter $d_{S,p}$. Therefore, the effective (practical) Sauter diameter d_{SV}, which is independent from the types of d, is to be considered for disperse systems with non-spherical particles. It is defined by six times the ratio of the actual total volume $V_{p,tot}$ to the actual total surface area $A_{p,tot}$, of all particles respectively, or by six divided by the volume-specific surface area $a_{v,tot}$ of all particles:

$$d_{SV} \coloneqq \frac{6V_{p,tot}}{A_{p,tot}} = \frac{6}{a_{v,tot}} \qquad \text{, for arbitrary particle shape.} \tag{2.48}$$

The effective Sauter diameter can also be derived from statistical moments, such as the Sauter diameter of spheres d_{32}; but the increase in surface area of individual particles compared to spheres of equal volume must be taken into account, e.g., through an average sphericity factor after Wadell [3], symbolized here with Ψ_{sph}. However, particle shape also varies in real systems of disperse solids. In order to maintain a low complexity level of equations, the assumption of uniform single particle sphericity ($\Psi_{sph,p}$ of Eq. 2.3) is used in practice: $\Psi_{sph} = \Psi_{sph,p}$. An average sphericity factor must then be adopted from literature or estimated image analyses with the two-dimensional counterpart: the so-called *circularity after Wadell* [3],

$$\text{circularity} = \frac{\text{perimeter of sphere of the same projected area}}{\text{actual projected perimeter of the particle}}. \tag{2.49}$$

But, latter can have quite large errors depending on the perspective. Grace a. Ebneyamini [21] have recently published comparisons between sphericity and circularity factors for different shapes and orientations of particles. The relation between effective Sauter diameter and the d_{32}-averages of the $d_{SV,p}$-, $d_{V,p}$-, and $d_{S,p}$-coordinate ensues from Eqs. 2.2 and 2.4 to:

$$d_{SV} = \begin{cases} \Psi_{sph}^{2} d_{32}(d = d_{SV,p}) & = \Psi_{sph}^{2} \frac{m_{3,0}(d=d_{SV,p})}{m_{2,0}(d=d_{SV,p})} \\ \Psi_{sph} d_{32}(d = d_{V,p}) & = \Psi_{sph} \frac{m_{3,0}(d=d_{V,p})}{m_{2,0}(d=d_{V,p})} \\ \Psi_{sph}^{3/2} d_{32}(d = d_{S,p}) & = \Psi_{sph}^{3/2} \frac{m_{3,0}(d=d_{S,p})}{m_{2,0}(d=d_{S,p})} \end{cases}. \tag{2.50}$$

2.1.3 Density-related characteristics of bulk solids

Intraparticle porosity - particle porosity

The intraparticle porosity of bulk solids ε_p, also called the relative void volume, void fraction, or voidage of single particles, or simply the particle porosity, is defined by the volume of voids $V_{p,void}$ distributed inside the particle divided by the entire particle volume:

$$\varepsilon_p = \frac{V_{p,void}}{V_p} = 1 - \frac{V_{p,s}}{V_p} = \varepsilon_{p,s}. \tag{2.51}$$

It can also be calculated from the volume of solid phase $V_{p,s}$. The intraparticle voids can be filled by gases, vapors, and/or liquids, as for instance by moist air and liquid water (product moisture) in bulk products of spray granulation processes. The particle porosity of Eq. 2.51 is an average characteristic of individual particles. It should not be confused with the pore size distribution. Since, the relative void volume can vary among individual particles, particle porosity is a distributed property of bulk solids.

Interparticle porosity - bulk porosity

The interparticle porosity of bulk solids ε_b, also called the bulk porosity, bulk voidage, or the relative interparticle void volume, is defined as the percentage of voids volume between particles $V_{b,void}$ in a total volume of the disperse system V_{tot}. It is the complementary proportion of the total volume of solids $V_{p,tot}$ in a disperse system:

$$\varepsilon_b = \frac{V_{b,void}}{V_{tot}} = 1 - \frac{V_{p,tot}}{V_{tot}} = \varepsilon_{b,s}. \tag{2.52}$$

The bulk porosity excludes intraparticle void fractions. The relative interparticle void volume is a characteristic quantity of packed beds, fluidized beds, or pneumatically transported bulk solids. The total volume of the disperse system V_{tot} (control volume) can be, for example, the package volume in bulk density measurements (packed bed), the entire holdup in bottom- or top-spray granulation processes (fluidized bed), or the volume of the interior of the riser tube in Wurster granulators (transported swarm). Depending on the application, the index of the interparticle porosity varies in this work. For example, ε_{sw} refers to sinking swarms of particles (Section 2.2.2), ε_{bed} to packed and fluidized beds (Section 2.2.3), ε_{mf} and ε_{elu} to the points of minimal fluidization and elutriation of a fluidized bed (Section 2.2.4), and ε_b to bulk density measurements (Section 9.3). In the two-zone continuum model of Wurster fluidization of Chapters 7 and 8, simply ε is used with reference to different local areas of the granulation system (Table 7.1) in order to summarize the interparticle void volume for the sinking particle swarm, the fluidized bed, and incoming and outgoing gas mass flows of the system in one variable.

Influence of particle arrangement on packed bed porosity

In practice, bulk materials or real packed beds are irregularly arranged, also referred to as *random packed beds*. Models of regular arrangement, such as the simple-cubic or body-centered-cubic structure of spheres, are not sufficient for the prediction of bulk porosity of random packages. The interparticle porosity must be therefore determined experimentally or estimated from literature data of similar materials. Using the latter, different states of arrangement have to be distinguished for random packed beds. These can be "loose", "dense", or "normal", as stated by Brown et al. [22]. The attribute "loose" denotes that the package was built by free flowing without any subsequent compression processes and has the highest bed porosity possible. A random packed bed is called "dense", when the minimum of bulk porosity has been reached after long-term vibration or shaking; but, compaction by pressing (e.g., tableting) is not meant by this term. The word "normal" shall indicate an intermediate state between "loose" and "dense" packages. In the scope of the present thesis, bulk porosities of loose random packed beds are of interest; by which for instance minimal fluidization conditions can be described, as shown later in Section 2.2.4.

Influence of mean size and shape of particles on packed bed porosity

Particle size of coarse-grained, randomly packed beds has hardly any influence on the relative bed-void volume. A critical point, below which the bed porosity starts to increase, is difficult to be defined by a general equation, as it depends on plenty of physical and chemical aspects, such as effective particle density, surface structure (roughness), particle shape, moisture content of particles, surface forces, but also on air temperature and humidity. Rather gradual transitions than critical diameters would appear in measurement results. Partridge a. Lyall [23], for example, have determined the interparticle porosity of several random and (nearly) monodisperse packages of spheres and sand with different particle diameters below a value of circa 0.55 mm. The findings are depicted in the left diagram of Figure 2.1, which shows that the gaps between the particles in these packings become slightly larger between diameters of around 0.28 mm and 0.55 mm, and rise more distinctly for the even smaller beds particles. It becomes further evident from these curves that the packages of sand have a higher bulk porosity than those of spheres with the same mean size, which is due to the difference in particle shape. The sphericity after Wadell (Eq. 2.3) is a useful parameter for describing the influence of particle shape on voidage of packed beds. A functional relationship of interparticle porosity depending on particle sphericity is presented in a graphic of Brown et al. (see "Fig. 223", p. 214 in [22]) for loose, normal, and dense random packages with a narrow particle size distribution. Geldart [24] has tabulated the corresponding values from the fit curves of this graphic for the loose and dense state. These are depicted in the right-hand diagram of Figure 2.1. It can be seen that bed porosity is the larger, the more the particle shape deviates from a sphere, after Wadell's definition. The size of the investigated particles is not stated in [22]; but, they can be presumed to be significantly larger than 0.5 mm when comparing these curves with correlations of Partridge a. Lyall (Figure 2.1, left). Moreover, a bulk porosity of 40 % seems to be a good estimate for perfect spheres bigger than circa 0.5 mm.

Empirical estimation method for bulk porosities of polydisperse packed beds of spheres

The bulk porosities in loose polydisperse packages ($\varepsilon_{b,pol}$) are smaller than in loose packages of mono-sized solids ($\varepsilon_{b,mon}$). Tsotsas [20, 25] suggests the following empirical polynomial equation

$$\frac{\varepsilon_{b,pol}}{\varepsilon_{b,mon}} = -0.112\zeta_{pol}^3 + 0.017\zeta_{pol}^2 - 0.259\zeta_{pol} + 1, \tag{2.53}$$

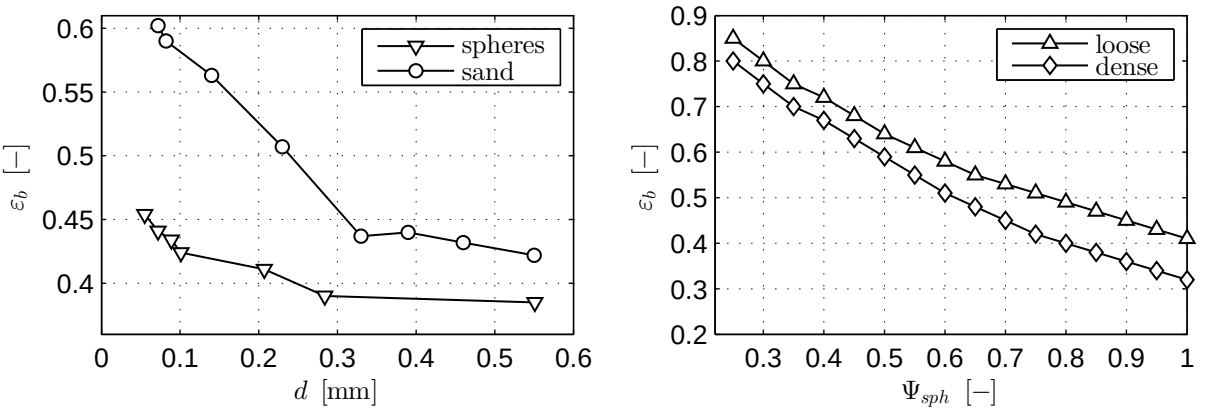

Figure 2.1: Left: bed porosity as function of particle size for packages of nearly mono-sized spheres and sand, measured by Partridge a. Lyall [23]; right: bed porosity as function of particle sphericity for "loose" and "dense" packages, as stated by Brown et al. [22]; values cited by Geldart [4].

wherewith the bulk porosity of polydisperse packages of spheres can be roughly estimated from a so-called *dispersion parameter* (in German: "Verteilungsparameter"), which is symbolized here by ζ_{pol}. The definition of the dispersion parameter is given in [25] and [26] with:

$$\zeta_{pol} = \left(\frac{\sum_{i=1}^{i_{max}} d_{i,mid}^{-2} \Delta Q_{3,i}}{\left(\sum_{i=1}^{i_{max}} d_{i,mid}^{-1} \Delta Q_{3,i} \right)^2} - 1 \right)^{1/2}, \tag{2.54}$$

in which different moments of the volume-based PSD ($r = 3$) are given in a numerical form (compare with Eqs. 2.18 to 2.26). The notation in Eq. 2.54 is adapted to the present thesis. Such a dispersity index ζ_{pol} is also used by Bauer [27] as influencing parameter of particle size variety on heat transport phenomena of fluids flowing through packed beds; but there, it is symbolized by "ζ_1". Tsotsas stated that the dispersity parameter of Eq. 2.54 was introduced by Rumpf a. Gupte [16]. But, latter authors have given a dispersity parameter in a different form such as in Eq. 2.44, where the relative standard deviation for an arbitrary dimensioning basis ζ_r is given. However, it is shown by a mathematical transformation in Appendix B.1 that the dispersity index ζ_{pol} of Eq. 2.54 conforms with the relative standard deviation of the length-based particle size distribution ζ_{q_1} (Eq. 2.44 for $r = 1$):

$$\zeta_{pol} = \left(\frac{\int_0^\infty d^{-2} q_3(d) \mathrm{d}d}{\left(\int_0^\infty d^{-1} q_3(d) \mathrm{d}d \right)^2} - 1 \right)^{1/2} = \left(\frac{m_{1,0} m_{3,0}}{m_{2,0}^2} - 1 \right)^{1/2} = \zeta_{q_1}. \tag{2.55}$$

Tsotsas also mentioned in [25] that other types of dispersion parameters are conceivable for describing porosities of polydisperse packages, but did not give any specific examples. Considering Eq. 2.44, three further dispersity indices could be derived from the generalized relative standard deviation ζ_r with the number basis ($r = 0$), the area basis ($r = 2$), or the volume basis ($r = 3$).

Compact particle density, effective particle density, and bulk density of packed beds

By neglecting the weight of the gas and the material moisture within the intra- and interparticle gaps, the following simple relationships between the effective particle density ρ_p, the compact solid density ρ_s, and the bulk density ρ_b of particulate system are obtained from Eqs. 2.51 and 2.52:

$$\rho_p = (1 - \varepsilon_p) \rho_s, \tag{2.56}$$

$$\rho_b = (1 - \varepsilon_b) \rho_p. \tag{2.57}$$

2.2 Characteristics of fluid-particle interactions

2.2.1 Stationary sinking of single particles in stagnant fluids

General stationary sinking velocity

The terminal sinking velocity of a single particle settling through stagnant fluids (symbolized by u_s) is derived from a stationary force balance. The relevant forces acting on the particle are the weight force $F_{gra,p}$, the buoyancy force $F_{bu,p}$, and the drag force $F_{d,p}$. The weight and the buoyancy forces are obtained from the effective particle density ρ_p, the single particle volume V_p, the gravitational constant g, and the fluid density ρ_{fl}, according to:

$$F_{gra,p} = \rho_p V_p g, \tag{2.58}$$

$$F_{bu,p} = \rho_{fl} V_p g. \tag{2.59}$$

The drag force is described by the commonly used *drag equation*:

$$F_{d,p} = c_d A_{proj} \frac{\rho_{fl}}{2} u_{ch}^2, \tag{2.60}$$

wherein c_d represents the drag coefficient, A_{proj} the projected surface area of the particle that faces against the flow, and u_{ch} the characteristic flow velocity. In case of sinking objects in stagnant fluids, the drag coefficient is related to the terminal Reynolds number Re_s, which is defined by the characteristic flow velocity of the drag equation (here u_s), a characteristic length of the particle L_{ch} (for spheres: d), and the kinetic viscosity of the fluid ν_{fl}:

$$Re_s = \frac{u_s L_{ch}}{\nu_{fl}}. \tag{2.61}$$

The shape and surface roughness of the particle affect the drag coefficient too:

$$c_d = c_d(Re_s, \text{shape, surface roughness}). \tag{2.62}$$

The stationary sinking velocity of spheres with smooth surfaces ensue from $F_{gra,p} = F_{bu,p} + F_{d,p}$ to:

$$u_s = \sqrt{\frac{4}{3 c_d(Re_s)} \frac{\rho_p - \rho_{fl}}{\rho_{fl}} dg}. \tag{2.63}$$

But this form does not yet provide a closed solution of the terminal sinking velocity due to the unknown $c_d(Re_s)$-relationship. Another dimensionless number of relevance for sinking phenomena is the Archimedes number Ar, which is formulated with:

$$Ar = \frac{\rho_p - \rho_{fl}}{\rho_{fl}} \frac{L_{ch}^3 g}{\nu_{fl}^2}. \tag{2.64}$$

With the terminal Reynolds number and corresponding Archimedes number, Eq. 2.63 can be converted to the (*general*) *dimensionless force balance*:

$$Re_s^2 = \frac{4}{3} \frac{Ar}{c_d(Re_s)}. \tag{2.65}$$

It is obvious in Eq. 2.65 that the Reynolds number is an implicit function of the Archimedes number, and therefore, directly related to material properties of particles and fluids. Thus, the drag coefficient can also be expressed in terms of the Archimedes number: $c_d = c_d(Ar)$. If a mathematical formula for the $c_d(Ar)$-relationship is known, an explicit solution for the terminal sinking velocity can be derived:

$$u_s = \frac{\nu_{fl}}{d} \sqrt{\frac{4}{3} \frac{Ar}{c_d(Ar)}}. \tag{2.66}$$

However, it is difficult to find simple and suitable Ar-functions, which match precisely with measurements for several scales of particle size or of Reynolds numbers (flow regimes). An overview on respective approaches on theoretical, semi-empirical, and empirical grounds can be found in various literature sources, such as in [8, 28–31].

Author	Stokes	transition	quadratic
Yang [8]	$Re_s < 0.2$	$0.2 < Re_s < 500$	$Re_s > 500$
Rhodes [9]	$Re_s < 0.3$	$0.3 < Re_s < 500$	$500 < Re_s < 2 \cdot 10^5$
Geldart [24]	$Re_s < 0.2$	$0.2 < Re_s < 1000$	$Re_s > 1000$
Kraume [28]	$Re_s \leq 0.25$	$0.25 < Re_s < 1000$	$1000 \leq Re_s \leq 3 \cdot 10^5$
Brauer a. Mewes [33]	$0 < Re_s \lesssim 1$	$1 \lesssim Re_s \lesssim 1000$	$1000 \lesssim Re_s \lesssim 3 \cdot 10^5$

Table 2.2: Bounds of characteristic flow regimes of stationary sinking spheres stated by different authors.

Flow regimes for spheres

The dependency of the drag coefficient on Reynolds number in a range below $3 \cdot 10^5$ can be divided into three domains of different flow characteristics, which are also named as flow regimes or flow regions. The first one is called the *Stokes* or *laminar regime*, the second the *transition* or *intermediate regime*, and the third the *Newton*, *turbulent*, or *quadratic regime*. Unified bounds of Reynolds numbers, by which the flow regimes can be differentiated from each other, do not exist; but, there are some recommendations in literature. A few of them are listed in Table 2.2. With Reynolds numbers greater than $3 \cdot 10^5$, the *drag crisis* sets in, in which the drag coefficient quickly drops to a lower value plateau. This effect is not regarded in this thesis, because such high Reynolds numbers do not occur in conventional processes of fluidized bed spray granulation.

In the Stokes regime, the flow pattern is entirely laminar around a sinking sphere. A *creeping flow* or a *viscous flow* is also spoken of here. Under those conditions, the drag force is mainly caused by *skin friction* on the whole particle surface. The drag force rises linearly with flow velocity (here u_s) in the Stokes regime. The flow pattern of the transition and quadratic regime is characterized by turbulences, as explained in the following. Increasing Reynolds number within the transition regime leads to *formation of vortices* in the fluid region behind the side of a particle that faces away from the flow (here above sinking particles). Taneda [32] analyzed how those vortices change with increasing Reynolds number by capturing images of spheres that were mechanically driven through water. The results are briefly described by Kraume in [28]. Kraume states that the laminar flow starts to separate from the sphere for Reynolds numbers at the lower margin of the intermediate regime ($Re_s \approx 20$) and forms *stationary, laminar vortices*. Those are lengthened and widened with increasing Reynolds number, and become unsteady for Reynolds numbers larger than $Re_s \approx 130$. The position of the *vortex shedding* oscillates for Reynolds numbers above circa $Re_s = 450$ and a so-called *Kármán vortex street* develops in the fluid having passed the particle. Due to this complex variation of flow pattern, the drag force increases non-linearly with the characteristic flow velocity in the intermediate regime. In addition to the *frictional forces*, *inertia effects* of the fluid have a significant influence on drag forces in the transition regime. In other words, the flow pattern contains laminar and turbulent parts. At this, the frictional drag acts mostly on the side of a particle that faces the flow (*partial skin friction*). The laminar proportion of the overall drag decreases with higher Reynolds number, and the inertial forces become more relevant. In the quadratic regime, turbulent effects dominate the overall flow resistance, so that the contribution of viscous forces becomes negligible. The Kármán vortex street still appears, but the location of *flow separation* (vortex shedding) shifts towards the equator of the sphere. Under those conditions, the drag coefficient remains in a narrow range of values, which is why, it is often assumed to be constant in the turbulent regime. The drag force grows then nearly proportional to the square of flow velocity, to which the designation "quadratic" of this regime is referred.

The differences in the flow regime result in a complex function of the drag coefficient on Reynolds number (or Archimedes number), as mentioned before. A $c_d(Re_s)$-relationship, that would be purely theoretical, provide analytical solutions for u_s, and be validated by experimental data over all three flow regimes, does not exist. But, many c_d-approaches of theoretical, semi-empirical, or purely empirical nature have been developed for different ranges of Reynolds numbers by several authors. The most recommended and easiest to use of them are outlined and compared below, in order to choose the best for calculating operation parameters of spray granulation applications.

Approximate solutions of Stokes and quadratic regime for spheres

An analytical equation of the drag force - $F_{d,p} = 3\pi\rho_{fl}\nu_{fl}du_s$, the so-called Stokes' law - was derived by Stokes [34] for purely laminar conditions. Combining this and the general drag equation (Eq. 2.60), the drag coefficient of the Stokes regime is derived as function of the Reynolds number, which can also be converted

to a function of the Archimedes number, via Eq. 2.65:

$$c_d(\text{Stokes}) = \frac{24}{Re_s} = \frac{432}{Ar}. \tag{2.67}$$

The corresponding dimensionless force balance, derived from Eq. 2.65, results in:

$$Re_s(\text{Stokes}) = \frac{Ar}{18}. \tag{2.68}$$

In 1966, Kürten et al. [30] compared the Stokes drag coefficient with measurement results and found a good agreement for $Re_s < 0.2$. This value is also mentioned by Zogg [10] as an upper limit for a flow regime with fully laminar conditions. Kraume [28] states that Reynolds numbers must be much lower than unity ($Re_s \ll 1$) to agree with theoretical conditions of the Stokes solution, but precise calculations are possible up to $Re_s < 0.25$. The latter limit is also given by Mörl et al. [29]. Only fine particles possess terminal sinking velocities and Reynolds numbers within the laminar regime.

A constant drag coefficient (symbolized by $c_{d,qu}$) can be assumed for large granules, which settle in the quadratic flow regime:

$$c_d(\text{quadratic}) \coloneqq c_{d,qu} \neq \text{f}(Re_s) \neq \text{f}(Ar). \tag{2.69}$$

This simplification is useful for rough engineering calculations, for instance when setting the operating range of fluidized beds of coarse particles. The dimensionless force balance of such conditions follows to:

$$Re_s(\text{quadratic}) = \sqrt{\frac{4}{3}\frac{Ar}{c_{d,qu}}}. \tag{2.70}$$

Kürten et al. [30] have also investigated the deviations of two values of $c_{d,qu}$ in different intervals of Reynolds number within the quadratic regime. At this, a maximal and minimal error of $\pm 4\,\%$ was ascertained for a value of $c_{d,qu} = 0.4$ in a more narrow range with $2 \cdot 10^3 \leq Re_s \leq 10^4$, while a value of $c_{d,qu} = 0.44$ was accompanied by errors between $-12\,\%$ and $+10\,\%$ for a wider range with $2 \cdot 10^3 \leq Re_s \leq 10^5$. From this, minimal and maximal values of measured drag coefficients can be deduced for these intervals, which results in $c_d(2 \cdot 10^3 \leq Re_s \leq 10^4) = 0.348 \,...\, 0.416$ and $c_d(2 \cdot 10^3 \leq Re_s \leq 10^5) = 0.387 \,...\, 0.484$.

Superposition approaches for all flow regimes of sinking spheres

The subsequent expression

$$Re_s(\text{inverse superposition}) = \frac{1}{\frac{18}{Ar} + \sqrt{\frac{3}{4}\frac{c_{d,qu}}{Ar}}} = \frac{Ar}{18 + \sqrt{\frac{3}{4}c_{d,qu}}\sqrt{Ar}} \tag{2.71}$$

corresponds to a *first-order inverse superposition* of the dimensionless asymptotes of the Stokes and quadratic regime, which are given in Eqs. 2.68 and 2.70. This inverse superposition (Eq. 2.71) coincides with the Stokes solution (Eq. 2.68) for very low Reynolds and Archimedes numbers, but also agrees with the quadratic approximation (Eq. 2.70) for very large Reynolds and Archimedes numbers. Equation 2.71 can also be solved for the Archimedes number given as an explicit function of the Reynolds number by substituting with $x^2 = Ar$ and finding the root x of the resulting quadratic equation, which ends up to:

$$Ar(\text{inverse superposition}) = \left(\sqrt{\frac{3}{16}c_{d,qu}}Re_s + \sqrt{\frac{3}{16}c_{d,qu}Re_s^2 + 18Re_s}\right)^2. \tag{2.72}$$

The drag coefficient can be expressed then either as function of the Reynolds number or of the Archimedes number with:

$$\begin{aligned} c_d(\text{inverse superposition}) &= \frac{4}{3}\left(\frac{18}{\sqrt{Ar}} + \sqrt{\frac{3}{4}c_{d,qu}}\right)^2 \\ &= \frac{4}{3}\left(\frac{18}{\sqrt{\frac{3}{16}c_{d,qu}}Re_s + \sqrt{\frac{3}{16}c_{d,qu}Re_s^2 + 18Re}} + \sqrt{\frac{3}{4}c_{d,qu}}\right)^2. \end{aligned} \tag{2.73}$$

Such an approach was published in 1958 by Goroshko et al. [35] in the form

$$Re_s(\text{Goroshko at al.}) = \frac{Ar}{18 + 0.61\sqrt{Ar}}, \tag{2.74}$$

where the constant drag coefficient of the quadratic regime was roughly estimated with $c_{d,qu} \approx 0.5$. It provides accurate sinking velocities for very low Reynolds numbers ($Re_s \ll 1$), in the Stokes regime; but it possesses relatively large errors in the transition and quadratic regime. However, Eq. 2.74 is recommended by Mörl et al. [29] as quick estimation method for setting operation parameters of fluidized bed processes (Section 2.2.4). The $Re_s(Ar)$-function of Goroshko et al. can be inverted to, firstly, $\sqrt{Ar} = 0.305Re_s + \sqrt{0.305^2 Re_s^2 + 18Re_s}$, and, secondly,

$$\begin{aligned} c_d(\text{Goroshko et al.}) &= \frac{4}{3}\left(\frac{18}{\sqrt{Ar}} + 0.61\right)^2 \\ &= \frac{4}{3}\left(\frac{18}{0.305Re_s + \sqrt{0.305^2 Re_s^2 + 18Re_s}} + 0.61\right)^2. \end{aligned} \tag{2.75}$$

The constant drag coefficient of the quadratic regime after Eq. 2.70 follows from Eq. 2.75 with $Re_s \to \infty$ to $c_{d,qu} = 4{\cdot}0.61^2/3 \approx 0.5$. The contribution of Goroshko et al. [35] is written in Russian, with its title translated by Sergeev [36] to "Approximate laws of suspended bed hydraulics and constrained fall". Translated excerpts can be found in a compilation of Russian literature, [37]. Another type of first-order superposition would be $c_d = 24/Re_s + 0.5$. For this approach, strong deviations from measurements between $-40\,\%$ and $+32\,\%$ were ascertained by Kürten et al. [30] within the investigation range of $Re_s < 10^5$. Strictly speaking, the equation of Goroshko et al. must be formally differentiated from $c_d = 24/Re_s + 0.5$; however, as both approaches are first-order superpositions of the Stokes and quadratic regime, similar errors can be expected for Eq. 2.75.

In 1972, Brauer a. Mewes [33] have recommended a dimensionless relationship between the Reynolds and Archimedes numbers for all three flow regimes ($0 \le Re_s \le 3 \cdot 10^5$), in form of the first line of Eq. 2.76. Dividing numerator and denominator by 1.74, shows in the second line that the proposed function of Brauer a. Mewes is very similar to that of Goroshko et al. (Eq. 2.75):

$$\begin{aligned} Re_s(\text{Brauer a. Mewes}) &= \frac{1.74Ar}{31.3 + \sqrt{Ar}} \\ &\approx \frac{Ar}{18 + 1.74^{-1}\sqrt{Ar}}, \end{aligned} \tag{2.76}$$

where $1.74^{-1} \approx 0.575$. The functions of Eqs. 2.74 and 2.76 are more closely together the lower the Reynolds and Archimedes numbers are. The drag coefficient of the superposition equation of Brauer a. Mewes can be derived in the same way as for Eq. 2.75:

$$\begin{aligned} c_d(\text{Brauer a. Mewes}) &= \frac{4}{3}\left(\frac{18}{\sqrt{Ar}} + 1.74^{-1}\right)^2 \\ &= \frac{4}{3}\left(\frac{18}{0.87^{-1}Re_s + \sqrt{0.87^{-2}Re_s^2 + 18Re_s}} + 1.74^{-1}\right)^2 \end{aligned} \tag{2.77}$$

From the upper limit this equation, where $Re_s \to \infty$, the constant drag coefficient of the quadratic regime is obtained with $c_{d,qu} = 4/(3 \cdot 1.74^2) \approx 0.44$. Therefore, the c_d-equation of Brauer a. Mewes matches better for with the aforementioned $c_{d,qu}$-constants suggested by Kürten et al. [30] (0.4 and 0.44) than c_d-equation of Goroshko et al. (Eq. 2.75). The approach of Brauer a. Mewes was also listed in the version of the first line of Eq. 2.76 by Mörl et al. [29]; but there it is referred to a different article by Mushtejev a. Uljanov [38] published in 1988.

Another way for approximating drag coefficients in the transition regime is by an inverse polynomial according to the first line of Eq. 2.78 with Re_s as independent variable and three constant parameters: $K_{s,1}$, $K_{s,2}$, and $K_{s,3}$. This method can also be seen as an *extended superposition of first order*. Through the second line of Eq. 2.78 is shown that such a polynomial can be transformed (by binomial theorem) to a squared binomial function of Re_s with two constants, but only when the second parameter $K_{s,2}$ is related to the

other constants with $K_{s,2} = \sqrt{4K_{s,1}K_{s,3}}$:

$$c_d(\text{extended superposition}) = \frac{K_{s,1}}{Re} + \frac{K_{s,2}}{\sqrt{Re_s}} + K_{s,3}$$
$$= K_{s,3}\left(\sqrt{\frac{K_{s,1}}{K_{s,3}Re_s}} + 1\right)^2 \qquad \text{, only for } K_{s,2} = \sqrt{4K_{s,1}K_{s,3}}. \tag{2.78}$$

For the binomial $c_d(Re_s)$-formulation of this equation, an analytical solution of the terminal Reynolds number can be obtained by inserting the second line of Eq. 2.78 in Eq. 2.65, substituting Re with x^2, finding the upper root x of the resulting quadratic equation, and re-substitute x with $\sqrt{Re_s}$. The final solution then given is:

$$Re_s(\text{extended superposition}) = \frac{K_{s,1}}{4K_{s,3}}\left(\sqrt{1 + \frac{1}{K_{s,1}}\sqrt{\frac{64K_{s,3}}{3}}\sqrt{Ar}} - 1\right)^2. \tag{2.79}$$

The drag coefficient can be defined by a function of Archimedes number after putting Eq. 2.79 into the second line of Eq. 2.78. At this point, it shall be noticed that closed solutions of u_s or Re_s cannot be derived from Eq. 2.78 if parameter relationship $K_{s,2} = \sqrt{4K_{s,1}K_{s,3}}$ is not fulfilled.

The following approach

$$c_d(\text{Kürten et al.}) = \frac{21}{Re_s} + \frac{6}{\sqrt{Re_s}} + 0.28 \tag{2.80}$$

was proposed by Kürten et al. [30], who found it, by comparison with other formulas, to be the best fit to measurement data with errors of maximal $\pm 4\,\%$ in a range of $0.1 \leq Re_s \leq 4000$. However, this c_d-equation converges to $21/Re_s$ for Reynolds number going to zero, and diverges therefore from the Stokes solution (Eq. 2.67) in the laminar regime. In the quadratic regime, the drag coefficient approaches a value of approximately 0.28, which is significantly smaller than the measured values (between 0.348 and 0.484). Beside this, the three constants do not fulfill the condition of the second line of Eq. 2.78: $K_{s,2} = \sqrt{4K_{s,1}K_{s,3}}$ ($6 \neq \sqrt{4 \cdot 21 \cdot 0.28} \approx 4.85$), wherefore the fit-equation of Kürten et al. matches only with the first line of Eq. 2.78 and cannot be transformed to a binomial expression. Consequently, the terminal Reynolds number Re_s and terminal sinking velocity u_s have to be determined iteratively. A similar approach with

$$c_d(\text{Kaskas}) = \frac{24}{Re_s} + \frac{4}{\sqrt{Re_s}} + 0.4, \tag{2.81}$$

which was used by Kaskas [39] in research on swarm effects during the sedimentation of suspensions, is also sometimes recommended for the transition regime, such as in [29]. Kraume [28] lists this equation too, but with reference to Brauer a. Mewes [33], who suggested this approximation for all three flow regimes: $0 < Re_s \leq 3{\cdot}10^5$. However, relatively large deviations to measurements can be expected for some locations in the transition and quadratic regime with maximal values of 20 %, as shown by Clift et al. [31]. The advantage of Kaskas' equation over that of Kürten et al. is that the lower and upper limiting cases agree better with the Stokes solution and the measured values in the quadratic regime. But, the function of Kaskas can also not be used to derive a closed solution of the terminal sinking velocity, as the constants in Eq. 2.81 do not match with the restriction of the second line of Eq. 2.78 too: $K_{s,2} = \sqrt{4K_{s,1}K_{s,3}}$ ($4 \neq \sqrt{4 \cdot 24 \cdot 0.4} \approx 6.2$).

Martin [40, 41] provided a drag coefficient approach, which fits to the first and second line of Eq. 2.78, as shown in the first line of Eq. 2.82. For this reason, Martin's c_d-approximation can be also described as function of the Archimedes number, as given in the second line of Eq. 2.82:

$$c_d(\text{Martin}) = \frac{1}{3}\left[\sqrt{\frac{72}{Re_s}} + 1\right]^2 = \frac{24}{Re_s} + \frac{\sqrt{32}}{\sqrt{Re_s}} + \frac{1}{3}$$
$$= \frac{1}{3}\left[\frac{2}{\sqrt{1 + \frac{1}{9}\sqrt{Ar}} - 1} + 1\right]^2. \tag{2.82}$$

The corresponding relation between the Reynolds number and the Archimedes number follows to:

$$Re_s(\text{Martin}) = 18\left[\sqrt{1 + \frac{\sqrt{Ar}}{9}} - 1\right]^2. \tag{2.83}$$

Martin's semi-empirical approach to c_d and Re_s can be seen as *left-fitted* or *Stokes-conform extrapolation equation*, because it converges to the c_d-approach of pure laminar conditions $c_d = 24/Re_s$ for very small Reynolds numbers, but also as extended superposition of first order, as Eqs. 2.82 and 2.83 agree with Eqs. 2.78 and 2.79. The limit for very high Reynolds numbers is given with 1/3. The approach of Martin was declared in [40] to be a sufficient approximation of the elutriation point for homogeneous fluidized beds (later used in Section 2.2.4) with a range of validity of $0 < Re_s < 10^5$. Comparison to empirical data in "Abb. 1" [40], however, shows that the c_d-function of Martin matches only precisely with measurement points for $Re_s < 10^4$, which still covers the entire laminar and intermediate regime, but only a lower part of the turbulent regime. For higher Reynolds number, within $10^4 < Re_s < 3{\cdot}10^5$, the deviations become larger with values up to round 45 % (estimated by 0.484/0.333). Zogg [10] suggests to apply Martin's approximation for Reynolds numbers lower than 10^4, too.

Summary of closed solutions for terminal sinking velocity

These of the described c_d- and u_s-approaches which provide analytical solutions are summarized in the following with the Archimedes number Ar according to Eq. 2.64:

$$u_s(\text{Stokes}) = \frac{1}{18}\frac{\rho_p - \rho_{fl}}{\rho_{fl}}\frac{d^2 g}{\nu_{fl}}, \tag{2.84}$$

$$u_s(\text{Goroshko et al.}) = \frac{\nu_{fl}}{d} \cdot \frac{Ar}{18 + 0.61\sqrt{Ar}}, \tag{2.85}$$

$$u_s(\text{Brauer a. Mewes}) = \frac{\nu_{fl}}{d} \cdot \frac{1.74Ar}{31.3 + \sqrt{Ar}}, \tag{2.86}$$

$$u_s(\text{Martin}) = \frac{\nu_{fl}}{d} \cdot 18\left[\sqrt{1 + \frac{\sqrt{Ar}}{9}} - 1\right]^2, \tag{2.87}$$

$$u_s(\text{quadratic}) = \sqrt{\frac{4}{3c_{d,qu}}\frac{\rho_p - \rho_{fl}}{\rho_{fl}}dg}. \tag{2.88}$$

Figure 2.2 shows the dependency of the terminal sinking velocity u_s and its corresponding Reynolds number Re_s on sphere diameter d for the approximation equations of Goroshko et al. (Eq. 2.85), Kürten et al. (iteratively solved by Eqs. 2.63 and 2.80), Brauer a. Mewes (Eq. 2.86), and Martin (Eq. 2.87). The depicted curves were calculated with an effective particle density of 1380 kg/m^3, which matches with Cellets®-materials (see later Table 9.1) employed in the granulation experiments of this study. It can be seen from the right diagram that the employed raw materials (size of 0.2 to 0.5 mm) settle in the intermediate flow regime. The curves show further that the calculation methods of Eqs. 2.84 to 2.87 provide deviating terminal sinking velocities. It is therefore important to pay attention to the range of validity in terms of the terminal Reynolds number, when choosing a proper sinking velocity approach. For fluidized bed granulation processes with materials smaller than round 2 mm, Martin's approach (Eqs. 2.82, 2.83, and 2.87) is suggested here, due to its accordance with Stokes law and measurements, and its ease of use.

Influence of particle shape

The motion of non-spherical particles in free fall differs from that of spheres, and can even be very complex and unsteady. The terminal sinking velocity can then only be used for rough approximations. Based on the definition of sphericity after Wadell [3], given in Eq. 2.3, and experimental data, Haider a. Levenspiel [42] developed a generalized fit-equation of the drag coefficient

$$c_d = \frac{24}{Re_s}\left(1 + 8.1716 \cdot \exp(-4.0655\Psi_{sph,p}) \cdot (Re_s)^{0.0964+0.5565\Psi_{sph,p}}\right) + \frac{73.69 Re_s \cdot \exp(-5.0748\Psi_{sph,p})}{Re_s + 5.378 \cdot \exp(6.2122\Psi_{sph,p})} \tag{2.89}$$

for non-spherical particles settling through fluids, in which the terminal Reynolds number is defined by the volume-equivalent diameter: $Re_s = d_{V,p}u_s/\nu_{fl}$. The constants were determined by "minimizing the root-mean-square (RMS) deviation of data points from correlation" with the Gauss-Newton method for four different isometric non-spherical particles with sphericities of 0.670, 0.806, 0.846, and 0.906 and for

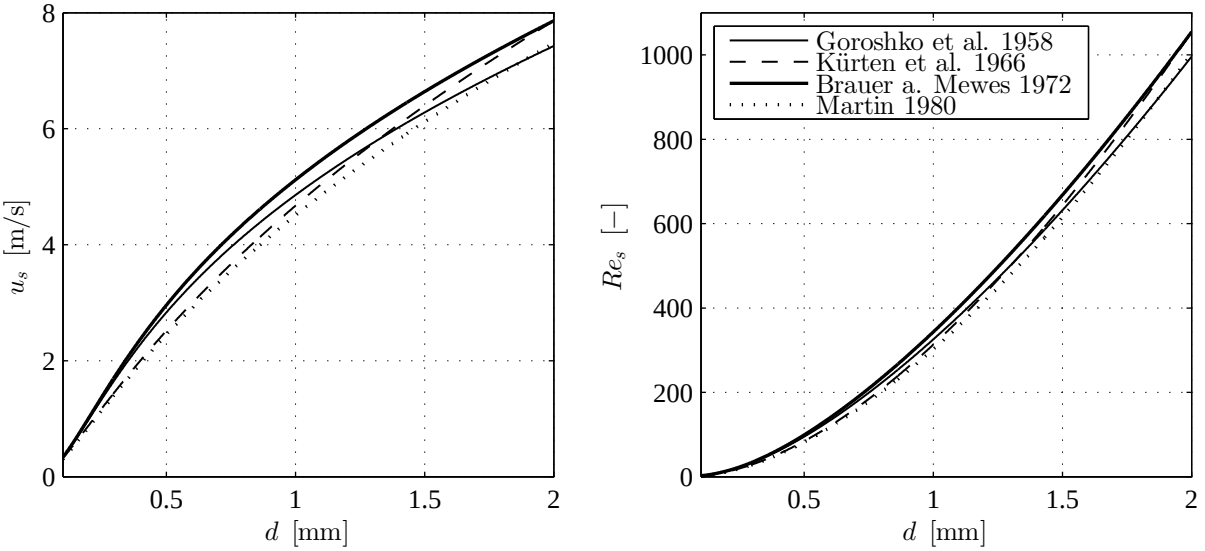

Figure 2.2: Terminal sinking velocity u_s (left) and its corresponding Reynolds number Re_s (right) in dependency on diameter d of spheres with an effective particle density of $\rho_p = 1380\,\mathrm{kg/m^3}$ settling in transition regime; calculated by the approximation methods of Goroshko et al. [35], Kürten et al. [30], Brauer a. Mewes [33], and Martin [40].

non-isometric, "thin free-falling disks" with sphericities of 0.026, 0.043, 0.123, and 0.230. The average RMS-deviation was larger for disk-shaped particles than for the isometric materials. The error of Eq. 2.89 is therefore expected to be higher for lower sphericities, on average. Kraume [28] reported about comparisons by Chhabra et al. [43] with empirical data, according to which Haider a. Levenspiel's equation was most recommendable for calculating the rate of descent of non-spherical particles. Therein, an average error of 20 % and a maximum error of 100 % were ascertained. The results of Haider a. Levenspiel [42] show that the c_d-Re_s-curves move to higher values for lower sphericities. Hence, the more the shape of a particle is different from a sphere, the slower it settles through stagnant fluid.

Wall effect

When sinking through a fluid, a *return flow* occurs around a particle due to the continuity condition. The fluid can therefore be stagnant (no flow), only far away from the particle, which is considered as the bulk region, whereas local flow velocities exist close to the particle. These velocities are higher for objects in vicinity of walls because of the lower free cross-section for the return flow. Hence, the presence of a wall has an impact on sinking velocity, even without direct particle-wall contact, but via the flow field. Larger local velocities enhance the momentum transfer from fluid to particles, which leads to greater drag forces and drag coefficients for particles sinking close to walls. Yang [8], for instance, suggests for laminar flow conditions a wall correction term to be added to Stokes' law, as follows:

$$F_{d,p} = 3\pi\rho_{fl}\nu_{fl}du_s(1 + k_{wa}\frac{d}{L_{wa}}) \qquad \text{, with } k_{wa} = \begin{cases} 0.563 & \text{, for a single planar wall} \\ 1.004 & \text{, for two planar walls} \\ 2.104 & \text{, for a circular cylinder} \end{cases} . \tag{2.90}$$

Therein, L_{wa} represents the distance from the particle center to the wall and k_{wa} a wall effect correction factor. The wall effect on sinking velocities can be disregarded in industrial fluidized bed processes because of large chamber diameters D. Instead, the particles would influence each other more than the walls do in fluidized beds. However, those fluid-particle-wall interactions could play an important role in thin classifiers, where particle concentration is desired to be low (see Section 2.2.7).

2.2.2 Stationary sinking of particle swarms

As just shown in the previous Section, particles sink slower in the vicinity of parallel walls, because fluid elements displaced by the settling objects (return flow) move upwards faster in a limited free space cross-section. This effect also appears when multiple particles (at least two) settle close together in unconfined fluids (practically: far away from walls), known as the *swarm effect*. The mutual hindrance of particles as they move through continuous media is a well-studied phenomenon that occurs in many industrial applications of sedimentation and fluidization. A brief overview of the first theoretical considerations and experimental findings on methods for calculating the swarm effect from publications of the first half of the twentieth century, is given for instance by Decker [44] and Singh a. Adhikari [45]. Kraume [28] illustrates the swarm effect using a model of Zehner [46], in which a fluid flows through a fixed cubic arrangement of spheres under laminar conditions. Velocity gradients on particle surfaces become larger due to neighboring particles, which leads to higher momentum transfer between fluid and particulate phase, and therefore, to higher drag coefficients and lower overall settling velocities. Kim et al. [47] and Ramachandran et al. [48] have shown that the drag on two sinking spheres (placed next to and behind one another) already differs significantly from the single particle drag at distances of ten times the sphere diameter, as quoted in [44]. Basic knowledge about swarm sinking can be found in textbooks, such as [9, 10, 28, 49]. However, there are many proposed calculation methods for settling velocities of swarms in literature, which vary in their mathematical structure and have been designed for different flow regimes. Some of the most proven and easiest to use are detailed below. These can be implemented, for instance, into the separation function of the three-compartment population balance model (Section 5.2) and the two-zone continuum model of Wurster fluidization (Section 7.7) of the present thesis.

Swarm correction factor

The swarm effect of settling kinetics in finite and infinite stagnant fluids can be represented by the swarm correction factor (symbolized by k_{sw}), which is generally defined as the ratio of the *swarm sinking velocity* (also called as sedimentation velocity or overall rate of decent) to the terminal sinking velocity (Section 2.2.1):

$$k_{sw} = \frac{u_{sw}}{u_s}. \tag{2.91}$$

This factor is also named as hindrance factor [49] or as relative swarm sinking velocity [28]. Richardson a. Zaki [50] demonstrated by theoretical considerations (including some of other authors too) about swarm settling under streamline conditions (Stokes regime) that the swarm correction factor depends on particle concentration (relative solid volume $\varepsilon_{s,sw}$) and the ratio of particle diameter (assuming to be a sphere) to the dimension of settling pipe (column diameter D). They have further shown by experimental data that the terminal Reynolds number (Re_s of Eq. 2.61) is another influencing factor for sedimentation velocity in the transition regime; whereas the latter is assumed to be only a function of particle concentration for turbulent conditions, with the following subdivision of Reynolds number intervals:

$$k_{sw} = \begin{cases} \mathrm{f}(\varepsilon_{s,sw}, \frac{d}{D}) & \text{, for } Re_s \lesssim 0.2 \\ \mathrm{f}(\varepsilon_{s,sw}, \frac{d}{D}, Re_s) & \text{, for } 0.2 \lesssim Re_s \lesssim 500 \\ \mathrm{f}(\varepsilon_{s,sw}) & \text{, for } 500 \lesssim Re_s \end{cases}. \tag{2.92}$$

Another result was that the hindrance factor k_{sw} grows with swarm porosity - $\varepsilon_{sw} = (1 - \varepsilon_{s,sw})$ - according to a power law, which is known as the widely applied *Richardson-Zaki equation*:

$$k_{sw}(\text{Richardson a. Zaki}) = \varepsilon_{sw}^{m_{sw}} = (1 - \varepsilon_{s,sw})^{m_{sw}}, \tag{2.93}$$

where m_{sw} represents the here so-called *Richardson-Zaki exponent* or power law exponent. This parameter was experimentally ascertained by Richardson a. Zaki [50] to be a one-dimensional function of d/D for laminar flow conditions, a two-dimensional function of d/D and Re_s in the intermediate regime, and independent from d/D and Re_s for turbulent flow conditions with $Re_s > 500$:

$$m_{sw}(\text{Richardson a. Zaki}) = \begin{cases} \mathrm{f}(\frac{d}{D}) & \text{, for } Re_s \lesssim 0.2 \\ \mathrm{f}(\frac{d}{D}, Re_s) & \text{, for } 0.2 \lesssim Re_s \lesssim 500 \\ \text{const.} & \text{, for } 500 \lesssim Re_s \end{cases}. \tag{2.94}$$

The empirical power law of Richardson a. Zaki was later confirmed by theoretical investigations of Hawksley [51], Maude a. Whitmore [52], and Thacker a. Lavelle [53], as stated in [49]. Di Felice a. Kehlenbeck [54] stated that the Richardson-Zaki equation occurred in a "somewhat different form" already two years earlier in a publication of Lewis a. Bowerman [55]. The empirical m_{sw}-approaches of Richardson a. Zaki (also summarized in [54]) are given below together with findings from other authors.

Stokes regime

For the Stokes regime, Richardson a. Zaki provided the following linear fit of the exponent m_{sw} over the particle-to-column diameter ratio ($\frac{d}{D}$, see first line of right hand side in Eq. 2.95), which goes to a constant value of 4.65 for column diameters much larger than the size of contained particles:

$$m_{sw}(\text{Richardson a. Zaki}) = \begin{cases} 4.65 + 19.5\frac{d}{D} & \text{, for } \frac{d}{D} > 0 \text{ and } Re_s \lesssim 0.2 \\ 4.65 & \text{, for } \frac{d}{D} \to 0 \text{ and } Re_s \lesssim 0.2 \end{cases}. \tag{2.95}$$

The ratio d/D was quite large in the measurements of Richardson a. Zaki due to the thin pipes (a few centimeters) employed in their experimental setting. But, those ratios are rather small in industrial processes such as in fluidized bed apparatuses, where $\frac{d}{D} \approx 0$. Changes in particle size have then only a minor influence on the Richardson-Zaki exponent of the laminar flow regime, which is why it is often regarded as constant with a value of $m_{sw} = 4.65$ in literature, as for instance by Kraume [28], Zehner [56], or Mier [57]. Deviations from this value between 4.65 and 5 still lead to sufficiently accurate settling velocities [49]. A value of 4.7 is suggested to be a good estimate of m_{sw} by Watanabe [58].

Brauer a. Kriegel [59] have developed a semi-empirical, but more complex, equation for the swarm correction factor, which is given with:

$$k_{sw}(\text{Brauer a. Kriegel}) = \frac{1 - \varepsilon_{s,sw}}{\left(1 + \frac{\varepsilon_{s,sw}}{(1-\varepsilon_{s,sw})^2}\right)\left(1 + \frac{1.2}{\sqrt{1+\left(\pi/(12\varepsilon_{s,sw})\right)^2} - 0.5}\right)}. \tag{2.96}$$

This approach underpins the independence from Reynolds number in the Stokes regime, as turned out from results of Richardson a. Zaki. Equation 2.96 is given in a textbook of Kraume [28] too, but with reference to a contribution published only by Brauer [60] a few years later than [59].

Zehner [56] compared the model equations of Richardson a. Zaki (Eq. 2.93 with $m_{sw} = 4.65$) and Brauer a. Kriegel (Eq. 2.96) with measurements from Molerus [61], which were conducted at Reynolds numbers of around 0.4. Both approaches match well with the experimental points for solid volume fractions up to $\varepsilon_{s,sw} = 0.4$. At higher values ($\varepsilon_{s,sw} > 0.4$), the model curve of Brauer a. Kriegel diverges from the empirical data, while the Richardson-Zaki equation still shows a good agreement for particle concentrations up to $\varepsilon_{s,sw} = 0.53$. An illustration of Molerus' measurements and the k_{sw}-curve of the Richardson-Zaki equation with $m = 4.65$ can also be found in [28], where k_{sw} is stated as relative fluid velocity (original, German: "bezogene Fluidgeschwindigkeit"). Furthermore, Kraume [28] confronted Eq. 2.93 (for $m_{sw} = 4.65$) and Eq. 2.96 with experimental data from Brauer [62] for $Re_s < 0.21$ in a separate plot. Therein, the Richardson-Zaki model fits again better to measurements for particle concentrations up to 50 % than the model of Brauer a. Kriegel, but the latter seems still appropriate for rough calculations. At this point, it is mentioned that higher swarm solid concentrations come close to conditions of loose random packed beds (Section 2.1.3) and are therefore limited, e.g., to around 60 % for mono-sized spheres.

Transition regime

As mentioned above, the relative swarm sinking velocity changes with the terminal Reynolds number Re_s in the transition regime. In order to consider this influence, Richardson a. Zaki [50] created the following experimental fit equations:

$$m_{sw}(\text{Richardson a. Zaki}) = \begin{cases} 4.35Re_s^{-0.03} + 17.5\frac{d}{D}Re_s^{-0.03} & \text{, for } \frac{d}{D} > 0 \text{ and } 0.2 \lesssim Re_s \lesssim 1 \\ 4.45Re_s^{-0.1} + 18\frac{d}{D}Re_s^{-0.1} & \text{, for } \frac{d}{D} > 0 \text{ and } 1 \lesssim Re_s \lesssim 200 \\ 4.45Re_s^{-0.1} & \text{, for } \frac{d}{D} > 0 \text{ and } 200 \lesssim Re_s \lesssim 500 \\ 4.35Re_s^{-0.03} & \text{, for } \frac{d}{D} \to 0 \text{ and } 0.2 \lesssim Re_s \lesssim 1 \\ 4.45Re_s^{-0.1} & \text{, for } \frac{d}{D} \to 0 \text{ and } 1 \lesssim Re_s \lesssim 500 \end{cases}, \tag{2.97}$$

in which the power law exponent of Eq. 2.93 is described as a two-dimensional function of the terminal Reynolds number and the particle-to-column diameter ratio for different Re_s-intervals in the first three lines of the right hand side. These 2D-fits are simplified for large columns (as in industrial fluidized beds) to 1D-equations depending only on the terminal Reynolds number, as given in the fourth and fifth line of Eq. 2.97. It is obvious that the Richardson-Zaki exponent hyperbolically decreases with growing Reynolds number. Thus, the hindering effect of sinking swarms is lower for larger particles in the intermediate regime.

A simpler approach is suggested by Kraume [28], through which the Richardson-Zaki exponent m_{sw} can be calculated from the Archimedes number via:

$$m_{sw}(\text{Kraume}) = 5.5Ar^{-0.06}. \tag{2.98}$$

This equation shows a similarity to the power expressions of Richardson a. Zaki in Eq. 2.97, and it found use for example in researches of Mier [57]. The Reynolds number interval of the transition regime is given with $0.25 < Re_s < 1000$ in [28]. The corresponding interval of Archimedes numbers ensues to round $5 < Ar < 402200$ using Martin's relation of stationary sinking spheres (Eq. 2.83), which provides very precise values for Reynolds numbers up to 10^4. As a conclusion, the exponents calculated from Kraume's approximation decrease from $m_{sw} = 4.99$ at $Re_s = 0.25$ to $m_{sw} = 2.54$ at $Re_s = 1000$. Equation 2.98 is not to be recommended for laminar ($Re_s < 0.25$) and turbulent flow conditions ($Re_s > 1000$), as can be seen later in Figure 2.4.

Quadratic regime

Richardson a. Zaki [50] detected an exponent with $m_{sw} = 2.39$ at a Reynolds number of $Re_s = 489$, and they assumed this value to be an appropriate approximation for even higher Reynolds numbers of the Newton regime:

$$m_{sw}(\text{Richardson a. Zaki}) = 2.39 \qquad \text{, for } Re_s \gtrsim 500. \tag{2.99}$$

Zehner [56], however, compared the Richardson-Zaki equation assuming an exponent of $m_{sw} = 2.4$ with measurements of Wilhelm a. Kwauk [63] generated for turbulent flow conditions (see also Table 2.2) at a terminal Reynolds number of $Re_s = 2180$. At this, the model curve lies clearly above the experimental data points. Kraume [28] even recommends a Richardson-Zaki exponent of $m_{sw} = 2.2$ for the quadratic regime, which is quite different from these of Richardson a. Zaki and of Zehner. But, using Kraume's value in the Richardson-Zaki equation would generate an even flatter curve of k_{sw} with $\varepsilon_{s,sw}$ (or ε_{sw}) and lead to an even larger deviation from Wilhelm a. Kwauk's empirical data. The differences might be due to the insufficient description of drag in the quadratic flow regime, which is affected by complex vortex shedding, as can also be seen in measurements of drag coefficients of single particles (Section 2.2.1).

Holistic equations for the three main flow regimes

Di Felice a. Kehlenbeck [54] recommended the approach of Rowe [64] with

$$\frac{4.7 - m_{sw}}{m_{sw} - 2.35} = 0.175Re_s^{0.75}$$

for the entire range of flow conditions, which can be solved for the exponent as follows:

$$m_{sw}(\text{Rowe}) = \frac{4.7 + 2.35 \cdot 0.175Re_s^{0.75}}{0.175Re_s^{0.75} + 1}. \tag{2.100}$$

The limits of this equation are 4.7 for $Re_s \to 0$ and 2.35 for $Re_s \to \infty$.

Khan a. Richardson [65] suggested a similar holistic approach, but with respect to the Archimedes number:

$$\frac{4.8 - m_{sw}}{m_{sw} - 2.4} = 0.043Ar^{0.57},$$

from which an explicit function of the exponent can be derived too:

$$m_{sw}(\text{Khan a. Richardson}) = \frac{4.8 + 2.4 \cdot 0.043Ar^{0.57}}{0.043Ar^{0.57} + 1}. \tag{2.101}$$

The lower and the upper limit are similar to these of Rowe with 4.8 for $Re_s \to 0$ and 2.4 for $Re_s \to \infty$. The approach of Khan a. Richardson can also be found in the textbook of Rhodes [9], where the right-hand side

of Eq. 2.101 is added by a factor with $(1 + 2.4(d/D)^{0.27})$ taking into account the particle-to-wall diameter ratio. However, this wall effect correction term can be neglected according to Di Felice a. Kehlenbeck [54].

Molerus [61] and Bertil Andersson [66] respectively created a sufficiently precise calculation method of the swarm effect for all three flow regimes, which is not based on the Richardson-Zaki equation. However, these approaches are rather cumbersome to apply, as stated by Zehner [56], who provided a semi-empirical alternative, in which the swarm correction factor is expressed by

$$k_{sw}(\text{Zehner}) = \left(1 - (\varepsilon_{s,sw})^{\frac{2}{3}(1+\delta_{bl})}\right)^{1.75\left(1+\frac{4}{3}\delta_{bl}\right)^2}, \tag{2.102}$$

with the Re_s-dependent, dimensionless boundary layer thickness δ_{bl}:

$$\delta_{bl} = \frac{1}{2 + \sqrt{0.5 Re_s}}. \tag{2.103}$$

Zehner's approach fits remarkably well to measurements of laminar [61,67], intermediate [56,68], and turbulent flow conditions [56,63]. Beside this, Zogg [10] refers to experimental investigations of Leu a. Ghosh [69] with the conclusion that the model of Zehner (Eqs. 2.102 and 2.103) suits as good approximation even for polydisperse swarms with a volume concentration up to 40 %. Furthermore, it can be said that the dimensionless boundary layer thickness δ_{bl} of Zehner's model becomes steadily constant for infinitely small and large terminal Reynolds numbers ($\delta_{bl}(Re_s \to 0) = 1/2$ and $\delta_{bl}(Re_s \to \infty) = 0$); which is why, this model is practically independent from the terminal Reynolds number in the Stokes regime for $Re_s \ll 1$ and in the Newton regime for $Re_s \gg 1000$. These limits agree with the aforementioned, theoretical relations of Richardson a. Zaki, as given in Eq. 2.92.

2.2.3 Upward flow of fluids through particle systems over perforated plates between confining straight walls

Subdivision into three main flow regimes of fluid-particle dynamics

It is distinguished between three different main flow regimes of fluid-particle transport dynamics when fluids flow vertically through particulate systems that are enclosed by a fluid-permeable plate at the bottom (called the inflow base or distributor plate) and side walls. These are the fixed bed, the fluidized bed, and the pneumatic transport regime. Which of these flow regimes is present depends on the strength of momentum transfer from fluid to particles, and can be therefore characterized by inlet flow velocity u_{in}. At low inflow velocities, particles stay in their positions and form a fixed bed (e.g., a random packed bed). The particles are loosened above a critical flow velocity, begin to move around near the bottom plate, and form a so-called fluidized bed. The lowest inlet flow velocity to generate such a state is known as the minimal fluidization point. Further increase in fluid velocity brings the particles to higher spatial positions, on average, so that interparticle voids enlarge, macroscopic particle concentration decreases, and the entire bed expands. The border between the regimes of fluidization and pneumatic transport is named as the elutriation point. At flow velocities above the elutriation limit, the bed material is carried out of the chamber. In the scope of this thesis, u_{mf} shall denote the inlet velocity at minimum fluidization for an isothermal homogeneous fluidized bed with vertically constant cross-section. The elutriation point for the same thermal conditions is symbolized by u_{elu}. Calculation methods of these limits are given below in Section 2.2.4.

Causes for vertical pressure changes

When passing a vertical packed bed or fluidized bed of the height H_{bed}, a decrease in absolute pressure (measurable) between the inlet and outlet flow emerges. This pressure difference (Δp_{tot}) is made up of so-called pressure losses (kinetic energy) and the potential energy of the fluid in the bed volume ($\rho_{fl} H_{bed} g$), which is known as hydrostatic pressure. The pressure losses, which are also referred to as pressure drop, are caused by friction on surfaces (skin friction) and inside the fluid (turbulences). In simple process chambers without any further built-in components, the overall pressure drop is due to the inflow base (symbolized by Δp_{dis}), losses from the bed particles (subsumed by Δp_{bed}), and wall friction. The latter can be disregarded, as losses by the bed particles (large surface) and the inflow plate (complex geometry) are much larger. In doing so, the overall pressure decrease of a packed or fluidized bed is expressed with:

$$\Delta p_{tot}(u_{in}) = \begin{cases} \Delta p_{dis}(u_{in}) + \Delta p_{bed}(u_{in}) + \rho_{fl} H_{bed} g & , \text{for } 0 < u_{in} < u_{mf} \\ \Delta p_{dis}(u_{in}) + \Delta p_{bed} \quad + \rho_{fl} H_{bed}(u_{in}) g & , \text{for } u_{mf} \le u_{in} < u_{elu} \end{cases}. \tag{2.104}$$

The bottom plate pressure drop increases with inlet flow velocity ($\Delta p_{dis}(u_{in})$) for both, fixed and fluidized beds; whereas the pressure drop of the particulate material ($\Delta p_{bed}(u_{in})$) grows with inlet gas velocity only within the fixed bed, but not in the fluidization regime ($\Delta p_{bed} \neq \mathrm{f}(u_{in})$). In opposite manner, the bed height remains unchanged for fixed bed conditions ($H_{bed} \neq \mathrm{f}(u_{in})$), but increases for higher inlet flow velocities in the regime of fluidization ($H_{bed}(u_{in})$). Some basics for calculating the pressure drop of perforated plates, based on researches of Hunt et al. [70] and McAllister et al. [71], are outlined by Hoppe a. Mittelstrass [72] or by Mörl et al. [29]. These are used in the context of the two-zone continuum model of Wurster fluidization, later in Section 7.4. A comprehensive overview of different types of distributor plates is given by Uhlemann a. Mörl (see "Kapitel 9" in [73]), who also recommend investigations of Brauer [60] for further understanding. The particle-related pressure drop of a packed bed Δp_{bed} can be calculated from diverse models, as described below. The hydrostatic term $\rho_{fl} H_{bed} g$ has a strong influence on measured pressure difference (conform with Δp_{tot}) for liquid-solid systems, but can be neglected when gaseous flow media are used, as also mentioned by Kunii a. Levenspiel [74].

Semi-empirical calculation methods of pressure drop across packed beds

A model that describes the packed-bed-related pressure loss Δp_{bed} is useful to derive an equation for the minimal fluidization point u_{mf}, as shown later in Section 2.2.4. Two types of such models exist, as mentioned by Wirth in [19]. The first one is based on the *channel flow notion*, in which the interparticle voids are considered as parallel connection of pores with a tube-equivalent diameter, known as the

$$\text{hydraulic diameter} = \frac{4 \cdot (\text{volume to permate by flow})}{\text{contact area of flow}}. \tag{2.105}$$

An advantage of this type of model is its simple structure, because the pressure drop is declared to be proportional to the kinetic flow energy ($\rho_{fl} u_0^2/2$) and to the reciprocal of the hydraulic diameter. In addition to this, the tube-equivalent diameter can be obtained from the volume-specific surface area $a_{v,tot}$ or the effective Sauter diameter d_{SV} (Eq. 2.48). Such a derivation is detailed by Kraume in [28] for a monodisperse package or by Schubert in [75] for beds of non-spherical particles using the volume-equivalent sphere diameter ($d = d_{V,p}$) and the sphericity after Wadell (Eq. 2.3). The *flow resistance factor* of the bed, which serves as proportionality constant in the channel flow concept, has to be adapted to empirical data, as for example by fit equations. This factor is comparable to the Fanning friction factor of flows in pipes, as stated by Rhodes [9], or to the drag coefficient of the terminal sinking velocity (see Eq. 2.62). For the sake of ease of use, those coefficients are correlated to a superficial Reynolds number, which is referred to the inlet flow velocity and the effective Sauter diameter: $Re_{in} = d_{SV} u_{in}/\nu_{fl}$. The inlet gas velocity conforms with superficial velocity inside the bed. Ergun [76] created such a fit with $(150(1-\varepsilon_{bed})/Re_{in} + 1.75)$ in a range of $1 < Re_{in} < 4500$ from measurements of many other authors, by means of which the today so-called *Ergun equation* was obtained with:

$$\frac{\Delta p_{bed}}{H_{bed}} = 150 \frac{(1-\varepsilon_{bed})^2}{\varepsilon_{bed}^3} \frac{\rho_{fl} \nu_{fl}}{d_{SV}^2} u_{in} + 1.75 \frac{1-\varepsilon_{bed}}{\varepsilon_{bed}^3} \frac{\rho_{fl}}{d_{SV}} u_{in}^2. \tag{2.106}$$

It relates the pressure loss gradient $\Delta p_{bed}/H_{bed}$ to the bed porosity ε_{bed}, the effective Sauter diameter d_{SV}, and the inlet gas velocity u_{in}. The effective Sauter diameter d_{SV} is denoted only as "effective diameter" in Ergun's publication, but its definition agrees with Eq. 2.48. Due to imprecise determination of the effective Sauter diameter, volume-specific surface area, or an average particle shape in practice, the Ergun equation is recommended in literature based on different particle-related simplifications. These can be found for instance

- in [9] for mono-sized spheres with $d_{SV} = d_{mon}$,
- in [28, 73, 77] for polydisperse spheres with $d_{SV} = d_{32}$,
- in [28] for polydisperse spheres, but given as function of the volume-specific surface area,
- in [78] for polydisperse non-spheres as function of diverse types of "mean diameter" and sphericity,
- in [75] for polydisperse non-spheres using the volume-equivalent diameter as size coordinate, which conforms with $d_{SV} = \Psi_{sph} d_{32}(d = d_{V,p})$ (see Eq. 2.50), or
- in [74] for polydisperse sphere-similar solids ("isotropic in shape") with an effective diameter obtained by sieving analysis, which resembles $d_{SV} = \Psi_{sph} d_{32}(d = d_{V,p})$.

Brauer [60] developed an alternative to Ergun's model, which provides similar results for Reynolds numbers below 1000, but diverges from Eq. 2.106 with further increasing Reynolds numbers.

The other type of model is not employed in the present thesis due to its high level of complexity, and shall be therefore only briefly described. This concept goes back to elaborations of Molerus [61] and essentially includes the effects of friction and flow separation on surfaces of single particles in packed beds, so that approaches of the terminal sinking velocity (Section 2.2.1) can be implemented into models of bulk solids. Thereby, intermediate flow conditions, under which neither frictional nor inertial effects dominate the overall flow resistance, are taken into account, in contrast to the *hydraulic diameter concept*.

Pressure drop of isothermal homogeneous fluidized beds

As seen in the Ergun equation (Eq. 2.106), the pressure drop increases steadily with superficial gas velocity. From the point of minimal fluidization on, this abruptly remains constant for beds with a uniform particle size. In the case of broad particle size distributions, the pressure loss merges into a constant range, as shown, for example, by Botterill et al. [79] for different operating temperatures. A simple calculation method for Δp_{bed} of the fluidization regime can be derived as follows. The pressure losses of chamber walls and a distributor plate do not have to be taken into account for a model conception of a swarm layer of particles that is homogeneously distributed from the bottom to H_{bed}, infinitely extended in radial direction, and floating in an upward flow of a fluid. The vertical, stationary momentum balance of such a suspension layer leads to a simple relationship between the total pressure difference Δp_{tot}, the area-specific weight of particles ($\rho_p(1-\varepsilon_{bed})H_{bed}g$), the area-specific buoyancy of particles ($\rho_{fl}(1-\varepsilon_{bed})H_{bed}g$), and the potential energy of fluid column ($\rho_{fl}H_{bed}g$), which results in:

$$\Delta p_{tot} = (\rho_p - \rho_{fl})(1-\varepsilon_{bed})H_{bed}g + \rho_{fl}H_{bed}g \qquad \text{, for } u_{mf} \leq u_{in} < u_{elu}. \tag{2.107}$$

From this equation, the dissipative pressure drop of gas-powered fluidized beds can be approximated with

$$\Delta p_{bed} \approx (\rho_p - \rho_{fl})(1-\varepsilon_{bed})H_{bed}g \qquad \text{, for } u_{mf} \leq u_{in} < u_{elu}, \tag{2.108}$$

where the hydrostatic pressure is disregarded. Equation 2.108 can be further simplified to a function of the bed mass ($M_{bed} = \rho_p(1-\varepsilon_{mf})A_{app}H_{bed}g$) with

$$\Delta p_{bed} \approx \rho_p(1-\varepsilon_{bed})H_{bed}g = \frac{M_{bed}g}{A_{app}} \qquad \text{, for } u_{mf} \leq u_{in} < u_{elu}, \tag{2.109}$$

where buoyancy of particles is neglected too. A somewhat different derivation, which leads also to Eq. 2.107, is illustrated by Wirth in [80].

2.2.4 Operation points of minimal fluidization and elutriation for isothermal homogeneous fluidized beds

As mentioned before, the points of minimal fluidization and elutriation are characteristic limits of the flow regime of fluidized beds. A few calculation methods of the limits, which are used for isothermal homogeneous fluidization in chambers with straight walls, are described below. The effect of higher local voids between particles in vicinity of walls and the consequent flow mal-distribution, as described for instance by Tsotsas a. Schlünder [81], are not taken into account here.

Bed porosity at minimal fluidization conditions

The bulk porosity of a fluidized bed at minimal fluidization conditions is represented here by ε_{mf}. It can be estimated via Eq. 2.57 by measurements of the effective particle density ρ_p and the bulk density ρ_b, or taken from literature data of "loose" random packed beds (see Section 2.1.3). The value of the minimal fluidization porosity depends on mean diameter, size variety, and shape of particles, whereat the influence of size on ε_{mf} can be neglected for coarse bulk materials with narrow PSDs:

$$\varepsilon_{mf} = \begin{cases} \mathrm{f}(d, \Psi_{sph}, \zeta_{q_r}) & \text{, for small particles} \\ \mathrm{f}(\Psi_{sph}, \zeta_{q_r}) & \text{, for coarse particles} \end{cases}. \tag{2.110}$$

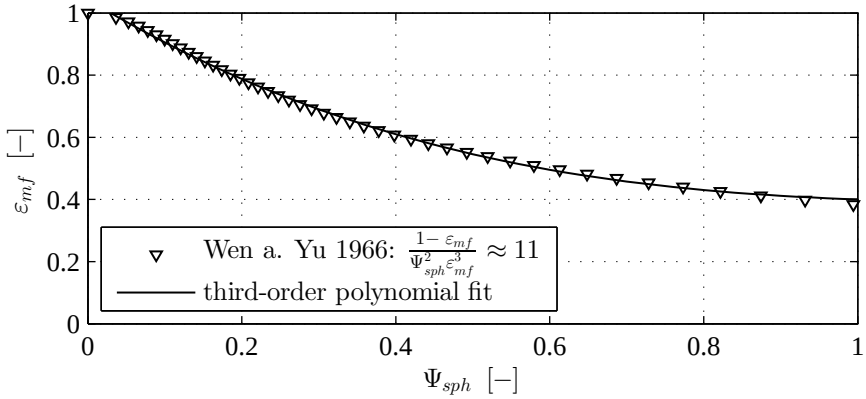

Figure 2.3: Implicit function of bed porosity at minimal fluidization depending on sphericity from Wen a. Yu [82] and the corresponding explicit fit function according to Eq. 2.112 for $\varepsilon_{mf,sph} = 40\,\%$.

Wen a. Yu [82] compared the following correlation

$$\frac{1-\varepsilon_{mf}}{\Psi_{sph}^2\varepsilon_{mf}^3} \approx 11 \tag{2.111}$$

between bed voidage of minimal fluidization and average particle sphericity with empirical data from several authors. This fit can depict the trend of measurement points, but can only be recommended for rough estimations due to large measurement fluctuations. Additionally, ε_{mf} must be determined by iterations, when using Eq. 2.111 for known sphericity factors. The following third-order polynomial

$$\varepsilon_{mf} = 0.2997(1-\Psi_{sph})^3 + 0.2549(1-\Psi_{sph})^2 + 0.0891(1-\Psi_{sph}) + \varepsilon_{mf,sph} \tag{2.112}$$

was fitted to Eq. 2.111 in order to provide a quicker calculation method. The advantage of such a formula is that the minimum fluidization porosity of spherical bed particles (symbolized by $\varepsilon_{mf,sph}$) can be exactly fixed to suggested values from literature, such as with 40 % for coarse spherical particles. Figure 2.3 illustrates that the fit-equation with $\varepsilon_{mf,sph} = 40\,\%$ matches precisely with the correlation of Wen a. Yu for almost the entire domain of the sphericity. It therefore nearly approaches the measurements shown in [82] for a range of sphericity between around 0.15 and 1. The disadvantage of the polynomial approximation is that values slightly above unity are obtain for sphericities below 0.03. But, those values are not of interest for applications of fluidized bed granulation.

Minimal fluidization point

There are many different approaches for calculating the minimal fluidization point in literature. Most of the recommended ones are based on the Ergun equation (Eq. 2.106), which can be combined with the simplified force balance (Eq. 2.108, neglecting the hydrostatic pressure) at minimum fluidization conditions of gas-solid systems. Defining the Reynolds number Re_{mf} at minimum fluidization velocity u_{mf} and the Archimedes number by the effective Sauter diameter d_{SV} with

$$Re_{mf} = \frac{u_{mf} d_{SV}}{\nu_{fl}} \tag{2.113}$$

and

$$Ar_{SV} = \frac{\rho_p - \rho_{fl}}{\rho_{fl}} \frac{d_{SV}^3 g}{\nu_{fl}^2}, \tag{2.114}$$

the point of minimal fluidization can be expressed in the following dimensionless form:

$$\frac{150(1-\varepsilon_{mf})}{\varepsilon_{mf}^3} Re_{mf} + \frac{1.75}{\varepsilon_{mf}^3} Re_{mf}^2 = Ar_{SV} \qquad \text{, for } u_{mf} \leq u_{in} < u_{elu}. \tag{2.115}$$

On the left side of this equation, the first term stands for laminar effects and the second for turbulent effects.

According to statements from an English-translation [37] of a compilation of several Russian publications, Goroshko et al. [35] provided the following "interpolation formula for the critical velocity for onset of fluidization":

$$Re_{mf}(\text{Goroshko et al.}) = \frac{Ar_{SV}}{150\frac{1-\varepsilon_{mf}}{\varepsilon_{mf}^3} + \sqrt{\frac{1.75}{\varepsilon_{mf}^3}Ar_{SV}}}. \tag{2.116}$$

This approach corresponds to an inverse superposition of a purely laminar solution ($150Re_{mf}(1-\varepsilon_{mf})/\varepsilon_{mf}^3 = Ar_{SV}$) and a purely turbulent solution ($1.75Re_{mf}^2/\varepsilon_{mf}^3 = Ar_{SV}$) of the Ergun equation, and it shows a similarity to another equation from Goroshko et al. (see Eq. 2.74) for terminal sinking velocities of spheres. By assuming a minimal fluidization porosity of 40 % for beds of round particles, the authors simplified Eq. 2.116 to:

$$Re_{mf}(\text{Goroshko et al.}) = \frac{Ar_{SV}}{1400 + 5.22\sqrt{Ar_{SV}}} \qquad \text{, for } \varepsilon_{mf} = 0.4, \tag{2.117}$$

and stated the latter equation to have an error of ±20 %. Nevertheless, Eq. 2.117 is recommended in literature (e.g., by Mörl et al. [29]) as a quick method for setting operation parameters of fluidized beds, due to its simple structure.

Equation 2.115 can be solved for Re_{mf} via the quadratic formula, which results in

$$Re_{mf}(\text{Ergun}) = \frac{A}{2B}(1-\varepsilon_{mf})\left(\sqrt{1 + \frac{4B}{A^2}\frac{\varepsilon_{mf}^3}{(1-\varepsilon_{mf})^2}Ar_{SV}} - 1\right) \tag{2.118}$$

with $A = 150$ and $B = 1.75$ by Martin in [40]. Martin stated this solution later with

$$Re_{mf}(\text{Martin}) = 42.9(1-\varepsilon_{mf})\left(\sqrt{1 + \frac{\varepsilon_{mf}^3}{(1-\varepsilon_{mf})^2}\frac{Ar_{SV}}{3214}} - 1\right), \tag{2.119}$$

where the quotients with A and B are rounded. Such an equation is also presented by Wirth [80] with values of the constants deviating a little:

$$Re_{mf}(\text{Wirth}) = 42.8(1-\varepsilon_{mf})\left(\sqrt{1 + 3.11\cdot 10^{-4}\frac{\varepsilon_{mf}^3}{(1-\varepsilon_{mf})^2}Ar_{SV}} - 1\right). \tag{2.120}$$

The influence of particle sphericity on Re_{mf} can be taken into account via the modified correlation of Wen a. Yu [82] in Eq. 2.112 and via equations of the effective Sauter diameter d_{SV} in Eq. 2.48 or Eq. 2.50. Ergun's equation [76] was fitted to measurements of superficial Reynolds numbers Re_{in} between around 1 and 4500. The measurements showed fluctuations, but Ergun's equation gives acceptable values.

Separately from the Ergun-based approximations (Eqs. 2.116 to 2.120), an empirical fit equation of similar structure with

$$Re_{mf}(\text{Wen a. Yu}) = \sqrt{33.7^2 + 0.0408Ar_V} - 33.7 \tag{2.121}$$

was created by Wen a. Yu [82] on the basis of many measurement points for Reynolds numbers between 10^{-3} and $5\cdot 10^3$. At this, the Archimedes number Ar_V (called as "Galileo number" in [82]) was calculated with the volume-equivalent diameter d_V of the particles instead of d_{SV}: $Ar_V = (\rho_p - \rho_{fl})d_V^3 g/(\rho_{fl}\nu_{fl}^2)$. The approach of Wen a. Yu is recommended by Wirth [80], as it can be applied without knowing the sphericity and bed porosity. However, since both parameters are not considered, the results can have large errors. Wen a. Yu stated averaged relative standard deviations with 21.3 % for non-spherical particles with $d \lesssim 0.5$ mm and with 37.6 % for non-spherical particles with $d \gtrsim 0.5$ mm. Because of these disadvantages, the Ergun-based equations (Eqs. 2.116 to 2.120) are to be preferred for the choice of an adequate calculation approach for minimal fluidization point.

Elutriation point

The elutriation point is expressed by means of inlet gas velocity with u_{elu} and the corresponding Reynolds number with Re_{elu}. The theoretical limit of homogeneous fluidization is characterized by an infinitely

index of method	CMFL-1	CMFL-2	CMFL-3
assumptions			
particle shape:	spherical	spherical	non-spherical, uniform
sphericity (Eq. 2.3):	$\Psi_{sph} = 1$	$\Psi_{sph} = 1$	$\Psi_{sph} < 1$
minimal fluidization			
ε_{mf}:	0.4	0.4	Eq. 2.112, modified from Wen a. Yu [82], with $\varepsilon_{mf,sph} = 0.4$
d_{ch}:	d_{32} (Eq. 2.46), or d_{SV} (Eq. 2.48)	d_{32} (Eq. 2.46), or d_{SV} (Eq. 2.48)	d_{SV} (Eq. 2.48), or d_{SV} (Eqs. 2.27 a. 2.50)
Re_{mf}:	Eq. 2.117, Goroshko et al. [35]	Eq. 2.119, Martin [41]	Eq. 2.119, Martin [41]
form of solution:	closed	closed	closed
elutriation			
d_{ch} for medium ζ_{q_r}:	d_{32} (Eq. 2.46)	d_{32} (Eq. 2.46)	$m_{1,0}(d = d_{V,p})$ (Eq. 2.27)
d_{ch} for large ζ_{q_r}:	d_{min}	d_{min}	$\min_{d_{V,p}}\big(q_0(d_{V,p})\big)$
$Re_{elu} = Re_s$:	Eq. 2.74, Goroshko et al. [35]	Eq. 2.83, Martin [41]	Eq. 2.65 (implicit form) force balance
c_d:	-	-	Eq. 2.89, Haider a. Levenspiel [42]
form of solution:	closed	closed	non-closed (iteration)

Table 2.3: Three suggested calculation methods for the operation limits of homogeneous fluidization, with different levels of accuracy and complexity and/or variable particle shape.

expanded bed ($H_{bed}(u_{elu}) \to \infty$) and an infinitely diluted particle concentration ($\varepsilon_{bed}(u_{elu}) \to 1$). Martin [41] suggested to approximate the elutriation point of homogeneous fluidized beds by the terminal sinking velocity

$$u_{elu} \coloneqq u_s \tag{2.122}$$

and its related Reynolds number

$$Re_{elu} \coloneqq Re_s = \frac{u_s d_{ch}}{\nu_{fl}}. \tag{2.123}$$

Section 2.2.1 outlines several approaches of the terminal sinking velocity with different levels of accuracy and complexity. Which type of characteristic diameter d_{ch} is to be used for Re_{elu}, depends on properties of the bed material such as the particle size distribution. But also, the employed calculation method of the minimal fluidization point should be considered for the choice of d_{ch}, as described below.

Choice of calculation methods

The inlet velocity of fluidized beds must be within the limits of minimal fluidization and elutriation. Several approaches of these limits are described above in this thesis. Three calculation methods of fluidization limits are composed at this point, which consist of different combinations of the approaches of minimal fluidization (above in this Section) and terminal sinking velocity (Section 2.2.1). They are indicated by CMFL-1, CMFL-2, and CMFL-3, and can be used for different accuracy requirements and/or different particle shapes. The corresponding assumptions and equation-references are summarized in Table 2.3. The first two calculation methods CMFL-1 and CMFL-2 are restricted to spherical particles, and the interparticle porosity at minimal fluidization is assumed to be 0.4 in each case. In the first calculation method CMFL-1, only superposition approaches from Goroshko et al. (Eq. 2.117 and Eq. 2.74, [35]) are combined due to their same mathematical structure, while CMFL-2 only contains approaches from Martin (Eq. 2.119 and Eq. 2.83, [41]) for the same reason. Martin suggested Eq. 2.83 for determining the elutriation point within a range of validity of $Ar < 2{\cdot}10^{10}$, which corresponds to $Re_s < 2.78{\cdot}10^5$. Iterations are not needed for CMFL-1 and CMFL-2, as both methods entirely consist of closed solutions. At this, the application of CMFL-1 is simpler, and CMFL-2 provide a little more precise results. In both cases, the errors are acceptable for the parameter setting of fluidized beds, as desired inlet velocities are supposed to be a few times higher than the minimal fluidization velocity and still far below the elutriation point. The third calculation method

CMFL-3 is conceptualized for non-spherical particles ($\Psi_{sph} < 1$). Martin's suggestion (Eq. 2.119) forms the basic equation of the minimal fluidization point in CMFL-3, in which the dependency on particle sphericity is implemented via the modified correlation of Wen a. Yu (Eq. 2.112, [82]) that estimates values for the bed porosity at minimal fluidization. The elutriation point of CMFL-3 is approached by the dimensionless force balance of a stationary sinking particle (Eq. 2.65) with the drag coefficient c_d described by the 2D-fit of Haider a. Levenspiel (Eq. 2.89, versus Re_s and Ψ_{sph}, [42]). Due to the complex equation structure, the elutriation velocity of CMFL-3 has to be determined iteratively.

For polydisperse systems, it is always advisable to use the effective Sauter diameter as characteristic property for the minimal fluidization point in presented calculation methods, because each of them is based on Ergun's equation. The purely statistical definition of the Sauter diameter d_{32} can be used too, when the bed material consists of spheres. The choice of a suitable characteristic diameter for the elutriation point must be considered in a more differentiated manner, as discharge of single particles significantly depends on particle size, which means that carrying-away of the fine fraction of fluidized beds appears already at lower velocities. An average particle size quantity can be used for narrow or somewhat wider particle size distributions neglecting particle size variety at small or medium relative standard deviations ζ_{q_r}. In this case, the effective Sauter diameter can be used for characterizing the elutriation point. It is then consistent with the minimal fluidization limit. For very broad PSDs (large ζ_{q_r}), a particle diameter representing the finest particles should be taken into account. This can be for instance the minimal diameter d_{min} (e.g., smallest sieve size) of manufacturer specification sheet, or the inverse value of the cumulative distribution function Q_r with e.g., $Q_r(d_{5\%}) = 5\,\%$. The Reynolds number of the c_d-correlation of Haider a. Levenspiel is related to the volume-equivalent diameter $d_{V,p}$. Therefore, it is recommended to use the first raw moment of the number-based density distribution over volume-equivalent diameter ($m_{1,0}(d = d_{V,p}) = \int_0^\infty d_{V,p} q_0(d = d_{V,p}) \mathrm{d}d$) as characteristic property of the elutriation point for narrow or somewhat wider bed-PSDs. For very large varieties in particle size, it would be better to employ the smallest volume-equivalent diameter of the bed material that can be determined. Other definitions of d_{ch} are conceivable for CMFL-3, as methods measuring and characterizing size of non-spherical particles can be deficient, especially for low sphericities. It should be further noticed at this point that CMFL-3 can only provide very rough approximations for materials with low sphericities (e.g., $\Psi_{sph} \ll 0.67$ according to [42]).

The influence of variety in apparent density and shape of the particles, particle surface roughness, and wall effects on the operation limits is not considered in any of the methods of Table 2.3.

2.2.5 Expansion of isothermal homogeneous fluidized beds

Fluidization number

The fluidization number f_{in} is defined as the ratio of inlet velocity u_{in} (or superficial velocity) to minimal fluidization velocity:

$$f_{in} = \frac{u_{in}}{u_{mf}}. \tag{2.124}$$

It is a dimensionless characteristic of the strength of fluidized bed expansion. Uhlemann a. Mörl ([73], "Bild 3-5") stated fluidization numbers between around 3.9 and 5.9 to be suitable for applications of fluidized bed spray granulation. Those numbers can be different for processes in Wurster equipment. The maximal fluidization number (symbolized here by f_{rn}, and by "f_{max}" in [73]) ensues from the elutriation point to

$$f_{rn} = \frac{u_{elu}}{u_{mf}} = \frac{Re_{elu}}{Re_{mf}}, \tag{2.125}$$

which is a measure of the width of fluidization regime and can therefore also referred to as *fluidization range number*. It can be described as function of the Archimedes number Ar, as for example by the first or second calculation method of the fluidization limits of Table 2.3:

$$f_{rn} = \begin{cases} \frac{1400+5.22\sqrt{Ar}}{18+0.61\sqrt{Ar}} & \text{, for CMFL-1 (Goroshko et al.)} \\ \frac{18\left(\sqrt{1+\frac{\sqrt{Ar}}{9}}-1\right)^2}{42.9(1-0.4)\left(\sqrt{1+\frac{0.4^3}{(1-0.4)^2}\frac{Ar}{3214}}-1\right)} & \text{, for CMFL-2 (Martin)} \end{cases}. \tag{2.126}$$

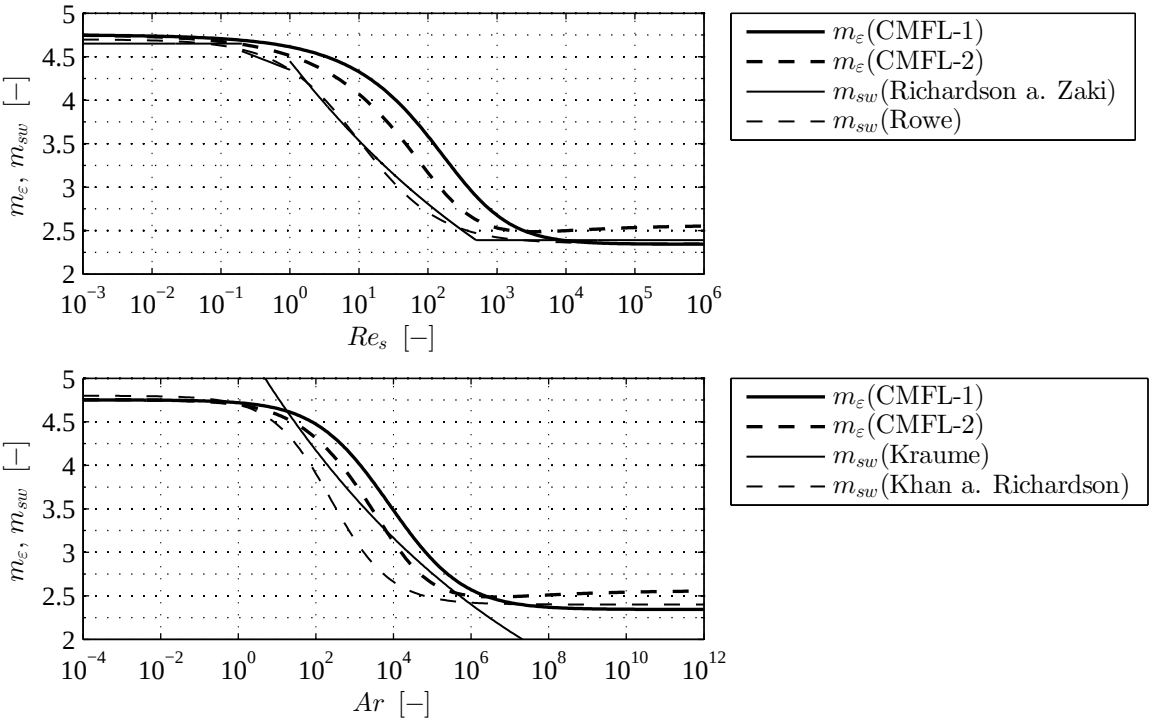

Figure 2.4: Fluidized bed expansion exponent after Brötz [83] and Richardson a. Zaki [50] calculated by different approximation equations: m_ε(CMFL-1) and m_ε(CMFL-2) with Eq. 2.126 and Eq. 2.129, m_{sw}(Richardson a. Zaki) with Eqs. 2.95, 2.97, and 2.99, m_{sw}(Rowe) with Eq. 2.100, m_{sw}(Kraume) with Eq. 2.98, and m_{sw}(Khan a. Richardson) with Eq. 2.101.

Expansion equations after Brötz and Richardson a. Zaki

As stated in [37], Brötz [83] "proposed" the following power law, that relates the inlet velocity to fluidized bed porosity by

$$\frac{u_{in}}{u_{mf}} = \left(\frac{\varepsilon_{bed}(u_{in})}{\varepsilon_{mf}}\right)^{m_\varepsilon}. \tag{2.127}$$

Through measurements of Brötz [84], the exponent m_ε could be identified as a function of particle diameter. Considering homogeneous fluidized beds as stationary settling swarms of particles, which are hold on a constant level (position in system coordinates), allows to apply the Richardson-Zaki equation (see Eq. 2.91 and Eq. 2.93) with reference to the elutriation velocity u_{elu}:

$$\frac{u_{in}}{u_{elu}} = \left(\frac{\varepsilon_{bed}(u_{in})}{\varepsilon_{elu}}\right)^{m_{sw}} \quad \text{, with } \varepsilon_{elu} = 1. \tag{2.128}$$

Using this equation for calculating the bed expansion is suggested for instance by Uhlemann a. Mörl [73] or by Mörl et al. [29]. It can be shown by inserting the minimal fluidization point ($u_{in} = u_{mf}$ and $\varepsilon_{bed} = \varepsilon_{mf}$) into Eq. 2.128, which results in $u_{mf}/u_{elu} = (\varepsilon_{mf}/\varepsilon_{elu})^{m_{sw}}$, and dividing this with Eq. 2.128, that the expansion equations of Brötz and Richardson a. Zaki are exchangeable, or in other words, formally the same. Consequently, the exponents m_ε and m_{sw} are identical in theory. However, empirical values of them can be different due to measurement errors of expanded bed porosities ε_{bed}, estimation errors of the minimal fluidization porosity ε_{mf}, and imprecise approaches of the minimal fluidization velocity u_{mf} and elutriation velocity u_{elu}.

As described in Section 2.2.2, Richardson a. Zaki have further demonstrated that the exponent m_{sw} is only a function of the terminal Reynolds number Re_s and the particle-to-column diameter ratio d/D. Translated to expanded fluidized beds, it means that this power law exponent is independent from the inlet velocity: $m_{sw} \neq \mathrm{f}(u_{in})$. The exponents, m_ε and m_{sw}, can then be derived from the minimal fluidization and elutriation limits with:

$$m_\varepsilon = m_{sw} = \frac{\ln(u_{mf}/u_{elu})}{\ln(\varepsilon_{mf})} = -\frac{\ln(f_{rn})}{\ln(\varepsilon_{mf})}, \tag{2.129}$$

which was also applied by Sathiyamoorthy a. Sridhar Rao [85,86], as stated in [29,73]. Equation 2.129 further implies that the sinking behavior of a swarm of particles with uniform size and density can also be described by the minimal fluidization velocity of a packed bed of same material and the stationary sinking velocity of a representative single particle situated in stagnant and unconfined fluids. But, as already indicated above, the approaches to minimal fluidization (Section 2.2.4) and stationary settling particles (Section 2.2.1) possess deficiencies (except for the one of Haider a. Levenspiel: Eq. 2.89) in quantifying the fluid-particle momentum transfer for all of the three main flow regimes (laminar, transitional, and turbulent).

The two calculation methods, CMFL-1 and CMFL-2, can be used for approximating the exponent m_ε via f_{rn} obtained by Eq. 2.126. Figure 2.4 illustrates a comparison between the approximation methods m_ε(CMFL-1) and m_ε(CMFL-2) with several functions for the Richardson-Zaki exponent m_{sw} proposed by different authors. From this it follows that both calculation methods m_ε(CMFL-1) and m_ε(CMFL-2) can be suggested for laminar flow conditions due to their good agreement with equations of Richardson a. Zaki (Eqs. 2.95, 2.97, and 2.99, [50]), Rowe (Eq. 2.100, [64]), and Khan a. Richardson (Eq. 2.101, [65]) at $Re_s < 0.1$. For the intermediate flow regime, it is recommended to apply the second calculation method CMFL-2, as it is closer to the correlations of Richardson a. Zaki, Rowe, and Khan a. Richardson than CMFL-1. In addition to this, m_ε(CMFL-2) provides results, which are very similar to the approximation proposed by Kraume (Eq. 2.98, [28]) for the transition regime. The first method CMFL-1 on the contrary matches better with m_{sw}-findings of Richardson a. Zaki, Rowe, and Khan a. Richardson in the quadratic regime.

Once decided for a calculation method for expansion exponent, the bed porosity that occurs at a certain inlet velocity can be calculated either from the point of minimal fluidization or elutriation according to:

$$\varepsilon_{bed}(u_{in}) = \varepsilon_{mf}\left(\frac{u}{u_{mf}}\right)^{1/m_\varepsilon} = \varepsilon_{elu}\left(\frac{u}{u_{elu}}\right)^{1/m_\varepsilon} \quad \text{, with } \varepsilon_{elu} = 1. \tag{2.130}$$

Through continuity conditions, the height of homogeneous fluidized beds H_{bed} can be obtained from the bed mass M_{bed} (or minimal bed height $H_{mf} = M_{bed}/\rho_p/(1-\varepsilon_{mf})/A_{app}$) with

$$H_{bed} = \frac{M_{bed}}{\rho_p(1-\varepsilon_{bed})A_{app}} = \frac{1-\varepsilon_{mf}}{1-\varepsilon_{bed}}H_{mf} \tag{2.131}$$

for cylindrical walls.

2.2.6 Outflow of particles from fluidized beds

Outflow of particles from fluidized beds through openings is caused by dispersion within the fluid (continuous phase) and/or by drag of fluids flowing through the opening. Hampel [2] stated two different approaches for calculating rates of bed discharge in terms of internal classifiers or chamber orifices. The first one was developed Mörl et al. [87] (as stated in [29]) and later used in population balance simulations by Heinrich et al. [88,89]. This approach is based on probability functions of particle-opening collisions, and is therefore seen as a dispersion model. It shall only be briefly mentioned here, as it is not employed in the present thesis. The other calculation method of bed discharge rates, named by Hampel, was introduced by Burgschweiger in [90] and proposed together with Tsotsas later in [91]. It is a semi-empirical approach, that considers fluidized beds as continuous suspension phases and presupposes Torricelli's outflow law to be applicable. Burgschweiger's outflow equation delivers mass flow rates of suspensions $\dot{M}_{out,tor}$ from this segmented function

$$\dot{M}_{out,tor} = \begin{cases} 0 & \text{, for } k_{pul} H_{bed} \leq H_{open} \\ \lambda_{tor} A_{open} \rho_p (1-\varepsilon_{bed}) \sqrt{2g(k_{pul} H_{bed} - H_{open})} & \text{, for } k_{pul} H_{bed} > H_{open} \end{cases}, \tag{2.132}$$

with λ_{tor} symbolizing an empirical flow correction coefficient, A_{open} the cross-section of the opening, $\rho_p(1-\varepsilon_{bed})$ the suspension density (bulk density of fluidized bed), k_{pul} a pulsation factor, and H_{open} the vertical distance from the bottom of fluidized bed to the outflow opening. The prefactor λ_{tor} is called as "inflow parameter" in [91] with reference to an internal classifier tube and is needed to compensate the difference of flow dynamics between conditions of fluidized beds and the Torricelli outflow law of pure liquids. The parameter k_{pul} takes into account pulsation of fluidized beds via

$$k_{pul} = \left(\frac{Re_{in}}{Re_{mf}} \right)^{m_{pul}} = \left(\frac{u_{in}}{u_{mf}} \right)^{m_{pul}}, \tag{2.133}$$

where m_{pul} is another empirical constant. Assuming cylindrical chamber walls, Burgschweiger converted Eq. 2.132 to the following expression

$$\dot{M}_{out,tor} = \begin{cases} 0 & \text{, for } k_{pul} H_{bed} \leq H_{open} \\ \lambda_{tor} \frac{A_{open}}{A_{app}} M_{bed} \sqrt{\frac{2g}{H_{bed}} (k_{pul} - \frac{H_{open}}{H_{bed}})} & \text{, for } k_{pul} H_{bed} > H_{open} \end{cases}, \tag{2.134}$$

wherein the dependency on cross-sectional area and on bed mass is illustrated. The empirical parameters have been determined with $\lambda_{tor} = 0.0316$ and $m_{pul} = 0.2605$ by experiments.

Due to the analogy to Torricelli outflow equation, Burgschweiger's model is less suitable for discharge rates that are dominated by dispersion kinetics, but rather for those mainly caused by the drag of outflowing fluids. The driving force of the Torricelli flow is the pressure difference in front of and behind the outflow cross-section, which is generated by the hydrostatic pressure of liquid columns. That is why, the modified Torricelli approach is seen as a reasonable method for describing the here so-called *Wurster suction rates* of the two-zone continuum model of Wurster fluidization, presented later in Section 7.7.

2.2.7 Size-selective particle separation by air classifiers

The individual particles of polydisperse solids have different sinking velocities, which leads to segregation and separation of particles during the free fall in a fluid. The larger particles settle faster than the smaller ones and concentrate downwards. This effect is used to separate particles according their size and/or density, as for instance in classification processes. A simple method of classification is to insert particles into an upward flow of air within a straight duct, for example in a tube.

Effects in straight-duct air classifiers

Under purely laminar flow conditions with homogeneous velocity u_g, three scenarios of movement of a single non-rotating sphere are possible in dependency on its terminal sinking velocity u_s. Particles settle down to the bottom outlet, if $u_s > u_g$, hover in a constant plane, if $u_s = u_g$, or rise up to the top outlet of the classifier, if $u_s < u_g$. Due to various random transport phenomena, however, the trajectories of particles are chaotic in practice. Rumpf a. Leschonski [92] have described several effects leading to undetermined

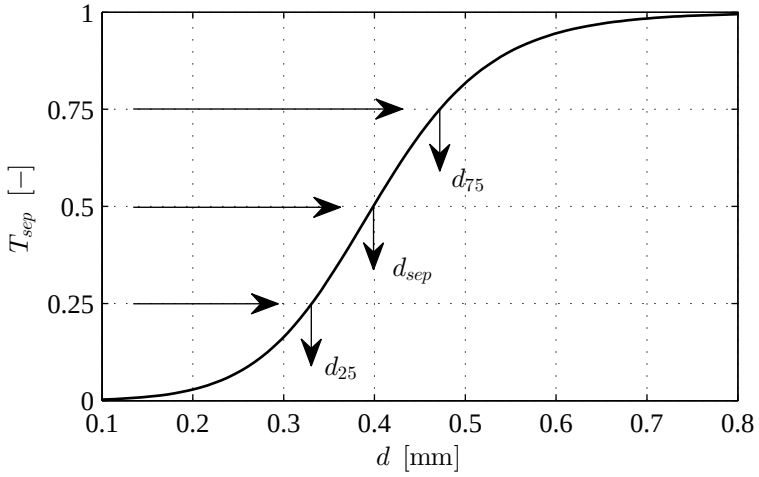

Figure 2.5: Illustration of an exemplary separation function T_{sep} and its characteristic parameters (d_{25}, d_{sep}, and d_{75}).

movement of particles in separators, which are for instance: turbulences of the fluid, the influence of flow separation at particle surfaces on bulk flow, particle-particle and particle-wall collisions, effects of adhesion and hindered sinking (swarm effects, Section 2.2.2), and some other equipment-dependent aspects.

Characteristics of separation curves

The effectiveness of classification processes is characterized by so-called separation curves, here symbolized by T_{sep}, which are defined as probability functions of being discharged in the coarse product outlet of a classifier system (*coarse-product discharge probability*). Their values lie therefore between zero and unity: $0 \leq T_{sep}(d, \rho_p) \leq 1$. The T_{sep}-value of an individual particle in a straight-duct air classifier depends on its sinking velocity, and hereby, on particle size and effective density, see also Section 2.2.1. The *separation diameter* d_{sep} is related to the coarse-product discharge probability of 50 %. It can formally be described by the inverse separation function $T_{sep,inv}$ with:

$$d_{sep} = T_{sep,inv}(T_{sep} = 0.5). \tag{2.135}$$

The particle diameters of coarse-product discharge probabilities of 25 % and 75 % are symbolized by d_{25} and d_{75}. The *separation sharpness* κ_{sep} is a characteristic parameter of separation functions, which represents the efficiency of separation processes. It is defined by the ratio of d_{25} to d_{75}:

$$\kappa_{sep} \coloneqq \frac{d_{25}}{d_{75}} = \frac{T_{sep,inv}(T_{sep} = 0.25)}{T_{sep,inv}(T_{sep} = 0.75)}. \tag{2.136}$$

Figure 2.5 illustrates the positions of d_{25}, d_{sep}, and d_{75} on an exemplary separation curve of spheres with uniform apparent density.

Mean convection velocity, dispersion coefficient, and Bodenstein number

Passing of bulk solids through classifiers can also be viewed as a residence time distribution problem of a partially back-mixed system. This requires the determination of mean axial convection velocities and axial dispersion coefficients of the material flows. Dispersion coefficients are measures of the intensity of back-mixing. At this point, the textbook of Levenspiel [93] is recommended for a deeper understanding of transport dynamics of coupled convection and dispersion. In vertical classifiers, the mean axial convection velocity of the gas is given by the average flow velocity u_g, and the mean axial convection velocity of the particles results from the difference of the average flow velocity to the terminal sinking velocity $u_g - u_s$. The latter can have positive values ($u_g - u_s > 0$), which means that a particle is likely to be raised by the gas flow, or negative values ($u_g - u_s < 0$), which means that a particle is likely to settle down against the flow. A mean convection velocity of zero ($u_g - u_s = 0$) occurs for particles with the separation diameter.

Dispersion coefficient of the fluid elements of a gas is symbolized by $D_{ax,g}$, and $D_{ax,p}$ represents the particle-related dispersion coefficient. Such a distinction was also made by Tomas a. Gröger [94], where the two mixing parameters $D_{ax,p}$ and $D_{ax,g}$ were referred to as turbulent diffusion coefficients (German: "turbulente Diffusionskoeffizienten"). The Bodenstein number is mostly given in literature [94–96] according to:

$$\text{Bodenstein number} = \frac{\text{(mean velocity of convective flow) x (length of flow path)}}{\text{dispersion coefficient}}. \tag{2.137}$$

Applying this to straight-duct air classifiers, the gas-flow-related Bodenstein numbers is obtained by

$$Bo_{ax,g} = \frac{u_g L_{sep}}{D_{ax,g}}, \tag{2.138}$$

and the Bodenstein number for axial dispersion of an individual particle follows from

$$Bo_{ax,p} = \frac{|u_g - u_s| L_{sep}}{D_{ax,p}}. \tag{2.139}$$

Practical values of Bodenstein numbers lie between 0.5 and 50 according to [94]. Levenspiel [93] defines the Bodenstein number by the reciprocal version of Eq. 2.137.

Tomas a. Gröger [94] have further reported that the dispersion coefficients of the gas and particles are equal to one another, if the turbulence field is homogeneous, the particles are much smaller than the size of vortices, and particle concentration is below 5 %. In this case, the axial dispersion coefficients of both material flows are summarized by a *generalized dispersion coefficient* D_{ax}:

$$D_{ax} \coloneqq D_{ax,g} \approx D_{ax,p} \qquad \text{, for } \varepsilon_{sw} > 0.95. \tag{2.140}$$

As quoted by Heinrich [88], it was shown by Tomas a. Gröger [94] that the axial dispersion coefficient of the fluid elements grows proportionally with the mean velocity of convective flow, as well as with the maximum possible vortex diameter, and thereby, with the channel width: $D_{ax,g} \sim u_g \cdot D_{chan}$. Introducing a proportionality constant, called the *turbulence constant* k_{tur} [94], the gas-related dispersion coefficient can be then described by this product:

$$D_{ax,g} \coloneqq k_{tur} u_g D_{chan}. \tag{2.141}$$

Distances between particles are on average smaller for higher particle concentrations, which reduces maximum possible vortex diameters. The turbulence constant is therefore a function of swarm volume fraction $\varepsilon_{sw,s}$. Heinrich et al. [88, 89] have written that the turbulence constant depends also on individual design of the separator

$$k_{tur} = \text{f}(\varepsilon_{sw,s}, \text{separator design}) \tag{2.142}$$

and must be derived from experimental results.

Axial dispersion coefficient of straight-tube classifiers with homogeneous turbulence field

The design of cylindrical straight-duct classifiers is characterized only by the tube length L_{sep}, the inner tube diameter D_{sep}, and the position of the feed. By definition, axial dispersion coefficients are independent from the length of the separation channel:

$$\{D_{ax}, D_{ax,g}, D_{ax,p}\} \neq \text{f}(L_{sep}). \tag{2.143}$$

According to Eq. 2.141, which implies that $D_{ax,g} \sim D_{sep}$, and to Eq. 2.143, the turbulence constant can only be a function of the swarm concentration:

$$k_{tur} = \text{f}(\varepsilon_{sw,s}) \qquad \text{, for straight-tube classifiers.} \tag{2.144}$$

At this point it should be noted that a functional relationship between a turbulence constant and the position of the particle feed does not make any physical sense, but the particle entry location has an impact on the separation behavior.

Drift-and-dispersion models of Molerus and Molerus a. Hoffmann

Molerus [97] considered the transport of particles in straight-duct air classifiers as a continuous-time Markov process, which can be described by the partial differential equation of Fokker [98], Plank [99] and Kolmogorov [100]. Different names for this equation can be found in the literature: e.g., often as "Fokker-Plank equation", in [97] as "Kolmogoroff-Fokker-Plank equation", and sometimes also as "Kolmogorov forward equation". Assuming that random motion of particles only depends on current state, and not on past processes, and the diffusion coefficient of particles to be constant, Molerus [97] derived the following separation function of a straight-duct air classifier by integrating the Fokker-Plank equation:

$$T_{sep}(d) = \frac{1}{1 + \exp\left(\frac{(u_g - u_s)L_{sep}}{2D_{mix}}\right)}, \tag{2.145}$$

where $u_g - u_s$ (in [97] symbolized by "u") denotes the absolute (system-related) average velocity of a particle in vertical direction, L_{sep} the total length of classifier channel, and D_{mix} (in [97] symbolized by "D") the intensity of mixing or irregular movement. The latter was introduced by Molerus as a constant substituent within the integration. This factor D_{mix} is called the mixing coefficient in [97] and should not be confused with the axial dispersion coefficient $D_{ax,p}$, which corresponds to the diffusion coefficient of the Brownian motion described by Einstein [101]. The meaning of coefficients of the Fokker-Plank equation was also explained earlier by Molerus in [102]. It is further stated in [97] that the entire argument of the exponential term in Eq. 2.145 can be seen as Bodenstein number (compare with Eq. 2.139). However, this definition is related to the sinking velocity of individual particles, and therefore, unsuitable as an overall measure for separation imperfections. But, Molerus [97] showed for the laminar case that the ratio $u_g L_{sep}/2D_{mix}$ correlates with the slope of the separation curve at the separation diameter d_{sep}, which is why $u_g L_{sep}/2D_{mix}$ is a measure of the separation sharpness.

Two years later, Molerus a. Hoffmann [103] have enhanced the approach of Eq. 2.145 to

$$T_{sep}(d) = \frac{1}{1 + \frac{u_s(d_{sep})}{u_s(d)} \exp\left(\frac{u_s(d_{sep})L_{sep}}{2D_{mix}}\left(1 - \frac{u_s(d)}{u_s(d_{sep})}\right)\right)}, \tag{2.146}$$

in which a pre-exponential term has been added and the sinking velocity of the separation diameter $u_s(d_{sep})$ (in [103] symbolized by "w_{ft}") was used instead of the mean gas velocity u_g. At this, it is determined that

$$u_s(d_{sep}) \coloneqq u_g, \tag{2.147}$$

in order to most reasonably meet the definition of the separation diameter in Eq. 2.135. The separation curves of Molerus (Eq. 2.145) and Molerus a. Hoffmann (Eq. 2.146) can be applied for straight-channel separators with arbitrary shapes of cross-section, because both approaches were derived from the one-dimensional variant of the Fokker-Plank equation and wall effects were neglected too.

The name "drift-and-dispersion model" shall indicate that the approaches of Molerus (Eq. 2.145) and Molerus a. Hoffmann (Eq. 2.146) were derived from the Fokker-Plank equation, which contains a *convective transport term* (*drift*) and a *diffusive transport term* (*dispersion*).

Heinrich's extension of the model of Molerus a. Hoffmann

Heinrich [88] employed the model of Molerus a. Hoffmann (Eq. 2.146) to calculate the internal classification of continuous granulation processes with

$$T_{sep}(d) = \frac{1}{1 + \frac{u_g}{u_s(d)} \exp\left(-\frac{(u_s - u_g)L_{sep}}{D_{ax,p}}\right)}, \tag{2.148}$$

as also presented later by Heinrich et al. [89,104]. Behind the argument of the exponential term in Eq. 2.148 hides the particle-related Bodenstein number of Eq. 2.139, as it was already indicated by Molerus in [97]. The particle-related axial dispersion coefficient was described by Heinrich with

$$D_{ax,p} \approx D_{ax,g} = k_{tur} u_g D_{sep}, \tag{2.149}$$

based on the aforementioned simplifications of Tomas a. Gröger (resulting in Eq. 2.141). Heinrich's extended version of Molerus a. Hoffmann was used later in simulation studies of Hampel [2] and of the author of the present thesis in cooperation with Bück and Tsotsas [105]. In [105], the separation function was reformulated to present it in a reduced form, where the mean gas velocity u_g and the gas-related Bodenstein number $Bo_{ax,g}$ are the only particle-size-independent parameters, which is detailed later in Section 5.2.

2.3 Reference case of the continuous granulation from Hampel

Continuous layerwise granulation with external product classification was investigated by Hampel [1, 2] experimentally and with population balance simulations. The experimental setup and the PB-model of Hampel (PB: population balance) form the starting point for the present thesis. The methods of Hampel's reference case are described in the following.

2.3.1 Experimental configuration and operation principle

The experiments of Hampel's work were conducted with a ProCell LabSystem of the company Glatt GmbH with a Wurster granulation chamber and an externally installed straight-duct air classifier, as illustrated in Figure 2.6. A more detailed description of the experimental configuration, the components used, and the main dimensions of the plant can be found in Section 9.2 and Figure C.2. The conical process chamber was joint to the nuclei feeding and classification equipment via double-pinch valves utilized as particle sluices. The feed-related double-pinch valve (nuclei feeder) and the classifier-related double-pinch valve (bed discharger) control the nuclei feed rate and particle inlet flow rate of the classifier, respectively. The design and operation principle of both particle sluices are detailed in Sections 9.4.1 and 9.4.2. A gas distributor plate, which consists of several sections of different perforation degrees, specified in Appendix C.2.3, was assembled at the bottom of the process chamber. The average perforation degree below the Wurster tube is larger than in the outer area of the distributor plate. Thereby, higher gas velocities are created in the middle region of the process chamber and particles are dragged through the Wurster tube, which is also sometimes denoted as "riser", [106]. A two-substance nozzle was installed in the center of the distributor plate, from where the nozzle orifices reached out into the lower part of the Wurster tube. There, the spray solution is atomized and deposits on up-flowing particles, due to which, the internal space of the Wurster tube is regarded as the *spray zone* (indicated by α). Process gas velocities are lowered above the spray zone, whereby particles fall back into the fluidized bed region, which is located in the exterior of the Wurster tube and which is referred to as the *drying zone* (indicated by $1-\alpha$). In the drying zone, the remaining spray solvent (often water) evaporates efficiently from particle surfaces. During operation, a moderate amount of bed granules passes the granulator-classifier connection channel (involving one double-pinch valve) and gets separated by the classifier air into a coarse and a fine fraction, mal-discharges by dispersion (Section 2.2.7) included. The granules coming out of the lower outlet of the separation tube is named the product discharge or, for short, just the product. The fine fraction is pneumatically conveyed back into the granulator via the upper classifier opening and a curved connection tube. These granules are related to the so-called recycle flow or just recycle. Beside this, the bed mass needs to be controlled in order to ensure appropriate fluidization and drying conditions and to avoid process instabilities. This had been achieved by manipulating the classifier gas velocity, and thus, the product discharge rate. The bed mass controller was designed according to a second-order cascade structure containing an inner and outer feed-back loop. A proportional-derivative controller formed the outer loop, where the bed mass (obtained by pressure drop measurements) serves as input signal, and which generates a target value for the classifier gas velocity as output signal. This target value is forwarded to a mass flow controller of the classifier gas, which is seen as the inner loop of the cascade structure, and which behaves after a proportional–integral–derivative control characteristic. The entire control system was able to keep the holdup (bed mass) in a range of stable granulation and fluidization in experiments lasting eight to ten hours. The inline detection method of the bed mass is described in Section 9.4.7. The control and monitoring system was modified in the scope of the present work, as shown in Section 9.4.8.

2.3.2 Three-compartment population balance model

Background of population balance models

The framework of population balances can be used to describe particle growth processes on a macroscopic level. Ramkrishna [107] provided a comprehensive introduction in the basics of this methodology. PB-modeling goes back to the work of Hulburt a. Katz [108] in the field of statistical mechanics, and was later employed by Randolph a. Larson [109] in the field of crystallization, and by Mörl et al. [29,110] for layerwise granulation with internal product classification. Using a population balance model with three functional compartments (zones), Hampel [1, 2] generated simulation results of continuous granulation with external product classification, which showed a good agreement with experimental data. A reproduction of Hampel's model structure can also be found in [105]. There, it is referred to as a "two-zone" population balance model,

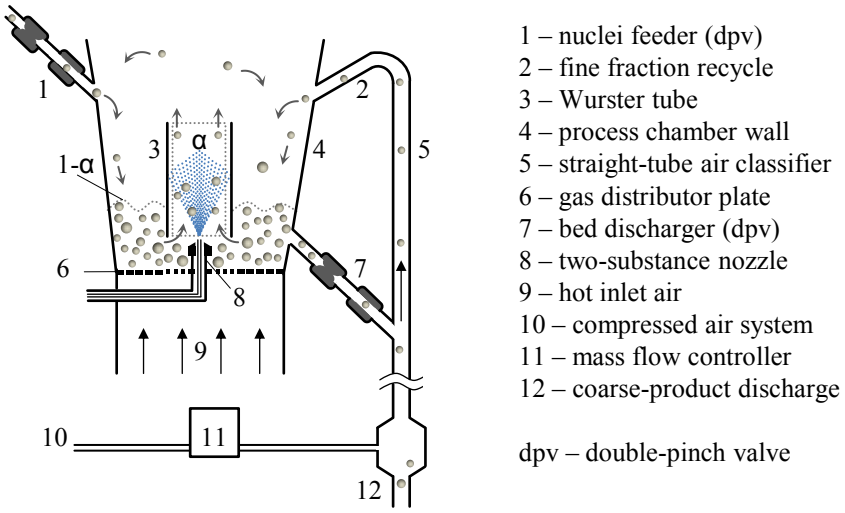

Figure 2.6: Illustration of the experimental setting of Hampel's reference case [1, 2].

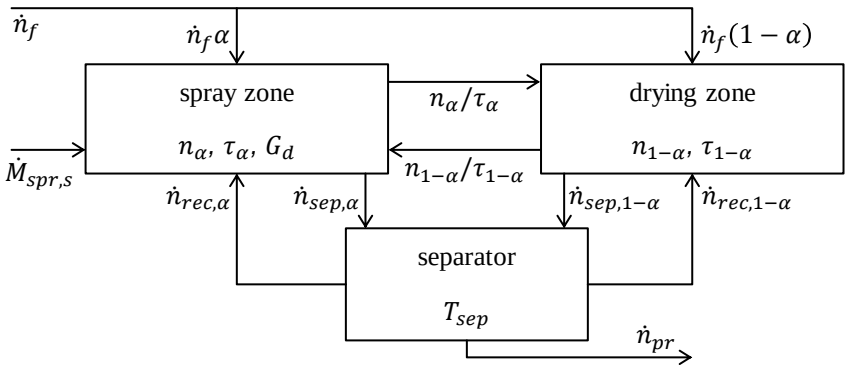

Figure 2.7: Flowsheet of Hampel's three-compartment population balance model [1, 2].

because only two PB-equations are needed to describe the processes in all three compartments, as explained below. Compartmental population balance models have been applied by many other authors before, as for instance with regard to calculation of layer porosities by Hoffmann et al. [111], prediction of layer volume distributions by Li et al. [112], influences of drying conditions on layer porosity by Rieck et al. [113], and influences of spray zone volume fraction and drying zone residence time on granulation stability by Bück et al. [114]. Hampel's three-compartment model is not to be confused with the PB-model of spray granulation from Maronga a. Wnukowski [115], which consists of a spray zone, a drying zone and a third zone, where particles are "not directly involved in the granulation process".

Main assumptions

The here so-called *three-compartment population balance model* of Hampel (not denoted by that in [1, 2]) is a simplified representation of the experimental process described in Section 2.3.1 and illustrated in Figure 2.6. For reasons of moderate complexity, the following assumptions have been made. The particles of the entire system are viewed to be spherical and their size (here diameter) to be the only distributed property. Typically, apparent granule density changes in layer-by-layer granulation processes, in particular, for core particles built up with coating layers of different materials. But a second internal coordinate of particle density is omitted in this model, as it would make the implementation and numerical simulation much more difficult. For example, the description of the initial condition of a two-dimensional distribution function for non-coated particles poses great challenges. In [1], the nuclei (core particles) and coating layers were considered to be the same type of material, but the value of its apparent density was not specified. In [2], the material properties of the two components were different, given with $\rho_f = 1380\,\mathrm{kg/m^3}$ for the effective density of the nuclei, with $\rho_{s,c} = 1440\,\mathrm{kg/m^3}$ for the compact solid density of the coating layer, and with $\varepsilon_c = 43\,\%$ for the coating layer porosity. The mass flow rates of nuclei feed $\dot{M}_f$ and sprayed solids $\dot{M}_{spr,s}$ are constant. Material losses of core and coating materials due to elutriation with process gas or adherence to chamber walls were disregarded. As the title of this subsection already reveals, granules are only situated in three compartments: the spray zone, the drying zone, and the separator. In Wurster granulation processes, the spray zone can be seen as the interior and the drying zone as the exterior of the Wurster tube. Applications of this model for top-spray or bottom-spray granulators are also possible. Exchange times between the zones, such as in the fall-down region above the drying zone, in the granulator-separator connection channel, or in the curved recycle tube are not taken into account. The residence time in the spray zone (symbolized by τ_α) and in the drying zone (symbolized by $\tau_{1-\alpha}$) are time-invariant and equal among all granules. The spray and drying zone shall be ideally back-mixed systems. The product classification is assumed to be quasi-stationary, so that the residence time of granules in the separator can be assumed with zero. Only layerwise growth takes place and other effects such as nucleation through premature drying of non-deposited spray droplets, particle-particle aggregation, or dis-aggregation by breakage and attrition are neglected. For an insight into a more precise description of PB-rates of those particle forming phenomena, reference is made to the contributions of Mörl [116], Hounslow et al. [117], Abberger [118], and Salman et al. [119]. The growth rate of single particles is supposed to be size-independent ($G_d \neq \mathrm{f}(d)$), which is known as even growth.

Structure of compartments and material flows

The structure of Hampel's model is illustrated by the flowsheet in Figure 2.7. The depicted flows of particulate materials are represented by several non-normalized and number-based density distribution flow rates, with $\dot{n}_f$ for the nuclei feed, n_α/τ_α for wet granules flowing from the spray zone to the drying zone, $n_{1-\alpha}/\tau_{1-\alpha}$ for dry granules being sucked from the drying zone into the spray zone, $\dot{n}_{sep,\alpha}$ and $\dot{n}_{sep,1-\alpha}$ for bed granules entering the separator, $\dot{n}_{rec,\alpha}$ and $\dot{n}_{rec,1-\alpha}$ for the fine fraction recycle from the classifier, and $\dot{n}_{pr}$ for the product discharge at the classifier bottom. The symbols n_α and $n_{1-\alpha}$ are the number density distributions of granules in the spray zone and in the drying zone. The reciprocals of the residences times τ_α and $\tau_{1-\alpha}$ are frequency factors for calculating the particle circulation in Wurster fluidization. The outlet of the spray zone conforms with the inlet of the drying zone, and vice versa. The constraint of Börner et al. (equation "19" in [106]):

$$\tau_{1-\alpha} = \tau_\alpha \frac{1-\alpha}{\alpha}, \tag{2.150}$$

was applied in the PB-model of Hampel. Equation 2.150 was derived from stationary mass balance of Wurster circulation with constant proportions in the spray zone and drying zone. The proportion factor α (equation "20" in [106]) was defined as mass fraction of spray zone particles with respect to the entire bed mass. On the contrary, the parameter α was referred to as volumetric ratio of the Wurster tube to the entire

fluidized bed in Hampel's work [1, 2]. However, the value of α was freely estimated with 1 % in simulations of [1] and much greater with 10 % in [2]. In either case, Hampel's simulation results approach the author's experimental PSD-curves of bed and product samples.

In the experiments of Hampel, the nuclei and fine fraction recycle of the classifier were fed only into the drying zone, and not into the spray zone. In the same way, bed particles could only be discharged from the drying zone to the separator, and not from the spray zone. In the simulations, however, these material flows are connected to both zones of the granulator. This may have hardly any significant influence on the overall development of simulated bed- and product-PSDs, due to the high exchange rates of the PB-equations. The flow rates of nuclei and the recycled granules are separated by proportion parameter α according to:

$$\dot{n}_{i,\alpha}(d) \coloneqq \dot{n}_{i,\alpha}(d) \cdot \alpha \qquad \text{, for } i \in \{f, rec\}, \tag{2.151}$$

$$\dot{n}_{i,1-\alpha}(d) \coloneqq \dot{n}_{i,1-\alpha}(d) \cdot (1-\alpha) \qquad \text{, for } i \in \{f, rec\}. \tag{2.152}$$

The distribution flow rates of the classifier inlet ($\dot{n}_{sep,\alpha}$ or $\dot{n}_{sep,1-\alpha}$) are defined by ratios of the corresponding number density distribution (n_α or $n_{1-\alpha}$) to a constant time parameter (symbolized by τ_{bed}):

$$\dot{n}_{sep,j}(d,t) \coloneqq \frac{n_j(d,t)}{\tau_{bed}} \qquad \text{, for } j \in \{\alpha, 1-\alpha\}. \tag{2.153}$$

The time parameter τ_{bed} roughly conforms with the mean residence time in the granulator under steady state conditions, but it clearly differs from the residence time in the entire granulator-separator system, which can be rather seen as a product growth time. The reciprocal of τ_{bed} represents a *separation frequency factor* of the bed granules, as continued later in Section 5.2.

PB-equations

The number density distribution of the entire granulator (symbolized by n_{bed}) is obtained by

$$n_{bed}(d,t) = n_\alpha(d,t) + n_{1-\alpha}(d,t) \tag{2.154}$$

at any time during simulation, but predefined with $n_{bed}(d, t=0) = n_\alpha(d, t=0)/\alpha = n_{1-\alpha}(d, t=0)/(1-\alpha)$ in the initial condition. The assumption of quasi-stationary classification delivers a simple relation between the number density flow rates of the classifier inlet $\dot{n}_{sep,j}$, the recycle $\dot{n}_{rec,j}$, and the product discharge $\dot{n}_{pr,j}$ with:

$$\dot{n}_{sep,j}(d,t) = \dot{n}_{rec,j}(d,t) + \dot{n}_{pr,j}(d,t) \qquad \text{, for } j \in \{\alpha, 1-\alpha\}; \tag{2.155}$$

but, it also allows to calculate the number density flow rates of the recycle and product outlets by the respective separator inlet flow rates $\dot{n}_{sep,j}$ and the separation function T_{sep} with:

$$\dot{n}_{rec,j}(d,t) = \dot{n}_{sep,j}(d,t)\big(1 - T_{sep}(d,t)\big) \qquad \text{, for } j \in \{\alpha, 1-\alpha\} \tag{2.156}$$

$$\dot{n}_{pr,j}(d,t) = \dot{n}_{sep,j}(d,t) T_{sep}(d,t) \qquad \text{, for } j \in \{\alpha, 1-\alpha\}. \tag{2.157}$$

In PB-modeling of ideally back-mixed systems, layerwise particle growth is described by convection of particles only along the internal size coordinate, which is mathematically expressed as the partial derivative of the product of the growth rate G_d and the number density distribution of particles involved in the growth process. In Hampel's reference case, a growth term is only considered in the population balance of the spray zone (n_α). However, the growth rate was calculated by

$$G_d(t) = \frac{\mathrm{d}d}{\mathrm{d}t} = \frac{2\dot{M}_{spr,s}}{\rho_c \int_0^\infty \pi d^2 n_{bed}(d,t)\mathrm{d}d}, \tag{2.158}$$

according to the approach of Mörl [29, 73] with the solids spray rate $\dot{M}_{spr,s}$ depositing on the total surface area of the entire bed $A_{bed} = \int_0^\infty \pi d^2 n_{bed} \mathrm{d}d$. The growth rate of Mörl is also described in Appendix B.2. At this point, it is mentioned that the G_d-definition used for the PB-simulations of the present thesis is somewhat different from Eq. 2.158 with $\int_0^\infty \pi d^2 n_\alpha \mathrm{d}d$ as sprayed surface area, more on this in Section 5.2. For calculating the external product classification, Heinrich's extended version [88, 89] of the drift-and-dispersion model of Molerus a. Hoffmann [103], given with

$$T_{sep}(d,t) = \frac{1}{1 + \frac{u_g(t)}{u_s(d)} \exp\left(-\frac{\big(u_s(d) - u_g(t)\big) L_{sep}}{k_{tur} u_g(t) D_{sep}}\right)}, \tag{2.159}$$

was employed. The background to the development of this separation curve is detailed in Section 2.2.7. The particularity here is that the classifying gas velocity u_g is manipulated for means of bed mass control (Eq. 2.162) and is therefore presented as a function of time in Eq. 2.159. The turbulence constant has been assumed with $k_{tur} = 2$.

Putting everything together, the population balances ensue to

$$\frac{\partial n_\alpha(d,t)}{\partial t} = -\frac{n_\alpha(d,t)}{\tau_\alpha} + \frac{n_{1-\alpha}(d,t)}{\tau_{1-\alpha}} + \dot{n}_f(d)\alpha - \frac{\partial}{\partial d}(G_d(t)n_\alpha(d,t)) - \frac{n_\alpha(d,t)}{\tau_{bed}}T_{sep}(d,t), \tag{2.160}$$

for the spray zone, and to

$$\frac{\partial n_{1-\alpha}(d,t)}{\partial t} = \frac{n_\alpha(d,t)}{\tau_\alpha} - \frac{n_{1-\alpha}(d,t)}{\tau_{1-\alpha}} + \dot{n}_f(d)(1-\alpha) - \frac{n_{1-\alpha}(d,t)}{\tau_{bed}}T_{sep}(d,t), \tag{2.161}$$

for the drying zone. Only these equations are seen as population balances in previous work [105]. But strictly speaking, population balances are to be made for each compartment of the model. Equation 2.155 is therefore a PB-equation too. However, it was neglected in [105] due to the assumption of a quasi-stationary conditions in the separator.

Bed mass controller

In contrast to the experiments, the bed mass controller of Hampel's PB-model [2] was designed according to a proportional single-loop structure:

$$u_g(t) = u_0 - K_m\big(M_{bed}(t) - M_{set}\big), \tag{2.162}$$

in which the separation gas velocity u_g is the manipulated variable. The P-control function of Eq. 2.162 was not presented in [1]. In [2], the gas velocity of *zero-control-deviation* u_0 (*offset*) was out. However, it is stringently required to be larger than zero, [105]; otherwise the control function would give out negative values, if the bed mass M_{bed} rises above the set point M_{set} (target value). Furthermore, Eq. 2.162 has the disadvantage that a velocity of zero or even negative values can be obtained, when the bed mass exceeds the zero root of the P-control function:

$$u_g(t) \leq 0 \qquad \text{, if } M_{bed}(t) \geq M_{set} + \frac{u_0}{K_m}. \tag{2.163}$$

This would lead either to division-by-zero errors or to inadequate values of the separation function T_{sep} in Eq. 2.159 within the simulation. Those bed mass excesses were not reached in the simulations of Hampel, so that the results could be evaluated. Nevertheless, such values might appear for different parameter settings, e.g., for higher solids spray rates, where bed mass grows faster during the startup. In order to avoid this, a *securing function* was implemented into bed mass controller of the present thesis, as shown later in Section 5.2. The gain factor K_m and the set point M_{set} were fixed with 12 m/s/kg and 1 kg, respectively, in [2].

3 Ideal continuous layerwise granulation model

The ideal continuous layerwise granulation model has been created in the framework of the present thesis in order

- to derive relations between process parameters and desired product characteristics,
- to work out diverse processing strategies within a simulation study with the three-compartment population balance model (Chapters 5 and 6) and in experiments (Sections 9.4 and 10.4), and
- to provide estimation methods of diverse average particle characteristics of the fluidized bed granules (in terms of size and apparent density) for calculating the limits of fluid-particle transport dynamics such as the minimal fluidization gas velocity and the elutriation gas velocity (Sections 2.2.4 and 7.6).

This model is also called ideal two-component particle growth model, ideal particle growth model, ideal granulation model or ICLG-model.

3.1 Model concept

3.1.1 Assumptions

The following simplifications have been made for the ideal two-component particle growth model.

1. Steady state conditions have been reached.
2. External nuclei (feed of core particles) and product granules are mono-sized and spherical.
3. Nuclei feed rate $\dot{M}_f$ and solids spray rate $\dot{M}_{spr,s}$ are constant.
4. Bed granules consist of two components: a spherical core and coating of either the same or of different type of material.
5. Effective core density ρ_f and effective coating layer density ρ_c are uniform in the entire bed.
6. The system residence time (time from entrance to product discharge) of the non-lost portion of bed granules (or cores) is uniform.
7. Particle growth only takes place layerwise and not through aggregation.
8. The core material does not break.
9. Nuclei of the coating component formed by premature drying of spray droplets and coating fragments due to breakage or attrition are immediately discharged with process gas and/or attached to walls.

A special case of the ideal particle growth model, where material losses and nucleation and breakage of the coating component are neglected, has also been shown in a previous publication of the presenter of this thesis in collaboration with Bück and Tsotsas [105]. Figure 3.1 illustrates the ideal particle growth process as convection along internal coordinates, whose relations are explained below.

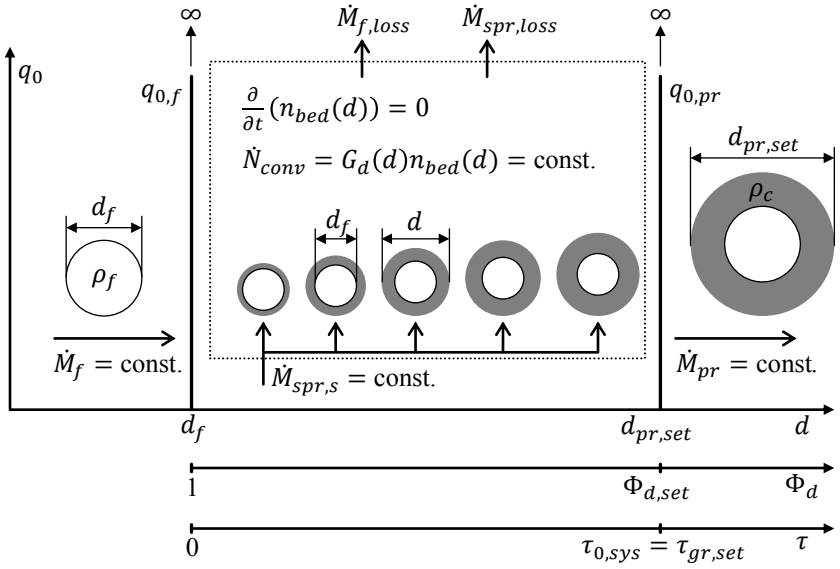

Figure 3.1: Illustration of the ideal continuous layerwise granulation model.

3.1.2 Similarities and differences to the granulation model of Mörl et al.

A layerwise granulation model similar to the present ICLG-model has been developed by Mörl et al. [110] and later cited in [73, 88, 116, 120]. A short summary of it was given by Mörl et al. in [29], see p. 53-58. The assumptions of the present granulation model, except for 4, 5, and 9, are the same in the model of Mörl et al. [110]. Moreover, Mörl et al. [110] restricted their model only to even growth, meaning that the spray liquid is "uniformly distributed onto particle surface". It is later shown that the assumptions 1-9 do not require the growth rate to be size-independent ($G_d \neq \text{f}(d)$), but the ICLG-model can be formulated for size-dependent growth ($G_d = \text{f}(d)$) too without any mathematical contradictions. In [110], the bed granules were also considered to be spheres, but a distinction between core and coating density was not made. In contrast to this, the materials of the components can be different or equal here: $\rho_f \neq \rho_c$ or $\rho_f = \rho_c$. In addition, the present model is combined with a one-dimensional population balance of the granulator (Section 3.3.1), by which the bed granule size distribution is described as function of the overall residence time and the growth rate function. Material losses of the cores ($\dot{M}_{f,loss}$) and the sprayed solids ($\dot{M}_{spr,loss}$) by discharge with process gas and adhesion to chamber walls are further considered here. Nuclei that are formed by sprayed solids (e.g., premature drying or destructive coating) are not taken into account in the population balance of the ICLG-model in Section 3.3.1. Instead, their effects on overall mass balances is subsumed by the material loss fraction (Section 3.2.1).

3.1.3 Definition of particle-related characteristics

The following parameters are introduced to describe and/or characterize continuous granulation processes according to the ideal particle growth model. The diameter of external nuclei (cores) d_f and the effective densities of the components ρ_f and ρ_c can be seen as given properties and the desired product diameter $d_{pr,set}$ as target value of granulation. Other characteristics can then be derived from them.

Desired particle growth ratio and relative bed granule diameter

The desired particle growth ratio $\Phi_{d,set}$ is defined by the ratio of the desired product size $d_{pr,set}$ to the nuclei feed diameter d_f:

$$\Phi_{d,set} \coloneqq \frac{d_{pr,set}}{d_f} > 1. \tag{3.1}$$

This ratio is also referred to as desired growth ratio or target-growth ratio. The desired product size shall be larger than external nuclei ($d_{pr,set} > d_f$), wherefore the desired growth ratio $\Phi_{d,set}$ has values greater than

unity. This way, division by zero is avoided in the calculation of moments of the bed particle size distribution, later on in Section 3.4. The desired particle growth ratio is seen as desired granule size enlargement and denoted by "dimensionless product diameter" in the similar model of Mörl et al. [29]. It is aimed in this thesis, to express diverse characteristics of the ICLG-model, such as

- the nuclei feed rate and solids spray rate (Section 3.2),
- the growth rate and required growth time (Section 3.4), or
- the relative product sinking velocity (Section 3.6),

as function of the desired particle growth ratio. The relative bed granule diameter Φ_d, also named as relative particle diameter, is given by the ratio of the arbitrary bed granule diameter d to the nuclei diameter d_f:

$$\Phi_d \coloneqq \frac{d}{d_f} \geq 1. \tag{3.2}$$

Its values range from unity to the target-growth ratio ($1 \leq \Phi_d \leq \Phi_{d,set}$) as also depicted in Figure 3.1. The relative particle diameter Φ_d is used to describe the change in effective bed particle density ρ_p with particle growth. The reciprocal of the third power of the relative particle diameter Φ_d^{-3} conforms with the volume fraction of the core in a particle of size d, and the coating volume fraction in a particle of size d is defined by $1 - \Phi_d^{-3}$.

Coating-to-core density ratio

The coating-to-core density ratio Φ_ρ, also referred to as component density ratio, is defined by the ratio of the effective coating density ρ_c to the effective density of the (core) nuclei material ρ_f:

$$\Phi_\rho = \frac{\rho_c}{\rho_f} = \frac{\rho_{s,c}(1-\varepsilon_c)}{\rho_{s,f}(1-\varepsilon_f)}. \tag{3.3}$$

It is related to the compact solid densities ($\rho_{s,f}$ and $\rho_{s,c}$) and porosities (ε_f and ε_c) of each component. In layer-by-layer granulation processes, where nuclei and coating are made of different types of materials, the component density ratio can be either unequal or equal to unity. In so-called layering processes, where the core and coating materials are the same, it is appropriate to assume a component density ratio of unity.

Effective density of bed and product granules

Based on the spherical two-component particle geometry and Eqs. 3.1 and 3.2, the effective density of bed granules ensues to

$$\rho_p = \rho_f \Phi_d^{-3} + \rho_c(1 - \Phi_d^{-3}) = \rho_f\big((1-\Phi_\rho)\Phi_d^{-3} + \Phi_\rho\big), \tag{3.4}$$

and the effective density of product particles to:

$$\rho_{pr} = \rho_f \Phi_{d,set}^{-3} + \rho_c(1 - \Phi_{d,set}^{-3}) = \rho_f\big((1-\Phi_\rho)\Phi_{d,set}^{-3} + \Phi_\rho\big). \tag{3.5}$$

The overall effective density of a two-component particle was also described by Heinrich [88] with factually the same equation, but with different notation.

Normalized effective particle density

The normalized effective particle density (symbolized by ξ_ρ) describes the relative change in bed particle density with growth in a dimensionless manner according to

$$\xi_\rho(\Phi_d) \coloneqq \frac{\rho_p(\Phi_d) - \rho_f}{\rho_c - \rho_f} = \frac{\rho_p(\Phi_d)/\rho_f - 1}{\Phi_\rho - 1} \qquad \text{, for } \Phi_\rho \neq 1, \tag{3.6}$$

with values between zero and unity, but only for coating-to-core density ratios not being unity. It can be shown by inserting Eq. 3.4 into Eq. 3.6 that the normalized effective particle density equals the volume fraction of the coating in a particle of size d:

$$\xi_\rho = 1 - \Phi_d^{-3} \qquad \text{, for } \Phi_\rho \neq 1. \tag{3.7}$$

The normalized effective particle density of the external nuclei is given with zero ($\xi_\rho(\Phi_d = 1) = 0$) and of the product with

$$\xi_{\rho,pr} = 1 - \Phi_{d,set}^{-3}. \tag{3.8}$$

The normalized effective particle density of bed granules increases with growth (Φ_d) and can reach unity for infinitely large desired particle growth ratios: $\xi_{\rho,pr}(\Phi_{d,set} \to \infty) = 1$. Through Eqs. 3.7 and 3.8, it becomes obvious that the normalized particle density is independent from the component densities: $\xi_\rho \neq \mathrm{f}(\rho_f, \rho_c)$.

3.1.4 Definition of process parameters

The fluidized bed mass, the nuclei feed rate, and the solids spray rate are process parameters that determine granulation kinetics. Based on them, the following parameters - material loss fractions, required and effective spray-to-feed rate ratio, and bed-mass-specific rates of nuclei feed and spray solids - are introduced to characterize continuous granulations processes.

Material loss fractions

In a real system, material losses of the core mass (denoted by $\dot{M}_{f,loss}$) and sprayed solids (denoted by $\dot{M}_{spr,loss}$) occur by adhesion to chamber walls and by mal-discharge in the exhaust gas. They must be considered in mass balances. For this reason, the mass loss fraction of external nuclei (cores)

$$\Phi_{f,loss} \coloneqq \frac{\dot{M}_{f,loss}}{\dot{M}_f} \tag{3.9}$$

and the mass loss fraction of sprayed solids (coating)

$$\Phi_{spr,loss} \coloneqq \frac{\dot{M}_{spr,loss}}{\dot{M}_{spr,s}} \tag{3.10}$$

are introduced. The core loss fraction $\Phi_{f,loss}$ can be neglected for large external nuclei. Both loss fractions are difficult to measure. Rough estimates of overall material loss (cores and coating) are generated from results of the discontinuous granulation experiments of this thesis (Section 10.1.4).

Required and effective spray-to-feed rate ratio

The required spray-to-feed rate ratio $\Phi_{m,set}$ is defined by the ratio of the solids spray rate $\dot{M}_{spr,s}$ to the feed rate of external nuclei $\dot{M}_f$:

$$\Phi_{m,set} \coloneqq \frac{\dot{M}_{spr,s}}{\dot{M}_f}. \tag{3.11}$$

It is later shown that this ratio is fixed by the desired growth ratio $\Phi_{d,set}$ due to the assumptions of the ICLG-model, to which the attribute "required" refers. The effective spray-to-feed rate ratio $\Phi_{m,eff}$ is formulated in the same way as $\Phi_{m,set}$, only that the material losses are excluded:

$$\Phi_{m,eff} \coloneqq \frac{\dot{M}_{spr,s}(1 - \Phi_{spr,loss})}{\dot{M}_f(1 - \Phi_{f,loss})}. \tag{3.12}$$

The numerator $\dot{M}_{spr,s}(1 - \Phi_{spr,loss})$ of this equation can be seen as effective solids spray rate and the denominator $\dot{M}_f(1 - \Phi_{f,loss})$ as effective nuclei feed rate.

Bed-mass-specific rates of nuclei feed and sprayed solids

The bed-mass-specific nuclei feed rate $\dot{m}_f$ (short specific feed rate) and the bed-mass-specific solids spray rate $\dot{m}_{spr,s}$ (short: specific solids spray rate) are introduced with

$$\dot{m}_f = \frac{\dot{M}_f}{M_{bed}}, \tag{3.13}$$

and

$$\dot{m}_{spr,s} = \frac{\dot{M}_{spr,s}}{M_{bed}} = \frac{\dot{M}_{spr} x_s}{M_{bed}}. \tag{3.14}$$

as measures for growth kinetic related characteristics such as the required growth time and the growth rate, more on this later.

3.2 Relationship between process and product parameters

3.2.1 Mass balances of the entire system

Particle-related mass flow rates

The nuclei feed rate $\dot{M}_f$ and the product discharge rate $\dot{M}_{pr}$ can be expressed by the respective total number flow rate of particles ($\dot{N}_f$ and $\dot{N}_{pr}$) and single particle masses (M_f and M_{pr}) with

$$\dot{M}_f = \dot{N}_f M_f = \dot{N}_f \rho_f \frac{\pi}{6} d_f^3 \tag{3.15}$$

and

$$\dot{M}_{pr} = \dot{N}_{pr} M_{pr} = \dot{N}_{pr} \rho_{pr} \frac{\pi}{6} d_f^3 \Phi_{d,set}^3. \tag{3.16}$$

As the product particles consist of the mass of two components (core and coating), the product discharge rate can be expressed by a sum of mass flow rates of the components according to:

$$\dot{M}_{pr} = \dot{M}_{pr,core} + \dot{M}_{pr,c}, \tag{3.17}$$

where $\dot{M}_{pr,core}$ stands for the core material fraction and $\dot{M}_{pr,c}$ for the coating material fraction in the product discharge. These component-related discharge rates are also associated with the total number discharge rate of the product $\dot{N}_{pr}$, the component densities (ρ_f and ρ_c), and the volume contents of the components ($\frac{\pi}{6} d_f^3$ and $\frac{\pi}{6} d_f^3 (\Phi_{d,set}^3 - 1)$), which results in

$$\dot{M}_{pr,core} = \dot{N}_{pr} \rho_f \frac{\pi}{6} d_f^3 \tag{3.18}$$

and

$$\dot{M}_{pr,c} = \dot{N}_{pr} \rho_c \frac{\pi}{6} d_f^3 \big(\Phi_{d,set}^3 - 1\big). \tag{3.19}$$

The number-based product discharge rate conforms with the number- and mass-based feed rate of external nuclei, when none of the core material is lost in the chamber: $\dot{N}_{pr}(\Phi_{f,loss} = 0) = \dot{N}_f$; but, it is less than the total number feed rate of external nuclei, when losses occur due to assumption 8 of Section 3.1.1: $\dot{N}_{pr}(\Phi_{f,loss} > 0) < \dot{N}_f$.

Partial and overall mass balances

Taking the material losses into account, two partial mass balances of the entire granulator-separator system are derived for steady state conditions, one for the core material with

$$\dot{M}_{pr,core} = \dot{M}_f \big(1 - \Phi_{f,loss}\big), \tag{3.20}$$

and one for the coating material with

$$\dot{M}_{pr,c} = \dot{M}_{spr,s} \big(1 - \Phi_{spr,loss}\big). \tag{3.21}$$

From Eqs. 3.17, 3.20 and 3.21, the product discharge rate $\dot{M}_{pr}$ can be expressed by the nuclei feed rate and the solids spray rate:

$$\dot{M}_{pr} = \dot{M}_f (1 - \Phi_{f,loss}) + \dot{M}_{spr,s} (1 - \Phi_{spr,loss}). \tag{3.22}$$

3.2.2 Spray-to-feed rate setting methods

Required and effective spray-to-feed rate ratio

The solids spray rate $\dot{M}_{spr,s}$ and the feed rate $\dot{M}_f$ are related to the mass discharge rate of coating and core material in the product by the partial mass balances Eq. 3.20 and Eq. 3.21. The required spray-to-feed rate ratio $\Phi_{m,set}$ can be therefore formed to:

$$\Phi_{m,set} = \frac{1 - \Phi_{f,loss}}{1 - \Phi_{spr,loss}} \frac{\dot{M}_{pr,c}}{\dot{M}_{pr,core}}. \tag{3.23}$$

Using Eqs. 3.3, 3.18, and 3.19, the required spray-to-feed rate ratio $\Phi_{m,set}$ is expressed in terms of the mass loss fractions of the components $\Phi_{f,loss}$ and $\Phi_{spr,loss}$, the coating-to-core density ratio Φ_ρ, and the target-growth ratio $\Phi_{d,set}$:

$$\Phi_{m,set} = \frac{1-\Phi_{f,loss}}{1-\Phi_{spr,loss}} \Phi_\rho \big(\Phi_{d,set}^3 - 1\big). \tag{3.24}$$

This relation transpires how the required spray-to-feed rate ratio $\Phi_{m,set}$ has to be adjusted to the desired particle growth ratio $\Phi_{d,set}$ and thus to the desired product size $d_{pr,set}$. It is the key element for controlling product size by operation parameters in continuous granulation, as later shown in the population balance study (Chapters 5 and 6) and in the experiments of continuous granulation (Sections 9.4.5 and 10.4) of this thesis. A similar relation to Eq. 3.24 has been stated within the context of the granulation model of Mörl et al. ([29], equations "83" and "84") in a different form, which was also presented by Heinrich ([88], equation "2.195"). There, the material losses are disregarded ($\Phi_{f,loss} = \Phi_{spr,loss} = 0$) and the component density ratio does not appear (e.g., $\Phi_\rho = 1$).

The effective spray-to-feed rate ratio follows from Eqs. 3.12 and 3.24 to:

$$\Phi_{m,eff} = \Phi_\rho \big(\Phi_{d,set}^3 - 1\big). \tag{3.25}$$

Conclusions for bed mass control

It shall be reminded here that fluidized bed mass needs to be controlled in continuous spray granulation. This could be done by manipulating the product discharge rate, the nuclei feed rate or the (solids) spray rate. However, choosing only one of the last two process parameters as manipulated variable would sacrifice the control of product size as a consequence of Eq. 3.24. This could only be avoided when the nuclei feed rate and solids spray rate are each manipulated to an extent which keeps their ratio constant. But such a control strategy is difficult to implement in practice, because it requires more devices (e.g., for inline detection, data acquisition, and mass flow control) and is associated with measurement errors and control deviations of even two operating parameters. Beside this, feeding nuclei by a double-pinch valve is limited and can have large dosing fluctuations, depending on the constructive design, as shown later in Section 10.2.

Practical restrictions

The setting of the nuclei feed rate $\dot{M}_f$ and the total spray rate $\dot{M}_{spr}$ (and so the solids spray rate $\dot{M}_{spr,s}$) is restricted by diverse practical aspects. For instance, the spray rate and the feed rate are limited by maximal conveying rates of ancillary equipment (e.g., pump-nozzle-system and double-pinch valve conveyor). Further, the spray rate is restricted by thermal limits of the process gas (e.g., process-gas saturation and agglomeration kinetics) as described later in Section 7. But also, the total inlet mass flow rate of solids $\dot{M}_{s,in} = \dot{M}_f + \dot{M}_{spr,s}$ is limited by the separator inlet mass flow rate $\dot{M}_{sep}$, as described later in Section 5.3. Otherwise the granulator would be overcharged, which leads to steady increase of bed mass and finally to process destabilization. The separator inlet mass flow can be controlled for instance by a double-pinch valve connecting the granulator with the separator, as realized in Hampel's reference case ([2], see also Section 2.3). The limits and conveying accuracy of such a double-pinch-valve bed discharger has been investigated experimentally, which is presented in Section 10.3.

Theoretical restrictions - freely selectable and dependent parameters

The desired particle growth ratio $\Phi_{d,set}$ and the production rate $\dot{M}_{pr}$ can be required process objectives in applications of continuous spray granulation. The nuclei feed rate $\dot{M}_f$ and the solids spray rate $\dot{M}_{spr,s}$ are related to the desired growth ratio $\Phi_{d,set}$ via Eqs. 3.11 and 3.24 and to the production rate $\dot{M}_{pr}$ via Eq. 3.22. This means that two of these four process parameters can be freely chosen, while the others follow from Eqs. 3.11, 3.22, and 3.24.

Three SFM-variants

The described theoretical restrictions result in three possible spray-to-feed rate setting methods (abbreviated by SFM1, SFM2, and SFM3) for a given desired particle growth ratio. These methods are also called as spray-to-feed rate setting variants or just as parameter setting methods in this thesis. The calculation steps of them are listed in Table 3.1. The nuclei feed rate $\dot{M}_f$ is predefined in the first variant SFM1, the solids spray rate $\dot{M}_{spr,s}$ in the second variant SFM2, and the production rate $\dot{M}_{pr}$ in the third variant SFM3.

indication	predefined parameter	calculation of ensuing parameters	equation
SFM1	$\dot{M}_f$	$\dot{M}_{spr,s} = \Phi_{m,set}\dot{M}_f$	Eq. 3.11
		$\dot{M}_{pr} = \dot{M}_f(1-\Phi_{f,loss}) + \dot{M}_{spr,s}(1-\Phi_{spr,loss})$	Eq. 3.22
SFM2	$\dot{M}_{spr,s}$	$\dot{M}_f = \Phi_{m,set}^{-1}\dot{M}_{spr,s}$	Eq. 3.11
		$\dot{M}_{pr} = \dot{M}_f(1-\Phi_{f,loss}) + \dot{M}_{spr,s}(1-\Phi_{spr,loss})$	Eq. 3.22
SFM3	$\dot{M}_{pr}$	$\dot{M}_f = \dot{M}_{pr}\big(1-\Phi_{f,loss}+\Phi_{m,set}(1-\Phi_{spr,loss})\big)^{-1}$	Eqs. 3.11 and 3.22
		$\dot{M}_{spr,s} = \Phi_{m,set}\dot{M}_f$	Eq. 3.11

Table 3.1: Parameter setting methods (indicated with SFM1, SFM2, and SFM3) for nuclei feed rate $\dot{M}_f$ and/or solids spray rate $\dot{M}_{spr,s}$, given as functions of the required spray-to-feed rate ratio $\Phi_{m,set}$, fixed by the desired particle growth ratio $\Phi_{d,set}$ via Eq. 3.24.

The second parameter setting method SFM2 was employed in the continuous granulation experiments (see Sections 9.4.11 and 10.4), whereas SFM3 was used within the PB-simulation study of the present work (see Section 6.1.1).

3.3 General solution for size-dependent growth

3.3.1 Derivation of bed particle size distribution from population balance

The size distribution of fluidized bed granules (n_{bed}) has an influence on the fluidization behavior. The present ideal continuous layerwise granulation model allows to approximate stationary bed granule size distributions by a one-dimensional population balance, which ensues from the previously stated assumptions 1-9 (beginning of this chapter) to:

$$\frac{\partial}{\partial t}\big(n_{bed}(d)\big) = \dot{n}_f(d) - \dot{n}_{pr}(d) - \frac{\partial}{\partial d}\big(\dot{N}_{conv}\big) = 0, \tag{3.26}$$

with n_{bed} given as the product of the total number of bed granules N_{bed} and the number-based normalized bed-PSD $q_{0,bed}$:

$$n_{bed}(d) = N_{bed}q_{0,bed}(d). \tag{3.27}$$

In addition, the population balance of Eq. 3.26 contains the number density distribution flow rate of the nuclei feed $\dot{n}_f$, the number density distribution flow rate of the product granules $\dot{n}_{pr}$, and the convection number flow rate $\dot{N}_{conv}$ of particles moving (virtually) along the internal size coordinate d. The feed- and product-related terms $\dot{n}_f$ and $\dot{n}_{pr}$ can be written as products of the total number flow rates ($\dot{N}_f$ or $\dot{N}_{pr}$) and the normalized particle size distribution ($q_{0,f}$ or $q_{0,pr}$) according to:

$$\dot{n}_i(d) = \dot{N}_i q_{0,i}(d) \qquad \text{, for } i \in \{f;pr\}. \tag{3.28}$$

The normalized particle size distributions of the mono-sized nuclei feed and product ($q_{0,f}$ and $q_{0,pr}$) can be described by two Gaussian distributions with

$$q_{0,i}(d) = \lim_{\sigma_i \to 0}\left(\frac{1}{\sigma_i\sqrt{2\pi}}\exp\left(-\frac{(d-d_i)^2}{2\sigma_i^2}\right)\right) \qquad \text{, for } i \in \{f;pr\}, \tag{3.29}$$

whose expectation values equal the respected diameter ($d_i = d_f$ or $d_i = d_{pr} = d_{pr,set}$), and whose standard deviation σ_i goes to zero, by which the two Dirac delta functions with

$$q_{0,i}(d) = \begin{cases} \infty & \text{, for } d = d_i \\ 0 & \text{, for } d \neq d_i \end{cases} \qquad \text{, for } i \in \{f;pr\} \tag{3.30}$$

are approached. Equations 3.29 and 3.30 are helpful in solving the population balance Eq. 3.26 analytically. The internal convection flow rate $\dot{N}_{conv}$ is defined by the product of the growth rate G_d and the number-based bed particle size distribution n_{bed}:

$$\dot{N}_{conv} = G_d(d)n_{bed}(d) = G_d(d)N_{bed}q_{0,bed}(d). \tag{3.31}$$

It follows from Eq. 3.30 that the inlet and outlet number density distribution flow rates ($\dot{n}_f$ and $\dot{n}_{pr}$) can be neglected in the population balance Eq. 3.26 within a bed particle size range of $d_f < d < d_{pr,set}$, which is called here the inner bed granule size range, where only particle sizes d greater than the feed diameter d_f and less than the desired product diameter $d_{pr,set}$ are considered. Thereby, the partial derivative of the internal convection number flow rate $\partial(\dot{N}_{conv})/\partial d$ becomes zero:

$$\frac{\partial}{\partial d}\left(\dot{N}_{conv}\right) = \frac{\partial}{\partial d}\Big(G_d(d)n_{bed}(d)\Big) = 0 \qquad \text{, for } d_f < d < d_{pr,set}. \tag{3.32}$$

As a conclusion, the internal convection number flow rate $\dot{N}_{conv}$ of the ideal granulation model is size-independent within the inner bed particle size range, as also illustrated in Figure 3.1. Further, the internal convection number flow rate $\dot{N}_{conv}$ is fixed by the feed-related boundary condition, where it equals the effective number flow rate of the feed $\dot{N}_f(1-\Phi_{f,loss})$. The latter can be obtained from the mass flow rate of the nuclei feed $\dot{M}_f$ by Eq. 3.15. Putting all together, it follows that:

$$\dot{N}_{conv} = G_d(d)n_{bed}(d) = \dot{N}_f(1-\Phi_{f,loss}) = \frac{\dot{M}_f(1-\Phi_{f,loss})}{\rho_f \frac{\pi}{6} d_f^3} \neq \mathrm{f}(d) \qquad \text{, for } d_f < d < d_{pr,set}. \tag{3.33}$$

The ratio of the total number of bed particles N_{bed} to the effective number flow rate of the nuclei feed $\dot{N}_f(1-\Phi_{f,loss})$ shall be defined as the effective number-based residence time of the particles (cores or coated nuclei) in the entire granulator-separator system $\tau_{0,sys}$:

$$\tau_{0,sys} \coloneqq \frac{N_{bed}}{\dot{N}_f(1-\Phi_{f,loss})} = \frac{N_{bed}\rho_f \frac{\pi}{6} d_f^3}{\dot{M}_f(1-\Phi_{f,loss})}. \tag{3.34}$$

The calculation of the total number of bed particles N_{bed} from the bed mass M_{bed} requires to know the bed particle size distribution, as it is shown later in Eq. 3.44. It can be seen from Eqs. 3.27 and 3.33 that the product of the growth rate G_d and the normalized bed particle size distribution $q_{0,bed}$ turns out to be the reciprocal of $\tau_{0,sys}$ for the inner particle size range $d_f < d < d_{pr,set}$:

$$G_d(d)q_{0,bed}(d) = \frac{\dot{N}_f(1-\Phi_{f,loss})}{N_{bed}} = \frac{1}{\tau_{0,sys}} \qquad \text{, for } d_f < d < d_{pr,set}. \tag{3.35}$$

In order to determine the bed particle size distribution $q_{0,bed}$ over the complete particle size range ($d_f \leq d \leq d_{pr,set}$), the limits ($G_d(d_f)q_{0,bed}(d_f)$ and $G_d(d_{pr,set})q_{0,bed}(d_{pr,set})$) of the left hand side of Eq. 3.35

$$G_d(d_i)q_{0,bed}(d_i) \coloneqq \lim_{d\to d_i}\big(G_d(d)q_{0,bed}(d)\big) = \frac{1}{\tau_{0,sys}} \qquad \text{, for } i \in \{f;pr,set\} \tag{3.36}$$

are added to the particle size range of Eq. 3.35 by definition. This way, the general bed particle size distribution $q_{0,bed}$ is expressed by the reciprocals of the effective number-based particle residence time of the granulator-separator system $\tau_{0,sys}$ and the size-dependent growth rate function $G_d(d)$:

$$q_{0,bed}(d) = \begin{cases} \frac{1}{\tau_{0,sys}} \frac{1}{G_d(d)} & \text{, for } d_f \leq d \leq d_{pr,set} \\ 0 & \text{, otherwise} \end{cases}. \tag{3.37}$$

3.3.2 Relationship between residence time, growth time, product size, and bed mass

Conformity of the effective number-based particle residence time and the required growth time

The assumptions of the ideal continuous layerwise granulation model (Section 3.1.1) stipulate that the total residence time of individuals in the granulator-separator system ($\tau_{0,sys}$, defined by Eq. 3.34) and the required

particle growth time (symbolized by $\tau_{gr,set}$) to enlarge granules from d_f to $d_{pr,set}$ must be the same. This conformity should be checked again in the following by means of integrations. With the normalization condition of distribution functions ($\int_{d_f}^{d_{pr,set}} q_{0,bed}\mathrm{d}d = 1$), integration of Eq. 3.37 from d_f to $d_{pr,set}$ relates $\tau_{0,sys}$ to an integral of the reciprocal growth rate function $G_d(d)^{-1}$:

$$\tau_{0,sys} = \int_{d_f}^{d_{pr,set}} G_d(d)^{-1}\mathrm{d}d. \tag{3.38}$$

The growth rate is defined as the differential change of the particle diameter with respect to the current retention time: $G_d = \mathrm{d}d/\mathrm{d}\tau$. The required growth time $\tau_{gr,set}$ is therefore the integral of the reciprocal growth rate function $G_d(d)^{-1}$ from the nuclei diameter d_f to the desired product diameter $d_{pr,set}$ too:

$$\tau_{gr,set} = \int_0^{\tau_{gr,set}} \mathrm{d}\tau = \int_{d_f}^{d_{pr,set}} G_d(d)^{-1}\mathrm{d}d. \tag{3.39}$$

Such a relationship between residence time and growth time of the granulation model of Mörl et al. [110] has also been stated in [29]; but there, the growth rate was assumed to be size-independent and the residence time was referred to nuclei mass (core mass) and nuclei feed rate, which leads to different equations. Nevertheless, attention should be drawn to the fact that the two interpretations of time coordinates are the same regardless of the type of the growth rate function. In addition, the residence time of the differential coating layers on product granules is distributed, and the average residence time of the differential coating layers is smaller than the overall residence time of the particles. For this reason, it is difficult to describe the residence time of particles by the bed mass M_{bed} and the product discharge rate $\dot{M}_{pr}$. The latter two quantities are measurable, however, using the ratio $M_{bed}/\dot{M}_{pr}$ for characterizing mean residence times in real systems involves some errors.

Independence of product size from bed mass

According to Eq. 3.38 and Eq. 3.39, it follows that the number-based residence time in the entire system $\tau_{0,sys}$ conforms to the required growth time $t_{gr,set}$ for the ICLG-model:

$$\tau_{0,sys} = \tau_{gr,set}, \tag{3.40}$$

regardless whether the growth rate is size-dependent or not. The higher the bed mass M_{bed} is, the lower is the growth rate G_d, and the longer it takes for the particles to grow to the desired product size $d_{pr,set}$. But, with higher bed mass, the total residence time increases in the same extent. As a conclusion of this, the target-growth ratio $\Phi_{d,set}$, but also the desired particle size $d_{pr,set}$, are independent from the bed mass M_{bed}:

$$\{\Phi_{d,set}, d_{pr,set}\} \neq \mathrm{f}(M_{bed}). \tag{3.41}$$

From this point of view, layerwise granulation with variable product size can be operated for different holdups M_{bed}, and hence, for different granulator scales. However, the required spray-to-feed rate $\Phi_{m,set}$ must be adapted to the desired particle growth ratio $\Phi_{d,set}$ by Eq. 3.24.

3.3.3 Determination of the total number of particles and the required growth time

In order to determine the total number of bed particles N_{bed} and the required growth time $\tau_{0,sys}$, the number-based average single particle mass $\bar{M}_{p,0}$ can be used. It is derived from the following integrals:

$$\bar{M}_{p,0} = \int_0^\infty \rho_p(d)\frac{\pi}{6}d^3 q_{0,bed}(d)\mathrm{d}d = \int_0^\infty \rho_f\big((1-\Phi_\rho)\Phi_d^{-3} + \Phi_\rho\big)\frac{\pi}{6}d^3 q_{0,bed}(d)\mathrm{d}d, \tag{3.42}$$

wherein the effective particle density ρ_p is replaced with Eq. 3.4. Using the third raw moment of the number-based particle size distribution $m_{3,0}$ (Eq. 2.27), the right-hand side of Eq. 3.42 is converted to:

$$\bar{M}_{p,0} = \rho_f\frac{\pi}{6}d_f^3\left(1 + \Phi_\rho\left(\frac{m_{3,0}}{d_f^3} - 1\right)\right). \tag{3.43}$$

From this, the total number of all bed particles N_{bed} is written with:

$$N_{bed} = \frac{M_{bed}}{\bar{M}_{p,0}} = \frac{M_{bed}}{\rho_f \frac{\pi}{6} d_f^3 \left(1 + \Phi_\rho \left(\frac{m_{3,0}}{d_f^3} - 1\right)\right)}. \tag{3.44}$$

Inserting this equation into Eq. 3.34 and using Eqs. 3.38 and 3.39, the required growth time $\tau_{gr,set}$ follows to

$$\tau_{gr,set} = \frac{M_{bed}}{\dot{M}_f (1 - \Phi_{f,loss}) \left(1 + \Phi_\rho \left(\frac{m_{3,0}}{d_f^3} - 1\right)\right)}, \tag{3.45}$$

which shows its dependency on bed mass M_{bed}, effective nuclei feed rate $\dot{M}_f(1-\Phi_{f,loss})$, component density ratio Φ_ρ, third moment of bed-PSD $m_{3,0}$, and the nuclei diameter d_f. The nuclei feed rate can be replaced by the spray rate. The required growth time $\tau_{gr,set}$ can also be expressed in terms of desired particle growth and the solids spray rate by recombination of Eqs. 3.11, 3.24, and 3.45:

$$\tau_{gr,set} = \frac{M_{bed}}{\dot{M}_{spr,s}(1 - \Phi_{spr,loss})} \frac{\Phi_\rho \left(\Phi_{d,set}^3 - 1\right)}{1 + \Phi_\rho \left(\frac{m_{3,0}}{d_f^3} - 1\right)}. \tag{3.46}$$

However, the number-based bed particle size distribution $q_{0,bed}$ is required in order to determine its third moment $m_{3,0}$. It can be analytically derived for instance for a size-independent growth rate function (even growth), as shown in Section 3.4.

3.3.4 Average characteristics of effective bed granule density

In case that the coating-to-core density ratio is not unity ($\Phi_\rho \neq 1$), the effective density of single bed granules is distributed in the present ideal granulation model (see Eq. 3.4). Diverse average characteristics of the bed particle density can be defined, as follows. They can be used for instance for calculating fluidization properties (Section 2.2.1 and Chapter 7). A simple one is the unweighted mean bed particle density $\bar{\rho}_{p,mid}$, which is obtained from the effective particle density definition of Eq. 3.4 and the unweighted mean particle diameter $d_{mid} = \frac{1}{2}(d_f + d_{pr,set})$ (see Eq. 2.42):

$$\bar{\rho}_{p,mid} = \rho_f \left(\frac{d_f}{d_{mid}}\right)^3 + \rho_c \left(1 - \left(\frac{d_f}{d_{mid}}\right)^3\right) = \rho_f \left((1 - \Phi_\rho)\left(\frac{d_f}{d_{mid}}\right)^3 + \Phi_\rho\right). \tag{3.47}$$

The main advantage of the unweighted mean bed particle density $\bar{\rho}_{p,mid}$ is that it can be determined independently from the bed particle size distribution, but it cannot guarantee any physically meaningful estimates. Similar to the definition of $\bar{\rho}_{p,mid}$, an average effective bed particle density can be formulated by inserting the mean bed particle diameter d_m into Eq. 3.4. It shall be represented by $\bar{\rho}_{p,m}$ and is given with:

$$\bar{\rho}_{p,m} = \rho_f \left(\frac{d_f}{d_m}\right)^3 + \rho_c \left(1 - \left(\frac{d_f}{d_m}\right)^3\right) = \rho_f \left((1 - \Phi_\rho)\left(\frac{d_f}{d_m}\right)^3 + \Phi_\rho\right). \tag{3.48}$$

In the same way, an average effective bed particle density can be related to the Sauter diameter $d_{32} = m_{3,0}/m_{2,0}$ (see Eq. 2.46), which is then symbolized by $\bar{\rho}_{p,32}$ and results in:

$$\bar{\rho}_{p,32} = \rho_f \left(\frac{d_f}{d_{32}}\right)^3 + \rho_c \left(1 - \left(\frac{d_f}{d_{32}}\right)^3\right) = \rho_f \left((1 - \Phi_\rho)\left(\frac{d_f}{d_{32}}\right)^3 + \Phi_\rho\right). \tag{3.49}$$

Another one is the number-based average effective particle density $\bar{\rho}_{p,q_0}$, which is defined by the following integral:

$$\bar{\rho}_{p,q_0} = \int_{d_f}^{d_{pr,set}} \rho_p(d) q_{0,bed}(d) \mathrm{d}d = \int_{d_f}^{d_{pr,set}} \left[\rho_f \left(\frac{d_f}{d}\right)^3 + \rho_c \left(1 - \left(\frac{d_f}{d}\right)^3\right)\right] q_{0,bed}(d) \mathrm{d}d. \tag{3.50}$$

This integral can be transformed to

$$\bar{\rho}_{p,q_0} = \rho_f d_f^3 m_{-3,0} + \rho_c \left(d_f^3 m_{-3,0} - 1\right) = \rho_f \left((1 - \Phi_\rho) d_f^3 m_{-3,0} + \Phi_\rho\right), \tag{3.51}$$

which reveals that $\bar{\rho}_{p,q_0}$ corresponds to Eq. 3.4 with an argument given by the power mean of the bed-PSD with $k = -3$ (i.e. $d^*_{-3,0} = (m_{-3,0})^{-1/3}$) according to Eqs. 2.33 and 2.37. Consequently, the number-based average effective particle density $\bar{\rho}_{p,q_0}$ can also be formulated as:

$$\bar{\rho}_{p,q_0} = \rho_f \left((1-\Phi_\rho) \Big(\frac{d_f}{d^*_{-3,0}} \Big)^3 + \Phi_\rho \right). \tag{3.52}$$

Moreover, the volume-based average effective bed particle density $\bar{\rho}_{p,q_3}$ can be defined with:

$$\bar{\rho}_{p,q_3} = \int_{d_f}^{d_{pr,set}} \rho_p(d) q_{3,bed}(d) \mathrm{d}d = \frac{\int_{d_f}^{d_{pr,set}} \rho_p(d) d^3 q_{0,bed}(d) \mathrm{d}d}{\int_{d_f}^{d_{pr,set}} d^3 q_{0,bed}(d) \mathrm{d}d}. \tag{3.53}$$

The volume-based average effective bed particle density $\bar{\rho}_{p,q_3}$ conforms with the ratio of the total bed mass M_{bed} to the total volume of bed particles $V_{tot,bed}$:

$$\bar{\rho}_{p,q_3} = \frac{\int_{d_f}^{d_{pr,set}} \rho_p(d) \frac{\pi}{6} d^3 n_{bed}(d) \mathrm{d}d}{\int_{d_f}^{d_{pr,set}} \frac{\pi}{6} d^3 n_{bed}(d) \mathrm{d}d} = \frac{M_{bed}}{V_{tot,bed}}. \tag{3.54}$$

Using the effective bed particle density ρ_p in Eq. 3.4, the volume-based average effective bed particle density $\bar{\rho}_{p,q_3}$ is formed to

$$\bar{\rho}_{p,q_3} = \rho_f \frac{d_f^3}{m_{3,0}} + \rho_c \left(1 - \frac{d_f^3}{m_{3,0}} \right) = \rho_f \left((1-\Phi_\rho) \frac{d_f^3}{m_{3,0}} + \Phi_\rho \right), \tag{3.55}$$

by which it turns out, according to Eq. 2.36, that $\bar{\rho}_{p,q_3}$ is associated to the third-power mean of the bed-PSD ($d^*_{3,0} = (m_{3,0})^{1/3}$):

$$\bar{\rho}_{p,q_3} = \rho_f \left((1-\Phi_\rho) \Big(\frac{d_f}{d^*_{3,0}} \Big)^3 + \Phi_\rho \right). \tag{3.56}$$

It shall be noted that the defined average bed particle densities of Eqs. 3.47, 3.48, 3.49, 3.52 and 3.56 consist of the same mathematical formula, which is generalized in Section 3.5. The influence of particle growth (represented by $\Phi_{d,set}$) on the described average characteristics of bed granule density is discussed later in Section 4.1.2.

3.4 Specific solution for size-independent growth

The growth rate is constant for all bed granules in the ideal continuous layerwise granulation model (steady-state conditions) with size-independent growth:

$$G_d = \text{const.} \neq \mathrm{f}(d,t). \tag{3.57}$$

Such conditions are also referred to as even growth and were described by Mörl et al. (see for instance [29,73]), which is further detailed in Appendix B.2. As a result of Eq. 3.37, a size-independent particle growth approach ($G_d \neq \mathrm{f}(d)$) implies that the bed particle size of the ICLG-model must be equally distributed according to:

$$q_{0,bed}(d) = \begin{cases} \frac{1}{d_{pr,set} - d_f} & , d_f \leq d \leq d_{pr,set} \\ 0 & , \text{otherwise} \end{cases}. \tag{3.58}$$

Once this distribution is mathematically defined, various properties of the ICLG-model can be derived as functions of pregiven process and material parameters ($\Phi_{d,set}$, Φ_ρ, d_f, $\dot{M}_f$, $\dot{M}_{spr,s}$, $\Phi_{f,loss}$, and $\Phi_{spr,loss}$) as follows. The k'th moment of the equal distribution of the bed granule size $q_{0,bed}$ is obtained by Eqs. 2.27 and 3.58 with:

$$m_{k,0} = \begin{cases} \frac{\ln\left(d_{pr,set}/d_f\right)}{d_{pr,set} - d_f} = \frac{1}{d_f} \frac{\ln(\Phi_{d,set})}{\Phi_{d,set} - 1} & , \text{for } k = -1 \\ 1 & , \text{for } k = 0 \\ \frac{1}{k+1} \frac{d_{pr,set}^{k+1} - d_f^{k+1}}{d_{pr,set} - d_f} = d_f^k \frac{1}{k+1} \frac{\Phi_{d,set}^{k+1} - 1}{\Phi_{d,set} - 1} & , \text{otherwise} \end{cases}. \tag{3.59}$$

With Eqs. 3.43 and 3.59, the average single bed particle mass $\bar{M}_{p,0}$ follows to:

$$\bar{M}_{p,0} = \rho_f \frac{\pi}{6} d_f^3 \left(1 + \Phi_\rho \left(\frac{1}{4}\frac{\Phi_{d,set}^4 - 1}{\Phi_{d,set} - 1} - 1\right)\right). \tag{3.60}$$

The total number of bed particles N_{bed} ensues from Eqs. 3.44 and 3.59 to:

$$N_{bed} = \frac{M_{bed}}{\bar{M}_{p,0}} = \frac{M_{bed}}{\rho_f \frac{\pi}{6} d_f^3 \left(1 + \Phi_\rho \left(\frac{1}{4}\frac{\Phi_{d,set}^4 - 1}{\Phi_{d,set} - 1} - 1\right)\right)}. \tag{3.61}$$

By inserting Eq. 3.59 with $k = 3$ into Eqs. 3.45 and 3.46 and using Eqs. 3.13 and 3.14, the required growth time $\tau_{gr,set}$ is specified in terms of the nuclei feed rate $\dot{M}_f$ or specific nuclei feed rate $\dot{m}_f$ with

$$\begin{aligned} \tau_{gr,set} &= \frac{M_{bed}}{\dot{M}_f (1 - \Phi_{f,loss}) \left(1 + \Phi_\rho \left(\frac{1}{4}\frac{\Phi_{d,set}^4 - 1}{\Phi_{d,set} - 1} - 1\right)\right)} \\ &= \frac{1}{\dot{m}_f (1 - \Phi_{f,loss}) \left(1 + \Phi_\rho \left(\frac{1}{4}\frac{\Phi_{d,set}^4 - 1}{\Phi_{d,set} - 1} - 1\right)\right)}, \end{aligned} \tag{3.62}$$

and in terms of solids spray rate $\dot{M}_{spr,s}$ or specific solids spray rate $\dot{m}_{spr,s}$ with

$$\begin{aligned} \tau_{gr,set} &= \frac{M_{bed}}{\dot{M}_{spr,s}(1 - \Phi_{spr,loss})} \frac{\Phi_\rho \left(\Phi_{d,set}^3 - 1\right)}{1 + \Phi_\rho \left(\frac{1}{4}\frac{\Phi_{d,set}^4 - 1}{\Phi_{d,set} - 1} - 1\right)} \\ &= \frac{1}{\dot{m}_{spr,s}(1 - \Phi_{spr,loss})} \frac{\Phi_\rho \left(\Phi_{d,set}^3 - 1\right)}{1 + \Phi_\rho \left(\frac{1}{4}\frac{\Phi_{d,set}^4 - 1}{\Phi_{d,set} - 1} - 1\right)}. \end{aligned} \tag{3.63}$$

The size-independent growth rate is obtained by integration of Eq. 3.38 or Eq. 3.39, which results in:

$$G_d = \frac{d_{pr,set} - d_f}{\tau_{gr,set}} = \frac{d_f(\Phi_{d,set} - 1)}{\tau_{gr,set}}. \tag{3.64}$$

From the required growth time $\tau_{gr,set}$ of Eq. 3.62, the growth rate G_d is obtained to:

$$\begin{aligned} G_d &= \frac{\dot{M}_f (1 - \Phi_{f,loss})}{M_{bed}} d_f (\Phi_{d,set} - 1) \left(1 + \Phi_\rho \left(\frac{1}{4}\frac{\Phi_{d,set}^4 - 1}{\Phi_{d,set} - 1} - 1\right)\right) \\ &= \dot{m}_f (1 - \Phi_{f,loss}) d_f (\Phi_{d,set} - 1) \left(1 + \Phi_\rho \left(\frac{1}{4}\frac{\Phi_{d,set}^4 - 1}{\Phi_{d,set} - 1} - 1\right)\right). \end{aligned} \tag{3.65}$$

Due to the stationary mass balance of the granulator, the feed rate $\dot{M}_f$ is related to the solids spray rate $\dot{M}_{spr,s}$ and the desired growth ratio $\Phi_{d,set}$, as shown above in Eq. 3.11 and Eq. 3.24. Thus, the growth rate G_d can also be formulated in terms of the solids spray rate with:

$$G_d = \frac{\dot{M}_{spr,s}(1 - \Phi_{spr,loss})}{M_{bed}} d_f \left(\left(\frac{1}{\Phi_\rho} - 1\right)\frac{\Phi_{d,set} - 1}{\Phi_{d,set}^3 - 1} + \frac{1}{4}\frac{\Phi_{d,set}^4 - 1}{\Phi_{d,set}^3 - 1}\right). \tag{3.66}$$

Several average characteristics of the even bed granule size distribution - d_m of Eq. 2.32, d_{32} of Eq. 2.46, $d_{-3,0}^*$ of Eq. 2.33 with $k = -3$, and $d_{3,0}^*$ of Eq. 2.33 with $k = 3$, - can be calculated with Eqs. 3.67 to 3.70, listed on the left of Table 3.2. These are derived with Eq. 3.59 and can be used to determine corresponding average characteristics of bed particle density - $\bar{\rho}_{p,m}$ of Eq. 3.48, $\bar{\rho}_{p,32}$ of Eq. 3.49, $\bar{\rho}_{p,q_0}$ of Eq. 3.52 and $\bar{\rho}_{p,3,0}$ of Eq. 3.56 - by Eqs. 3.71 to 3.74, given on the right of Table 3.2. At this point, it is mentioned that the mean diameter equals the unweighted average particle diameter for an even bed-PSD: $d_m = d_{mid}$; and so the corresponding average bed particle densities do: $\bar{\rho}_{p,m} = \bar{\rho}_{p,mid}$.

$$d_m = d_f \frac{1}{2}(\Phi_{d,set} + 1) \tag{3.67}$$

$$d_{32} = d_f \frac{3}{4} \frac{\Phi_{d,set}^4 - 1}{\Phi_{d,set}^3 - 1} \tag{3.68}$$

$$d_{-3,0}^* = d_f \left(2 \frac{\Phi_{d,set}^2}{\Phi_{d,set} + 1} \right)^{\frac{1}{3}} \tag{3.69}$$

$$d_{3,0}^* = d_f \left(\frac{1}{4} \frac{\Phi_{d,set}^4 - 1}{\Phi_{d,set} - 1} \right)^{\frac{1}{3}} \tag{3.70}$$

$$\bar{\rho}_{p,m} = \rho_f \left((1 - \Phi_\rho) \frac{8}{(\Phi_{d,set} + 1)^3} + \Phi_\rho \right) \tag{3.71}$$

$$\bar{\rho}_{p,32} = \rho_f \left((1 - \Phi_\rho) \left(\frac{4}{3} \frac{\Phi_{d,set}^3 - 1}{\Phi_{d,set}^4 - 1} \right)^3 + \Phi_\rho \right) \tag{3.72}$$

$$\bar{\rho}_{p,q_0} = \rho_f \left((1 - \Phi_\rho) \frac{1}{2} \frac{\Phi_{d,set} + 1}{\Phi_{d,set}^2} + \Phi_\rho \right) \tag{3.73}$$

$$\bar{\rho}_{p,q_3} = \rho_f \left((1 - \Phi_\rho) 4 \frac{\Phi_{d,set} - 1}{\Phi_{d,set}^4 - 1} + \Phi_\rho \right) \tag{3.74}$$

Table 3.2: Diverse average bed particle diameters and the corresponding average particle densities for even growth of particles and equal bed particle size distribution.

3.5 Normalized particle density of different average size characteristics for size-dependent and -independent growth

The general normalized particle density (symbolized by $\xi_{\rho,j}$) is introduced here to describe, unify, and compare the relative change of diverse particle density characteristics with granule size enlargement (Φ_d and $\Phi_{d,set}$) in a generalized manner, which is illustrated and discussed later in Figure 4.2 and Section 4.1.2. It is formulated with

$$\xi_{\rho,j} \coloneqq \frac{\rho_j(d_j) - \rho_f}{\rho_c - \rho_f} = \frac{\rho_j(d_j)/\rho_f - 1}{\Phi_\rho - 1} \qquad \text{, for } \Phi_\rho \neq 1, \tag{3.75}$$

according to the variable normalized particle density ξ_ρ of Eq. 3.7. In Eq. 3.75, ρ_j stands for a general effective particle density, which can be ρ_{pr} of Eq. 3.5, $\bar{\rho}_{p,mid}$ of Eq. 3.47, $\bar{\rho}_{p,m}$ of Eq. 3.48, $\bar{\rho}_{p,32}$ of Eq. 3.49, $\bar{\rho}_{p,q_0}$ of Eq. 3.52 or $\bar{\rho}_{p,q_3}$ of Eq. 3.56, and d_j represents the general particle size characteristic associated to ρ_j, which can be $d_{pr,set}$, d_{mid}, d_m of Eq. 3.67, d_{32} of Eq. 3.68, $d_{-3,0}^*$ of Eq. 3.69, and $d_{3,0}^*$ of Eq. 3.70. All of these characteristic properties are associated with each other ($\xi_{\rho,j}(\rho_j(d_j))$. The normalized densities of these characteristic points must lie on a single curve according to Eq. 3.6 and can therefore, be expressed by a general equation with:

$$\xi_{\rho,j} = 1 - \left(\frac{d_f}{d_j} \right)^3. \tag{3.76}$$

It is obvious in Eq. 3.76 that all normalized particle densities of $\xi_{\rho,j}$ are independent from the effective densities of the single components ($\xi_{\rho,j} \neq \mathrm{f}(\rho_f, \rho_c)$) and also from coating-to-core density ratio ($\xi_{\rho,j} \neq \mathrm{f}(\Phi_\rho)$), which allows to compare the different characteristic points regardless of the material types used. Following Eq. 3.76, the normalized effective density of the product $\xi_{\rho,pr}$ results with $d_{pr,set} = d_f \Phi_{d,set}$ in:

$$\xi_{\rho,pr} = 1 - \Phi_{d,set}^{-3}, \tag{3.77}$$

which can be determined without regard to the bed particle size distribution $q_{0,bed}$. The normalized average particle density of the unweighted average bed particle diameter $\bar{\rho}_{p,mid}$ does not depend on the bed particle size distribution. It ensues from Eq. 3.76 and the unweighted particle diameter $d_{mid} = \frac{1}{2}(d_f + d_{pr,set})$ to:

$$\xi_{\rho,mid} = 1 - \left(\frac{d_f}{d_{mid}} \right)^3 = 1 - \frac{8}{(\Phi_{d,set} + 1)^3}. \tag{3.78}$$

The normalized average particle densities of the mean bed particle diameter $\xi_{\rho,m}(d_m)$, of the Sauter diameter $\xi_{\rho,32}(d_{32})$, of the number-based average bed particle diameter $\xi_{\rho,q_0}(d_{-3,0}^*)$ and of the volume-based average bed particle diameter $\xi_{\rho,q_3}(d_{3,0}^*)$ are listed in Table 3.3 with general expressions on the left (for size-dependent growth) and with specific solutions for size-independent growth on the right. As the unweighted particle diameter d_{mid} equals the mean diameter d_m for an equal bed particle size distribution, the corresponding normalized average particle densities $\xi_{\rho,mid}$ (Eq. 3.78) and $\xi_{\rho,m}$ (Eq. 3.83) are the same.

size-dependent growth $G_d = \mathrm{f}(d)$		size-independent growth $G_d \neq \mathrm{f}(d)$	
$\xi_{\rho,m} = 1 - \left(\frac{d_f}{d_m}\right)^3$	(3.79)	$\xi_{\rho,m} = 1 - \frac{8}{(\Phi_{d,set}+1)^3}$	(3.83)
$\xi_{\rho,32} = 1 - \left(\frac{d_f}{d_{32}}\right)^3$	(3.80)	$\xi_{\rho,32} = 1 - \left(\frac{4}{3}\frac{\Phi_{d,set}^3 - 1}{\Phi_{d,set}^4 - 1}\right)^3$	(3.84)
$\xi_{\rho,q_0} = 1 - \frac{d_f^3}{m_{-3,0}^{-1}} = 1 - \left(\frac{d_f}{d_{-3,0}^*}\right)^3$	(3.81)	$\xi_{\rho,q_0} = 1 - \frac{1}{2}\frac{\Phi_{d,set}+1}{\Phi_{d,set}^2}$	(3.85)
$\xi_{\rho,q_3} = 1 - \frac{d_f^3}{m_{3,0}} = 1 - \left(\frac{d_f}{d_{3,0}^*}\right)^3$	(3.82)	$\xi_{\rho,q_3} = 1 - 4\frac{\Phi_{d,set}-1}{\Phi_{d,set}^4 - 1}$	(3.86)

Table 3.3: Diverse normalized particle densities for a general size-dependent growth function $G_d = \mathrm{f}(d)$ and a size-independent growth rate function $G_d \neq \mathrm{f}(d)$ (even growth).

3.6 Influence of particle growth on product settling characteristics

It was previously shown that the terminal sinking velocity u_s (Section 2.2.1) is the mainly used property to calculate the elutriation limit of the fluidized bed operation range (Section 2.2.4) or the separation curve of the straight-duct air classifier (Section 2.2.7). The terminal sinking velocity strongly depends on particle size d and effective particle density ρ_p (see also Eq. 2.63). Both of these particle properties are distributed in layerwise granulation processes, when cores and coatings have different apparent densities. The change in effective particle density with granule size enlargement ($\Phi_d \uparrow$) can be approached by the present ICLG-model using Eq. 3.4 for the case that the component density ratio is unequal to unity: $\Phi_\rho \neq 1$. Regarding the analytical solutions in Eqs. 2.84 to 2.88, it is to be expected that the terminal sinking velocity of bed granules increases with particle growth for layering with $\Phi_\rho = 1$ and coating with $\Phi_\rho > 1$. In the case of coating layers which are significantly lighter than the core material, the terminal sinking velocity can also be reduced by particle growth. The reason behind this is the strong reduction of the overall effective particle density ρ_p (see Eqs. 3.4 and 3.5), especially in the beginning of granulation. For such conditions, the classification, whose separation principle is based on higher sinking velocities of the product, is not suitable as discharge method in continuous granulation processes. In the following, different approaches for laminar and turbulent flow conditions are to be worked out, with which the influence of particle growth and coating-to-core density ratio on terminal sinking velocity can be determined. From this, two critical characteristics of layerwise granulation are derived. The first one is the critical component-density ratio (symbolized by $\Phi_{\rho,cr}$), below which the sinking velocity lowers with incipient granule size enlargement. The second one is the minimum particle growth ratio (symbolized by $\Phi_{d,min}$), from which the product sinking velocity exceeds that of the external nuclei for undercritical component-density ratios ($\Phi_\rho < \Phi_{\rho,cr}$). This point is also called the minimum required particle growth ratio. With these critical characteristics, it can be decided whether the continuous granulation is to be realized by classification or by a different apparatus (e.g., horizontal fluidized bed), depending on the desired particle growth ratio and the material densities.

3.6.1 General equations of definition

Terminal sinking velocity of external nuclei and product granules

According to Eq. 2.63, the terminal sinking velocity of external nuclei (symbolized by $u_{s,f}$) and of the product (symbolized by $u_{s,pr}$) is given with

$$u_{s,f} = \begin{cases} \sqrt{\frac{4}{3c_{d,f}}\frac{\rho_f - \rho_g}{\rho_g} d_f g} & , \text{for } F_{bu} > 0 \\ \sqrt{\frac{4}{3c_{d,f}}\frac{\rho_f}{\rho_g} d_f g} & , \text{for } F_{bu} = 0 \end{cases} \tag{3.87}$$

and

$$u_{s,pr} = \begin{cases} \sqrt{\frac{4}{3c_{d,pr}}\frac{\rho_{pr} - \rho_g}{\rho_g} d_{pr,set} g} & , \text{for } F_{bu} > 0 \\ \sqrt{\frac{4}{3c_{d,pr}}\frac{\rho_{pr}}{\rho_g} d_{pr,set} g} & , \text{for } F_{bu} = 0 \end{cases}, \tag{3.88}$$

each of the equations distinguishing between two different cases: with the buoyancy force taken into account (denoted by $F_{bu} > 0$) and without buoyancy force (denoted by $F_{bu} = 0$). Equations 3.87 and 3.88 shall be reformulated in order to describe the influence of particle growth on product sinking velocity in a dimensionless manner in the following. For this purpose, Eq. 3.5 is used to replace the effective product density ρ_{pr} by terms of the target-growth ratio $\Phi_{d,set}$ and the component density ratio Φ_ρ, the nuclei-to-gas density ratio ρ_f/ρ_g is factored out, and the desired product diameter $d_{pr,set}$ is substituted by $d_f\Phi_{d,set}$, which results in

$$u_{s,f} = \begin{cases} \sqrt{\frac{4}{3c_{d,f}}\frac{\rho_f}{\rho_g}\left(1-\frac{\rho_g}{\rho_f}\right)d_f g} & \text{, for } F_{bu} > 0 \\ \sqrt{\frac{4}{3c_{d,f}}\frac{\rho_f}{\rho_g}d_f g} & \text{, for } F_{bu} = 0 \end{cases}, \tag{3.89}$$

and

$$u_{s,pr} = \begin{cases} \sqrt{\frac{4}{3c_{d,pr}}\frac{\rho_f}{\rho_g}\left(\left((1-\Phi_\rho)\Phi_{d,set}^{-3}+\Phi_\rho\right)-\frac{\rho_g}{\rho_f}\right)d_f\Phi_{d,set}g} & \text{, for } F_{bu} > 0 \\ \sqrt{\frac{4}{3c_{d,pr}}\frac{\rho_f}{\rho_g}\left((1-\Phi_\rho)\Phi_{d,set}^{-3}+\Phi_\rho\right)d_f\Phi_{d,set}g} & \text{, for } F_{bu} = 0 \end{cases}. \tag{3.90}$$

Terminal sinking velocities can be still sufficiently approximated with disregarded buoyancy ($F_{bu} = 0$) for solid-gas systems due to their large density difference ($\rho_g \ll \rho_f$).

Gas-to-nuclei density ratio

The gas-to-nuclei density ratio Φ_{bu} is introduced with

$$\Phi_{bu} \coloneqq \frac{\rho_g}{\rho_f} \tag{3.91}$$

to represent the influence of buoyancy on the relative product sinking velocity by means of a dimensionless quantity, as shown below. In the case of neglected buoyancy force ($F_{bu} = 0$), the gas-to-nuclei density ratio is by definition still larger than zero ($\Phi_{bu} > 0$); however, it does not then appear in the solutions of the relative product sinking velocity.

Relative product sinking velocity

The relative product sinking velocity $\Phi_{u_{s,pr}}$ is defined as product-to-nuclei ratio of terminal sinking velocities:

$$\Phi_{u_{s,pr}} \coloneqq \frac{u_{s,pr}}{u_{s,f}}. \tag{3.92}$$

After division of Eq. 3.90 by Eq. 3.89, the relative product sinking velocity $\Phi_{u_{s,pr}}$ is formulated with

$$\Phi_{u_{s,pr}} = \begin{cases} \sqrt{\frac{c_{d,f}}{c_{d,pr}}\frac{(1-\Phi_\rho)\Phi_{d,set}^{-3}+\Phi_\rho-\Phi_{bu}}{1-\Phi_{bu}}\Phi_{d,set}} & \text{, for } \Phi_\rho \neq 1 \text{ and } F_{bu} > 0 \\ \sqrt{\frac{c_{d,f}}{c_{d,pr}}\left((1-\Phi_\rho)\Phi_{d,set}^{-3}+\Phi_\rho\right)\Phi_{d,set}} & \text{, for } \Phi_\rho \neq 1 \text{ and } F_{bu} = 0 \\ \sqrt{\frac{c_{d,f}}{c_{d,pr}}\Phi_{d,set}} & \text{, for } \Phi_\rho = 1 \end{cases} \tag{3.93}$$

for three different cases. The first and second case are both expressions for components of different effective densities ($\Phi_\rho \neq 1$), e.g., for coating applications with thick layers. The difference between them is that the first case considers buoyancy ($F_{bu} > 0$), while the second does not ($F_{bu} = 0$). The third case presupposes a homogeneous intraparticle density ($\Phi_\rho = 1$), as for instance in layering applications, whereby it turns out that the buoyancy does not influence the relative product sinking velocity $\Phi_{u_{s,pr}}$ anyway. The product-to-nuclei ratio of the drag coefficients $c_{d,pr}/c_{d,f}$ depends on the terminal Reynolds numbers ($Re_{s,f} = u_{s,f}d_f/\nu_g$ and $Re_{s,pr} = u_{s,pr}d_{pr,set}/\nu_g$), which correspond to nuclei and product properties:

$$\frac{c_{d,pr}}{c_{d,f}} = \mathrm{f}(Re_{s,f}, Re_{s,pr}). \tag{3.94}$$

Diverse c_d-approaches are presented in Section 2.2.1. Some of them provide closed solutions for the terminal sinking velocity, and hence, for the relative product sinking velocity. These are for example the Stokes approximation for $Re_s < 0.25$ (Eqs. 2.68, 2.67, and 2.84), the suggestions of Martin [40, 41] with exact

values for $Re_s < 10^4$ (Eqs. 2.83, 2.82, and 2.87), or the quadratic solution with fluctuating errors within a range of $10^3 < Re_s < 3 \cdot 10^5$ (Eqs. 2.69, 2.70, and 2.88). The product of the relative product sinking velocity and the desired particle growth ratio conforms with the product-to-nuclei ratio of terminal Reynolds numbers: $\Phi_{u_{s,pr}} \Phi_{d,set} = Re_{s,pr}/Re_{s,f}$.

3.6.2 Approximate solutions for the Stokes and the quadratic flow regime

Relative product sinking velocity

The product-to-nuclei ratio of drag coefficient of Eq. 3.94 is simplified for the laminar and turbulent flow regimes, as follows:

$$\frac{c_{d,pr}}{c_{d,f}} = \begin{cases} \frac{Re_{s,f}}{Re_{s,pr}} = \frac{1}{\Phi_{u_{s,pr}} \Phi_{d,set}} & \text{, for the Stokes regime} \\ 1 & \text{, for the quadratic regime} \end{cases}. \tag{3.95}$$

Using the relations of Eq. 3.95, each of three cases of the relative product sinking velocity $\Phi_{u_{s,pr}}$ of Eq. 3.93 is given only as function of material characteristics ($\Phi_{d,set}$, Φ_ρ, and Φ_{bu}) with

$$\Phi_{u_{s,pr}}(\text{Stokes}) = \begin{cases} \frac{(1-\Phi_\rho)\Phi_{d,set}^{-3} + \Phi_\rho - \Phi_{bu}}{1-\Phi_{bu}} \Phi_{d,set}^2 & \text{, for } \Phi_\rho \neq 1 \text{ and } F_{bu} > 0 \\ \left((1-\Phi_\rho)\Phi_{d,set}^{-3} + \Phi_\rho\right)\Phi_{d,set}^2 & \text{, for } \Phi_\rho \neq 1 \text{ and } F_{bu} = 0 \\ \Phi_{d,set}^2 & \text{, for } \Phi_\rho = 1 \end{cases} \tag{3.96}$$

for the Stokes regime and with

$$\Phi_{u_{s,pr}}(\text{quadratic}) = \begin{cases} \sqrt{\frac{(1-\Phi_\rho)\Phi_{d,set}^{-3} + \Phi_\rho - \Phi_{bu}}{1-\Phi_{bu}} \Phi_{d,set}} & \text{, for } \Phi_\rho \neq 1 \text{ and } F_{bu} > 0 \\ \sqrt{\left((1-\Phi_\rho)\Phi_{d,set}^{-3} + \Phi_\rho\right)\Phi_{d,set}} & \text{, for } \Phi_\rho \neq 1 \text{ and } F_{bu} = 0 \\ \sqrt{\Phi_{d,set}} & \text{, for } \Phi_\rho = 1 \end{cases}. \tag{3.97}$$

for the quadratic regime. It is noticeable that the limiting case solutions for the homogeneous intraparticle product density ($\Phi_\rho = 1$) are each of a simple structure; but, they are also independent from the solids density overall.

Slope functions of the relative product sinking velocity

It can be seen in the first and second case of Eqs. 3.96 and 3.97 (for $\Phi_\rho \neq 1$) that the solutions of $\Phi_{u_{s,pr}}$ contain the hyperbolic term $(1-\Phi_\rho)\Phi_{d,set}^{-3}$ for both limiting flow regimes. This term influences relative product sinking velocity $\Phi_{u_{s,pr}}$ strongly in the beginning of particle growth ($\Phi_{d,set} \to 1$) and vanishes for large desired particle growth ratios ($\Phi_{d,set} \to \infty$). Due to the hyperbolic term, the relative product sinking velocity $\Phi_{u_{s,pr}}$ can decline in the beginning when the coating-to-core density ratio Φ_ρ is too low. In order to find the critical coating-to-core density ratio $\Phi_{\rho,cr}$, under which the relative product sinking velocity decreases in the beginning of growth, the first derivative of the relative product sinking velocity with respect to the desired particle growth ratio $\Phi_{d,set}$ is introduced:

$$\Phi'_{u_{s,pr}} := \frac{\mathrm{d}}{\mathrm{d}\Phi_{d,set}}(\Phi_{u_{s,pr}}). \tag{3.98}$$

This derivative can be solved for the laminar and turbulent regimes, which ensues from Eqs. 3.96, 3.97, and 3.98 to the here so-called slope functions of the relative product sinking velocity with

$$\Phi'_{u_{s,pr}}(\text{Stokes}) = \begin{cases} \frac{2\left(\Phi_\rho - \Phi_{bu}\right)\Phi_{d,set} - (1-\Phi_\rho)\Phi_{d,set}^{-2}}{1-\Phi_{bu}} & \text{, for } \Phi_\rho \neq 1 \text{ and } F_{bu} > 0 \\ 2\Phi_\rho \Phi_{d,set} - (1-\Phi_\rho)\Phi_{d,set}^{-2} & \text{, for } \Phi_\rho \neq 1 \text{ and } F_{bu} = 0 \\ 2\Phi_{d,set} & \text{, for } \Phi_\rho = 1 \end{cases} \tag{3.99}$$

for the Stokes regime and with

$$\Phi'_{u_{s,pr}}(\text{quadratic}) = \begin{cases} \frac{1}{2\sqrt{1-\Phi_{bu}}} \frac{\Phi_\rho - \Phi_{bu} - 2(1-\Phi_\rho)\Phi_{d,set}^{-3}}{\sqrt{(1-\Phi_\rho)\Phi_{d,set}^{-2} + (\Phi_\rho - \Phi_{bu})\Phi_{d,set}}} & \text{, for } \Phi_\rho \neq 1 \text{ and } F_{bu} > 0 \\ \frac{1}{2} \frac{\Phi_\rho - 2(1-\Phi_\rho)\Phi_{d,set}^{-3}}{\sqrt{(1-\Phi_\rho)\Phi_{d,set}^{-2} + \Phi_\rho \Phi_{d,set}}} & \text{, for } \Phi_\rho \neq 1 \text{ and } F_{bu} = 0 \\ \frac{1}{2\sqrt{\Phi_{d,set}}} & \text{, for } \Phi_\rho = 1 \end{cases} \tag{3.100}$$

for the quadratic regime. Both slope functions (Eqs. 3.99 and 3.100) are derived for different component densities ($\Phi_\rho \neq 1$). In the beginning of this chapter, the desired particle growth ratio was defined to be larger than unity (Eq. 3.1: $\Phi_{d,set} > 1$) to avoid division-by-zero contractions in the ICLG-model equations (e.g., Eq. 3.59). The incipient slopes of the relative product sinking velocity (symbolized by $\Phi'_{u_{s,pr,0}}$) are therefore derived from the limits of Eqs. 3.99 and 3.100 for the desired particle growth ratio approaching unity ($\Phi_{d,set} \to 1$), which follows to

$$\Phi'_{u_{s,pr,0}}(\text{Stokes}) = \lim_{\Phi_{d,set}\to 1}\left(\Phi'_{u_{s,pr}}(\text{Stokes})\right) = \begin{cases} \frac{3\Phi_\rho - 2\Phi_{bu} - 1}{1-\Phi_{bu}} & \text{, for } \Phi_\rho \neq 1 \text{ and } F_{bu} > 0 \\ 3\Phi_\rho - 1 & \text{, for } \Phi_\rho \neq 1 \text{ and } F_{bu} = 0 \\ 2 & \text{, for } \Phi_\rho = 1 \end{cases}, \tag{3.101}$$

for Stokes conditions and to

$$\Phi'_{u_{s,pr,0}}(\text{quadratic}) = \lim_{\Phi_{d,set}\to 1}\left(\Phi'_{u_{s,pr}}(\text{quadratic})\right) = \begin{cases} \frac{1}{2}\frac{3\Phi_\rho - \Phi_{bu} - 2}{1-\Phi_{bu}} & \text{, for } \Phi_\rho \neq 1 \text{ and } F_{bu} > 0 \\ \frac{1}{2}(3\Phi_\rho - 2) & \text{, for } \Phi_\rho \neq 1 \text{ and } F_{bu} = 0 \\ \frac{1}{2} & \text{, for } \Phi_\rho = 1 \end{cases}. \tag{3.102}$$

for quadratic conditions.

Critical coating-to-core density ratio - critical component density ratio

By setting the incipient slopes of Eqs. 3.101 and 3.102 to zero, respectively, the critical coating-to-core density ratio $\Phi_{\rho,cr}$ is obtained with

$$\Phi_{\rho,cr}(\text{Stokes}) = \begin{cases} \frac{1+2\Phi_{bu}}{3} & \text{, for } F_{bu} > 0 \\ \frac{1}{3} & \text{, for } F_{bu} = 0 \end{cases} \tag{3.103}$$

for the Stokes regime and with

$$\Phi_{\rho,cr}(\text{quadratic}) = \begin{cases} \frac{2+\Phi_{bu}}{3} & \text{, for } F_{bu} > 0 \\ \frac{2}{3} & \text{, for } F_{bu} = 0 \end{cases} \tag{3.104}$$

for the quadratic regime. The third case with $\Phi_\rho = 1$ does not apply here for logical reasons.

Minimum required particle growth ratio

As described before, the product sinking velocity $u_{s,pr}$ is lowered by initial layerwise particle growth for undercritical component density ratios $\Phi_\rho < \Phi_{\rho,cr}$, because the effective particle density significantly decreases in the beginning of granulation. In such a case the relative product sinking velocity $\Phi_{u_{s,pr}}$ falls below unity for low desired particle growth ratios $\Phi_{d,set}$, as can also be deduced from the hyperbolic term $(1-\Phi_\rho)\Phi_{d,set}^{-3}$ in Eqs. 3.96 and 3.97. But after sufficiently large particle growth, the overall density gradually takes on the value of the coating material, which is also illustrated by the normalized effective product density ($\xi_{\rho,pr} = 1 - \Phi_{d,set}^3$) later in Figure 4.2. A further granule size enlargement then raises the product sinking velocity again under nearly constant particle density conditions, so that it exceeds the terminal sinking velocity of external nuclei at the here so-called minimum required particle growth ratio $\Phi_{d,min}$, which is defined by:

$$\Phi_{d,min} = \Phi_{d,set}(\Phi_{u_{s,pr}} \coloneqq 1, \Phi_\rho) > 1 \qquad \text{, for } \Phi_{bu} < \Phi_\rho < \Phi_{\rho,cr}. \tag{3.105}$$

The minimum required particle growth ratio $\Phi_{d,min}$ can be used as a criterion of minimal desired particle growth ratio for continuous granulation with air classification, as shown later in Chapter 4. Its dependency on the coating-to-core density ratio Φ_ρ can be derived for the Stokes and quadratic regime by setting the relative product sinking velocity of Eqs. 3.96 and 3.97 to unity and transforming both equations to the following third order polynomials:

$$0 = \Phi_d^{*3} - (K_{\Phi_\rho} + 1)\Phi_d^* + K_{\Phi_\rho} \qquad \text{, for the Stokes regime,} \tag{3.106}$$

$$0 = \Phi_d^{*3} - (K_{\Phi_\rho} + 1)\Phi_d^{*2} + K_{\Phi_\rho} \qquad \text{, for the quadratic regime,} \tag{3.107}$$

where K_{Φ_ρ} is given with

$$K_{\Phi_\rho} = \begin{cases} \frac{1-\Phi_\rho}{\Phi_\rho-\Phi_{bu}} & \text{, for } F_{bu} > 0 \text{ and } \Phi_{bu} < \Phi_\rho < \Phi_{\rho,cr} = \begin{cases} \frac{1+2\Phi_{bu}}{3} & \text{, for the Stokes regime} \\ \frac{2+\Phi_{bu}}{3} & \text{, for the quadratic regime} \end{cases} \\ \frac{1-\Phi_\rho}{\Phi_\rho} & \text{, for } F_{bu} = 0 \text{ and } \quad 0 < \Phi_\rho < \Phi_{\rho,cr} = \begin{cases} \frac{1}{3} & \text{, for the Stokes regime} \\ \frac{2}{3} & \text{, for the quadratic regime} \end{cases} \end{cases}. \tag{3.108}$$

In Eqs. 3.106 and 3.107, Φ_d^* represents the variables of the third-order polynomials, for each of which there are three roots in the order: $\Phi_{d1}^* < \Phi_{d2}^* < \Phi_{d3}^*$. The minimum required particle growth ratio must correspond to the largest root of the polynomial equations ($\Phi_{d,min} = \Phi_{d3}^*$), since with further granule enlargement no intersection point with $\Phi_{u_{s,pr}} = 1$ appears, and hence no further root of the polynomials. In addition to this, the relative product sinking velocity is by definition already given as unity at the beginning of granulation: $\Phi_{u_{s,pr}}(\Phi_{d,set} \to 1) = 1$. This means that the second roots of the polynomials are always located at unity ($\Phi_{d2}^* = 1$) independently from the component density ratio. Once one of the three roots is known, the third-order polynomials can be reduced to quadratic equations by polynomial division with the linear factor $(\Phi_d^* - 1)$. The roots of these quadratic polynomials then correspond to the first and third roots (Φ_{d1}^* and Φ_{d3}^*) of the third order polynomials. As the value of Φ_{d3}^* is larger than that of Φ_{d1}^*, the minimum required particle growth ratio $\Phi_{d,min}$ conforms with the upper root of the quadratic polynomials, which provides analytical expressions of the minimum required particle growth ratio according to

$$\Phi_{d,min}(\text{Stokes}) = \begin{cases} \sqrt{K_{\Phi_\rho} + \frac{1}{4}} - \frac{1}{2} & \text{, for } \Phi_\rho < \Phi_{\rho,cr} \text{ with } K \text{ by Eq. 3.108} \\ 1 & \text{, for } \Phi_\rho \geq \Phi_{\rho,cr} \end{cases}, \tag{3.109}$$

for the Stokes regime and to

$$\Phi_{d,min}(\text{quadratic}) = \begin{cases} \frac{1}{2}K_{\Phi_\rho} + \sqrt{\frac{1}{4}K_{\Phi_\rho}^2 + K_{\Phi_\rho}} & \text{, for } \Phi_\rho < \Phi_{\rho,cr} \text{ with } K_{\Phi_\rho} \text{ by Eq. 3.108} \\ 1 & \text{, for } \Phi_\rho \geq \Phi_{\rho,cr} \end{cases} \tag{3.110}$$

for the quadratic regime, where the trivial solutions of critical and overcritical component density ratios ($\Phi_{d,min}(\Phi_\rho \geq \Phi_{\rho,cr}) = 1$) are included, respectively. The dependency of minimum required particle growth ratios of the Stokes and quadratic regime on component density ratio is illustrated and discussed later in Section 4.2.3 for the case of neglected buoyancy.

Cross-check

The solutions of the minimum required particle growth ratio $\Phi_{d,min}$ for the Stokes regime and the quadratic regime can be cross-checked by inserting the critical component density ratio $\Phi_{\rho,cr}$ into Eqs. 3.108 to 3.110. The substitute K_{Φ_ρ} follows then to

$$K_{\Phi_\rho}(\Phi_\rho = \Phi_{\rho,cr}) = \frac{1-\Phi_{\rho,cr}}{\Phi_{\rho,cr}-\Phi_{bu}} = \frac{1-\frac{1+2\Phi_{bu}}{3}}{\frac{1+2\Phi_{bu}}{3}-\Phi_{bu}} = \frac{3-1-2\Phi_{bu}}{1+2\Phi_{bu}-3\Phi_{bu}} = \frac{2-2\Phi_{bu}}{1-\Phi_{bu}} = 2,$$

for the Stokes regime, and to

$$K_{\Phi_\rho}(\Phi_\rho = \Phi_{\rho,cr}) = \frac{1-\Phi_{\rho,cr}}{\Phi_{\rho,cr}-\Phi_{bu}} = \frac{1-\frac{2+\Phi_{bu}}{3}}{\frac{2+\Phi_{bu}}{3}-\Phi_{bu}} = \frac{3-2-\Phi_{bu}}{2+\Phi_{bu}-3\Phi_{bu}} = \frac{1-\Phi_{bu}}{2-2\Phi_{bu}} = \frac{1}{2},$$

for the quadratic regime. By

$$\Phi_{d,min}\big(\text{Stokes, } K_{\Phi_\rho}(\Phi_\rho = \Phi_{\rho,cr}) = 2\big) = \sqrt{2+\frac{1}{4}} - \frac{1}{2} = \sqrt{\frac{8+1}{4}} - \frac{1}{2} = 1 \qquad \text{, and by}$$

$$\Phi_{d,min}\big(\text{quadratic, } K_{\Phi_\rho}(\Phi_\rho = \Phi_{\rho,cr}) = \frac{1}{2}\big) = \frac{1}{2}\frac{1}{2} + \sqrt{\frac{1}{4}\frac{1}{4} + \frac{1}{2}} = \frac{1}{4} + \sqrt{\frac{1}{16} + \frac{8}{16}} = 1,$$

it shows that the corresponding minimum required particle growth ratio ensues to unity at the critical coating-to-core density ratio for both limiting cases, as to be expected.

4 Results of the ideal continuous layerwise granulation model

The ideal continuous layerwise granulation model (ICLG-model) of Chapter 3 allows to roughly estimate required operating parameters and diverse characteristics of bed and product particles for continuous layering or coating processes. Based on the ICLG-model, the influence of layerwise particle growth on

- characteristics related to particle density (Section 4.1.2),
- required process parameters (Section 4.1.3),
- required growth time (Section 4.1.4), and
- product settling characteristics (Section 4.2)

shall be illustrated and discussed in the following in dependency on the desired particle growth ratio $\Phi_{d,set}$ for different combinations of coating and core materials, which are represented by different values of the coating-to-core density ratio Φ_ρ. The results provide the basis for the development of operation concepts for continuous layer-by-layer granulation processes, some of which are also used in the experimental part of this thesis (Sections 9.4 and 10.4).

4.1 Influence of particle growth on product and process characteristics

4.1.1 Parameter setting

The desired growth ratio $\Phi_{d,set}$ is chosen as main variable over which the product characteristics shall be plotted in the following. In plots, the coating-to-core density ratio $\Phi_\rho = \rho_c/\rho_f$ is used as curve parameter. Five different values of the component density ratio are defined, which are summarized in Table 4.1. Two of them are referred to materials employed in the experiments of the present thesis. These are Cellets® and glass beads (as core particles) and sodium benzoate (as coating). From this, two different binary component systems are formulated: Cellets® with sodium benzoate coatings and glass beads with sodium benzoate coatings. The component density ratio Φ_ρ of both binary component systems is calculated as described in the following. The manufacturer specifications of the core materials are listed in Table 9.1. The effective core material densities (represented by ρ_f according to the ICLG-model) are given with $1380\,\mathrm{kg/m^3}$ for Cellets® (stated also in [2]) and with $2500\,\mathrm{kg/m^3}$ for glass beads. The compact solid density of sodium benzoate (symbolized here with $\rho_{s,c}$) is given with $1440\,\mathrm{kg/m^3}$, [2]. Hampel [2] has determined a value of the average coating layer porosity ε_c with 43 % for sodium benzoate coatings on Cellets®. At this, the coating has been created by discontinuous Wurster granulation with an inlet gas temperature of 70°C, an inlet gas mass flow rate of 70 kg/h, and a total spray rate of 1.1 kg/h with a mass fraction of 30 %. The effective coating density $\rho_c = \rho_{s,c}(1-\varepsilon_c)$ of sodium benzoate with a porosity of 43 % ensues to $820.8\,\mathrm{kg/m^3}$, The corresponding component density ratios are given then with $\Phi_\rho = 0.595$ for sodium benzoate layers on Cellets®-cores and with $\Phi_\rho = 0.328$ for sodium benzoate coatings on glass beads, as listed in Table 4.2. Another value for the parameter setting of the coating-to-core density ratio is unity, which represents particle growth processes with homogeneous intraparticle density, as a proper assumption for layering processes. The last two values of the component density ratio are chosen with 1.4 and 1.7 to have nearly equal intervals between pairs of parameter values.

4.1.2 Density characteristics

Effective product density

Figure 4.1 depicts the effective product density ρ_{pr} with increasing target-growth ratio $\Phi_{d,set}$ calculated by Eq. 3.5 for the five different coating-to-core density ratios Φ_ρ of Table 4.1 with an effective core density

parameter	parameter variation
Φ_ρ	$\{0.328, 0.595, 1, 1.4, 1.7\}$

Table 4.1: Setting of the component density ratio Φ_ρ to be used as curve parameter.

binary component system	ρ_f [kg/m^3]	Φ_ρ [–]
Cellets® with sodium benzoate coating	1380	0.595
glass beads with sodium benzoate coating	2500	0.328

Table 4.2: Reference values of the component density ratio Φ_ρ for an effective coating density of $\rho_c = 820.8\,\mathrm{kg/m^3}$ and for two different binary component systems.

of $1380\,\mathrm{kg/m^3}$. For the component density ratio of unity ($\Phi_\rho = 1$), the effective product density is by definition not affected during granulation. It can be seen that the effective product density ρ_{pr} declines for the first two component density ratios ($\Phi_\rho = 0.328$ and $\Phi_\rho = 0.595$) and rises for the last two component density ratios ($\Phi_\rho = 1.4$ and $\Phi_\rho = 1.7$). For each of the curves with different component densities ($\Phi_\rho \neq 1$), the effective product density gradually takes on the value of the effective coating density according to $\rho_c = \rho_f \Phi_\rho$. Regardless of the value of the component density ratio, the effective product density changes significantly before doubling of the grain size ($\Phi_{d,set} < 2$), and only slightly for even larger particle growth ratios ($\Phi_{d,set} > 2$). The value of effective coating density is almost reached after tripling the granule size ($\Phi_{d,set} = 3$).

Normalized effective particle density

Several normalized effective particle densities $\xi_{\rho,j}$ are defined in Section 3.5, which are referred to diverse characteristic particle diameters. These include the normalized effective particle density related to the product diameter $\xi_{\rho,pr}(d_{pr,set})$, to the unweighted average bed particle diameter $\xi_{\rho,mid}(d_{mid})$, the mean diameter of the bed $\xi_{\rho,m}(d_m)$, and the Sauter diameter of the bed $\xi_{\rho,32}(d_{32})$, as well as the number-based average normalized effective particle density $\xi_{\rho,q_0}((d^*_{-3,0}))$ and the volume-based normalized effective particle density $\xi_{\rho,q_3}(d^*_{3,0})$. All of them are by definition independent from component densities, see Eqs. 3.7, 3.8, and 3.76. The described normalized effective particle densities represent the relative change in effective particle density with particle growth. They can be expressed by functions of only the desired particle growth ratio $\Phi_{d,set}$ (see Eqs. 3.77 to 3.86), when size-independent growth is assumed ($G_d \neq \mathrm{f}(d)$). These functions are shown in Figure 4.2 for desired growth ratios $\Phi_{d,set}$ between 1 and 4. The normalized effective particle densities are zero for desired particle growth ratio approaching unity: $\xi_{\rho,j}(\Phi_{d,set} \to 1) = 0$, which is the lower limit of smallest granulation with $\rho_{pr} \to \rho_f$. In contrast to this, the normalized effective particle densities converge to unity (100 % in Figure 4.2) for infinitely large desired particle growth ratios: $\xi_{\rho,j}(\Phi_{d,set} \to \infty) = 1$. The normalized effective particle density of the unweighted average bed particle diameter $\xi_{\rho,mid}$ equals that of the mean diameter $\xi_{\rho,m}$ for an even growth rate function. Both of which are

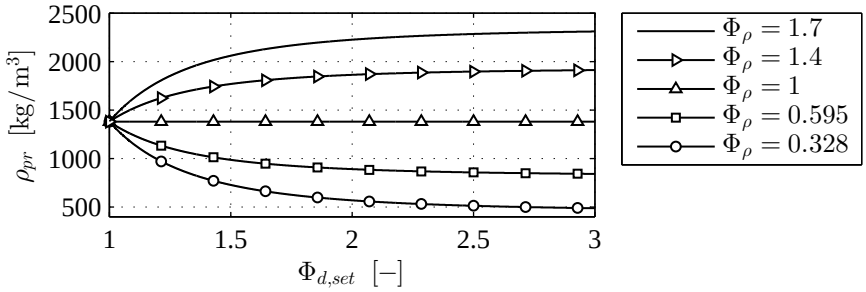

Figure 4.1: Effective product density ρ_{pr} in dependency on the desired particle growth ratio $\Phi_{d,set}$ for different coating-to-core density ratios Φ_ρ.

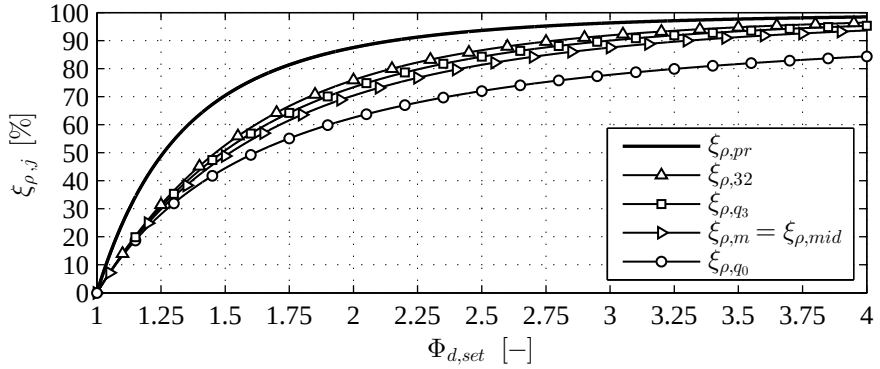

Figure 4.2: Normalized effective particle densities $\xi_{\rho,j}$ of different particle characteristics*) versus the desired particle growth ratio $\Phi_{d,set}$; *) related to the product diameter $\xi_{\rho,pr}$ (Eq. 3.77), the Sauter diameter of the bed $\xi_{\rho,32}$ (Eq. 3.84)**), the volume-based average bed particle density ξ_{ρ,q_3} (Eq. 3.86)**), the mean diameter of the bed $\xi_{\rho,m}$ (Eq. 3.83, conforms with $\xi_{\rho,mid}$)**), and the number-based average bed particle density ξ_{ρ,q_0} (Eq. 3.85)**); **) for size-independent (even) growth rate, given in Table 3.3.

illustrated by the same curve in Figure 4.2, indicated with $\xi_{\rho,mid} = \xi_{\rho,m}$. It turns out that the normalized effective density of the number-based average bed particle density ξ_{ρ,q_0} has the smallest values followed by that of the mean bed particle diameter $\xi_{\rho,m}$, of the unweighted average bed particle diameter $\xi_{\rho,mid}$, of the volume-based average bed particle density ξ_{ρ,q_3}, and of the Sauter diameter $\xi_{\rho,32}$ of the product diameter $\xi_{\rho,pr}$ with largest values:

$$\xi_{\rho,q_0} < \xi_{\rho,mid} = \xi_{\rho,m} < \xi_{\rho,q_3} < \xi_{\rho,32} < \xi_{\rho,pr} \qquad \text{, for } \Phi_{d,set} > 1,\ \Phi_\rho \neq 1, \text{ and } G_d \neq \mathrm{f}(d). \tag{4.1}$$

The normalized effective particle densities increase strongly for low desired growth ratios $\Phi_{d,set} < 2$ and slighter for larger desired growth ratios $\Phi_{d,set} > 2$. It is obvious that the normalized average effective density of the number-based average effective bed particle density ξ_{ρ,q_0} is far less than the other normalized average effective bed particle densities ($\xi_{\rho,mid}$, $\xi_{\rho,m}$, $\xi_{\rho,32}$, and ξ_{ρ,q_3}). The normalized average effective densities of the mean diameter $\xi_{\rho,m}$, of the Sauter diameter $\xi_{\rho,32}$, and of the volume-based average effective particle density ξ_{ρ,q_3} are closer together.

4.1.3 Required nuclei feed rate and solids spray rate

Required and effective spray-to-feed rate ratio

It is shown by Eq. 3.24 in Section 3.2 that, under conditions of the ideal particle growth model (Section 3.1.1), the required spray-to-feed rate ratio $\Phi_{m,set}$ is defined by the material losses of external nuclei $\Phi_{f,loss}$ and sprayed solids $\Phi_{spr,loss}$, the coating-to-core density ratio Φ_ρ and the target-growth ratio $\Phi_{d,set}$. It conforms to the effective spray-to-feed rate ratio $\Phi_{m,eff}$ of Eq. 3.25 for vanishing material losses: $\Phi_{m,set}(\Phi_{f,loss} = 0, \Phi_{spr,loss} = 0) = \Phi_{m,eff}$. Figure 4.3 is illustrates the cubic increase of the effective spray-to-feed rate ratio $\Phi_{m,eff}$ on desired particle growth ratio $\Phi_{d,set}$ for the five values of the different component density ratio Φ_ρ of Table 4.1. The context shows that higher spray rates and/or lower nuclei feed rates are required in order to increase the granule size enlargement. The ratio of spray-to-feed rate must be even greater for higher component density ratios.

Conclusions for the spray-to-feed rate setting methods

As described in Section 3.2.2, the nuclei feed rate $\dot{M}_f$, the solids spray rate $\dot{M}_{spr,s}$, and the production rate $\dot{M}_{pr}$ are related with each other by two equations (Eqs. 3.24 and 3.22); wherefore, only one of them can be freely chosen. This leads to the three different setting variants of the nuclei feed rate and solids spray rate (SFV1, SFM2, and SFM3), as listed in Table 3.1. In the first variant SFM1, where the nuclei feed rate is predefined, higher desired particle diameters can be achieved by larger solids spray rates. But, the solids spray rate is limited by the drying capacity of the inlet gas (process-gas saturation), the solubility of solids in

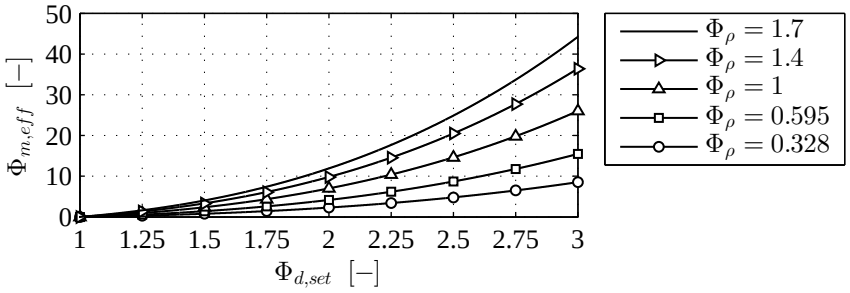

Figure 4.3: Effective spray-to-feed rate ratio $\Phi_{m,eff}$ versus the desired particle growth ratio $\Phi_{d,set}$ for five different values of the coating-to-core density ratio Φ_ρ from Table 4.1.

the employed spray liquid, drying kinetics, agglomeration tendency, and conveying limits of the pump-nozzle equipment. Drying capacity of process gas can be enlarged, and drying kinetics improved, by using

- larger granulator chamber to increase the cross-section area of the inlet,
- several granulator-classifier stages,
- horizontal fluidized beds,
- higher inlet gas velocities, and/or
- higher inlet gas temperatures.

At this, bigger granulator chambers or plants with several granulator-separator stages are related to higher investment costs and restricted by construction limitations. The setting of the inlet gas velocity depends on fluidization conditions and, hence, on material properties such as particle size and effective particle density, as shown in Section 2.2.4. Too high inlet gas temperatures lead to unwanted effects such as degradation for thermally sensitive materials. In the second spray-to-feed rate setting method SFM2, where the spray rate can be set properly, lower feed rate is needed to achieve greater desired product diameters. The feed rate is not limited by thermal characteristics, however, smaller feed rates are accompanied by lower production rates (see Eq. 3.22). Thus, with the SFM2 method, a reduced production rate has to be accepted in order to obtain larger granules. When aiming at a certain production rate, parameter setting method SFM3, has to be used. In this case, both a larger solids spray rate and lower nuclei feed rate must be guaranteed to gain higher desired particle growth ratios. The limitations of the spray rate must be considered here too. The influence of desired particle growth ratio, nuclei feed rate, and solids spray rate on required growth time $\tau_{gr,set}$, and thus, on duration of startup periods is illustrated and discussed in the following section.

4.1.4 Required growth time for even growth and for different spray-to-feed rate setting methods

The required growth time $\tau_{gr,set}$ is a measure for average total residence time of particles in the granulator-separator system, and thus, for the duration of startup periods in continuous processes. In the following, the dependence of the required growth time on the desired growth ratio $\Phi_{d,set}$ and the component density ratio Φ_ρ for the first two parameter setting variants SFM1 and SFM2 and for process-like conditions of the continuous granulation experiments are shown for even growth, such as in the size-independent growth rate approach of Mörl (even growth, see Appendix B.2). Beside the desired particle growth ratio and the component density ratio, the bed mass M_{bed}, the nuclei feed rate $\dot{M}_f$, the solids spray rate $\dot{M}_{spr,s}$, the material losses of the nuclei feed $\Phi_{f,loss}$, and sprayed solids $\Phi_{spr,loss}$ determine the required growth time too. Latter can be calculated for even growth conditions by Eq. 3.62 for fixed nuclei feed rate (SFM1) and by Eq. 3.63 for fixed solids spray rate (SFM2). It turns out from these equations that the functional relationship between the required growth time $\tau_{gr,set}$ and the desired particle growth ratio $\Phi_{d,set}$ is different for the parameter setting methods SFM1 and SFM2. This difference is illustrated below using two parameter examples for each of the two methods, which are listed in Table 4.3. The bed mass is assumed to be given with 1 kg, the solids mass fraction of the spray solution x_s with 32.25 %, the material losses of the nuclei feed and the sprayed solids with zero, respectively ($\Phi_{f,loss} = \Phi_{spr,loss} = 0$), the nuclei feed rates with 110 g/h

variant	SFM1:		SFM2:		
parameter	$\dot{M}_f$	$\dot{m}_f$	$\dot{M}_{spr}$	$\dot{M}_{spr,s}$	$\dot{m}_{spr,s}$
unit	[g/h]	[h^{-1}]	[g/h]	[g/h]	[h^{-1}]
example 1	110	0.11	800	258	0.258
example 2	150	0.15	1000	325.5	0.3225

Table 4.3: Calculation of two example values of the bed-mass-specific feed rate $\dot{m}_f$ for method SFM1 and of the bed-mass-specific solids spray rates $\dot{m}_{spr,s}$ for method SFM2, with $M_{bed} = 1\,\text{kg}$ and $x_s = 32.25\,\%$.

and 150 g/h for the method SFM1, and the solids spray rate with 258 g/h and 325.5 g/h. The values of the specific nuclei feed rate and the specific solids spray rate ensue from Eqs. 3.13 and 3.14. The values of the solids spray rate are chosen according to $\dot{M}_{spr,s} = \dot{M}_{spr} x_s$ with values of total spray rates that are applied in the experiments.

Curves of required growth time with desired particle growth ratio for different granulation conditions

Figure 4.4 shows the required growth time $\tau_{gr,set}$ with target-growth ratio $\Phi_{d,set}$ for the five different component density ratios Φ_ρ of Table 4.1 and the different parameter settings of Table 4.3. It can be seen that higher specific nuclei feed rates $\dot{m}_f$ and larger specific solids spray rates $\dot{m}_{spr,s}$ reduce the required growth time. The required growth time declines with increasing desired particle growth ratios for fixed nuclei feed rates (SFM1). The reason for this is that the solids spray rate is set to larger values by Eq. 3.11 and Eq. 3.24 for a fixed feed rate, which enlarges the growth rate. On the other hand, the required growth time increases with greater desired particle growth ratios for fixed solids spray rates (SFM2). Here, the feed rate $\dot{M}_f$ has to be reduced to raise the granule size enlargement ratio $\Phi_{d,set}$. It follows from Eq. 3.62 that lower feed rates are accompanied by longer required growth times. Further, the required spray-to-feed rate ratio (see Eq. 3.11 and Eq. 3.24) depends on the component density ratio Φ_ρ. Thereby, the component density ratio influences the required growth time $\tau_{gr,set}$. It is shown in Figure 4.4 that larger component density ratios lead to lower required growth times for the spray-to-feed rate setting method SFM1, where the feed rate is fixed. In contrast to this, higher growth times are required for larger component density ratios in the second spray-to-feed rate setting method SFM2, where the spray rate is fixed.

Conclusions for experiments

A lower required growth time is favored in granulation processes as it yields higher production rates. But, the spray rate is restricted by thermal limitations of the process gas (e.g., saturation) and agglomeration tendency of the bed, as mentioned above. In order to avoid such effects, it is recommended to set the spray rate to values with appropriate process conditions. This way, the second spray-to-feed rate setting method SFM2 has to be employed to set larger desired growth ratios with the disadvantage of large required growth times and lower production rates. Further, longer startup periods are needed for higher required growth times. For instance, a required growth time of nearly $\tau_{gr,set} = 6\,\text{h}$ is obtained for the second spray-to-feed rate setting method SFM2 at a desired growth ratio of $\Phi_{d,set} = 2$ and a component density ratio of $\Phi_\rho = 0.595$, which represents Cellets® with sodium benzoate coatings. The startup period would be longer than 6 h in this case. For this reason, several startup strategies of enhancing growing up kinetics are conceptualized in Section 9.4.10 and applied to the continuous granulation experiments of this thesis in Section 10.4.

4.2 Influence of particle growth on product settling characteristics

The terminal product sinking velocity $u_{s,pr}$ and the associated relative product sinking velocity $\Phi_{u_{s,pr}}$ are parameters of the ideal granulation model that characterize how efficient product granules can be separated from a real granulator system by air classifiers in continuous operation. In those processes, the terminal sinking velocity should be much larger than that of external nuclei $u_{s,f}$, which means that the relative product sinking velocity has to be significantly larger than unity. Diverse calculation methods of these product settling characteristics are derived in Section 3.6. There, it can be seen that $u_{s,pr}$ and $\Phi_{u_{s,pr}}$ depend on size and effective density of external nuclei d_f and ρ_p, the desired particle growth ratio $\Phi_{d,set}$, and

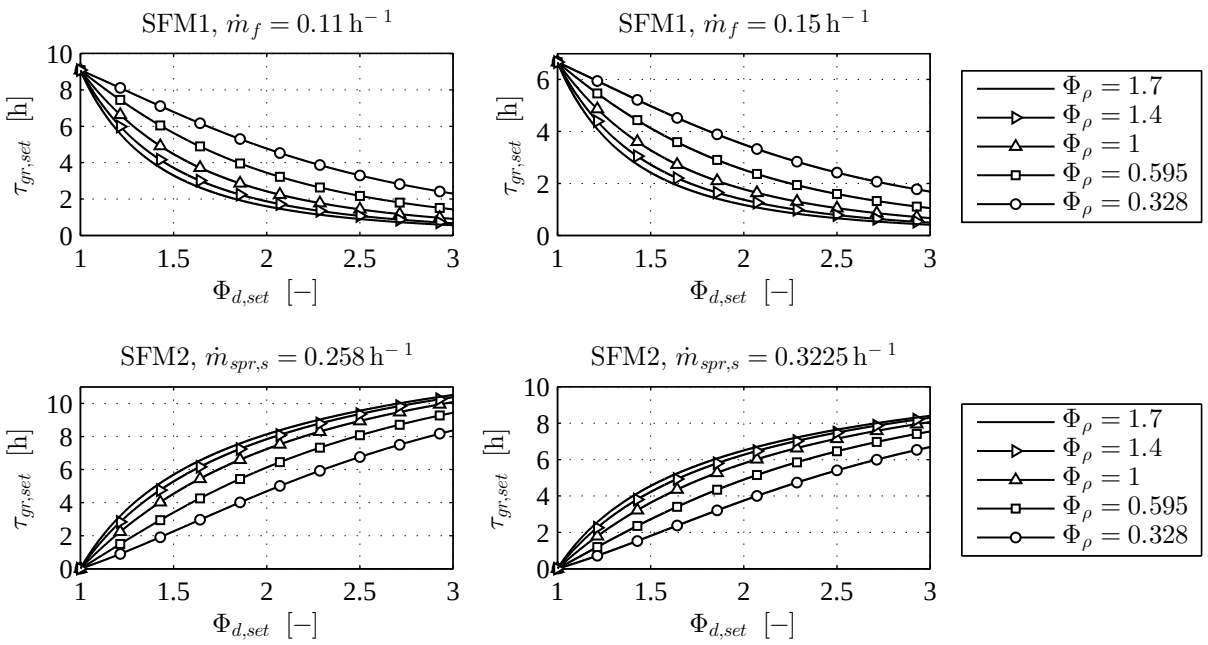

Figure 4.4: Functional relationship between required growth time $\tau_{gr,set}$ and desired particle growth ratio $\Phi_{d,set}$ for method SFM1 with two examples of bed-mass-specific nuclei feed rate $\dot{m}_f$ and for method SFM2 with two examples of bed-mass-specific solids spray rate $\dot{m}_{spr,s}$, each of them calculated for different coating-to-core density ratios Φ_ρ.

the component density ratio Φ_ρ. The influence of these properties shall be illustrated and discussed in the following using the example of the terminal product sinking velocity. In addition, the functional relationships between relative product sinking velocity and the desired particle growth ratio of the Stokes and quadratic regimes are contrasted for different component density ratios. By this, it shall be shown that continuous granulation with external product classification can only be applied to large-growth granulation conditions ($\Phi_{d,set} \gg 1$) at low component-density ratios ($\Phi_\rho \ll 1$).

4.2.1 Product sinking velocity according to Martin's approach

Figure 4.5 shows the evolution of the terminal product sinking velocity with desired particle growth ratio for the five component density ratios of Table 4.1, each of which calculated by the approach of Martin [40,41] in Eq. 2.87, for the effective core density of the Cellets®-materials (left diagram: $\rho_f = 1380\,\mathrm{kg/m^3}$) and of the glass beads (right diagram: $\rho_f = 2500\,\mathrm{kg/m^3}$), which have been used in the experimental part of this thesis (Chapters 9 and 10), and for a nuclei diameter of $d_f = 3\,\mathrm{mm}$. As to be expected, it can be seen from the curves that the product sinking velocity is the higher, the larger the effective density of external nuclei ρ_f and the component density ratio Φ_ρ is. All of the $u_{s,pr}$-curves, except for these of the lowest coating-to-core density ratio ($\Phi_\rho = 0.328$), steadily increase with the desired particle growth ratio from the beginning of granulation on. At each of the examples with $\Phi_\rho = 0.328$, an initial decline of the product sinking velocity is ascertained, which lasts until a granule size enlargement of around 1.25, from where on the terminal product sinking velocities start to grow and then exceed the terminal sinking velocity of external nuclei at around 1.5. As a conclusion, air classifiers should be only applied as method of size-selective product discharge in continuous granulation processes for desired particle growth ratios that are significantly larger than 1.5, when the component density ratio is given with $\Phi_\rho = 0.328$. It is explained in Section 3.6, that the terminal product sinking velocity can decrease for low (undercritical) coating-to-core density ratios, as the effective particle density lowers strongly in the beginning of granulation for such material combinations. In Section 3.6.2, it is even shown that the critical values of the component density ratio $\Phi_{\rho,cr}$ lie at around 1/3 for the Stokes regime ($Re_s \lesssim 0.25$) and at around 1/6 for the quadratic regime ($Re_s \gtrsim 1000$). The flow conditions of the presented sinking velocity curves fall within the lower area of the transition regime ($0.25 \lesssim Re_s \lesssim 1000$), as can be deduced from the right diagram in Figure 2.2. The point where the relative product sinking velocity exceeds unity is the minimum required particle growth ratio $\Phi_{d,min}$, as mentioned before in Section

Φ_ρ [–]	K [–]	$\Phi_{d,min}$(Stokes) [–]	$\Phi_{d,min}$(quadratic) [–]
Eq.	3.108	3.109	3.110
2/3	0.5	1	1
1/3	2	1	2.73
1/6	5	1.79	5.85
1/10	9	2.54	9.91

Table 4.4: Minimum required particle growth ratios $\Phi_{d,min}$ for four different component density ratios Φ_ρ, each calculated for the Stokes and for the quadratic flow regime.

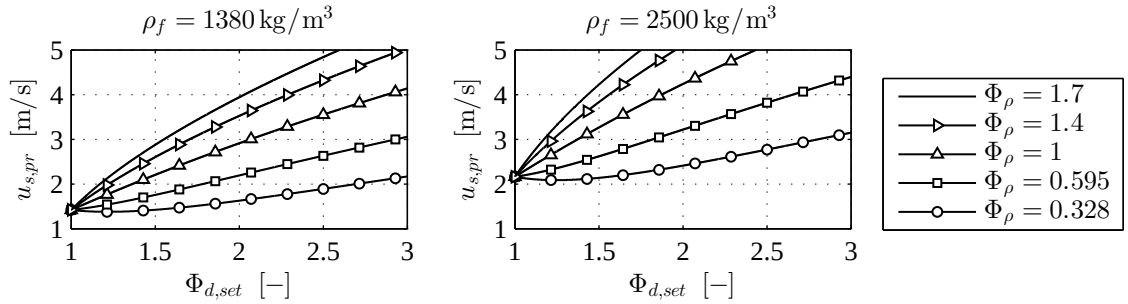

Figure 4.5: Terminal sinking velocity of the product $u_{s,pr}$ versus desired particle growth ratio $\Phi_{d,set}$ for a feed diameter of $d_f = 3\,\mathrm{mm}$, two different effective core densities ρ_f, and five examples of the coating-to-core density ratio Φ_ρ.

3.6. Based on the criterion of Eq. 3.105, the critical desired particle growth ratios are read out of Figure 4.5 with $\Phi_{d,min} = 1.487$ for the left diagram ($\rho_f = 1380\,\mathrm{kg/m^3}$) and with $\Phi_{d,min} = 1.562$ for the right diagram ($\rho_f = 2500\,\mathrm{kg/m^3}$).

4.2.2 Relative product sinking velocity for the Stokes and the quadratic flow regime

Figure 4.6 shows the dependency of the relative product sinking velocity $\Phi_{u_{s,pr}}$ on the desired growth ratio $\Phi_{d,set}$ for five different component density ratios with $\Phi_\rho \in \{1, 2/3, 1/3, 1/6, 1/10\}$, each of which calculated for the Stokes regime by Eq. 3.96 (left diagram) and for the quadratic regime by Eq. 3.97 (right diagram) with negligence of buoyancy ($F_b = 0$). The first example of the coating-to-core density ratio represents the case of homogeneous intraparticle density (e.g., layering). These curves are simply defined by the square function for dominating laminar flow conditions (Stokes) and by the square root function for dominating

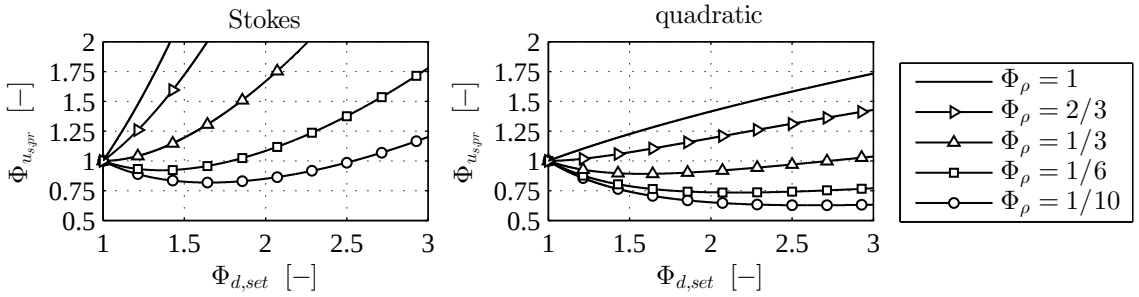

Figure 4.6: Relative product sinking velocity $\Phi_{u_{s,pr}}$ versus the desired particle growth ratio $\Phi_{d,set}$ for five examples of the coating-to-core density ratio Φ_ρ, each calculated for the Stokes and the quadratic flow regimes.

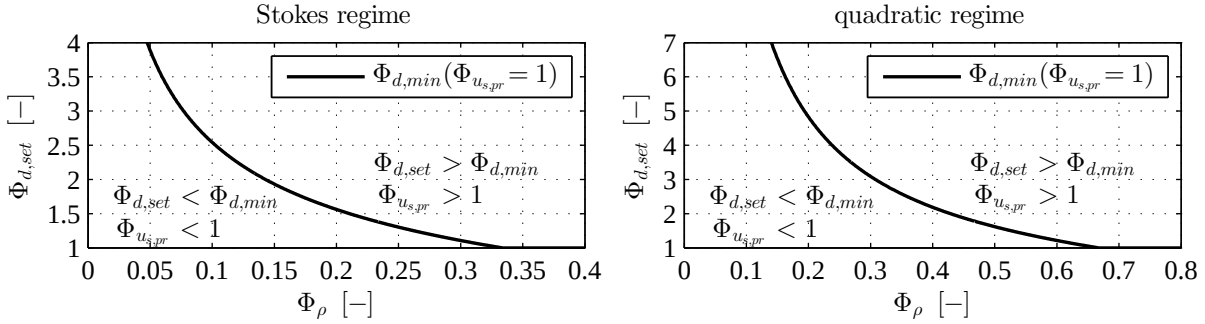

Figure 4.7: Domains of insufficient particle growth ($\Phi_{d,set} < \Phi_{d,min}$) and sufficient particle growth ($\Phi_{d,set} > \Phi_{d,min}$) of product separability in dependency on the coating-to-core density ratio Φ_ρ for the Stokes regime and the quadratic regime.

turbulent flow conditions (quadratic). The component density ratio of $\Phi_\rho = 2/3$ corresponds to the critical component density ratio $\Phi_{\rho,cr}$ of the quadratic regime, while 1/3 equals the critical component density ratio of the Stokes regime. It can be seen that the incipient slope of the relative product sinking velocities are zero ($\Phi'_{u_{s,pr}}(\Phi_{d,set} \to 1) = 0$) for the curves of critical component density ratios. The last two Φ_ρ-examples are deliberately chosen to be small enough to better demonstrate the effect of an initial decrease in terminal product sinking velocity with particle growth. Further, it is obvious that the relative product sinking velocity increases stronger with the desired particle growth ratio $\Phi_{d,set}$ in the Stokes regime than in the quadratic regime. The relative product sinking velocity falls below unity $\Phi_{u_{s,pr}} < 1$ within a certain range of particle size enlargement ratios ($1 < \Phi_{d,set} < \Phi_{d,min}$) for undercritical component density ratios. This range is smaller for the Stokes regime than for the quadratic regime at the same component density ratio. In other words, the minimum required particle growth ratio $\Phi_{d,min}$ is larger for the turbulent flow regime at the same coating-to-core density ratio. The minimum required particle growth ratios of the given component density ratios from Figure 4.6, except for the first example, are listed in Table 4.4. They are calculated by Eqs. 3.108 and 3.109 for the Stokes regime and by Eqs. 3.108 and 3.110 for the quadratic flow regime. The minimum required particle growth ratio of the last two examples of component density ratios for the quadratic solutions are even outside the plot at round $\Phi_{d,min} \approx 5.85$ and $\Phi_{d,min} \approx 9.91$.

4.2.3 Minimum required particle growth ratio for the Stokes and the quadratic flow regime

The minimum required particle growth ratio of the Stokes regime and the quadratic regime is derived in Section 3.6 It can be calculated by Eq. 3.108, Eq. 3.109 and Eq. 3.110. Figure 4.7 illustrates the minimum required particle growth ratio in dependency on the component density ratio Φ_ρ for the Stokes regime (left) and for quadratic regime (right). These curves are determined with neglected buoyancy force ($F_b = 0$). The following points are ascertained for both limiting cases. The minimum required particle growth ratio goes to infinity for component density ratios approaching zero: $\Phi_{d,min}(\Phi_\rho \to 0) \to \infty$. It declines with higher component density ratios up to the critical component density ratio $\Phi_{\rho,cr}$, which is given with $\Phi_{\rho,cr} = 1/3$ for the Stokes regime and with $\Phi_{\rho,cr} = 2/3$ for the quadratic regime. The minimum required particle growth ratio is unity for supercritical component density ratios $\Phi_\rho > \Phi_{\rho,cr}$, as it is also shown by Eq. 3.109 and Eq. 3.110. The minimum required particle growth ratio $\Phi_{d,min}$ divides the diagrams of Figure 4.7 into two parameter domains of the desired particle growth ratio and the component density ratio, one where particle growth is insufficiently proceeded and one where particle growth is sufficiently large to obtain product sinking velocities larger than the feed particle sinking velocity $u_{s,pr} > u_f$. The domain of insufficient particle growth is characterized by a desired particle growth ratio less than the minimum required particle growth ratio $\Phi_{d,set} < \Phi_{d,min}$ and a relative product sinking velocity less than unity $\Phi_{u_{s,pr}} < 1$. The domain of sufficient particle growth is characterized by a desired particle growth ratio larger than the minimum required particle growth ratio $\Phi_{d,set} > \Phi_{d,min}$ and a relative product sinking velocity higher than unity $\Phi_{u_{s,pr}} > 1$. As a result, air classification is not a suitable method of product separation in continuous granulation for parameter combinations ($\Phi_{d,set}$ and Φ_ρ) in the domain of insufficient particle growth. The minimum required particle growth ratio curve of the quadratic regime lies above the curve of the Stokes

regime. Hence, the minimum required particle growth ratio depends on the scale of particle size.

5 Supplements of Hampel's three-compartment population balance model

5.1 Deficiencies of Hampel's model

The three-compartment population balance model of Hampel ([1, 2], recapitulated in Section 2.3.2) is the base of the PB-simulation study in the present thesis. There are some deficiencies in Hampel's reference case, which are named in the following. The structure of Hampel's model (see flowsheet in Figure 2.7) does not entirely match with the material flows of the experimental setting (see Figure 2.6). As mentioned before, external nuclei cannot be fed directly into the spray zone (interior of Wurster tube) due to the wall of the Wurster tube, and only granules from the drying region (exterior of Wurster tube) can enter the separator, as the separator inlet is located at the lower part of the process chamber wall. The size distribution of the nuclei used in Hampel's research has not been specified in [1,2]. Moreover, the following aspects of the model design of the reference case do not cope with overall mass conversation. For one thing, the growth rate of Hampel's model has been related to the total surface area of the bed particles A_{bed}, but particle growth was assumed to take place only in the spray zone (compare Eqs. 2.158 and 2.160). For another thing, the particle size was supposed to be the only distributed property of the bed, which assumes the granule density to be uniform, but the effective material densities of the nuclei and of the coating layer have been set differently in [2]. Further, Hampel's processing strategy has focused only on bed mass control. Desired product characteristics such as growth ratio ($\Phi_{d,set}$), product size ($d_{pr,set}$) or coating thickness have not been defined. The employed proportional bed mass controller (Eq. 2.162) can influence product characteristics in an undesirable manner due to the manipulation of the separation gas velocity u_g. The zero control deviation gas velocity u_0 of the P-controller was not related to wanted product characteristics. An adaption of the solids spray rate $\dot{M}_{spr,s}$ and nuclei feed rate $\dot{M}_f$ to the desired particle growth ratio $\Phi_{d,set}$, as it is required by the ideal continuous layerwise granulation model according to Eqs. 3.11 and 3.24, was not implemented. The particle growth ratios being obtained in Hampel's investigations are relatively small ($\Phi_d < 2$). For example, the results of the ideal granulation model in Sections 3.6 and 4.2 show that air classification for separating products from continuously operated granulation systems is only suitable for sufficiently large growth ratios, when the coating density is significantly smaller than that of the core material (nuclei). On the other hand, the product discharge by classification with low separation sharpness κ_{sep} is more efficient for large desired particle growth ratios. Besides, Hampel's concept is unsuitable for thin-layer coating processes in practice, due to possible size dispersity of primary particles, residence time distribution in granulation chambers and imperfections of classifiers. It is only recommended for thick-layer coating processes when different materials are to be put on core particles. Otherwise, products with low coating efficiencies (fraction of coated surface area of particles) are obtained. For these reasons, the three-compartment population balance model of Hampel is extended with some relationships from the ideal particle growth model of Chapter 3, with the goal to develop a processing strategy by which stable continuous layerwise granulation with fluidized bed and adjustable product size can be realized and higher particle growth ratios can be achieved.

5.2 Modified three-compartment population balance

Flowsheet

The flow structure of Hampel's model (see Figure 2.7) is adapted to the material flows of the experimental setting with Wurster equipment (see Figure 2.6), as illustrated in Figure 5.1. Therein, the feed of external nuclei and the fine fraction recycle enter only the drying zone, and only particles from the drying zone are conveyed into the separator. The rest of Hampel's flowsheet is maintained in the modified three-compartment population balance model.

Predefined parameters

Predefined parameters for the present PB-simulation study in Chapter 6 are: the desired particle growth ratio, the general particle density ρ_p, the initial bed mass $M_{bed,0}$, the mean diameter of external nuclei $d_{m,f}$, the standard deviation of the PSD of external nuclei σ_f, the separation time constant τ_{sep}, the spray zone residence time τ_α, the spray zone particle fraction α, the separation sharpness κ_{sep}, the minimal separation gas velocity $u_{g,min}$, the gain factor K_m, and the set bed mass M_{set}. Other properties are calculated from these parameters, as described in the following.

Uniform effective particle density

The effective material densities of the nuclei ρ_f and the coating layer ρ_c are assumed to be equal. Hence, they conform with the effective bed particle density ρ_p and the effective product density ρ_{pr}:

$$\rho_f = \rho_c = \rho_p = \rho_{pr}. \tag{5.1}$$

In the context of the PB-model, the effective material densities of the nuclei and the coating layer are represented by the effective particle density ρ_p.

Characteristics of external nuclei supply and bed material

The number-based particle size distribution of the external nuclei $q_{0,f}$ is approached by the Gaussian distribution:

$$q_{0,f}(d) \coloneqq \frac{1}{\sigma_f\sqrt{2\pi}}\exp\left(-\frac{(d-d_{m,f})^2}{2\sigma_f^2}\right), \tag{5.2}$$

with $d_{m,f}$ as expectation value and σ_f as standard deviation. The particle size distribution of the initial bed material shall be the same as that of the external nuclei $q_{0,f}$. The number density flow rate of the nuclei feed $\dot{n}_f$ and the number density distribution of initial bed particles $n_{bed,0}$ are approximately derived from the normalized PSD of the external nuclei $q_{0,f}$ with

$$\dot{n}_f(d) \approx \frac{\dot{M}_f}{\int_0^\infty \rho_p \frac{\pi}{6} d^3 q_{0,f}(d)\,\mathrm{d}d} q_{0,f}(d) \tag{5.3}$$

and

$$n_{bed,0}(d) \approx \frac{M_{bed,0}}{\int_0^\infty \rho_p \frac{\pi}{6} d^3 q_{0,f}(d)\,\mathrm{d}d} q_{0,f}(d). \tag{5.4}$$

The feed rate $\dot{M}_f$ is adapted to the desired growth ratio $\Phi_{d,set}$, as shown later. It should be noticed that the Gaussian particle size distribution $q_{0,f}$ is defined over the domain from negative infinity to positive infinity, but PSDs of real systems can only lie in the positive diameter domain: $d > 0$. However, the density function of the Gaussian distribution is used here due to its simple structure. The values of the standard deviation σ_f can then not be chosen too large, otherwise, a significant part of the size distribution would be counted in the negative domain, which would lead to errors in the number density distribution flow rate of the nuclei feed $\dot{n}_f$ and the number density distribution of initial bed material $n_{bed,0}$. The initial number density distributions of spray zone particles and drying zone particles are calculated according to $n_{\alpha,0} = \alpha n_{bed,0}$ and $n_{1-\alpha,0} = (1-\alpha)n_{bed,0}$, respectively. The subsequent bed masses M_{bed} are calculated by the following integral:

$$M_{bed}(t) = \int_0^\infty \rho_p \frac{\pi}{6} d^3 n_{bed}(d,t)\,\mathrm{d}d. \tag{5.5}$$

Number density distribution flow rate of separator inlet

The number density distribution flow rate of the separator inlet $\dot{n}_{sep}$ shall be defined as the product of a separation frequency factor k_{sep} and the number density distribution of the drying zone particles $n_{1-\alpha}$:

$$\dot{n}_{sep}(d,t) = k_{sep} n_{1-\alpha}(d,t). \tag{5.6}$$

A distinction between two different approaches of the separation frequency factor k_{sep} is made, which are indicated by SFF1 and SFF2. In SFF1, k_{sep} is given by the reciprocal of a separation time constant τ_{sep}:

$$k_{sep}(\mathrm{SFF1}) = \frac{1}{\tau_{sep}} \neq \mathrm{f}(d,t), \tag{5.7}$$

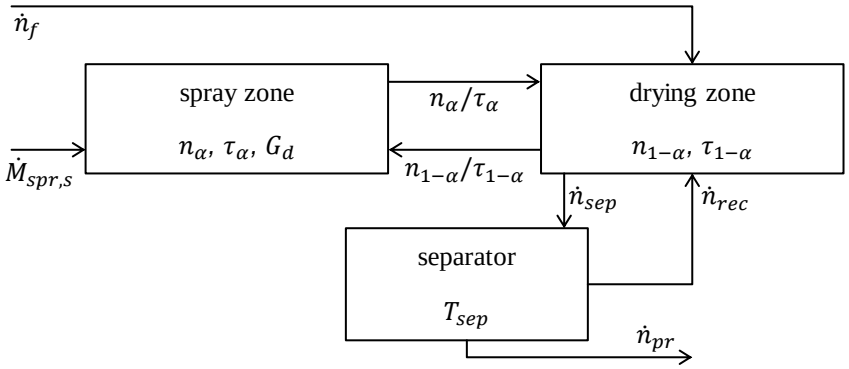

Figure 5.1: Flowsheet of the modified three-compartment population balance model based on Hampel's reference case [1, 2].

as it was used in Hampel's simulations ([1, 2], see also Eq. 2.153). This way, the separation frequency factor is independent from particle size d and constant with time t. But in contrast to Hampel's model, the number density distribution flow rate of the separator inlet $\dot{n}_{sep}$ is only related to the number density distribution of drying zone particles $n_{1-\alpha}$ here. The separation time constant can be understood somewhat as the approximately average residence time that the bed granules need to fall into the separator. The second separation frequency factor, used in approach SFF2, is defined as the ratio of a separator inlet mass flow rate $\dot{M}_{sep}$ (short: separator input rate), used as fixed parameter, to the current bed mass M_{bed}:

$$k_{sep}(\text{SFF2}) = \frac{\dot{M}_{sep}}{M_{bed}(t)}. \tag{5.8}$$

The particle mass flow rate of the separator inlet $\dot{M}_{sep}$ can be also referred to as bed discharge rate, when only one classifier is joined to the granulator. The change in bed mass M_{bed} during the startup period is considered by the separation frequency factor k_{sep}. The approach SFF2 was also proposed by Hampel (not named as SFF2 in [2]), but only SFF1 was applied there. The separator inlet mass flow rate $\dot{M}_{sep}$ can be roughly determined by bed discharge experiments, as done so for the present thesis (see Section 10.3). When using a bed discharge equipment, such as in Hampel's case, the separator inlet mass flow rate $\dot{M}_{sep}$ can be manipulated by the switching times of the classifier-related double-pinch valve. However, accuracy and temporal fluctuations in the conveying rate depend on many aspects such as fluidization conditions (e.g., Sections 2.2.5 and 2.2.6) or apparative design, as explained in Section 9.4.2.

Partial differential equations

According to Hampel's three-compartment population balance model, the separation process is assumed to be quasi-stationary. From this, the difference of the separator-inlet-related number density distribution flow $\dot{n}_{sep}$ to the recycle-related number density distribution flow rate $\dot{n}_{rec}$ is expressed with:

$$\dot{n}_{sep}(d,t) - \dot{n}_{rec}(d,t) = \dot{n}_{pr}(d,t) = k_{sep} n_{1-\alpha}(d,t) T_{sep}(d,t). \tag{5.9}$$

Following Eqs. 5.6 and 5.9 and the flowsheet in Figure 5.1, the modified three-compartment population balance is formulated with:

$$\frac{\partial}{\partial t}\big(n_\alpha(d,t)\big) = -\frac{n_\alpha(d,t)}{\tau_\alpha} + \frac{n_{1-\alpha}(d,t)}{\tau_{1-\alpha}} - \frac{\partial}{\partial d}\big(G_d(t) n_\alpha(d,t)\big) \tag{5.10}$$

$$\frac{\partial}{\partial t}\big(n_{1-\alpha}(d,t)\big) = \frac{n_\alpha(d,t)}{\tau_\alpha} - \frac{n_{1-\alpha}(d,t)}{\tau_{1-\alpha}} + \dot{n}_f(d) - k_{sep} n_{1-\alpha}(d,t) T_{sep}(d,t). \tag{5.11}$$

The drying zone residence time follows from spray zone residence time τ_α and the spray zone particle fraction α via Eq. 2.150 with $\tau_{1-\alpha} = \tau_\alpha(1-\alpha)/\alpha$.

Growth rate

As mentioned before, the growth rate G_d has been related to the particle surface area of the entire bed in Hampel's reference case (Section 2.3.2), but growth was assumed to take place only in the spray zone. In the modified three-compartment population balance model, the growth rate bases on the approach of Mörl (Eq. B.1) too, but is implemented in a different way for reasons of mass conservation. On the one hand, the growth rate is related to the surface area of particles being situated only in the spray zone $A_{\alpha,tot} = \int_0^\infty \pi d^2 n_\alpha(d)\,\mathrm{d}d$. On the other hand, effective material densities of the nuclei (cores) ρ_f and the coating layer ρ_c are uniform, which is why the effective coating density is represented by the effective particle density ρ_p (Eq. 5.1). In doing so, the growth rate is formulated with

$$G_d = \frac{2\dot{M}_{spr,s}}{\int_0^\infty \rho_p \pi d^2 n_\alpha(d)\,\mathrm{d}d}, \tag{5.12}$$

wherein the solids spray rate $\dot{M}_{spr,s} = \dot{M}_{spr} x_x$ is used.

Reformulation of the separation function

Likewise to Hampel's reference case (Eq. 2.159), Heinrich's extended approach of Molerus a. Hoffmann (Section 2.2.7, Eqs. 2.148 and 2.149) for defining separation functions of straight-duct air classifiers is implemented into the modified three-compartment population balance model too. But, it is given in a form that relates to the Bodenstein number for axial dispersion of fluid elements $Bo_{ax,g}$ (Eq. 2.138) in order to calculate the separation curves in dependency on predefined separation sharpnesses κ_{sep} (Eq. 2.136) in the PB-simulation study of Chapter 6. The meaning of the Bodenstein number for axial dispersion is described in more detail in Section 2.2.7. According to Eqs. 2.138 and 2.149, the gas-related Bodenstein number can be expressed as the ratio of the classifier length L_{sep} to the product of the turbulence constant k_{tur} and the inner diameter of classifier D_{sep}:

$$Bo_{ax,g} \coloneqq \frac{L_{sep} u_g}{D_{ax,g}} = \frac{L_{sep} u_g}{k_{tur} u_g D_{sep}} = \frac{L_{sep}}{k_{tur} D_{sep}} \approx \frac{L_{sep} u_g}{D_{ax,p}}. \tag{5.13}$$

Inserting Eq. 2.149 in Eq. 2.148 and substituting $L_{sep}/(k_{tur} D_{sep})$ by $Bo_{ax,g}$ through Eq. 5.13, Heinrich's version is reformulated to

$$T_{sep}(d,t) = \frac{1}{1 + \frac{u_g(t)}{u_s(d)} \exp\left(Bo_{ax,g}\left(1 - \frac{u_s(d)}{u_g(t)}\right)\right)}, \tag{5.14}$$

which is formally more similar to the model of Molerus a. Hoffmann in Eq. 2.146. It turns out from Eq. 5.14 that the gas-related Bodenstein number $Bo_{ax,g}$ and the separation gas velocity u_g are the only characteristic parameters defining the separation curves. At this, the gas-related Bodenstein number has a strong influence on the inclination, but not on the position of separation curve, while the separation gas velocity only slightly influences the inclination and sets the location on the d-coordinate. As a conclusion of Eq. 5.14, a two-dimensional function of the separation sharpness κ_{sep} depending on the Bodenstein number $Bo_{ax,g}$ and the separation gas velocity u_g can be formulated

$$\kappa_{sep} = \mathrm{f}(Bo_{ax,g}, u_g), \tag{5.15}$$

which is shown later in Section 6, Figure 6.1. The terminal sinking velocity of particles with separation diameter $u_s(d_{sep}, \rho_p)$ is equal to the current separation gas velocity u_g. Such particles have a 50-50 % coarse-product discharge probability:

$$T_{sep}\Big(u_s\big(d_{sep}(t), \rho_p\big) = u_g(t)\Big) = 0.5. \tag{5.16}$$

However, as mentioned before, the separation gas velocity u_g is manipulated by the proportional bed mass controller (Eq. 5.18), and therefore, a function of time. Hence, the separation diameter of the classifier is also changing with time: $d_{sep} = \mathrm{f}(t)$.

Extension of the bed mass control function

The bed mass controller used in this work is a version of Hampel's proportional controller from Eq. 2.162 with the following supplements. The zero control deviation gas velocity u_0 is replaced by the set separation gas velocity $u_{g,set}$, which shall be associated with desired product characteristics, as shown later in Section 5.3. An offset mode is added to the bed mass controller (see Eq. 5.18), where the gain factor is given with $K_m = 0$ and the proportional term $K_m(M_{set} - M_{bed})$ is deactivated. The separation gas velocity u_g equals then the set separation gas velocity $u_{g,set}$, which is, in this case, also called simply as offset. The offset option sacrifices bed mass control, but enables full control of the separation gas velocity, and hereby, a targeted influence on desired product characteristics. The activated part of the proportional bed mass controller, which is defined for $K_m > 0$, is further extended with a securing, wherewith values of or below zero for the separation gas velocity u_g are avoided by two domains. As mentioned in Section 2.3.2, only using Hampel's proportional controller Eq. 2.162 can provide negative separation gas velocities at bed masses above the zero root of the control function. For this reason, a minimal separation gas velocity $u_{g,min}$ and a corresponding critical bed mass $M_{bed,cr}$ are introduced. Using the linear control function of Eq. 2.162, the critical bed mass is obtained from the set bed mass M_{set}, the separation set gas velocity $u_{g,set}$, the minimal separation gas velocity $u_{g,min}$, and the gain factor K_m with:

$$M_{bed,cr} = M_{set} + \frac{u_{g,set} - u_{g,min}}{K_m} \qquad \text{, for } K_m > 0. \tag{5.17}$$

The minimal separation gas velocity $u_{g,min}$ must be larger than zero ($u_{g,min} > 0$) to avoid division-by-zero errors in the separation function T_{sep} of Eq. 5.14. The critical bed mass $M_{bed,cr}$ is used to divide the bed mass coordinate into two domains: one with undercritical bed mass values ($M_{bed} < M_{bed,cr}$) and one with bed masses equal to or larger than the critical bed mass ($M_{bed} \geq M_{bed,cr}$). The controller output u_g is calculated by the P-control function for the undercritical domain, while it is set to the minimal separation gas velocity $u_{g,min}$ for critical or overcritical bed mass values:

$$u_g(t) = \begin{cases} u_{g,set} & \text{, for } K_m = 0 \text{ (offset mode)} \\ u_{g,set} - K_m\big(M_{bed}(t) - M_{set}\big) & \text{, for } K_m > 0 \text{ (activated mode) and } M_{bed}(t) < M_{bed,cr} \\ u_{g,min} & \text{, for } K_m > 0 \text{ (activated mode) and } M_{bed}(t) \geq M_{bed,cr} \end{cases}. \tag{5.18}$$

The different modes of the bed mass controller are distinguished from each other with the denotation $K_m = 0$ for the offset mode and with $K_m > 0$ for the activated mode. Figure 5.2 illustrates the P-control function of Eq. 5.18 for different gain factors in a), bed masses in b), and set separation gas velocities in c). Some of the curve parameter values are adapted to the process parameters of the simulation studies in Chapter 6 and the continuous granulation experiments in Section 10.4. It can be seen that greater gain factors lead to sharper control functions and lower critical bed masses. An increase in the set bed mass shifts the control function to the right and enlarges the critical bed mass by the same amount. A higher set separation gas velocity raises the P-control curve upwards, which leads also to larger critical bed mass values. For an existing fluidized bed system of a certain scale, the value of the set bed mass should match the optimal fluidization and granulation conditions. The choice of an optimal set separation gas velocity strongly depends on product characteristics, e.g., the desired product diameter $d_{pr,set}$, more on this below and in Chapter 6. To find an appropriate gain factor value, many aspects that affect dynamics of bed mass development, have to be considered. Those are for instance the nuclei feed rate, the solids spray rate, the growth rate, the set bed mass, the set separation gas velocity, the desired product diameter, and the conveying rate from granulator to the separator. The influence of various gain factors on simulated process behavior is shown and discussed later in Section 6.2. In practice, measurement errors and fluctuations of the inline detection of the current fluidized bed mass can result in undesirably strong changes in separation gas velocity, as it is observed by some continuous granulation experiments in Section 10.4.2. By these examples, an optimal gain factor was worked out.

Particle size characteristics of bed and product granules

The normalized particle size distribution of the bed material $q_{0,bed}$ is obtained according to Eq. 2.6 with the basis $r = 0$ by

$$q_{0,bed}(d,t) = \frac{n_{bed}(d,t)}{\int_0^\infty n_{bed}(d,t)\mathrm{d}d}. \tag{5.19}$$

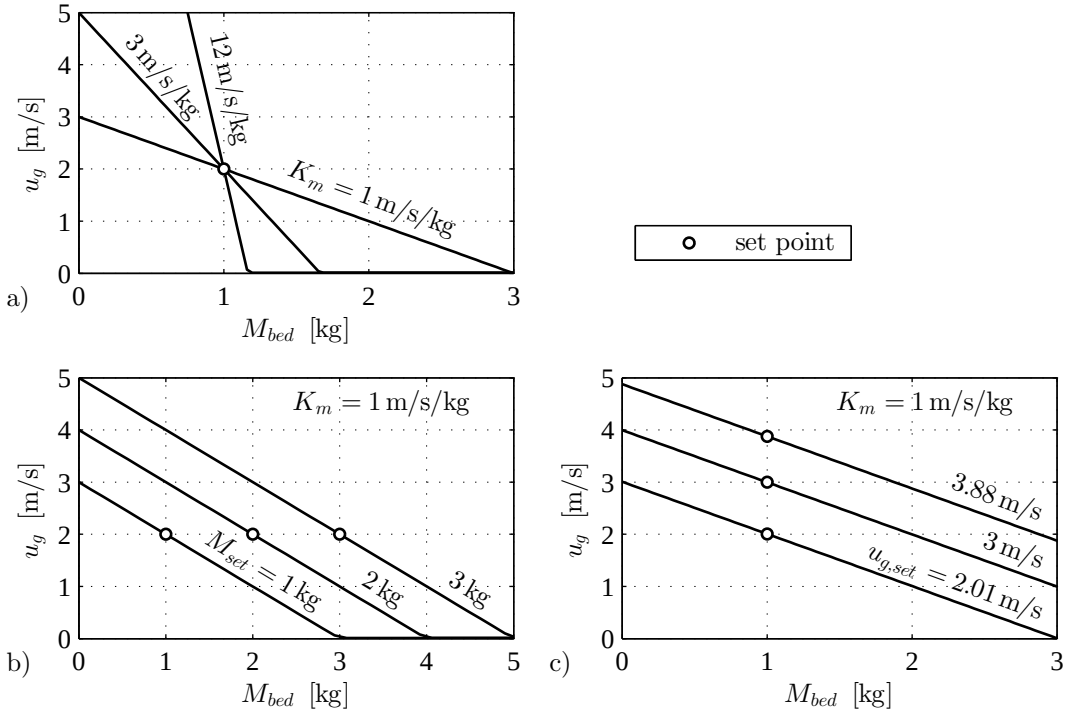

Figure 5.2: P-control function $u_g(M_{bed})$ for different parameter variations: gain factor K_m in a), set bed mass M_{set} in b), and set separation gas velocity $u_{g,set}$ in c).

The product size distribution $q_{0,pr}$ is derived from $\dot{n}_{pr} = \dot{n}_{sep} T_{sep}$ and Eq. 5.6, so that it can be calculated by the number density distribution of drying zone particles $n_{1-\alpha}$ and the separation function T_{sep}:

$$q_{0,pr}(d,t) = \frac{\dot{n}_{pr}(d,t)}{\int_0^\infty \dot{n}_{pr}(d,t)\mathrm{d}d} = \frac{n_{1-\alpha}(d,t) T_{sep}(d,t)}{\int_0^\infty n_{1-\alpha}(d,t) T_{sep}(d,t)\mathrm{d}d}. \tag{5.20}$$

From Eqs. 5.19 and 5.20, several scalar PSD-characteristics (e.g., from Section 2.1.2) can be derived, such as the mean diameter of the bed material $d_{m,bed}$ with Eq. 5.21, the mean diameter of the product $d_{m,pr}$ with Eq. 5.22, the standard deviation of the bed-PSD σ_{bed} with Eq. 5.23, and the standard deviation of the product-PSD σ_{pr} with Eq. 5.24:

$$d_{m,bed}(t) = \int_0^\infty d q_{0,bed}(d,t)\mathrm{d}d, \tag{5.21}$$

$$d_{m,pr}(t) = \int_0^\infty d q_{0,pr}(d,t)\mathrm{d}d, \tag{5.22}$$

$$\sigma_{bed}(t) = \sqrt{\int_0^\infty (d - d_{m,bed})^2 q_{0,bed}(d,t)\mathrm{d}d}, \tag{5.23}$$

$$\sigma_{pr}(t) = \sqrt{\int_0^\infty (d - d_{m,pr})^2 q_{0,pr}(d,t)\mathrm{d}d}. \tag{5.24}$$

Bed discharge rate and production rate

In general, the bed discharge rate denotes the mass flow rate of bed granules that are currently leaving the granulator. In this work, the granulator is only coupled to one classification tube in the simulation series shown later in Chapter 6. In this case, the bed discharge rate always corresponds to the separator input rate. Therefore, both terms are used synonymously here, and the bed discharge rate is also symbolized by $\dot{M}_{sep}$. The bed discharge rate is defined by this integral: $\dot{M}_{sep} = \int_0^\infty \rho_p \frac{\pi}{6} d^3 \dot{n}_{sep}(d,t)\mathrm{d}d$. When using the

SFF1-approach of the separation frequency factor in Eq. 5.7, the bed discharge rate is a function of time and can be calculated by

$$\dot{M}_{sep}(\text{SFF1}) = \rho_p \frac{\pi}{6} \frac{1}{\tau_{bed}} \int_0^\infty d^3 n_{1-\alpha}(d,t)\mathrm{d}d. \tag{5.25}$$

In case of the approach SFF2, the bed discharge rate is constant in time, as one of the predefined parameters. When using several classification tubes, the bed discharge rate ensues from the sum of the individual classifier input rates. The production rate follows from the general integral $\dot{M}_{pr}(t) = \int_0^\infty \rho_p \frac{\pi}{6} d^3 \dot{n}_{pr}(d,t)\mathrm{d}d$. By Eqs. 5.6 to 5.9, it is transformed to

$$\dot{M}_{pr}(\text{SFF1}) = \rho_p \frac{\pi}{6} \frac{1}{\tau_{bed}} \int_0^\infty d^3 n_{1-\alpha}(d,t) T_{sep}(d,t)\mathrm{d}d \tag{5.26}$$

for the method SFF1, and to

$$\dot{M}_{pr}(\text{SFF2}) = \rho_p \frac{\pi}{6} \frac{\dot{M}_{sep}}{M_{bed}(t)} \int_0^\infty d^3 n_{1-\alpha}(d,t) T_{sep}(d,t)\mathrm{d}d \tag{5.27}$$

for the method SFF2.

5.3 Adaption of process control parameters to the desired product size

Desired particle growth ratio

The desired particle growth ratio $\Phi_{d,set}$ has been introduced in the scope of the ideal particle growth model in Chapter 3 (see Eq. 3.1), where external nuclei and product granules are assumed to be mono-sized. The external nuclei of the three-compartment population balance model, however, are polydisperse. The desired particle growth ratio must be, therefore, defined by a quotient of the desired product diameter $d_{pr,set}$ to an average size characteristic of the nuclei-PSD. Several of those characteristics are outlined in Section 2.1.2, but it is not yet clear, which of them is most expedient for defining the desired particle growth ratio for the PB-model. For the sake of simplicity, the desired particle enlargement ratio is referred to the mean diameter of the external core material $d_{m,f}$:

$$\Phi_{d,set} = \frac{d_{pr,set}}{d_{m,f}}. \tag{5.28}$$

The desired growth ratio $\Phi_{d,set}$ is used as an objective-parameter for the PB-simulations and to determine required process parameters in terms of product size control, as described in the following.

Nuclei feed rate and solids spray rate

The relationship between the required spray-to-feed rate ratio $\Phi_{m,set}$ and the target-growth ratio $\Phi_{d,set}$ from the ICLG-model (see Chapter 3, Eq. 3.24) shall be applied with

$$\Phi_{m,set} = \frac{\dot{M}_{spr,s}}{\dot{M}_f} = \Phi_{d,set}^3 - 1, \tag{5.29}$$

in one of the investigated processing strategies (indicated by CM3) of the PB-simulation study for uniformity of effective particle density ($\Phi_\rho = 1$) and with disregarded material losses of cores and sprayed solids ($\Phi_{f,loss} = \Phi_{spr,loss} = 0$). The nuclei feed rate $\dot{M}_f$ and the solids spray rate $\dot{M}_{spr,s}$ are then adapted to the desired particle growth ratio via the parameter setting method SFM3 from Table 3.1, as shown later in Section 6.1.1.

Set separation gas velocity

As mentioned before, the current separation gas velocity u_g specifies the separation diameter d_{sep} of the classifier with time according to Eqs. 5.14 and 5.16. Although the separation gas velocity is the manipulated variable in the control concept (Eq. 5.18 for $K_m > 0$), it should aim to approach the separation diameter $d_{sep}(u_g(t))$ to the desired product diameter $d_{pr,set}$ within the PB-simulations. For this purpose, the set

separation gas velocity $u_{g,set}$ of the P-controller is calculated by the product-related terminal sinking velocity $u_{s,pr}$, which is associated to desired product diameter $d_{pr,set} = d_{m,f}\Phi_{d,set}$ via:

$$u_{g,set} \coloneqq u_{s,pr} = \sqrt{\frac{4}{3c_d(Re_{s,pr})}\frac{\rho_{pr}-\rho_g}{\rho_g}d_{m,f}\Phi_{d,set}g}. \tag{5.30}$$

Due to the assumption of uniform particle density in the PB-model, effective product density ρ_{pr} in Eq. 5.30 is equal to the effective particle density ρ_p (see Eq. 5.1). There are two methods to achieve a separation diameter d_{sep} that equals or approximates to the desired product diameter $d_{pr,set}$. The first one is realized by the offset mode ($K_m = 0$) of the control function, where the control deviation of the separation gas velocity becomes zero ($u_g - u_{g,set} = 0$) and the separation diameter corresponds exactly to the desired product diameter:

$$d_{sep,set} = d_{sep}(u_{g,set}) \coloneqq d_{pr,set} \qquad \text{, for } K_m = 0 \text{ (offset mode).} \tag{5.31}$$

However, this procedure carries the risk of inadequate bed mass development, which can lead to process instability. The second method presupposes that steady-state conditions can be reached for the activated mode of the bed mass controller ($K_m > 0$), and it pursues to minimize the absolute control deviations of separation gas velocity $|u_g - u_{g,set}|$ and of the separation diameter $|d_{sep} - d_{pr,set}|$. This can also be formulated as an optimization problem of process parameters with

$$\text{find}_{\min,|d_{sep}-d_{pr,set}|}\left(|d_{sep}(\Phi_{d,set}, \kappa_{sep}, M_{set}, K_m, ...) - d_{pr,set}|\right) \quad \text{, for } K_m > 0 \text{ (activated mode),} \tag{5.32}$$

where the separation diameter is influenced for example by the desired particle growth ratio $\Phi_{d,set}$, the separation sharpness of the classifier κ_{sep}, the set bed mass M_{set}, and the gain factor K_m. At this point, it should be noted that three process success indices from Section 5.4 are formulated for solving the optimization problem of the PB-study.

Differences to experiments

The adaptions of the required spray-to-feed rate ratio $\Phi_{m,set}$ and the set separation gas velocity $u_{g,set}$ to desired product characteristics are also made for the continuous experiments of the present thesis (Sections 9.4.5 and 9.4.6); but there, material losses of sprayed solids are taken into account, different material densities of the cores (nuclei) and coating layers ($\rho_f \neq \rho_c$) are considered, and the effective product density ρ_{pr} is calculated by Eq. 3.5 of the ICLG-model.

5.4 Relative control deviations as process success indices

For validation of process objectives in the PB-simulation studies in Sections 6.1 and 6.2, three controlled process variables (coordinates) are considered, from each of which a dimensionless process success index is derived in the following. The controlled process variables are the bed mass M_{bed}, the separation gas velocity u_g, and the product mean diameter $d_{m,pr}$. The state on these coordinates is represented in summary by the generalized controlled process variable P_j with $j \in \{m, u, d\}$ and $P_j \in \{P_m = M_{bed}, P_u = u_g, P_d = d_{m,pr}\}$. All three of them are seen as the state vector of controlled process variables (in short: controlled variables). It should be noted here that the bed mass is viewed as a closed-loop controlled variable by manipulating the separation gas velocity, the separation gas velocity as an open-loop controlled variable by setting constant process parameters, and the product mean diameter as an open-loop controlled variable that follows the separation gas velocity again via the separation curve. The individual PB-simulations shall be calculated up to a predefined total process time, symbolized by t_{end}, which is also referred to as the terminal simulation point. The state vector of controlled variables at the terminal simulation point, denoted by $P_{j,end}$ with $P_{j,end} \in \{M_{bed,end}, u_{g,end}, d_{m,pr,end}\}$, depends on many process parameters and material properties, as for instance the nuclei feed rate $\dot{M}_f$, the solids spray rate $\dot{M}_{spr,s}$, the size distribution of the external nuclei $q_{0,f}$, and the initial bed mass $M_{bed,0}$. The set values of the controlled variables are summarized by the set point vector $P_{j,end}$ with $P_{j,set} \in \{P_{m,set} = M_{set}, P_{u,set} = u_{g,set}, P_{d,set} = d_{pr,set}\}$. The difference between the controlled variables and set values ($P_j - P_{j,set}$) is named as control deviation. The relative control deviation (symbolized by ζ_j) is defined as quotient of the control deviation by the associated set value:

$$\zeta_j(t) = \frac{|P_j(t) - P_{j,set}|}{P_{j,set}} \qquad \text{, for } j \in \{m, u, d\} \text{ and } P_j \in \{M_{bed}, u_g, d_{m,pr}\}. \tag{5.33}$$

It is the aim to obtain nearly stationary conditions at terminal simulation points with lowest control deviations possible for each of the controlled variables, as large deviations can lead to unfavorable consequences for fluidization behavior and product characteristics. But, even in a steady state, the vector of controlled variables most likely deviates from the desired set values. Those states shall be investigated by means of relative control deviations at the terminal simulation point according to:

$$\zeta_{j,end} = \frac{|P_{j,end} - P_{j,set}|}{P_{j,set}} \qquad \text{, for } j \in \{m,u,d\} \text{ and } P_{j,end} \in \{M_{bed,end}, u_{g,end}, d_{m,pr,end}\}. \tag{5.34}$$

in terms of bed mass with $\zeta_{m,end}$, of separation gas velocity with $\zeta_{u,end}$ and of product mean diameter with $\zeta_{d,end}$. These three quantities are used as dimensionless process success indices for evaluating different processing strategies that are defined later in Section 6.1.1. In [105], the generalized controlled variable is symbolized by "ξ_j" and the generalized relative control deviation by "$\Delta\xi_j$". Instead of the previous notation, P is used here to refer to the term "process variable" and ζ to refer generally to deviation quantities, similarly as in case of relative standard deviations, see for example in Eqs. 2.44 and 2.55.

The control deviation of separation gas velocity is linearly connected to the control deviation of the bed mass, when the activated mode of bed mass controller is used (see Eq. 5.18 for $K_m > 0$) and bed mass values are below the critical bed mass ($M_{bed} < M_{bed,cr}$, see also Eq. 5.17). In this case, relative control deviations of the separation gas velocity and of the bed mass are correlated via

$$\zeta_u(t) = \frac{K_m M_{set}}{u_{g,set}} \zeta_m(t) \qquad \text{, for } K_m > 0 \text{ and } M_{bed} < M_{bed,cr}. \tag{5.35}$$

It shows up again by Eq. 5.35 that larger gain factors K_m are accompanied by lower bed mass control deviations and higher control deviations in the separation gas velocity. Consequently, lower gain factors are favorable for better control of product size, but worsen bed mass control accuracy. However, as long as the obtained bed mass is situated within a range of adequate process conditions (e.g., stable Wurster fluidization or low agglomeration kinetics), low gain factor can be applied. A proportional bed mass control function has also been employed within continuous granulation experiments of the present thesis, as described in Section 9.4.8. In addition, different gain factors (Table 10.13) have been used, of which an optimum is worked out in Section 10.4.2 with a compromise between controlled bed mass and manipulated separation gas velocity.

6 Results of the modified three-compartment population balance model

Different processing strategies for continuous granulation shall be examined by simulations based on the supplemented three-compartment population balance model of Chapter 5 for different separation conditions in Section 6.1. In addition, simulations with the two approaches to the separation frequency factor (Eqs. 5.7 and 5.8) are contrasted for different control parameters in Section 6.2. The PB-model has been implemented into MATLAB R2015a. The partial differential equations have been transformed into a system of ordinary differential equations by the finite volume method, and the particle growth is calculated by the first-order upwind scheme.

6.1 Influence of processing strategies and separation performance on process stability and product characteristics

The influence of different processing strategies and the separation sharpness on continuous granulation with product classification is investigated in the following. The focus lies on the control of the bed mass as a characteristic of process stability and on product size distribution. The separation frequency factor SFF1 of Eq. 5.7 is used in the study of this section.

6.1.1 Processing strategies and parameter setting

Processing strategies

Three different processing strategies of continuous granulation, which are denoted by CM1, CM2, and CM3, are conceptualized within the partial study of this thesis. The abbreviations refer to previous work [105] and stand for "control method". The distinctive features of them are listed in Table 6.1. The first processing strategy CM1 shall refrain from active feed-back control of fluidized bed mass. Therefore, the control function in Eq. 5.18 is set to offset mode (indicated with $K_m = 0$) with a gain factor of zero and the separation gas velocity u_g to the set separation gas velocity $u_{g,set}$ for the entire simulated process time. Manipulation of separation gas flow is omitted in CM1, which enables a better control on product characteristics. However, process instability might occur with the absence of bed mass control under certain process conditions (e.g., solids spray rate, nuclei feed rate, and separation properties), as discussed later on. In the processing strategies CM2 and CM3, bed mass shall be controlled by manipulating the separation gas velocity u_g with the active mode (indicated with $K_m > 0$) of the proportional controller in Eq. 5.18. The adaption of the required spray-to-feed rate ratio $\Phi_{m,set}$ to the desired particle growth ratio $\Phi_{d,set}$ via Eq. 5.29 is only considered by the processing strategy CM3. At this, the nuclei feed rate $\dot{M}_f$ and the solids spray rate $\dot{M}_{spr,s}$ are calculated according to the spray-to-feed rate setting method SFM3 (Section 3.2.2, Table 3.1). The set separation gas velocity $u_{g,set}$ is adapted to the desired growth ratio $\Phi_{d,set}$ by Eq. 5.30 for each of the described processing strategies.

Uniform parameters

The parameters that are uniform for each of the three processing strategies (CM1, CM2, and CM3) are listed in Table 6.2. The values of the spray zone particle fraction α, the spray zone residence time τ_α, the separation time constant τ_{sep}, and the set bed mass M_{set} are adapted from one of Hampel's studies in [1]. The values of the nuclei characteristics (mean diameter $d_{m,f}$, standard deviation σ_f, and effective particle density ρ_p) conform roughly with the characteristics of Cellets®200, which has been used in granulation experiments of Hampel [1,2] and of the present thesis (Section 10.4). The initial bed mass $M_{bed,0}$ shall be equal to the set bed mass M_{set}. The production rate is defined with 600 g/h in order to agree with one of Hampel's experimental conditions [1], where a nuclei feed rate of $\dot{M}_f = 300\,\mathrm{g/h}$ and a solids spray rate of $\dot{M}_{spr,s} = 300\,\mathrm{g/h}$ were

processing strategy	CM1	CM2	CM3
active control of bed mass	no	yes	yes
manipulation of separation gas velocity	no	yes	yes
mode of control function Eq. 5.18	offset	activated	activated
gain factor	$K_m = 0$	$K_m > 0$	$K_m > 0$
adaption of $\Phi_{m,set}$ by Eq. 5.29	no	no	yes
spray-to-feed rate setting method	none	none	SFM3
adaption of $u_{g,set}$ by Eq. 5.30	yes	yes	yes

Table 6.1: Distinctive features of the processing strategies CM1, CM2, and CM3.

α [%]	τ_α [s]	τ_{sep} [s]	M_{set} [kg]	$d_{m,f}$ [mm]	σ_f [mm]	ρ_p [kg/m^3]	$M_{bed,0}$ [kg]	$\dot{M}_{pr}$ [g/h]
1	0.1	1800	1.1	0.3	0.02	1380	1.1	600

Table 6.2: Uniform parameters for simulations shown in Section 6.1.

given. Neglecting the material losses of nuclei and sprayed solids ($\Phi_{f,loss} = \Phi_{spr,loss} = 0$), the production rate $\dot{M}_{pr}$ follows from Eq. 3.22.

Non-uniform parameters

The following parameters are constant within the simulations, but different among the processing strategies CM1, CM2, and CM3. The gain factor of the proportional controller is given with zero ($K_m = 0$) for CM1 by definition of this strategy. The gain factors of the strategies CM2 and CM3 are specified with $K_m = 12\,\mathrm{m/kg/s}$, respectively, in accordance to validated simulations of Hampel from [2]. The minimal separation gas velocity $u_{g,min}$ of the control function Eq. 5.18 is not needed to be defined for the first process strategy CM1, whereas, it is for CM2 and CM3. The minimal separation gas velocity is chosen with $0.001\,\mathrm{m/s}$, whereby the following recommendation should be met. The minimal separation gas velocity $u_{g,min}$ should be much less than set separation gas velocity $u_{g,set}$, which varies in the simulation study, as described below. But, set separation gas velocity is supposed to be always larger than the terminal sinking velocity of the mean diameter of the external nuclei - $u_{g,set} > u_{s,f}(d_{m,f})$ - due to the premise of desired particle growth ratio larger unity $\Phi_{d,set} > 1$. Product sinking velocities can be even lower than that of nuclei with mean diameter, as a result of the ideal continuous layerwise granulation model shown in Sections 3.6 and 4.2, but only for coating-to-core density ratios much lower than unity ($\Phi_\rho \ll 1$), which is not the case in the present PB-model (here $\Phi_\rho = 1$). The sinking velocity of the mean nuclei diameter $u_{s,f}(d_{m,f})$ ensues to $1.42\,\mathrm{m/s}$ from Martin's closed solution ([40], Eq. 2.87) or to $1.46\,\mathrm{m/s}$ from the iterative approach of Kürten et al. ([30], Eqs. 2.63 and 2.80). Both values are much larger than the minimal separation gas velocity $u_{g,min}$ used. The overall simulation duration t_{end} is given with $40\,\mathrm{h}$ for the processing strategies CM2 and CM3. The overall simulation time varies for processing strategy CM1, for reasons of very long transient conditions, as described later on. In the processing strategies CM1 and CM2, the feed rate $\dot{M}_f$ and the solids spray rate $\dot{M}_{spr,s}$ are fixed at $300\,\mathrm{g/h}$, respectively. At this, the ratio of the solids spray rate to the nuclei feed rate is unity.

Varied parameters

The PB-simulations of this section have been conducted for various desired particle growth ratios $\Phi_{d,set}$ and separation sharpnesses κ_{sep} for each of the processing strategies (CM1, CM2, and CM3) in order to study the following aspects. Firstly, the transient behavior of the bed mass $M_{bed}(t)$, the separation gas velocity $u_g(t)$, and the product size distribution $q_{0,pr}(t)$ (mean size $d_{m,pr}(t)$ too) is investigated for two different desired particle growth ratios ($\Phi_{d,set} = 4/3$ and $\Phi_{d,set} = 8/3$) and a separation sharpness of $\kappa_{sep} = 0.85$ (Section 6.1.2). At this, the desired particle growth ratio of 4/3 represents a parameter setting for slight-growth granulation and of 8/3 a parameter setting of large-growth granulation. The corresponding objective-product diameter is $d_{pr,set} = 0.4\,\mathrm{mm}$ for the slight-growth example and $d_{pr,set} = 0.8\,\mathrm{mm}$ for the large-growth example. Secondly, relative control deviations according to Eq. 5.34, which are related to the bed mass $\zeta_{m,end}$ and the product mean size $\zeta_{d,end}$, are determined from the end point of the simulations

slight-growth granulation $\Phi_{d,set} = 4/3$, $u_{g,set} = 2.01\,\mathrm{m/s}$					large-growth granulation $\Phi_{d,set} = 8/3$, $u_{g,set} = 3.88\,\mathrm{m/s}$				
	$M_{bed,cr}$ [kg]	$\Phi_{m,set}$ [−]	$\dot{M}_f$ [g/h]	$\dot{M}_{spr,s}$ [g/h]		$M_{bed,cr}$ [kg]	$\Phi_{m,set}$ [−]	$\dot{M}_f$ [g/h]	$\dot{M}_{spr,s}$ [g/h]
CM2	1.27	-	-	-	CM2	1.42	-	-	-
CM3	1.27	1.37	253.1	346.9	CM3	1.42	17.96	31.6	568.4

Table 6.3: Process parameters which are adapted to the desired particle growth ratio $\Phi_{d,set}$ according to the different processing strategies CM1, CM2, and CM3, each of which calculated for the slight-growth granulation and the large-growth granulation example.

t_{end} (terminal simulation point) for a two-dimensional parameter array, in which the desired particle growth ratio is defined within a range of values of $1.02 \leq \Phi_{d,set} \leq 3.5$ and the separation sharpness within a range of values of $0.25 \leq \kappa_{sep} \leq 0.95$ (Section 6.1.3).

Adaption of process parameters to the desired particle growth ratio

According to the processing strategies of Table 6.1, some of the process parameters shall be adapted to the target-growth ratio $\Phi_{d,set}$. These are shown in Table 6.3 for the examples of slight-growth granulation with $\Phi_{d,set} = 4/3$ and of large-growth granulation with $\Phi_{d,set} = 8/3$. Regardless of which of the three processing strategies is to be applied, the set separation gas velocity $u_{g,set}$ is given with 2.01 m/s for the slight-growth example and with 3.88 m/s for the large-growth example. The critical bed mass $M_{bed,cr}$ is only needed for the strategies CM2 and CM3. It is obtained from Eq. 5.17 with 1.27 kg for $\Phi_{d,set} = 4/3$ and with 1.42 kg for $\Phi_{d,set} = 8/3$. The values of the critical bed mass are not much larger than the set bed mass due to the relatively large gain factor of 12 m/s/kg. The adaption of the spray-to-feed rate ratios, and thereby, of nuclei feed rates and solids spray rates to the desired particle growth ratio by Eq. 5.29 is only made for strategy CM3. In each simulation with strategies CM1 and CM2 and with desired particle growth ratios of $\Phi_{d,set} = 4/3$ and $\Phi_{d,set} = 8/3$, both the nuclei feed rate $\dot{M}_f$ and the solids spray rate $\dot{M}_{spr,s}$ are defined with 300 g/h. The desired particle growth ratio that corresponds to such spray-to-feed rate conditions ($\dot{M}_{spr,s}/\dot{M}_f = 1$) follows from Eq. 5.29 with nearly 1.26. This value is not very different from that of the example of slight-growth granulation. A particle size ratio of around 1.26 should be compared with the product mean diameter curves of the CM1- and CM2-simulations presented below. It becomes further obvious from Table 6.3 that the spray-to-feed rate ratio of the large-growth example is many times larger than this of the other example, which is owed to the third power of $\Phi_{d,set}$ in Eq. 5.29. Using the spray-to-feed rate setting method SFM3 (Table 3.1) and neglecting material losses ($\Phi_{f,loss} = \Phi_{spr,loss} = 0$), the nuclei feed rates $\dot{M}_f$ and solids spray rate $\dot{M}_{spr,s}$ of the strategy CM3 are calculated by

$$\dot{M}_f = \frac{\dot{M}_{pr}}{1 + \Phi_{m,set}} \tag{6.1}$$

and

$$\dot{M}_{spr,s} = \Phi_{m,set} \dot{M}_f. \tag{6.2}$$

Two-dimensional function for separation sharpness

It was shown before (Eqs. 5.13 to 5.15) that the separation sharpness κ_{sep} of the separation function $T_{sep}(d)$ used in the present model (derived from Heinrich's extension of the model of Molerus a. Hoffmann, Section 2.2.7) depends only on the gas-related Bodenstein number for axial dispersion $Bo_{ax,g}$ and on the separation gas velocity u_g. This two-dimensional function for the separation sharpness was created numerically via interpolation after Eq. 2.136 from several separation curves for various Bodenstein numbers and separation gas velocities. The sinking velocities of the separation functions were calculated for a broad and finely discretized d-coordinate with a uniform effective particle density of $\rho_p = 1380\,\mathrm{kg/m^3}$ and with air at normal conditions as separation gas. The 2D-plot of $\kappa_{sep}(Bo_{ax,g}, u_g)$ is illustrated in Figure 6.1. It is visible that higher separation sharpnesses are obtained at greater Bodenstein numbers, and that the separation gas velocity only slightly influences the separation sharpness. This leads to the conclusion in a practical sense

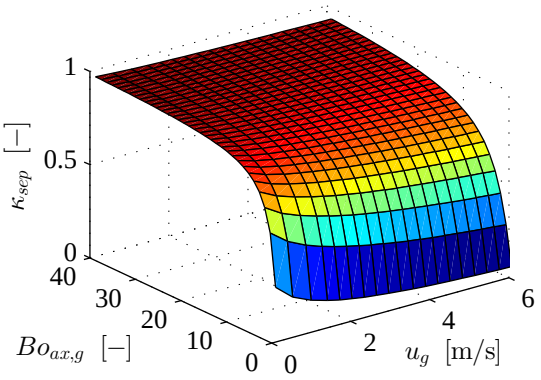

Figure 6.1: Separation sharpness κ_{sep} as two-dimensional function of Bodenstein number for axial gas dispersion $Bo_{ax,g}$ and separation gas velocity u_g.

$\Phi_{d,set}$ [–]	$u_g = u_{g,set}$ [m/s]	$Bo_{ax,g}$ [–]
4/3	2.01	11.93
8/3	3.88	14.74

Table 6.4: Bodenstein number for axial dispersion of the separation gas $Bo_{ax,g}$ for the slight- and large-growth granulation examples, $\Phi_{d,set} = 4/3$ and $\Phi_{d,set} = 8/3$, used for simulations with the processing strategy CM1 and a separation sharpness of $\kappa_{sep} = 0.85$.

that mainly longer and thinner tubes lead to better separation performances considering Eq. 5.13. But, the classifier should not be too thin in practice, because it can worsen the separation performance due to larger particle concentrations at required granule charge (e.g., separation inlet mass flow rate $\dot{M}_{sep}$), higher flow mal-distribution of laminar velocity profiles ($u_g D_{sep}/\nu_g \ll 2320$, from equation "3-51" in [121]) and lowering of sinking velocities in vicinity of walls (e.g., Eq. 2.90).

Adaption of Bodenstein number to the separation sharpness

As mentioned before, the separation sharpness κ_{sep} shall be one of the predefined parameters for the individual PB-simulations and is, therefore, supposed to be constant with simulated process time. In order to obtain a separation function $T_{sep}(d)$ after Eq. 5.14 with a desired value of the separation sharpness at a given separation gas velocity u_g, the gas-related Bodenstein of axial dispersion $B_{ax,g}$ has to be adapted via the two-dimensional function (here 2D-array of data) that is illustrated in Figure 6.1. In the processing strategy CM1, the separation gas velocity ($u_g(\text{CM1}) = u_{g,set}$) is also time-invariant according to the offset mode ($K_m = 0$) of the control function Eq. 5.18. As a result of the $\kappa_{sep}(Bo_{ax,g}, u_g)$-function, the gas-related Bodenstein number is a constant simulation parameter too for the case of CM1. Table 6.4 shows the Bodenstein number for axial gas dispersion for the slight- and large-growth granulation examples, each of which calculated for a separation sharpness of 85 %. In the processing strategies CM2 and CM3, where the bed mass controller is in active mode ($K_m > 0$), the separation gas velocity u_g is changing during the simulations. The Bodenstein number $Bo_{ax,g}$ is adapted to the current separation gas velocity $u_g(t)$ with the 2D-function of Figure 6.1 during the entire CM2- and CM3-simulations in order to maintain the predefined value of separation sharpness κ_{sep}.

Comparison to separation parameters of Hampel's PB-simulations

In the PB-simulations of Hampel's reference model ([2], recapitulated in Section 2.3), the separation curves were calculated with a classifier length of $L_{sep} = 1.1\,\text{m}$, an inner diameter of the classifier of $D_{sep} = 0.032\,\text{m}$ and a turbulence constant of $k_{tur} = 2$. Just to give an example for such a classifier design, a gas-related Bodenstein number of 11.93 would correspond to a turbulence constant of $k_{tur} = 2.88$ via Eq. 5.13 and a gas-related Bodenstein number of 14.74 to a turbulence constant of $k_{tur} = 2.33$, which are not so much

L_{sep} [m]	D_{sep} [m]	κ_{sep} [−]	$Bo_{ax,g}$ [−]	k_{tur} [−]
1.1	0.032	0.8	8.8	3.9
1.5	0.032	0.9	19.5	2.4

Table 6.5: Bodenstein numbers and turbulence factors estimated from Hampel's measurements [24].

different from Hampel's assumption. However, the determination of the classifier length L_{sep}, the inner diameter of classifier D_{sep}, and the turbulence constant k_{tur} is not needed within PB-simulations with the present model (Chapter 5), when the gas-related Bodenstein number is known.

Derivation of gas-related Bodenstein numbers and turbulence constants from Hampel's classification experiments

Hampel (see "Section 6.4" in [2]) has conducted two classification experiments with straight-duct air classifiers of different tube lengths ($L_{sep} = 1.1\,\mathrm{m}$ and $L_{sep} = 1.5\,\mathrm{m}$) and of same inner tube diameter ($D_{sep} = 0.032\,\mathrm{m}$). The author ascertained a separation sharpness of $\kappa_{sep} = 0.8$ for the shorter tube and of $\kappa_{sep} = 0.9$ for the longer tube. The employed separation gas velocity is not stated clearly in [2], but it is deduced to be $2\,\mathrm{m/s}$, which matches roughly to the separation diameter of Hampel's continuous experiments. Recalling Figure 6.1, the Bodenstein numbers and the corresponding turbulence factors are calculated from these measurements and listed in Table 6.5. It can be seen that the Bodenstein number of the long-tube example is larger than for the shorter classifier. This is to be expected according to its definition (see Eq. 2.138). On the contrary, the turbulence constant does not depend on the separation channel length, as shown in Section 2.2.7. The calculated turbulence constants in Table 6.5, however, are different. Deviations of experimental conditions can be a reason for this difference. For example, the particle inlet of the longer classifier assembly was at a higher position than for the other. But also, the double-pinch valve employed as particle feeder possesses strong dosage fluctuations. Causes for the dosing inaccuracy of such an equipment are described in Sections 9.4.1 and 9.4.2 and analyzed by experiments shown in Sections 10.2 and 10.3.

6.1.2 Temporal evolution of characteristic quantities for slight- and large-growth granulation

The simulation results of six process examples with a separation sharpness of $\kappa_{sep} = 0.85$ are illustrated and described in the following to compare the three processing strategies of Section 6.1.1 (CM1, CM2, and CM3), each for a small and a large desired particle growth ratio ($\Phi_{d,set} = 4/3$ and $\Phi_{d,set} = 8/3$).

Product size distribution

The startup evolution of the product size distribution $q_{0,pr}$ of each processing strategy is illustrated in Figure 6.2 for the slight-growth example ($\Phi_{d,set} = 4/3$) on left-hand side and the large-growth example ($\Phi_{d,set} = 8/3$) on the right-hand side. In simulations of slight-growth granulation, it is obvious that the product size distributions of all three processing strategies grow similarly to higher diameter values, become wider over time and no longer change significantly after around 7 h. Only the $q_{0,pr}$-curves of CM3 achieve somewhat larger diameters in total. It should be emphasized that the modal value of the CM3 product size distribution ends up very close to the desired product size of $d_{pr,set} = 0.4\,\mathrm{mm}$, while a slight deviation of the PSD-modals remains for the first two strategies CM1 and CM2. In the diagrams of the large-growth example, the product size distributions of processing strategy CM1 and CM2 does not, whereas the product size distribution of CM3 does reach the desired product diameter of $d_{pr,set} = 0.8\,\mathrm{mm}$. The simulation with CM1 and $\Phi_{d,set} = 8/3$ has the longest startup period regarding the product size distribution (see also bed mass later on) among all plots. The product size distributions of the slight- and large-growth granulation examples of method CM2 are very similar. At this point it is mentioned again that the nuclei feed rate and solids spray rate are identical between both simulations, and that neither of their spray-to-feed rate ratios (given with unity $\dot{M}_{spr,s}/\dot{M}_f = 1$) is adapted to the desired growth ratio $\Phi_{d,set}$, such as the required spray-to-feed rate ratio $\Phi_{m,set}$ used in strategy CM3. In the simulated process of strategy CM3 with the large-growth target, the time evolution of the product size distribution is completely different than in CM1- and CM2-results. There, a steady particle growth to much higher particle diameters with nearly constant PSD-variance is visible for the first 0.8 h, whereafter the product size distribution stops increasing and

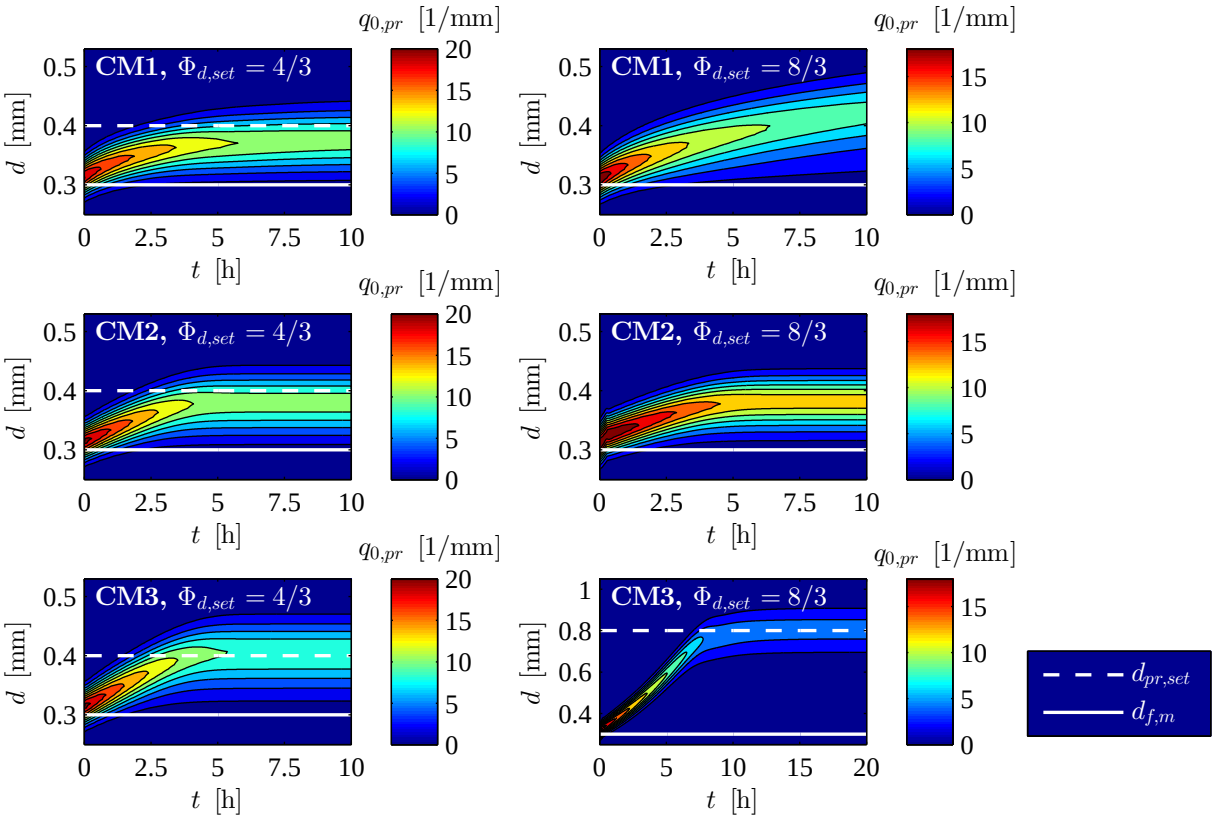

Figure 6.2: Transient evolution of product size distribution $q_{0,pr}$ for three different processing strategies (CM1, CM2, and CM3) and two different desired particle growth ratios $\Phi_{d,set}$.

becomes clearly broader than in other simulations. As noticed for the slight-growth process with strategy CM3, the modal value of the product-PSD precisely meets to the desired product diameter $d_{pr,set}$ too in the CM3-simulation of the large-growth granulation example. Moreover, it can be stated that the product size distribution is nearly symmetric in all of the shown examples of Figure 6.2. For such conditions, the modal value of the product size distribution is close to the mean value. The latter is calculated for each of the described process examples, as shown below.

Fluidized bed mass, separation gas velocity, and product mean size

The temporal evolution of the bed mass, the separation gas velocity, and the product mean diameter of the six simulations examples is illustrated in Figure 6.3, where the left diagrams show each processing strategy for the slight-growth granulation example ($\Phi_{d,set} = 4/3$) and the right diagrams each processing strategy for the large-growth granulation example ($\Phi_{d,set} = 8/3$). The time curves of the total bed mass $M_{bed}(t)$ are calculated numerically from the simulated number density distribution of bed particles $n_{bed}(t)$ by Eq. 5.5. As described before, the separation gas velocity u_g is constant in the processing strategy CM1, but time-variant in CM2 and CM3. The current separation gas velocity $u_g(t)$ of the CM2- and CM3-simulations follow from the bed mass via the control function Eq. 5.18. The time curve of product mean diameter $d_{m,pr}(t)$ is determined by the first moment (see Eq. 2.27 for $k = 1$ and $r = 0$) of the normalized product size distribution $q_{0,pr}(d,t)$.

For the slight-growth example, each processing strategy turns out to be stable regarding the bed mass curves even though in variant CM1 no feed-back control is employed. The bed mass of the first processing strategy CM1 increases in the first 1.25 h and then declines to a value of 0.73 kg under almost stationary conditions at 20 h. In the methods CM2 and CM3, the values of the bed mass only exceed slightly the set bed mass of 1.1 kg in the first 3 h. After this, the bed mass values fall below the set point, but with marginal control deviations. The separation gas velocities of CM2 and CM3 proceed inversely proportional to the corresponding bed mass curves, but with a more distinctive control error (see Eq. 5.34) due to the high gain

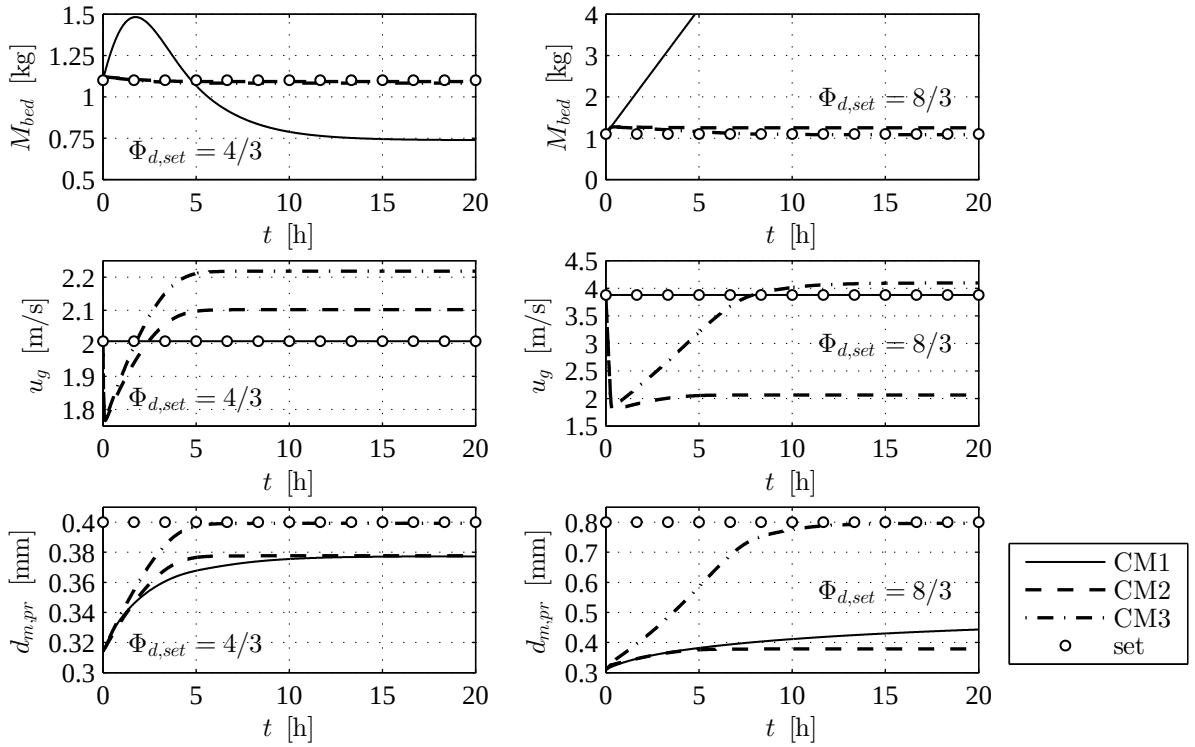

Figure 6.3: Transient evolution of bed mass M_{bed}, separation gas velocity u_g and product mean size $d_{m,pr}$ for three different processing strategies (CM1, CM2, and CM3) and two different desired particle growth ratios $\Phi_{d,set}$.

factor of $K_m = 12\,\mathrm{m/kg/s}$. As it can also be ascertained from Figure 6.2, the product mean diameter grows in the startup period until it reaches a constant value for each processing strategy. At this, CM1 takes the longest to arrive to stationary product mean diameters with nearly 10 h, whereas CM2 and CM3 generate such conditions almost twice as fast, which is due to the following reason. The initial increase of the bed mass in the case of CM1 leads to a higher surface area of the entire fluidized bed, which lowers the growth rate of single particles and hereby enlarges the duration of startup. It can be further seen that both variants CM1 and CM2 achieve values of stationary product mean diameter of around 0.38 mm, which deviates somewhat from the desired product size of $d_{pr,set} = 0.4\,\mathrm{mm}$. The particle growth ratio is obtained for CM1 and CM2 with round 1.267. The spray-to-feed rate ratio of the CM1- and CM2-process is given with unity ($\dot{M}_{spr,s}/\dot{M}_f = 1$), respectively, which corresponds to a target-growth ratio $\Phi_{d,set}$ of around 1.26 according to Eq. 5.29. Such a target value would match better with the CM1- and CM2-curves. It appears that the adaption of spray-to-feed rate ratio $\Phi_{m,set}$ to $\Phi_{d,set}$ has a stronger influence on stationary product size distribution (especially on the mean value) than the adaption of set separation gas velocity to $\Phi_{d,set}$. Even the operation with zero control deviation of the separation gas velocity u_g in CM1 is not capable to discharge product granules with a mean diameter that hardly deviates from the target value $d_{pr,set}$. Presumably, the operated spray-to-feed rate ratio of unity ($\dot{M}_{spr,s}/\dot{M}_f = 1$) is too low in this case. In the processing strategy CM3, where both the required spray-to-feed rate ratio $\Phi_{m,set}$ and the set separation gas velocity $u_{g,set}$ are adapted to the desired particle growth ratio $\Phi_{d,set}$, the stationary product mean diameter is almost exactly equal to the desired product size of 0.4 mm, as also ascertained before with respect to the modal value.

The temporal curves of large-growth granulation simulations ($\Phi_{d,set} = 8/3$) differ from the slight-growth granulation results in some points. The absence of bed mass control in variant CM1 leads to an enduring increase of the bed mass for higher set separation gas velocities (here 3.88 m/s). As a consequence for practical applications, the process chamber can be overloaded for such conditions and sub-processes such as fluidization, mixing, and homogeneous spraying and drying cannot be realized properly. In the variants CM2 and CM3, total bed mass stability can be ensured by the proportional feed-back controller not only for the slight-growth, but also for the large-growth example. The separation gas velocity u_g of the processing strategy CM1 is constant anyway, as no manipulation takes place in this case. The separation gas velocity of

the CM2- and CM3-simulations drops down in the beginning of the simulations to a value of nearly 1.78 m/s at a time of 0.38 h due the initial bed mass enlargements. The u_g-curve of the CM2-results persists at low values, whereas the u_g-values of the CM3 example increase up to values slightly above set separation gas velocity of $u_{g,set} = 3.88\,\mathrm{m/s}$. The reason for this is explained as follows. The ratio of solids spray rate to nuclei feed rate $\dot{M}_{spr,s}/\dot{M}_f$ is not adapted to the desired granule size enlargement ratio $\Phi_{d,set}$ in the strategy CM2, in contrast to CM3. At this, the solids spray rate $\dot{M}_{spr,s}$ is given with 300 g/h for the variant CM2 and with 568.4 g/h for CM3. In addition, the bed mass is controlled in a range of nearly constant values in both simulations. Hence, the growth rate of the CM2-granulation is much lower than in the CM3-process during the entire simulation, whereby longer growth periods to reach the target-product size $d_{pr,set}$ (here 0.8 mm) are needed in variant CM2. Higher growth times would lead to an accumulation of bed mass when the separation gas velocities u_g are close to the set point. However, the proportional controller (Eq. 5.18 for $K_m > 0$) reacts with low separation gas velocities in CM2 to prevent the bed mass from further enlargement by a sufficiently large product mass flow rate. In contrast to this, particles faster reach the desired product size in the CM3-simulation due to larger growth rates, whereby they can be separated from the granulator by the classifier more quickly (in terms of residence time) and higher mass flow rate of the product discharge even at low separation gas velocities is obtained. Consequently, the total bed mass is lowered, which leads to an increase of the separation gas velocity with proceeding time up to steady-state conditions, at which the production rate $\dot{M}_{pr}$ approaches the value of the total mass input of solids (here 600 g/h). Specifically, separation gas velocities of 2.06 m/s for CM2 and 4.09 m/s for CM3 are ascertained after 20 h of large-growth granulation. The product mean diameter of large-growth granulation with processing strategy CM1 raises to higher values than in case of slight-growth granulation (Figure 6.3, left) up to a value of 0.47 mm at a simulation time of 40 h (out of plot), where stationarity has still not been reached due to the enduring bed mass accumulation. But observed product mean size curve of CM1 is far below the objective-size of 0.8 mm, where the spray-to-feed rate ratio is not adapted to the desired particle growth ratio. However, such conditions are not relevant for practical applications as the bed mass evolution turns out to be instable. The product mean diameter curve of large-growth granulation with strategy CM2 is located even lower than the CM1-curve within the simulated time period of 20 h for the reason that the separation gas velocity of variant CM2 is much lower than in the CM1-simulation. It can be seen moreover that the CM2-curves of the product mean size are almost identical for the slight- and the large-growth example, although the set separation gas velocity $u_{g,set}$ differs by a factor of around 2. But the spray-to-feed rate ratio is given with unity in both cases of CM2. Hence, it can be ascertained again, that the spray-to-feed rate ratio has a stronger influence on the terminal average product diameter than the set separation gas velocity. In other words the average product size cannot be controlled when only the set separation gas velocity is conformed to the desired particle growth ratio and the adaption of the spray-to-feed rate ratio is refrained, as it is the case in CM1 and CM2. Hence, it turns out that variant CM2 is not suitable as processing strategy with adjustable average product size. The product mean size of the third variant CM3 however meets the target value very closely also for large-growth granulation, but it becomes constant only after 15 h, whereas it takes only 5 h for strategy CM2. As a conclusion from this, large-growth granulation can be realized properly by the processing strategy CM3, but it takes longer than in CM2 to obtain stationarity.

Comparison to required growth time of the ideal continuous layerwise granulation model

It is observed from the CM3-results of slight- and large-growth granulation that the bed mass M_{bed} is controlled to nearly constant values in vicinity of the set point M_{set} for the entire simulation. In addition, the required spray-to-feed rate ratio $\Phi_{m,set}$ is adapted to the desired growth ratio $\Phi_{d,set}$, and even growth is presupposed to take place. These conditions allow a comparison between the CM3-results and the presented ideal granulation model of Chapter 3. A relation for the required growth time (see Eq. 3.63) has been derived from the ICLG-model. This equation can be adapted to the assumptions of the present three-compartment population balance model, in which the spray loss fraction is set to zero ($\Phi_{spr,loss} = 0$), and the component density ratio is assumed with unity ($\Phi_\rho = 1$). By this, the required growth time ensues to:

$$\tau_{gr,set} = \frac{M_{set}}{\dot{M}_{spr,s}} \frac{4(\Phi_{d,set}^3 - 1)(\Phi_{d,set} - 1)}{\Phi_{d,set}^4 - 1}. \tag{6.3}$$

The adapted solids spray rates are given with 346.9 g/h for the slight-growth example and with 568.4 g/h for the large-growth example, as shown in Table 6.5. Using these solids spray rates, a set bed mass of $M_{bed} = 1.1\,\mathrm{kg}$, and Eq. 6.3, the required growth time follows with $\tau_{gr,set} = 2.68\,\mathrm{h}$ for the slight-growth example and with $\tau_{gr,set} = 4.68\,\mathrm{h}$ for large-growth example. It can be seen from the temporal curves in

Figure 6.3 that the evolution of product mean size takes around twice as long as the required growth time to reach stationarity at the objective-product size for both target formulations ($\Phi_{d,set} = 4/3$ and $\Phi_{d,set} = 8/3$).

6.1.3 Terminal control deviations for various desired particle growth ratios and separation sharpnesses

The influence of the desired particle growth ratio $\Phi_{d,set}$ and the separation sharpness κ_{sep} on the terminal relative control deviations of the fluidized bed mass ζ_m and the average product diameter ζ_d is discussed in the following for each processing strategy of Section 6.1.1 (CM1, CM2, and CM3). All of the quantities shown below were determined from the terminal operation point τ_{end}.

Relative control deviations

The terminal relative control deviations of bed mass $\zeta_{m,end}$ and product mean size $\zeta_{d,end}$ from their set values are calculated according to Eq. 5.34 for each of the suggested processing strategies CM1, CM2, and CM3. They are pictured as two-dimensional functions of the target-growth ratio $\Phi_{d,set}$ and the separation sharpness κ_{sep} in Figure 6.4. Therein can be seen under which process conditions the control errors are small and process objectives (bed mass stability and precise control in product size) can be realized. It is visible in the left plot of CM1 that large desired particle growth ratios $\Phi_{d,set}$ and high separation sharpnesses cause enormously high bed mass values, shown here with simulated control deviations up to 8000 %. Large control errors of bed mass can exceed the load capacity of the process chamber or lead to instable fluidization conditions. The immense enlargement of the bed mass is caused by several factors such as constant high values of the set separation gas velocities $u_{g,set}$ for the method CM1 and decreasing growth rates, which is explained in more detail later on in Section 6.1.4. For slight-growth granulation with CM1, the terminal control errors of both the bed mass $\zeta_{m,end}$ and the product mean diameter $\zeta_{d,end}$ are low regardless of the value of the separation sharpness. The terminal operation points of the CM2- and CM3-simulations show different results. In variant CM2, the relative control errors of the terminal bed mass $\zeta_{m,end}$ range from 0.19 to 25 %, which is still in an acceptable range of proper fluidization conditions. At higher separation sharpnesses (e.g., $\kappa_{sep} > 0.8$), an enlargement of the set separation gas velocity $u_{g,set}$ in CM2 leads to higher control deviations in terms of the bed mass and the product mean size. In variant CM3, the relative control deviations of both the total bed mass $\zeta_{m,end}$ and the product mean diameter $\zeta_{d,end}$ are the lower, the higher the separation sharpness κ_{sep} is. Hence, better product size distributions are achieved by improving the separation performance for the processing strategy CM3. For this reason, the process objectives of granulation with stable fluidization and of adjustable product size can be realized simultaneously, when a proportional bed mass controller (see Eq. 5.18) is used, the required spray-to-feed rate ratio $\Phi_{m,set}$ is conformed to the desired growth ratio $\Phi_{d,set}$, and the set separation gas velocity $u_{g,set}$ of P-controller is adapted to the objective-product size $d_{pr,set}$, but only for good separation performances ($\kappa_{sep} > 0.8$).

6.1.4 Discussion of large control deviations

Processing strategy CM1

As stated before, the immense bed mass increase of CM1-simulations for larger desired growth ratios $\Phi_{d,set}$ from around 1.5 up to 3.5 at high separation sharpness κ_{sep} is caused by the relatively large values of the set separation gas velocity $u_{g,set}$ and the growth conditions. Especially in the startup period, initial bed particles must grow quickly to larger particle size values, when the bed mass is not controlled by manipulating the separation gas velocity. Otherwise not enough particles can pass against the constant classifying flow and leave the entire system from the product outlet, which leads to a lack of product discharge rate and a steady increase of total bed mass in the process beginning. This reduces the growth rate of single granules again and keeps the product discharge rate low with proceeding simulation time. A steady state of the simulations can nevertheless be achieved after very long process times for the following reasons. A small amount of fine particles is still discharged from the product outlet due to imperfections of the separation function T_{sep}. The model-based bed discharge rate ($\dot{M}_{sep} = \int_0^\infty \rho_p \frac{\pi}{6} d^3 k_{sep} n_{1-\alpha}(d) \mathrm{d}d$ - classifier entry rate) of this PB-study is calculated from the number density distributions flow at the separator inlet $\dot{n}_{sep}$ in Eq. 5.6 with a constant separation frequency factor k_{sep} in Eq. 5.7, indicated as SFF1-approach. Due to the small spray zone proportion factor of $\alpha = 0.01$, the number density distribution of granules in the drying zone is nearly linearly connected to the number density distribution of the entire bed:

$$n_{1-\alpha}(d) \approx (1-\alpha) n_{bed}(d). \tag{6.4}$$

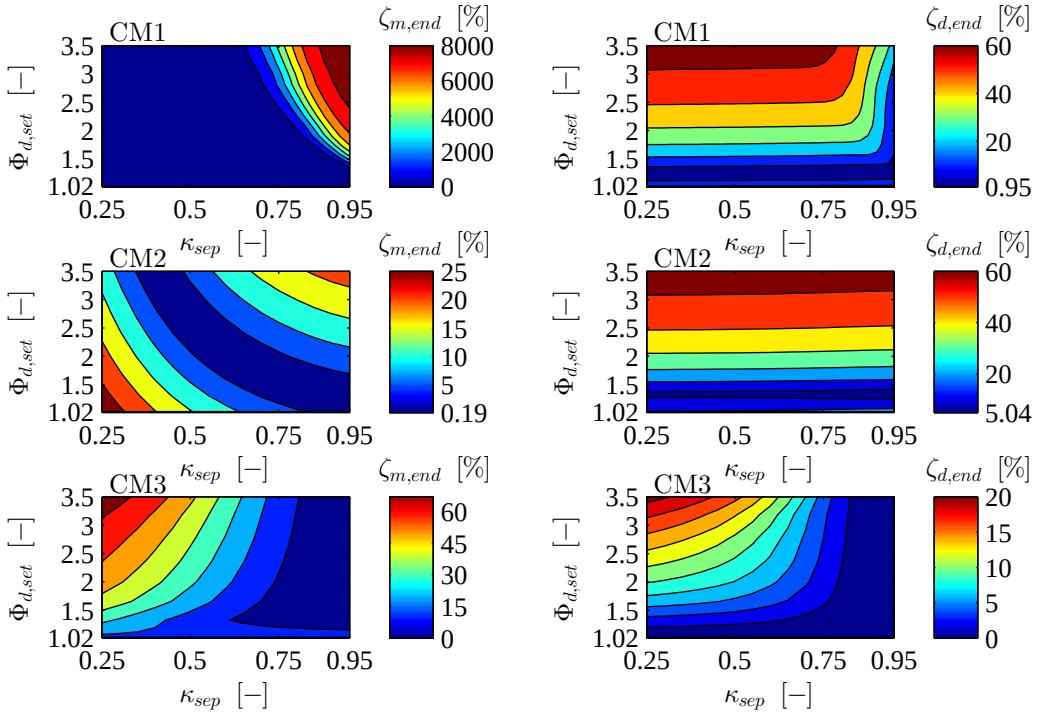

Figure 6.4: Relative control deviations (process success indices) at the terminal simulation point for the bed mass $\zeta_{m,end}$ (left) and the product mean size $\zeta_{d,end}$ (right) for three different processing strategies (CM1, CM2, and CM3) in dependency on desired particle growth ratio $\Phi_{d,set}$ and separation sharpness κ_{sep}.

Consequently, the bed discharge rate $\dot{M}_{sep}$ can be expressed by

$$\begin{aligned}\dot{M}_{sep} &= \int_0^\infty \rho_p \frac{\pi}{6} d^3 \dot{n}_{sep}(d)\mathrm{d}d \\ &\approx k_{sep}(1-\alpha) \int_0^\infty \rho_p \frac{\pi}{6} d^3 n_{bed}(d)\mathrm{d}d = k_{sep}(1-\alpha) M_{bed},\end{aligned} \tag{6.5}$$

from which is shown that the bed discharge rate is directly proportional to the total mass of drying zone particles ($M_{1-\alpha} = \int_0^\infty \rho_p \frac{\pi}{6} d^3 n_{1-\alpha}(d)\mathrm{d}d$), but also ca. proportional to the mass of the entire bed ($M_{bed} = \int_0^\infty \rho_p \frac{\pi}{6} d^3 n_{bed}(d)\mathrm{d}d$). Using Eqs. 5.9 and 6.5, the production rate $\dot{M}_{pr} = \int_0^\infty \rho_p \frac{\pi}{6} d^3 \dot{n}_{pr}\mathrm{d}d$ can be approximated by the number density distribution of all bed granules n_{bed} and the separation curve T_{sep} according to:

$$\begin{aligned}\dot{M}_{pr} &= k_{sep} \int_0^\infty \rho_p \frac{\pi}{6} d^3 n_{1-\alpha}(d) T_{sep}(d)\mathrm{d}d \\ &\approx k_{sep}(1-\alpha) \int_0^\infty \rho_p \frac{\pi}{6} d^3 n_{bed}(d) T_{sep}(d)\mathrm{d}d.\end{aligned} \tag{6.6}$$

At this, the separation function is time-independent for the CM1-simulations. From Eq. 6.6, it can be seen that a steadily enlarging bed mass raises the product mass flow rate as long as it reaches a value of the total mass input of solids ($\dot{M}_f + \dot{M}_{spr,s}$). Hence, the CM1-simulations of large-growth granulation with high separation sharpnesses can become stationary even for the immense bed mass excesses, but after a very long time. For example, a stationary bed mass of the presented large-growth granulation with processing strategy CM1 (Figure 6.3) is obtained after more than 30, 000 h. However, those process conditions are not of interest for practical applications.

Processing strategy CM2

As shown in Figures 6.2, 6.3, and 6.4, the product size distribution cannot be controlled by the processing strategy CM2, where only the set separation gas velocity of the bed mass controller is adapted to the desired

particle growth ratio, but the spray-to-feed rate ratio is fixed to a freely chosen point. The control deviations in product size are low for small desired particle growth ratios, which is less a result of strategy CM2, but more of the spray-to-feed rate setting. When taking a higher spray-to-feed rate ratio and using the method CM2 at high separation sharpnesses, the range of minimal control errors in product size would probably shift to larger $\Phi_{d,set}$-values. The insufficient adjustability of product size of method CM2 can be explained for the large-growth granulation example of Figure 6.3 with a desired product diameter $d_{pr,set} = 0.8\,\mathrm{mm}$ and a desired particle growth ratio of $\Phi_{d,set} = 8/3$. There, the initial set separation gas velocity and initial separation diameter were given with $u_{g,set,0} = 3.88\,\mathrm{m/s}$ and $d_{sep}(u_{g,set,0}) = 0.8\,\mathrm{mm}$, by which less granules are discharged as product and the bed mass raises in the process beginning. According to the proportional controller in Eq. 5.18, the separation gas velocity u_g and the corresponding separation diameter d_{sep} decline in response with increasing bed mass. The reaction of the proportional controller is strong because of the high gain factor $K_m = 12\,\mathrm{m/kg/s}$, what results in large changes of the separation gas velocity. After a certain simulation time (0.38 h for this example), the separation diameter has decreased to a value where a product discharge rate $\dot{M}_{pr}$ as large as the total mass input of solids ($\dot{M}_{spr,s} + \dot{M}_f$) is obtained. At this point, the fluidized bed mass accumulation has arrived at a maximum, from where the bed mass slightly lowers again and takes on a stationary value after 5 h. At the same time, the classifying gas speed passes through a minimum and then changes steadily to a constant value. The growth rate is relatively low in the CM2-example with $\Phi_{d,set} = 8/3$, as the solids spray rate (300 g/h for this example) is not conformed to the desired product size. For this reason, the separation gas velocity remains at a stationary value, where an equilibrium between the particle residence times and the growth kinetics is arrived, so that bed mass can be hold on a constant level. The controller ensures a constant bed mass close to the target value through low gas velocities and, however, sacrifices a product mean size close to the target value.

6.1.5 Summary and conclusions

The goal of the present PB-simulation study was to find a processing strategy and proper process conditions, which can accomplish a stable continuous fluidized bed spray granulation process with freely adjustable product mean size up to a desired granule size enlargement ratio $\Phi_{d,set}$ of 3.5. Three different processing strategies (features in Table 6.1) have been tested by simulations with a modified version of Hampel's three-compartment population balance model [1,2] for various desired particle growth ratios ($1.02 \leq \Phi_{d,set} \leq 3.5$) and separation sharpnesses ($0.25 \leq \kappa_{sep} \leq 0.95$). The first processing strategy CM1 operates without bed mass control (offset mode of Eq. 5.18), with freely chosen spray-to-feed rate ratio (here $\dot{M}_{spr,s}/\dot{M}_f = 1$), and with constant set separation gas velocity ($u_g = u_{g,set} = \mathrm{f}(\Phi_{d,set})$ via Eq. 5.30) that is adapted to the desired product size $d_{pr,set}$. The parameter setting in processing strategy CM2 is the same as in CM1, but the fluidized bed mass is additionally controlled by a proportional feed-back structure (activated mode of Eq. 5.18) in CM2. In the third processing strategy CM3, the proportional feed-back controller is employed likewise to CM2, and both the required spray-to-feed rate ratio $\Phi_{m,set}$ and set separation gas velocity $u_{g,set}$ are adapted to the desired particle growth ratio.

Successes of the processing strategies

The process behavior of the three strategies could essentially be ascertained as follows. In strategy CM1, the bed mass can exceed a range of values of process stability and even granulator capacities for certain parameter conditions. In the simulation examples shown, this has occurred for processes with high separation sharpness and high desired particle growth ratios at a relatively low spray-to-feed rate ratio. Strategy CM2 can ensure bed mass stability for all the parameter settings used, but the product mean diameter $d_{m,pr}$ does not follow the desired product diameter $d_{pr,set}$ for the arbitrary desired particle growth ratios. From the processing strategies presented, only operation with CM3 and sufficiently large separation sharpnesses ($\kappa_{sep} > 0.8$) can achieve bed mass stability and free control in product mean size at the same time. A processing strategy, where only the spray-to-feed rate ratio is adapted to the desired particle growth ratio and set separation gas velocity is freely selected, has not been investigated within the present PB-simulation study. Nevertheless, the processing strategy CM3 shall be the basis for the continuous granulation experiments in Section 10.4.

Separation performance

In general, processes with high separation performance are preferred to achieve narrow product size distributions. As shown in Figure 6.1, high separation sharpnesses in a straight-duct classifier tube can be reached

for larger Bodenstein numbers of axial gas dispersion. It follows from the definition of the Bodenstein number (Eq. 5.13) that longer and thinner tubes as well as lower turbulence factors improve the separation performance. The separation gas velocity has only a slight influence on the separation sharpness within the range of 0.5 to 5 m/s, especially for Bodenstein numbers larger than 20. As a consequence, the set separation gas velocity, and so, the desired granule size enlargement ratio can be varied without significant changes in the separation efficiency for higher Bodenstein numbers. But set separation gas velocities above 5 m/s would be needed for granulation processes of much larger and more dense nuclei particles. In this case, the separation sharpness would decrease more strongly. So in order to obtain the same separation sharpness, even longer or thinner tubes must be applied. As mentioned before, the inner diameter of the classifier cannot be chosen too small, however, due to diverse effects, such as higher particle concentrations for a certain required classification load ($\dot{M}_{sep} > \dot{M}_f(1-\Phi_{f,loss}) + \dot{M}_{spr,s}(1-\Phi_{spr,loss})$), lower terminal sinking velocities of single particles and swarms in proximity of walls (e.g., Eq. 2.90 for single particles or approaches of Richardson a. Zaki [50] in Section 2.2.2 for swarms), and laminar velocity profiles of separation gas. But those effects have not been considered in this PB-study. Furthermore, high particle concentration can be avoided in practice by distributing the particles among several straight-duct classifiers in parallel arrangement. Alternatively, zig-zag classifiers with many separation stages can be used to increase separation performance.

Application to different configurations of granulators

Hampel's PB-model ([1, 2], Section 2.3), the present modification (Section 5.2) of it, and the processing strategy CM3 are not only restricted to continuous granulation processes with Wurster equipment. They can also be applied to granulators with top-, bottom-, or side-spray configuration, or to spouted beds; because, the division of the granulation chamber into a spray zone and a drying zone is also useful for those processes. It is crucial that the proportion of agglomeration should be low, so that granules are mainly built up in layers. The simulation parameters, such as the spray zone fraction α, the spray zone residence time τ_α, and the drying zone residence time $\tau_{1-\alpha}$, would be different for other granulator configurations.

Further disregarded aspects and outlook to subsequent investigations of this thesis

The creation of internal nuclei (e.g., overspray) by, for instance, premature drying of spray droplets is not regarded in this study. In case of strong internal nucleation, the spray-to-feed rate adaption according to the ideal granulation model, which is utilized in strategy CM3 via the setting method SFM3 (Table 3.1), could be only applied effectively, when the majority of internal nuclei is lost by wall adhesion and elutriation with exhaust gas, and not discharged in the product. Recycling of dust material from the exhaust gas, which can be used for layering applications, is also not considered here. Another aspect that is not covered by the present PB-study, are the spray limits by process-gas saturation and drying kinetics, which may lead to over-wetting and destabilization of the fluidized bed through agglomeration. A calculation method for the process-gas-saturation limit for the example of Wurster granulation with the equipment of Hampel's experiments is derived later in Sections 7.10 and 7.11. Realization of strategy CM3 requires a precise control of nuclei feed rates and spray rates in practice. Possible ranges of these process parameters are restricted by the design and operation principle of the employed equipment, see for instance Section 9.4.1. Especially the nuclei feed rate is hard to be controlled, as shown later in Section 10.2. Therefore, different feed rate control methods are developed in Section 9.4.3. Fast startups were also not part of the simulation objectives. Especially large-growth granulation (e.g., $\Phi_{d,set} = 8/3$) requires long transient periods. For this reason, two strategies for faster growth during process startups are conceptualized in Section 9.4.10 and found use in the continuous granulation experiments.

6.2 Simulations for two types of separation frequency factor, various gain factors, and different desired particle growth ratios

In Section 6.1, the CM3 method has proven to be a promising processing strategy for continuous granulation with adjustable product size, which will also be investigated experimentally later. However, due to the model assumptions, there are still some deviations from the experiments. For instance, the dosing behavior analysis of the feed-out double-pinch valve (see Figure 2.6, No. 7) has shown that the conveying rate from the granulator to the separator (bed discharge rate $\dot{M}_{sep}$) fluctuates around a long-term average value.

Therefore, using the SFF2-type of the separation frequency factor k_{sep} (constant $\dot{M}_{sep}$, Eq. 5.8) within the PB-model is more realistic than the SFF1-approach (constant residence time, Eq. 5.7). In addition to this, an optimal gain factor of $K_m = 3\,\mathrm{m/s/kg}$ was worked out of the first continuous granulation experiments of this thesis in Section 10.4.2 for process conditions of Hampel's reference case. In simulations of Section 6.1 (of Hampel [2] too), however, the gain factor is given much larger with $K_m = 12\,\mathrm{m/s/kg}$. Smaller gain factors make bed mass control dynamics slower and also influence the control deviations of bed mass (as controlled variable) and separation gas velocity (as manipulated variable). It is not yet clear, if the processing strategy CM3 can still achieve the same successes in process stability and product size control with a much lower gain factor, and how strongly each of the stationary control deviations in bed mass, separation gas velocity, and product mean size is affected then. For these reasons, it is aimed in this Section

- to improve the PB-model of Chapter 5 by the SFF2-approach,
- to generate simulation results that come closer to the experimental conditions,
- to investigate influence of the gain factor on temporal evolution of the three controlled variables,
- to test the processing strategy CM3 for a lower gain factor in terms of process dynamics and terminal control deviations for different growth targets,
- to better understand the control behavior of bed mass, separation gas velocity, and product mean size as well as the startup behavior, and
- to draw conclusions with regard of possible control and startup strategies, not only in general, but also for the experiments in this work (Section 10.4.3).

The following PB-study consists of two parts. The first part includes simulations with both k_{sep}-approaches SFF1 and SFF2 for different gain factors at slight-growth conditions with $\Phi_{d,set} = 4/3$. Based on this, both methods SFF1 and SFF2 are compared, and the influence of the gain factor on temporal development of the three controlled variables - bed mass M_{bed}, separation gas velocity u_g, and product mean diameter $d_{m,pr}$ - is analyzed. The second part contains granulation processes with different growth targets ($\Phi_{d,set}$), which were only simulated with the SFF2-variant and the empirical optimum of the gain factor. Therein, success and process dynamics of strategy CM3 are inspected.

6.2.1 Parameter setting

Uniform parameters and assumptions

As mentioned before, the processing strategy CM3 of Table 6.1 shall be used for each of the simulations. This means that both the required spray-to-feed rate ratio $\Phi_{m,set}$ and the set separation gas velocity $u_{g,set}$ are adapted to the desired particle growth ratio via Eqs. 5.29, 5.30, 6.1, and 6.2. The uniform parameters of this PB-simulation study are listed in Table 6.6. The particle size distributions of the external nuclei and the initial bed material are defined with the Gaussian distribution in Eq. 5.2 again. The spray zone fraction factor α, the residence time of granules in the spray zone τ_α, the nuclei mean size $d_{m,f}$, the standard deviation of the nuclei-PSD σ_f, and the production rate $\dot{M}_{pr}$ are adopted from the previous simulation study in Table 6.2. They have been used in Hampel's simulations [2], which were validated by experiments. The residence time of granules in the drying zone ensues from Eq. 2.150 to $\tau_{1-\alpha} = 9.9\,\mathrm{s}$. The effective densities of external nuclei, initial bed granules, and coatings are supposed to be equal with $\rho_p = 1380\,\mathrm{kg/m^3}$. The coating-to-core density ratio follows therefore with unity: $\Phi_\rho = 1$. The set bed mass M_{set} and the initial bed mass $M_{bed,0}$ are both given here with 1 kg, slightly smaller than for the simulations in Section 6.1. The minimal separation gas velocity $u_{g,min}$ of the proportional bed mass controller (Eq. 5.18) is the same as in the CM2- and CM3-simulations of Section 6.1. The drag coefficient, used for calculating the terminal sinking velocity u_s in the separation function (Eq. 5.14) or the set separation gas velocity $u_{g,set}$ in Eq. 5.30, is determined iteratively with the correlation of Kürten et al. ([30], see Eq. 2.80). During each simulation, the gas-related Bodenstein number for axial dispersion $Bo_{ax,g}$ of the classifier function (Eq. 5.14) is steadily adapted to a fixed separation sharpness of $\kappa_{sep} = 90\,\%$ by means of the 2D-data array of the function shown in Figure 6.1. Mass losses of the core and coating materials are neglected: $\Phi_{f,loss} = \Phi_{spr,loss} = 0$.

α [%]	τ_α [s]	$\tau_{1-\alpha}$ [s]	$d_{m,f}$ [mm]	σ_f [mm]	ρ_p [kg/m^3]	$\dot{M}_{pr}$ [g/h]	$M_{bed,0}$ [kg]	M_{set} [kg]	$u_{g,min}$ [m/s]
1	0.1	9.9	0.3	0.02	1380	600	1	1	0.001

Table 6.6: Uniform parameters for simulations shown in Section 6.2.

variation of K_m with $\Phi_{d,set} = 4/3$ for SFF1 and SFF2		variation of $\Phi_{d,set}$ with $K_m = 3\,\mathrm{m/s/kg}$ only for SFF2						
K_m [m/s/kg]	$M_{bed,cr}$ [kg]	$\Phi_{d,set}$ [−]	$\Phi_{m,set}$ [−]	$\dot{M}_f$ [g/h]	$\dot{M}_{spr,s}$ [g/h]	$u_{g,set}$ [m/s]	$M_{bed,cr}$ [kg]	$\tau_{gr,set}$ [h]
1	3.01	**4/3**	1.37	253.1	346.9	2.01	1.67	2.44
3	1.67	**5/3**	3.63	129.6	470.4	2.52	1.84	3.06
5	1.40	**6/3**	7.00	75.0	525.0	3.00	2.00	3.56
7	1.29	**7/3**	11.70	47.2	552.8	3.45	2.15	3.94
12	1.17	**8/3**	17.96	31.6	568.4	3.88	2.29	4.25

Table 6.7: Values of varied and dependent process parameters.

Differences in simulation parameters

A separation time constant of $\tau_{sep} = 1800\,\mathrm{s}$ was used for the SFF1-simulations. In the simulations with SFF2, the bed discharge rate is assumed to be $\dot{M}_{sep} = 3.82\,\mathrm{kg/h}$. This value is derived from experiments of Hampel [2], where bed discharge curves of tracer particles were measured. Table 6.7 gives an overview on the parameter variation of this PB-study with five values of the gain factor K_m (1, 3, 5, 7, and 12 m/s/kg) on the left and five values of the desired particle growth ratio $\Phi_{d,set}$ (4/3, 5/3, 6/3, 7/3, and 8/3) on the right. For each of these examples, a PB-simulation is carried out, with diverse characteristic quantities calculated and described in Section 6.2.2. The dependent parameters are also listed in Table 6.7. When varying the gain factor, only the critical bed mass of the proportional controller (Eq. 5.18 for $K_m > 0$) has to be adapted via Eq. 5.17. For the variation of the desired granule size enlargement ratio $\Phi_{d,set}$, the required spray-to-feed rate ratio $\Phi_{m,set}$, the nuclei feed rate $\dot{M}_f$, the solids spray rate $\dot{M}_{spr,s}$, the set separation gas velocity $u_{g,set}$, and the critical bed mass $M_{bed,cr}$ are changed. As depicted in Figure 5.2, the P-control function becomes steeper by larger gain factors, and thus, the critical bed mass becomes smaller; whereas higher desired growth ratios shift the control curve to the right by larger set separation gas velocities and thereby raise the value of the critical bed mass. Furthermore, the required growth time $\tau_{gr,set}$ according to the ideal granulation model is calculated by Eq. 6.3 for each of the $\Phi_{d,set}$-examples and listed in Table 6.7 too. The required growth time of the ICLG-model increases degressively with the desired granule size enlargement ratio, because the spray-to-feed rate setting method SFM3 of Table 3.1 is employed as a part of strategy CM3. The values of $\tau_{gr,set}$ shall be compared to visually estimated startup times below.

6.2.2 Temporal evolution of diverse characteristic quantities

Comparison between SFF1 and SFF2 approach for different gain factors at slight-growth granulation conditions

Figure 6.5 shows the temporal curves of the bed mass M_{bed}, the separation gas velocity u_g, and the product mean diameter $d_{m,pr}$ for the PB-simulations of the five different gain factors K_m of Table 6.7, each of which calculated with the SFF1-approach of separation frequency factor (Eq. 5.7), depicted on the left, and with the SFF2-approach of separation frequency factor (Eq. 5.8), depicted on the right. It is evident that simulation with either the first or the second type of separation frequency factor leads to almost the same results for each of the gain factor examples. It can also be seen that, for smaller gain factor, the bed mass deflects more from the setpoint in both the transient and stationary phase. At this, maximal relative control deviations in bed mass are observed with +21 % for the startup period and with −6 % at steady-state conditions. These control errors are still in an acceptable range of stable fluidization for the equipment (ProCell LabSystem, see Section 9.2) used by Hampel [1,2] and in the granulation experiments of this thesis. In the simulations with larger gain factors, the bed mass controller reacts earlier with a reduction of the

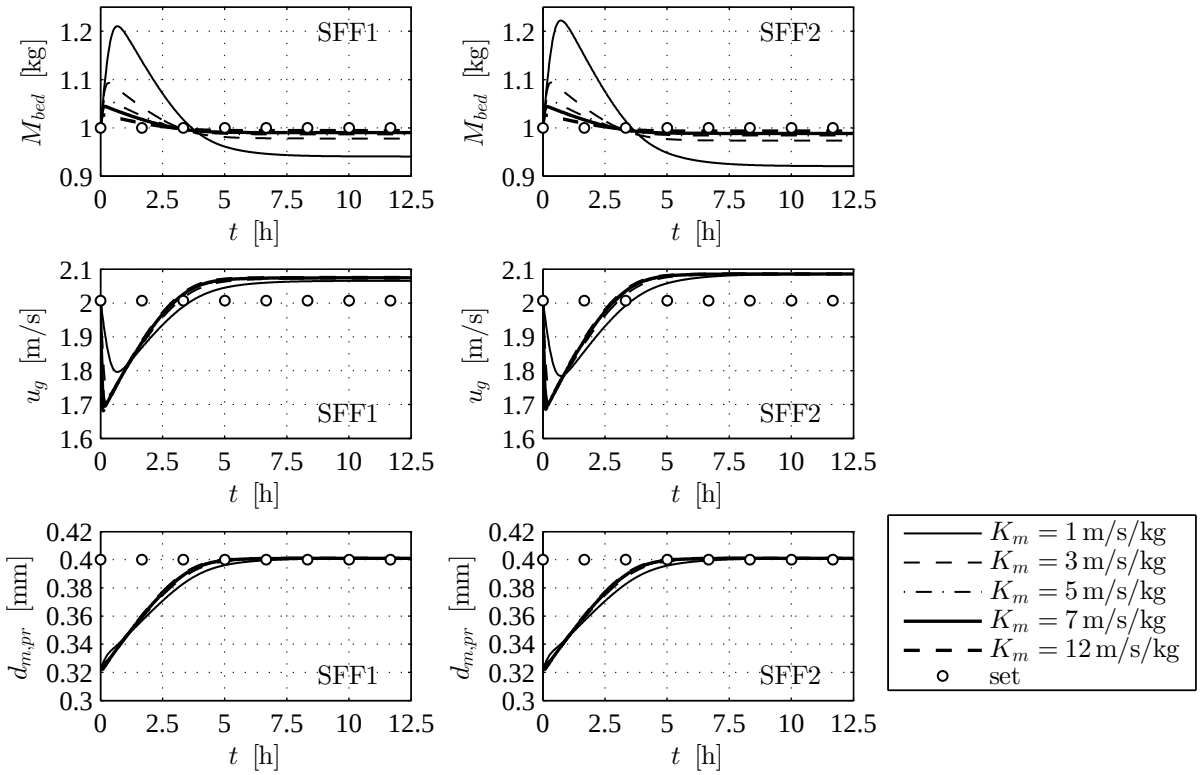

Figure 6.5: Transient evolution of bed mass M_{bed}, separation gas velocity u_g and product mean size $d_{m,pr}$ for different gain factors K_m and two different approaches to the separation frequency factor k_{sep} (SFF1 and SFF2).

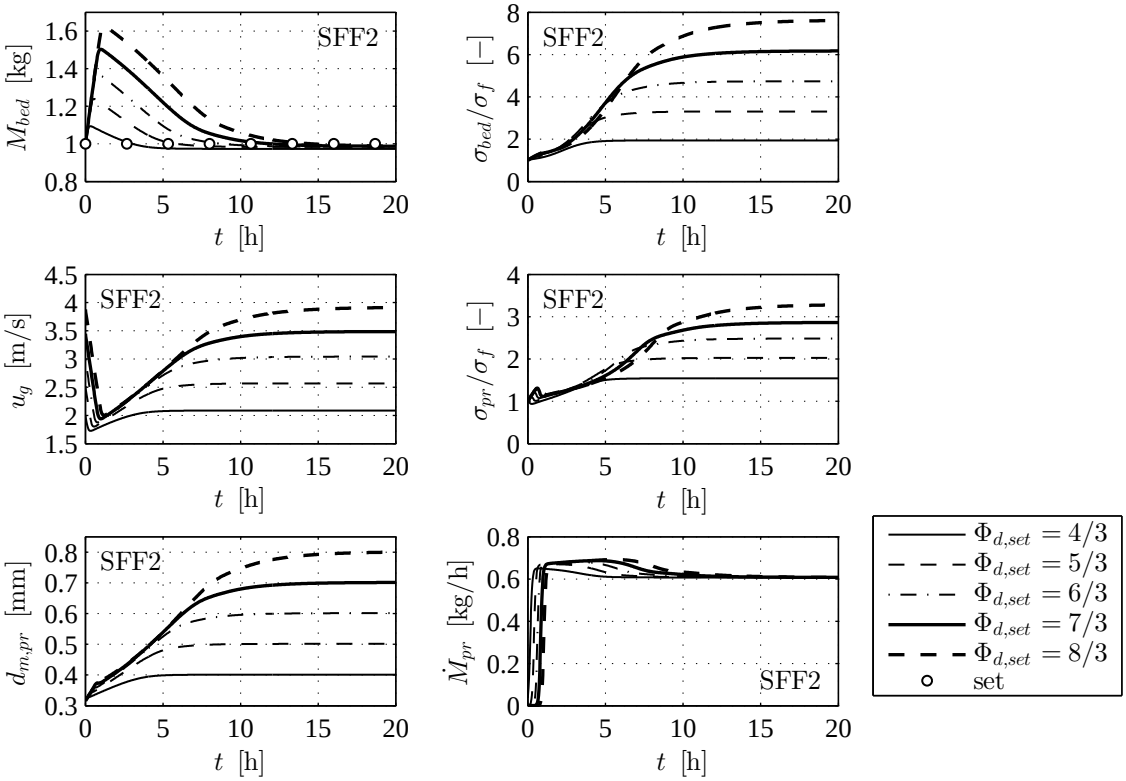

Figure 6.6: Transient evolution of diverse properties for different desired particle growth ratios $\Phi_{d,set}$, each simulation calculated with the SFF2-approach for k_{sep}.

separation gas velocity in the process beginning, which dampens the increase in bed mass more strongly. At this, the u_g-curves of $K_m \geq 3\,\mathrm{m/s/kg}$ are closer together than the u_g-curve of $K_m = 1\,\mathrm{m/s/kg}$. The stationary separation gas velocity $u_g(t \to \infty)$ is raised by growing gain factors, but only very slightly. The development of the product mean diameter during the entire startup and the stationary period is also hardly affected by varying the gain factor. Only the product mean diameter of the smallest K_m-example takes a little longer to reach stationarity. The terminal relative control deviation of the separation gas velocity $\zeta_{u,end}$ is detected with 3.94 % at maximum and of the product mean diameter $\zeta_{d,end}$ with 0.25 % at maximum among all simulations presented in Figure 6.5. Again, it is particularly noteworthy that the product mean diameter exactly matches the target-product size $d_{pr,set}$. This is due to the employed processing strategy CM3, which has already proven itself in Section 6.1 for the adjustable control of the product size in continuous granulation. The reason for the different influences of gain factors on the control deviations in bed mass, separation gas velocity, and product mean size is discussed below.

Simulations with the separation frequency factor SFF2 and a moderate gain factor for various desired particle growth ratios

The PB-simulations with the SFF2-approach for the five different desired particle growth ratios $\Phi_{d,set}$ of Table 6.7 are described in the following by means of the bed mass M_{bed}, the separation gas velocity u_g, the product mean diameter $d_{m,pr}$, the bed-to-nuclei ratio of PSD-standard-deviations σ_{bed}/σ_f from Eq. 5.23 with $\sigma_f = 0.02\,\mathrm{mm}$, the product-to-nuclei ratio of PSD-standard-deviations σ_{pr}/σ_f from Eq. 5.24, and the production rate $\dot{M}_{pr}$ from Eq. 5.27. The time courses of these six process characteristics are shown in Figure 6.6. In each simulation, an initial increase in bed mass is observed, which is the stronger the higher the desired particle growth ratio is. The bed mass controller takes also longer for larger growth targets to lower the bed mass towards the setpoint and reach stationarity. With a gain factor of $K_m = 3\,\mathrm{m/s/kg}$, the relative control deviation ζ_m has reached its maximum of around 60 % for the largest desired particle growth ratio $\Phi_{d,set}$. Larger excesses in bed mass could endanger process stability for granulation processes with the experimental equipment (Section 9.2.1) used in this thesis. The critical bed mass $M_{bed,cr}$ of the

P-controller (Table 6.7) is not exceeded in any of the depicted examples. Moreover, a clear inflection point is visible in the bed mass curves. At these points, the bed granules have become sufficiently large, so that the product discharge rate is higher than the total solids input (here $\dot{M}_f + \dot{M}_{spr,s} = 0.6\,\mathrm{kg/h}$), as can be seen in the $\dot{M}_{pr}$-t-diagram. The bed mass then becomes smaller as a result. The separation gas velocity behaves inversely due to the control function, i. e. each of the u_g-curves initially drops to a turning point, and then rises to a steady state. In contrast to the bed mass curves, however, the target values for the separation gas velocity vary between the simulations, whereby the stationary points also differ significantly from one another. For each $\Phi_{d,set}$-example, the terminal bed mass is slightly below the setpoint, while the terminal separation gas velocity is always a little bit above the set separation gas velocity of Table 6.7. The product mean diameters increase steadily from the process beginning on and take on stationary values, which are again very close to the target diameters. The terminal relative control deviations $\zeta_{j,end}$ lie between 1.35 and 2.64 % for the bed mass (below setpoints), 1.04 and 3.94 % for the separation gas velocity (above setpoints), and 0.16 and 0.25 % for the product mean diameter (above setpoints). The absolute values of the relative control deviations decrease with $\Phi_{d,set}$ for each of the controlled variables. The standard deviations of the particle size distributions of the bed and product material σ_{bed} and σ_{pr} increase in the transient phase and reach a multiple of that of the core material. Large product size varieties of bed granules are part of the principle of the procedure, and thus, inevitable. However, the variance in the product-PSD may be one of the process objectives or costumer requirements. In layering application, for example, σ_{pr} should be as small as possible, if it is pursued to produce monodisperse bulk solids. To achieve this, a particularly high separation sharpness is required here, but also a narrow residence time distribution of the bed particles.

Taking into account all the variables presented in Figure 6.6, the following startup times for reaching the full steady state are roughly determined by eye with 5 h for $\Phi_{d,set} = 4/3$, 7.5 h for $\Phi_{d,set} = 5/3$, 11 h for $\Phi_{d,set} = 6/3$, 15 h for $\Phi_{d,set} = 7/3$, and 20 h for $\Phi_{d,set} = 8/3$. From this becomes obvious that startup times grow over-proportionally with the desired particle growth ratio; whereas, the required growth times $\tau_{gr,set}$ of Table 6.7 increase degressively with $\Phi_{d,set}$. In the slight-growth example with $\Phi_{d,set} = 4/3$, the startup period to reach stationarity is around twice as large as the required growth time. In the simulation of the largest growth target $\Phi_{d,set} = 8/3$, it even takes four times the required growth time. The reason for this goes back to the enlarged bed mass excesses for higher desired particle growth ratios. Thereby, growth rates of single particles (Eq. 5.17) are lowered, which extends the startup phase.

6.2.3 Conclusions and outlook

Evaluation of method SFF2

Two bed discharge methods have been compared within this section. In the first one, denoted by SFF1, the granulator residence time of bed particles is uniform and time-invariant (τ_{sep} =const.), the separation frequency factor is determined by the reciprocal of the granulator residence time ($k_{sep} = 1/\tau_{sep}$, Eq. 5.7), and the bed discharge rate changes during the transient phase of the simulations ($\dot{M}_{sep} = \mathrm{f}(t)$). In the second one, denoted by SFF2, the bed discharge rate is given as one of the constant parameters ($\dot{M}_{sep}$ =const.), the separation frequency factor is obtained from the ratio of current bed mass to the bed discharge rate ($k_{sep} = M_{bed}(t)/\dot{M}_{sep}$, Eq. 5.8), and granulator residence time varies during the startup ($\tau_{sep} = \mathrm{f}(t)$). Figure 6.5 shows that each of the three controlled variables (M_{bed}, u_g, and $d_{m,pr}$) of the PB-simulations with both methods SFF1 and SFF2 evolves almost equally; but, these curves were only calculated for the slight-growth granulation example with $\Phi_{d,set} = 4/3$. However, the stationary points of the three controlled variables of SFF2-simulations with larger growth targets in Figure 6.6 can be compared with the terminal relative control deviations of Figure 6.4, which were created by SFF1-simulations. It can be seen from this that the control deviations obtained in the final state are practically the same for both methods, even in the case of higher growth ratios. It is, therefore, recommended for future research to apply the bed discharge calculation method SFF2. In doing so, the bed discharge rate can be estimated from experiments; but, it also allows to simulate continuous granulation processes with multiple classifiers (at least two). The bed discharge rate has to be calculated by the sum of several separator input rates ($\sum_i \dot{M}_{sep,i}$).

Mutual independence of bed mass and product mean size for stationary conditions

It turns out from the M_{bed}- and $d_{m,pr}$-curves in Figure 6.5 that stationary bed mass values are different for the five K_m-examples, while the product mean diameters fall on almost the same stationary point. This observed behavior goes along with one of the conclusions of the ideal particle growth model, shown in Section 3.3.2, that says: the product diameter to be set ($d_{pr,set}$) is independent from the bed mass under the given

model conditions (Section 3.1.1), one of which is the assumption of stationarity. In order to substantiate this statement, simulations with the present PB-model can be made for a broader range of setpoints of the bed mass in future work. By this, the processing strategy CM3 (Table 6.1) could be tested for different plant scales. The bed discharge calculation method SFF2 can then be of advantage, as the granulator residence times of $\tau_{sep} = 1800\,\mathrm{s}$ used by Hampel [2] would be inappropriate for systems of different desired holdups.

Control behavior of processing strategy CM3 - advantage of proportional bed mass control

Recapitulating all the simulated process conditions of Section 6.2, the stationary product size can also be controlled by the processing strategy CM3 (Table 6.1) with a lower gain factor. But, when using a proportional bed mass controller, as with Eq. 5.18, certain remaining control deviations in the bed mass, the separation gas velocity, and hence, the separation diameter must be still expected for steady states. These are only zero for certain settings of the process parameters. However, the results show that zero-control-deviations in bed mass ($M_{bed,end} \rightarrow M_{set}$) and/or separation gas velocity ($u_{g,end} \rightarrow u_{g,set}$) are not needed to achieved a precise control in product mean diameter ($d_{m,pr,end} \rightarrow d_{pr,set}$). The deficiency of a P-controller to transfer the present granulator-separator system into states with (almost always) non-zero control deviations even proves to be advantageous for product size control, which is explained as follows. For example, in each of the simulations of both Figures 6.5 and 6.6, the terminal separation gas velocity $u_{g,end}$ exceeds the set separation gas velocity $u_{g,set}$ more than the product mean diameter $d_{m,pr}$ exceeds the target value $d_{pr,set}$. This means that the terminal separation diameter $d_{sep,end}$ is somewhat larger than the terminal product mean diameter $d_{m,pr,end}$ and even a little bit more larger than desired product diameter: $d_{sep,end}(u_{g,end}) > d_{m,pr,end} > d_{pr,set}$. As a conclusion, the product mean size can be precisely controlled despite existing control deviations of the separation gas velocity. At this, the proportionally controlled granulator-separator-system evades to a stationary point of the bed mass $M_{bed,end}$ and separation gas velocity $u_{g,end}$ in such a way that the core and coating masses of incoming and outgoing material flows can become equal. Depending on the shape of the separation curve, the stationary separation gas velocity then takes on a value at which the discharged core and coating components of the production rate $\dot{M}_{pr}$ correspond to the ratio of the solids spray rate $\dot{M}_{spr,s}$ to the nuclei feed rate $\dot{M}_f$. Thus, the spray-to-feed rate ratio $\Phi_{m,set}$ dictates not only the product mean size $d_{m,pr,end}$, but also the steady state of the separation gas velocity, and finally the bed mass too. Even when the gain factor of the bed mass control function changes, the steady-state separation gas velocities and product mean diameters stay approximately constant, as shown in Figure 6.5. Instead, the P-controller converts the bed mass into a suitable stationary point, at which the incoming and outgoing partial masses can become the same. According to Eq. 5.35, the final bed mass deviation must then be greater for smaller gain factors in order to guarantee certain separation gas velocities that are necessary for stationary mass balances and thus for constant bed mass conditions.

Possible consequences for simulations with a proportional-integrative bed mass controller

The control deviations of the bed mass and separation gas velocity can be reduced to zero by adding an integrative term to undercritical part ($M_{bed} < M_{bed,cr}$) of the proportional control function in Eq. 5.18. But, as described before, the proportional bed mass controller enables precise product size control, in particular, due to the remaining control deviations. When using an integrative control term, the separation gas velocity would be forced to converge to the set separation gas velocity that is adapted to the desired product size: $u_{g,end} \rightarrow u_{g,set}(d_{pr,set} = d_{m,f}\Phi_{d,set})$. But, the PB-simulation can only become stationary at separation gas velocities, where the incoming and outgoing material flows of the core and coating materials are equal. The results of this section show that those stationary separation gas velocities are somewhat different from the set separation gas velocity in most cases. In other words, the PI-controller would shift the system away from the state of stationary partial mass balances, which are dictated by the spray-to-feed rate ratio $\Phi_{m,set}$. It could perhaps result in an oscillating behavior. However, this would still have to be confirmed by simulations with such a proportional-integrative bed mass controller. For the process objectives of the present thesis, a PI-controller is irrelevant. An exact bed mass control is also not necessary for precise grain size enlargement if the steady state of the two controlled variables does not depend on each other.

Necessity of adapting the set separation gas velocity to the desired particle growth ratio

Another processing strategy, denoted by CM4, which includes the adjustment of the spray-to-feed rate ratio $\Phi_{m,set}$ to the desired particle growth ratio $\Phi_{d,set}$ via the SFM3 method, but in which the set separation gas

velocity $u_{g,set}$ is freely chosen, was not examined in Section 6.1. However, from the findings of the control behavior described above, the following stationary states of the granulation process can be presumed for such a processing strategy. In case of CM4, the simulated terminal product mean diameters $d_{m,pr,end}$ would probably still come close to the target value $d_{pr,set}$. The P-controller would presumably adjust such bed mass values with corresponding stationary separation gas velocities, for which the partial mass flows of the inlets (nuclei feed and sprayed solids) and the outlet (core and coating of the product) are again the same. According to Eq. 5.35, if the deviations between $u_{g,set}$ and $u_{g,end}$ were very high, also very large control deviations in bed mass would occur, which in turn may endanger process stability in the practical realization. This effect would be even greater for smaller gain factors, what can also be seen from Eq. 5.35. It is therefore recommended not just to use the spray-to-feed rate method SFM3 (or SFM1 and SFM2), but also to adapt the set separation gas velocity to the desired particle growth ratio, and thus, to keep the control deviations in bed mass low.

Process stability for slow bed mass control dynamics

Stability of fluidized bed spray granulation would be guaranteed in practice for each of the granulation examples in Figure 6.6, up to a target-growth ratio of $\Phi_{d,set} = 8/3$. However, in processes with still larger growth ratios, the bed mass peaks within the startup phase (see $0 < t < 2\,\mathrm{h}$) could reach values out of the stable operation range of a real fluidized bed granulator. This is due to the low gain factor of $K_m = 3\,\mathrm{m/s/kg}$, wherewith the bed mass control dynamics is relatively slow under the present process conditions. Higher gain factors would dampen such bed mass excesses, as can be seen from the previous results in Figure 6.5, and could hereby enable faster startups for the large $\Phi_{d,set}$-examples. Nevertheless, the gain factor of $K_m = 3\,\mathrm{m/s/kg}$ has proven as practical optimum in the continuous granulation experiments in Section 10.4.1. At larger gain factors, the fluctuations in the detected bed mass are transferred more strongly to the separation gas velocity, with possible undesirable effects on product characteristics, when using a simple P-control structure. Those fluctuations could be dampened with a PI-controller; but, the precise control of product size would be presumably sacrificed in this case, as explained before. Instead of this, a calculation method for a moving average of the bed mass could be implemented into the control and monitoring system (Section 9.4.8). But, this can be difficult or perhaps not be possible depending on the predefined tools and functions that are available in the data acquisition software (e.g., DASYLab®) used. As an alternative to such a smoothing function, parts of the bed mass could also be discharged unclassified by switching off the separating gas flow in the startup phase, discarding the first product granules. Such a manual bed mass control strategy is described in more detail later in Sections 9.4.9 and 9.4.10. When doing so, the discarded product from the unsteady phase can be mixed into large batches of external nuclei material in coating applications or used to prepare the spray solution in layering applications, just to give two examples.

Measures for fast startups in experiments

It is one of the objectives of this thesis to conduct continuous experiments of large-growth granulation with $\Phi_{d,set} > 2$. The results of Figure 6.6 have shown that higher growth targets lead to an over-proportional increase of the time to reach steady state. The startup time of the third example $\Phi_{d,set} = 6/3 = 2$ was estimated already with 11 h. The experiments would have to be carried out even longer to show constant PSD-curves of bed and product samples, which is quite challenging. The required growth times $\tau_{gr,set}$ of Table 6.7, however, indicate that startup periods can be shorter. The long growth phases of the product mean diameter arise because the initial overloads of bed mass lower the growth rate of single granules in the process beginning. To avoid this, higher gain factors are needed. But, as explained before, the gain factors of a simple proportional bed mass controller cannot be chosen too high for practical reasons. The manual bed mass control strategies of Sections 9.4.9 and 9.4.10, which are mentioned above, can be applied for a certain period of time to avoid large bed masses and shorten the startup. Another method would be to operate with higher gain factors in the process beginning and to successively lower the gain factor towards the value of the practical optimum (here $K_m = 3\,\mathrm{m/s/kg}$).

7 Two-zone continuum model of Wurster fluidization

A two-zone continuum model of Wurster fluidization (short TZC-model) with injection of pure water has been developed within the scope of the present thesis in order to

- investigate the influence of different process parameters such as inlet gas velocity, bed mass, water spray rate, and inlet gas temperature on diverse average characteristics of the Wurster tube interior and exterior such as residence times (τ_α and $\tau_{1-\alpha}$), gaseous volume fractions (ε_α and $\varepsilon_{1-\alpha}$, counterpart to particle concentrations), and proportions of granules (α_m and $1-\alpha_m$), which can be used for instance for the parameter setting of the three-compartment population balance model of Chapter 5,
- describe and characterize Wurster fluidization processes by means of dimensionless quantities,
- analyze the influence of heat losses and evaporation on process gas properties,
- define several process limits in terms of minimal fluidization, process-gas saturation, and maximal fluidized bed expansion within a Wurster granulator, and
- propose process parameters for stable operation conditions, which are also taken into account for the parameter setting of the continuous granulation experiments in Section 10.4.1.

The main structure, assumptions, and the material flowsheet of the model are given in Section 7.1. The dimensions and several geometric relations of the process chamber are specified in Section 7.2. In Section 7.3, several calculation methods for diverse material properties of the gas phase (e.g., density, viscosity, and enthalpy) and for changes of thermodynamic state variables due to evaporation processes can be found. Sections 7.4 to 7.8 show the main implementation sequence of the TZC-model, where diverse quantities of fluid dynamics (e.g., superficial gas velocity) are calculated by analytical equations, first, and quantities of fluid-particle interactions (e.g., particle concentrations and fluidized bed expansion) are determined by an iteration sequence, second. Furthermore, five different dimensionless process parameters are introduced in Section 7.9 for describing the parameter conditions and state properties of Wurster fluidization in a generalized form. These are the dimensionless inlet gas velocity ξ_{in}, the dimensionless water spray rate $\dot{\mu}_w$, the dimensionless nozzle air rate $\dot{\mu}_{g,noz}$, the dimensionless bed mass μ_{bed}, and the normalized bed height of the drying zone $\Phi_{h,1-\alpha}$. Based on these dimensionless quantities, here so-called limits of process-gas saturation, non-isothermal minimal Wurster fluidization, and Wurster-tube exceedance are generally formulated by critical condition equations in Section 7.10. Some analytical solutions for the approximation of these process limits are derived in Section 7.11.

7.1 Model structure and assumptions

Functional compartments and flowsheet network

Despite of its name, the two-zone continuum model consists of four functional compartments in total. These are the compartment of the inlet gas distributor plate, the compartment of nozzle gas injection, the spray zone, and the drying zone. The model structure is illustrated in Figure 7.1 a in terms of material flows through and between the functional compartments. The term "two zone" in the name of the model only refers to the spray zone and drying zone, since this is where the main processes of Wurster fluidization take place. These include fluid-particle transport dynamics, as for instance, pneumatic conveying through the Wurster tube and fluidized bed expansion, but also wetting and drying of particle surfaces. The other two compartments are of secondary importance, but still necessary, as they determine the inlet conditions. The spray zone comprises the entire interior space of the Wurster tube, while the drying zone is located in the process chamber space around the Wurster tube. As can also be seen in Figure 7.1 a, the TZC-model is built up by a network of several spots (indicated by circles). These are located at the inlet and outlet interfaces

of each functional compartment, at the nozzle gas inlet, and in the middle of the spray zone and the drying zone. The distributor plate is also referred to as inflow plate or bottom plate in the following.

Main assumptions

Due to a certain distribution of perforation degree over the distributor plate cross-section (specified in Section 7.4), the inlet gas flow splits into two separate plug flows of different gas velocities. Heat losses of the hot inlet gas only occur when flowing through the distributor plate compartment. This assumption is suitable for perforated metal plates with relatively high thickness (here 3 mm), as those insert components possess a high thermal conductivity and have a large contact area to the process gas. The injected nozzle gas perfectly mixes with the process gas that enters the spray zone. The sprayed liquid (here water) does not contain any solid components, completely deposits on particulate surface, and evaporates only in the spray zone and drying zone. No external solids are fed into the system, nor are bed particles discharged from the process chamber. The bed material is assumed to be situated only in the spray zone and the drying zone. The residence times of particles being transported from the top of the spray zone to the top of the drying zone are set to zero. The particles being sucked from the drying zone into the spray zone do not flow through the nozzle injection compartment. In real systems, a spatial distinction between a nozzle gas injection compartment and the spray zone does not exist actually, because the nozzle gas injection and the spray atomization are located in the lower part of the Wurster tube. In addition, the presence of a two-substance nozzle (liquid-gas) within the process chamber and the spray cone in the Wurster tube affect the flow pattern of the process gas. Such effects of nozzles installed in real Wurster granulators are not considered in the present model to lower the level of complexity. For more details, reference is made to the work of Börner et al. [106]. Material losses by entrainment with exhaust gas or adhesion to walls do not emerge. Thus, the entire bed mass is constant in time. The wet Wurster fluidization process takes place under stationary conditions, so that thermodynamic state variables, material properties and flow rates are time-invariant at each location. The bed granules are assumed to be spheres of same size and uniform effective particle density. Hence, particle formulation processes such as nucleation, aggregation, dis-aggregation, or layerwise growth are excluded. The process gas flows through the spray zone with a homogeneous and one-dimensional velocity profile. The particles are evenly distributed in the fluid inside the spray zone and dragged with constant raising velocity. In the drying zone, both the fluid and the solid phase are ideally back-mixed. Influences of changing pressure and temperature by the injected water on material properties and process behavior are neglected. Especially, pressure changes are relatively low in comparison to temperature changes.

State vector of fluid-particle properties and thermodynamic indices of the network spots

At each of the network spots, different state properties of the fluid-particle system (e.g., thermodynamic state variables and particle concentration) are given. In order to fully describe the state of fluid-particle transport dynamics within the present model concept, at least four quantities must be considered, which are for instance, the gas mass flow rate $\dot{M}_g$, the gas temperature T, the moisture content in the gas Y, and the interparticle porosity ε. The latter can be exchanged by solids concentration according to their definitions ($\varepsilon = 1 - \varepsilon_s$, see Eq. 2.52). Superficial gas velocities u and interstitial gas velocities u_ε ensue from the mass flow rate, temperature, moisture content, and the cross-section area A of the respective spots, as described later in Section 7.3. In Figure 7.1 a, the different state properties are represented by the state vector of fluid-particle transport dynamics

$$S = \left(\dot{M}_g,\, T,\, Y,\, \varepsilon\right) \tag{7.1}$$

and a variable indication that is to be adapted to the related network location. A summary of the indices and their affiliations can be found in Table 7.1. When symbolizing relationships that are valid for all nodes of the model network, the index is omitted in the following. Some of the network spots have the same thermodynamic state in terms of temperature T and moisture load Y. These (T, Y)-states are indicated by the slanted numbers, *1*, *2*, *2′*, *3*, *3′*, and *3″*, as shown in Figure 7.1a. The different thermodynamic states, that the process gas experiences when flowing through the four compartments, are illustrated in a schematic Mollier-diagram in Figure 7.1b with the help of the numerical indices. The numerical denotations of the thermodynamic states (thermodynamic state index) and their associations to the network spots are also presented in Table 7.1.

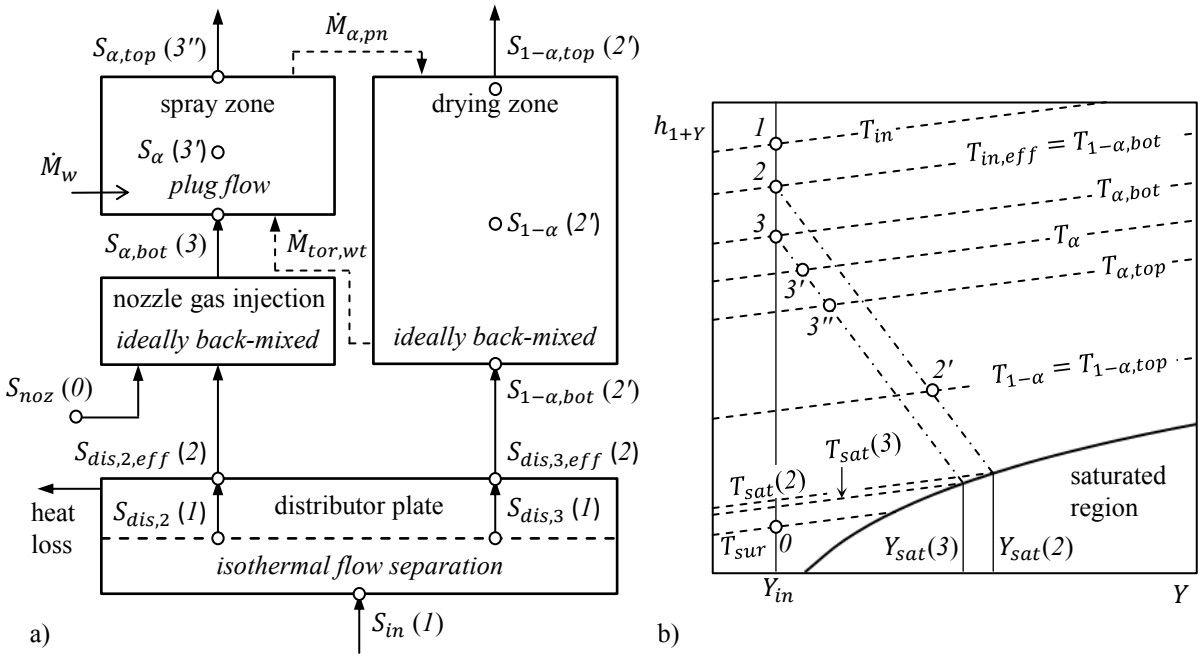

Figure 7.1: Flowsheet of the present two-zone continuum model in (in a) and an illustration of thermodynamic states of the process gas in a schematic Mollier-diagram (in b).

indication of the spot	appellation	thermodynamic state index	ε
noz	nozzle gas	0	1
in	inlet gas	1	1
$dis,2$	inlet gas flowing into the second distributor plate section under isothermal conditions	1	1
$dis,3$	inlet gas flowing into the third distributor plate section under isothermal conditions	1	1
$dis,2,eff$	inlet gas leaving the second distributor plate section after heat exchange	2	1
$dis,3,eff$	inlet gas leaving the third distributor plate section after heat exchange	2	1
α,bot	bottom of spray zone	3	$\in]\varepsilon_{mf},1[$
α	average state of spray zone	$3'$	$\in]\varepsilon_{mf},1[$
α,top	top of spray zone	$3''$	$\in]\varepsilon_{mf},1[$
$1-\alpha,bot$	bottom of drying zone	$2'$	$\in]\varepsilon_{mf},1[$
$1-\alpha$	average state of drying zone	$2'$	$\in]\varepsilon_{mf},1[$
$1-\alpha,top$	top of drying zone	$2'$	$\in]\varepsilon_{mf},1[$

Table 7.1: Appellation of the network spots of the two-zone continuum model (Figure 7.1a), the corresponding thermodynamic state indices of the schematic Mollier-diagram (Figure 7.1b), and the domain of definition for the interparticle spot porosities ε.

Changes of state properties

The properties of the inlet gas S_{in}, the nozzle gas S_{noz}, and the water spray rate $\dot{M}_w$ must be predefined process parameters in the implementation of the TZC-model. As described later in Section 7.4, the model's distributor plate consists of three sections, one of which is blocked by the nozzle assembly (indicated with $dis,1$) and the other two being gas-permeable (indicated with $dis,2$ and $dis,3$), but with different perforations. The passage of the inlet gas (here air) through the model distributor plate is divided into two steps. In the first step, the inlet gas of the state $S_{in}\,(1)$ flows into the two perforated distributor plate sections under isothermal conditions, where it is separated into one flow with the state $S_{dis,2}\,(1)$ and one flow with the state $S_{dis,3}\,(1)$. At this, only the mass flow rates of the state vectors S_{in}, $S_{dis,2}$, and $S_{dis,3}$ are different. In the second step, the inlet gas temperature T_{in} decreases to the here so-called effective inlet gas temperature $T_{in,eff}$ due to heat losses through walls, as shown with the (*1-2*)-line in the Mollier-diagram. The separated flows leaving the distributor plate are then related to the states $S_{dis,2,eff}\,(2)$ and $S_{dis,3,eff}\,(2)$, respectively. The other compartments have adiabatic walls. Both temperatures T_{in} and $T_{in,eff}$ are equal for entirely adiabatic systems. The process gas of the second distributor plate section with the state $S_{dis,2,eff}\,(2)$ is perfectly mixed with nozzle gas with the state $S_{noz}\,(0)$ within the nozzle gas injection compartment. The process gas temperature gets thereby a little bit reduced to $T_{\alpha,bot}$, as the nozzle gas is given with the temperature of the surroundings T_{sur}, which is also depicted in the Mollier-diagram with the (*2-3*-0)-line. The mixed gas of nozzle gas injection compartment flows to the spray zone bottom with the state $S_{\alpha,bot}\,(3)$. The evaporation of sprayed liquids lead to decreasing process gas temperature and increasing process gas moisture contents, as illustrated by the (*3-3′-3″*)-line for the spray zone and the (*2-2′*)-line for the drying zone. The state of the spray zone center $S_{\alpha}\,(3')$ differs from the state of the spray zone outlet $S_{\alpha,out}\,(3'')$, since the gas flows through this compartment under plug flow conditions (no back-mixing). In the drying zone, the state vector of the center $S_{1-\alpha}\,(2')$ and the outlet $S_{1-\alpha,out}\,(2')$ are equal, which results from the assumption that both phases, gas and solids, are ideally back-mixed. However, process gas velocities are different for these spots, when the process chamber is build by conical walls, as described later in Sections 7.2 and 7.5.

Defined value range of interparticle porosity of the network spots

The values that the interparticle porosities of the different network spots can take are listed in Table 7.1. The inlet gas, the nozzle gas, and the process gas leaving the distributor plate sections are assumed to be particle-free. Therefore, the related interparticle porosities are set to unity: $\varepsilon_{noz} = \varepsilon_{in} = \varepsilon_{dis,2} = \varepsilon_{dis,3} = 1$. The interparticle porosity in spray zone and drying zone are not predefined, but they must be calculated by iterations as explained later on. Due to the assumption of homogeneous particle concentration, the interparticle porosities of the bottom, the average spot, and the top are defined to be equal for the spray zone

$$\varepsilon_{\alpha,bot} = \varepsilon_{\alpha} = \varepsilon_{\alpha,top} \tag{7.2}$$

and for the drying zone

$$\varepsilon_{1-\alpha,bot} = \varepsilon_{1-\alpha} = \varepsilon_{1-\alpha,top}, \tag{7.3}$$

having values between the minimal fluidization point ε_{mf} and the elutriation point $\varepsilon_{elu} = 1$.

Circulating Wurster fluidization

The mass flow rate of bed particles being sucked from the drying zone into the spray zone is called the *Wurster suction rate* and symbolized by $\dot{M}_{tor,wt}$. At this, the index *tor* refers to a modified Torricelli approach that is used later to define the Wurster suction rate. The mass flow rate of particles that are pneumatically dragged through the Wurster tube shall be represented here by the shorter term *pneumatic conveying rate* and the symbol $\dot{M}_{\alpha,pn}$. Both the Wurster suction rate and the pneumatic conveying rate follow certain laws, as shown later in Section 7.7. By assuming stationary Wurster circulation, the two flow rates can be equated:

$$\dot{M}_{tor,wt} = \dot{M}_{pn,\alpha}. \tag{7.4}$$

With the help of this relation, several characteristics of fluid-particle transport dynamics can be iteratively determined for the circulating Wurster fluidization process, which are for example the particle concentrations in the spray and the drying zone or the fluidized bed height outside the Wurster tube, but also parameters for the three-compartment population balance model such as the proportions of bed granules and residence times in the two zones (α, $1-\alpha$, τ_{α}, and $\tau_{1-\alpha}$).

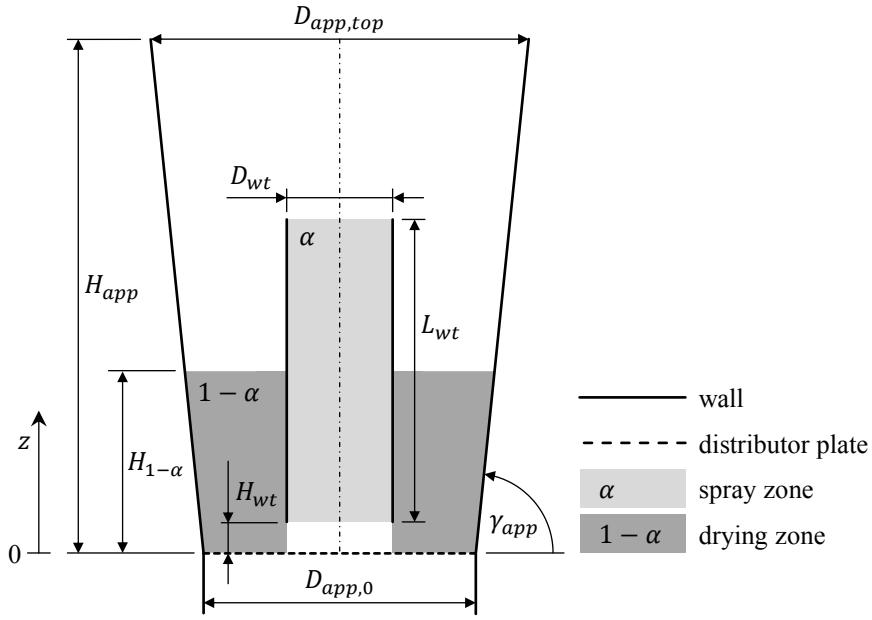

Figure 7.2: Setup of the process chamber of the two-zone continuum model.

7.2 Specifications of the process chamber

The process chamber of the two-zone continuum model is adapted to the experimental plant of the present thesis, which has also been employed in Hampel's investigations to validate the reference case of the three-compartment population balance model (Section 2.3).

Overall space

The process chamber of the TZC-model and its dimensions are illustrated in Figure 7.2. It consists of a distributor plate at the chamber bottom, a conical outer wall, and a Wurster tube fixed in the center of the chamber slightly above the distributor plate. The specifications of the process chamber are listed in Table 7.2. The symbol z defines the vertical coordinate of the process chamber with $z = 0$ indicating the position of the distributor plate. The inclination angle of the process chamber wall is given by γ_{app}. It can be calculated from the bottom diameter $D_{app,0}$, the upper diameter $D_{app,top}$, and the height H_{app} of the process chamber by the following geometric relation:

$$\gamma_{app} = \arctan\left(\frac{2H_{app}}{D_{app,top} - D_{app,0}}\right). \tag{7.5}$$

With known inclination angle, the expanding process chamber diameter D_{app} can be obtained according to

$$D_{app}(z) = D_{app,0} + \frac{2}{\tan(\gamma_{app})} z \qquad \text{, for } 0 \leq z \leq H_{app}. \tag{7.6}$$

Spray zone and drying zone

The spray zone is assumed to be situated in the complete interior of the Wurster tube. The cross-sectional area of the spray zone $A_\alpha = \pi D_{wt}^2/4$ is constant with z, due to which the spray zone volume can be calculated by the cylinder equation: $V_\alpha = A_\alpha L_{wt}$. The spray zone dimensions are fixed parameters of the two-zone continuum model, which are independent from process parameters such as mass flow rates and temperatures of the inlet and nozzle gas. By contrast, the extent of the drying zone is influenced by process parameter conditions, as the drying zone volume is defined by the bounds of the fluidized bed in the outer region of the

$D_{app,0}$ [cm]	$D_{app,top}$ [cm]	H_{app} [cm]	γ_{app} [°]	D_{wt} [cm]	H_{wt} [cm]	L_{wt} [cm]
18	25	34	84.12	7	2	20

Table 7.2: Specification of the process chamber of the two-zone continuum model.

Wurster tube. The cross-sectional area of the drying zone $A_{1-\alpha}$ grows quadratically with z via Eq. 7.6 and

$$A_{1-\alpha}(z) = \frac{\pi}{4}\big(D_{app}^2(z) - D_{wt}^2\big). \tag{7.7}$$

Integrating the cross-sectional area of the drying zone over the vertical coordinate z from the bottom $z = 0$ to the top of the drying zone $H_{1-\alpha}$ provides a general expression of the drying zone volume $V_{1-\alpha}$ with:

$$V_{1-\alpha}(z) = \int_{z=0}^{H_{1-\alpha}} A_{1-\alpha}(z)\,\mathrm{d}z. \tag{7.8}$$

After inserting Eqs. 7.6 and 7.7 into Eq. 7.8, the general volume integral is solved to a third-order polynomial of the fluidized bed height $H_{1-\alpha}$ with

$$V_{1-\alpha} = \frac{\pi}{3}\frac{1}{\tan^2(\gamma_{app})}H_{1-\alpha}^3 + \frac{\pi}{2}\frac{1}{\tan(\gamma_{app})}D_{app,0}H_{1-\alpha}^2 + \frac{\pi}{4}(D_{app,0}^2 - D_{wt}^2)H_{1-\alpha},$$

which is converted to

$$V_{1-\alpha} = \frac{\pi D_{app,0}H_{1-\alpha}^2}{2\tan(\gamma_{app})}\left(\frac{2}{3\tan(\gamma_{app})}\frac{H_{1-\alpha}}{D_{app,0}} + 1\right) + \frac{\pi}{4}(D_{app,0}^2 - D_{wt}^2)H_{1-\alpha} \tag{7.9}$$

by factoring the term $\pi D_{app,0}H_{1-\alpha}^2/(2\tan(\gamma_{app}))$ of the first and second summand out of the right-hand side. The reciprocal of the tangent function of γ_{app} converges to zero for straight walls: $1/\tan(\gamma_{app} \to 90°) = 0$. Based on this, the third-order polynomial of the drying zone volume $V_{1-\alpha}$ can be approximated by a quadratic polynomial for high angles of inclination γ_{app} close to 90° (steep chamber walls). For walls that are much steeper than 45°, the factor $2H_{1-\alpha}/(3\tan(\gamma_{app})D_{app,0})$ is much smaller than unity

$$\left(\frac{2}{3\tan(\gamma_{app})}\frac{H_{1-\alpha}}{D_{app,0}}\right)\Bigg|_{\gamma_{app}\gg 45°} \ll 1 \tag{7.10}$$

and can therefore be neglected. In doing so, the drying zone volume simplifies to a quadratic function of the bed height, as follows:

$$V_{1-\alpha}(\gamma_{app} \gg 45°) \approx V_{1-\alpha,quad} \coloneqq \frac{\pi}{2\tan(\gamma_{app})}D_{app,0}H_{1-\alpha}^2 + \frac{\pi}{4}(D_{app,0}^2 - D_{wt}^2)H_{1-\alpha}. \tag{7.11}$$

From this, an equation of the bed height depending on the drying zone volume can be derived analytically, which ends up to:

$$\begin{aligned} H_{1-\alpha}(\gamma_{app} \gg 45°) \approx &-\frac{\tan(\gamma_{app})}{4}\frac{D_{app,0}^2 - D_{wt}^2}{D_{app,0}} \\ &+\sqrt{\left(\frac{\tan(\gamma_{app})}{4}\frac{D_{app,0}^2 - D_{wt}^2}{D_{app,0}}\right)^2 + \frac{2\tan(\gamma_{app})}{\pi}\frac{V_{1-\alpha}}{D_{app,0}}}. \end{aligned} \tag{7.12}$$

The bed height $H_{1-\alpha}$ is necessary to determine the Wurster suction rate $\dot{M}_{tor,wt}$ as described later on.

Error of quadratic approximation of the drying zone volume for three examples of inclination angles

In order to show the deviation of the quadratic solution in Eq. 7.11 from the cubic formula according to Eq. 7.9, the factor $2/(3\tan(\gamma_{app}))$ and the volume error $V_{1-\alpha,quad}/V_{1-\alpha,cub} - 1$ have been calculated for three different inclination angles (45°, 70°, and 84.12°) and two different bed heights (12 cm and 22 cm).

γ_{app} [°]	$H_{1-\alpha}$ [cm]	$\frac{2}{3\tan(\gamma_{app})}\frac{H_{1-\alpha}}{D_{app,0}}$ [−]	$\frac{V_{1-\alpha,quad}}{V_{1-\alpha,cub}}-1$ [%]
45	12	0.444	-21.36
45	22	0.815	-37.69
70	12	0.162	-5.56
70	22	0.297	-13.18
84.12	12	0.046	-0.63
84.12	22	0.084	-1.88

Table 7.3: Deviation of the quadratic solution from the cubic solution of the drying zone volume for different inclination angles γ_{app}, different bed heights $H_{1-\alpha}$ and a bottom diameter of $D_{app,0} = 18\,\text{cm}$.

The results are listed in Table 7.3. The bed height of 12 cm is an empirical value that has been experienced in the experimental investigations of this thesis, and the height of 22 cm is the theoretical maximum of bed expansion that corresponds to the height of the top of the Wurster tube: $z_{max} = H_{wt} + L_{wt}$. It is seen that inclination angles of 45° and 70° lead to large drying zone volume errors. The inclination angle of 84.12° is employed in the present TZC-model. This value of the inclination angle has been determined from the dimensions of the experimental plant used in the present thesis. The deviation of the quadratic solution from the cubic solution for the inclination angle of 84.12° is less than −1.88 %, which justifies to neglect the cubic term in Eq. 7.9.

7.3 Determination of gas properties

Several approaches to calculate different gas properties in dependency on process gas temperature T and moisture content Y are shown in the following. These gas properties are the specific enthalpies of dry air, water, and moist air, the isenthalpic saturation temperature, the saturation vapor pressure, the saturation moisture content, the temperature and moisture content of the spray zone and drying zone outlets, the gas density, the kinematic viscosity, the mass flow rate, and the superficial gas velocity. The definition equations of them are needed multiple times within the implementation of the TZC-model. Pressure changes of the process gas within the granulator are neglected, as mentioned in Section 7.1. Hence, the changes in thermodynamic state properties are seen as isobaric with a constant system pressure p_{sys}. The empirical correlations used for model implementation are related to 1-bar-measurements.

Enthalpy of humid air

The specific enthalpies of dry air h_{air} and water vapor h_{vap} shall be calculated by empirical functions of temperature, which are fitted to data from [122, 123]. As widely applied for thermodynamic calculations of moist air, the reference enthalpies of the dry air $h_{air,0}$ and the liquid water phase $h_{w,0}$ are defined to be zero for a reference temperature of 0℃:

$$h_{air,0} = h_{air}(T = 0℃) \coloneqq 0, \tag{7.13}$$

$$h_{w,0} = h_{w}(T = 0℃) \coloneqq 0. \tag{7.14}$$

The specific reference enthalpy of water vapor $h_{vap,0}$ in air conforms then with the evaporation enthalpy $\Delta h_{eva,0}$ at the reference temperature:

$$h_{vap,0} = h_{vap}(T = 0℃) \coloneqq \Delta h_{eva,0}, \tag{7.15}$$

which is given with $\Delta h_{eva,0} = 2500941.6\,\text{J/kg}$ in [123]. The empirical fits of the specific enthalpies of dry air $h_{air}(T)$ and water vapor $h_{vap}(T)$ are created here by the following third-order polynomials with T as independent variable:

$$h_{air}[\text{J/kg}] = 1.4164 \cdot 10^{-4}T^3 + 6.1822 \cdot 10^{-3}T^2 + 1006T \quad \text{, for } 0 \leq T \leq 200℃,\ 1\,\text{bar}, \tag{7.16}$$

$$h_{vap}[\text{J/kg}] = -1.154 \cdot 10^{-2}T^3 + 0.55625T^2 + 1808.1T + 2500941.6 \quad \text{, for } 0 \leq T \leq 200℃,\ 1\,\text{bar}. \tag{7.17}$$

The specific enthalpies of dry air and water vapor are used to calculate the dry-air-specific enthalpy of humid air h_{1+Y} with

$$h_{1+Y}(T,Y) = h_{air}(T) + Y h_{vap}(T) \tag{7.18}$$

for a certain thermodynamic state (T, Y) in the unsaturated region. The dry-air-specific enthalpy is useful to calculate isenthalpic saturation temperatures T_{sat}, and temperatures and moisture contents related to the spray zone and the drying zone via a lever principle, as described below in more detail. The specific enthalpy h_g is related to the entire mass of dry air and water vapor, and follows thereby from:

$$h_g = \frac{1}{1+Y} h_{air}(T) + \frac{Y}{1+Y} h_{vap}(T). \tag{7.19}$$

Average specific heat capacity of humid air

The heat capacity of a material (here humid air) depends on temperature and pressure. In isobaric systems, only specific heat capacity at a certain constant system pressure is to be considered (symbolized here by $c_{p,g}$), which is only a function of temperature: $c_{p,g}(T)$. According to the mean value theorem, the average specific heat capacity $\bar{c}_{p,g,0}$ is derived from this function with

$$\bar{c}_{p,g,0} = \frac{\int_0^T c_{p,g}(T)\mathrm{d}T}{T[^\circ\mathrm{C}]}. \tag{7.20}$$

Since the specific enthalpy of humid air h_g is given by the definite integral of $c_{p,g}(T)$-function from the reference temperature (0°C) to the present temperature T

$$h_g = \int_0^T c_{p,g}(T)\mathrm{d}T, \tag{7.21}$$

the average specific heat capacity $\bar{c}_{p,g,0}$ can be related to the specific enthalpy of humid air h_g with:

$$\bar{c}_{p,g,0} = \frac{h_g(T,Y)}{T[^\circ\mathrm{C}]}. \tag{7.22}$$

This equation allows to calculate the average specific heat capacity $\bar{c}_{p,g,0}$ from empirical fit-curves via Eqs. 7.16, 7.17, and 7.19, which finds use later for determining $T_{\alpha,bot}$, the temperature of the mixed gas entering the bottom of the spray zone.

Isenthalpic saturation point of humid air

The concept of the isenthalpic saturation point is used for the TZC-model to approximate the maximum vapor intake capacity of humid air (e.g., process-gas-saturation limit in Sections 7.10.2 and 7.11.4) at a certain thermodynamic state (T,Y), and to determine the final states of process gas in evaporation processes in the spray zone and drying zone (see lever principle below). The isenthalpic saturation point is characterized by a dry-air-specific enthalpy of saturated conditions $h_{1+Y,sat}$, the here so-called isenthalpic saturation temperature T_{sat}, the corresponding vapor pressure p_{sat}, and the corresponding moisture content Y_{sat}. In this order, they shall be calculated for a certain thermodynamic starting point (T,Y) without using iterations. For this purpose, the following calculation sequence was developed. The main assumption of the concept is that the thermodynamic state of humid air changes with constant dry-air-specific enthalpy in evaporation processes. According to this, the dry-air-specific enthalpy of the isenthalpic saturation point (after maximal evaporation) is equal to the dry-air-specific enthalpy of the initial state (before maximal evaporation):

$$h_{1+Y,sat}(T_{sat}, Y_{sat}) \coloneqq h_{1+Y}(T,Y). \tag{7.23}$$

Via this equation the saturation state (T_{sat},Y_{sat}) is coupled to the initial state (T,Y), which is also illustrated by dash-dotted lines in Figure 7.1b. The dry-air-specific enthalpy of the initial state $h_{1+Y}(T,Y)$ is obtained by Eqs. 7.13 to 7.18. In order to calculate the isenthalpic saturation temperature T_{sat} from the associated dry-air-specific enthalpy $h_{1+Y,sat}$, an empirical correlation was developed in the scope of this thesis in the following way. Firstly, a list of the saturation vapor pressures of pure water vapor p_{sat} and corresponding saturation temperatures T_{sat} ranging from 0 to 95°C has been taken from [123]. The corresponding saturation moisture contents Y_{sat} have been calculated by Eq. 7.28 for a system pressure of $p_{sys} = 1\,\mathrm{bar}$, and

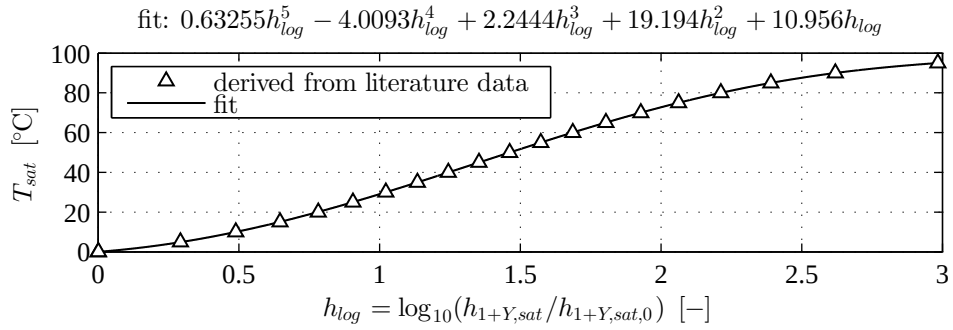

Figure 7.3: Fit-curve on literature data of the saturation points of humid air [123]: isenthalpic saturation temperature T_{sat} versus the corresponding relative logarithmic enthalpy h_{log} for a system pressure of $p_{sys} = 1\,\mathrm{bar}$.

subsequently, the corresponding dry-air-specific enthalpy of the saturation point $h_{1+Y,sat}(T_{sat})$ by Eqs. 7.16 to 7.18. In addition, the dry-air-specific enthalpy of saturated air at the reference temperature $h_{1+Y,sat,0}$ was determined by

$$h_{1+Y,sat,0} = h_{1+Y,sat}(0℃) = Y_{sat} h_{vap,0}, \tag{7.24}$$

which results in $h_{1+Y,sat,0} = 9567.78\,\mathrm{J/kg}$. Using this reference parameter, the relative logarithmic enthalpy of the saturation point h_{log} is defined with:

$$h_{log} \coloneqq \log_{10}\left(\frac{h_{1+Y,sat}(T_{sat}, Y_{sat})}{h_{1+Y,sat,0}}\right) = \log_{10}\left(\frac{h_{1+Y}(T,Y)}{h_{1+Y,sat,0}}\right), \tag{7.25}$$

which has been calculated for each point of (p_{sat},T_{sat})-list from the measurement data of [123]. The given saturation temperatures T_{sat} were plotted versus calculated relative logarithmic enthalpies, as shown in Figure 7.3. Therein, the following fifth-order polynomial:

$$T_{sat}[℃] = 0.63255h_{log}^5 - 4.0093h_{log}^4 + 2.2444h_{log}^3 + 19.194h_{log}^2 + 10.956h_{log} \tag{7.26}$$

could be very precisely fitted to the data points of T_{sat} and h_{log}. At this, the coefficient of determination of the fit curve is almost exactly equal to unity. It should be further noted that the isenthalpic saturation temperature is not to be confused with the adiabatic saturation temperature, but it is an approximation of it. The approximation error is the smaller, the lower the temperature and the higher the moisture content of the initial state (T,Y) is. The vapor pressure of the isenthalpic saturation point p_{sat} follows from an Antoine equation of the form

$$p_{sat}[\mathrm{Pa}] = \exp\left(23.4588 - \frac{3977.378231}{233.317217 + T_{sat}[℃]}\right), \tag{7.27}$$

which has been stated by Burgschweiger ([90], p.117, equation "A.17"). The moisture content of saturated humid air can be generally obtained from:

$$Y_{sat} = \frac{\tilde{M}_{vap}}{\tilde{M}_{air}} \frac{p_{sat}}{p_{sys} - p_{sat}}. \tag{7.28}$$

Lever principle and drying potential of evaporation processes

Based on the assumption that the dry-air-specific enthalpy of the process air h_{1+Y} does not change during the evaporation process, the states before water vapor absorption (indicated by T and Y) and after water vapor absorption (indicated by T' and Y') lie on a straight line in the Mollier diagram. As a result, the process gas temperature falls linearly with the increase in moisture content when the injected water is dried. According to this, the lever principle is formulated with respect to the isenthalpic saturation point:

$$\frac{T' - T_{sat}(T,Y)}{T - T_{sat}(T,Y)} = \frac{Y_{sat}\big(T_{sat}(T,Y)\big) - Y'}{Y_{sat}\big(T_{sat}(T,Y)\big) - Y}. \tag{7.29}$$

zone	T	Y	T'	Y'
spray zone	$T_{\alpha,bot}$	Y_{in}	$T_{\alpha,top}$	$Y_{\alpha,top}$
drying zone	$T_{in,eff}$	Y_{in}	$T_{1-\alpha,top}$	$Y_{1-\alpha,top}$

Table 7.4: Allocation of thermodynamic states before and after evaporation to spots of the spray zone and the drying zone.

The lever principle is applied later for describing changes in process gas properties of the spray zone and drying zone. There, the initial states (T, Y) correspond to the inlet spots and the states after evaporation (T', Y') to the outlets spots of the compartments, what is sorted again in Table 7.4. The final thermodynamic states of both zones cannot be determined with the lever principle alone. Another relation is required, with which exactly one set of final state variables (T',Y') is determined at the output of either zone. In contrast to the drying zone, the final state of the spray zone is dictated by the drying kinetics, as for common process conditions the residence times of the water droplets are shorter than their necessary drying times. However, an approach to the evaporation kinetics in the spray zone is missing. Instead, an empirical equation for the drying potential at the top of the spray zone

$$\eta_{dry,\alpha,top} = \frac{T_{\alpha,top} - T_{sat}(T_{\alpha,bot}, Y_{in})}{T_{\alpha,bot} - T_{sat}(T_{\alpha,bot}, Y_{in})} = \frac{Y_{sat}(T_{\alpha,bot}, Y_{in}) - Y}{Y_{sat}(T_{\alpha,bot}, Y_{in}) - Y_{in}}, \tag{7.30}$$

can be acquired by temperature measurements, as shown later in Section 7.5. Moreover, the evaporation of sprayed liquid within the spray zone can even be neglected in rough calculations, as the vast majority of liquid evaporates in the drying zone. In this case, the drying potential of the spray zone outlet gas is given with unity: $\eta_{dry,\alpha,top} = 1$. Such a simplification is useful to derive a closed solution of the process-gas-saturation limit (see Sections 7.10.2 and 7.11.6). The outlet state of the drying zone $\eta_{dry,1-\alpha}$ can be obtained by the overall mass balance of the sprayed water when the drying potential of the spray zone is known, as shown below in Section 7.5.

Density and kinematic viscosity of humid air

Since humid air is used as process gas, its density is calculated by the ideal gas law of a binary system with

$$\rho_g = \frac{1+Y}{1+Y\frac{\tilde{M}_{air}}{\tilde{M}_{vap}}} \frac{\tilde{M}_{air} p_{sys}}{\tilde{R}T} \tag{7.31}$$

for different thermodynamic states (T,Y); whereas, for reasons of simplicity, the overall kinematic viscosity of the process gas ν_g shall be approximated only by the prevailing part of it, which is the kinematic viscosity of dry air:

$$\nu_g \coloneqq \nu_{air}(T). \tag{7.32}$$

Based on data in [122], the following quadratic fit depending on temperature has been generated for a temperature range from 0 to 200℃ and a system pressure of 1 bar for the kinematic viscosity of dry air:

$$\nu_{air}[\mathrm{m^2/s}] = 9.82678 \cdot 10^{-11} T^2 + 8.99401 \cdot 10^{-8} T + 13.4838 \cdot 10^{-6} \quad \text{, for } 0 \leq T \leq 200℃,\ 1\,\mathrm{bar}. \tag{7.33}$$

Flow-related characteristics

For each of the model spots, the volume flow rate $\dot{V}_g$, the superficial velocity u, the mass flow rate $\dot{M}_g$, and the dry-air mass flow rate $\dot{M}_{dry}$ of the gas phase can be mutually calculated with the aid of the cross-sectional area A, the process gas density ρ_g, and the moisture content Y by the following relationships:

$$\dot{V}_g = A \cdot u, \tag{7.34}$$

$$\dot{M}_g = \rho_g(T,Y)\dot{V}_g, \tag{7.35}$$

$$\dot{M}_{dry} = \frac{\dot{M}_g}{1+Y}. \tag{7.36}$$

The interstitial gas velocity follows from the quotient of the superficial gas velocity over the interparticle porosity:

$$u_\varepsilon = \frac{u}{\varepsilon}. \tag{7.37}$$

The cross-sectional areas are fixed parameters for different spots of the TZC-model, except for the drying zone. There, the cross-sectional area of the centered spot and the outlet spot depend on the fluidized bed height $H_{1-\alpha}$.

The subsequent equations of Section 7.4 to Section 7.8 are presented in the order of their implementation in the present model, as far as possible.

7.4 Characteristics of fluid dynamics and heat losses in the distributor plate compartment

Diverse calculation methods are derived for the isothermal flow separation ($S_{in} \rightarrow (S_{dis,2}, S_{dis,3})$) of the distributor plate compartment in Section 7.4.2 and for the influence of heat losses on inlet gas temperature ($S_{dis,2} \rightarrow S_{dis,2,eff}$ and $S_{dis,3} \rightarrow S_{dis,3,eff}$) in Section 7.4.3.

7.4.1 Perforation design

The perforation design of the model distributor plate shall be adapted to the real inflow plate of the granulation experiments of this thesis, which is illustrated in Figure 7.4 and described in more detail later in Section 8.1. The specifications of the real bottom plate are summarized in Section C.2.2. In the following, diverse characteristics of the model plate's perforation design are outlined, and their relations are derived. The cross-section of the model inflow plate is divided into three concentric circular sections with different degrees of perforation, inner diameters D_{i-1}, and outer diameters D_i. For reasons of mathematical completeness in Eq. 7.38, the center of the bottom plate is indicated by $i = 0$ and its diameter given with zero $D_{dis,i=0} = 0$. The first section ($i = 1$) and the second section ($i = 2$) should be located below the spray zone (Wurster tube interior) and the third section ($i = 3$) below the drying zone (Wurster tube exterior). The outer diameter of the first section ($D_{dis,1}$) should be as large as the nozzle assembly. The outer diameter of the second section shall conform with the Wurster diameter ($D_{dis,2} = D_{wt}$) and the outer diameter of the third section be equal to the diameter of the entire process chamber bottom ($D_{dis,3} = D_{app,0}$). The cross-sectional area of each distributor plate section $A_{dis,i}$ is obtained by

$$A_{dis,i} = \frac{\pi}{4}\left(D_{dis,i}^2 - D_{dis,i-1}^2\right) \qquad \text{, for } i \in \{1,2,3\}. \tag{7.38}$$

The total cross-sectional area of the process chamber bottom $A_{app,0}$ is calculated either by the sum of the sectional areas or as the circle area of the entire inlet cross-section:

$$A_{app,0} = \sum_{i=1}^{3} A_{dis,i} = \frac{\pi}{4} D_{app,0}^2. \tag{7.39}$$

Further, the area fraction $\varphi_{dis,i}$ of the distributor plate section i in the entire cross-section is introduced with:

$$\varphi_{dis,i} = \frac{A_{dis,i}}{A_{app,0}} \qquad \text{, for } i \in \{1,2,3\}. \tag{7.40}$$

As mentioned above, the first distributor plate section $i = 1$ is occupied by the nozzle assembly, and therefore, does not contain any perforation holes, and is also not passable for the process gas. The annular sections ($i \in \{2,3\}$), on the contrary, are perforated with cylindrical holes. The diameters of the holes ($d_{dis,2}$ and $d_{dis,3}$) are supposed to be constant within each of the two sections. They can be of the same size, but they do not have to be, as described below. Based on these assumptions, the void areas of the second and third distributor plate sections (areas of free cross-section: $A_{dis,\varepsilon,2}$ and $A_{dis,\varepsilon,3}$) are determined by the number of holes $N_{dis,i}$ and the hole diameters $d_{dis,i}$ with:

$$A_{dis,\varepsilon,i} = N_{dis,i} \frac{\pi}{4} d_{dis,i}^2 \qquad \text{, for } i \in \{2,3\}. \tag{7.41}$$

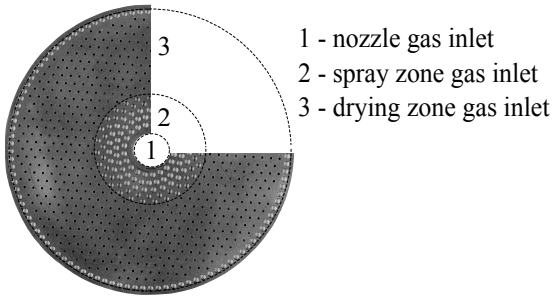

Figure 7.4: Subdivision of the experimental distributor plate into three sections for the parameter setting of the present two-zone continuum model.

The perforation degree $\Psi_{dis,i}$, also called as opening ratio [29], is another characteristic quantity of the distributor plate sections. It is defined as the ratio of the void area $A_{dis,\varepsilon,i}$ to the cross-section area $A_{dis,i}$ of section i, which follows to:

$$\Psi_{dis,i} = \frac{A_{dis,\varepsilon,i}}{A_{dis,i}} = N_{dis,i} \frac{d_{dis,i}^2}{\left(D_{dis,i}^2 - D_{dis,i-1}^2\right)} \qquad \text{, for } i \in \{2,3\}. \tag{7.42}$$

The opening ratio of a perforated plate characterizes the flow resistance, and is therefore the decisive factor for the flow separation in the distributor plate compartment, as shown in Section 7.4.2. In Wurster fluidization processes, the average gas velocity in the spray zone should be higher than that in the drying zone. To achieve this, the perforation degree of the second distributor plate section must be larger than in the third section:

$$\Psi_{dis,2} \overset{!}{>} \Psi_{dis,3} > 0. \tag{7.43}$$

The constraint in Eq. 7.43 can also be fulfilled for hole diameters of the second section being smaller than the holes of the third section ($d_{dis,2} < d_{dis,3}$) when there are enough holes in section $i = 2$ and/or not too many holes in section $i = 3$. In this case, the holes of the second section would be much closer together on average than in the third section. In practice, however, it is common to create bigger holes in the region below the Wurster tube. As can be seen in Figure 7.4 (pictured sharper in Figure C.3), the real inflow plate of this work contains holes of even five different diameters. For this case, an average hole diameter has to be derived for each of the annular distributor plate sections, which is done so in Section 8.1. There, the average diameter of the second section is clearly larger than the average diameter of the third section.

7.4.2 Isothermal flow separation

Definition of inlet gas velocity properties

In the implementation of TZC-model, the temperature and moisture content of the inlet gas have to be predefined. The related interparticle porosity of it is given with unity by definition. Of the inlet flow variables - mass flow rate $\dot{M}_{in}$, volume flow rate $\dot{V}_{in}$, and average gas velocity u_{in} - at least one variable must be specified. The others are obtained from these relations:

$$\dot{V}_{in} = u_{in} A_{app,0}, \tag{7.44}$$

$$\rho_{g,in} = \rho_g(T_{in}, Y_{in}) = \frac{1 + Y_{in}}{1 + Y_{in} \frac{\tilde{M}_{air}}{\tilde{M}_{vap}}} \frac{\tilde{M}_{air} p_{sys}}{\tilde{R} T_{in}}, \tag{7.45}$$

$$\dot{M}_{in} = \rho_{g,in} \dot{V}_{in}. \tag{7.46}$$

A distinction between superficial and interstitial gas velocity is not needed here; instead, u_{in} is only referred to as inlet gas velocity.

Stationary flow through parallel-connected resistances

In order to determine the state properties of the separated flows $S_{dis,2}$ and $S_{dis,3}$, several equations are derived in the following from the model concept of a stationary flow through parallel-connected resistances.

At this, the annular distributor plate sections ($i \in \{2,3\}$) are seen as the flow resistances. The calculation of fluid-dynamics-related characteristics of the separated flows is described further from Eq. 7.61 onwards. The stationary mass balance of the isothermal part of the distributor plate compartment results in this sum equation:

$$\dot{M}_{in} = \dot{M}_{dis,2} + \dot{M}_{dis,3}. \tag{7.47}$$

Neglecting changes of gas density by pressure losses, the inlet gas volume flow rate $\dot{V}_{in}$ equals the sum of separated volume flow rates $\dot{V}_{dis,i}$ under isothermal conditions too:

$$\dot{V}_{in} = \dot{V}_{dis,2} + \dot{V}_{dis,3}. \tag{7.48}$$

The sectional volume flow rates $\dot{V}_{dis,i}$ are defined as the product of the corresponding superficial gas velocity $u_{dis,i}$ and cross-sectional area $A_{dis,i}$:

$$\dot{V}_{dis,i} = u_{dis,i} A_{dis,i} = u_{dis,i} \varphi_{dis,i} A_{app,0} \qquad \text{, for } i \in \{2,3\}. \tag{7.49}$$

Combining Eqs. 7.44, 7.48, and 7.49, a relationship between inlet gas velocity u_{in} and the sectional superficial gas velocities $u_{dis,i}$ can be derived to:

$$u_{in} = u_{dis,2}\varphi_{dis,2} + u_{dis,3}\varphi_{dis,3}. \tag{7.50}$$

It is further assumed that the pressure drop of the distributor plate is constant in radial direction, so that the pressure drops of the second and third distributor plate sections are equal:

$$\Delta p_{dis,2} = \Delta p_{dis,3}. \tag{7.51}$$

As stated in [73], a basic approach to the pressure drop across perforated plates is given by Brauer [60], where the pressure drop is defined by the product of a drag coefficient and the kinetic energy of the flow ($\rho_g u^2/2$). Adopting this to the distributor plate section, the sectional pressure drop can be formulated with:

$$\Delta p_{dis,i} = c_{dis,i} \frac{\rho_{g,in}}{2} u_{dis,i}^2 \qquad \text{, for } i \in \{2,3\}. \tag{7.52}$$

Hunt et al. [70] suggested an approach by which the sectional drag coefficients $c_{dis,i}$ can be expressed as function of a corresponding pressure drop coefficient $K_{dis,i}$ and the corresponding opening ratio $\Psi_{dis,i}$:

$$c_{dis,i} = K_{dis,i} \Psi_{dis,i}^{-2} \left(0.4(1.25 - \Psi_{dis,i}) + (1 - \Psi_{dis,i})^2\right) \qquad \text{, for } i \in \{2,3\}. \tag{7.53}$$

A relation between the pressure drop coefficient $K_{dis,i}$ and the ratio of the plate thickness (symbolized by s_{dis}) to the hole diameter was created by McAllister et al. [71], who had investigated the pressure drop for several types of perforated plates with different plate thicknesses and hole diameters. A third-order polynomial can be fitted to these results with a good agreement to the data points, which given by

$$K_{dis,i} = 1.6959 - 0.763579 \frac{s_{dis}}{d_{dis,i}} + 0.213827 \left(\frac{s_{dis}}{d_{dis,i}}\right)^2 - 0.0165174 \left(\frac{s_{dis}}{d_{dis,i}}\right)^3 \qquad \text{, for } i \in \{2,3\}, \tag{7.54}$$

with reference to the notation of this work. Equation 7.53 is also cited by Mörl et al. [29], however the authors presented the correlation between $K_{dis,i}$ and $s_{dis}/d_{dis,i}$ only by means of a graphical plot. Therein, the pressure drop coefficient $K_{dis,i}$ is called as "flow coefficient of perforated plate". Perforation coefficient would also be an appropriate designation for $K_{dis,i}$, as well as perforation ratio or relative hole length for $s_{dis}/d_{dis,i}$.

Furthermore, the superficial gas velocity ratio $\omega_{2,3}$ of the second section $i = 2$ to third section $i = 3$ is introduced with:

$$\omega_{2,3} \coloneqq \frac{u_{dis,2}}{u_{dis,3}} \gg 1. \tag{7.55}$$

This ratio is referred to as *binary velocity distribution ratio*,*binary velocity split ratio*, or in short *velocity split ratio*. It can be expressed only by constructive properties of the distributor plate after inserting Eqs. 7.52 and 7.53 into Eq. 7.51:

$$\omega_{2,3} = \sqrt{\frac{c_{dis,3}}{c_{dis,2}}} = \sqrt{\frac{K_{dis,3} \Psi_{dis,3}^{-2} \left(0.4(1.25 - \Psi_{dis,3}) + (1 - \Psi_{dis,3})^2\right)}{K_{dis,2} \Psi_{dis,2}^{-2} \left(0.4(1.25 - \Psi_{dis,2}) + (1 - \Psi_{dis,2})^2\right)}} \qquad \text{, for } i \in \{2,3\}. \tag{7.56}$$

In addition to this, the ratio of the sectional superficial gas velocity of i to the inlet gas velocity $\omega_{i,in} \coloneqq u_{dis,i}/u_{in}$ and its inverse ratio $\omega_{in,i} \coloneqq u_{in}/u_{dis,i}$ are introduced. They can be related to the cross-sectional area fractions of the second and third distributor plate section ($\varphi_{dis,2}$ and $\varphi_{dis,3}$) and the binary velocity distribution ratio $\omega_{2,3}$ via Eqs. 7.50 and 7.56, which results in

$$\omega_{i,in} \coloneqq \frac{u_{dis,i}}{u_{in}} = (\varphi_{dis,2}\omega_{2,3} + \varphi_{dis,3})^{-1}\omega_{2,3}^{3-i} \qquad \text{, for } i \in \{2,3\} \tag{7.57}$$

and

$$\omega_{in,i} \coloneqq \frac{u_{in}}{u_{dis,i}} = (\varphi_{dis,2}\omega_{2,3} + \varphi_{dis,3})\omega_{2,3}^{i-3} \qquad \text{, for } i \in \{2,3\}. \tag{7.58}$$

When referring to the second section, $\omega_{2,in}$ is larger than unity, wherefore it is called *inlet gas velocity enhancement factor*, *inlet gas acceleration factor*, or in short *acceleration factor*. The gas velocity ratio of the third section $\omega_{3,in}$ is named as *inlet gas velocity reduction factor*, *inlet gas throttling factor*, or just *throttling factor*, since it is less than unity. Another dimensionless characteristic of the flow separation by the distributor plate is $\Omega_{i,in}$, the ratio of a sectional mass flow rate $\dot{M}_{dis,i}$ of i to the inlet gas mass flow rate $\dot{M}_{in}$. It conforms with the ratio of sectional dry mass flow rate $\dot{M}_{dis,i,dry}$ of i to the dry mass flow rate of the inlet gas $\dot{M}_{in,dry}$ according to Eq. 7.36:

$$\Omega_{i,in} \coloneqq \frac{\dot{M}_{dis,i}}{\dot{M}_{in}} = \frac{\dot{M}_{dis,i,dry}}{\dot{M}_{in,dry}} \qquad \text{, for } i \in \{2,3\}. \tag{7.59}$$

The ratios $\Omega_{2,in}$ and $\Omega_{3,in}$ are mass fractions of the inlet gas going into the spray zone and into the drying zone. The inlet gas mass fraction for the spray zone $\Omega_{2,in}$ can be seen as *bypass fraction of the overall drying power*, and is therefore called as *drying power bypass fraction*, or abbreviated as *bypass fraction*. The inlet gas mass fraction for the drying zone $\Omega_{3,in}$ is referred to as *drying gas mass fraction*. Both *inlet gas split fractions* $\Omega_{2,in}$ and $\Omega_{3,in}$ can be related by the sectional area fractions $\varphi_{dis,i}$ and the binary velocity split ratio $\omega_{2,3}$ as follows:

$$\Omega_{i,in} = \varphi_{dis,i}\omega_{i,in} = \varphi_{dis,i}(\varphi_{dis,2}\omega_{2,3} + \varphi_{dis,3})^{-1}\omega_{2,3}^{3-i} \qquad \text{, for } i \in \{2,3\}. \tag{7.60}$$

From Eqs. 7.56 to 7.60, it turns out that the velocity ratio split ratio $\omega_{2,3}$, the inlet-gas-related sectional velocity ratios $\omega_{i,in}$, their reciprocals $\omega_{in,i}$, and the inlet gas split fractions $\Omega_{i,in}$ are determined only by the specifications of the model distribution plate, and is therefore independent from inlet gas properties such as mass flow rate, temperature, and moisture content. Especially, the inlet gas throttling factor ($\omega_{3,in} = \varphi_{dis,2}\omega_{2,3} + \varphi_{dis,3}$) is useful for a dimensionless description of process limits, later on in Section 7.10.

Calculation of fluid-dynamics-related characteristics of the separated flows

Following Eqs. 7.57 and 7.60, the sectional gas velocities $u_{dis,2}$ and $u_{dis,3}$ and the sectional mass flow rates $\dot{M}_{dis,2}$ and $\dot{M}_{dis,3}$ are calculated with:

$$u_{dis,2} = u_{in}\omega_{2,in} = u_{in}\frac{\omega_{2,3}}{\varphi_{dis,2}\omega_{2,3} + \varphi_{dis,3}}, \tag{7.61}$$

$$u_{dis,3} = u_{in}\omega_{3,in} = u_{in}\frac{1}{\varphi_{dis,2}\omega_{2,3} + \varphi_{dis,3}}, \tag{7.62}$$

$$\dot{M}_{dis,2} = \dot{M}_{in}\Omega_{2,in} = \dot{M}_{in}\frac{\varphi_{dis,2}\omega_{2,3}}{\varphi_{dis,2}\omega_{2,3} + \varphi_{dis,3}}, \tag{7.63}$$

$$\dot{M}_{dis,3} = \dot{M}_{in}\Omega_{3,in} = \dot{M}_{in}\frac{\varphi_{dis,3}}{\varphi_{dis,2}\omega_{2,3} + \varphi_{dis,3}}. \tag{7.64}$$

The respective dry mass flow rates can be obtained from Eq. 7.36. The interstitial gas velocities of the distributor plate sections are not relevant for the implementation of the TZC-model.

7.4.3 Temperature drop by heat losses

As shown later in Chapter 8, the two-zone continuum model shall be implemented for completely isothermal systems, completely adiabatic walls, and non-adiabatic conditions. These options shall be considered in the model implementation by means of the relative temperature drop (symbolized by Θ_{loss}) across the

distributor plate section, which is defined by the absolute temperature drop divided by the maximal possible temperature drop:

$$\Theta_{loss} \coloneqq \frac{T_{in} - T_{in,eff}}{T_{in} - T_{sur}}. \tag{7.65}$$

In completely isothermal or completely adiabatic systems, the relative temperature drop of process gas is given with zero. In case of non-isothermal or non-adiabatic systems, the relative temperature drop could be approached by models of heat transfer kinetics. But that is quite cumbersome and complex for the given construction of the process chamber. Instead, measurements of the inlet gas temperature right below the plate and of the effective inlet gas temperature right above the plate could be made to determine the relative temperature drop. Those measurements have been carried out in this thesis, as shown in Section C.6.1, by which an empirical function of the relative temperature drop depending on the inlet gas velocity at standard temperature and pressure conditions of dry air ($u_{in,stp}$) was derived. Using this, the following optional function of Θ_{loss} is designed for isothermal and/or adiabatic systems as well as for non-adiabatic systems with:

$$\Theta_{loss} = \begin{cases} 0 & \text{, isothermal and/or adiabatic} \\ \frac{1}{1+19.5628\left(u_{in,stp}[\mathrm{m/s}]\right)^{1.743}} & \text{, non-adiabatic (empirical)} \end{cases}. \tag{7.66}$$

From this, the effective inlet gas temperature can be obtained by

$$T_{in,eff} = T_{in} - \Theta_{loss}(T_{in} - T_{sur}) \tag{7.67}$$

for given temperatures of the inlet gas T_{in} and the surroundings T_{sur}. The superficial gas velocities of the distributor plate section outlet $u_{dis,i,eff}$ are calculated with the help of the ideal gas law according to:

$$u_{dis,i,eff} = u_{dis,i}\frac{T_{in,eff}[\mathrm{K}]}{T_{in}[\mathrm{K}]} \qquad \text{, for } i \in \{2,3\}, \tag{7.68}$$

wherein the influence of the pressure drop is neglected. The moisture content of the inlet gas remains constant when passing the inflow plate: $Y_{in} = Y_{in,eff}$. Back-mixing of vapor from the process chamber interior against the main flow into the distributor plate holes can be disregarded. The mass flow rates of the process gas at the inlet and outlet of the distributor plate sections must be equal due to the assumption of stationary flow and the law of conservation of mass:

$$\dot{M}_{dis,i,eff} = \dot{M}_{dis,i} \qquad \text{, for } i \in \{2,3\}. \tag{7.69}$$

The sectional mass flow rates $\dot{M}_{dis,i}$ are significant to determine the drying power of the process gas in the spray zone and drying zone, and thus, to define thermal process limits such as the process-gas-saturation point.

7.5 Fluid dynamics and drying of sprayed liquid in the Wurster fluidized bed

In the following, analytical relationships of the nozzle gas injection and the gas transport as well as the evaporation of the spray liquid in the spray zone and drying zone are derived.

Nozzle gas injection

In real Wurster processes, three different gas flows - the process gas of the second distributor plate section, the nozzle gas, and the process gas sucked from the drying region - enter the Wurster tube, where they are only then mixed. In order to lower the complexity level of the two-zone continuum model, the gas flow from the drying zone is neglected, and the other two gas flows are assumed to be perfectly mixed before going into the Wurster tube (spray zone). This sub-process of the model shall take place in the nozzle gas injection compartment (see Figure 7.1a), as described before. The mass flow rate of the nozzle gas $\dot{M}_{g,noz}$ belongs to the predefined parameters in the implementation of the TZC-model. It should have values in the range of the experimental conditions of this thesis, where it is set by the nozzle gas excess pressure $p_{g,noz}$. Those values can be estimated from the specification sheet of the nozzle-manufacturer, which is described in

Appendix C.2.3. The calculation of $\dot{M}_{dis,2}$ is shown in the previous section. The stationary mass balance of nozzle gas injection compartment relates the gas mass flow rate of the spray zone inlet $\dot{M}_{g,\alpha,bot}$ to the sum of the process gas mass flow rates from the second distributor plate section and the nozzle gas:

$$\dot{M}_{g,\alpha,bot} = \dot{M}_{dis,2} + \dot{M}_{g,noz}. \tag{7.70}$$

Since the nozzle gas injection compartment is assumed to be free of particles and spray droplets, no evaporation takes place there, and hence, the moisture content of the mixed gas flow is still equal to that of the inlet gas:

$$Y_{\alpha,bot} = Y_{in,eff} = Y_{in}. \tag{7.71}$$

The gas temperature of the spray zone inlet $T_{\alpha,bot}$ is firstly estimated by this approximation

$$T^*_{\alpha,bot} \coloneqq \frac{\dot{M}_{dis,2} T_{in,eff} + \dot{M}_{g,noz} T_{g,noz}}{\dot{M}_{g,\alpha,bot}}, \tag{7.72}$$

in which the dependency of the gas heat capacity on temperature is neglected. The gas temperature of the spray zone inlet is then obtained from the energy balance of the nozzle gas injection compartment according to

$$T_{\alpha,bot} = \frac{\dot{M}_{dis,2} h_g(T_{in,eff}, Y_{in}) + \dot{M}_{g,noz} h_g(T_{g,noz}, Y_{in})}{\dot{M}_{g,\alpha,bot} \bar{c}_{p,g,0}(T^*_{\alpha,bot})}, \tag{7.73}$$

where the specific enthalpies h_g of the process gas and the nozzle gas are to be calculated by Eq. 7.19, and the average heat capacity of the mixed gas $\bar{c}_{p,g,0}$ is obtained from Eqs. 7.19 and 7.22 with the estimated temperature $T^*_{\alpha,bot}$ of Eq. 7.72.

Gas transport and evaporation in the spray zone

The evaporation of sprayed water affects process gas properties within the Wurster tube in real processes, but only to a small extent, so that those effects are neglected in the implementation of the TZC-model. However, if spray zone evaporation were taken into account, the drying potential at the spray zone outlet $\eta_{dry,\alpha,top}$ would be a practicable, characteristic measure for the amount of evaporated water in the spray zone. The drying potential of the spray zone outlet is given with unity ($\eta_{dry,\alpha,top} = 1$) for conditions without evaporation in the spray zone, and otherwise described by empirical correlations ($\mathrm{f_{emp}}$), as in the following optional equation:

$$\eta_{dry,\alpha,top} = \begin{cases} 1 & \text{, no evaparation in spray zone} \\ \mathrm{f_{emp}}(\dot{M}_{in}, T_{in}, \dot{M}_w, A_{app,0}, D_{wt}, \omega_{2,3}, ...) < 1 & \text{, with evaparation in spray zone} \end{cases}. \tag{7.74}$$

The simplification of $\eta_{dry,\alpha,top} = 1$ is also useful for creating approximate solutions of the operation limits of non-isothermal minimal Wurster fluidization and process-gas saturation, which can be determined without implementing the entire two-zone continuum model, as shown later in Sections 7.10.1 and 7.10.2. In Appendix C.6.2, two empirical fit equations are shown, one depending on the area-specific water spray rate $\dot{m}_w = \dot{M}_w / A_{app,0}$ and one depending on the inlet gas temperature T_{in}, which were derived from temperature measurements according to the experimental setting in Figure 9.5 b. But, these correlations provide only very rough estimates due to large fluctuations of the measured temperatures. The employment of a heat and mass transfer model for calculating the drying potential of the spray zone outlet would substantially enhance the level of complexity. The following equations of process gas characteristics in the spray zone can be used for both cases: without and with evaporation in the spray zone. Once the drying potential of the spray zone outlet is known, the temperature $T_{\alpha,top}$ and the moisture content $Y_{\alpha,top}$ of the spray zone outlet gas can be calculated with the help of the saturation states of the spray zone inlet gas $T_{sat}(T_{\alpha,bot}, Y_{in})$ and $Y_{sat}(T_{\alpha,bot}, Y_{in})$ (obtained from Eqs. 7.23 to 7.28) and the lever principle (Eq. 7.29):

$$T_{\alpha,top} = T_{sat}(T_{\alpha,bot}, Y_{in}) + \eta_{dry,\alpha,top}\big(T_{\alpha,bot} - T_{sat}(T_{\alpha,bot}, Y_{in})\big), \tag{7.75}$$

$$Y_{\alpha,top} = Y_{sat}(T_{\alpha,bot}, Y_{in}) - \eta_{dry,\alpha,top}\big(Y_{sat}(T_{\alpha,bot}, Y_{in}) - Y_{in}\big). \tag{7.76}$$

The average gas temperature of the spray zone T_α can be approached for instance by the mean value of the inlet and outlet temperatures of the spray zone:

$$T_\alpha \coloneqq \frac{1}{2}(T_{\alpha,bot} + T_{\alpha,top}). \tag{7.77}$$

The average moisture content of the spray zone gas Y_α ensues from the lever principle again:

$$Y_\alpha = Y_{\alpha,top} - \frac{T_{\alpha,bot} - T_\alpha}{T_{\alpha,bot} - T_{sat}(T_{\alpha,bot}, Y_{in})}\big(Y_{sat}(T_{\alpha,bot}, Y_{in}) - Y_{in}\big). \tag{7.78}$$

Based on constant mass flow rates of dry air ($\dot{M}_{dry,\alpha,bot} = \dot{M}_{dry,\alpha} = \dot{M}_{dry,\alpha,top}$) and Eq. 7.36, the total mass flow rates of the spray zone outlet $\dot{M}_{g,\alpha,top}$ and the spray zone average point $\dot{M}_{g,\alpha}$ can be obtained from:

$$\dot{M}_{g,\alpha,top} = \dot{M}_{g,\alpha,bot}\frac{1 + Y_{\alpha,top}}{1 + Y_{in}}, \tag{7.79}$$

$$\dot{M}_{g,\alpha} = \dot{M}_{g,\alpha,bot}\frac{1 + Y_{\alpha}}{1 + Y_{in}}. \tag{7.80}$$

The difference in moisture content between the inlet and outlet process gas of the spray zone can also be used to calculate the total evaporation rate of the spray zone $\dot{M}_{eva,\alpha}$ by:

$$\dot{M}_{eva,\alpha} = \dot{M}_{g,\alpha,bot}\frac{Y_{\alpha,top} - Y_{in}}{1 + Y_{in}}. \tag{7.81}$$

It is assumed that the complete amount of sprayed water deposits on particle surface, and the discharged particles come directly into the drying zone. The amount of water on surface of particles that leave the spray zone is represented by $\dot{M}_{w,p,\alpha}$. It can be calculated by the difference of the water spray rate $\dot{M}_w$ to the total evaporation rate in the spray zone $\dot{M}_{\alpha,eva}$:

$$\dot{M}_{w,p,\alpha} = \dot{M}_w - \dot{M}_{eva,\alpha}. \tag{7.82}$$

The amount of deposited water ($\dot{M}_{w,p,\alpha}$) is dried by the process gas of the drying zone. The superficial gas velocity of the spray zone average state u_α is defined with:

$$u_\alpha = \frac{\dot{M}_{g,\alpha}}{\rho_g(T_\alpha, Y_\alpha)\frac{\pi}{4}D_{wt}^2} \tag{7.83}$$

It is needed to determine the pneumatic transport of particles in the spray zone, later in Section 7.7.

Gas transport and evaporation in the drying zone

The mass flow rate of process gas entering the drying zone is the same as the mass flow rate of the gas passing the distributor plate section below the drying zone:

$$\dot{M}_{g,1-\alpha,bot} = \dot{M}_{dis,3}. \tag{7.84}$$

At steady state conditions, the overall evaporation rate in the drying zone $\dot{M}_{eva,1-\alpha}$ must equal the mass flow rate of deposited water $\dot{M}_{w,p,\alpha}$ (see Eq. 7.82):

$$\dot{M}_{eva,1-\alpha} = \dot{M}_{w,p,\alpha}. \tag{7.85}$$

The total mass flow rate of gas in the drying zone results from the sum of the drying zone inlet flow and the evaporated amount of water:

$$\dot{M}_{g,1-\alpha} = \dot{M}_{g,1-\alpha,bot} + \dot{M}_{eva,1-\alpha}. \tag{7.86}$$

The saturation point of the drying zone ($T_{sat}(T_{in,eff}, Y_{in})$ and $Y_{sat}(T_{in,eff}, Y_{in})$) is calculated by Eqs. 7.23 to 7.28 with the effective inlet gas temperature $T_{in,eff}$ and the inlet gas moisture content Y_{in} as initial state. As described before, the drying zone is assumed to be an ideally back-mixed system for both the gas and the solid phase. Hence, the property state vector of the drying zone outlet gas conforms with that of drying zone average spot: $S_{1-\alpha,top} = S_{1-\alpha}$. The respective moisture contents follow from the partial mass balance of water ($\dot{M}_{dry,1-\alpha}Y_{1-\alpha} = \dot{M}_{dry,1-\alpha,bot}Y_{1-\alpha,bot} + \dot{M}_{eva,1-\alpha}$) and Eq. 7.36

$$Y_{1-\alpha,bot} = Y_{1-\alpha} = Y_{1-\alpha,top} = Y_{in} + (1 + Y_{in})\frac{\dot{M}_{eva,1-\alpha}}{\dot{M}_{g,1-\alpha,bot}}, \tag{7.87}$$

and the respective temperatures ensue from the lever principle of Eq. 7.29

$$T_{1-\alpha,bot} = T_{1-\alpha} = T_{1-\alpha,top} = T_{sat}(T_{in,eff}, Y_{in}) + \frac{Y_{sat}(T_{in,eff}, Y_{in}) - Y_{1-\alpha}}{Y_{sat}(T_{in,eff}, Y_{in}) - Y_{in}} \big(T_{in,eff} - T_{sat}(T_{in,eff}, Y_{in})\big). \tag{7.88}$$

By disregarding changes in pressure along the vertical coordinate z, the density of the drying zone gas $\rho_{g,1-\alpha}$ is determined according to Eq. 7.31:

$$\rho_{g,1-\alpha} = \rho_g(T_{1-\alpha}, Y_{1-\alpha}) = \frac{1 + Y_{1-\alpha}}{1 + Y_{1-\alpha}\frac{\tilde{M}_{air}}{\tilde{M}_{vap}}} \frac{\tilde{M}_{air} p_{sys}}{\tilde{R} T_{1-\alpha}}. \tag{7.89}$$

The superficial gas velocity at the bottom of drying zone $u_{1-\alpha,bot} = u_{1-\alpha}(z = 0)$ can be calculated from

$$u_{1-\alpha,bot} = \frac{\dot{M}_{g,1-\alpha}}{\rho_{g,1-\alpha} A_{dis,3}}, \tag{7.90}$$

whereas the superficial gas velocity at the top of drying zone $u_{1-\alpha,top} = u_{1-\alpha}(z = H_{1-\alpha})$ requires a known fluidized bed height $H_{1-\alpha}$. The latter must be determined iteratively, as shown below in Section 7.7.

7.6 Reference characteristics of fluid-particle transport dynamics in the Wurster fluidized bed

The terminal sinking velocity of single particles (Section 2.2.1) and the points of minimal fluidization and elutriation of homogeneous fluidized beds (Section 2.2.4) are the main characteristics of fluid-particle transport dynamics, wherewith pneumatic transport and swarm sinking in the spray zone and bed expansion in drying zone is later calculated (Section 7.7) to find process conditions of stationary circulating Wurster fluidization. These characteristics shall be determined by approaches of Martin ([40, 41], see Eqs. 2.83, 2.87, and 2.119), which are functions of the Archimedes number. However, the Archimedes number depends on gas properties, and thus, on the thermodynamic state of the process gas (T,Y). Therefore, two different Archimedes numbers are calculated by

$$Ar_\alpha = \frac{\rho_p - \rho_g(T_\alpha, Y_\alpha)}{\rho_g(T_\alpha, Y_\alpha)} \frac{d^3 g}{\nu_g^2(T_\alpha)} \tag{7.91}$$

for the spray zone, and by

$$Ar_{1-\alpha} = \frac{\rho_p - \rho_g(T_{1-\alpha}, Y_{1-\alpha})}{\rho_g(T_{1-\alpha}, Y_{1-\alpha})} \frac{d^3 g}{\nu_g^2(T_{1-\alpha})} \tag{7.92}$$

for the drying zone. The effective particle density ρ_p and the particle diameter d are given process parameters of the two-zone continuum model. Martin's equation of the minimal fluidization velocity (Eq. 2.119) is only needed for calculating the fluidized bed expansion in the drying zone, with:

$$u_{mf,1-\alpha} = \frac{\nu_g(T_{1-\alpha})}{d} 42.9(1 - \varepsilon_{mf}) \left(\sqrt{1 + \frac{\varepsilon_{mf}^3}{(1 - \varepsilon_{mf})^2} \frac{Ar_{1-\alpha}}{3214}} - 1 \right). \tag{7.93}$$

By contrast, the terminal sinking velocity of Martin's approximate solution (Eq. 2.87) is used for both the spray zone with

$$u_{s,\alpha} = \frac{\nu_g(T_\alpha)}{d} \cdot 18 \left[\sqrt{1 + \frac{\sqrt{Ar_\alpha}}{9}} - 1 \right]^2, \tag{7.94}$$

and the drying zone with

$$u_{elu,1-\alpha} = u_{s,1-\alpha} = \frac{\nu_g(T_{1-\alpha})}{d} \cdot 18 \left[\sqrt{1 + \frac{\sqrt{Ar_{1-\alpha}}}{9}} - 1 \right]^2, \tag{7.95}$$

where the terminal sinking velocity and the elutriation point of drying zone $u_{elu,1-\alpha}$ are assumed to be equal. The ratio of the elutriation velocity to the minimal fluidization velocity defines the fluidization range number f_{rn} (maximal fluidization number), which is given with

$$f_{rn,1-\alpha} = \frac{u_{elu,1-\alpha}}{u_{mf,1-\alpha}} \tag{7.96}$$

for the drying zone. The fluidization range number is useful for describing the fluidized bed expansion process below in Section 7.7 and diverse dimensionless characteristics of process limits shown later in Sections 7.9 to 7.11.

7.7 Iterative calculation of the circulating Wurster fluidization

The pneumatic transport of particles in the spray zone and the fluidized bed expansion in the drying zone must be calculated by iterating Eqs. 7.97 to 7.119. The iteration rounds are counted by j, where $j = 1$ defines the first round. The model quantities that change within the iteration are marked with "(j)".

Pneumatic transport in the spray zone

In the first iteration round, the interparticle porosity (swarm porosity) of the spray zone $\varepsilon_\alpha(j = 1)$ must be estimated with a low start value (symbolized by $\varepsilon_{\alpha,0}$) in order to avoid creation of complex numbers within the computation, and thus, to obtain converging iterations, as explained below in more detail. From the second iteration round on ($j > 1$), the spray zone swarm porosity ε_α is set to a new approximated value (symbolized by $\varepsilon_{\alpha,new}$)

$$\varepsilon_\alpha(j) \coloneqq \begin{cases} \varepsilon_{\alpha,0} & \text{, if } j = 1 \\ \varepsilon_{\alpha,new}(j-1) & \text{, if } j > 1 \end{cases}, \tag{7.97}$$

which is determined by Eq. 7.118 at the end of this iteration sequence. Using the interparticle porosity of Eq. 7.97, the interstitial gas velocity in the spray zone $u_{\varepsilon,\alpha}$ follows from:

$$u_{\varepsilon,\alpha}(j) = \frac{u_\alpha}{\varepsilon_\alpha(j)}. \tag{7.98}$$

The Richardson-Zaki exponent

$$m_{sw,\alpha} = 5.5 Ar_\alpha^{-0.06} = 5.5 \left(\frac{\rho_p - \rho_{g,\alpha}}{\rho_{g,\alpha}} \frac{dg}{\nu_g^2} \right)^{-0.06}, \tag{7.99}$$

suggested by Kraume ([28], see Eq. 2.98), is employed to calculate the swarm sinking correction factor

$$k_{sw,\alpha}(j) = \big(\varepsilon_\alpha(j)\big)^{m_{sw,\alpha}} \tag{7.100}$$

according to the Richardson-Zaki equation ([50], Eq. 2.93). It should be noted at this point that Eq. 7.99 only provides reliable values for the transition flow regime of sinking particles ($0.25 < Re_s < 1000$), which is also demonstrated in Section 2.2.5 (Figure 2.4), where Kraume's approach is compared with empirical correlations of other authors (described in Section 2.2.2). Especially the holistic equations of Rowe ([64], Eq. 2.100) and of Khan a. Richardson ([65], Eq. 2.101) are recommendable, as they can be easily implemented into the TZC-model and cover the Stokes and quadratic regime too. The swarm sinking velocity $u_{sw,\alpha}$ results from multiplication of the swarm correction factor $k_{sw,\alpha}$ and the terminal sinking velocity of single particles $u_{s,\alpha}$:

$$u_{sw,\alpha}(j) = k_{sw,\alpha}(j) u_{s,\alpha}. \tag{7.101}$$

The pneumatic transport velocity $u_{pn,\alpha}$ ensues from the difference of the swarm sinking velocity $u_{sw,\alpha}$ to the interstitial gas velocity $u_{\varepsilon,\alpha}$:

$$u_{pn,\alpha}(j) = u_{\varepsilon,\alpha}(j) - u_{sw,\alpha}(j). \tag{7.102}$$

The pneumatic transport velocity $u_{pn,\alpha}$ can also be called as average rising velocity of particles in the spray zone. Since all particles are assumed to be evenly distributed within the Wurster tube interior, the total dry mass of them M_α is obtained by:

$$M_\alpha(j) = \rho_p \big(1 - \varepsilon_\alpha(j)\big) \frac{\pi}{4} D_{wt}^2 L_{wt}. \tag{7.103}$$

Setting of the start value of swarm porosity in the spray zone

It can be seen from Eqs. 7.98 to 7.101 that a larger swarm porosity ($\varepsilon_\alpha \uparrow$) leads to a lower interstitial gas velocity ($u_{\varepsilon,\alpha} \downarrow$) and a higher swarm sinking velocity ($u_{sw,\alpha} \uparrow$). For this reason, the interstitial gas velocity $u_{\varepsilon,\alpha}$ can become smaller than the swarm sinking velocity $u_{sw,\alpha}$, when the start value of the swarm porosity $\varepsilon_{\alpha,0}$ is chosen above a certain critical value (symbolized by $\varepsilon_{\alpha,0,cr}$). In this case, negative values would be obtained for the particle rising velocity $u_{pn,\alpha}$, which should be actually stringently larger than zero in the context of the TZC-model. To ensure this, the start value of the swarm porosity $\varepsilon_{\alpha,0}$ could be chosen, for example, as low as possible. However, iterations with lower start values take longer to find nearly constant solutions. Therefore, the critical start values $\varepsilon_{\alpha,0,cr}$ could also be calculated a priori with

$$\varepsilon_{\alpha,0,cr} = \left(\frac{u_\alpha}{u_{s,\alpha}}\right)^{1/(m_{sw,\alpha}+1)}, \tag{7.104}$$

which is derived by inserting Eqs. 7.98 to 7.101 into the right-hand side of Eq. 7.102 and setting the pneumatic transport velocity to zero ($u_{pn,\alpha} = 0$). Alternatively, a value of 0.4 can be taken for $\varepsilon_{\alpha,0}$, because it conforms well with common bulk porosity values at minimal fluidization conditions ε_{mf} (see Section 2.2.4), and the interparticle porosity of the spray zone can be expected to be much larger than 0.4 in Wurster fluidization.

Fluidized bed expansion in the drying zone

The calculation part of the iteration sequence, that refers to several fluidized bed characteristics of the drying zone, is presented in the following. At this, the moisture content of the drying zone particles is neglected, and only the dry bed mass of particles $M_{1-\alpha}$ shall be considered for calculating the bed expansion. The dry bed mass results from the difference of the total bed mass M_{bed} (predefined parameter) to the dry mass of all spray zone particles:

$$M_{1-\alpha}(j) = M_{bed} - M_\alpha(j). \tag{7.105}$$

As shown by the example of isothermal homogeneous fluidization in Section 2.2.5, the average bed porosity of the drying zone is related to the corresponding superficial gas velocity $u_{1-\alpha}$. However, the latter decreases into vertical direction due to the conical process chamber: $u_{1-\alpha} = \mathrm{f}(z)$. The particles can therefore not be evenly distributed in space, and the fluidized bed of the drying zone cannot be homogeneous, as a consequence of the expansion equations of Brötz (Eq. 2.127) and Richardson a. Zaki (Eq. 2.128). In order to simplify the problem, the bed porosity $\varepsilon_{1-\alpha}$ is nevertheless assumed to be constant here for the entire drying zone ($0 \leq z \leq H_{1-\alpha}$); but, the local changes of the superficial gas velocity in the drying zone are taken into account. The bed height, the superficial gas velocity at the drying zone gas outlet $u_{1-\alpha,top}$, and the superficial gas velocity at the average spot $\bar{u}_{1-\alpha}$ are therefore approximated by another iteration sequence, where k represents the counter variable of the new internal iteration loop (within j'th sequence), and $k = 1$ defines the first iteration round. The start value of the average gas velocity $\bar{u}_{1-\alpha}(j, k = 1)$ of the first iteration is set to the superficial gas velocity of the drying zone inlet $u_{1-\alpha,bot}$, which was calculated before by Eq. 7.90. A new value of the average superficial gas velocity (symbolized by $\bar{u}_{1-\alpha,new}$) is approached at the end of the k-related iteration sequence by Eq. 7.112, which is then used as start value for the next iteration round ($k > 1$) and so on:

$$\bar{u}_{1-\alpha}(j,k) = \begin{cases} u_{1-\alpha,bot} & \text{, if } k = 1 \\ \bar{u}_{1-\alpha,new}(j,k-1) & \text{, if } k > 1 \end{cases}. \tag{7.106}$$

The bed porosity $\varepsilon_{1-\alpha}$ is determined according to Eq. 2.130:

$$\varepsilon_{1-\alpha}(j,k) = \varepsilon_{mf}\left(\frac{\bar{u}_{1-\alpha}(j,k)}{u_{mf,1-\alpha}}\right)^{-ln(\varepsilon_{mf})/ln(f_{rn,1-\alpha})}, \tag{7.107}$$

The bed volume $V_{1-\alpha}$ is obtained from the definition of the interparticle porosity, the bed mass, and the swarm density ($\rho_p(1-\varepsilon_{1-\alpha})$):

$$V_{1-\alpha}(j,k) = \frac{M_{1-\alpha}(j)}{\rho_p\big(1-\varepsilon_{1-\alpha}(j,k)\big)}, \tag{7.108}$$

The quadratic approximation for steep conical process chambers, derived in Section 7.2, is used to calculate the bed height $H_{1-\alpha}$:

$$H_{1-\alpha}(j,k) \coloneqq \frac{\tan(\gamma_{app})}{4}\frac{D_{app,0}^2 - D_{wt}^2}{D_{app,0}} + \sqrt{\left(\frac{\tan(\gamma_{app})}{4}\frac{D_{app,0}^2 - D_{wt}^2}{D_{app,0}}\right)^2 + \frac{2\tan(\gamma_{app})}{\pi}\frac{V_{1-\alpha}(j,k)}{D_{app,0}}}. \quad (7.109)$$

The cross-sectional area of the drying zone outlet $A_{1-\alpha,top}$ follows with the bed height from:

$$A_{1-\alpha,top}(j,k) = \frac{\pi}{4}\left(\left(D_{app,0} + \frac{2}{\tan(\gamma_{app})}H_{1-\alpha}(j,k)\right)^2 - D_{wt}^2\right). \quad (7.110)$$

From this, the superficial gas velocity at the drying zone outlet is calculated with:

$$u_{1-\alpha,top}(j,k) = \frac{\dot{M}_{g,1-\alpha}}{\rho_p\big(1-\varepsilon_{1-\alpha}(j,k)\big)A_{1-\alpha,top}(j,k)}. \quad (7.111)$$

The new value of the average superficial gas velocity $\bar{u}_{1-\alpha,new}$ is approached by the mean value of the superficial gas velocities of the drying zone inlet and outlet:

$$\bar{u}_{1-\alpha,new}(j,k) \coloneqq \frac{1}{2}\big(u_{1-\alpha,bot} + u_{1-\alpha,top}(j,k)\big). \quad (7.112)$$

The iterations of Eqs. 7.106 to 7.112 are conducted until the iteration error of the average superficial gas velocity is less than a certain permissible error $\epsilon_{u,1-\alpha}$ (predefined parameter):

$$k \coloneqq \begin{cases} k+1 & \text{, if } \left|\big(\bar{u}_{1-\alpha,new}(j,k) - \bar{u}_{1-\alpha}(j,k)\big)/\bar{u}_{1-\alpha}(j,k)\right| > \epsilon_{u,1-\alpha} \\ k_{end} & \text{, if } \left|\big(\bar{u}_{1-\alpha,new}(j,k) - \bar{u}_{1-\alpha}(j,k)\big)/\bar{u}_{1-\alpha}(j,k)\right| \leq \epsilon_{u,1-\alpha} \end{cases}. \quad (7.113)$$

Mass flow rates of circulating particles in Wurster fluidization

The mass flow rate of pneumatically transported particles in the spray zone (pneumatic conveying rate $\dot{M}_{pn,\alpha}$) of the current iteration is given by:

$$\dot{M}_{pn,\alpha}(j) = \rho_p\big(1-\varepsilon_{\alpha}(j)\big)\frac{\pi}{4}D_{wt}^2 u_{pn,\alpha}(j). \quad (7.114)$$

The mass flow rate of particles being sucked from the drying zone into the Wurster tube (Wurster suction rate $\dot{M}_{tor,wt}$) shall be described by a semi-empirical fluid-bed outflow equation, which is derived from the modified Torricelli outflow equation from Burgschweiger a. Tsotsas ([90,91], Section 2.2.6) with adaptation to the Wurster chamber construction of the TZC-model. The equation of this approach (see Eq. 2.134) was applied for calculating the particle entry rate of vertical internal classification tubes. For the present conditions, the opening area of the internal classifier A_{open} of Eq. 2.134 is replaced by the free suction area below the Wurster tube inlet (Wurster tube gap: $\pi D_{wt} H_{wt}$), and the height of the internal classifier inlet H_{open} of Eq. 2.134 is set to zero, because Wurster tube gap is located on the bottom of the fluidized bed in the present model. The pulsation factor k_{pul} of Eq. 2.133 follows to

$$k_{pul}(j) = \left(\frac{\bar{u}_{1-\alpha}(j,k_{end})}{u_{mf,1-\alpha}}\right)^{m_{tor}}, \quad (7.115)$$

and the equation of the Wurster suction rate ensues to

$$\dot{M}_{tor,wt}(j) = \lambda_{tor}\pi D_{wt} H_{wt}\rho_p\big(1-\varepsilon_{1-\alpha}(j,k_{end})\big)\sqrt{2g k_{pul}(j) H_{1-\alpha}(j,k_{end})}. \quad (7.116)$$

The pneumatic conveying rate must equal the Wurster suction rate due to the assumption of stationary particle circulation (Eq. 7.4: $\dot{M}_{pn,\alpha} = \dot{M}_{tor,wt}$). In the iterations, however, the j-related pneumatic conveying rate and the Wurster suction rate are different ($\dot{M}_{pn,\alpha}(j) \neq \dot{M}_{tor,wt}(j)$), as the estimated and calculated swarm porosities still contain a certain error.

Transition to the next iteration loop

It is the aim of the j-related iteration to minimize the errors of the interparticle porosities of the spray zone and drying zone, the pneumatic conveying rate, and the Wurster suction rate. For this purpose, a vector containing a domain of spray zone swarm porosities is introduced, which is symbolized by ε_α^* and called the free variable of the swarm porosity. In order to find the next start value of the iteration $\varepsilon_{\alpha,new}(j)$, the free variable of the swarm porosity is used to generate a function vector of the pneumatic conveying rate by

$$\dot{M}_{pn,\alpha}(\varepsilon_\alpha^*) = \rho_p(1-\varepsilon_\alpha^*)\frac{\pi}{4}D_{wt}^2\left(\frac{u_\alpha}{\varepsilon_\alpha^*} - (\varepsilon_\alpha^*)^{m_{sw,\alpha}}u_{s,\alpha}\right), \tag{7.117}$$

for the entire domain of ε_α^*. The $\dot{M}_{pn,\alpha}(j,\varepsilon_\alpha^*)$-function of Eq. 7.117 decreases monotonically with the free variable of the swarm porosity ε_α^*, and it has one intercept with the Wurster suction rate $\dot{M}_{tor,wt}(j)$ of the current iteration round j. The location of this intercept can be found by a minimal search method (here "min" in MATLAB®), from which the abscissa-value of the intercept is set to the new spray zone porosity $\varepsilon_{\alpha,new}$ according to:

$$\varepsilon_{\alpha,new}(j) = \mathrm{find}_{\min,\varepsilon_\alpha^*}\Big(\big|\dot{M}_{pn,\alpha}(\varepsilon_\alpha^*) - \dot{M}_{tor,wt}(j)\big|\Big). \tag{7.118}$$

Subsequently, the error of the new spray zone porosity with reference to the start value of the iteration round $|(\varepsilon_{\alpha,new}(j)-\varepsilon_\alpha(j))/\varepsilon_\alpha|$ is determined and compared with a desired iteration error $\epsilon_{\varepsilon,\alpha}$ (predefined parameter). Another iteration sequence starts from Eq. 7.97 when the iteration error is larger than the target error, where the iteration counter is increased by unity $j := j+1$. In the opposite case ($j := j_{end}$), no further iterations are conducted, and the calculated quantities of the current iteration round are seen as the solution of the TZC-model:

$$j := \begin{cases} j+1 & \text{, if} \big|\big(\varepsilon_{\alpha,new}(j)-\varepsilon_\alpha(j)\big)/\varepsilon_\alpha(j)\big| > \epsilon_{\varepsilon,\alpha} \\ j_{end} & \text{, if} \big|\big(\varepsilon_{\alpha,new}(j)-\varepsilon_\alpha(j)\big)/\varepsilon_\alpha(j)\big| \le \epsilon_{\varepsilon,\alpha} \end{cases}. \tag{7.119}$$

7.8 Average parameters of the spray zone and the drying zone

Drying potentials

As described before in Section 7.5, the drying potential of the spray zone outlet is difficult to calculate by heat and transfer models, when the evaporation of sprayed water is to be taken into account; instead, it is recommended to use empirical functions of process parameters from measurements of individual systems (e.g., in Appendix C.6.2), as illustrated in Eq. 7.74. For neglected spray zone evaporation or for isothermal implementations of the two-zone continuum model, the drying potential of the spray zone is assumed with unity, what is still sufficient for moderate accuracy requirements. In the drying zone, which is a perfectly back-mixed system, the thermodynamic states (T,Y) of drying zone average gas and drying zone outlet gas are equal, and so also the respective drying potentials ($\eta_{1-\alpha} = \eta_{1-\alpha,top}$). The drying potentials of these drying zone spots are by no means equal to unity, as the main part of sprayed water evaporates here. They follow from this equation:

$$\begin{aligned}\eta_{dry,1-\alpha} &= \eta_{dry,1-\alpha,top} \\ &= \frac{T_{1-\alpha}-T_{sat}(T_{in,eff},Y_{in})}{T_{in}-T_{sat}(T_{in,eff},Y_{in})} = \frac{Y_{sat}(T_{in,eff},Y_{in})-Y_{1-\alpha}}{Y_{sat}(T_{in,eff},Y_{in})-Y_{in}}.\end{aligned} \tag{7.120}$$

Mass fractions of bed particles

The mass fraction α_m of bed particles being situated in the spray zone is defined by:

$$\alpha_m := \frac{M_\alpha(j_{end})}{M_{bed}}. \tag{7.121}$$

The values of α_m can be used for the spray zone proportion factor α in the three-compartment population balance model of Hampel ([1, 2], recapitulated in Section 2.3.2) or its supplemented version of Section 5.2, which is consistent with Börner's definition of α [106]. According to Eq. 7.105, the mass fraction of drying zone particles in the entire bed is expressed with $1-\alpha_m$.

Particle residence times

The particle residence times of the spray zone τ_α and the drying zone $\tau_{1-\alpha}$ are further parameters of the three-compartment population balance model. They can be calculated from the mass of all particles in the respective zones divided by the circulation mass flow rate, which is defined by both the pneumatic conveying rate $\dot{M}_{pn,\alpha}$ and the Wurster suction rate $\dot{M}_{tor,wt}$. This way, the residence times of both zones follow from:

$$\tau_\alpha = \frac{M_\alpha(j_{end})}{\dot{M}_{pn,\alpha}(j_{end})} = \frac{\alpha_m M_{bed}}{\dot{M}_{pn,\alpha}(j_{end})} = \frac{L_{wt}}{u_{pn,\alpha}(j_{end})}, \tag{7.122}$$

$$\tau_{1-\alpha} = \frac{M_{1-\alpha}(j_{end})}{\dot{M}_{tor,wt}(j_{end})} = \frac{(1-\alpha_m)M_{bed}}{\dot{M}_{tor,wt}(j_{end})}. \tag{7.123}$$

At this, the spray zone residence time ensues also out of the space-time law ($\tau_\alpha = L_{wt}/u_{pn,\alpha}$) with the Wurster tube length as necessary distance to flow through.

7.9 Definition of reference process characteristics and dimensionless process parameters

The following five dimensionless process parameters are introduced in this Section: the dimensionless inlet gas velocity ξ_{in}, the dimensionless water spray rate $\dot{\mu}_w$, the dimensionless nozzle air rate $\dot{\mu}_{g,noz}$, the dimensionless bed mass μ_{bed}, and the normalized bed height $\Phi_{h,1-\alpha}$. They are used

- for describing process limits of minimal Wurster fluidization, process-gas saturation, and Wurster-tube exceedance in Sections 7.10 and 7.11,
- for the parameter setting in the sensitivity analysis of the two-zone continuum model of Section 8.2,
- for recommending operation points (ranges) of a stable Wurster granulation for different system scales in a general manner, as for example in Section 8.4.

Reference characteristics of the regime of isothermal homogeneous fluidization

Some of the dimensionless quantities defined below are based on reference characteristics of the flow regime of an isothermal homogeneous fluidized bed with the same thermodynamic state as that of the inlet gas from the TZC-model. These are the reference point of minimal fluidization with

$$u_{mf,ref} \coloneqq u_{mf}(T_{in}, Y_{in}, d, \rho_p), \tag{7.124}$$

the reference point of elutriation with

$$u_{elu,ref} \coloneqq u_{elu}(T_{in}, Y_{in}, d, \rho_p), \tag{7.125}$$

and the corresponding reference fluidization range number with

$$f_{rn,ref} \coloneqq \frac{u_{elu,ref}}{u_{mf,ref}}. \tag{7.126}$$

The reference points of minimal fluidization $u_{mf,ref}$ and elutriation $u_{elu,ref}$ are calculated by Martin's correlations [40, 41] (see Eqs. 2.87 and 2.119) in this thesis, but other approaches are conceivable too. A few different calculation methods for u_{mf} and u_{elu}, in general, have been suggested and described in Section 2.2.4, see for instance Table 2.3. As mentioned above, the fluidized bed of the two-zone continuum model is assumed to be monodisperse. Bed particle size distributions of continuous granulation processes, however, are polydisperse. In this case, it is recommended to calculate the minimal fluidization gas velocity and the elutriation gas velocity with respect to average particle characteristics (e.g., Sauter diameter) of the ideal continuous layerwise granulation model that are derived in Section 3.4.

Reference saturation point

The isenthalpic saturation point that ensues from the thermodynamic state of the inlet gas (T_{in},Y_{in}) and Eqs. 7.16 to 7.18 and 7.23 to 7.28 shall be represented in the following by the so-called reference saturation temperature $T_{sat,ref}$ with

$$T_{sat,ref} \coloneqq T_{sat}(T_{in}, Y_{in}, p_{sys}) \tag{7.127}$$

and the reference saturation moisture content $Y_{sat,ref}$ with

$$Y_{sat,ref} \coloneqq Y_{sat}(T_{in}, Y_{in}, p_{sys}). \tag{7.128}$$

The reference saturation point ($T_{sat,ref}$,$Y_{sat,ref}$) is used within the definition of the dimensionless water spray rate and for describing some of the approximate process limit characteristics in Section 7.11.

Dimensionless inlet gas velocity

The dimensionless inlet gas velocity ξ_{in} is defined by

$$\xi_{in} \coloneqq \frac{u_{in}(T_{in}, Y_{in}) - u_{mf,ref}}{u_{elu,ref} - u_{mf,ref}} = \frac{u_{in}(T_{in}, Y_{in})/u_{mf,ref} - 1}{f_{rn,ref} - 1}, \tag{7.129}$$

which relates it to the inlet gas conditions (T_{in} and Y_{in}) and the bed characteristics such as particle diameter d and effective particle density ρ_p via the reference points of minimal fluidization $u_{mf,ref}$ and elutriation $u_{elu,ref}$ of Eqs. 7.124 and 7.125. As can be seen on the right-hand side of Eq. 7.129, the dimensionless inlet gas velocity ξ_{in} can also be expressed in terms of the reference fluidization range number $f_{rn,ref}$ of Eq. 7.126. The values of the dimensionless inlet gas velocity ξ_{in} would be lower than unity for isothermal and homogeneous fluidized beds with straight chamber walls. However, the fluidization limits of spray fluidized beds in conical chambers are different. The dimensionless inlet gas velocity of the operation range of such systems can have values larger than unity for the following reasons. On one hand, spraying and evaporation have a cooling effect on the process gas, which reduces not only its temperature, but also its average velocity. On the other hand, conical walls lead to decreasing average process gas velocities in the direction of the flow. In spray fluidized bed systems with Wurster equipment, the process gas velocity of the fluidized bed region (drying zone) is even smaller than the inlet gas velocity due to lower perforation degrees of the distributor plate in this area. Besides, the dimensionless inlet gas velocity can also have negative values, when the inlet gas velocity is lower than the reference minimal fluidization point ($u_{in} < u_{mf,ref}$); but such operation conditions are not relevant for practical applications.

Dimensionless water spray rate

The dimensionless water spray rate $\dot{\mu}_w$ is defined as the ratio of the water spray rate $\dot{M}_w$ to the maximal drying capacity of an inlet gas flow with the velocity of the reference elutriation point $u_{elu,ref}$ of Eq. 7.125:

$$\dot{\mu}_w \coloneqq \frac{(1 + Y_{in})\dot{M}_w}{\rho_{g,in} \frac{\pi}{4} D_{app,0}^2 u_{elu,ref} (Y_{sat,ref} - Y_{in})}. \tag{7.130}$$

The maximal drying capacity is seen as the maximal evaporation rate that can be taken up by the entire inlet gas flow, at which it becomes saturated. The elutriation point characterizes here the upper limit of the inlet gas velocity for non-isothermal fluidization processes. The values of the dimensionless water spray rate, which are suitable for the practice, are most likely much less than unity, because those processes are operated with inlet gas velocity significantly lower than elutriation gas velocity and with sufficiently large inlet gas temperatures wherewith process-gas saturation can be avoided.

Dimensionless nozzle air rate

The dimensionless nozzle air rate $\dot{\mu}_{g,noz}$ is defined as the ratio of the nozzle air mass flow rate $\dot{M}_{g,noz}$ to the inlet gas mass flow rate of the reference elutriation point $u_{elu,ref}$:

$$\dot{\mu}_{g,noz} \coloneqq \frac{\dot{M}_{g,noz}}{\rho_{g,in} \frac{\pi}{4} D_{app,0}^2 u_{elu,ref}}. \tag{7.131}$$

The dimensionless water spray rate and nozzle air rate occur in the dimensionless description of the process-gas-saturation limit of Wurster fluidization, as shown later in Section 7.10.2.

Dimensionless bed mass

The dimensionless bed mass μ_{bed} is defined as the ratio of actual bed mass M_{bed} to the maximal bed mass that fits into the Wurster tube exterior from the chamber bottom to the top edge of the Wurster tube for static conditions ($u_{in} = 0$):

$$\mu_{bed} \coloneqq \frac{M_{bed}}{\rho_p(1-\varepsilon_{mf})V_{1-\alpha,max}}. \tag{7.132}$$

At this, the interparticle porosity of the stagnant bed is assumed to be equal to the interparticle bed porosity under minimal fluidization conditions ε_{mf} (predefined in the TZC-model). In order to achieve adequate Wurster fluidization in practice, the chamber should be filled up only to the lower area of the Wurster tube. The values of the dimensionless bed mass are therefore between zero and unity for proper parameter settings of real Wurster systems, but closer to zero than to unity. The maximal volume of the drying zone $V_{1-\alpha,max}$ can be calculated by Eq. 7.9 with $H_{1-\alpha,max} = H_{wt} + L_{wt}$ as input variable. Furthermore, the dimensionless bed mass is employed for defining an approximate solution of the Wurster-tube-exceedance limit, more on this in Section 7.11.5.

Normalized bed height of the drying zone

The normalized bed height of the drying zone $\Phi_{h,1-\alpha}$ is defined as the ratio of bed height in the drying zone $H_{1-\alpha}$ to the distance between the distributor plate and the top edge of the Wurster tube:

$$\Phi_{h,1-\alpha} \coloneqq \frac{H_{1-\alpha}}{H_{wt} + L_{wt}}. \tag{7.133}$$

It is introduced to illustrate the bed expansion in dependency on dimensionless inlet gas velocity, later in Section 8.2, and to characterize the operation point, where the bed expansion of the drying zone reaches the top edge of the Wurster tube by $\Phi_{h,1-\alpha} = 1$, which is the Wurster-tube-exceedance limit. A general description of this process limit is given in Section 7.10.3, and an approximate solution of it can be found in Section 7.11.5. The height $H_{1-\alpha}$ of Eq. 7.133 can be adopted by that $H_{1-\alpha}(j_{end}, k_{end})$ resulting from the iteration sequence of Section 7.7.

7.10 General description of process limits

Based on the concept of the present two-zone continuum model, the process limits of non-isothermal minimal Wurster fluidization (Section 7.10.1), process-gas saturation (Section 7.10.2), and Wurster-tube exceedance (Section 7.10.3) shall be described by general functions of the reference limits of isothermal homogeneous fluidization $u_{mf,ref}$ and $u_{elu,ref}$ and several corrections factors that are related to the flow separation and heat losses of the distributor plate and evaporation cooling effects. In addition, a critical dimensionless water spray rate is defined in Section 7.10.4, for which the limiting curves of non-isothermal minimum Wurster fluidization and process-gas saturation intersect.

7.10.1 Non-isothermal minimal-Wurster-fluidization limit

Criterion

The non-isothermal minimal-Wurster-fluidization limit (symbolized by u_{mwf}) characterizes that point of inlet gas velocity, where the process gas velocity at the drying zone bottom $u_{1-\alpha,bot}$ equals the minimal fluidization gas velocity of isothermal homogeneous fluidization for the thermodynamic state of the drying zone $u_{mf}(T_{1-\alpha},Y_{1-\alpha})$:

$$u_{mwf} \coloneqq u_{in}\big(u_{1-\alpha,bot}(\dot{M}_{1-\alpha,dry} = \dot{M}_{dis,3,dry}, T_{1-\alpha}, Y_{1-\alpha}) = u_{mf}(T_{1-\alpha}, Y_{1-\alpha}, d, \rho_p)\big) \tag{7.134}$$

with

$$\{\dot{M}_{1-\alpha,dry}, T_{1-\alpha}, Y_{1-\alpha}\} = \mathrm{f}(u_{in}, T_{in}, Y_{in}, \dot{M}_w, \varphi_{dis,3}, \omega_{3,in}, \eta_{dry,\alpha,top}, ...). \tag{7.135}$$

In this way, the non-isothermal minimal-fluidization limit takes into account changes in process gas velocity by heat losses through walls, by flow separation in the distributor plate, by gas cooling through evaporation, and by increase in mass flow rate due to evaporated water. The influence of conical chamber walls is disregarded here for the sake of simplicity. The non-isothermal minimal-fluidization limit of the inlet gas flow can also be represented by the corresponding volume flow rate $\dot{V}_{mwf} = A_{app,0}u_{mwf}$, mass flow rate $\dot{M}_{mwf} = \rho_{g,in}\dot{V}_{mwf}$, or dimensionless gas velocity ξ_{mwf}.

General relation to reference limits of isothermal homogeneous fluidization with correction factors

In the following, general formulations of the inlet gas velocity of non-isothermal minimal Wurster fluidization u_{mwf} and its corresponding dimensionless inlet gas velocity ξ_{mwf} are derived. At first, the inlet gas velocity of non-isothermal minimal Wurster fluidization u_{mwf} is related to the process gas velocity at the bottom of the drying zone $u_{1-\alpha,bot}$ via three factors of different velocity ratios:

$$u_{mwf}(T_{in}, Y_{in}) = \frac{u_{mwf}(T_{in})}{u_{dis,3}(T_{in})} \frac{u_{dis,3}(T_{in})}{u_{dis,3}(T_{in,eff})} \frac{u_{dis,3}(T_{in,eff})}{u_{1-\alpha,bot}(T_{1-\alpha}, Y_{1-\alpha})} u_{1-\alpha,bot}(T_{1-\alpha}, Y_{1-\alpha}). \tag{7.136}$$

Using the inlet gas throttling factor $\omega_{3,in} = u_{dis,3}/u_{mwf}$ (Eq. 7.57), the definition of gas density (Eq. 7.31), and the criterion of the non-isothermal minimal-Wurster-fluidization limit (Eq. 7.135), the inlet gas velocity of non-isothermal minimal Wurster fluidization is changed to this form:

$$u_{mwf}(T_{in}, Y_{in}) = \frac{1}{\omega_{3,in}} \frac{T_{in}[\mathrm{K}]}{T_{in,eff}[\mathrm{K}]} \frac{T_{in,eff}[\mathrm{K}]}{T_{1-\alpha}[\mathrm{K}]} \frac{\tilde{M}_{vap} + Y_{in}\tilde{M}_{air}}{\tilde{M}_{vap} + Y_{1-\alpha}\tilde{M}_{air}} u_{mf}(T_{1-\alpha}, Y_{1-\alpha}, d, \rho_p). \tag{7.137}$$

Therein, the effect of flow separation by the distributor plate is included by velocity ratio $\omega_{3,in}$. The temperature ratios in Eq. 7.137 are substituted by the *gas velocity reduction factor of heat losses* $\Phi_{u,T,dis}$ with

$$\Phi_{u,T,dis} = \frac{T_{in,eff}[\mathrm{K}]}{T_{in}[\mathrm{K}]} \tag{7.138}$$

and by the *gas velocity reduction factor of evaporation cooling* $\Phi_{u,T,eva}$ with

$$\Phi_{u,T,eva} = \frac{T_{1-\alpha}[\mathrm{K}]}{T_{in,eff}[\mathrm{K}]}. \tag{7.139}$$

At this, the temperatures of Eq. 7.138 and Eq. 7.139 have to be given in Kelvin, since they are derived from the gas density equation (Eq. 7.31). Additionally, the *gas velocity enhancement factor of released water vapor* $\Phi_{u,Y,eva}$ is introduced with

$$\Phi_{u,Y,eva} = \frac{\tilde{M}_{vap} + Y_{1-\alpha}\tilde{M}_{air}}{\tilde{M}_{vap} + Y_{in}\tilde{M}_{air}}. \tag{7.140}$$

Inserted into Eq. 7.137, the inlet gas velocity of non-isothermal minimal Wurster fluidization is rewritten by:

$$u_{mwf}(T_{in}, Y_{in}) = \frac{1}{\omega_{3,in}\Phi_{u,T,dis}\Phi_{u,T,eva}\Phi_{u,Y,eva}} u_{mf}(T_{1-\alpha}, Y_{1-\alpha}). \tag{7.141}$$

The dimensionless factors of Eq. 7.141 are summarized by the substituent K_{mwf}:

$$K_{mwf} = \frac{1}{\omega_{3,in}\Phi_{u,T,dis}\Phi_{u,T,eva}\Phi_{u,Y,eva}}. \tag{7.142}$$

The corresponding dimensionless inlet gas velocity is obtained by putting Eqs. 7.141 and 7.142 into Eq. 7.129:

$$\xi_{mwf} = \frac{u_{mwf}(T_{in}, Y_{in})/u_{mf,ref} - 1}{f_{rn,ref} - 1} = \frac{K_{mwf}u_{mf}(T_{1-\alpha}, Y_{1-\alpha})/u_{mf,ref} - 1}{f_{rn,ref} - 1}. \tag{7.143}$$

It turns out from Eqs. 7.141 and 7.143 that neither the inlet gas velocity of non-isothermal minimal Wurster fluidization nor its corresponding dimensionless inlet gas velocity can be calculated by closed solutions, as the effective inlet gas temperature and the thermodynamic state properties of the drying zone process gas are functions of the inlet gas velocity: $\{T_{in,eff}, T_{1-\alpha}, Y_{1-\alpha}\} = \mathrm{f}(u_{in} = u_{mwf})$. The process gas conditions depend also on further parameters such as the cross-section area of the process gas inlet $A_{app,0}$, the water spray rate $\dot{M}_w$, and the drying potential of the spray zone outlet gas $\eta_{dry,1-\alpha,top}$:

$$\begin{pmatrix} T_{1-\alpha} \\ Y_{1-\alpha} \end{pmatrix} = \mathrm{f}(u_{mwf} = u_{in}). \tag{7.144}$$

Consequently, the gas velocity reduction factor of heat losses $\Phi_{u,T,dis}$, the gas velocity reduction factor of evaporation cooling $\Phi_{u,T,eva}$, and the gas velocity enhancement factor of released water vapor $\Phi_{u,Y,eva}$ are also functions of the inlet gas velocity:

$$\begin{pmatrix} \Phi_{u,T,dis} \\ \Phi_{u,T,eva} \\ \Phi_{u,Y,eva} \end{pmatrix} = \mathrm{f}(u_{mwf} = u_{in}). \tag{7.145}$$

Furthermore, the *overall gas velocity correction factor of evaporation* $\Phi_{u,eva}$ can be defined by

$$\Phi_{u,eva} = \Phi_{u,T,eva}\Phi_{u,Y,eva}, \tag{7.146}$$

wherein, the gas velocity reduction factor of evaporation cooling $\Phi_{u,T,eva}$ and the gas velocity enhancement factor of evaporated water $\Phi_{u,Y,eva}$ are summarized. The range of values of the three velocity correction factors of evaporation $\Phi_{u,T,eva}$, $\Phi_{u,Y,eva}$, and $\Phi_{u,eva}$ are later presented for different inlet gas temperatures and drying potentials of the drying zone in Figure 8.8. In the Mollier-diagram of the TZC-model, Figure 7.1 b, the isothermal flow separation step ($\omega_{2,3}$) lies on point *1*, while $\Phi_{u,T,dis}$ represents the (*1-2*)-line and $\Phi_{u,eva}$ the (*2-2′*)-line.

Limits of the gas velocity correction factors

In adiabatic systems, the gas velocity reduction factor of heat losses $\Phi_{u,T,dis}$ can be set to unity. It also converges to unity for non-adiabatic systems with infinitely large cross-section area $A_{app,0}$

$$\lim_{A_{app,0}\to\infty}\big(\Phi_{u,T,dis}\big) = 1 \tag{7.147}$$

or for infinitely large inlet gas velocities u_{in}

$$\lim_{u_{in}\to\infty}\big(\Phi_{u,T,dis}\big) = 1. \tag{7.148}$$

That means that the error of neglected heat losses is lower for bigger granulators and for larger and heavier particles of bed material. The gas velocity reduction factor of evaporation cooling $\Phi_{u,T,eva}$ and the gas velocity enhancement factor of released water vapor $\Phi_{u,Y,eva}$ approach unity for vanishing water spray rates $\dot{M}_w$ or infinitely large cross-sectional areas of the process chamber bottom $A_{app,0}$. Hence, the limit of these factors is unity for vanishing area-specific water spray rates $\dot{m}_w = \dot{M}_w/A_{app,0}$:

$$\lim_{\dot{m}_w\to 0}\begin{pmatrix}\Phi_{u,T,eva}\\ \Phi_{u,Y,eva}\end{pmatrix} = \begin{pmatrix}1\\ 1\end{pmatrix}. \tag{7.149}$$

In the present thesis, the definition of the inlet gas velocity of non-isothermal minimal fluidization is derived for Wurster granulators (u_{mwf}), but it can also be used for spray granulation with overall homogeneous fluidization (e.g., top-spray), whereat the throttling factor $\omega_{3,in}$ becomes unity.

7.10.2 Process-gas-saturation limit

The process-gas-saturation limit (symbolized here by u_{sat}) is defined as the point of inlet gas velocity u_{in}, at which the process gas of the drying zone becomes saturated, which means that the associated drying potential becomes zero for the given process parameters ($\eta_{dry,1-\alpha} = 0$):

$$u_{sat} \coloneqq u_{in}\big(\eta_{dry,1-\alpha}(u_{in}, T_{in}, Y_{in}, \dot{M}_w, A_{app,0}, \varphi_{dis,3}, \omega_{3,in}, \eta_{dry,\alpha,top}, ...) = 0\big). \tag{7.150}$$

The saturation state (T_{sat} and Y_{sat}) of the drying zone gas depends on many process characteristics such as the thermodynamic state of the inlet gas (T_{in} and Y_{in}), the water spray rate $\dot{M}_w$, the cross-section area of the process gas inlet $A_{app,0}$, and the flow separation characteristics of the distributor plate ($\varphi_{dis,3}$, $\omega_{3,in}$). The process-gas-saturation limit can also be described in terms of inlet gas volume flow rate $\dot{V}_{sat} = A_{app,0}u_{sat}$, inlet gas mass flow rate $\dot{M}_{sat} = \rho_{g,in}\dot{V}_{sat}$, or dimensionless inlet gas velocity ξ_{sat}. In the following, an equation describing the minimal inlet gas velocity of process-gas saturation for Wurster fluidization is derived, which starts from the overall mass balance of water. The overall mass balance of water ($\dot{M}_w = \dot{M}_{eva,\alpha} + \dot{M}_{eva,1-\alpha}$) can be written as:

$$\dot{M}_w = \dot{M}_{g,\alpha,dry}\big(Y_{\alpha,top} - Y_{in}\big) + \dot{M}_{g,1-\alpha,dry}\big(Y_{sat}(T_{in,eff}) - Y_{in}\big). \tag{7.151}$$

The dry mass flow rates of Eq. 7.151 can be replaced by $\dot{M}_{g,\alpha,dry} = (\dot{M}_{dis,2,dry} + \dot{M}_{g,noz,dry})$ for the spray zone term and by $\dot{M}_{g,1-\alpha,dry} = \dot{M}_{dis,3,dry}$ for the drying zone term. By this, the nozzle flow rates (water spray rate and nozzle air rate) can be separated and taken to the left-hand side:

$$\dot{M}_w - \dot{M}_{g,noz,dry}\big(Y_{\alpha,top} - Y_{in}\big) = \dot{M}_{dis,2,dry}\big(Y_{\alpha,top} - Y_{in}\big) + \dot{M}_{dis,3,dry}\big(Y_{sat}(T_{in,eff}) - Y_{in}\big). \tag{7.152}$$

Division of Eq. 7.152 by the dry mass flow rate of the inlet gas ($\dot{M}_{sat,dry} = \dot{M}_{sat}/(1+Y_{in})$) and division by the specific drying capacity of the effective inlet gas temperature ($Y_{sat}(T_{in,eff}) - Y_{in}$) lead to the following form of the overall water mass balance:

$$\frac{\dot{M}_w}{\dot{M}_{sat,dry}} \frac{1}{Y_{sat}(T_{in,eff}, Y_{in}) - Y_{in}} - \frac{\dot{M}_{g,noz,dry}}{\dot{M}_{sat,dry}} \frac{Y_{\alpha,top} - Y_{in}}{Y_{sat}(T_{in,eff}, Y_{in}) - Y_{in}} = \frac{\dot{M}_{dis,2,dry}}{\dot{M}_{sat,dry}} \frac{Y_{\alpha,top} - Y_{in}}{Y_{sat}(T_{in,eff}) - Y_{in}} + \frac{\dot{M}_{dis,3,dry}}{\dot{M}_{sat,dry}}. \tag{7.153}$$

By replacing the inlet gas mass flow rate of the process-gas-saturation limit with $\dot{M}_{sat,dry} = \rho_g A_{app,0} u_{sat}/(1+Y_{in})$ and inserting a unity quotient whose numerator and denominator are each given by the reference elutriation point ($u_{elu,ref}/u_{elu,ref}$), the first term of the left-hand side of Eq. 7.153 can firstly be changed to:

$$\frac{\dot{M}_w}{\dot{M}_{sat,dry}} \frac{1}{Y_{sat}(T_{in,eff}, Y_{in}) - Y_{in}} = \frac{u_{elu,ref}}{u_{sat}(T_{in}, Y_{in})} \frac{\dot{M}_w(1+Y_{in})}{\rho_{g,in} A_{app,0} u_{elu,ref} \big(Y_{sat}(T_{in,eff}, Y_{in}) - Y_{in}\big)}, \tag{7.154}$$

and then be expressed by means of the dimensionless water spray rate $\dot{\mu}_w$ (Eq. 7.130):

$$\frac{\dot{M}_w}{\dot{M}_{sat,dry}} \frac{1}{Y_{sat}(T_{in,eff}) - Y_{in}} = \frac{u_{elu,ref}}{u_{sat}(T_{in}, Y_{in})} \frac{Y_{sat,ref} - Y_{in}}{Y_{sat}(T_{in,eff}, Y_{in}) - Y_{in}} \dot{\mu}_w. \tag{7.155}$$

The dry mass flow rate ratio of nozzle air to inlet gas $\dot{M}_{g,noz,dry}/\dot{M}_{sat,dry}$ equals the ratio of total mass flow rates of nozzle air to inlet gas $\dot{M}_{g,noz}/\dot{M}_{sat}$. This ratio can be related to the dimensionless nozzle air rate $\dot{\mu}_{g,noz}$ (Eq. 7.131) according to:

$$\frac{\dot{M}_{g,noz,dry}}{\dot{M}_{sat,dry}} = \frac{\dot{M}_{g,noz}}{\dot{M}_{sat}} = \frac{u_{elu,ref}}{u_{sat}(T_{in}, Y_{in})} \frac{\dot{M}_{g,noz}}{\rho_g A_{app,0} u_{elu,ref}} = \frac{u_{elu,ref}}{u_{sat}(T_{in}, Y_{in})} \dot{\mu}_{g,noz}. \tag{7.156}$$

Furthermore, the drying capacity reduction factor of heat losses $\Theta_{Y,dis}$ and the drying capacity reduction factor of nozzle gas injection $\Theta_{Y,noz}$ are introduced with:

$$\Theta_{Y,dis} = \frac{Y_{sat}(T_{in,eff}, Y_{in}) - Y_{in}}{Y_{sat,ref} - Y_{in}}, \tag{7.157}$$

$$\Theta_{Y,noz} = \frac{Y_{sat}(T_{\alpha,bot}, Y_{in}) - Y_{in}}{Y_{sat}(T_{in,eff}, Y_{in}) - Y_{in}}. \tag{7.158}$$

The term $(Y_{\alpha,top} - Y_{in})/(Y_{sat}(T_{in,eff}, Y_{in}) - Y_{in})$ from Eq. 7.153 can be factorized by the drying capacity reduction factor of nozzle gas injection $\Theta_{Y,noz}$ and saturation degree of the spray zone outlet $(1 - \eta_{dry,\alpha,top})$ via:

$$\frac{Y_{\alpha,top} - Y_{in}}{Y_{sat}(T_{in,eff}, Y_{in}) - Y_{in}} = \frac{Y_{sat}(T_{\alpha,bot}, Y_{in}) - Y_{in}}{Y_{sat}(T_{in,eff}, Y_{in}) - Y_{in}} \frac{Y_{\alpha,top} - Y_{in}}{Y_{sat}(T_{\alpha,bot}, Y_{in}) - Y_{in}} = \Theta_{Y,noz}(1 - \eta_{dry,\alpha,top}). \tag{7.159}$$

The dry mass flow rate ratios ($\dot{M}_{dis,i,dry}/\dot{M}_{sat,dry}$) of the annular distributor plate sections to the inlet gas on the right-hand side of Eq. 7.153 can be substituted with the mass fraction $\Omega_{i,in}$ by Eq. 7.59 for $i \in \{2,3\}$:

$$\frac{\dot{M}_{dis,2,dry}}{\dot{M}_{sat,dry}} = \frac{\dot{M}_{dis,2}}{\dot{M}_{sat}} = \varphi_{dis,2}\omega_{2,in} = \Omega_{2,in}, \tag{7.160}$$

$$\frac{\dot{M}_{dis,3,dry}}{\dot{M}_{sat,dry}} = \frac{\dot{M}_{dis,3}}{\dot{M}_{sat}} = \varphi_{dis,3}\omega_{3,in} = \Omega_{3,in}. \tag{7.161}$$

Putting Eqs. 7.155 to 7.160 into Eq. 7.153, the minimal inlet gas velocity of process-gas saturation is formulated in terms of the reference elutriation point $u_{elu,ref}$ and several dimensionless characteristics with

$$u_{sat}(T_{in}, Y_{in}) = u_{elu,ref} \frac{\dot{\mu}_w - \Theta_{Y,dis}\Theta_{Y,noz}(1 - \eta_{dry,\alpha,top})\dot{\mu}_{g,noz}}{\Theta_{Y,dis}\big(\Theta_{Y,noz}(1 - \eta_{dry,\alpha,top})\Omega_{2,in} + \Omega_{3,in}\big)}, \tag{7.162}$$

which takes into account size and density of particles, inlet gas conditions, chamber size, distributor plate design, heat losses, spraying of water, injection of nozzle air, and spray zone evaporation. The drying capacity reduction factor of heat losses $\Theta_{Y,dis}$, the drying capacity reduction factor of nozzle gas injection $\Theta_{Y,noz}$, the drying potential at the spray zone top $\eta_{dry,\alpha,top}$, and the inlet gas split fractions $\Omega_{2,in}$ and $\Omega_{3,in}$ can be summarized in a prefactor of the dimensionless water spray rate $K_{sat,w}$ with

$$K_{sat,w} = \frac{1}{\Theta_{Y,dis}\big(\Theta_{Y,noz}(1-\eta_{dry,\alpha,top})\Omega_{2,in}+\Omega_{3,in}\big)} \tag{7.163}$$

and another prefactor of the dimensionless nozzle air rate $K_{sat,noz}$ with

$$K_{sat,noz} = \frac{\Theta_{Y,noz}(1-\eta_{dry,\alpha,top})}{\Theta_{Y,dis}\big(\Theta_{Y,noz}(1-\eta_{dry,\alpha,top})\Omega_{2,in}+\Omega_{3,in}\big)}. \tag{7.164}$$

The dimensionless inlet gas velocity of process-gas saturation follows from the general definition in Eq. 7.129 to:

$$\xi_{sat} \coloneqq \frac{u_{sat}(T_{in},Y_{in})/u_{mf,ref}-1}{f_{rn,ref}-1}. \tag{7.165}$$

Inserting the inlet gas velocity of process-gas saturation in Eq. 7.162, and the substitutes of Eqs. 7.163 and 7.164 into Eq. 7.165, the dimensionless inlet gas velocity of process-gas saturation ξ_{sat} ensues to:

$$\xi_{sat} = \frac{f_{rn,ref}(K_{sat,w}\dot{\mu}_w - K_{sat,noz}\dot{\mu}_{noz})-1}{f_{rn,ref}-1}. \tag{7.166}$$

As shown in Section 7.4, the mass fractions of sectional process gas flow to the inlet gas flow are independent from the inlet gas velocity ($\Omega_{i,in} \neq \mathrm{f}(u_{in})$) for both the second and the third distributor plate section ($i \in \{2,3\}$). But, the mass fraction of nozzle gas injection flow to inlet gas flow and the drying capacity reduction factors, $\Theta_{Y,dis}$ and $\Theta_{Y,noz}$, depend on the inlet gas velocity u_{in}:

$$\begin{pmatrix}\Theta_{Y,dis}\\ \Theta_{Y,noz}\end{pmatrix} = \mathrm{f}(u_{sat}=u_{in}). \tag{7.167}$$

As a conclusion, the minimal inlet gas velocity of process-gas saturation u_{sat} and its corresponding dimensionless equivalent ξ_{sat} must be determined by iterations. However, an iterative calculation of the process-gas-saturation limit can be avoided by approximate solutions under certain conditions, as shown in Section 7.11.4.

7.10.3 Wurster-tube-exceedance limit

In practical Wurster granulation processes, the fluidized bed in the drying zone should only expand to a lower area of the Wurster tube, so that the dimensionless bed height of Eq. 7.133 is significantly smaller than unity ($\Phi_{h,1-\alpha} \ll 1$). Expansion to the upper opening of the riser tube, which is characterized by a dimensionless bed height of unity ($\Phi_{h,1-\alpha}=1$), or even higher beds ($\Phi_{h,1-\alpha}>1$), should be avoided in any case to ensure process stability. For this purpose, the here so-called Wurster-tube-exceedance limit is introduced. It shall be represented by the inlet gas velocity u_{exc} and the corresponding dimensionless inlet gas velocity ξ_{exc}. The inlet gas volume flow rate ($\dot{V}_{exc}$) or mass flow rate ($\dot{M}_{exc}$) are further possible quantities, by means of which the Wurster-tube-exceedance limit can be formulated. The inlet gas velocity of this limit is defined by that value of inlet gas velocity, for which the dimensionless bed height of the drying zone becomes unity ($\Phi_{h,1-\alpha}=1$) with all other given process parameters such as inlet gas temperature T_{in}, inlet gas moisture content Y_{in}, water spray rate $\dot{M}_w$, bed mass M_{bed}, chamber bottom cross-section $A_{app,0}$, and the inlet gas throttling factor $\omega_{3,in}$:

$$u_{exc} \coloneqq u_{in}(\Phi_{h,1-\alpha}(u_{in},T_{in},Y_{in},\dot{M}_w,M_{bed},A_{app,0},\omega_{3,in},\eta_{dry,\alpha,top},...)=1). \tag{7.168}$$

The corresponding dimensionless inlet gas velocity ξ_{exc} follows from Eqs. 7.129 and 7.168 to:

$$\xi_{exc} = \frac{u_{exc}(T_{in},Y_{in})/u_{mf,ref}-1}{f_{rn,ref}-1}. \tag{7.169}$$

The parameters of the Wurster-tube-exceedance point u_{exc} and ξ_{exc} are later used as the upper limit of the parameter setting in the sensitivity analysis study of the TZC-model in Section 8.2. However, the

characteristics of Eqs. 7.168 and 7.169 must be calculated iteratively, as described in more detail in Section 8.2.1. But, when assuming the entire system as isothermal and the total bed to be situated in the drying zone, an analytical approximation method for the Wurster-tube-exceedance limit can be derived, which is continued in Section 7.11.5.

7.10.4 Critical water spray rate and its dimensionless equivalent

The inlet gas velocities of non-isothermal minimal Wurster fluidization u_{mwf} and process-gas saturation u_{sat} define a lower process parameter limit, respectively. Depending on other parameters (e.g., T_{in}, Y_{in}, and $\dot{M}_w$), one of these two quantities is greater, and thus, determines the absolute lower limit of the inlet gas velocity. For example, the inlet gas velocity of the process-gas saturation is equal to zero, when no water is sprayed into the system (see Eq. 7.162 with $\dot{\mu}_w = 1$ and $\eta_{dry,\alpha,top} = 1$), which is definitely less than that of the minimal Wurster fluidization of Eq. 7.141:

$$u_{sat}(\dot{M}_w = 0) = 0 < u_{mwf}(\dot{M}_w = 0). \tag{7.170}$$

However, the $u_{sat}(\dot{M}_w)$-function increases strongly in contrast to the $u_{mwf}(\dot{M}_w)$-function, which is also shown later in Section 8.3 for adiabatic conditions and under negligence of spray zone evaporation. Therefore, the u_{sat}-limit exceeds the u_{mwf}-limit already at low water spray rates. This intercept shall to be characterized by the here so-called critical water spray rate (symbolized by $\dot{M}_{w,cr}$):

$$u_{sat}(\dot{M}_{w,cr}) = u_{mwf}(\dot{M}_{w,cr}). \tag{7.171}$$

The critical point of Eq. 7.171 can also be expressed by means of the corresponding dimensionless inlet gas velocities (ξ_{sat} and ξ_{mwf}) and the critical dimensionless water spray rate $\dot{\mu}_{w,cr}$:

$$\xi_{sat}(\dot{\mu}_{w,cr}) = \xi_{mwf}(\dot{\mu}_{w,cr}). \tag{7.172}$$

By inserting Eqs. 7.166 and 7.143 into Eq. 7.172, the critical dimensionless water spray rate is formulated with:

$$\dot{\mu}_{w,cr} = \frac{K_{mwf}}{K_{sat,w}} \frac{u_{mf}\big(T_{sat}(T_{in,eff}, Y_{in}), Y_{sat}(T_{in,eff}, Y_{in})\big)}{u_{elu,ref}} + \frac{K_{sat,noz}}{K_{sat,w}} \dot{\mu}_{noz}. \tag{7.173}$$

The critical dimensionless water spray rate $\dot{\mu}_{w,cr}$ can only be determined by iterations, since the substitutes K_{mwf}, $K_{sat,w}$, and $K_{sat,noz}$ depend on the inlet gas velocity u_{in}. A closed solution for the critical dimensionless water spray rate can be derived as approximation for an adiabatic system under negligence of spray zone evaporation, which is shown below in Section 7.11.6.

7.11 Approximate solutions for process limits

Diverse analytical calculation methods for the process limits and the critical water spray rate from Section 7.10 are presented in the following. These include

- the minimal-Wurster-fluidization limit of isothermal systems in Section 7.11.1,
- the minimal-Wurster-fluidization limit of adiabatic systems derived from the drying potential of the drying zone process gas (symbolized there by $\eta_{dry,1-\alpha,ad}$, predefined with $\eta_{dry,1-\alpha,ad} \in [0,1]$) in Section 7.11.2,
- the minimal-Wurster-fluidization limit of adiabatic systems with $\eta_{dry,\alpha,top} = 1$ derived from the drying potential of the drying zone process gas (symbolized there by $\eta^*_{dry,1-\alpha,ad}$, predefined with $\eta^*_{dry,1-\alpha,ad} \in [0,1]$) in Section 7.11.3,
- the process-gas-saturation limit of adiabatic systems with $\eta_{dry,\alpha,top} = 1$ in Section 7.11.4,
- the Wurster-tube-exceedance limit of isothermal systems with $\alpha_m = 0$ in Section 7.11.5, and
- the critical water spray rate of adiabatic systems with $\eta_{dry,\alpha,top} = 1$ in Section 7.11.6,

in which $\eta_{dry,\alpha,top} = 1$ indicates that spray zone evaporation is neglected and $\alpha_m = 0$ that the entire bed mass is assumed to be situated in the drying zone. In isothermal systems neither heat losses occur nor water is injected. Consequently, the relative temperature is defined with zero ($\Theta_{loss} = 0$), the influence of evaporation cooling and increase of mass flow rate by released water vapor on process gas velocity does not have to be considered, and the gas velocity reduction factor of heat losses $\Phi_{u,T,dis}$, the gas velocity reduction factor of evaporation cooling $\Phi_{u,T,eva}$, the gas velocity enhancement factor by intake of evaporated water $\Phi_{u,Y,eva}$, and the overall velocity correction factor of evaporation $\Phi_{u,eva}$ are given with unity:

$$\Phi_{u,T,dis} = \Phi_{u,T,eva} = \Phi_{u,Y,eva} = \Phi_{u,eva} = 1 \qquad \text{, for isothermal systems,} \tag{7.174}$$

and so do the drying potentials of the centers and outlets of the spray zone and drying zone too:

$$\eta_{dry,\alpha} = \eta_{dry,\alpha,top} = \eta_{dry,1-\alpha} = \eta_{dry,1-\alpha,top} = 1 \qquad \text{, for isothermal systems.} \tag{7.175}$$

The assumption of an entirely adiabatic process chamber only implies a relative temperature drop of zero and a gas velocity reduction factor by heat losses of unity:

$$\Phi_{u,T,dis}(\Theta_{loss} = 0) = 1 \qquad \text{, for adiabatic systems.} \tag{7.176}$$

Changes in process gas properties by evaporation have to be taken into account for adiabatic systems, when water is sprayed ($\dot{M}_w > 0$). An adiabatic implementation of the two-zone continuum model with a water spray rate of zero $\dot{M}_w = 0$ conforms with the isothermal case. The neglect of heat losses to the environment is particularly well justified for large process chambers, high gas velocities, or apparatuses with insulated walls. The temperature measurements presented in Appendix C.6.2, which were carried out with the experimental setting of Figure 9.5 b), have shown that the drying potential of the spray zone outlet gas $\eta_{dry,\alpha,top}$ approaches unity for higher inlet gas temperatures. In most of these experiments, drying potentials of the spray zone outlet gas larger than 0.9 were obtained, which supports the assumption of negligible evaporation processes in the spray zone.

7.11.1 Isothermal minimal-Wurster-fluidization limit

The characteristic minimal fluidization velocities of drying zone and inlet gas conditions are equal for isothermal systems:

$$u_{mf}(T_{1-\alpha}, Y_{1-\alpha}) = u_{mf}(T_{in}, Y_{in}) = u_{mf,ref} \qquad \text{, for isothermal systems.} \tag{7.177}$$

Based on Eqs. 7.141, 7.174, and 7.177, the inlet gas velocity of isothermal minimal-Wurster fluidization $u_{mwf,iso}$ is obtained in the following simple form

$$u_{mwf,iso} = \frac{1}{\omega_{3,in}} u_{mf,ref}, \tag{7.178}$$

and its corresponding dimensionless inlet gas velocity $\xi_{mwf,iso}$ follows by Eqs. 7.178 and 7.129 to:

$$\xi_{mwf,iso} = \frac{\frac{1}{\omega_{3,in}} - 1}{f_{rn,ref} - 1}. \tag{7.179}$$

The isothermal process limit of minimal-Wurster-fluidization is used later in Section 8.2.3 as lower limit of the parameter setting for the sensitivity analysis of the isothermal implementation of the two-zone continuum model. The inlet gas velocity reduction factor $\omega_{3,in}$ only depends on the distributor plate design, as mentioned before. It can be calculated by Eq. 7.57 with $i = 3$, which is for example shown in Section 8.1.

7.11.2 Adiabatic minimal-Wurster-fluidization limit

Functional relationships

The inlet gas velocity of the adiabatic minimal-Wurster-fluidization limit $u_{mwf,ad}$ and the corresponding dimensionless inlet gas velocity $\xi_{mwf,ad}$ are derived from Eqs. 7.141 to 7.143 with Eqs. 7.146 and 7.176 to:

$$u_{mwf,ad} = \frac{1}{\omega_{3,in}\Phi_{u,eva,ad}} u_{mf}(T_{1-\alpha}, Y_{1-\alpha}), \tag{7.180}$$

$$\xi_{mwf,ad} = \frac{\frac{1}{\omega_{3,in}\Phi_{u,eva,ad}} \frac{u_{mf}(T_{1-\alpha}, Y_{1-\alpha})}{u_{mf,ref}} - 1}{f_{rn,ref} - 1}. \tag{7.181}$$

Therein, the velocity correction factor of evaporation $\Phi_{u,eva,ad}$ and the characteristic minimal fluidization velocity of the drying zone ($u_{mf,1-\alpha,ad} = u_{mf}(T_{1-\alpha}, Y_{1-\alpha})$) are determined by the thermodynamic state of the drying zone process gas, and the latter in turn by the inlet gas parameters ($u_{in} \coloneqq u_{mwf,ad}$, T_{in}, and Y_{in}), the water spray rate $\dot{M}_w$, the drying potential of the spray zone outlet $\eta_{dry,\alpha,top}$, and the drying gas mass fractions $\Omega_{3,in}$:

$$\{\Phi_{u,eva,ad}, u_{mf,1-\alpha,ad}\} = \mathrm{f}\big(\{T_{1-\alpha}, Y_{1-\alpha}\} = \mathrm{f}(u_{in} \coloneqq u_{mwf,ad}, T_{in}, Y_{in}, \dot{M}_w, \Omega_{3,in}, \eta_{dry,\alpha,top})\big). \tag{7.182}$$

The drying potential of the drying zone process gas is fixed by the same properties given on the right-hand side of Eq. 7.182:

$$\eta_{dry,1-\alpha,ad} = \mathrm{f}(u_{in}, T_{in}, Y_{in}, \dot{M}_w, \Omega_{3,in}, \eta_{dry,\alpha,top}). \tag{7.183}$$

The adiabatic minimal-Wurster-fluidization limit is only needed to be considered for undercritical water spray rates larger than zero: $0 < \dot{M}_w < \dot{M}_{w,cr,ad}$; under which conditions the drying potential of the drying zone process gas is larger than zero and less than unity

$$0 < \eta_{dry,1-\alpha,ad}(0 < \dot{M}_w < \dot{M}_{w,cr,ad}) < 1, \tag{7.184}$$

and the thermodynamic state of the drying zone process gas ($T_{1-\alpha}$ and $Y_{1-\alpha}$) cannot be a priori calculated for the predefined process parameters (e.g., T_{in}, Y_{in}, $\dot{M}_w$, $\eta_{dry,\alpha,top}$, and $\Omega_{3,in}$), so that the adiabatic minimal-Wurster-fluidization limit still has to be determined iteratively with the TZC-model (only Sections 7.1 to 7.5).

Limiting cases of non-spraying and critical water spray rates

There are two limiting cases for the adiabatic minimal-Wurster-fluidization point, which can be calculated without any help of iterations. One is given for a water spray rate of zero (non-spraying conditions: $\dot{M}_w = 0$), where the drying potential of the drying zone process gas stays unity

$$\eta_{dry,1-\alpha,ad}(\dot{M}_w = 0) = 1, \tag{7.185}$$

and one is defined by the adiabatic critical water spray rate ($\dot{M}_w = \dot{M}_{w,cr,ad}$, see also Section 7.11.6), where the process gas of the drying zone gets saturated and the associated drying potential is reduced to zero:

$$\eta_{dry,1-\alpha,ad}(\dot{M}_w = \dot{M}_{w,cr,ad}) = 0. \tag{7.186}$$

As already mentioned, the TZC-model of adiabatic systems without water injection agrees with the isothermal version of the model, where $T_{1-\alpha} = T_{in}$ and $Y_{1-\alpha} = Y_{in}$. As a result, if there is no water injection, the overall velocity correction factor of evaporation is unity and the adiabatic minimal-Wurster-fluidization limit is equal to the isothermal minimal-Wurster-fluidization limit of Eqs. 7.178 and 7.179:

$$\Phi_{u,eva,ad}\big(\eta_{dry,1-\alpha,ad}(\dot{M}_w = 0) = 1\big) = 1, \tag{7.187}$$

$$u_{mwf,ad}\big(\eta_{dry,1-\alpha,ad}(\dot{M}_w = 0) = 1\big) = u_{mwf,iso}, \tag{7.188}$$

$$\xi_{mwf,ad}\big(\eta_{dry,1-\alpha,ad}(\dot{M}_w = 0) = 1\big) = \xi_{mwf,iso}. \tag{7.189}$$

The overall velocity correction factor of evaporation at critical water spray rates (symbolized by $\Phi_{u,eva,ad,cr}$) can be derived from Eqs. 7.139, 7.140, and 7.146 with process-gas-saturation conditions, which results in:

$$\begin{aligned}\Phi_{u,eva,ad,cr} &= \Phi_{u,eva,ad}\big(\eta_{dry,1-\alpha}(\dot{M}_w = \dot{M}_{w,cr,ad}) = 0\big) \\ &= \frac{T_{sat,ref}[\mathrm{K}]}{T_{in}[\mathrm{K}]}\,\frac{\tilde{M}_{vap} + Y_{sat,ref}\tilde{M}_{air}}{\tilde{M}_{vap} + Y_{in}\tilde{M}_{air}}.\end{aligned} \tag{7.190}$$

Therein, the saturation temperature T_{sat} and corresponding saturation moisture content Y_{sat} can be estimated by the isenthalpic saturation point given in Section 7.3. The inlet gas velocity of the adiabatic minimal-Wurster-fluidization limit for critical water spray rates and its corresponding dimensionless inlet gas velocity follow from Eqs. 7.180 to 7.181 and 7.190 to:

$$u_{mwf,ad}\big(\eta_{dry,1-\alpha}(\dot{M}_w = \dot{M}_{w,cr,ad}) = 0\big) = \frac{1}{\omega_{3,in}\Phi_{u,eva,ad,cr}}u_{mf}(T_{sat,ref}, Y_{sat,ref}), \tag{7.191}$$

$$\xi_{mwf,ad}\big(\eta_{dry,1-\alpha}(\dot{M}_w = \dot{M}_{w,cr,ad}) = 0\big) = \frac{\frac{1}{\omega_{3,in}\Phi_{u,eva,ad,cr}}\frac{u_{mf}(T_{sat,ref},Y_{sat,ref})}{u_{mf,ref}} - 1}{f_{rn,ref} - 1}. \tag{7.192}$$

After these equations, the drying potential of the spray zone outlet $\eta_{dry,\alpha,top}$ needs not be defined to calculate the adiabatic minimal-Wurster-fluidization limit of saturated process gas conditions in the drying zone.

Domain of the adiabatic minimal-Wurster-fluidization limit

The thermodynamic state variables of the drying zone process gas can be expressed by the lever principle of Eq. 7.120 for adiabatic conditions ($T_{in,eff} = T_{in}$) with:

$$T_{1-\alpha,ad} = T_{sat,ref} + \eta_{dry,1-\alpha}(T_{in} - T_{sat,ref}), \tag{7.193}$$

$$Y_{1-\alpha,ad} = Y_{sat,ref} - \eta_{dry,1-\alpha}(Y_{sat,ref} - Y_{in}). \tag{7.194}$$

The overall velocity correction factor of evaporation follows then from:

$$\Phi_{u,eva,ad} = \frac{T_{1-\alpha,ad}[\mathrm{K}]}{T_{in}[\mathrm{K}]} \frac{\tilde{M}_{vap} + Y_{1-\alpha,ad}\tilde{M}_{air}}{\tilde{M}_{vap} + Y_{in}\tilde{M}_{air}}. \tag{7.195}$$

The adiabatic minimum-Wurster-fluidization point can therefore be calculated without iterations, by applying Eqs. 7.193 to 7.195 first and Eqs. 7.180 to 7.181 second, when the inlet gas temperature T_{in}, the inlet gas moisture content Y_{in}, and the drying potential of the process gas of the drying zone $\eta_{dry,1-\alpha}$ are specified. By this, an entire range of possible inlet gas velocities of the adiabatic minimal-Wurster-fluidization limit can determined for the total domain of the drying potential of the drying zone ($0 \leq \eta_{dry,1-\alpha} \leq 1$), which is as also presented later in Section 8.3.1 for different inlet gas conditions.

7.11.3 Approximate adiabatic minimal-Wurster-fluidization limit

The inlet gas velocity of the approximate adiabatic minimal-Wurster-fluidization limit $u^*_{mwf,ad}$ and its corresponding dimensionless inlet gas velocity $\xi^*_{mwf,ad}$ can be determined for an entire predefined domain of the drying potential of the drying zone process gas (symbolized here by $\eta^*_{dry,1-\alpha,ad}$) from the following equation sequence

$$\eta^*_{dry,1-\alpha,ad} \in [0,1], \tag{7.196}$$

$$T^*_{1-\alpha,ad} = T_{sat,ref} + \eta^*_{dry,1-\alpha,ad}(T_{in} - T_{sat,ref}), \tag{7.197}$$

$$Y^*_{1-\alpha,ad} = Y_{sat,ref} - \eta^*_{dry,1-\alpha,ad}(Y_{sat,ref} - Y_{in}), \tag{7.198}$$

$$\Phi^*_{u,eva,ad} = \frac{T^*_{1-\alpha,ad}[\mathrm{K}]}{T_{in}[\mathrm{K}]} \frac{\tilde{M}_{vap} + Y^*_{1-\alpha,ad}\tilde{M}_{air}}{\tilde{M}_{vap} + Y_{in}\tilde{M}_{air}}, \tag{7.199}$$

$$u^*_{mwf,ad} = \frac{1}{\omega_{3,in}\Phi^*_{u,eva,ad}} u_{mf}(T^*_{1-\alpha,ad}, Y^*_{1-\alpha,ad}), \tag{7.200}$$

$$\xi^*_{mwf,ad} = \frac{\frac{1}{\omega_{3,in}\Phi^*_{u,eva,ad}} \frac{u_{mf}(T^*_{1-\alpha,ad}, Y^*_{1-\alpha,ad})}{u_{mf,ref}} - 1}{f_{rn,ref} - 1}, \tag{7.201}$$

such as described for the adiabatic minimal-Wurster-fluidization limit in the previous section. The difference there to here is that the drying potential of the spray zone outlet gas can have arbitrary values between zero and unity ($0 \leq \eta_{dry,\alpha,top} \leq 1$), whereas it is given with unity ($\eta_{dry,\alpha,top} = 1$) for the approximate adiabatic minimal-Wurster-fluidization limit. The latter can be related to the water spray rate (here symbolized by $\dot{M}^*_{w,ad}$) for the case that $\eta_{dry,\alpha,top} = 1$ by combining the water mass balance Eqs. 7.81, 7.82, 7.85, 7.87, and 7.120, which results in:

$$\begin{aligned} \dot{M}^*_{w,ad} = \dot{M}_{w,ad}(\eta_{dry,\alpha,top} = 1) &= \frac{\Omega_{3,in}\rho_{g,in}\frac{\pi}{4}D^2_{app,0}u^*_{mwf,ad}}{1 + Y_{in}}(Y^*_{1-\alpha,ad} - Y_{in}) \\ &= \frac{\Omega_{3,in}\rho_{g,in}\frac{\pi}{4}D^2_{app,0}u^*_{mwf,ad}}{1 + Y_{in}}\big(Y_{sat,ref} - Y_{in}\big)(1 - \eta^*_{dry,1-\alpha,ad}). \end{aligned} \tag{7.202}$$

The corresponding dimensionless water spray rate (here symbolized by $\dot{\mu}^*_{w,ad}$) ensues from Eqs. 7.130 and 7.202 to:

$$\dot{\mu}^*_{w,ad} = \dot{\mu}_{w,ad}(\eta_{dry,\alpha,top} = 1) = \Omega_{3,in}\frac{u_{mwf,ad}}{u_{elu,ref}}(1 - \eta^*_{dry,1-\alpha,ad}). \tag{7.203}$$

The values of $\dot{\mu}^*_{w,ad}$ reach from zero for $\eta_{dry,1-\alpha} = 1$ to the approximate adiabatic critical dimensionless water spray rate $\dot{\mu}^*_{w,cr,ad}$ of Eq. 7.221 for $\eta_{dry,1-\alpha} = 0$. A direct calculation of the approximate adiabatic

minimal-Wurster-fluidization limit based on a predefined water spray rate $\dot{M}_w$ or dimensionless water spray rate $\dot{\mu}_w$ is not possible without a specified drying potential of the process gas in the drying zone. However, using Eqs. 7.196 to 7.203, spray-rate-dependent process limit curves in terms of the inlet gas velocity ($u^*_{mwf,ad}(\dot{\mu}^*_{w,ad})$) and the dimensionless inlet gas velocity ($\xi^*_{mwf,ad}(\dot{\mu}^*_{w,ad})$) can be created numerically, as shown later in Section 8.3.2.

7.11.4 Approximate adiabatic process-gas-saturation limit

The process-gas-saturation limit of Eqs. 7.162 to 7.166 is simplified for adiabatic conditions ($\Theta_{Y,dis} = 1$) and with negligence of evaporation in the spray zone ($\eta_{dry,\alpha,top} = 1$) to the here so-called approximate adiabatic process-gas-saturation limit. The inlet gas velocity of the approximate adiabatic process-gas-saturation limit $u^*_{sat,ad}$, its corresponding substitution prefactors of the dimensionless water spray rate $K^*_{sat,w,ad}$ and the dimensionless nozzle air rate $K^*_{sat,noz,ad}$, and its corresponding dimensionless inlet gas velocity $\xi^*_{sat,ad}$ ensue then to:

$$u^*_{sat,ad} = u_{sat,ad}(\eta_{dry,\alpha,top} = 1) = \frac{1}{\Omega_{3,in}} \frac{(1 + Y_{in})\dot{M}_w}{\rho_{g,in} \frac{\pi}{4} D^2_{app}(Y_{sat,ref} - Y_{in})}$$
$$= u_{elu,ref} \frac{1}{\Omega_{3,in}} \dot{\mu}_w, \tag{7.204}$$

$$K^*_{sat,w,ad} = K_{sat,w,ad}(\eta_{dry,\alpha,top} = 1) = \frac{1}{\Omega_{3,in}} = \frac{1}{\varphi_{dis,3}\omega_{3,in}}, \tag{7.205}$$

$$K^*_{sat,noz,ad} = K_{sat,noz,ad}(\eta_{dry,\alpha,top} = 1) = 0, \tag{7.206}$$

$$\xi^*_{sat,ad} = \xi_{sat,ad}(\eta_{dry,\alpha,top} = 1) = \frac{f_{rn,ref} \frac{1}{\Omega_{3,in}} \dot{\mu}_w - 1}{f_{rn,ref} - 1}. \tag{7.207}$$

It can be seen that the process-gas-saturation limit increases linearly with the dimensionless water spray rate when the reference elutriation gas velocity is a fixed parameter, which means that, after the definition of the dimensionless water spray rate (Eq. 7.130), the process-gas-saturation limit can be lowered for smaller water spray rates $\dot{M}_w$, larger cross-section areas of the process chamber bottom ($\pi D^2_{app,0}/4$), higher inlet gas temperatures T_{in}, and lower inlet gas moisture contents Y_{in}. Although the reference elutriation gas velocity $u_{elu,ref}$ occurs in Eq. 7.204, the process-gas-saturation limit does not depend on it, as the dimensionless water spray rate by definition is inversely proportional to the reference elutriation gas velocity. It is further visible that higher drying gas mass fractions $\Omega_{3,in}$ can reduce the process-gas-saturation limit. However, this mass ratio should not be too large in order to achieve proper Wurster fluidization conditions, which means higher gas velocities within the Wurster tube. The adiabatic approximate solution of the process-gas-saturation limit can be used for rough estimations of the process parameter setting for Wurster granulation.

7.11.5 Approximate isothermal Wurster-tube-exceedance limit

In the following, the calculation method of the here so-called approximate isothermal Wurster-tube-exceedance limit shall be derived, which does not require to implement the entire presented TZC-model. With the help of Eq. 7.174 and the assumption that the entire bed mass lies in the drying zone ($M_{1-\alpha} = M_{bed} \Leftrightarrow \alpha_m = 0$), the general criterion of the Wurster-tube-exceedance limit from Section 7.10.3 can be simplified to:

$$u^*_{exc,iso} \coloneqq u_{in}\big(\Phi_{h,1-\alpha}(T_{1-\alpha} = T_{in}, Y_{1-\alpha} = Y_{in}, M_{1-\alpha} = M_{bed}) = 1\big). \tag{7.208}$$

The bed height of this limit is given by $H_{1-\alpha,exc,iso} = H_{wt} + L_{wt}$ and the corresponding bed volume $V_{1-\alpha,exc,iso}$ follows from Eq. 7.9 with $H_{1-\alpha,exc,iso}$ as input variable. The dimensionless bed mass μ_{bed} is obtained from Eq. 7.132 with $V_{1-\alpha,max} = V_{1-\alpha,exc,iso}$. The bed porosity of the drying zone $\varepsilon_{1-\alpha,exc,iso}$ can be calculated either with the bed mass, the effective particle density, and the bed volume according to

$$\varepsilon_{1-\alpha,exc,iso} = 1 - \frac{M_{bed}}{\rho_p V_{1-\alpha,exc,iso}}, \tag{7.209}$$

or with the bed porosity of minimal fluidization conditions ε_{mf} (predefined parameter) and the dimensionless bed mass according to

$$\varepsilon_{1-\alpha,exc,iso} = 1 - (1 - \varepsilon_{mf})\mu_{bed}. \tag{7.210}$$

The conical chamber geometry shall be taken into account by means of the so-called cross-sectional expansion factor (symbolized by $\Phi_{a,exc}$), which results from the ratio of the maximum to the minimum cross-sectional area ($A_{1-\alpha,top}$ to $A_{1-\alpha,bot}$) in the drying zone. It can be derived from Eqs. 7.5 to 7.7,

$$\Phi_{a,exc} = \frac{A_{1-\alpha,top}}{A_{1-\alpha,bot}} = \frac{\left(D_{app,0} + \frac{2}{\tan(\gamma_{app})}(H_{wt} + L_{wt})\right)^2 - D_{wt}^2}{D_{app,0}^2 - D_{wt}^2} \tag{7.211}$$

for given chamber characteristics as illustrated in Figure 7.2. The superficial gas velocity decreases with the flow in the drying zone due to the cross-sectional expansion. Under isothermal conditions, the superficial process gas velocities in different locations of the drying zone can be related to the inlet gas velocity of the approximate isothermal Wurster-tube-exceedance limit $u_{exc,iso}^*$, as for instance for the superficial gas velocity of the drying zone bottom $u_{1-\alpha,bot}$ by definition of the inlet gas throttling factor $\omega_{3,in}$

$$u_{1-\alpha,bot} = \omega_{3,in} u_{exc,iso}^*, \tag{7.212}$$

and for the drying zone outlet gas velocity $u_{1-\alpha,top}$ by the definition the cross-sectional expansion factor $\Phi_{a,exc}$ and continuity conditions in the drying zone ($u_{1-\alpha,top} = u_{1-\alpha,bot}/\Phi_{a,exc}$)

$$u_{1-\alpha,top} = \frac{\omega_{3,in}}{\Phi_{a,exc}} u_{exc,iso}^*. \tag{7.213}$$

As explained before, the throttling factor $\omega_{3,in}$ is a parameter depending only on the inflow plate construction and can be specified by Eqs. 7.54, 7.56, and 7.57. For defining the inlet gas velocity of the approximate isothermal Wurster-tube-exceedance limit $u_{exc,iso}^*$ as function of bed porosity at minimal fluidization ε_{mf}, the dimensionless bed μ_{bed}, the cross-sectional expansion factor $\Phi_{a,exc}$, the throttling factor $\omega_{3,in}$ of Eq. 7.57, the reference elutriation velocity $u_{elu,ref}$ of Eq. 7.125, and the reference fluidization range number $f_{rn,ref}$ of Eq. 7.126, the mean value ($\bar{u}_{1-\alpha} \coloneqq \frac{1}{2}(u_{1-\alpha,bot} + u_{1-\alpha,top})$) of the two process gas velocities from Eqs. 7.212 and 7.213 is used:

$$\bar{u}_{1-\alpha} = \omega_{3,in} \frac{\Phi_{a,exc} + 1}{2\Phi_{a,exc}} u_{exc,iso}^*. \tag{7.214}$$

The average velocity of the drying zone $\bar{u}_{1-\alpha}$ of Eq. 7.214 and the bed porosity $\varepsilon_{1-\alpha}$ of Eq. 7.210 (or Eq. 7.209) are assumed to be decisive for the overall bed expansion behavior, their relationship to each other to be defined by the Richardson a. Zaki equation ([50], Eq. 2.130) with the suggestion of Sathiyamoorthy a. Sridhar Rao ([85], Eq. 2.129) for the Richardson-Zaki exponent, which ends up to:

$$\bar{u}_{1-\alpha} = u_{elu,ref} (\varepsilon_{1-\alpha,exc,iso})^{-\ln(f_{rn,ref})/\ln(\varepsilon_{mf})}. \tag{7.215}$$

Combining Eqs. 7.214 and 7.215, the subsequent expressions of the approximate isothermal Wurster-tube-exceedance limit are found: in terms of the inlet gas velocity with

$$u_{exc,iso}^* = u_{elu,ref} \frac{1}{\omega_{3,in}} \frac{2\Phi_{a,exc}}{\Phi_{a,exc} + 1} \left(1 - (1 - \varepsilon_{mf})\mu_{bed}\right)^{-\ln(f_{rn,ref})/\ln(\varepsilon_{mf})} \tag{7.216}$$

and of the dimensionless inlet gas velocity (according to Eq. 7.129) with

$$\xi_{exc,iso}^* = \frac{f_{rn,ref} \frac{1}{\omega_{3,in}} \frac{2\Phi_{a,exc}}{\Phi_{a,exc}+1} \left(1 - (1 - \varepsilon_{mf})\mu_{bed}\right)^{-\ln(f_{rn,ref})/\ln(\varepsilon_{mf})} - 1}{f_{rn,ref} - 1}. \tag{7.217}$$

Later in Section 8.2, the approximate isothermal Wurster-tube-exceedance limit of different process conditions is compared to the non-isothermal Wurster-tube-exceedance limit, which results from the implementation of the entire TZC-model for non-isothermal conditions with a certain amount of the bed mass situated in the drying zone ($\alpha_m > 0$). There, it turns out that the mass fraction of bed particles being in the spray zone α_m approaches zero for high inlet gas velocities around the Wurster-tube-exceedance limit, which supports the assumption in Eq. 7.208 that all of the bed mass is in the drying zone.

7.11.6 Approximate adiabatic critical water spray rate and its dimensionless equivalent

As mentioned above in Section 7.10.4, the critical dimensionless water spray rate $\dot{\mu}_{w,cr}$ can be approximated by a closed solution for adiabatic systems in which no spray zone evaporation takes place ($\eta_{dry,\alpha,top} = 1$).

In this case, the approximated adiabatic critical water spray rate (symbolized by $\dot{M}^*_{w,cr,ad}$) is spoken of. The corresponding dimensionless water spray rate (symbolized by $\dot{\mu}^*_{w,cr,ad}$) follows from Eq. 7.130. The approximate adiabatic critical water spray rate $\dot{M}^*_{w,cr,ad}$ defines the intercept of the approximate adiabatic minimal-Wurster-fluidization limit of the 7.197 to 7.203 with $\eta^*_{dry,1-\alpha,ad} = 0$ and the approximate adiabatic process-gas-saturation limit of Eqs. 7.204 to 7.207:

$$u^*_{mwf,ad}\big(\eta^*_{dry,1-\alpha,ad}(\dot{M}^*_{w,cr,ad}) = 0\big) = u^*_{sat,ad}(\dot{M}^*_{w,cr,ad}), \tag{7.218}$$

$$\xi^*_{mwf,ad}\big(\eta^*_{dry,1-\alpha,ad}(\dot{\mu}^*_{w,cr,ad}) = 0\big) = \xi^*_{sat,ad}(\dot{\mu}^*_{w,cr,ad}). \tag{7.219}$$

These equations can be solved for the approximate adiabatic critical water spray rate $\dot{M}^*_{w,cr,ad}$ and its dimensionless equivalent $\dot{\mu}^*_{w,cr,ad}$ by inserting Eqs. 7.200, 7.201, 7.204, and 7.207 into 7.218 and 7.219. With $\Omega_{3,in} = \varphi_{dis,3}\omega_{3,in}$, they follow to:

$$\dot{M}^*_{w,cr,ad} = \frac{\varphi_{dis,3}}{\Phi_{u,eva,ad,cr}} \frac{\rho_{g,in}\frac{\pi}{4}D^2_{app,0}u_{mf}(T_{sat,ref}, Y_{sat,ref})}{1 + Y_{in}}, \tag{7.220}$$

$$\begin{aligned}\dot{\mu}^*_{w,cr,ad} &= \frac{\varphi_{dis,3}}{\Phi_{u,eva,ad,cr}} \frac{u_{mf}(T_{sat,ref}, Y_{sat,ref})}{u_{elu,ref}} \\ &= \frac{\varphi_{dis,3}}{\Phi_{u,eva,ad,cr}} \frac{1}{f_{rn,ref}} \frac{u_{mf}(T_{sat,ref}, Y_{sat,ref})}{u_{mf,ref}},\end{aligned} \tag{7.221}$$

where the cross-sectional area fraction $\varphi_{dis,3}$ of Eq. 7.40 for $i = 3$, the overall velocity correction factor of evaporation $\Phi_{u,eva,ad,cr}$ of Eq. 7.190, the characteristic minimal fluidization velocity related to the reference saturation point $u_{mf}(T_{sat,ref}, Y_{sat,ref})$ (Eqs. 7.127 and 7.128), and the reference elutriation velocity $u_{elu,ref}$ of Eq. 7.125 are used. The latter can be replaced by the reference minimal fluidization number $f_{rn,ref}$ and the reference minimal fluidization velocity $u_{mf,ref}$ of Eq. 7.124 according Eq. 7.126.

The values of the approximate adiabatic critical dimensionless water spray rate is low for process conditions such as in Hampel's reference case (Section 2.3), as also shown later in Section 8.3.2. The third distributor plate section measures around 85 % of the entire bottom cross-section, see $\varphi_{dis,3}$ in Table 8.1. The values of critical adiabatic overall velocity correction factor of evaporation $\Phi_{u,eva,ad,cr}$ are in a range of nearly 84 to 90 % for inlet gas temperatures from 70 to 110°C according to the right diagram of Figure 8.8 at the saturation point $\eta_{dry,1-\alpha} = 0$. The quotient $\varphi_{dis,3}/\Phi_{u,eva,ad,cr}$ from Eq. 7.221 is therefore in proximity of unity. The reference fluidization range number is significantly larger than unity: $f_{rn,ref} \gg 1$. The characteristic minimal fluidization velocities at saturated gas and inlet gas conditions are also not much different. In summary, according to Eq. 7.221, the approximated adiabatic critical dimensionless water spray rate is well below unity ($\dot{\mu}^*_{w,cr,ad} \ll 1$) for the Wurster equipment used in Hampel's reference case (see Figures C.2 and C.3 and Section 9.2.2).

The approximate adiabatic critical dimensionless water spray rate $\dot{\mu}^*_{w,cr,ad}$ of Eq. 7.221 serves as a quick decision criterion for the prevailing lower process limit of the inlet gas velocity, which can be defined either by the minimal-Wurster-fluidization or by process-gas-saturation depending on the value of the dimensionless water spray rate $\dot{\mu}_w$ to be operated with. When the dimensionless water spray rate is significantly below the critical point ($\dot{\mu}_w < \dot{\mu}^*_{w,cr,ad}$), the minimal-Wurster-fluidization limit has to be considered; whereas in the opposite case ($\dot{\mu}_w > \dot{\mu}^*_{w,cr,ad}$), the minimal inlet gas velocity is determined by the process-gas-saturation limit. If the dimensionless water spray rate is only slightly smaller or larger than the critical dimensionless water spray rate ($\dot{\mu}_w \lesssim \dot{\mu}^*_{w,cr,ad}$ or $\dot{\mu}_w \gtrsim \dot{\mu}^*_{w,cr,ad}$), neglected side effects (heat losses and spray zone evaporation) can lead to incorrect assignment of the dominant process limit. In this case, the values of the two limits are quite close to each other, so that both can serve as a guide measure, because the inlet gas velocities to be used in real terms must be significantly higher anyway to ensure process stability. Further, a general minimal inlet gas velocity (symbolized by $u^*_{min,ad}$) and a general minimal dimensionless inlet gas velocity (symbolized by $\xi^*_{min,ad}$) can be defined by means of the approximate adiabatic critical dimensionless water spray rate $\dot{\mu}^*_{w,cr,ad}$, which conjoins the isothermal minimal-Wurster-fluidization limit ($u_{mwf,iso}$ and $\xi_{mwf,iso}$) of Section 7.11.1, the approximate adiabatic minimal-Wurster-fluidization limit ($u^*_{mwf,ad}$, and $\xi^*_{mwf,ad}$) of Section 7.11.3, and the approximate adiabatic process-gas-saturation limit ($u^*_{sat,ad}$ and $\xi^*_{sat,ad}$) of Section

7.11.4 by the following section-wise functions:

$$u^*_{min,ad} = \begin{cases} u_{mwf,iso} & \text{, for } \dot{M}_w = 0 \\ u^*_{mwf,ad} & \text{, for } 0 < \dot{M}_w < \dot{M}^*_{w,cr,ad}, \text{ with } \dot{M}_w = \dot{M}^*_{w,ad} \\ u^*_{sat,ad} & \text{, for } \dot{M}_w \geq \dot{M}^*_{w,cr,ad} \end{cases}, \tag{7.222}$$

$$\xi^*_{min,ad} = \begin{cases} \xi_{mwf,iso} & \text{, for } \dot{\mu}_w = 0 \\ \xi^*_{mwf,ad} & \text{, for } 0 < \dot{\mu}_w < \dot{\mu}^*_{w,cr,ad}, \text{ with } \dot{\mu}_w = \dot{\mu}^*_{w,ad} \\ \xi^*_{sat,ad} & \text{, for } \dot{\mu}_w \geq \dot{\mu}^*_{w,cr,ad} \end{cases}. \tag{7.223}$$

The criterion of Eqs. 7.222 and 7.223 is used later for the parameter variation analysis of the two-zone continuum model (Section 8.2) and for illustrating the influence of particle size on $\xi^*_{min,ad}$ in Section 8.3.3.

8 Results of the two-zone continuum model of Wurster fluidization

8.1 Characteristics of the distributor plate and isothermal flow separation

As described in Section 7.4.1, the distributor plate of the TZC-model is adapted to the experimental distributor plate employed in the granulation experiments of the present thesis (Section 10.4). The model inflow plate shall consist of three sections of different hole design (indicated by $i \in \{1, 2, 3\}$, see Figure 7.4), while the experimental bottom plate is divided into five differently perforated sections (indicated by $j \in \{\mathrm{A}, \mathrm{B}, \mathrm{C}, \mathrm{D}, \mathrm{E}\}$, see Figure C.3). The specifications of the real bottom plate are given in Table C.2. The distributor plate characteristics which are relevant for the implementation of the TZC-model are listed in Table 8.1. The outer diameter of the first section of the model inflow plate is the same as that of the experimental one ($D_{dis,1} = D_{dis,\mathrm{A}} = 0.03\,\mathrm{m}$). The outer diameter of the second section of the model plate conforms with that of the third section of the real plate and with the Wurster tube diameter ($D_{dis,2} = D_{dis,\mathrm{C}} = D_{wt} = 0.07\,\mathrm{m}$). The outer diameter of the third model plate section equals that of the fifth section of the experimental plate and the diameter of process chamber inlet ($D_{dis,3} = D_{dis,\mathrm{E}} = D_{app,0} = 0.18\,\mathrm{m}$). The area fractions $\varphi_{dis,i}$ of all three model sections are calculated by Eqs. 7.38 and 7.40. The first section of the experimental bottom plate ($j = \mathrm{A}$) is occupied by a nozzle assembly during operation. Hence, this section is not passable for the inlet gas, which is also assumed in the TZC-model. For this reason, further characteristics of the first section of the model distributor plate are not needed to be considered. The characteristics of the annular sections of the model distributor plate, for which $i \in \{2, 3\}$, are derived from the specifications of the experimental distributor plate sections from B to E in the following way. The total numbers of holes in the annular model sections $N_{dis,2}$ and $N_{dis,3}$ ensue from summation of these of the overlapped experimental distributor plate sections:

$$N_{dis,2} = N_{dis,\mathrm{B}} + N_{dis,\mathrm{C}}, \tag{8.1}$$

$$N_{dis,3} = N_{dis,\mathrm{D}} + N_{dis,\mathrm{E}}. \tag{8.2}$$

The sectional hole diameters $d_{dis,2}$ and $d_{dis,3}$ are defined as number-based mean values of the corresponding experimental inflow plate sections according to:

$$d_{dis,2} \coloneqq \frac{N_{dis,\mathrm{B}} d_{dis,\mathrm{B}} + N_{dis,\mathrm{C}} d_{dis,\mathrm{C}}}{N_{dis,\mathrm{B}} + N_{dis,\mathrm{C}}}, \tag{8.3}$$

$$d_{dis,3} \coloneqq \frac{N_{dis,\mathrm{D}} d_{dis,\mathrm{D}} + N_{dis,\mathrm{E}} d_{dis,\mathrm{E}}}{N_{dis,D} + N_{dis,E}}. \tag{8.4}$$

The opening ratios $\Psi_{dis,2}$ and $\Psi_{dis,3}$ follow from Eq. 7.42. The model plate shall have a thickness of $s_{dis} = 3\,\mathrm{mm}$ such as in the real case. The sectional pressure drop coefficients $K_{dis,2}$ and $K_{dis,3}$, and drag coefficients $c_{dis,2}$ and $c_{dis,3}$, are obtained from Eqs. 7.54 and 7.53. The binary velocity split ratio results with $\omega_{2,3} = 5.58$ from Eq. 7.56. This means that the superficial velocity of the gas passing the second section $u_{dis,2}$ is 5.58-times higher than that going through the third section $u_{dis,3}$. The inlet gas acceleration velocity $\omega_{2,in}$ and the inlet gas throttling velocity $\omega_{3,in}$ are calculated via Eq. 7.57. In the present case, the superficial gas velocity of the second section is round 3.63-times larger than the inlet gas velocity and the superficial gas velocity of the third section is only circa 35 % smaller than the inlet gas velocity. The inlet gas split fractions $\Omega_{2,in}$ and $\Omega_{3,in}$ are determined by Eq. 7.60. Thereby, it turns out that, although the cross-sectional area fraction of the third section is much larger with $\varphi_{dis,3} = 84.88\,\%$ than that of the second section with $\varphi_{dis,2} = 12.35\,\%$, only 55.2 % of the inlet gas is flowing through third section due to its lower perforation degree $\Psi_{dis,3} = 4.75\,\%$. The described characteristics of the model distributor plate are constant within the entire sensitivity analysis of the TZC-model.

section number i:			1	2	3
property	symbol	unit			
outer diameter of section i	$D_{dis,i}$	[m]	0.03	0.07	0.18
area fraction of section i	$\varphi_{dis,i}$	[%]	2.78	12.35	84.88
number of holes in section i	$N_{dis,i}$	[−]	0	128	796
hole diameter of section i	$d_{dis,i}$	[mm]	-	2.789	1.281
opening ratio of section i	$\Psi_{dis,i}$	[%]	-	24.89	4.75
pressure drop constant of section i	$K_{dis,i}$	[−]	-	1.101	0.868
drag coefficient of section i	$c_{dis,i}$	[−]	-	17.15	533.58
ratio of sectional gas velocity to inlet gas velocity	$\omega_{i,in}$	[−]	-	3.63	0.65
sectional mass fraction of inlet gas	$\Omega_{i,in}$	[%]	-	44.8	55.2

Table 8.1: Specifications of the gas distributor plate sections employed in the present two-zone continuum model of Wurster fluidization.

8.2 Sensitivity analysis of characteristics of fluid-particle transport dynamics

8.2.1 Setting of fixed and varied parameters

Constant parameters

The parameters of the model distributor plate and the isothermal flow separation step shall be constant within this sensitivity analysis and adopted from Section 8.1, see also Table 8.1. Further constant parameters are listed in Table 8.2 and described in the following. The diameter d and the effective particle density ρ_p of the monodisperse and spherical bed material are adopted from the external nuclei characteristics used in the population balance simulation study in Chapter 6, which is also comparable to the experimentally employed Cellets®200-cores. The bed porosity of minimal fluidization conditions ε_{mf} is chosen with 0.4, as it is a common value for loose packed beds of spherical particles (see Sections 2.1.3 and 2.2.4). The constructive parameters of the process chamber ($D_{app,0}$, D_{wt}, L_{wt}, and H_{wt}, Figure 7.2) conform to the experimental setting of this thesis that is detailed in Section 9.2 and Figure C.2. The moisture content of the inlet gas is defined with $Y_{in} = 1\,\mathrm{g/kg}$, which roughly corresponds to the outlet conditions of the air condition system in front of the experimental plant (Figure 9.4). This value was determined by dew point measurement. The material properties of the process gas are calculated for the system pressure of $p_{sys} = 1\,\mathrm{bar}$. At this, pressure changes within the process chamber, as for instance across the distributor plate or the fluidized bed, are neglected. In the experiments, the process gas and the nozzle gas are delivered by the same air conditioning system. The moisture load of the nozzle gas and of the inlet gas are therefore assumed to be equal here: $Y_{g,noz} = Y_{in}$. The mass flow rate of the nozzle gas $\dot{M}_{g,noz}$ is set to $4\,\mathrm{kg/h}$, which approximately matches the spray conditions of the granulation experiments with a nozzle air excess pressure of 1.75 bar. A relation between mass flow rates and excess pressures of the nozzle air is deduced from a specification sheet of the company Düsen-Schlick GmbH for the two-substance nozzle type "model 970 S4" [124], as shown in Appendix C.2.3. The outflow coefficient λ_{tor} and the exponent m_{pul} of the pulsation factor k_{pul}, which are used for defining the Wurster suction rate via Eq. 7.116, are taken over from empirical values suggested by Burgschweiger a. Tsotsas [90, 91]. The molar gas constant $\tilde{R}$ and the acceleration constant of gravity are given in Table A.1. The molar mass of dry air $\tilde{M}_{air}$ and water vapor $\tilde{M}_{vap}$ are adopted from data of [122, 123], which are listed in Table A.2. Heat losses through walls and evaporation of the spray liquid in the spray zone shall not be regarded within the entire parameter variation study of the present section, what is to be implemented by a relative temperature drop of zero ($\Theta_{loss} = 0$) and a drying potential at the top of the spray zone of unity ($\eta_{dry,\alpha,top} = 1$).

Overview on varied parameters

The present study is divided into three parameter variation series, which are indicated by TZCM-1, TZCM-2, and TZCM-3. Table 8.3 gives an overview on these sub-studies with regard to mainly varied parameters, types of thermodynamic system, and spraying conditions. Four parameters are varied in total. These are the dimensionless inlet gas velocity ξ_{in} as variation coordinate over which the ensuing quantities of the

property	symbol	unit	value
particle diameter	d	[mm]	0.3
effective particle density	ρ_p	[kg/m^3]	1380
interparticle porosity at minimal fluidization	ε_{mf}	[−]	0.4
chamber diameter of process gas inlet	$D_{app,0}$	[m]	0.18
diameter of Wurster tube	D_{wt}	[m]	0.07
length of Wurster tube	L_{wt}	[m]	0.20
gap height of Wurster tube	H_{wt}	[m]	0.02
moisture content of inlet gas	Y_{in}	[g/kg]	1
absolute pressure of process gas	p_{sys}	[bar]	1
mass flow rate of nozzle air	$\dot{M}_{g,noz}$	[kg/h]	4
outflow coefficient of modified Torricelli flow	λ_{tor}	[−]	0.0316
exponent of pulsation factor (modified Torricelli flow)	m_{pul}	[−]	0.2605
relative temperature drop	Θ_{loss}	[−]	0
drying potential of spray zone outlet gas	$\eta_{dry,\alpha,top}$	[−]	1

Table 8.2: Constant parameters for the sensitivity analysis of the present two-zone continuum model of Wurster fluidization.

parameter variation series	TZCM-1	TZCM-2	TZCM-3
varied parameter coordinate	ξ_{in}	ξ_{in}	ξ_{in}
varied curve parameter	M_{bed}	$\dot{M}_w$	T_{in}
thermodynamic type of system	isothermal	adiabatic	adiabatic
spray activity	off	on	on
bed mass M_{bed}	various, Table 8.4	1 kg	1 kg
water spray rate $\dot{M}_w$	0	various, Table 8.4	600 g/h
inlet gas temperature T_{in}	70℃	70℃	various, Table 8.4
temperature of nozzle air $T_{g,noz}$	70℃	20℃	20℃

Table 8.3: Overview on mainly varied parameters (ξ_{in}, M_{bed}, $\dot{M}_w$, and T_{in}), types of thermodynamic system, and spraying conditions for the three parameter variation series TZCM-1, TZCM-2, and TZCM-3.

parameter variation series	TZCM-1	TZCM-2	TZCM-3
curve parameter	M_{bed}	$\dot{M}_w$	T_{in}
unit	[kg]	[g/h]	[℃]
value 1	0.5	200	60
value 2	1	400	70
value 3	1.5	600	80
value 4	2	800	90
value 3	3	1000	100

Table 8.4: Values of the second varied parameter for the parameter variation series TZCM-1, TZCM-2, and TZCM-3.

TZC-model shall be illustrated for each of the three series (Section 8.2.3), the fluidized bed mass M_{bed} as curve parameter for the TZCM-1 series, the water spray rate $\dot{M}_w$ as curve parameter for the TZCM-2 series, and the inlet gas temperature T_{in} as curve parameter for the TZCM-3 series. The curve parameters are given with five different values for each parameter variation series, as listed in Table 8.4. The first parameter variation series TZCM-1 is conducted for an isothermal system, where spraying of water is refrained, and the process gas temperatures of all the flowsheet locations of the TZC-model (Figure 7.1 a) are given with 70℃. The TZCM-2 and TZCM-3 series shall be non-isothermal implementations with entirely adiabatic walls, active spraying of water, and a bed mass of 1 kg. The value range of water spray rate of the TZCM-2 series is applicable for Wurster granulation with the present process chamber design. At this, 600 g/h and 800 g/h most closely match the spray conditions of the continuous granulation experiments of this thesis (see Section 10.4.1). The water spray rate of TZCM-3 is set to 600 g/h. The inlet gas temperature of TZCM-2 is assumed with 70℃, wherewith also some of the granulation experiments of Hampel's reference case ([2], Section 2.3) were carried out. In the isothermal series TZCM-1, the nozzle gas temperature conforms with the respective inlet gas temperature (70℃), whereas it is defined to be at room temperature (20℃) for the TZCM-2 and TZCM-3 series to get more realistic process conditions.

8.2.2 Ensuing characteristic parameters of process conditions and limits

Diverse dimensionless characteristics of process conditions and limits of Sections 7.9 to 7.11 are calculated for the three parameter variation series TZCM-1, TZCM-2, and TZCM-3, as shown in the following. These include the dimensionless bed mass μ_{bed} from Eq. 7.132, the isenthalpic saturation temperature of inlet gas conditions $T_{sat,ref}$ (reference saturation temperature) from Eqs. 7.16 to 7.18, 7.23 to 7.26, and 7.127, its corresponding saturation moisture content $Y_{sat,ref}$ from Eqs. 7.27, 7.28, and 7.128, the reference minimal fluidization velocity $u_{mf,ref}$ from Eq. 7.124, the reference elutriation velocity $u_{elu,ref}$ from Eq. 7.125, the reference fluidization range number $f_{rn,ref}$ from Eq. 7.126, the terminal Reynolds number Re_s from Eq. 2.61, the dimensionless water spray rate $\dot{\mu}_w$ from Eq. 7.130, the approximate adiabatic critical dimensionless water spray rate $\dot{\mu}^*_{w,cr,ad}$ from Eq. 7.221 (with negligence of spray zone evaporation $\eta_{dry,1-\alpha,top} = 1$), the isothermal minimal-Wurster-fluidization limit $\xi_{mf,iso}$ from Eq. 7.179, the approximate adiabatic process-gas-saturation limit $\xi^*_{sat,ad}$ from Eq. 7.207, the Wurster-tube-exceedance limit ξ_{exc} from Eqs. 7.168 and 7.169 with $\xi_{exc} = \xi_{exc,iso}$ for the TZCM-1 series and with $\xi_{exc} = \xi^*_{exc,ad}$ for the TZCM-2 and TZCM-3 series, the approximate isothermal Wurster-tube-exceedance limit $\xi^*_{exc,iso}$ from Eq. 7.217, and the bed mass fraction of the spray zone from Eq. 7.121 at the iterative isothermal Wurster-tube-exceedance limit $\alpha_m(\xi_{exc,iso})$. Those of these quantities that are constant within the sub-studies TZCM-1, TZCM-2, and TZCM-3 are listed in Table 8.5 and those that change are given in Tables 8.6 to 8.9.

Dimensionless bed mass

The dimensionless bed mass μ_{bed} is independent from inlet gas and spraying conditions and serves as orientation for choosing the bed mass values in Wurster granulation processes with plants of different scales, as shown later on. The calculation of the dimensionless bed mass μ_{bed} requires the maximum volume of the drying zone $V_{1-\alpha,max}$, which is given with $6.279 \cdot 10^{-3}\, m^3$ for the present process chamber specification. The latter is obtained by Eq. 7.9 using $H_{wt} + L_{wt}$ as the maximum height of the drying zone. The dimensionless bed mass values that correspond to each of the investigated bed mass examples of TZCM-1 are listed in Table 8.6. The solutions of the TZCM-2 and TZCM-3 series are related to a dimensionless bed mass of 19.24 %.

Isenthalpic saturation temperature with reference to inlet gas conditions

The saturation point is not needed to be taken into account for the isothermal parameter variation series TZCM-1. For the second series TZCM-2 (Table 8.5), the reference saturation temperature is constantly given with $T_{sat,ref} = 24.1$℃ and the corresponding moisture content with $Y_{sat,ref} = 19.26$ g/kg, as the thermodynamic state of the inlet gas is uniformly set with $T_{in} = 70$℃ and $Y_{in} = 0.01$g/kg here. In the TZCM-3 series (Table 8.8), the reference saturation temperature is getting bigger from 21.5 to 30.5℃ over the different inlet gas temperature examples. At this, the reference saturation temperature only rises by circa 42 % in total, while the inlet gas temperature was increased by around 67 % from 60 and 100℃. The moisture load at saturation $Y_{sat,ref}$ grows somewhat over-proportionally from 16.38 g/kg to 28.42 g/kg with inlet gas temperature values of TZCM-3 (Table 8.8).

Reference characteristics of isothermal homogeneous fluidization

The reference minimal fluidization velocity, the reference elutriation velocity, the reference fluidization range number, and the terminal Reynolds number are given with $u_{mf,ref} = 41.7\,\mathrm{mm/s}$, $u_{elu,ref} = 1395\,\mathrm{mm/s}$, $f_{rn,ref} = 33.49$, and $Re_s = 20.66$ for the entire TZCM-1 and TZCM-2 series (Table 8.5). These characteristics vary with the inlet gas temperatures of the third series TZCM-3 (Table 8.8) with decreasing values from 42.58 to 39.22 mm/s for the reference minimal fluidization velocity $u_{mf,ref}$, from 1400 to 1382 mm/s for the reference elutriation velocity, from 21.83 to 17.67 for the terminal Reynolds number Re_s, and with increasing values from 32.87 to 35.24 for the reference fluidization range number $f_{rn,ref}$. The reference points of minimal fluidization and elutriation have been calculated by Martin's approaches according to Eqs. 2.87 and 2.119 [40, 41]. The elutriation point corresponds here to the terminal sinking velocity. As the terminal Reynolds numbers of bed particles with the present size and density lie in the lower area of the transition flow regime (Table 2.2), the sinking velocity approach of Martin can be employed, more on this in Section 2.2.1. But also Kraume's correlation of the Richardson-Zaki exponent m_{sw} and the Archimedes number (see Eq. 2.98 or Eq. 7.99) can be used for calculating the swarm correction factor inside the spray zone $k_{sw,\alpha}$ as long as the bed particles settle in the transition regime. However, the obtained terminal Reynolds number are quite close to the Stokes regime ($Re_s < 1$). Therefore, it is recommended to use other approaches of the Richardson-Zaki exponent, such as this of Rowe in Eq. 2.100 or Khan a. Richardson in Eq. 2.101, when the TZC-model is applied for smaller and/or lighter particles than these of the present investigation (Table 8.2).

Dimensionless water spray rate and approximate adiabatic critical dimensionless water spray rate

The dimensionless water spray rate $\dot{\mu}_w$ is given with zero for the isothermal parameter variation series TZCM-1 (Table 8.3), increases from 8.453 to 42.26 % with the five water spray rate examples of the TZCM-2 series (Table 8.7), and decreases from 29.15 to 18.54 % with the five inlet gas temperature examples of the TZCM-3 series (Table 8.9). The approximate adiabatic critical dimensionless water spray rate $\dot{\mu}^*_{w,cr,ad}$ marks the point of the water spray rate at which the process-gas-saturation limit exceeds the minimal-Wurster-fluidization limit (described in Sections 7.10.4 and 7.11.6). It needs not to be considered for the first series TZCM-1 due to the assumption of isothermal conditions. The approximate adiabatic critical dimensionless water spray rate $\dot{\mu}^*_{w,cr,ad}$ depends on the inlet gas conditions and material characteristics. It is therefore given with a constant value of round 3.19 % for the TZCM-2 series (Table 8.5) and varies in a narrow range of 3.15 to 3.35 % for the third series TZCM-3 (Table 8.9).

Lower and upper limit of the permissible range of dimensionless inlet gas velocity

The coordinate of the dimensionless inlet gas velocity ξ_{in} shall be finely discretized between the minimal operation point ξ_{min} and maximal operation point ξ_{max} that are defined by relevant process limits. The isothermal minimal-Wurster-fluidization limit $\xi_{mwf,iso}$ is used as minimal dimensionless inlet gas velocity for the TZCM-1 series (Table 8.5). The minimal dimensionless inlet gas velocity of the non-isothermal implementations TZCM-2 and TZCM-3 can either be fixed by minimal-fluidization or process-gas saturation conditions, as explained in Section 7.10.4. The approximate adiabatic critical dimensionless water spray rate $\dot{\mu}^*_{w,cr,ad}$ can serve as a rough indicator for the prevailing lower limit, which is also exemplified in Eq. 7.223. Since the dimensionless water spray rates $\dot{\mu}_w$ of the TZCM-2 and TZCM-3 series are clearly larger than the approximate adiabatic critical dimensionless water spray rate $\dot{\mu}^*_{w,cr,ad}$ for every parameter setting, the approximate adiabatic process-gas-saturation limit $\xi^*_{sat,ad}$ defines the minimal dimensionless inlet gas velocity here. As maximal value of the domain of the dimensionless inlet gas velocity, the iterative version of the Wurster-tube-exceedance limit is employed for each of the three sub-studies, which is in general symbolized by ξ_{exc}, as in Section 7.10.3, but here according to the assumptions by $\xi_{exc,iso}$ for the isothermal series TZCM-1 and by $\xi^*_{exc,ad}$ for non-isothermal series TZCM-2 and TZCM-3. The isothermal minimal-Wurster-fluidization limit is constantly given with round $\xi_{mwf,iso} = 1.66\,\%$ in the TZCM-1 series. The approximate adiabatic process-gas-saturation limit $\xi^*_{sat,ad}$ increases linearly from 12.71 to 75.86 % with the water spray rate values of TZCM-2 (Table 8.7) and decreases almost hyperbolically from 51.33 to 31.66 % with the inlet gas temperature values of TZCM-3 (Table 8.9). The dimensionless inlet gas velocities of the Wurster-tube-exceedance limit of all the three parameter variation series ($\xi_{exc,iso}$ and $\xi^*_{exc,ad}$) were determined by iterating the entire TZC-model of Sections 7.1 to 7.7 as long as the calculated dimensionless bed height $\Phi_{h,1-\alpha}$ (Eqs. 7.109 and 7.133) is sufficiently close to unity, so that the Wurster-tube-exceedance criterion of Eq. 7.168 is

parameter variation series	TZCM-1	TZCM-2	TZCM-3
μ_{bed} [%]	various, Table 8.6	19.24	19.24
$T_{sat,ref}$ [°C]	-	24.1	various, Table 8.8
$Y_{sat,ref}$ [g/kg]	-	19.26	various, Table 8.8
$u_{mf,ref}$ [mm/s]	41.7	41.7	various, Table 8.8
$u_{elu,ref}$ [mm/s]	1395	1395	various, Table 8.8
$f_{rn,ref}$ [−]	33.49	33.49	various, Table 8.8
Re_s [−]	20.66	20.66	various, Table 8.8
$\dot{\mu}_w$ [%]	0	various, Table 8.7	various, Table 8.9
$\dot{\mu}^*_{w,cr,ad}$ [%]	-	3.193	various, Table 8.9
ξ_{min}	$\xi_{mwf,iso}$	$\xi^*_{sat,ad}$	$\xi^*_{sat,ad}$
ξ_{max}	$\xi_{exc,iso}$	$\xi^*_{exc,ad}$	$\xi^*_{exc,ad}$
$\xi_{mwf,iso}$ [%]	1.66	-	-
$\xi^*_{sat,ad}$ [%]	-	various, Table 8.7	various, Table 8.9
$\xi^*_{exc,ad}$ [%]	various, Table 8.6	various, Table 8.7	various, Table 8.9
$\xi^*_{exc,iso}(T_{in}, Y_{in})$ [%]	various, Table 8.6	120.8	various, Table 8.9

Table 8.5: Overview on diverse characteristics of process conditions and limits for the three parameter variation series TZCM-1, TZCM-2, and TZCM-3.

M_{bed} [kg]	μ_{bed} [%]	$\xi_{exc,iso}$ [%]	$\xi^*_{exc,iso}$ [%]	$\alpha_m(\xi_{exc,iso})$ [%]
0.5	9.618	154.9	154.7	0.28
1	19.24	119.9	120.8	0.37
1.5	28.85	91.51	92.6	0.50
2	38.47	68.43	69.4	0.71
3	57.71	35.60	35.8	1.62

Table 8.6: Different characteristics that change within the parameter variation series TZCM-1: dimensionless bed mass μ_{bed}, iterative Wurster-tube-exceedance limit $\xi_{exc,iso}$, approximate isothermal Wurster-tube-exceedance limit $\xi^*_{exc,iso}$, and the bed mass fraction of the spray zone at the iterative Wurster-tube-exceedance limit $\alpha_m(\xi_{exc,iso})$.

fulfilled with a deviation of less than 10^{-6} %. The approximate isothermal Wurster-tube-exceedance limit $\xi^*_{exc,iso}$ of Eq. 7.217 was used as start value in first iteration round. The dimensionless inlet gas velocity of the Wurster-tube-exceedance limit $\xi^*_{exc,ad}$ strongly declines from 154.7 to 35.8 % with a slight hyperbolic tendency over the five bed mass values of the TZCM-1 series (Table 8.6), grows a little from 121.1 to 129.3 % with almost linear dependency over the five water spray rates of the TZCM-2 series (Table 8.7), and marginally decreases from 125.7 to 123.8 % over the five inlet gas temperatures of the TZCM-3 series (see Table 8.9). The reason for the increase of the Wurster-tube-exceedance limit $\xi^*_{exc,ad}$ with the water spray rate comes from the evaporation cooling effect, at which higher water spray rates significantly reduce the process gas temperature in the drying zone, lower thereby the process gas velocity, and lessen the fluidized bed expansion.

Comparison of the approximate and iterative Wurster-tube-exceedance limits

The dimensionless inlet gas velocity of the approximate isothermal Wurster-tube-exceedance limit $\xi^*_{exc,iso}$ was calculated for each of the three parameter setting series TZCM-1, TZCM-2, and TZCM-3 regardless of whether the system is isothermal or non-isothermal. In the series TZCM-1 and TZCM-3 (Tables 8.6 and 8.9), the approximate isothermal Wurster-tube-exceedance limit $\xi^*_{exc,iso}$ changes with the bed mass M_{bed} and the inlet gas temperature T_{in} in the same qualitative manner as the iterative Wurster-tube-exceedance limit $\xi^*_{exc,ad}$. It can be seen in the TZCM-1 results that the approximations of the isothermal Wurster-tube-exceedance limit are very close to that of the iterative solutions ($\xi^*_{exc,iso}$(TZCM-1)$\approx \xi^*_{exc,ad}$(TZCM-1)) with a relative error (according to $(\xi^*_{exc,ad} - \xi^*_{exc,iso})/\xi^*_{exc,ad}$) up to maximal 1.19 %. The approximate and

$\dot{M}_w$ [g/h]	$\dot{\mu}_w$ [%]	$\xi^*_{sat,ad}$ [%]	$\xi^*_{exc,ad}$ [%]
200	8.453	12.71	121.1
400	16.91	28.50	123.1
600	25.36	44.28	125.2
800	33.81	60.07	127.3
1000	42.26	75.86	129.3

Table 8.7: Diverse process characteristics that change within the second parameter variation series TZCM-2: dimensionless water spray rate $\dot{\mu}_w$ and dimensionless inlet gas velocity of the approximate adiabatic process-gas-saturation limit $\xi^*_{sat,ad}$ and the approximate adiabatic Wurster-tube-exceedance limit $\xi^*_{exc,ad}$.

T_{in} [°C]	$T_{sat,ref}$ [°C]	$Y_{sat,ref}$ [g/kg]	$u_{mf,ref}$ [mm/s]	$u_{elu,ref}$ [mm/s]	$f_{rn,ref}$ [–]	Re_s [–]
60	21.50	16.38	42.58	1400	32.87	21.83
70	24.10	19.26	41.67	1395	33.49	20.66
80	26.44	22.24	40.81	1391	34.08	19.59
90	28.56	25.30	40.00	1387	34.67	18.59
100	30.50	28.42	39.22	1382	35.24	17.67

Table 8.8: Diverse characteristics of the isenthalpic saturation point with reference to inlet gas conditions and of fluid-particle transport dynamics for the third parameter variation series TZCM-3.

T_{in} [°C]	$\dot{\mu}_w$ [%]	$\dot{\mu}^*_{w,cr,ad}$ [%]	$\xi^*_{sat,ad}$ [%]	$\xi^*_{exc,ad}$ [%]	$\xi^*_{exc,iso}$ [%]
60	29.15	3.148	51.33	125.7	121.1
70	25.36	3.193	44.28	125.2	120.8
80	22.51	3.242	39.00	124.7	120.5
90	20.30	3.294	34.91	124.3	120.2
100	18.54	3.348	31.66	123.8	119.9

Table 8.9: Diverse characteristics of process limits for the third parameter variation series TZCM-3.

iterative solutions of the Wurster-tube-exceedance limits of the TZCM-3 series are somewhat more different with relative errors between −3.66 to −3.15 %. The approximate isothermal Wurster-tube-exceedance limit of the entire second parameter variation series is constantly given with $\xi^*_{exc,iso}$(TZCM-2)= 120.8 % (Table 8.5), but the corresponding iterative Wurster-tube-exceedance limit $\xi^*_{exc,ad}$ increases with $\dot{M}_w$, as mentioned before. Here a maximum relative deviation of 6.6 % between the approximate and iterative solution is ascertained for the largest water spray rate example (1000 g/h). Although this error is not negligible small, the approximate isothermal Wurster-tube-exceedance limit $\xi^*_{exc,iso}$ can still serve as rough calculation method for the maximal permissible inlet gas velocity, since practical inlet gas velocities are to be set far below the Wurster-tube-exceedance limit to obtain fluidized beds that only float around the lower part of the Wurster tube. The water spray rate has the biggest influence on the differences between $\xi^*_{exc,ad}$ and $\xi^*_{exc,iso}$ among the varied curve parameters of Table 8.4 due to strong influence of the cooling effect on fluidized bed expansion, as described above.

Bed mass fraction in the spray zone at the Wurster-tube-exceedance limit

The concept of the approximate isothermal Wurster-tube-exceedance limit assumes that the entire bed mass is located in the drying zone, which is equivalent to a zero bed mass fraction of the spray zone: $M_{1-\alpha} = M_{bed} \Leftrightarrow \alpha_m = 0$. The bed mass fractions of the spray zone that result from the iterative solutions of Wurster-tube-exceedance limit $\alpha_m(\xi_{exc,iso})$ are also listed in Table 8.6. It turns out that these spray zone mass fractions are still relatively low, so that the assumption that the entire bed mass is in the drying zone is justified.

8.2.3 Iterative solutions of spray zone and drying zone quantities

Several quantities of the fluid-particle transport dynamics of the spray zone and drying zone in the TZC-model are illustrated and discussed in the following using the examples of the three different parameter variation series (TZCM-1, TZCM-2, and TZCM-3) of Section 8.2.1 and within the process limits of Section 8.2.2. The different quantities shown are calculated by iterating the entire TZC-model described in Sections 7.1 to 7.8. The results are presented as functions of the dimensionless inlet gas velocity ξ_{in} within a permissible operation range $\xi_{min} < \xi_{in} < \xi_{max}$ (see Table 8.5) for the three different curve parameters of Table 8.4: the bed masses M_{bed} of the TZCM-1 series, the water spray rates $\dot{M}_w$ of the TZCM2 series, and the inlet gas temperatures T_{in} of the TZCM-3 series. The spray zone quantities to be investigated include the mass fraction of bed material in the spray zone α_m from Eq. 7.121, the swarm porosity ε_α from Eq. 7.118, the swarm sinking correction factor $k_{sw,\alpha}$ from Eq. 7.100, the swarm sinking velocity $u_{sw,\alpha}$ from Eq. 7.101, the pneumatic transport velocity $u_{pn,\alpha}$ from Eq. 7.102, and the particle residence time τ_α from Eq. 7.122. They are the most important characteristics of the TZC-model that represent the pneumatic transport behavior in the Wurster tube and are depicted in Figure 8.1 for the TZCM-1 series, in Figure 8.3 for the TZCM-2 series, and in Figure 8.5 for TZCM-3. The relevant drying zone characteristics are the bed porosity $\varepsilon_{1-\alpha}$ from Eq. 7.107, the normalized bed height $\Phi_{h,1-\alpha}$ from Eq. 7.133, the Wurster suction rate $\dot{M}_{wt,tor}$ from Eq. 7.116, the particle residence time $\tau_{1-\alpha}$ from Eq. 7.123, the process gas temperature $T_{1-\alpha}$ from Eq. 7.88, and the drying potential $\eta_{dry,1-\alpha}$ from Eq. 7.120. The results of them can be found in Figure 8.2 for TZCM-1, in Figure 8.4 for TZCM-2, and in Figure 8.6 for TZCM-3. At this, the process gas temperature $T_{1-\alpha}$ and the drying potential $\eta_{dry,1-\alpha}$ are excluded in the TZCM-1 results of the drying zone, because this series contains only isothermal solutions of the TZC-Model.

Influence of (dimensionless) inlet gas velocity

The (dimensionless) inlet gas velocity has a substantial influence on each of the spray zone and drying zone quantities depicted in Figures 8.1 to 8.6 for all the three parameter variation series TZCM-1, TZCM-2, and TZCM-3. The qualitative dependency on the dimensionless inlet gas velocity is same among the three presented series. But the difference between them is that the lower limits of the operation range in terms of dimensionless inlet gas velocity ($\xi^*_{sat,ad} < \xi_{in} < \xi^*_{exc,ad}$) are given by one single point of the isothermal minimal-Wurster-fluidization limit (1.66 %) in the TZCM-1 series and by several process-gas-saturation points in the TZCM-2 and TZCM-3 series (see also Tables 8.7 and 8.9), as described already in Section 8.2.2. At this, the operation range is the smaller the larger the bed mass, the higher the water spray rate, and the lower the inlet gas temperature is. An increase in the inlet gas velocity leads to lower bed mass fractions of the spray zone α_m and shorter residence times τ_α. The swarm porosities ε_α are the lowest at the minimal dimensionless inlet gas velocities, increases steadily with a growing inlet gas velocity, and converges

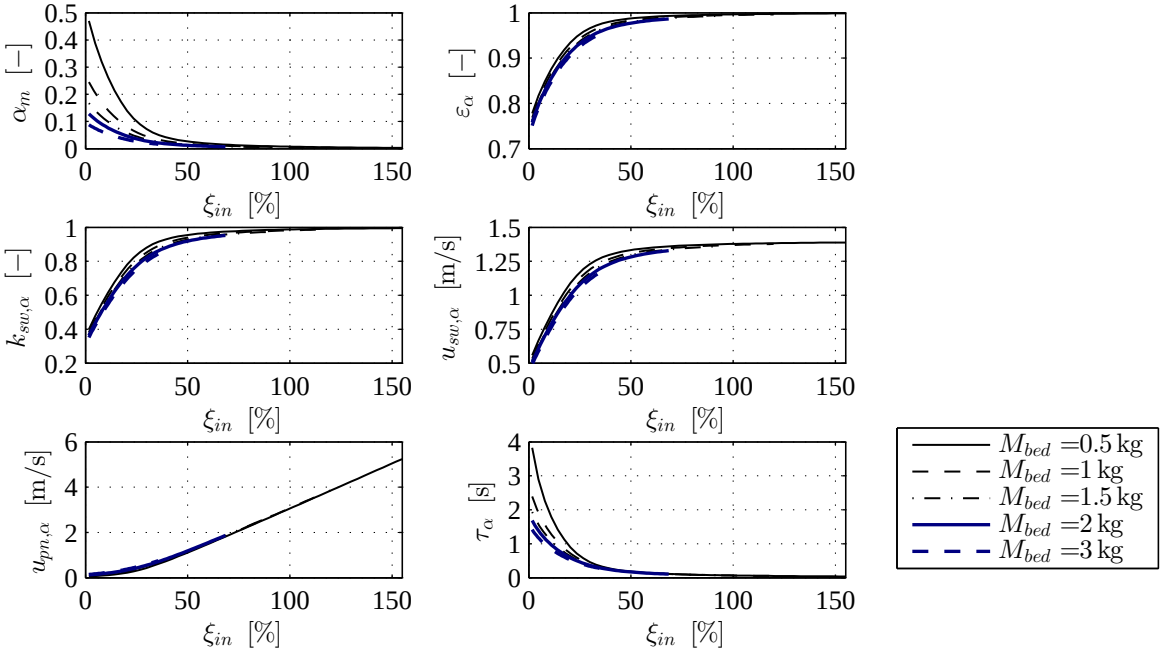

Figure 8.1: Diverse characteristics of the spray zone in dependency on the dimensionless inlet gas velocity ξ_{in} for different bed masses M_{bed}.

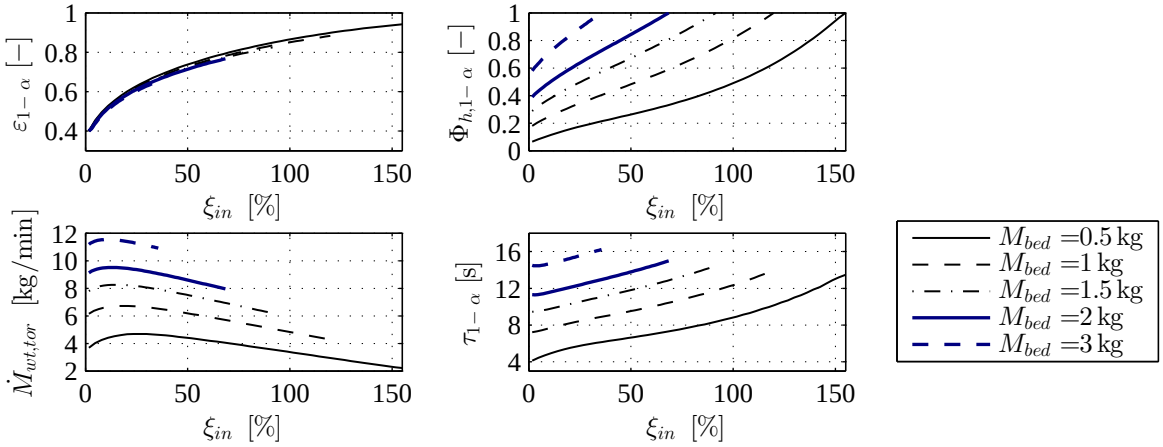

Figure 8.2: Diverse characteristics of the drying zone in dependency on the dimensionless inlet gas velocity ξ_{in} for different bed masses M_{bed}.

finally to unity, which is already approximately reached for dimensionless inlet gas velocities higher than around 70 %. Due to Eqs. 7.100 to 7.101, the swarm sinking factor $k_{sw,\alpha}$ and the swarm sinking velocity $u_{sw,\alpha}$ show the same qualitative functional relationship to the inlet gas velocity as the swarm porosity does. At this, the asymptotic upper limit of the swarm sinking correction factor $k_{sw,\alpha}$ is given by unity and that of the swarm sinking velocity $u_{sw,\alpha}$ by terminal sinking velocity of the bed granules $u_{s,\alpha}$. The latter is equivalent to the reference elutriation velocity in the isothermal series (u_s(TZCM-1)= $u_{elu,ref} = 1.395\,\mathrm{m/s}$, see also Table 8.8). The pneumatic transport velocity $u_{pn,\alpha}$ slightly increases with dimensionless inlet gas velocity at lower values (here $< 30\,\%$) and somewhat more at larger values with a transition to a quasi-linear dependency. The particle residence time τ_α is hyperbolically related to the particle rising velocity $u_{pn,\alpha}$ according to Eq. 7.122, wherefore it gradually declines with the inlet gas velocity towards zero as asymptotic lower limit. The obtained drying zone quantities show a typical bed expansion behavior as it is the case in a chamber with a homogeneous fluidized bed over the entire cross-section. The bed porosity has the minimal fluidization value ($\varepsilon_{mf} = 0.4$) at the inlet gas velocity of the isothermal minimal-Wurster-fluidization limit (1.66 %), which can only be seen for TZCM-1 results (Figure 8.2). The bed porosity $\varepsilon_{1-\alpha}$, the dimensionless bed height $\Phi_{h,1-\alpha}$, and the particle residence time $\tau_{1-\alpha}$ are raised by increasing dimensionless inlet gas velocity over the entire considered range of values. The functional relation between the Wurster suction rate $\dot{M}_{wt,tor}$ and the dimensionless inlet gas velocity is clearly distinguished from these of the other described quantities, which is shown by the TZCM-1 results (Figure 8.2). The Wurster suction rate grows at lower inlet gas velocities, reaches a maximum, and then decrease constantly. The reason for this is discussed below in Section 8.5. For the non-isothermal model investigations TZCM-2 and TZCM-3, the influence of inlet gas velocity on temperature and drying potential of the process gas in the drying zone can be read from Figures 8.4 and 8.6. These two quantities increase with the dimensionless inlet gas velocity, because larger entry flows at constant water spray rates are less cooled by evaporation and have higher drying capacities.

Influence of bed mass

Of the spray zone and drying zone quantities in Figures 8.1 and 8.2, the swarm porosity ε_α, the swarm sinking factor $k_{sw,\alpha}$, the swarm sinking velocity $u_{sw,\alpha}$, the pneumatic transport velocity $u_{pn,\alpha}$, and the bed porosity $\varepsilon_{1-\alpha}$ are only little affected by varying bed mass M_{bed}. The bed mass fraction of the spray zone α_m and the particle residence time τ_α are somewhat more influenced, especially at lower dimensionless inlet gas velocities ($\xi_{in} \ll 50\,\%$ for α_m and $\xi_{in} \ll 40\,\%$ for τ_α). The significant decrease in α_m with M_{bed} is due to the normalization to the total bed mass by Eq. 7.121. The absolute bed mass fraction in the spray zone M_α does not change that much for the various M_{bed}-examples, as can be deduced from the curves in the ε_α-ξ_{in}-diagram and Eq. 7.103. Through the hyperbolic relationships of Eq. 7.122, the small change in the pneumatic transport velocity $u_{pn,\alpha}$ is transferred more strongly to the spray zone residence time τ_α at the lower inlet gas velocities; but, this influence becomes negligible at dimensionless inlet gas velocities greater than around 40 %. The curves of the dimensionless bed height $\Phi_{h,1-\alpha}$, the Wurster suction rate $\dot{M}_{wt,tor}$, and the particle residence time of the drying zone $\tau_{1-\alpha}$ shift most strongly with different bed mass. At this, larger bed masses are followed by greater bed heights, higher Wurster suction rates, and longer particle residence times. The five $\Phi_{h,1-\alpha}$-curves reach unity at the Wurster-tube-exceedance limits $\xi^*_{exc,ad}$ of Table 8.6, as it is supposed to be by the corresponding criterion of Eq. 7.168.

Influence of water spray rate

It can be seen from the TZCM-2 results (Figure 8.3) that none of the depicted spray zone quantities is affected by the water spray rate $\dot{M}_w$, because evaporation of sprayed water in the spray zone is neglected here (in TZCM-3 too). In contrast to this, evaporation of sprayed water takes place in the drying zone for the TZCM-2 implementation. Hence, water spray rate has an influence on drying zone quantities, as shown in Figure 8.4. But, the bed porosity $\varepsilon_{1-\alpha}$, the normalized bed height $\Phi_{h,1-\alpha}$, the Wurster suction rate $\dot{M}_{wt,tor}$, and the particle residence time $\tau_{1-\alpha}$ change only slightly with the water spray rate for the entire operation range of dimensionless inlet gas velocity. The temperature and the drying potential of the drying zone process gas, however, strongly decrease with higher water spray rates at constant (dimensionless) inlet gas velocity, which is due to a stronger cooling effect and limited drying capacity.

Influence of inlet gas temperature

It is ascertained by the TZCM-3 results in Figures 8.5 and 8.6 that the inlet gas temperature T_{in} has hardly any influence on most of the fluid-particle transport characteristics of the spray zone and drying zone, which

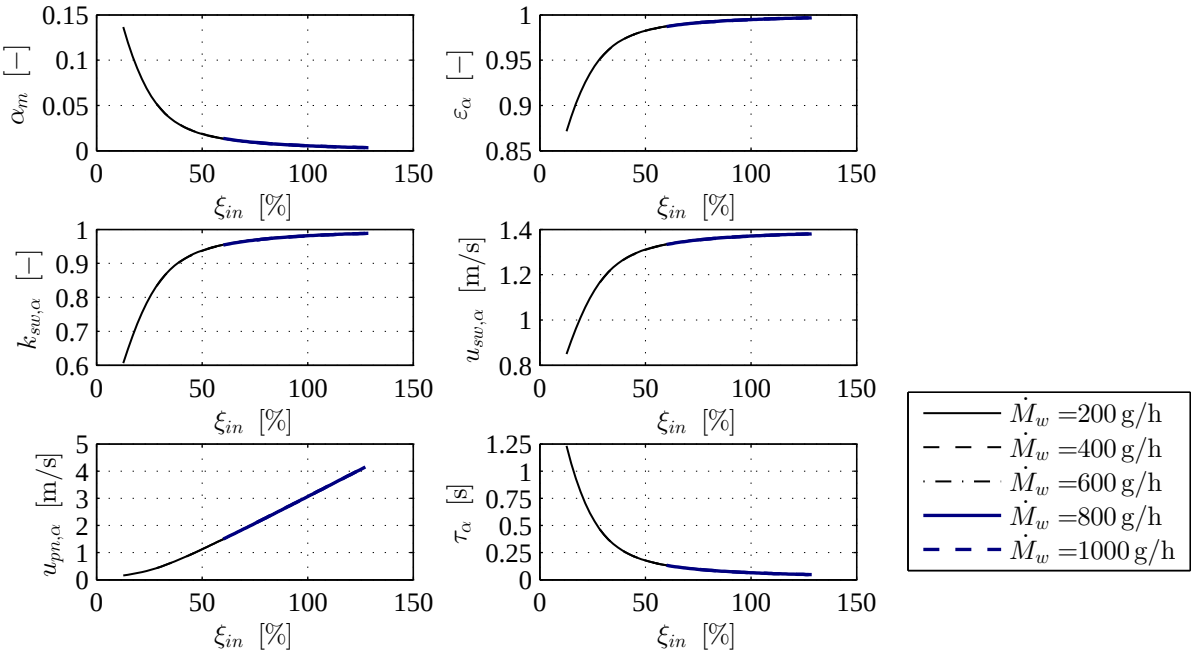

Figure 8.3: Diverse characteristics of the spray zone in dependency on the dimensionless inlet gas velocity ξ_{in} for different water spray rates $\dot{M}_w$.

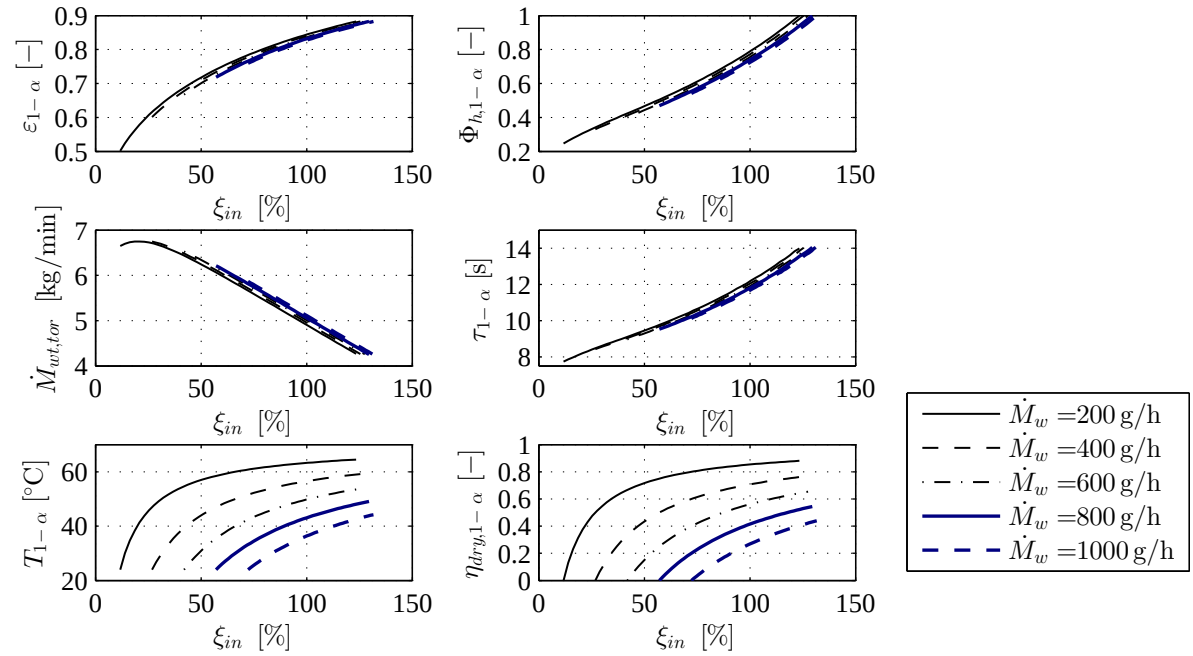

Figure 8.4: Diverse characteristics of the drying zone in dependency on the dimensionless inlet gas velocity ξ_{in} for different water spray rates $\dot{M}_w$.

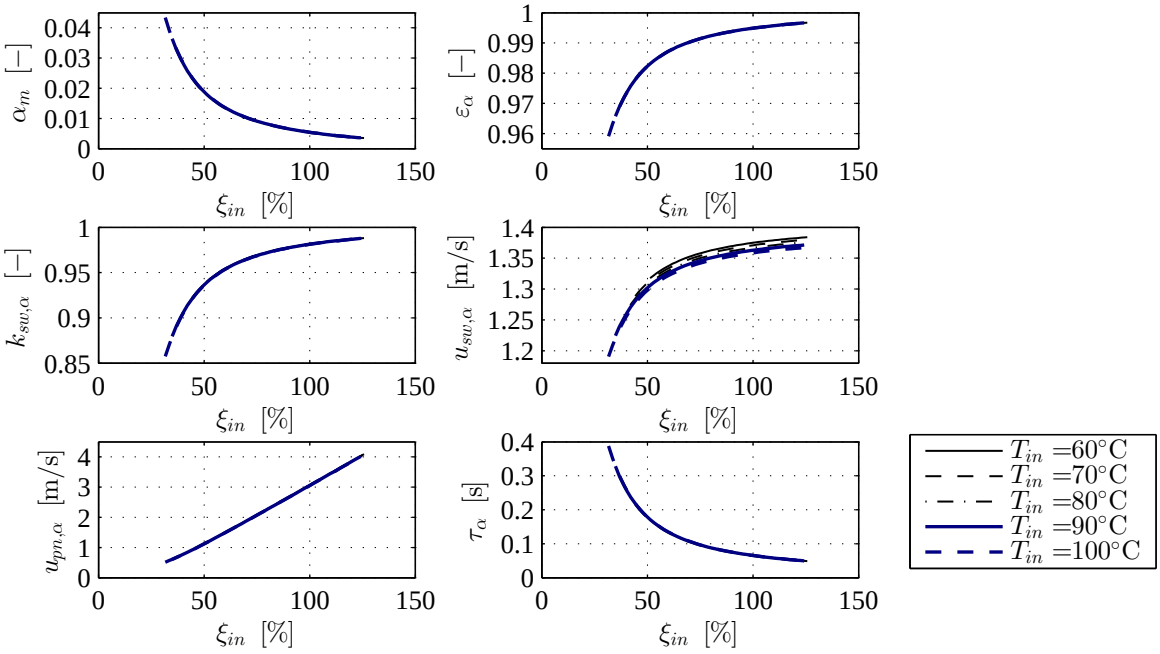

Figure 8.5: Diverse characteristics of the spray zone in dependency on the dimensionless inlet gas velocity ξ_{in} for different inlet gas temperatures T_{in}.

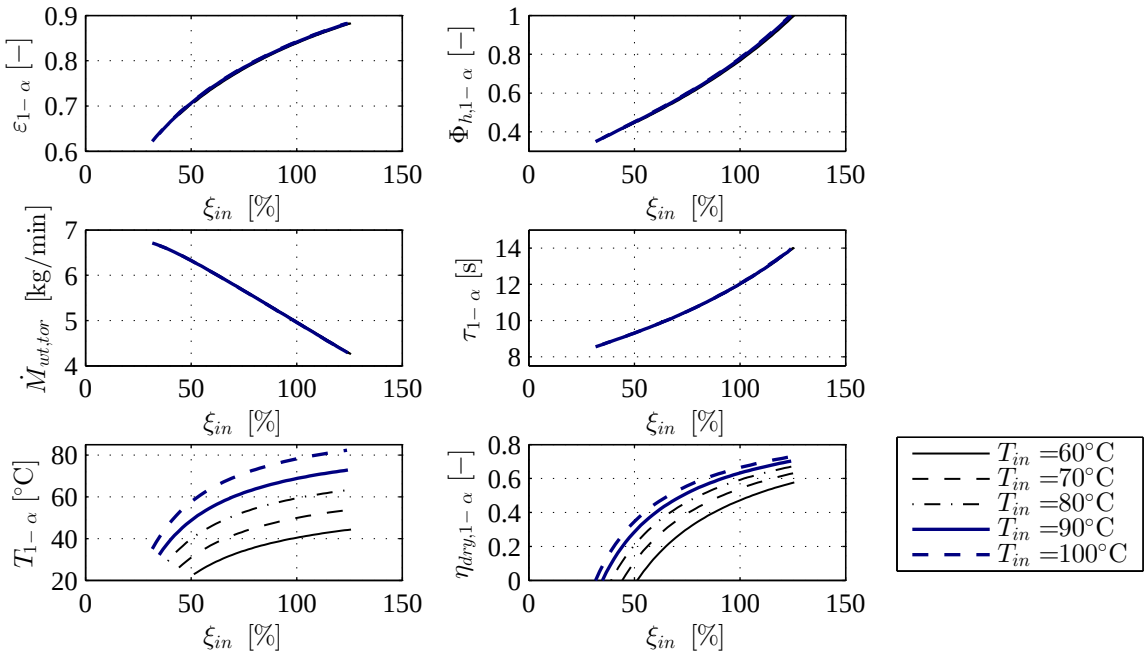

Figure 8.6: Diverse characteristics of the drying zone in dependency on the dimensionless inlet gas velocity ξ_{in} for different inlet gas temperatures T_{in}.

are the bed mass fraction of the spray zone α_m, the swarm porosity ε_α, the swarm sinking factor k_{sw}, the pneumatic transport velocity $u_{pn,\alpha}$, the particle residence in the spray zone τ_α, the bed porosity $\varepsilon_{1-\alpha}$, the bed height $\Phi_{h,1-\alpha}$, the Wurster suction rate $\dot{M}_{wt,tor}$, and the particle residence in the drying zone $\tau_{1-\alpha}$. The independence of these quantities from the inlet gas temperature is based on the mutual relationships in the iteration cycle structure of Eqs. 7.97 to 7.119. The swarm sinking velocity $u_{sw,\alpha}$, however, decreases a little with the inlet gas temperature, but still in a small margin, which is due to the following reason. According to Eq. 7.101, the swarm sinking velocity $u_{sw,\alpha}$ is obtained by the product of the swarm sinking correction factor $k_{sw,\alpha}$ and the terminal sinking velocity $u_{s,\alpha}$ from Eq. 7.94, and the latter lowers slightly, as can also be seen with the reference elutriation gas velocities $u_{elu,ref}$ in Table 8.8. Despite reduced swarm sinking velocities, the pneumatic transport velocity $u_{pn,\alpha}$ (obtained from Eq. 7.102) remains almost unchanged with a temperature increase, because the interstitial gas velocity $u_{\varepsilon,\alpha}$ from Eq. 7.98 (not illustrated here) grows a little too. The process gas temperature of the drying zone $T_{1-\alpha}$ and the drying potential $\eta_{dry,1-\alpha}$ are clearly higher for the larger inlet gas temperatures. The remaining drying power of the drying zone gas is larger then, and thus, higher water spray rates could be applied without reaching process-gas saturation.

Saturation points

The lower diagrams of Figures 8.4 and 8.6 (TZCM-2 and TZCM-3) show that at the minimal dimensionless inlet gas velocities (here approximate adiabatic process-gas-saturation limits $\xi^*_{sat,ad}$ of Table 8.7), the drying zone gas temperatures coincide with the respective isenthalpic saturation temperature T_{sat} (see Tables 8.5 and 8.8), and the drying potential of the drying zone process gas becomes zero at these points, as it is to be expected for process-gas-saturation conditions.

8.3 Sensitivity analysis of diverse characteristics of process limits

It has already been ascertained in Section 8.2.2 that the process limits of Wurster granulation, which are conceptualized in Sections 7.10 and 7.11, react sensitively to changed process parameter settings. In the following, various influences due to heat losses, spraying and evaporation, inlet temperature, and product diameter on diverse characteristics of process limits are shown in more detail. The different correction factors for velocity and the drying capacity of the process gas are analyzed. These are the gas velocity reduction factor of heat losses $\Phi_{u,T,eva}$ from Eq. 7.138, the drying capacity reduction factor of heat losses $\Theta_{Y,dis}$ from Eq. 7.157, the gas velocity reduction factor of evaporation cooling $\Phi_{u,T,eva}$ from Eq. 7.139, the gas velocity enhancement factor of released water vapor $\Phi_{u,Y,eva}$ from Eq. 7.140, and the overall gas velocity correction factor of evaporation $\Phi_{u,eva}$ from Eq. 7.146. In addition to this, the focus is placed on the limits of the inlet gas velocity that are referred to minimal Wurster fluidization and process-gas saturation. Unless otherwise stated, the results presented are based on the constant parameters of Tables 8.1 and 8.2.

8.3.1 Influence of heat losses and evaporation on correction factors of process gas velocity and drying capacity for different inlet gas temperatures

Heat losses

Heat losses through walls have an effect on the minimal-Wurster-fluidization limit (Section 7.10.1) and the process-gas-saturation limit (Section 7.10.2). The relative temperature drop Θ_{loss} of Eq. 7.65 and the effective inlet gas temperature $T_{in,eff}$ of Eq. 7.67 are used to quantify heat losses within the two-zone continuum model. The gas velocity reduction factor $\Phi_{u,T,dis}$ and the drying capacity reduction factor $\Theta_{Y,dis}$ (Eqs. 7.138 and 7.157) were introduced to represent the influence of the heat losses on the process limits of minimal Wurster fluidization and process-gas saturation through dimensionless factors and also to take them into account in the calculation equations of the process limits (Eqs. 7.141 to 7.143, 7.162, 7.163, and 7.166). The change in these correction factors with the relative temperature drop of heat losses Θ_{loss} from 0 to 20 % is illustrated in Figure 8.7 for three different inlet gas temperatures: 70°C, 90°C, and 110°C. It is seen that both the gas velocity reduction factor $\Phi_{u,T,dis}$ and the drying capacity reduction factor $\Theta_{Y,dis}$ decrease with higher relative temperature drop Θ_{loss} and with larger inlet gas temperature T_{in}. The decline of the gas velocity reduction factor is somewhat lower than that of the drying capacity reduction factor. The smallest values are ascertained with round $\Phi_{u,T,dis} = 0.953$ for the gas velocity reduction factor of heat losses and with round $\Theta_{Y,dis} = 0.82$ for the smallest drying capacity reduction factor. Consequently, calculating process limits for an adiabatic system with the given parameters of Figure 8.7 has relative errors below 5 % for the

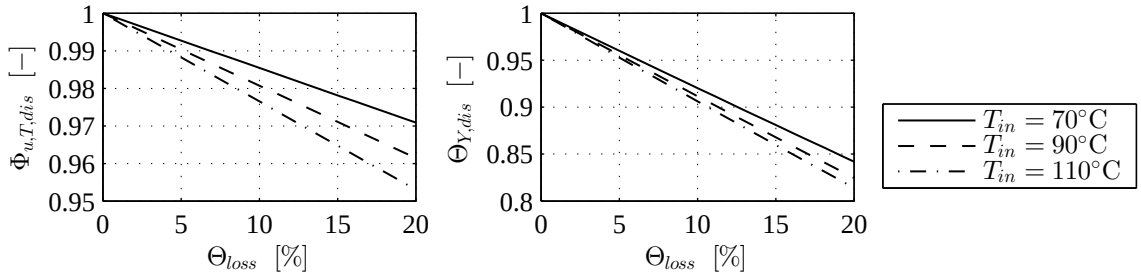

Figure 8.7: Influence of relative temperature drop of heat losses Θ_{loss} on gas velocity reduction factor of heat losses $\Phi_{u,T,dis}$, and on drying capacity reduction factor of heat losses $\Theta_{Y,dis}$ for different inlet gas temperatures T_{in}.

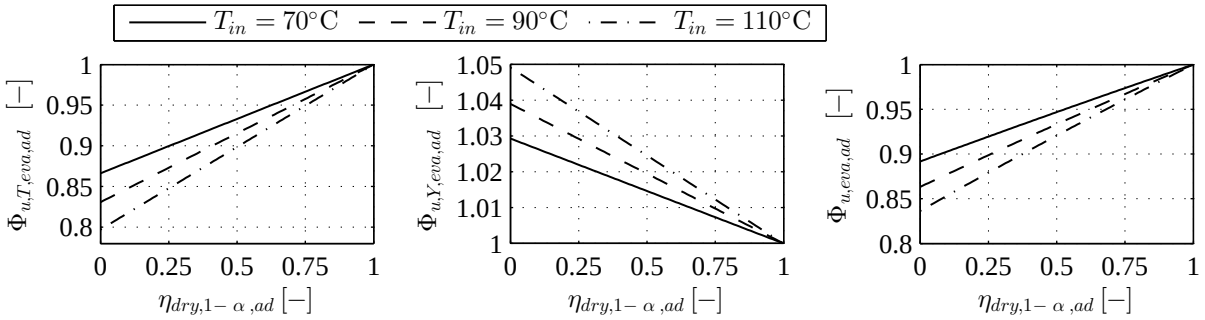

Figure 8.8: Influence of the drying potential of the drying zone process gas $\eta_{dry,1-\alpha}$ on the gas velocity reduction factor of evaporation cooling $\Phi_{u,T,eva}$, on the gas velocity enhancement factor of water vapor release $\Phi_{u,Y,eva}$, and on the overall gas velocity correction factor of evaporation $\Phi_{u,eva}$ for three different inlet gas temperatures.

minimal-Wurster-fluidization limit and below 18 % for the process-gas-saturation limit. Measurements of the relative temperature drop Θ_{loss}, which were generated with the experimental granulation plant used in this thesis (Section 9.2.1), are shown in Appendix C.6.1. The results (see Figures C.10 and C.11) include values from around $\Theta_{loss} = 13\,\%$ for an inlet gas mass flow rate of 60 kg/h (normal inlet gas velocity 0.5 m/s) to around $\Theta_{loss} = 5\,\%$ for an inlet gas mass flow rate of 120 kg/h (normal inlet gas velocity 1 m/s). This means that the described relative errors of adiabatic process limits (in terms of $\Phi_{u,T,dis}$ and $\Theta_{Y,dis}$) are even smaller for the employed experimental plant.

Spraying and evaporation

Evaporation of injected water affects process gas properties and thus also the point of minimal Wurster fluidization. The gas velocity reduction factor of evaporation cooling $\Phi_{u,T,eva}$ and the gas velocity enhancement factor of released water vapor $\Phi_{u,Y,eva}$ quantify opposing partial effects on the process gas velocity. The product of both, known as the overall gas velocity correction factor of evaporation $\Phi_{u,eva}$, determines in which direction and how much the process gas velocity changes due to water evaporation. All the three correction factors are functions of the water spray rate. As also described in Section 7.11.2, the decisive factor for this influence is not the water spray rate $\dot{M}_w$, but the drying potential of the process gas in the drying zone $\eta_{dry,1-\alpha}$ obtained from the lever principle in Eq. 7.120. The drying potential can have values from zero to one. Higher drying potentials represent a lower water spray rate and vice versa. The exact values of drying potential depend on many factors, as for instance shown in Eq. 7.183. However, the changes in minimal-Wurster-fluidization limit (presented in Section 8.3.2) and the related correction factors need only be considered within the value domain of the drying potential $0 \leq \eta_{dry,1-\alpha} \leq 1$, since over-saturated states are not relevant anyway. A drying potential of unity is obtained within the TZC-model if either spraying is completely refrained ($\eta_{dry,1-\alpha}(\dot{M}_w = 0) = 1$) or if all of the sprayed water has already evaporated in the

spray zone ($\eta_{dry,1-\alpha}(\dot{M}_w = \dot{M}_{eva,\alpha} > 0) = 1$). The mal-discharge of water droplets with the exhaust gas over the spray zone (Wurster tube) is not even considered. The drying potential becomes zero (saturation state) either at an inlet gas velocity of the minimal-Wurster-fluidization limit with a critical water spray rate ($\eta_{dry,1-\alpha}(u_{in} = u_{mwf}, \dot{M}_w = \dot{M}_{w,cr}) = 0$) or at an inlet gas velocity of the process-gas-saturation limit with a supercritical water spray rate ($\eta_{dry,1-\alpha}(u_{in} = u_{sat}, \dot{M}_w > \dot{M}_{w,cr}) = 0$). Only the first case is examined here. The relationships between the three gas velocity correction factors ($\Phi_{u,T,eva}$, $\Phi_{u,Y,eva}$, and $\Phi_{u,eva}$) and the drying potential of the drying zone process gas $\eta_{dry,1-\alpha}$ are illustrated in Figure 8.8 for three different inlet gas temperatures T_{in}. For each of the depicted inlet gas temperature examples, the following observation is made. All the three factors are by definition unity for a drying potential of unity. As expected, the gas velocity reduction factor of evaporation cooling $\Phi_{u,T,eva}$ drops to values below unity for higher evaporation rates ($\dot{M}_w \uparrow \Leftrightarrow \dot{M}_{eva,1-\alpha} \uparrow \Leftrightarrow \eta_{dry,1-\alpha} \downarrow$), while the gas velocity enhancement factor of released water vapor $\Phi_{u,Y,eva}$ increases to values above unity. At this, the reduction factor $\Phi_{u,T,eva}$ decreases more strongly than the enhancement factor $\Phi_{u,Y,eva}$ grows, so that the overall gas velocity correction factor takes on values below unity: $\Phi_{u,eva}(\eta_{dry,1-\alpha} < 1) < 1$. This means that evaporation cooling is the prevailing effect on process gas velocity and not the enlargement of gas volume by released water vapor. The decline of $\Phi_{u,T,eva}$-factor, the increase of the $\Phi_{u,Y,eva}$-factor, and the decrease of the $\Phi_{u,eva}$-factor are the steeper, the higher the evaporation rate and the inlet gas temperature is. Thus, spraying reduces the process gas velocity more distinctly for larger inlet gas temperatures. It can be seen from the $\Phi_{u,eva}$-diagram that the process gas velocity is lowered at saturation conditions by around 10.5 to 14 % for the investigated inlet gas temperatures.

8.3.2 Influence of spraying and evaporation on limits of minimal Wurster fluidization and process-gas-saturation for different inlet gas temperatures

The influence of spraying conditions on the limits of minimal Wurster fluidization and process-gas saturation is illustrated in the following for the example of an adiabatic system, in which evaporation does not take place, so that the relative temperature drop is zero ($\Theta_{loss} = 0$), the inlet gas temperature and the effective inlet gas temperature are equal ($T_{in} = T_{in,eff}$), and the gas velocity reduction factor of heat losses, the drying capacity reduction factor of heat losses, and the drying potential of the spray zone outlet gas are unity ($\Phi_{u,T,dis} = \Theta_{Y,dis} = \eta_{dry,\alpha,top} = 1$). The characteristics used as independent variables to represent spraying and evaporation conditions here are the drying potential of the drying zone process gas $\eta_{dry,1-\alpha}$ (as in Section 8.3.1), the water spray rate $\dot{M}_w$, and the dimensionless water spray rate $\dot{\mu}_w$.

Adiabatic minimal-Wurster-fluidization limit versus drying potential of the drying zone process gas

As mentioned before in Section 7.11.2, the inlet gas velocity of the adiabatic minimal-Wurster-fluidization limit $u_{mwf,ad}$ and its corresponding dimensionless inlet gas velocity $\xi_{mwf,ad}$ can be determined without iterations by the sequence of Eqs. 7.16 to 7.18, 7.23 to 7.28, 7.180, 7.181, and 7.193 to 7.195, when the inlet gas temperature T_{in}, the inlet gas moisture content Y_{in}, and the drying potential of the drying zone gas $\eta_{dry,1-\alpha,ad}$ are specified. According to this, $u_{mwf,ad}$ and $\xi_{mwf,ad}$ were calculated for the entire domain of the drying potential of the drying zone gas ($0 \leq \eta_{dry,1-\alpha,ad} \leq 1$), each of which for three different inlet gas temperatures: 70℃, 90℃, and 110℃. The results of them are shown in the left and the middle diagram of Figure 8.9. Both for the inlet gas velocity and its dimensionless equivalent of the adiabatic minimal-Wurster-fluidization limit, the same behavior is found with decreasing drying potential. The adiabatic minimal-Wurster-fluidization limit possesses values of the isothermal minimal-Wurster-fluidization limit at a drying potential of unity (see also Eqs. 7.188 and 7.189). The isothermal minimal-Wurster-fluidization limit is slightly raised by increasing inlet gas temperatures. The adiabatic minimal-Wurster-fluidization limit $\xi_{mwf,ad}$ becomes larger with decreasing drying potential, which is due to the reduced overall gas velocity correction factors of evaporation $\Phi_{u,eva}$ (see right diagram of Figure 8.8) and Eq. 7.180. The slope of the adiabatic minimal-Wurster-fluidization limit is flatter for higher inlet gas temperatures; wherefore, the $u_{mwf,ad}$- and $\xi_{mwf,ad}$-curves intersect. The point of intersection of the gas velocity is at a significantly lower drying potential of around 32 % compared to that of the dimensionless gas velocity at a drying potential of around 75 %.

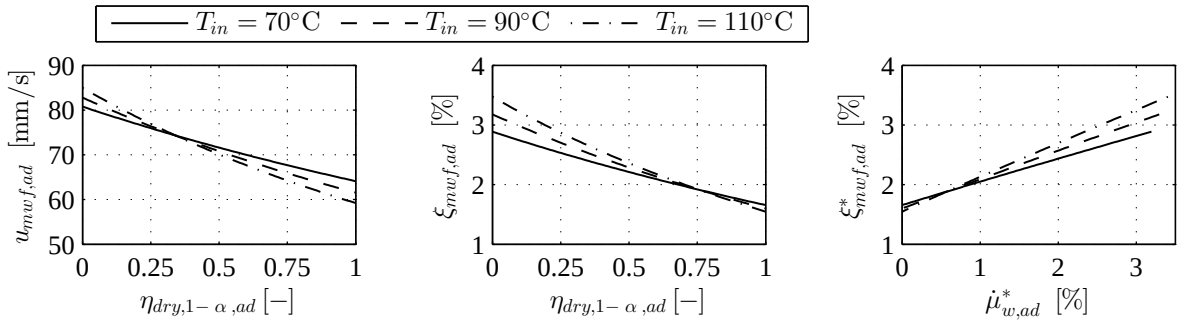

Figure 8.9: Influence of spraying (represented by $\eta_{dry,1-\alpha,ad}$ and $\dot{\mu}^*_{w,ad}$) on the minimal-Wurster-fluidization limit (represented by $u_{mwf,ad}$, $\xi_{mwf,ad}$, and $\xi^*_{mwf,ad}$) for three different inlet gas temperatures.

Approximate adiabatic minimal-Wurster-fluidization limit versus dimensionless water spray rate

When the system has adiabatic walls and the drying potential of the spray zone outlet gas $\eta_{dry,\alpha,top}$ is predefined, the adiabatic water spray rate $\dot{M}_{w,ad}$ and its dimensionless equivalent $\dot{\mu}_{w,ad}$ are exactly related to the drying potential of the drying zone process gas $\eta_{dry,1-\alpha,ad}$ and to the adiabatic minimal-Wurster-fluidization limit ($u_{mwf,ad}(\eta_{dry,1-\alpha,ad})$ and $\xi_{mwf,ad}(\eta_{dry,1-\alpha,ad})$, see first two diagrams of Figure 8.9) by the partial mass balance of water. The calculation of such a relationship is described by Eqs. 7.196 to 7.203 in Section 7.11.3 for the case example of the approximate adiabatic minimal-Wurster-fluidization limit $\xi^*_{mwf,ad}(\dot{\mu}^*_{w,ad})$, for which the absence of evaporation in the spray zone is assumed, so that the drying potential of the spray zone outlet gas is given with $\eta_{dry,\alpha,top} = 1$. Based on this, the dimensionless inlet gas velocity of the approximate adiabatic minimal-Wurster-fluidization limit $\xi^*_{mwf,ad}$ and the corresponding dimensionless water spray rates $\dot{\mu}^*_{w,ad}$ were calculated for the entire domain of the drying potential of the drying zone process gas ($0 < \eta^*_{dry,1-\alpha,ad} < 1$), each of which for the inlet gas temperatures considered here. The obtained $\xi^*_{mwf,ad}(\dot{\mu}^*_{w,ad})$-curves are shown in the third diagram of Figure 8.9. The values of the depicted dimensionless water spray rates range from zero up to the approximate adiabatic critical dimensionless water spray rate of Eq. 7.221: $0 \leq \dot{\mu}^*_{w,ad} \leq \dot{\mu}^*_{w,cr,ad}$. The critical point grows a little with the inlet gas temperature from around 3.19 to 3.4 % (compare with Table 8.9). It is further visible that $\xi^*_{mwf,ad}$ increases almost linearly with $\dot{\mu}^*_{w,ad}$ for each of the T_{in}-examples. It should be particularly emphasized that the dimensionless inlet gas velocity and the dimensionless water spray rate presented in Figure 8.9 take on relatively small values between round 1.5 and 3.5 % for $\xi_{mwf,ad}$ and $\xi^*_{mwf,ad}$ and between 0 and 3.4 % for $\dot{\mu}^*_{w,ad}$ in contrast to the process-gas-saturation limit (Figure 8.10), more on this below.

Approximate adiabatic process-gas-saturation limit

It is already known through Eqs. 7.204 and 7.207 in Section 7.11.4 that both the inlet gas velocity of the approximate adiabatic process-gas-saturation limit $u^*_{sat,ad}$ and its corresponding dimensionless inlet gas velocity $\xi^*_{sat,ad}$ grow linearly with the dimensionless water spray rate $\dot{\mu}_w$ and via Eq. 7.130 also with the water spray rate $\dot{M}_w$. Nevertheless, the functions of $u^*_{sat,ad}$ versus $\dot{M}_w$, of $u^*_{sat,ad}$ versus $\dot{\mu}_w$, and of $\xi^*_{sat,ad}$ versus $\dot{\mu}_w$ are shown in Figure 8.10 for three different inlet gas temperatures T_{in}: 70℃, 90℃, and 110℃. It can be seen that the inlet gas velocity of the approximate adiabatic process-gas-saturation limit $u^*_{sat,ad}$ increases the stronger with the water spray rate $\dot{M}_w$, the lower the inlet gas temperature is. The reason for this is that the drying power is less at reduced inlet gas temperatures, so that higher inlet gas velocities are needed to provide the required evaporation energy. When plotted against the dimensionless water spray rate $\dot{\mu}_w$, the slope of the inlet gas velocity of process-gas-saturation limit $u^*_{sat,ad}$ is only marginally lowered with higher inlet gas temperatures, which is due to the very slight decline of the reference elutriation gas velocity $u_{elu,ref}$ (compare with Table 8.8). The influence of the inlet gas temperature on the $\xi^*_{sat,ad}(\dot{\mu}_w)$-curves is even smaller, although the reference fluidization range number $f_{rn,ref}$ varies among these curves. This speaks for using a ξ_{sat}-$\dot{\mu}_w$-diagram as a general process parameter map of stable Wurster fluidization, where the process-gas-saturation limit defines the border between an unsaturated regime and a saturated regime. Such a map is created below in Section 8.4, where the limits of minimal-Wurster-fluidization and

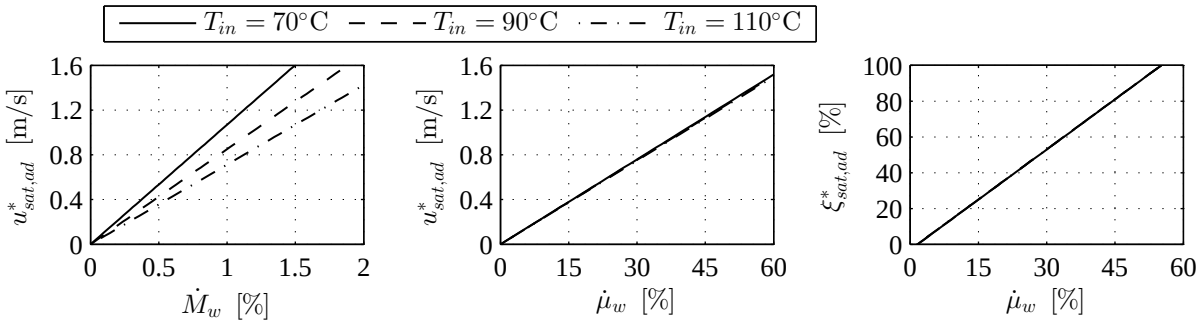

Figure 8.10: Influence of spraying (represented by $\dot{M}_w$ and $\dot{\mu}_w$) on the process-gas-saturation limit (represented by $u^*_{sat,ad}$ and $\xi^*_{sat,ad}$) for three different inlet gas temperatures.

Wurster-tube-exceedance are considered too. The ranges of values of the dimensionless water spray rate and the dimensionless inlet gas velocity that are relevant for the process-gas-saturation limit are much wider than those of the minimal-Wurster-fluidization limit. The $\xi^*_{sat,ad}(\dot{\mu}_w)$-curves are also many times steeper than the $\xi_{mwf,ad}(\dot{\mu}_w)$-curves. Therefore, the process-gas-saturation limit exceeds the minimal-Wurster-fluidization limit already at low (dimensionless) water spray rates, which is already described in Section 7.11.6 and is taken into account in the next section.

8.3.3 Influence of particle size on minimal inlet gas velocity

The influence of particle size on spray-rate-dependent curves of the general minimum inlet gas velocity $u^*_{min,ad}(\dot{M}_w)$ of Eq. 7.222 and its corresponding dimensionless equivalent $\xi^*_{min,ad}(\dot{\mu}_w)$ of Eq. 7.223 is illustrated and discussed in this section. Both functions place the isothermal minimal-Wurster-fluidization limit ($u_{mwf,iso}$ and $\xi_{mwf,iso}$, Section 7.11.1), the approximate adiabatic minimal-Wurster-fluidization limit ($u^*_{mwf,ad}(\dot{M}_w)$ and $\xi^*_{mwf,ad}(\dot{\mu}_w)$, Section 7.11.3), and the approximate adiabatic process gas saturation limit ($u^*_{sat,ad}(\dot{M}_w)$ and $\xi^*_{sat,ad}(\dot{\mu}_w)$, Section 7.11.4) on a continuous curve in the $u_{in}(\dot{M}_w)$-diagram and the $\xi_{in}(\dot{\mu}_w)$-diagram, respectively. These curves shall be created for three different bed particle diameters (d: 0.3 mm, 0.8 mm, and 2 mm). The inlet gas temperature in this section is constantly given with $T_{in} = 70℃$. The associated reference isenthalpic saturation point $T_{sat,ref}$ and $Y_{sat,ref}$ can be read from the second row of Table 8.8. The overall gas velocity correction factor of evaporation for saturated process gas conditions ensues from Eq. 7.190 to $\Phi_{u,eva,ad,cr} = 0.892$.

Calculation of characteristic curve parameters

For creating the $u^*_{min,ad}(\dot{M}_w)$- and $\xi^*_{min,ad}(\dot{\mu}_w)$-curves for each of the three particle diameters, the characteristic parameters of Table 8.10 were calculated. These are the terminal Reynolds number Re_s (Eq. 2.83), the reference minimal fluidization velocity $u_{mf,ref}$ (Eqs. 2.113, 2.119, and 7.124), the reference elutriation velocity $u_{elu,ref}$ (Eqs. 2.87, 2.122, 7.125), the reference fluidization range number $f_{rn,ref}$ (Eq. 7.126), the inlet gas velocity of the isothermal minimal-Wurster-fluidization limit $u_{mwf,iso}$ (Eq. 7.178) and its dimensionless equivalent $\xi_{mwf,iso}$ (Eq. 7.179), and the approximate adiabatic critical water spray rate $\dot{M}^*_{w,cr,ad}$ (Eq. 7.220) and its dimensionless equivalent $\dot{\mu}^*_{w,cr,ad}$ (Eq. 7.221). As to be expected by the fundamentals of Sections 2.2.1 and 2.2.4, the terminal Reynolds number Re_s, the reference minimal fluidization velocity $u_{mf,ref}$, and the reference elutriation velocity $u_{elu,ref}$ become larger for bigger particles. The listed terminal Reynolds numbers Re_s show that all three particle diameter examples are situated in the transition flow regime after the criteria of [24, 28, 33], stated in Table 2.2. The reference fluidization range number $f_{rn,ref}$, on the contrary, strongly decreases with higher particle diameters in the transition regime, which means that the fluidization range is smaller for larger particles. A relation between $f_{rn,ref}$ and d was also illustrated by Mörl et al. ([29], "Fig. 11") in an inverse form by a Re_{mf}/Re_{elu}-Ar-diagram. The depicted curve was generated on basis of the calculation method CMFL-1 of Table 2.3 (see also Eq. 2.126). From this, it can be deduced that the maximal reference fluidization number converges to an upper limit for particle diameters going to zero ($f_{rn}(\text{CMFL-1}, d \to 0) = 77.8$) and to a lower limit for infinitely growing particle diameters ($f_{rn}(\text{CMFL-1}, d \to \infty) = 8.6$). In the present TZCM-study, the calculation method CMFL-2 of Table 2.3 is

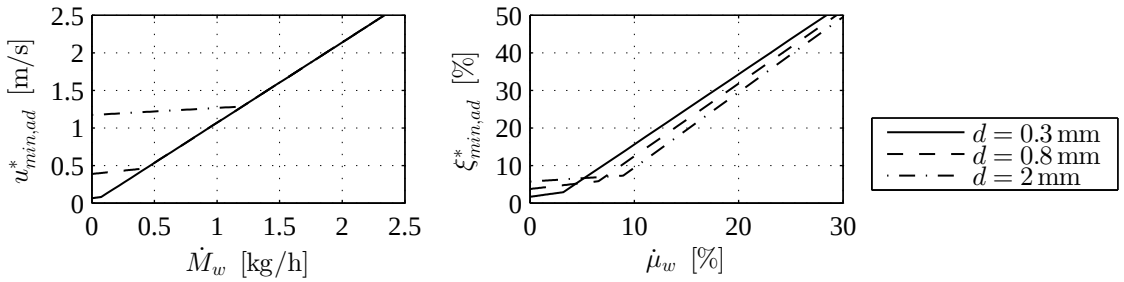

Figure 8.11: Influence of particle size on the spray-rate-dependent curves of the minimal inlet gas velocity $u^*_{min,ad}$ and minimal dimensionless inlet gas velocity $\xi^*_{sat,ad}$.

d [mm]	Re_s [–]	$u_{mf,ref}$ [mm/s]	$u_{elu,ref}$ [mm/s]	$f_{rn,ref}$ [–]	$u_{mwf,iso}$ [mm/s]	$\xi_{mwf,iso}$ [%]	$\dot{M}^*_{w,cr,ad}$ [g/h]	$\dot{\mu}^*_{w,cr,ad}$ [%]
0.3	20.66	41.67	1395	33.5	64.11	1.66	75.56	3.193
0.8	153.0	251.4	3875	15.4	386.8	3.74	432.1	6.578
2	782.3	761.7	7925	10.4	1172	5.73	1202	8.946

Table 8.10: Approximate adiabatic critical water spray rate and the corresponding dimensionless water spray rate for three different particle diameters.

applied. The $f_{rn}(Ar)$-dependency of CMFL-2 (see Eq. 2.126) is much more complex than that of CMFL-1, but both provide roughly the same tendency of f_{rn}-values for $10^{-4} \leq Ar \leq 10^{12}$, as shown previously with Figure 2.4 and Eq. 2.129. The inlet gas velocity of the isothermal minimal-Wurster-fluidization limit $u_{mwf,iso}$ rises linearly with the reference minimal fluidization velocity according to Eq. 7.178. But also the corresponding dimensionless inlet gas velocity $\xi_{mwf,iso}$ increases a little with d due to Eq. 7.179 and significantly with decreasing reference fluidization range number $f_{rn,ref}$ within the transition regime. The change in $u_{mf}(T_{sat,ref}, Y_{sat,ref})$ and $f_{rn,ref}$ with particle size leads to an enlargement of the approximate adiabatic critical water spray rate $\dot{M}^*_{w,cr,ad}$ and its corresponding dimensionless water spray rate $\dot{\mu}^*_{w,cr,ad}$ via Eqs. 7.220 and 7.221.

Spray-rate-dependent curves of minimal inlet gas velocity and minimal dimensionless inlet gas velocity

Figure 8.11 shows the $u^*_{min,ad}(\dot{M}_w)$-curves for the three diameters in the left diagram, and the $\xi^*_{min,ad}(\dot{\mu}_w)$-curves in the right diagram. At zero spray rate, the general minimal inlet gas velocity and its dimensionless equivalent coincide with the isothermal minimal-Wurster-fluidization limit given in Table 8.10: $u^*_{min,ad}(\dot{M}_w = 0) = u_{mwf,iso}$ and $\xi^*_{min,ad}(\dot{\mu}_w) = \xi_{mwf,iso}$. Therefore, the general minimal inlet gas velocity of non-spraying conditions is clearly risen with larger diameters, while the corresponding dimensionless inlet gas velocity is enhanced a little. Since the approximate adiabatic critical water spray rate $\dot{M}^*_{w,cr,ad}$ and its corresponding dimensionless water spray rate $\dot{\mu}^*_{w,cr,ad}$ of Table 8.10 grow with the diameter d, the depicted range of the minimal Wurster fluidization ($0 < \dot{M}_w < \dot{M}_{w,cr}$ and $0 < \dot{\mu}_w < \dot{\mu}^*_{w,cr,ad}$) is wider for the larger particles. The $u^*_{min,ad}(\dot{M}_w)$- and $\xi^*_{min,ad}(\dot{\mu}_w)$-slopes of this range are positive, but flat, and they are not much different between the three d-examples. In the diagram on the left, all three curves fall on the same saturation line ($u^*_{min,ad}(\dot{M}_w \geq \dot{M}_{w,cr,ad}) = u^*_{sat,ad}$), as this is by definition (Eq. 7.204) independent of particulate properties. The $\xi^*_{min,ad}(\dot{\mu}_w)$-slopes of the saturated range ($\dot{\mu}_w \geq \dot{\mu}^*_{w,cr,ad}$) get slightly higher for greater particles. But, they are much steeper than for the unsaturated regime and intercept, therefore, the $\xi^*_{min,ad}$-curves of the bigger particles in their range of undercritical dimensionless water spray rates. Contrary to the minimum-Wurster-fluidization limit, the dimensionless inlet gas velocity of the process-gas-saturation limit shifts downwards for larger particles under the present parameter conditions.

8.4 Characterization of experimental conditions from Hampel's case study

Some of the experimental conditions of Hampel's case study ([1, 2], recapitulated in Section 2.3) shall be assessed by the two-zone continuum model with regard to process stability and to Wurster fluidization kinetics in this section. Therefore, several corresponding dimensionless process parameters and characteristics of circulating Wurster fluidization are to be determined and presented in Section 8.4.1. The dimensionless process parameters can be used for setting stable operating points for granulation systems of different scales. The characteristics of circulating Wurster fluidization can serve as parameters for Hampel's three-compartment population balance model and its supplemented version of Chapter 6. The experimental operation points are, in addition, illustrated within two operation maps of stable Wurster fluidization from Section 8.4.2, which are created on basis of approximate process limits of Section 7.11.

All results shown here are based on the following assumptions. The bed material consists of mono-sized, spherical particles with a diameter of $d = 0.3\,\mathrm{mm}$ and an effective particle density of $\rho_p = 1380\,\mathrm{kg/m^3}$. The given particulate properties match roughly with the specifications of Cellets®200 (see Tables 9.1 and C.1) employed as initial material in granulation experiments of Hampel and the present thesis (Section 10.4). The parameters of the dimensions of the model distributor plate and of the model process chamber are adopted from Tables 8.1 and 8.2. They accord also with Hampel's experimental setting (described in Section 9.2.1). The bed mass is constantly given with $M_{bed} = 1\,\mathrm{kg}$. Heat losses are disregarded, so that the relative temperature drop is zero ($\Theta_{loss} = 0$).

8.4.1 Model characteristics of several experimentally applied operation points

The experimental process conditions of Hampel to be described by the TZC-model, some corresponding dimensionless process parameters and limits, and some corresponding model characteristics of circulating Wurster fluidization are listed in Table 8.11.

Combinations of experimental process parameters

The process parameters from Hampel's experiments to be investigated here are combinations of two different inlet gas temperatures T_{in} (70℃ and 90℃), three different inlet gas mass flow rates $\dot{M}_{in}$ (70 kg/h, 85 kg/h, and 100 kg/h), and two different water spray rates $\dot{M}_w$ (542 g/h and 677.5 g/h). A total of twelve experimental operating conditions result from this, as listed by No. 1 - 12 in Table 8.11. The water spray rate examples conform with the total desired spray rates of $\dot{M}_{spr,set} = 800\,\mathrm{g/h}$ and $\dot{M}_{spr,set} = 1000\,\mathrm{g/h}$ that are used in the granulation experiments of the present thesis (see Table 10.15), for which a sodium benzoate spray solution with a solids mass fraction of $x_s = 32.25\,\%$ was prepared.

Corresponding dimensionless process parameters and limits

The reference isenthalpic saturation temperature $T_{sat,ref}$ of Eq. 7.127, the associated moisture content $Y_{sat,ref}$ of Eq. 7.128, the reference minimal fluidization velocity $u_{mf,ref}$ of Eq. 7.124, the reference elutriation velocity $u_{elu,ref}$ of Eq. 7.125, the reference fluidization range number $f_{rn,ref}$ of Eq. 7.126, and the approximate adiabatic critical dimensionless water spray rate $\dot{\mu}^*_{w,cr,ad}$ of Eq. 7.221 are only affected by the inlet gas temperature from the independent process parameters of Table 8.11 (T_{in}, $\dot{M}_{in}$, and $\dot{M}_w$). They were previously determined as part of the TZCM-3 study and can be found in the second and fourth row of Tables 8.8 and 8.9. Table 8.11 shows further dimensionless process parameters that vary between the operation point examples of No. 1 - 12. These are the dimensionless water spray rate $\dot{\mu}_w$, the dimensionless inlet gas velocity to be operated with ξ_{in}, the dimensionless inlet gas velocity of the approximate adiabatic process-gas-saturation limit $\xi^*_{sat,ad}$, and the dimensionless inlet gas velocity of the Wurster-tube-exceedance limit $\xi^*_{exc,ad}$. The dimensionless water spray rate $\dot{\mu}_w$ follows from Eq. 7.130 with values between 18.34 and 28.63 %. It does not depend on the inlet gas mass flow rate $\dot{M}_{in}$, but it becomes lower with increasing inlet gas temperatures T_{in} and higher for the larger water spray rates $\dot{M}_w$. However, for each of the depicted operation points, the dimensionless water spray rate is supercritical ($\dot{\mu}_w > \dot{\mu}^*_{w,cr,ad}$ for No. 1 - 12), so that the approximate adiabatic process-gas-saturation limit defines the general minimal (dimensionless) inlet gas velocity, drying and agglomeration kinetics excluded. The obtained values of the dimensionless inlet gas velocity ξ_{in} lie between 52.56 % (No. 1 and 4) and 81.6 % (No. 9 and 12). They enlarge somewhat with the inlet gas temperature T_{in} and strongly with the inlet gas mass flow rate $\dot{M}_{in}$, but stay constant for the

No. [–]	T_{in} [℃]	$\dot{M}_{in}$ [kg/h]	$\dot{M}_w$ [g/h]	$\dot{\mu}_w$ [℃]	ξ_{in} [%]	$\xi^*_{sat,ad}$ [%]	$\xi^*_{exc,ad}$ [%]	α_m [%]	τ_α [s]	$\tau_{1-\alpha}$ [s]
1	70	70	542	22.91	52.56	39.72	129.5	1.72	0.203	11.6
2	70	85	542	22.91	64.49	39.72	129.5	1.19	0.138	11.5
3	70	100	542	22.91	76.41	39.72	129.5	0.88	0.104	11.7
4	70	70	677.5	28.63	**52.56**	**50.42**	131.2	1.73	0.203	11.5
5	70	85	677.5	28.63	64.49	50.42	131.2	1.20	0.138	11.4
6	70	100	677.5	28.63	76.41	50.42	131.2	0.88	0.104	11.6
7	90	70	542	18.34	56.23	31.26	128.9	1.56	0.182	11.5
8	90	85	542	18.34	68.91	31.26	128.9	1.07	0.125	11.5
9	90	100	542	18.34	81.60	31.26	128.9	0.79	0.095	11.9
10	90	70	677.5	22.92	56.23	39.81	130.6	1.57	0.182	11.4
11	90	85	677.5	22.92	68.91	39.81	130.6	1.08	0.125	11.5
12	90	100	677.5	22.92	81.60	39.81	130.6	0.80	0.095	11.8

Table 8.11: Characteristics of the TZC-model in terms of dimensionless process parameters ($\dot{\mu}_w$ and ξ_{in}), process limits ($\xi^*_{sat,ad}$, and $\xi^*_{exc,ad}$), the bed mass fraction of the spray zone α_m, and the residence times of the spray zone τ_α and drying zone $\tau_{1-\alpha}$ for different operation points (T_{in}, $\dot{M}_{in}$, and $\dot{M}_w$) of Hampel's case study [1, 2].

two water spray rates $\dot{M}_w$. The dimensionless inlet gas velocities of the approximate adiabatic process-gas-saturation limit $\xi^*_{sat,ad}$ are smaller with values from 31.26 to 50.42 %. They are the higher the lower the inlet gas temperature T_{in} and the larger the water spray rate $\dot{M}_w$ is, and they are independent from the inlet gas mass flow rate $\dot{M}_{in}$. It should be particularly emphasized that the dimensionless inlet gas velocity of the operating point No. 4 is quite close to the saturation limit, which is taken into account again later in the parameter setting of the continuous granulation experiments. The dimensionless inlet gas velocities of the Wurster-tube-exceedance limit $\xi^*_{exc,ad}$ are only slightly influenced by each of the three process parameters of Table 8.11. Their values range from 128.9 to 131.2 %.

Corresponding model characteristics of circulating Wurster fluidization

The TZC-model characteristics of circulating sprayed Wurster fluidization to be considered here are the bed mass fractions of the spray zone α_m and the particle residence times of the spray zone τ_α and the drying zone $\tau_{1-\alpha}$. The calculated bed mass fractions of the spray zone have values between 0.8 and 1.72 %, which are not far from the bed mass fraction (1 %) used the PB-simulation studies of Hampel [1] and this thesis (Chapter 6, [105]) for continuous granulation with external product classification. The spray zone residence time τ_α of the operation points is quite small with 0.095 s as minimum and 0.203 s as maximum, but again close to the spray zone residence time τ_α of PB-studies of Hampel and this work (0.1 s). The best agreement between of the TZC-model results and the PB-parameter values of α_m and τ_α are given for the processes of Table 8.11 with 100 kg/h as inlet gas mass flow rate. The drying zone residence time $\tau_{1-\alpha}$ hardly changes between 11.4 s and 11.8 s among the different process conditions.

8.4.2 Classification in operating maps of Wurster fluidization

Two operation maps of Wurster granulation shown in Figure 8.12 have been created in form of a ξ_{in}-$\dot{\mu}_w$-diagram for the inlet gas temperatures of 70℃ and 90℃, respectively. Either map includes three curves of the general approximate adiabatic minimal dimensionless inlet gas velocity $\xi^*_{min,ad}(\dot{\mu}_w)$ of Eq. 7.223 for different spray loss fractions ($\Phi_{spr,loss} \in \{0, 10\,\%, 20\,\%\}$), one curve of the Wurster-tube-exceedance limit $\xi^*_{exc,ad}(\dot{\mu}_w)$ of Section 7.10.3, and the experimentally applied operating points No. 1-12 (T_{in}, $\dot{M}_{in}$, $\dot{M}_w$) of Table 8.11.

Spray-rate-dependent process limit curves

Each of $\xi^*_{min,ad}$-curves unifies the isothermal minimal-Wurster-fluidization limit $\xi_{mwf,iso}$ of Section 7.11.1 at $\dot{\mu}_w = 0$, the approximate adiabatic minimal-Wurster-fluidization limit $\xi^*_{mwf,ad}$ of Section 7.11.3 for $0 <$

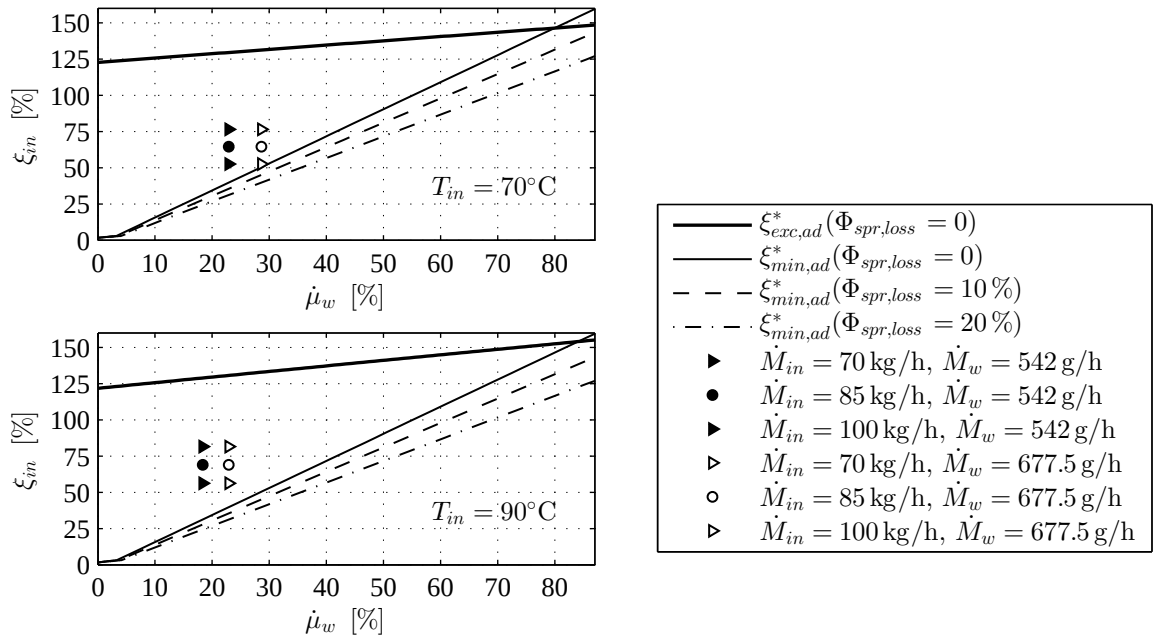

Figure 8.12: Dimensionless operation map of Wurster granulation containing process limit curves ($\xi^*_{min,ad}$ and $\xi^*_{exc,ad}$) and several appropriate operation points of experiment application.

$\dot{\mu}_w < \dot{\mu}_{w,cr,ad}$, and the approximate adiabatic process-gas-saturation limit $\xi^*_{sat,ad}$ of Section 7.11.4 for $\dot{\mu}_w \geq \dot{\mu}_{w,cr,ad}$. The $\xi^*_{exc,ad}$-curves were determined by iterating the implemented TZC-model from Sections 7.1 to 7.7 using the criterion in Eq. 7.168 and neglecting spray zone evaporation ($\eta_{dry,1-\alpha,top} = 1$). The spray loss fraction $\Phi_{spr,loss}$ shall represent here the amount of sprayed water which is not deposited on particle surfaces, but is discharged with the exhaust gas and dried above the Wurster tube. At this point it is remarked that mal-discharged droplets can be evaporated in the exhaust gas, even when the drying zone process gas is saturated, since the spray zone outlet gas flow is around 45 % of the inlet gas mass flow rate (drying power bypass fraction $\Omega_{2,in}$ in Table 8.1) and has still enough drying potential (see Appendix C.6.2). It can be seen that higher spray loss fractions reduce the slope of the $\xi^*_{sat,ad}(\dot{\mu}_w)$-function and shift therefore the entire curve of the general minimal dimensionless inlet gas velocity $\xi^*_{min,ad}$ downwards. Further, the general minimal dimensionless inlet gas velocity $\xi^*_{min,ad}$ and the Wurster-tube-exceedance limit $\xi_{exc,ad}$ enclose a region of permissible process parameters, wherein sprayed Wurster fluidization should be realized. At this, the dimensionless inlet gas velocity has to be above the general minimal dimensionless inlet gas velocity and below the Wurster-tube-exceedance limit: $\xi^*_{min,ad}(\dot{\mu}_w) < \xi_{in} < \xi_{exc,ad}(\dot{\mu}_w)$. It is obvious that this range is the largest at dimensionless water spray rates close to zero and becomes smaller with an increasing dimensionless water spray rate. Finally the lower and upper limit curves intersect at relatively high dimensionless water spray rates, which lie for the case of zero spray losses ($\xi^*_{sat,ad}(\Phi_{spr,loss} = 0) = \xi^*_{exc,ad}$) at a dimensionless water spray rate of round 80 % for the 70℃-diagram and of round 83 % for the 90℃-diagram.

Recommendations for easier creation of operation maps

It has already been shown in Figure 8.9 that the dimensionless inlet gas velocity of the approximate adiabatic minimal-Wurster-fluidization limit $\xi^*_{mwf,ad}$ increases almost linearly with the dimensionless water spray rate $\dot{\mu}_w$. The dimensionless inlet gas velocity of the approximate adiabatic process-gas-saturation limit $\xi^*_{sat,ad}$ is by definition a straight line in the ξ_{in}-$\dot{\mu}_w$-diagram, see Eq. 7.207. The process maps in Figure 8.12 also show that the dimensionless inlet gas velocity of the Wurster-tube-exceedance limit $\xi^*_{exc,ad}$ depends quasi-linearly on the water spray rate $\dot{\mu}_w$. To create such operation maps for practice, it is therefore sufficient to determine only the following (corner) points and to connect them linearly with one another: $\xi_{mwf,iso}$ at $\dot{\mu}_w = 0$, $\xi^*_{sat,ad}$ at $\dot{\mu}_w = \dot{\mu}^*_{w,cr,ad}$, $\xi^*_{exc,ad}$ at $\dot{\mu}_w = 0$, and $\xi^*_{exc,ad} = \xi^*_{sat,ad}$ where $\eta_{dry,1-\alpha} = 0$. For the last-mentioned point, the associated dimensionless water spray rate must be determined iteratively. The calculations can, however, be further simplified by using the approximate isothermal Wurster-tube-exceedance limit $\xi^*_{exc,iso}$ of Section

7.11.5 instead of the iterative Wurster-tube-exceedance limit $\xi^*_{exc,ad}$, once with inlet gas conditions (T_{in}, Y_{in}) for the y-intercept ($\dot{\mu}_w = 0$) and once with the reference saturation point ($T_{sat,ref}$, $Y_{sat,ref}$) for the point of intersection with the saturation line ($\xi^*_{exc,iso} = \xi^*_{sat,ad}$). For the latter point of intersection, a maximal approximate dimensionless water spray rate according to $\dot{\mu}^*_{w,max,ad} = \dot{\mu}_w(\xi^*_{exc,iso} = \xi^*_{sat,ad})$ can be derived by equating Eqs. 7.207 and 7.217.

Experimental operation points

It has already been recognized from the dimensionless inlet gas velocities ξ_{in}, the process-gas-saturation limits $\xi^*_{sat,ad}$, and the Wurster-tube-exceedance limits $\xi^*_{exc,ad}$ of Table 8.11 that all the operation points No. 1 -12 are located in the region of permissible process parameters of sprayed Wurster fluidization, which again becomes clear in Figure 8.12. It is noticeable that all of the operating points depicted are closer to the lower than to the upper process limit. They are the closer to the saturation line, the smaller the dimensionless inlet gas velocity and the higher the water spray rates are. At this, all operation point examples have a clear distance from the saturation limit, except for No. 4. The latter is nearby the process-gas-saturation limit with a spray loss fraction of zero $\xi^*_{min,ad}(\Phi_{spr,loss} = 0)$. This process limit would be lower in practice as a small amount of water evaporates already in the spray zone and some droplets are mal-discharged with process gas. Nevertheless, drying kinetics in the drying zone is slow when the process gas is almost completely saturated. This causes an increase in wet surfaces of the bed material, and thus, enlarges the tendency towards unwanted agglomeration and the risk of process destabilization. The process stability would be more endangered than when a solids containing liquid of higher viscosity is sprayed, what increases the binding effect. The inlet gas conditions of the parameter example No. 4 (70℃, 70 kg/h) were employed within the discontinuous granulation study of Section 10.1, in which it was found to be prone to destabilization (see Table 10.2: EB-21-1 to EB-21-5). For these reasons, an inlet gas temperature of 70℃ is excluded from the choice of process parameters for the continuous granulation experiments in Section 10.4.1. Instead of this, an inlet gas temperature of 90℃ is preferred. Aspects of spraying, such as the nozzle gas excess pressure and spray losses, are also taken into account for the design of operation concepts of continuous granulation. These are investigated in the batch experiments.

8.5 Discussion and conclusions

8.5.1 Discussion

Difference between the approximate and iterative Wurster-tube-exceedance limits

The iterative Wurster-tube-exceedance limit of Section 7.10.3 and the approximate isothermal Wurster-tube-exceedance limit were determined for each of the parameter variation series TZCM-1, TZCM-2, and TZCM-3. The results of them are given in Table 8.6 (see $\xi_{exc,iso}$- and $\xi^*_{exc,iso}$-values), Table 8.7 (see $\xi^*_{exc,ad}$-values), and Table 8.9 (see $\xi^*_{exc,ad}$- and $\xi^*_{exc,iso}$-values) in the order of the varied parameters of Table 8.4. The iterative Wurster-tube-exceedance limit of the TZCM-2 series must be compared to the approximate isothermal Wurster-tube-exceedance limit of 1 kg bed mass from Table 8.6 ($\xi^*_{exc,iso} = 120.8\,\%$). The deviations between the iterative and approximate upper limits are the lowest in the isothermal series TZCM-1, where spraying is refrained. When water injection is activated, these deviations increase, and even more the higher the water spray rate is. Variation of the inlet gas temperature slightly influences the error between the iterative and approximate Wurster-tube-exceedance limit. Changes in process gas state properties (T,Y) within the drying zone due to evaporation effects are the main reason for these differences. Evaporation cooling is dominant compared to the mass increase of the gas flow, which leads to a reduction of process gas velocity in the fluidized bed region, as also shown in Figure 8.8 by the overall gas velocity correction factor $\Phi_{u,eva,ad}$. Larger water spray rates lower the drying potential of the process gas in the drying zone $\eta_{dry,1-\alpha,ad}$, and thus, the overall gas velocity correction factor $\Phi_{u,eva,ad}$ too. Therefore, higher inlet gas velocities are necessary to reach the Wurster-tube-exceedance limit. In contrast to the iterative approach of this limit, the approximated variant remains unaffected by evaporation effects. Consequently, the deviation between the iterative and approximate solutions increases with the water spray rate. The largest error occurs for saturated process gas conditions. This corresponds to the operation points of Figure 8.12, at which the $\xi^*_{exc,ad}(\dot{\mu}_w)$- and the $\xi^*_{min,ad}(\dot{\mu}_w)$-curves cross each other. Another error source is that the bed heights of the $\xi_{exc,iso}$-, $\xi^*_{exc,ad}$- and $\xi^*_{exc,iso}$-limits were calculated by slightly different methods. At this, the quadratic approximation of the drying zone volume depending on the drying zone bed height of Eq. 7.12 with the maximal bed height $H_{1-\alpha,max} = H_{wt} + L_{wt}$ as input variable was employed for the iterative Wurster-tube-exceedance limits

$\xi_{exc,iso}$ and $\xi^*_{exc,ad}$; whereas the approximate isothermal Wurster-tube-exceedance limit $\xi^*_{exc,iso}$ is based on the cubic relation of Eq. 7.9 and with maximal volume of the drying zone $V_{1-\alpha,max}$ as input variable.

Qualitative dependency of Wurster suction rate on dimensionless inlet gas velocity

The entire qualitative dependency of the Wurster suction rate $\dot{M}_{wt,tor}$ on the dimensionless inlet gas velocity ξ_{in} from the point of minimal Wurster fluidization up to the Wurster-tube-exceedance limit shall be explained in more detail at this point by analyzing the results of the isothermal parameter variation study TZCM-1 given in Figure 8.2. As already stated, the functional relationship of $\dot{M}_{wt,tor}(\xi_{in})$ is clearly characterized by a maximum for dimensionless inlet gas velocities in vicinity of the lower limit. The bed porosity of the drying zone $\varepsilon_{1-\alpha}$ and the bed height $H_{1-\alpha}$ contrarily affect the Wurster suction rate $\dot{M}_{wt,tor}$ according to the modified Torricelli approach in Eq. 7.116. The bed porosity $\varepsilon_{1-\alpha}$ increases steadily with the dimensionless inlet gas velocity. This has a lessening effect on the Wurster suction rate, since the particle concentration $(1-\varepsilon_{1-\alpha})$ becomes lower then, and thus, fewer particles are present in the sucked suspension flow. At the same time, the bed mass fraction of the spray zone α_m declines very sharply with a growing dimensionless inlet gas velocity nearby the minimal-Wurster-fluidization limit, that results in a strong enlargement of the bed mass in the drying zone $M_{1-\alpha}$. Hence, the bed height $H_{1-\alpha}$ rises once by a greater bed mass and once by stronger bed expansion. Larger bed heights again have an increasing effect on the Wurster suction rate, which is stronger than the dilution effect of smaller particle concentrations. Thereby the Wurster suction rate initially increases to a maximum at low dimensionless inlet gas velocities. From this point on, the bed height no longer rises quite as strongly, and the bed porosity also approaches the unity mark, wherefore the Wurster suction rate decreases again with even faster inlet flows.

Characteristics of the fluid-particle transport dynamics

The characteristics of the fluid-particle transport dynamics of the spray zone and drying zone include bed mass fractions (α_m and $1-\alpha_m$), relative void volumes (ε_α and $\varepsilon_{1-\alpha}$), the particle residence times (τ_α and $\tau_{1-\alpha}$), and the Wurster suction rate $\dot{M}_{wt,tor}$. The solutions of these quantities presented here were calculated on the basis of the values proposed by Burgschweiger a. Tsotsas [90,91] for an empirical flow correction coefficient λ_{tor} and the exponent m_{pul} of the modified Torricelli-approach of Eqs. 7.115 and 7.116 (compare with Section 2.2.6). The results are therefore to be viewed critically, although they show quite reasonable values. Especially the bed mass proportion α_m and residence times τ_α and $\tau_{1-\alpha}$ from Hampel's experimental reference operation points in Table 8.11 agree quite well with Hampel's PB-simulation parameters. Nevertheless, an experimental validation of the characteristics of fluid-particle transport dynamics from the TZC-model is missing. It makes sense to examine the sensitivity of the TZC-model with regard to the flow correction coefficient λ_{tor} for future work and to investigate the variability of those characteristics. In addition, the residence times and the relative void volumes (or average particle concentrations) of the TZC-model can be compared with average values from DEM-CFD simulations. It might be better to omit the pulsation term k_{pul} of Eq. 7.115 when using Eq. 7.116. The pulsation factor was introduced by Burgschweiger for calculating particle entry rates into an elevated classification tube opening inside a granulator, which is not necessary in the case of the Wurster suction gap at the bottom of the fluidized bed.

8.5.2 Process stability

The main conclusions of the investigations of Sections 8.2 to Section 8.4 are summarized in the following.

Sufficient pneumatic conveyability through the Wurster pipe at low dimensionless gas inlet velocities

The parameter variation series TZCM-1 (Tables 8.5 and 8.6) shows that all the pneumatic transport velocities obtained are positive ($u_{pn,\alpha} > 0$) for the entire ranges of the dimensionless inlet gas velocity ($\xi_{mf,iso} \leq \xi_{in} \leq \xi_{exc,iso}$) and for each of the bed mass examples. Hence, the swarm sinking velocity is always lower than the interstitial gas velocity ($u_{sw,\alpha} < u_{\varepsilon,\alpha}$). Especially at low dimensionless inlet gas velocities ($\xi_{in} \to \xi_{mwf,iso}$), the superficial gas velocity of the spray zone u_α can become lower than the sinking velocity of single particles $u_{s,\alpha}$; but, the enhanced swarm effect (lowered swarm porosity $\varepsilon_\alpha \Leftrightarrow$ enlarged particle concentration $1-\varepsilon_\alpha$ $\Leftrightarrow$ smaller $k_{sw,\alpha}$-values) at these conditions still sufficiently reduces the swarm sinking velocity $u_{sw,\alpha}$, so that particles can be raised through the spray zone, and stable circulating Wurster fluidization can be

guaranteed even in vicinity of the minimal-Wurster-fluidization limit (here $\xi_{mwf,iso}$). However, the TZCM-1-results only represent the isothermal case, and therefore, disregard the process-gas-saturation limit (Section 7.10.2) of sprayed Wurster fluidization in contrast to the non-isothermal parameter variation series TZCM-2 and TZCM-3. In particular, lower dimensionless inlet gas velocities can lead to over-saturated process gas conditions for higher water spray rates $\dot{M}_w$ and/or lower inlet gas temperatures T_{in}, as shown by the $\xi^*_{sat,ad}$-limits of the TZCM-2 and TZCM-3 series given in Tables 8.7 and 8.9 or by Hampel's employed operation points in Table 8.11.

Insufficient drying kinetics at low dimensionless inlet gas velocities

Operation points close to the process-gas-saturation limit are also not recommendable, even when the drying potential of the drying zone process gas is still greater than zero, since drying must be still fast enough to steadily evaporate the entire amount of sprayed water. Insufficient drying kinetics lead to high overall wetting degree of the bed (ratio of wet to total particle surface area), enhance agglomeration rates, and risk the process stability of Wurster granulation. A critical point at which dominant agglomeration processes occur cannot be described by the TZC-model presented yet. For this purpose, the model would have to be expanded using agglomeration kinetic approaches. In addition, a drying model, based on droplets lying on individual bed particles, could be implemented to calculate an average drying time. This should be strictly shorter than the residence time of the particles in the drying zone: $\tau_{dry} \ll \tau_{1-\alpha}$. Otherwise there would be a steady accumulation of bed moisture and ultimately a collapse of the Wurster fluidized bed. At this point, it is referred to recent investigations of Rieck et al. [125,126], who have worked out process parameter regimes of dominant particle size enlargement mechanisms for layerwise growth and agglomeration, which also makes use of drying-kinetic approaches for wetted single particles.

Reduced drying power in using Wurster equipment

By inline-measurements within some discontinuous granulation experiments of this thesis (see Figures 10.2 and 10.3) and Wurster fluidization experiments, where pure water is sprayed (Appendix C.6.2), it is shown that fluidized bed gas is strongly cooled with reference to the inlet gas temperature, whereas the temperatures of the spray zone outlet gas shrink only a little. This leads to the conclusion that, in granulation applications with Wurster equipment, the vast majority of sprayed water is to be evaporated outside of the Wurster tube, which is why this region can rightly be called the drying zone. In addition, it turns out from the flow separation results of the distributor plate (see Table 8.1: $\varphi_{dis,3}$ and $\Omega_{3,in}$), that only around 55 % of the overall drying power of the hot inlet gas flows into the drying zone, even though the cross-sectional inlet area below the drying region $\varphi_{3,dis}$ is about 85 % of the entire inflow plate cross-section. This is caused by a higher opening ratio (perforation degree) of the distributor plate section below the spray zone $\Psi_{dis,2}$ than below the drying zone $\Psi_{dis,3}$. As a consequence, process-gas saturation at large water spray rates is reached earlier in granulation processes with Wurster equipment than in top-spray configurations, where the drying power of the inlet gas is completely exploited. From this point of view, continuous layerwise granulation in top-spray setting could be operated with higher spray rates; whereby, growth rates were increased, larger granules were produced, and shorter startup periods were achievable. However, agglomeration tendency of top-spray processes is higher than that in Wurster granulation, since the latter operates with greater shear forces in the spray zone. Consequently, the Wurster process is to be preferred for the layerwise, agglomeration-free granulation due to its process stability, but bypass losses of the inlet gas drying power through the spray zone channel must be accepted.

Effects at high dimensionless inlet gas velocities

The inlet gas velocity cannot be chosen too high due to the following restrictions. The overall upper limit in terms of (dimensionless) inlet gas velocity is the elutriation point. But this needs not be considered for Wurster granulation, since the Wurster-tube-exceedance limit is already arrived at a little lower inlet gas velocities: $u_{exc} < u_{elu}$ and $\xi_{exc} < \xi_{elu}$. In practice, bed particles can be raised above the top of the Wurster tube at even lower inlet gas velocities than those of the Wurster-tube-exceedance limit, since real fluidized beds pulsate to a certain extent. The latter effect is neglected within the concept of the Wurster-tube-exceedance limit of this thesis, because the fluidized bed region is regarded to be homogeneous. The results of the sensitivity analysis of Section 8.2 (Figures 8.1, 8.3, and 8.5) show further that the swarm porosity of the spray zone has almost reached unity for dimensionless inlet gas velocities going to the Wurster-tube-exceedance limit: $\varepsilon_\alpha(\xi_{in} \to \xi_{exc}) \approx 1$. Hence, the particle concentration inside the Wurster tube $(1 - \varepsilon_\alpha)$

takes on values close to zero under those conditions. But, in practical applications, a minimal particle concentration is required in order to properly distribute spray droplets on particle surfaces to avoid wetting of the inner wall of the Wurster tube, to minimize spray losses, and to ensure process stability. For long-term requirements of continuous granulation with Wurster equipment, it is especially important to prevent the Wurster tube from being steadily coated with the spray solution, as it narrows the free cross-section of the spray zone and leads to process destabilization in permanent operation. For these reasons, it is suggested to run Wurster granulation processes well below the Wurster-tube-exceedance limit: $\xi_{in,set} \ll \xi_{exc}$.

Difficulties at too low and high dimensionless bed masses

In the isothermal parameter variation series TZCM-1, circulating Wurster fluidization is investigated by means of the TZC-model for different bed masses M_{bed} from 0.5 to 3 kg that correspond to dimensionless bed masses μ_{bed} from 9.6 to 57.7 % (Table 8.6). The risk of small dimensionless bed mass values in Wurster granulation is that the fluidized bed ring in the drying zone no longer completely covers the Wurster suction gap and/or that, due to an insufficient pressure gradient in the bed, no stable suction of granules into the Wurster tube is more possible. In the example of the smallest (dimensionless) bed mass of the TZCM-1 series, very high bed mass proportions α_m of up to nearly 50 % arise in the spray zone for dimensionless inlet gas velocities approaching the minimal-Wurster-fluidization limit ($\xi_{in} \to \xi_{exc,iso}$, see Figure 8.1). Under such extreme conditions, just 250 g of bed mass would be present in the drying zone. This amount would correspond to a homogeneous bed height of approximately 6.4 mm for the used constant model parameters of Table 8.2, under minimal fluidization conditions, and assuming straight chamber walls. The Wurster gap height, here $H_{wt} = 20$ mm, were then clearly above the fluidized bed, and adequate Wurster suction is not guaranteed. At higher bed masses, the Wurster-tube-exceedance limit shifts downwards to the limit of minimal inlet gas velocity, which narrows the operating range of admissible inlet gas velocities, compare for instance $\xi_{exc,iso}$-values of Table 8.6 with the $\xi^*_{sat,ad}$-value of the second example of Table 8.9. It can be shown by the present study of the TZC-model that, for the granulation processes with the experimental equipment from Section 9.2.1 and a material with an effective particle density of $\rho_p = 1380\,\mathrm{kg/m^3}$, a bed mass of already 2 kg ($\mu_{bed} = 38.47\,\%$) leads to severe limitations in possible operating points, while a bed mass of 3 kg ($\mu_{bed} = 57.71\,\%$) very likely endangers the process stability. For this purpose, the results of the last two examples of the TZCM-1 series in Table 8.6 can be compared with those of the TZCM-2 and TZCM-3 series in Tables 8.7 and 8.9 and of the parameter examples from Hampel in Table 8.11. The dimensionless inlet gas velocity of the Wurster-tube-exceedance limit of the 2-kg-example is around $\xi_{exc,iso} = 68.4\,\%$ and that of the 3 kg-example is around $\xi_{exc,iso} = 35.6\,\%$. These upper limits come very close to the calculated saturation limits of the parameter examples of the partial studies TZCM-2 and TZCM-3 and of Hampel's granulation experiments, and some even fall below them. At an inlet gas temperature of 70 °C and water spray rates above roughly 600 g/h, stable Wurster circulation can be regarded as quite jeopardized with a bed mass of 2 kg and excluded with a bed mass of 3 kg. At higher inlet gas temperatures (see ≥ 90 °C) the saturation points also fall below the Wurster-tube-exceedance limit of the 3 kg-example, but only very slightly. Since the model is also subject to assumptions and errors, and since the drying kinetics must also be sufficiently large, the dimensionless inlet gas velocity to be set should be well above the saturation line ($\xi_{in,set} \gg \xi_{sat}$), as previously described. The bed mass should therefore not exceed a certain value. The TZCM-1 example with a bed mass of 1.5 kg ($\mu_{bed} = 28.85\,\%$) shows an acceptable Wurster-tube-exceedance limit with $\xi_{exc,iso} = 91.51\,\%$. In the continuous granulation experiments of this work, the bed mass controller used should keep the holdup below the 1.5-kg-mark. However, a certain leeway in bed mass values is still necessary for a precise control of a desired product mean diameter, as it is ascertained in the PB-study of Chapter 6 and is also shown later in the experiments in Section 10.4.

Choice of optimal bed mass for different plant scales and materials

A bed mass of 0.7 to 1.5 kg has proved to be a suitable value for stable Wurster fluidization of Cellets® in the experimental process chamber. The effective particle density of Cellets® is around $1380\,\mathrm{kg/m^3}$. From Eq. 7.132, the corresponding limits of the dimensionless bed mass μ_{bed} follow to 13.5 and 28.9 %. These limits of the dimensionless bed mass are suggested as rough orientation for setting holdups in Wurster process chambers of different scales. In order to recalculate the range of optimal bed masses, the converted version of Eq. 7.132 can be used:

$$M_{bed} = \mu_{bed}\rho_p(1-\varepsilon_{mf})V_{1-\alpha,max}. \tag{8.5}$$

The maximal volume of the drying zone $V_{1-\alpha,max}$ is to be obtained by Eq. 7.9 with the corresponding bed height $H_{1-\alpha,max} = H_{wt} + L_{wt}$.

Restrictions of enhancing drying power for Wurster granulation

It follows from the results of the ideal continuous layerwise granulation model in Chapter 4, the PB-simulation study in Chapter 6, and the TZC-model that high spray rates are favorable for large-growth granulation and fast startups, but they require enough drying power, which is subject to significant losses in processes with Wurster equipment. The lack of drying power can be compensated by various measures. On the one hand, the inlet gas velocity u_{in} can be increased for this purpose, but only up to a certain point to stay well below the Wurster-tube-exceedance limit. From this point of view, lower bed masses permit higher inlet gas velocities. On the other hand, higher inlet temperatures T_{in} enlarge the drying power too. These should not be chosen too high either for different reasons. Very high inlet gas temperatures lead to greater solid spray losses $\Phi_{spr,loss}$ due to premature drying effects, can decompose thermally sensitive materials, and/or can enhance electrostatic-induced particle-particle aggregations and particle-wall adhesion, as was also observed in the experiments with Cellets®. The velocity and temperature of the inlet gas also have a decisive influence on the morphological structure of the on-sprayed layers, which can be rather smooth and compact for fast drying conditions or rough and porous for slow drying conditions, see for example [2, 127]. The inlet gas parameters can thus also be limited by morphological product requirements. Furthermore, the drying power can be improved by using larger apparatus diameters $D_{app,0}$. By this, higher spray rates $\dot{M}_{spr}$, and hence, larger particle growth ratios Φ_d are possible in continuous granulation processes; but, with the cross-sectional area of the process chamber $A_{app,0}$, the bed mass required for a stable Wurster fluidization also grows. Whether the possible growth rates of single particles will then be raised or decreased, is not clarified within the scope of this thesis. However, higher bed-mass-specific solids spray rates $\dot{m}_{spr,s}$ (Eq. 3.14) should be pursued, since they reduce the growth times $\tau_{gr,set}$, according to the ideal granulation model (see Figure 4.4), and accelerate therefore startups of real continuous granulation processes.

Reduced drying power by heat losses

Heat losses reduce the drying power of the inlet gas, and thus, require even higher inlet gas velocities in order to remain well above the process-gas-saturation limit. To avoid excessively saturated gas states in the drying zone, heat losses must be taken into account under certain circumstances, when the granulation chamber has no thermal insulation. However, it is not the heat loss flow rate that is decisive for the effective drying power in the fluidized bed region, but the effective inlet gas temperature ($T_{in,eff}$ of Eq. 7.67) or the absolute temperature drop across the distributor plate ($\Delta T_{loss} = T_{in} - T_{in,eff}$). Several temperature measurements were conducted by empty operation (without bed material and without spraying) with the non-insulated granulation system of this work (ProCell LabSystem, Section 9.2.1), as illustrated in Figure C.11. The results show that the temperature drop ΔT_{loss} decreases with lower inlet gas temperatures T_{in} and with higher inlet gas velocities u_{in} (or mass flow rates $\dot{M}_{in}$). However, reducing the inlet gas temperature T_{in} is not advisable for compensating the decrease in drying power of heat losses. Instead, the inlet gas temperature would have to be increased and bigger operating costs would have to be accepted. Better still, the inlet gas velocity could be set higher, which not only enhances the drying power, but also lessens the temperature drops ΔT_{loss}. This strategy is advantageous in granulation of larger and/or heavier bed materials, since they require higher gas velocities to achieve similar fluidization conditions (e.g., fluidization number f_{rn}, Eq. 2.125). As can be seen in the example of Figure 8.11, the gas velocity of the minimum-Wurster-fluidization limit ($u^*_{mwf,ad} = u^*_{min,ad}(\dot{M}_w < \dot{M}_{w,cr})$) increases with the particle diameter d. Here, clearly visibly, higher inlet gas velocities have to be used, but the Wurster-tube-exceedance limit cannot be reached as quickly as with smaller and lighter particles. Heat losses when flowing through the distributor plate are therefore rather negligible for granulation of larger particles. The granulation experiments of this thesis were carried out on a laboratory scale. With the diameter of the system used ($D_{app,0} = 18\,\mathrm{cm}$), the heat losses have a significant influence on the saturation limit. In industrial equipment, the heat losses can presumably be neglected in the calculation of process limits.

9 Experimental basics

Different experimental sub-studies were carried out in the scope of this thesis in order to understand the interaction and the limitations of various sub-processes in continuous fluidized bed spray granulation with external product classification, and thereby, to improve process control strategies in terms of stability, fast startup, and product size. These include

- several multi-stage discontinuous granulation experiments (Section 10.1),
- dosing behavior analyses of the nuclei feeding equipment (Section 10.2),
- measurements of bed discharge dynamics (Section 10.3), and
- continuous granulation experiments with different processing strategies (Section 10.4).

Moreover, heat losses through chamber walls (Appendix C.6.1) and process gas cooling within the Wurster tube due to droplet evaporation (Appendix C.6.2) were investigated. In this chapter, the main basics of all the experimental sub-studies of this thesis are described.

9.1 Raw bulk materials

In total seven different raw bulk materials were used for the experimental investigations of this thesis. They are identified by the abbreviation from IM-1 to IM-7, where IM stands for "initial material" and the number differentiates the bulk solids products.

Manufacturer's specification

The names of the particulate raw materials of IM-1 to IM-7 and some of their manufacturer specifications are listed in Table 9.1 including the minimal particle diameter d_{min}, the maximal particle diameter d_{max}, the effective particle density ρ_p, and the bulk density ρ_b. The first six initial materials are different size-related fractions of Cellets® from the company HARKE Pharma GmbH. The test materials IM-2 and IM-3 are both of the type Cellets®200, but they come from different production batches, and have clear variances in their grain size spectrum, as shown in C.1. Cellets® are manufactured by the rotor granulation process and subsequent sieving. They consist of micro-crystalline cellulose and, according to the manufacturer's sheet, they have an effective particle density of $\rho_p = 1380\,\mathrm{kg/m^3}$. As the seventh test material, IM-7, glass beads with particle diameters between 200 and 300 µm were chosen, because glass beads have a significantly higher effective particle density with $\rho_p = 2500\,\mathrm{kg/m^3}$ than Cellets®. Bulk densities ρ_b measured by the manufacturer are also listed in Table 9.1. From these and the effective particle densities, the bulk porosities ε_b of the last column in Table 9.1 were derived via Eq. 2.57. Their values are a little higher than 40 %, which is recommended in Section 2.2.4 as an adequate bed porosity for the minimal fluidization state of spherical bulk solids (ε_{mf}), as it is applied for analysis of the two-zone continuum model on Chapter 8. However, the deviations are still acceptable.

Analysis of different bulk characteristics

In addition to the manufacturer's information, the following product characteristics of the initial materials of Table 9.1 were also determined. These included the particle size distributions illustrated in Figure C.1 and diverse scalar characteristics given in Table C.1. The particle size distributions were measured through dynamic image analysis by a CAMSIZER® of the company Retsch® Technology (today Microtrac MRB) on the basis of the circle-equivalent diameter of project particle surface $d_{PA,p}$, that is defined in Eq. 2.1. The scalar quantities from the d_{50,q_0}-line to the ζ_{q_1}-line of Table C.1 were derived from the depicted PSDs via some of the equations described in Section 2.1.2. In addition, the CAMSIZER® also calculated the mean sphericities Ψ_{sph} of Table C.1 (after Wadell [3], as in Eq. 2.3), which, strictly speaking, are mean circularities after Eq. 2.49 due to the image analysis. This parameter shows that the Cellets® (IM-1 to IM-6) are very

index of initial material	product name	d_{min} [µm]	d_{max} [µm]	ρ_b [kg/m^3]	ρ_p [kg/m^3]	ε_b [%]
IM-1	Cellets®100	100	200	790	1380	42.75
IM-2	Cellets®200	200	355	790	1380	42.75
IM-3	Cellets®200	200	355	790	1380	42.75
IM-4	Cellets®350	350	500	790	1380	42.75
IM-5	Cellets®500	500	710	810	1380	41.30
IM-6	Cellets®700	700	1000	810	1380	41.30
IM-7	glass beads	200	300	1440	2500	42.40

Table 9.1: Manufacturer's specification of different initial bulk materials used in the present thesis.

experimental substudy	labeling	Section	IM-1	IM-2	IM-3	IM-4	IM-5	IM-6	IM-7
discontinuous granulation	EB	10.1	-	x	-	x	-	-	x
feed rate analysis	EF	10.2	x	x	-	x	x	x	x
bed discharge dynamics	EBD	10.3	-	x	-	-	-	-	-
continuous granulation	EC	10.4	-	x	x	-	-	-	-

Table 9.2: Overview on the use of seven different initial bulk materials (IM-1 to IM-7) in experimental sub-studies of the present thesis.

spherical, while the glass beads (IM-7) only slightly resemble to spheres. The bulk densities ρ_b of Table C.1 were measured gravimetrically after the bulk solids had been poured into a known cylinder volume. They differ a little from these of the manufacturer. The effective particle densities ρ_p of Table C.1 were determined by means of volume displacement of water in a measuring beaker. Their values are somewhat higher than that of Table 9.1. The bulk porosity ε_b according to Eq. 2.57 was also calculated for each of the density measurements carried out here. Particularly noticeable is the increasing tendency of the bulk porosity of the smaller Cellets®. As explained in more detail in Section 2.1.3, it is already known in literature that interparticle porosity of bulk solids increases with decreasing particle diameter below a critical grain size.

Overview of applications in this thesis

The seven bulk solids variants of Table 9.1 were employed for various purposes within the experimental sub-studies of this thesis, as summarized in Table 3. The initial materials IM-2 and IM-4 served as core particles in the discontinuous multi-stage granulation processes of Section 10.1. For the feed rate analysis study in Section 10.2, almost all raw materials, except IM-3, were used, in particular for investigating the influence of particle size and density on the conveying behavior of the nuclei feeding equipment. The bed discharge experiments in Section 10.3 were carried out only with the IM-2 material. The external nuclei and initial bed material of the continuous granulation experiments of Section 10.4 consisted of the IM-2 or IM-3 materials. At this point it should be noted that both Cellets® and glass beads are mechanically very stable, so that breakage phenomena during fluidization, conveying, and classification processes can be excluded, and they are also quite spherical. These properties are suitable for validation of process concepts such as the spray-to-feed setting methods of the ideal particle growth model in Section 3.2.2.

9.2 Equipment and setups of the process-related experimental investigations

The equipment and setups used for the process-related experimental investigations of this thesis are outlined in this section. The different experimental setups are shown schematically in Figures 9.1 to 9.5, and the dimensions of the classifier, granulator, and nuclei feeding equipment are illustrated and specified in Figure C.2.

9.2.1 Overview on utilized equipment

A rough overview on the utilized equipment (depicted in Figures 9.1 and 9.5) is given below.

Granulator plant

The experimental sub-studies were conducted with the ProCell LabSystem of the company Glatt GmbH. This granulation plant is designed for laboratory scale processes with holdups of around 1 kg depending on the material type. Its modular structure allows to exchange process chambers of different functionalities, whereby granulation can be realized for instance through fluidized beds with top- or bottom-spray configuration, spraying in spouted beds, or sprayed Wurster fluidized beds. In all experiments of this thesis, except for the dosing analysis of the feed-related double-pinch valve, the processing insert of the type GF3 from the Glatt-company has been utilized in Wurster configuration. The GF3 assembly consists of one lower component with a cylindrical cross-section (smaller part), one upper component (bigger part), which widens conically towards the top, and one gas distributor plate (exchangeable) clammed inbetween. In the experimental investigations of this thesis, a perforated metal disc was used as gas distributor plate. A photograph and a detailed description of the perforation structure of this distributor plate are given in Appendix C.2.2. The conical component of the GF3 insert is considered as the process chamber of the plant. The Wurster tube was positioned in the lower center of the process chamber. The dimensions of the process chamber and of the Wurster tube are shown in Figure C.2. The supply channel of a two-substance nozzle was installed in the cylindrical part of the GF3 insert. The orifice of the two-substance nozzle reached into the interior of the Wurster tube. Further, the ProCell LabSystem includes an expansion zone (conical walls) and a calming zone (cylindrical walls) above the process chamber. In these granulator compartments, the process gas velocity decreases during operation to prevent granules from being mal-discharged in the exhaust gas. Dust filters can also be installed within the calming zone of the plant; but, this was omitted in the granulation experiments. Further, the LabSystem of Glatt integrates a control panel. Herewith, set values of the inlet gas mass flow rate, inlet gas temperature, and the nozzle air excess pressure can be predefined.

Components for particle transport: classification and nuclei feeding equipments

A screw conveyor and a zig-zag classifier belong to the additional equipment of ProCell LabSystem, which enables to operate granulation in continuous mode. In the previous investigations of Hampel ([1,2], reference case in Section 2.3), however, both the separation performance of the zig-zag classifier and the dosing accuracy of screw conveyor turned out to be insufficient for continuous operation with the materials employed (Cellets®200). Therefore, a different classification and nuclei feeding equipment had been constructed in the scope of Hampel's work, which is adopted for this thesis. The nuclei feeding and classifier equipment contain one double-pinch valve (particle sluice), respectively, by which the nuclei feed rate and the mass flow of particles entering the classifier shall be controlled within the continuous granulation experiments. In each of the particle sluices, two single pinch valves are joined in series via a plastic cylinder. The pinch valves were produced by the company AKO GmbH, as stated in [2]. The dimensions of the pinch valves and plastic cylinders are identical. Latter have a length of 5 cm, an inner diameter of 2 cm, and an outer diameter of 2.6 cm. In order to better distinguish between the two particle sluices, the following denotations are used. The double-pinch valve of the nuclei feeding equipment is called as feed-in, feed-related, nuclei-related, or nuclei feeding double-pinch valve, or in short just nuclei feeder. The double-pinch valve of the classifier equipment is called as feed-out, classifier-related, bed outlet or bed discharge double-pinch valve, or only bed discharger. Furthermore, the feeding equipment comprises a container for storing nuclei during the continuous granulation experiments, whose feeding hopper is joined to the upper end of the feed-related particle sluice. The classifier is made of a vertical, cylindrical, and straight duct (tube). The straight-duct air classifier and nuclei feeding equipment are connected to the granulator via flexible hoses. The working principles of both particle conveyors are described in more detail later in Sections 9.4.1 and 9.4.2. Relevant dimensions of classifier and nuclei feeding equipment are shown in Figure C.8 such as the classifier length ($L_{sep} = 110\,\text{cm}$), the inner diameter of the classifier ($D_{sep} = 3.2\,\text{cm}$), the nuclei container size, and the size and inclination angle of the installed double-pinch valves.

Components for delivery of fluids: pneumatic control gas, classification gas, process gas, nozzle gas, and spray liquid

In the different experiments of this thesis, technical air was used as medium for pneumatic control of the two double-pinch valves, as classification gas, as process gas for providing drying energy and fluidizing bed materials, and as nozzle gas for atomizing liquids within the spray zone. The technical air was delivered by a compressed air system and dehumidified by an air conditioning system of the company Munters (type ML270). The switching positions of the double-pinch valves (open or closed) were set by a pneumatic control

unit, which had also been assembled in the context of Hampel's investigations [1,2], more on this in Sections 9.4.1 and 9.4.2. To set a certain separation gas velocity in the classifier, a mass flow controller (MFC) of the company Bronkhorst Mättig (type IP40) was employed in the continuous granulation experiments. At this, the classifier-MFC was connected to the air supply system (see Figure 9.4). The mass flow of the process gas (or inlet gas) was generated by two ventilators: a pressure fan situated in front of the process chamber and a vacuum fan adjoined behind the granulator system. The pressure fan (upstream ventilator) is integrated within the ProCell LabSystem; whereas, the vacuum fan (downstream ventilator) was added to the laboratory plant system of Glatt. By setting both ventilators at different powers, the absolute pressure of the process gas can be regulated. The nozzle air excess pressure can be set at the control panel of the granulation laboratory system to adjust nozzle air supply rates. A peristaltic pump of Watson-Marlow (type 323-S-314D2/400) and a two-substance nozzle of Düsen-Schlick GmbH (model 970 S4, [124]) were employed for spraying liquids (aqueous NaB-solution or pure water) in the experiments of Figures 9.1, 9.4, and 9.5 b. Liquids to be injected into the process chamber were pumped via flexible silicone tubes out of a beaker. The latter stood on a cylinder (here an elongated plastic bucket) to generate a liquid suction level above the pump wheel, a continuous downward gradient of the silicone tube, and finally, stability in pumping. The beaker of the spray liquid and the plastic cylinder were put on a weight balance standing on the working surface of the ProCell LabSystem. This way, spray rates could be monitored during experiments by measuring filling levels at different time points.

Inline data acquisition system for monitoring and recording process-related measurement parameters as well as for controlling bed mass and product size

Several measurement properties can be monitored during operation on the control panel of the ProCell LabSystem such as the inlet gas temperature, the process gas temperature inside the fluidized bed region (a few centimeters above the inflow plate), the outlet gas temperature, and the pressure drop across the GF3 insert. However, the results of this measurement system were not examined in this thesis. Instead of this, an external data acquisition system, which was added to ProCell LabSystem in the scope of previous work [1, 2], was used here to record process variables such as temperatures and absolute pressures of the inlet and outlet gas, fluidized bed temperature, and classifier gas velocity. These properties were measured inline during the experiments through several thermocouples and pressure sensors. The signals of them were synchronized by a data logger system (Gantner, type ISK-100) and then submitted to an external personnel computer, wherewith the measurement quantities of the conducted experiments of Figures 9.1, 9.4, and 9.5 were monitored and saved via programs of the DASYLab-Software (version V5.5). But also, the bed mass was controlled in the continuous granulation experiments via a DASYLab-sheet, as explained later in Section 9.4.8.

9.2.2 Experimental setups

The setups of the different experimental sub-studies are briefly described in the following. From all the equipment listed in Section 9.2.1, only the air delivery system (compressed air system and air conditioner) was used in each of the sub-studies; while the others were not always needed.

Discontinuous granulation

The setup of the discontinuous granulation experiments of Section 10.1 is illustrated in Figure 9.1 and described in the following. The batch experiments were realized in the ProCell LabSystem with Wurster equipment, the downstream ventilator, and the previously described spraying equipment. The classification and nuclei feeding equipment were not employed. The orifices of the granulator, whereat the classifier- and feed-related double-pinch valves can be connected with, were closed by sealing plugs. The inlet gas temperature T_{in}, the inlet gas pressure p_{in}, the process gas temperature in the fluidized bed region T_{bed}, the outlet gas temperature T_{out}, and the outlet gas pressure p_{out} were measured inline by thermocouples and pressure sensors. These quantities are helpful for detecting occurrences of process instability (e.g., excessive agglomeration) during operation. The difference of the inlet and outlet gas pressure is used for the inline detection method of bed mass implemented by Hampel ([2], described in Section 9.4.7), which shall be examined within the discontinuous granulation study of this thesis. The different measurement properties were recorded via the above detailed data acquisition and monitoring system (data logger and external PC).

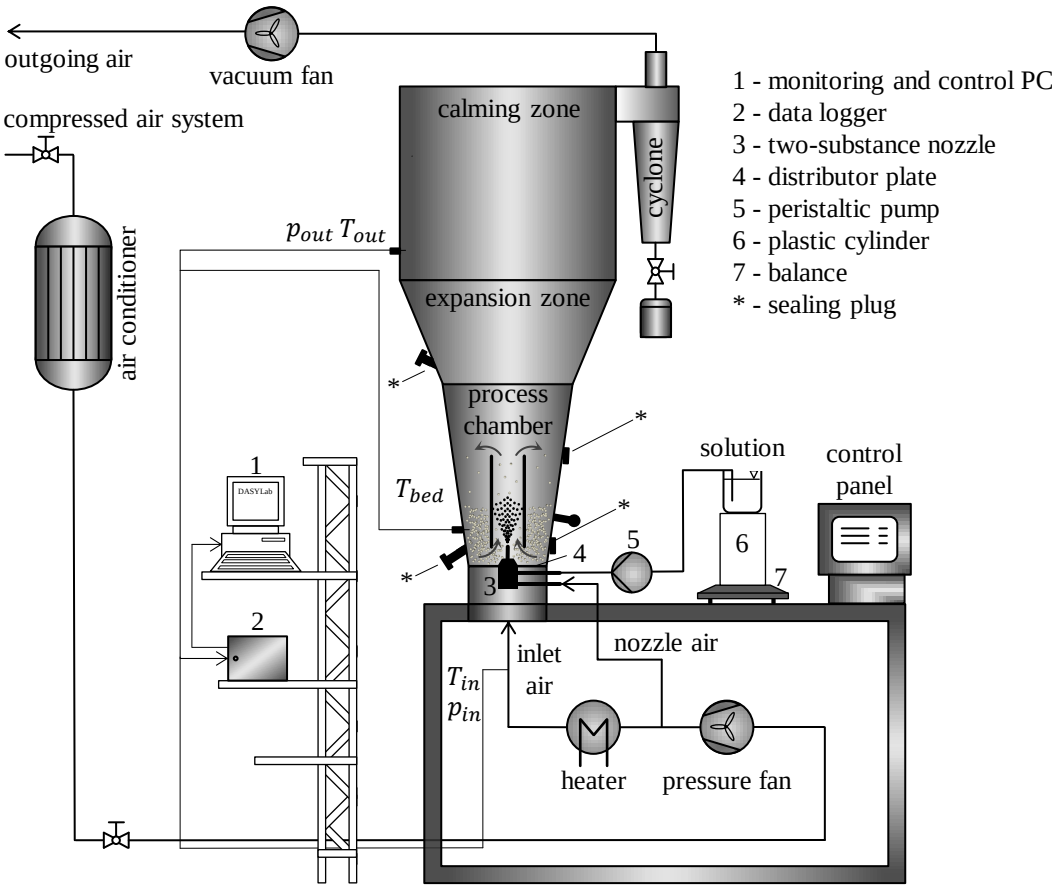

Figure 9.1: Experimental setup for the discontinuous granulation study in Section 10.1.

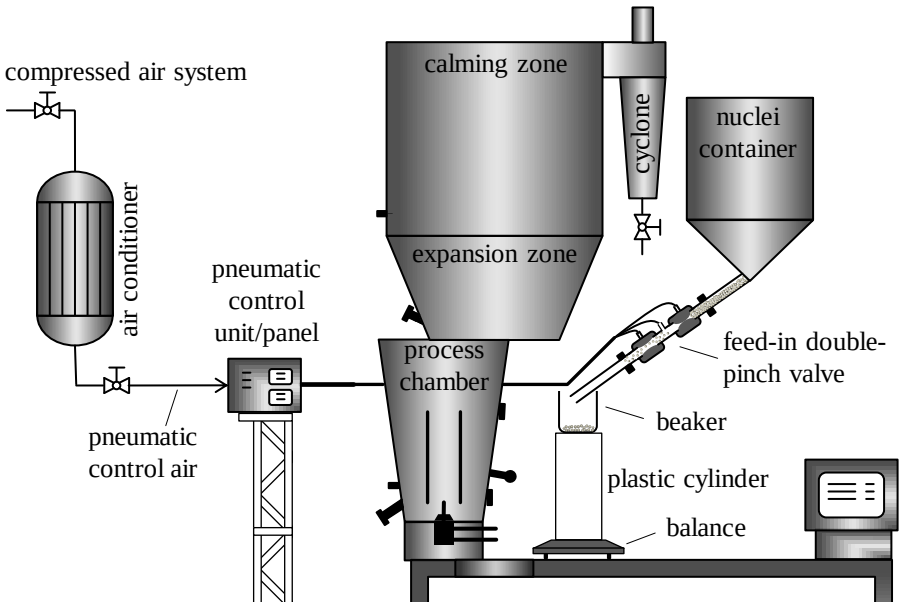

Figure 9.2: Experimental setup for the dosing analysis of the feed-in double-pinch valve in Section 10.2.

Dosing behavior analysis of the feed-in double-pinch valve

The setup of the experiments for the dosing analysis of the feed-in double-pinch valve of Section 10.2 is depicted in Figure 9.2. In this substudy, only the nuclei feeding system of all the aforementioned equipments was employed; but, it was assembled at the ProCell LabSystem likewise to the setup of the continuous granulation experiments in Figure 9.4. The feeding container was filled with a certain amount of nuclei (raw bulk materials, see Tables 9.1 and 9.2), and single dosages of them were conveyed by the feed-related double-pinch valve into a measurement beaker. The height position of the latter was prepared in the same way as for the storage and level measurement of the spray solution (see Figure 9.4), but with the difference that the weight balance and the elongated plastic cylinder (bucket) were placed very close to the process chamber here in order to measure single dosing masses under process-like conditions of the continuous granulation experiments. However, a slight difference in the angle of inclination of the nuclei feeder remained between the dosing behavior and continuous granulation sub-studies. The individual dosing masses were mostly determined by video recording the weight balance. Only in a few long-term experiments, that lasted up to over 30 h, the weight balance was connected to the data acquisition system (not illustrated in Figure 9.2). Switching times of the single pinch valves were set on the control panel of the pneumatic air control unit.

Bed discharge dynamics

Figure 9.3 shows the setup of the bed discharge dynamics study (Section 10.3). This setup involves the ProCell LabSystem, the downstream ventilator, the pneumatic control unit, and a part of the classifier equipment. Different masses of nuclei (here Cellets®200) were fluidized by hot air within the process chamber. Spraying of any liquids into the granulator was not carried out, because strong agglomeration would occur at low bed masses, even if pure water were injected. Classification and reflux of particles were omitted in these experiments too. The classifier-MFC, the recycle tube, the product outlet trap, and the product sampler (No. 7, 8, 10, and 11 in Figure 9.4) were disconnected from the classifier equipment for the bed discharging experiments. The openings of the classifier and the granulator at the recycle channel were sealed. The classifier tube was only connected to the bed outlet orifice of the process chamber via the feed-out double-pinch valve (No. 2 in Figure 9.3). Only the straight part of the classifier was used to align sluiced particles, so that they can fall into a sample container (measurement beaker), which was positioned around the lower classifier outlet. This container was exchanged every thirty seconds with another empty one. These time intervals are referred to as *sampling units* in the context of this substudy. The mass of a sampling unit was weighed and recorded by hand during the experiments (No. 7 and 8 in Figure 9.3), while the next sampling

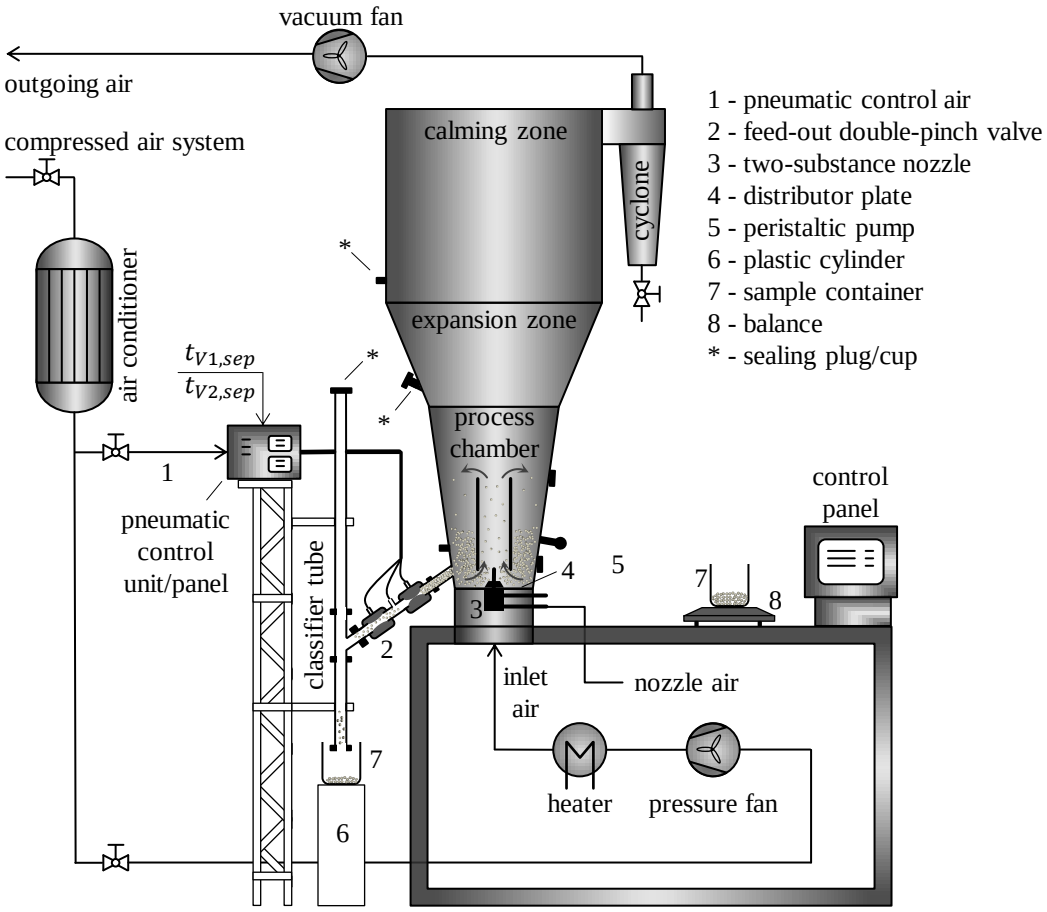

Figure 9.3: Experimental setup for the bed discharge dynamics analysis in Section 10.3.

1 - pneumatic control air
2 - classification air
3 - process and nozzle air
4 - pneumatic control unit/panel
5 - monitoring and control PC
6 - data logger
7 - mass flow controller of the classifier air (MFC)
8 - fine fraction recycle
9 - feed-out double-pinch valve
10 - product trap
11 - product sample container
12 - two-substance nozzle
13 - distributor plate
14 - bed sampling device
15 - peristaltic pump
16 - plastic cylinder
17 - balance
18 - feed-in double-pinch valve
19 - dust container

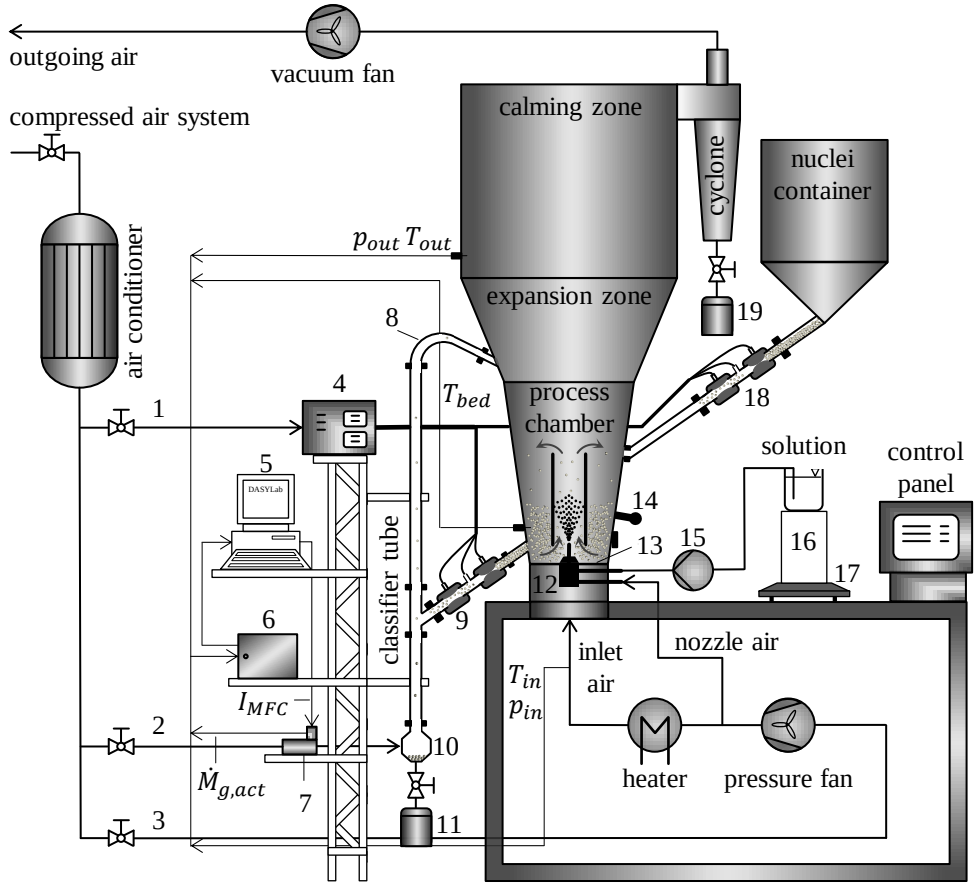

Figure 9.4: Experimental setup for the continuous granulation study in Section 10.4.

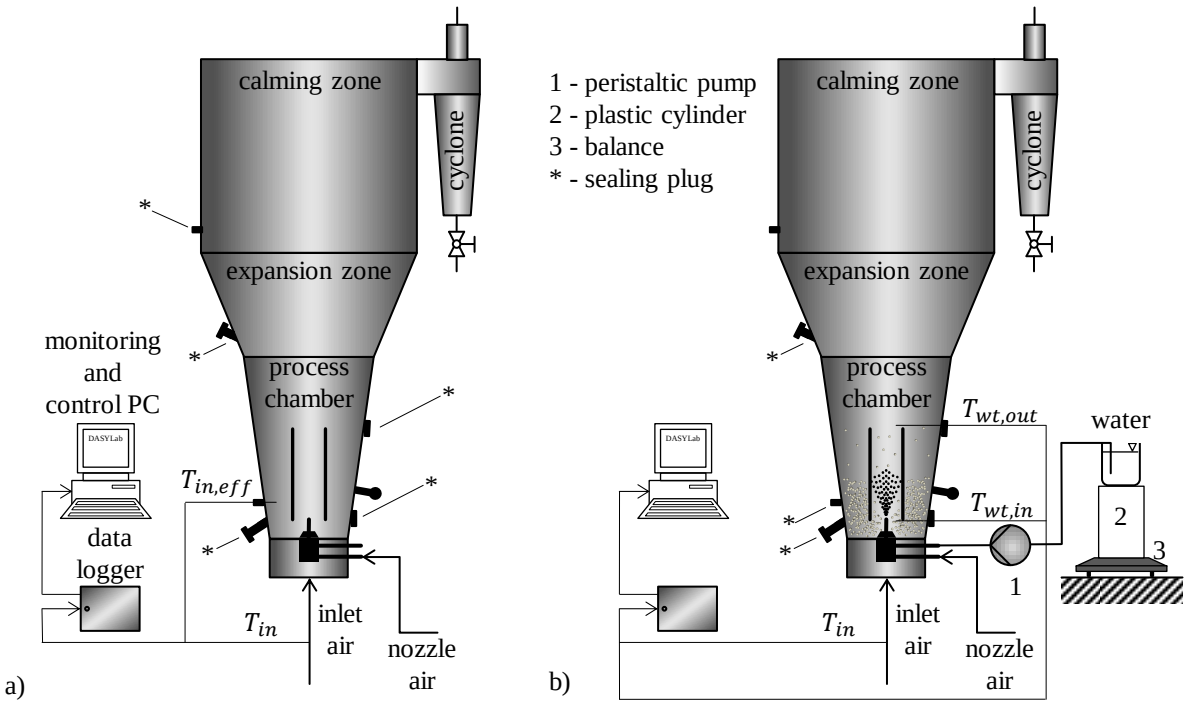

Figure 9.5: Experimental setup for the temperature measurements of the present thesis to investigate heat losses in a) and evaporation cooling of process gas within Wurster tube in b).

unit was collected simultaneously.

Continuous granulation

The experimental setup of the continuous granulation experiments is pictured in Figure 9.4. In these experiments, all the equipment listed in Section 9.2.1 was utilized, which are the technical air delivery system, the data acquisition systems, the ProCell LabSystem with Wurster equipment, the downstream ventilator, the pneumatic control unit of the double-pinch valves, and the equipments for classification, feeding of external nuclei, and spraying liquids. The nuclei feeding container was connected via the feed-in double-pinch valve to the orifice of the process chamber that lies circa at that level of the top edge of the Wurster tube. The product separation system was joined via the feed-out double-pinch valve to the granulator at the bed outlet orifice of the process chamber, as it was the case in the partial study of bed discharge dynamics. But in the continuous granulation experiments, the recycle of the classifier was connected to the LabSystem at the orifice of the expansion zone. Further, the classifier-MFC, the product trap at the classifier bottom, and exchangeable product sample containers were used here. As in the discontinuous granulation experiments, the inlet gas temperature T_{in}, inlet gas pressure p_{in}, the process gas temperature of the fluidized bed region T_{bed}, the outlet gas temperature T_{out}, and the outlet gas pressure p_{out} were measured inline and saved by the data acquisition system. In addition to this, a feed-back structure for controlling the fluidized bed mass during the continuous granulation experiments had been implemented into the data acquisition program (DASYLab-file) by Hampel [1, 2]. In order to couple bed mass control with a product size control concept (see Section 9.4.6), Hampel's implementation was modified for this thesis, as explained in more detail in Section 9.4.8. A signal value (here electric current I_{MFC}) calculated by the supplemented control system is submitted to the classifier-MFC during the experiments. This input signal dictates a current set mass flow rate, which should be created by the MFC to obtain a current desired separation gas velocity $u_g(t)$ of the bed mass controller, see also Section 9.4.8. Moreover, the output signal of the classifier-MFC representing the actual current mass flow rate $\dot{M}_{g,act}(t)$ was recorded including a measurement error of the MFC. From this measurement property, actual current separation gas velocities ($u_{g,act}(t)$, Figure 9.9) were determined in dependency on the inner classifier diameter D_{sep}. The delivery equipment of the spray solution (here sodium benzoate dissolved in water) was prepared such as above described for the discontinuous experiments.

Heat losses through walls and process gas cooling within Wurster tube by droplet evaporation

The setups of the heat loss measurements in Appendix C.6.1 and the experimental investigation of process gas cooling by droplet evaporation within the Wurster tube in Appendix C.6.2 are illustrated in Figure 9.5 a and 9.5 b. In both sub-studies, the ProCell LabSystem was put into operation together with the vacuum fan for different inlet gas temperatures and inlet gas mass flow rates. The difference between these studies was that fluidization and spraying were omitted in the heat loss measurements, whereas in the evaporation cooling study, pure water was sprayed on 1 kg of Cellets®200 in Wurster fluidization. In both experimental series of Figure 9.5, nozzle air was injected into the granulator, since the nozzle air delivery system has to be activated to run the entire laboratory system. In the heat loss analysis, the so-called effective inlet gas temperature $T_{in,eff}$ was detected by the same thermocouple that was used to monitor and record the fluidized bed temperature T_{bed} in the granulation experiments. To investigate the evaporation cooling effect inside the Wurster tube, the process gas temperatures were measured by two thermocouples, one placed at the Wurster tube inlet $T_{wt,in}$ and the other at the Wurster tube outlet $T_{wt,out}$. They were inserted into the process chamber via the orifice of the external nuclei entry and another orifice at the level of the Wurster tube gas inlet. The latter was blinded in the other experimental setups, as it is just an optional chamber opening, which offers for instance granulation experiments with bottom-spray configuration. The heads of the thermocouples were positioned two centimeters far from the inner wall of the Wurster tube. The spraying equipment was set up exactly as in the granulation experiments.

9.3 Estimation method for average coating density from bulk characteristics

A proper value of the effective coating density is needed for the parameter setting strategies of Sections 9.4.5 and 9.4.6, which are conceptualized for the continuous granulation experiments of the present work. In the discontinuous granulation study of Section 10.1, the core materials IM-2, IM-4, and IM-7 of Table 9.1 were coated with the same material (sodium benzoate) in various multi-stage batch experiments with different process parameters (e.g., inlet gas mass flow rate $\dot{M}_{in}$ and inlet gas temperature T_{in}). An average effective coating density ρ_c and a corresponding coating layer porosity ε_c shall be calculated from bulk properties of some of the stage products with the following method. The single stages of the batch experiments are indicated by $j \in \{0, 1, 2, ...\}$, where a stage number of zero ($j = 0$) represents the initial materials. The bulk properties to be measured are the bulk density $\rho_{b,j}$, number-based particle size distribution $q_{0,j}$, and the volume-based particle size distribution $q_{3,j}$. The bulk densities $\rho_{b,j}$ were determined gravimetrically by filling the pure core materials or the products into a small container with known volume capacity. The PSDs of the products have been created by a CAMSIZER®-device of the company Retsch® Technology (today Microtrac MRB) likewise to these of the raw bulk materials, see Section 9.1. The interparticle porosity of the core materials $\varepsilon_{b,0}$ ensues from the raw material bulk density $\rho_{b,0}$ and the associated effective particle density $\rho_{p,0}$ with:

$$\varepsilon_{b,0} = \varepsilon_{b,j=0} = 1 - \frac{\rho_{b,0}}{\rho_{p,0}}. \tag{9.1}$$

The effective particle density of the core materials $\rho_{p,0}$ could be measured by water displacement in a measuring cylinder, since the used materials (Cellets® and glass beads) are water-insoluble and have no open pores. The results of $\rho_{b,0}$, $\rho_{p,0}$, and $\varepsilon_{b,0}$ are given in Table C.1. The coated particles, however, cannot be inserted into a water column, as sodium benzoate layers would be dissolved then. For this reason, the effective particle density of the stage products $\rho_{p,j}$ with $j > 0$ is derived here from the corresponding bulk density $\rho_{b,j}$ and interparticle porosity $\varepsilon_{b,j}$. The latter depends on the degree of dispersity of the product size distribution, as described in Section 2.1.3. The empirical approach of Eqs. 2.53 and 2.54 suggested by Tsotsas [25] should be therefore applied for estimating interparticle porosities of the stage products from their particle size distributions. It could be shown in Appendix B.1 that the dispersion parameter ζ_{pol} of Eq. 2.54 conforms with the relative standard deviation (coefficient of variation) of a certain length-based particle size distribution ζ_{q_1} that is defined in Eq. 2.44 with $r = 1$. In the present context, such a dispersion parameter (symbolized here by $\zeta_{q_1,j}$) is to be calculated for the initial materials and each stage product by:

$$\zeta_{q_1,j} = \frac{\sigma_{q_1,j}}{d_{m,q_1,j}} = \left(\frac{\int_0^\infty d^{-2} q_{3,j}(d) \mathrm{d}d}{\left(\int_0^\infty d^{-1} q_{3,j}(d) \mathrm{d}d \right)^2} - 1 \right)^{1/2} \quad \text{, for } j \in \{0, 1, 2, 3, ...\}. \tag{9.2}$$

Further, the interparticle porosity of a monodisperse reference system $\varepsilon_{b,mon}$ has to be defined, which is assumed to be a constant parameter for both the initial materials ($j = 0$) and the batch products ($j > 0$). It can be recalculated from the interparticle porosity $\varepsilon_{b,0}$ and the relative standard deviation $\zeta_{q_1,0}$ of the initial material according to:

$$\varepsilon_{b,mon} = \frac{\varepsilon_{b,0}}{-0.112\zeta_{q_1,0}^3 + 0.017\zeta_{q_1,0}^2 - 0.259\zeta_{q_1,0} + 1}. \tag{9.3}$$

From this, the interparticle porosity $\varepsilon_{b,j}$ and the effective particle density $\rho_{p,j}$ of the stage products follow then from

$$\varepsilon_{b,j} = \varepsilon_{b,mon}\left(-0.112\zeta_{q_1,j}^3 + 0.017\zeta_{q_1,j}^2 - 0.259\zeta_{q_1,j} + 1\right) \qquad \text{, for } j \in \{1,2,3,...\}, \tag{9.4}$$

and from

$$\rho_{p,j} = \frac{\rho_{b,j}}{1 - \varepsilon_{b,j}} \qquad \text{, for } j \in \{1,2,3,...\}. \tag{9.5}$$

An average volume fraction of the core to the product particles is needed in addition. For this, the mean particle volume of the initial materials $V_{p,m,j=0}$ and the stage products $V_{p,m,j>0}$ are used. Both ensue from the third moments of the respective number-based particle size distributions with:

$$V_{p,m,j} = \frac{\pi}{6}\int_0^\infty d^3 q_{0,j}\mathrm{d}d = \frac{\pi}{6} m_{3,0,j} \qquad \text{, for } j \in \{0,1,2,3,...\}. \tag{9.6}$$

Due to Eq. 9.6, the average core-to-particle volume fraction of the stage products ($V_{p,m,0}/V_{p,m,j}$) equals the ratio of the third raw moment of the initial material PSD $m_{3,0,0}$ to that of the stage product $m_{3,0,j}$. Both moments can be related again to the mean-volume-equivalent particle diameter $d^*_{3,0}$ of Eq. 2.36. The ratio of $d^*_{3,0,j}$ to $d^*_{3,0,0}$ is referred to as the particle growth ratio on basis of mean-volume-equivalent particle diameter, which is symbolized here by $\Phi_d(d^*_{3,0})$. The latter is used to express the average core-to-particle volume fraction of the stage products according to this relationship:

$$\frac{V_{p,m,0}}{V_{p,m,j}} = \frac{m_{3,0,0}}{m_{3,0,j}} = \left(\frac{d^*_{3,0,0}}{d^*_{3,0,j}}\right)^3 = \Phi_{d,j}^{-3}(d^*_{3,0}) \qquad \text{, for } j \in \{1,2,3,...\}. \tag{9.7}$$

The expression $\Phi_d^{-3}(d^*_{3,0})$ shall represent the number-based average core-to-particle volume fraction in the following of this thesis. According to the ideal continuous layerwise granulation model of Chapter 3, the effective particle density can be expressed in terms of the component densities (core and coating) and the core-to-particle volume fraction of Eq. 9.7:

$$\rho_{p,j} = \rho_{p,0}\Phi_{d,j}^{-3}(d^*_{3,0}) + \rho_{c,j}\left(1 - \Phi_{d,j}^{-3}(d^*_{3,0})\right) \qquad \text{, for } j \in \{1,2,3,...\}. \tag{9.8}$$

By this, the average effective coating density can be determined from:

$$\rho_{c,j} = \frac{\rho_{p,j} - \rho_{p,0}\Phi_{d,j}^{-3}(d^*_{3,0})}{1 - \Phi_{d,j}^{-3}(d^*_{3,0})} \qquad \text{, for } j \in \{1,2,3,...\}. \tag{9.9}$$

The average coating layer porosity of the stage products $\varepsilon_{c,j}$ can be finally estimated by

$$\varepsilon_{c,j} = 1 - \frac{\rho_{c,j}}{\rho_{s,c}} \qquad \text{, for } j \in \{1,2,3,...\} \tag{9.10}$$

for a known compact solid density of the coating material $\rho_{s,c}$. The latter is given with $1440\,\mathrm{kg/m^3}$ for sodium benzoate, as stated in [2].

The described estimation method of the effective coating density and the corresponding layer porosity is not suitable for thin coatings for the following reasons. Core-to-particle volume fractions ($m_{3,0,0}/m_{3,0,j}$) are accompanied by measurement errors in particle size distributions, and the values of such a volume ratio are close to unity for products with thin coatings. Due to this, the denominator of Eq. 9.9 can become negative for thin-coating conditions; but, even for positive denominators of Eq. 9.9, the influence of PSD measurement errors on $\rho_{c,j}$ would also be strongly enhanced, when the core-to-particle volume ratio is close to unity: $m_{3,0,0}/m_{3,0,j} \to 1$. As a conclusion, the results of higher stage products are more reliable. It is further ascertained from the ideal granulation model (see Figure 4.2), where coatings are uniform and

homogeneous, that the effective particle density converges to the effective coating density for larger product-to-core size ratios: $\rho_p(\Phi_d \to \infty) \to \rho_c \Leftrightarrow \xi_\rho(\Phi_d \to \infty) \to 1$. At this, the effective product density of granules, whose particle growth ratio is greater than 3, has a relative deviation from the apparent coating density of less than round 3.7 % $(1 - \xi_{\rho,j})$. Therefore, it is aimed in the discontinuous granulation study of Section 10.1 to create thicker coatings and to conduct more stages in series. Local changes of apparent density and porosity inside the coatings, that can occur in large-growth granulation processes, are not considered by the present estimation method. Moreover, nucleation of particles of pure coating material, which can lead to errors in the bulk density measurements, is also disregarded here. Those nuclei are often smaller than the coated products, wherefore the nuclei fraction can be removed by sieving with mesh sizes lower than the minimal diameter d_{min} of the raw bulk materials, see Table 9.1.

9.4 Methods for continuous fluidized bed spray granulation

9.4.1 Feeding nuclei into the granulator by a double-pinch valve

As mentioned before, the nuclei feeding equipment utilized in the continuous granulation experiments of Section 10.4 comprises a storage container and a double-pinch valve, as shown in Figure 9.4. The double-pinch valve is used as particle sluice for inserting external nuclei into the granulator with certain feed rates. The working principle of the nuclei feeder and side effects on its dosing accuracy are described in the following.

Operation principle

The operation principle of the feed-related double-pinch valve is illustrated in Figures 9.6 and 9.7. A certain amount of primary particles (nuclei filling level) is stored in the nuclei container. The feed-in particle sluice prevents nuclei from free flow and process gas from being ejected out of the granulator. The pinch valves of the nuclei feeder can be either open or closed. These switching positions are realized by a pneumatic control system. During operation, the two valves are switched synchronously with inverse switching positions, so that one is always open, while the other is closed at the same time. In this way, nuclei are sluiced into the process chamber within two steps. In the first step, shown in Figure 9.6 a, the upper pinch valve (inlet pinch valve, indicated by V1) is opened, and the lower pinch valve (outlet pinch valve, indicated by V2) is closed. Thereby, the sluice channel between the valves gets filled with core material. At this, free particle flow is enhanced by higher filling levels of the container. In the second step, shown in Figure 9.6 b, the upper pinch valve is locked and the lower pinch valve is unclosed. The nuclei can slip through the outlet pinch valve then, while the amplification of the filling level pressure on free flow of nuclei is suppressed through the closed inlet pinch valve V1. Therefore, air is needed to be flushed into the sluice volume to quickly purge out the particles and to minimize adhesion at inner walls (fouling). The open-state times of the pinch valves, also called as opening times or switching times here, are represented by $t_{V1,f}$ and $t_{V2,f}$, respectively. They can be set separately on the panel of the pneumatic control system (see for instance Figure 9.2 or 9.4). The opening time of the upper pinch valve $t_{V1,f}$ dictates the time interval for which the channel of the lower pinch valve $t_{V2,f}$ is blocked, and vice versa (see Figure 9.7). Operation with equal open-state times shall be named in the following as *even switching rhythm* (with even switching times: $t_{V1,sep} = t_{V2,sep}$) and with unequal open-state times as *uneven switching rhythm* (with uneven switching times: $t_{V1,sep} \neq t_{V2,sep}$). The sum of the switching times of the single valves is symbolized by $t_{dpv,f}$:

$$t_{dpv,f} = t_{V1,f} + t_{V2,f}. \tag{9.11}$$

It can also be called *double-switch time*, single dosage time step, dosing time step, *dosing cycle time*, or in short just cycle time. The double-switch time is important for calculation and adjustment of feed rates, as detailed later in Sections 9.4.3 and 9.4.12. In the experimental equipment of the present thesis, the pinching gas and the flushing gas are provided from same pneumatic control system with the same pressure: the here so-called pressure of the pneumatic control air, which is symbolized by $p_{g,dpv}$.

Dosing inaccuracy

Dosing inaccuracies can be caused by several phenomena. A few could be observed visually during the experimental study of the dosing behavior of the feed-related double-pinch valve in Section 10.2. These are named here as the memory, the fouling, and the flush-back effect. The *memory effect* takes place in the rubber material of the pinch valves, whose back-reformation to a complete open-state gap distance slows

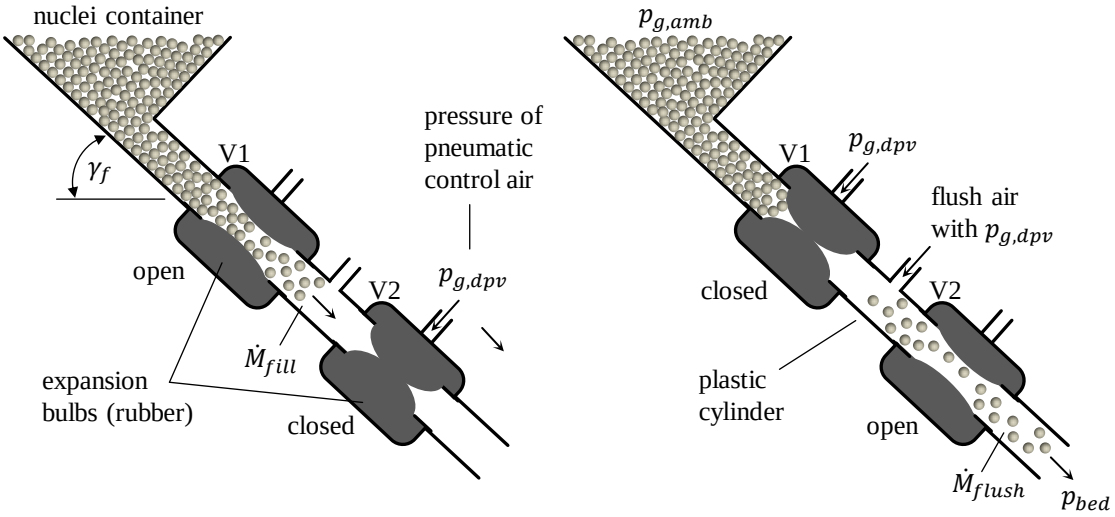

Figure 9.6: Operation principle of the feed-related double-pinch valve illustrated by two steps in a) and b).

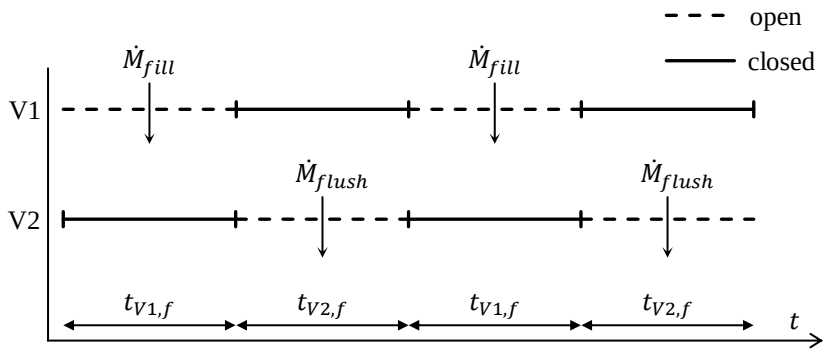

Figure 9.7: Illustration of the synchronous switching mode with inverse switching positions of the pinch valves V1 and V2 with time.

down a little in permanent operation. Consequently, the channel cross-section is constricted inside the pinch valves, whereby average feed rates can be lowered in a long-term perspective. In the *fouling effect*, a certain amount of particles attaches to inner walls of the sluice channel by adhesion forces, which reduces the dosage mass, and thus, the nuclei feed rate. The name *flush-back effect* already reveals its reason for dosing imperfections. A certain proportion of nuclei in the sluice volume is purged through the upper pinch valve, when it is not closed quickly or pressed together strongly enough. It is assumed that the extent of the flush-back effect (mass of mal-discharged particles) depends on process properties such as the internal gas pressure in the fluidized bed (symbolized by p_{bed}), the pinching gas pressure inside the upper expansion bulb (here $p_{g,dpv}$), the pressure of the flushing gas (here $p_{g,dpv}$), the ambient pressure acting inside the nuclei container (symbolized by $p_{g,amb}$), the nuclei filling level M_{fill}, and on nuclei characteristics such as particle size and density. In fluidized bed spray granulation, the gas pressure inside the process chamber fluctuates relatively strongly due to effects of real fluidization such as gas bubble formation. Especially those fluctuations can lead to significant temporal changes in the strength of the flush-back effect and, therefore, in the mass of single dosages.

9.4.2 Conveying bed granules to the separator by a double-pinch valve

In continuous granulation with internal classification (see for instance [14,15,88,89]), where the particle inlet and the fine-fraction recycle of the classifier share the same tube opening, pressure fluctuations of the fluidized bed gas can affect the turbulence of classification gas flow with the result of worse separation performances (see also Section 2.2.7). Such an effect can be avoided through external product classification, where the granulator and particle inlet opening of the classifier are connected with each other by a gas-tight particle sluice, and where the fine fraction recycle is joined to granulator at a different location. In the present thesis, a double-pinch valve is used as a particle sluice (outlined in Section 9.2). This makes it possible to control (throttle) bed outlet rates, and thereby, to improve classification conditions without changing constructive design of the process chamber. The classifier-related double-pinch valve is denoted by several names in this thesis, as for example the feed-out double-pinch valve, the bed discharge conveyor, bed outlet particle sluice, or the bed granule discharger. The operation principle of the feed-out double-pinch valve is illustrated in Figure 9.8. The graphic shows two different types of possible bed discharge dynamics, which are described below.

Operation principle of the feed-out double-pinch valve

In the present work, the dimensions of the feed-in and feed-out double-pinch valves are identical in terms of their pinch valves, sluice volumes (plastic cylinders), and pneumatic air orifices. The operation principle of the classifier-related double-pinch valve is almost the same as this of the nuclei feeding equipment (Section 9.4.1). The pinch valves of the bed discharge sluice switch synchronously with inverse switching position, so that the upper pinch valve (inlet pinch valve, indicated by V1) is open when the lower pinch valve (outlet pinch valve, indicated by V2) is closed, and vice versa. The difference to the nuclei feeder is that the particle concentration of the fluidized bed can have a direct impact on bed discharge dynamics. The cycle time of the feed-out particle sluice (symbolized by $t_{dpv,sep}$) is defined likewise to that of the nuclei feeder: by the sum of the open-state times of the single pinch valves:

$$t_{dpv,sep} = t_{V1,sep} + t_{V2,sep}. \tag{9.12}$$

This time period is also called as double-switch time or dosing time step of the feed-out double-pinch valve, likewise to $t_{dpv,f}$ of Eq. 9.11. It has an effect on the conveying rates of the bed material discharger, as explained below.

When bed granules are conveyed from a granulator to a separator through a double-pinch valve, essentially two particle transport mechanisms (bed discharging steps) occur one after the other. In the first mechanism, the particles of the bed fall into (hit) the conveyor inlet channel. This sub-process is called *drop-out mechanism* (*step*) or *granulator exit mechanism* (*step*) of the bed material. It is based on particle dispersion in the fluidized bed and success probabilities of particles passing the bed outflow opening. The second particle transport mechanism is generated by the conveying principle of the double-pinch valve, such as it also takes place in the nuclei feeding equipment. Therein, particles situated in the conveyor inlet channel firstly flow into the sluice volume, after the upper pinch valve V1 has opened, and get subsequently flushed out of this intermediate volume by the pneumatic control air, after the lower pinch valve V2 has been unlocked. This part of the bed discharge process is the *sluice passage mechanism* (*step*) or simply the *conveying mechanism*

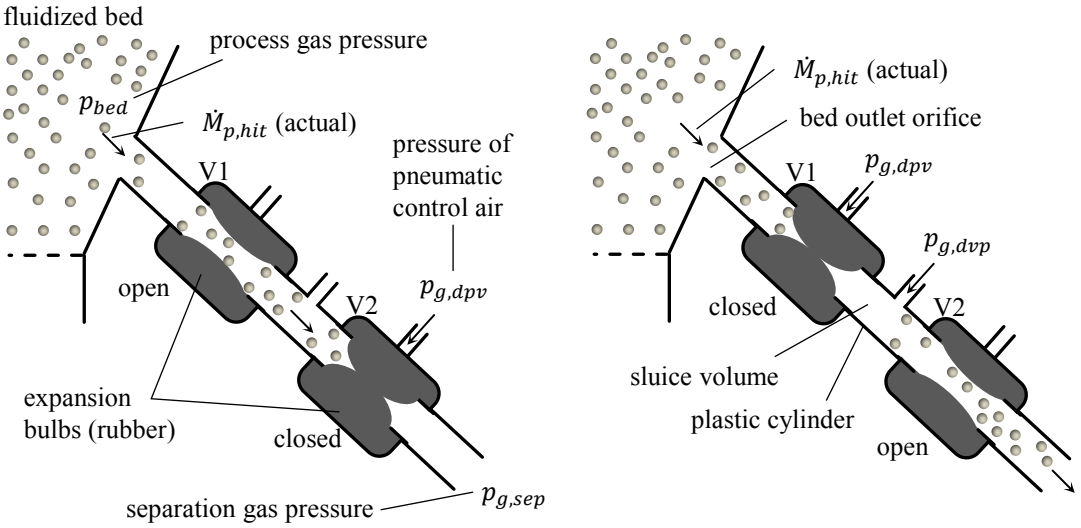

a) limitation by slow drop-out mechanism ($\dot{M}_{sep} = \dot{M}_{p,hit} < \dot{M}_{dpv,sep}$)

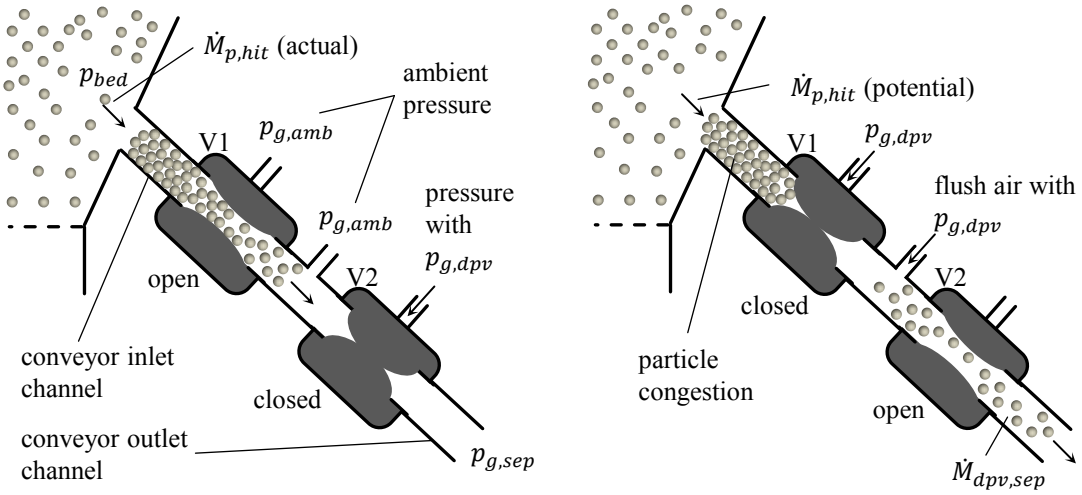

b) limitation by slow particle sluice mechanism ($\dot{M}_{sep} = \dot{M}_{dpv,sep} < \dot{M}_{p,hit}$)

Figure 9.8: Operation principle of the feed-out double-pinch valve with two limitation types of bed discharge dynamics illustrated separately in a) and b).

(*step*) of the double-pinch valve. The slower of the described particle transport mechanisms dictates the overall bed discharge dynamics due to their serial combination.

Overall conveying rates

Various designations can be used for the mass flow rate of granules passing the entire bed outlet channel (double-pinch valve and connection channels), as for example the granule conveying rate, the bed outlet flow rate, the bed discharge rate, the mass flow rate of particles entering the classifier, the granule or solids feed rate of the separator, the particle loading rates of the classifier, or simply the classifier entry rate. The granule conveying rate of the feed-out double-pinch valve is a time-averaged property. The smallest time period, for which bed discharge rates can be calculated, is the dosing time step of the classifier-related particle sluice $t_{dpv,sep}$. At this, the bed outlet flow rate is defined by the ratio of the mass of sluiced particles (single dosage mass, symbolized by $M_{dos,sep,i}$) to the double-switch time:

$$\dot{M}_{sep,i} = \frac{M_{dos,sep,i}}{t_{dpv,sep}} = \frac{M_{dos,sep,i}}{t_{V1,sep} + t_{V2,sep}}, \tag{9.13}$$

where i indicates a certain single dosing cycle or dosage. At this, it is mentioned that the symbol $\dot{M}_{sep}$ has two different meanings in this thesis. One is for describing the long-term average of fluctuating bed discharge rates of single dosages $\dot{M}_{sep,i}$, where the observation time period is several times longer than $t_{dpv,sep}$, and the other refers to bed discharge rates under stationary or quasi-stationary conditions, such as in the population balance model of Chapter 5.

Limitation types of bed discharge dynamics - potential mass flow rates of single particle transport mechanisms

As mentioned above, there are two different limitation types of bed discharge dynamics, which are the limitation of a slow drop-out mechanism, depicted in Figure 9.8 a, and the limitation of a slow particle sluice mechanism, depicted in Figure 9.8 b. Both particle transport mechanisms can be described by potential mass flow rates, as follows. The potential mass flow rate of the drop-out step (symbolized by $\dot{M}_{p,hit}$) is named as the *bed outlet hit rate*. It shall represent the maximal mass of bed granules that can enter the conveyor inlet channel per time unit by particle dispersion (random motion) for the case that the bed outlet orifice is totally free. The mass flow rate that can be maximally generated by the double-pinch valve at a certain parameter setting ($t_{V1,sep}$, $t_{V2,sep}$, and $p_{g,dpv}$) is called as the *potential conveyor rate* (symbolized by $\dot{M}_{dpv,sep}$) of the double-pinch valve. The latter is not to be confused with the actual conveying rate of a single dosage $\dot{M}_{sep,i}$. The long-term conveying rate obtained, $\dot{M}_{sep}$, is dominated by the slower of the transport mechanisms, and thus, is either defined by the bed outlet hit rate $\dot{M}_{p,hit}$ or by the potential conveyor rate $\dot{M}_{dpv,sep}$:

$$\dot{M}_{sep} = \begin{cases} \dot{M}_{p,hit} & \text{, for limitation by drop-out mechanism } (\dot{M}_{p,hit} < \dot{M}_{dpv,sep}) \\ \dot{M}_{dpv,sep} & \text{, for limitation by particle sluice mechanism } (\dot{M}_{p,hit} > \dot{M}_{dpv,sep}) \end{cases}. \tag{9.14}$$

A critical state, where both potential mass flow rates are equal ($\dot{M}_{p,hit} = \dot{M}_{dpv,sep}$), can also be formulated. But such conditions are very unlikely to happen in real systems. A distinctive feature of the types of bed discharge dynamics is that the major part of volume in the conveyor inlet channel remains free of particles when the drop-out mechanism dominates the overall transport dynamics; whereas particle congestion in the complete conveyor inlet channel appears when the particle sluice mechanism defines the overall bed discharge rate. The bed outlet hit rate $\dot{M}_{p,hit}$ depends on the cross-sectional area and the position of the bed outlet orifice, but also on properties that influence fluidization behavior. The latter include for instance particle properties such as size and density, process gas properties such as pressure and temperature, and chamber design such as cross-sectional diameter, type of gas distributor plate or other internal elements (e.g., Wurster tube). Manipulation of the feed-out rates of the dispersive limitation type requires changes in the fluidization bed properties or in the constructive design of the bed outlet opening. Assuming that the bed outlet hit rate is not affected by an operating double-pinch valve (e.g., by flush-back effects or leaky pinching) for a dominating drop-out mechanism, the conveying rates can be considered as independent from switching times of the single pinch valve. The potential conveyor rate of the classifier-related double-pinch valve $\dot{M}_{dpv,sep}$ is affected by several properties such as the open-state times of the pinch valves, the sluice volume, pressures of the process gas, the pneumatic control air, and the separation gas, as well as wall adhesion properties such as size, density and moisture of granules. The bed discharge rates can be controlled roughly (fluctuations

involved) by opening times of the pinch valves when the particle sluice mechanism determines the overall bed discharge dynamics.

Discharge experiments of Hampel

Diverse bed discharge experiments were made by Hampel [2] with the same equipment of the present work, through which single dosage masses ($M_{dos,sep,i}$), discharge times of tracer particles (coarse fraction of a blend of small and large Cellets®), and separation sharpnesses of the classifier (κ_{sep}) had been investigated for different switching frequencies (inverse of open-state times) of the double-pinch valve in even switching mode ($t_{V1,sep} = t_{V2,sep}$). In each of the experiments, Cellets® with an initial mass of 1 kg were brought into Wurster fluidization with an inlet gas mass flow rate of 70 kg/h and inlet gas temperature of 25 °C. The dimensions of the sluice volume (plastic cylinder), the pressure of the pneumatic control air, and parameters of the separation gas flow are not stated. It is assumed that the sluice volume in Hampel's experiments was bigger (longer plastic cylinder) than in this thesis, because some of single dosage masses measured by Hampel are several times larger than these of the present work, more on this later in Section 10.3. However, it turned out from the results of Hampel that the bed discharge dynamics depended strongly on the switching frequencies (opening times) of the double-pinch valve, which speaks for the particle sluice mechanism being the dominating step of bed discharge dynamics with the utilized equipment. This hypothesis is examined again through the bed discharge study in Section 10.3, but for fluidization parameters (inlet gas) that are closer the process conditions of the continuous granulation experiments.

Dosing inaccuracy

The so-called memory, fouling, and flush-back effects, which were recognized in the dosing analysis of the feed-out double-pinch valve (described in Section 9.4.1), can also emerge in the bed granule discharger with the result of dosing fluctuations. It is not clear whether reduction of cross-section inside pinch valves in permanent operation, which is a consequence of the memory effect, has a significant influence on dosing rates of the feed-out double-pinch valve. The fouling effect, on the other hand, could be observed visually during the bed discharge experiments of Section 10.3. The amount of bed granules that stuck to the inner wall of the transparent plastic cylinder changed clearly between the dosing cycles. In contrast to the nuclei feeder, the flush-back effect of the classifier-related particle sluice could not be detected visually during operation, due to the metal walls of the process chamber and unfavorable position of the chamber windows.

9.4.3 Feed rate control methods

A precise setting of the feed rate is needed to adjust the product mean size in layerwise granulation processes, as it is ascertained from the ideal particle growth model in Section 3.2 and the simulation study with a modified three-compartment population balance in Section 6.1. In continuous granulation experiments of the present thesis, feeding of nuclei shall be realized by a double-pinch valve, as described in Section 9.4.1. For this purpose, a proper feed rate control method has to be designed. Four different feed rate control methods (indicated by F1, F2, F3, and F4) can be suggested for a double-pinch valve feeder, the control principles of which are given in the following list:

- F1 - delay of single dosages by large open-state times of both pinch valves $t_{V1,f}$ and $t_{V2,f}$ with a *maximal single dosage mass* (fluctuations disregarded);
- F2 - delay of single dosages by large open-state times of the lower pinch valve $t_{V2,f}$ and reduction of single dosage masses by *partially filling of the sluice volume* (see Figure 9.6 a);
- F3 - delay of single dosages by large open-state times of the upper pinch valve $t_{V1,f}$ and reduction of single dosage masses by *partially purging of the sluice volume* (see Figure 9.6 b);
- F4 - conveying a precisely *prepared dosage mass* (symbolized by $M_{dos,f}$) after predefined *dosing time gaps* (symbolized by $\Delta t_{dos,f}$).

The main differences of these strategies are summarized in Table 9.3. In the first three strategies (F1 to F3), the double-pinch valve is operated in automatic mode of the pneumatic control system, and the feed container has to be filled with a sufficient charge of nuclei. In addition to this, the feed rate is achieved to be controlled only by setting the open-state times: $t_{V1,f}$ and $t_{V2,f}$. The corresponding feed rate of a single

dosage $\dot{M}_{f,i}$ ensues from the ratio of a single dosage mass $M_{dos,f,i}$ (sluice package) to the double-switch time $t_{dpv,i}$:

$$\dot{M}_{f,i} = \frac{M_{dos,f,i}}{t_{dpv,f}} = \frac{M_{dos,f,i}}{t_{V1,f} + t_{V2,f}} \qquad \text{, for F1, F2, and F3.} \tag{9.15}$$

However, estimation of the single dosage mass is difficult, as it is accompanied by fluctuations in practice. A mathematical description of the single dosage mass can be formulated as follows, where different effects are separated by statistical factors.

In the first control method F1, it is aimed to sluice maximally possible single dosages and to define feed rates through specified cycle times of double-pinch valve $t_{dpv,f}$. The open-state times of the inlet and outlet pinch valves must be therefore long enough to completely fill and flush off the sluice volume. The maximally possible single dosage mass can be defined by the bulk density of the nuclei material (symbolized here by $\rho_{b,f}$) and the sluice volume $V_{dpv,sl}$ between both pinch valves. The bulk density of nuclei feed material can be determined by gravimetric measurement or from $\rho_{b,f} = \rho_f(1 - \varepsilon_b)$ for a given effective nuclei density ρ_f and assuming the bulk porosity with 40 % for spherical particles. As mentioned before in Section 9.4.1, a memory, a fouling, and a flush-back effect of the double-pinch valve lead to lower single dosage masses on average and to dosing fluctuations. These effects can be subsumed by the dosage fluctuation factor $\Phi_{dpv,i}$, whose values are lower than unity: $\Phi_{dpv,i} < 1$. Putting all this together, the single dosage mass obtained $M_{dos,f,i}$ is expressed with:

$$M_{dos,f,i} = \rho_{b,f} V_{dpv,sl} \Phi_{dpv,i} \neq f(t_{V1,f}, t_{V2,f}) \qquad \text{, for F1.} \tag{9.16}$$

The single dosage mass $M_{dos,f,i}$ does not depend on the opening times of the two pinch valves $t_{V1,f}$ and $t_{V2,f}$ for the feed rate control method F1. Variations of single dosages, and associated to this, the dosage fluctuation factor $\Phi_{dpv,i}$ are caused by many different aspects. The memory effect depends on time of operation t. The fouling effect is affected by the inclination angle of the conveying channel γ_f (see Figures 3.2 and 9.6 a), surfaces forces, types of materials of the nuclei and feeding equipment, the ambient temperature $T_{g,amb}$, size and density of the nuclei material, and pressure of the pneumatic control air $p_{g,dpv}$. The flush-back effect is influenced by the filling level of the nuclei container, the size and density of the nuclei material, the gas pressure in the nuclei container $p_{g,amb}$ (ambient pressure here), the pressure of pneumatic control air $p_{g,dpv}$ (changeable), and the pressure of the process gas in the fluidized bed p_{bed}, which fluctuates due to inhomogeneous fluidization. The sluice volume $V_{dpv,sl}$ or the maximally possible dosage mass $\rho_{b,f} V_{dpv,sl}$ are difficult to measure by dosage masses of the method F1, since they are reduced by the fouling and flush-back effect. As shown later in Section 10.2.2, dosing accuracy is better when both open-state times are high (here $\gg 1\,\text{s}$). It was further detected that the dosage mass becomes nearly independent from the single open-state times ($t_{V1,f}$ and $t_{V2,f}$) for method F1. Beside this, lower feed rates are required for larger particle growth ratios in continuous granulation according to the spray-to-feed rate setting methods of Table 3.1(SFM2 applied here) of the ICLG-model. This can be achieved by larger double-switch times in F1.

In contrast to method F1, the feed rate is controlled by reducing the filling-up time in F2 and lowering the flushing-out time in F3. To accomplish this, the open-state times must be very short in the respective cases: here with $t_{V1,f} \ll 1\,\text{s}$ for F2 and $t_{V2,f} \ll 1\,\text{s}$ for F3. The restriction of sluice volume filling level in F2 can be represented by another reduction factor $\Phi_{fill,i}$, which depends on the open-state time of the upper pinch valve $t_{V1,f}$ and the inclination angle of double-pinch valve channel γ_f. The single dosage mass can then be approached by

$$M_{dos,f,i} = \rho_{b,f} V_{dpv,sl} \Phi_{dpv,i} \Phi_{fill,i}(t_{V1,f}, \gamma_f) \qquad \text{, for F2.} \tag{9.17}$$

The limitation of particle outflow from the sluice volume can be considered by a flush-out reduction factor $\Phi_{flush,i}$, wherewith the single dosage mass ensues to

$$M_{dos,f,i} = \rho_{b,f} V_{dpv,sl} \Phi_{dpv,i} \Phi_{flush,i}(t_{V2,f}) \qquad \text{, for F3.} \tag{9.18}$$

The open-state times act as main control variables corresponding to functional relations of $M_{dos,f,i}$ on $t_{V1,f}$ in Eq. 9.17 and on $t_{V2,f}$ in Eq. 9.18.

The feed rate control method F4 has to be operated manually. The storage container of nuclei feeding equipment is only filled by a precisely weighed dosage mass $M_{dos,f}$, which should be inserted into the granulator after defined time gaps of dosing $\Delta t_{dos,f}$. Feeding-in is realized by the double-pinch valve; but, several dosing cycles must be executed to compensate fouling and flush-back effects. The pneumatic control system is deactivated during time gaps of dosing. After completely sluicing the dosage mass $M_{dos,f}$, another

index	operation mode	container filling level	main control property	open-state time of V1 $t_{V1,f}$	open-state time of V2 $t_{V2,f}$
F1	automatic	$M_{fill,0}$ (large)	$t_{dpv,f}$	high ($\gg 1\,\mathrm{s}$)	high ($\gg 1\,\mathrm{s}$)
F2	automatic	$M_{fill,0}$ (large)	$t_{V1,f}$	low ($\ll 1\,\mathrm{s}$)	high ($\gg 1\,\mathrm{s}$)
F3	automatic	$M_{fill,0}$ (large)	$t_{V2,f}$	high ($\gg 1\,\mathrm{s}$)	low ($\ll 1\,\mathrm{s}$)
F4	manual	$M_{dos,f}$ (dosage only)	$M_{dos,f}$ (low) $\Delta t_{dos,f}$	around 1 s	around 1 s

Table 9.3: Features of four different feed rate control tactics for sluicing particles through a double-pinch valve.

nuclei dosage of the same amount has to be refilled into the container. This way, a long-term feed rate (in the scale of minutes and hours) can be generated that conforms to the ratio of the prepared dosage mass $M_{dos,f}$ to the time gap of dosing $\Delta t_{dos,f}$:

$$\dot{M}_f = \frac{M_{dos,f}}{\Delta t_{dos,f}} \qquad \text{, for F4.} \tag{9.19}$$

The advantage of method F4 is that the long-term feed rate is controlled precisely, but sacrificing automatic operation. However, this method can be used in continuous granulation experiments to avoid an error in feed rate (only in long-term perspective) and to better evaluate the parameter setting concept of the ICLG-model.

As shown later in Section 10.4, the methods F1 and F4 are employed in continuous granulation experiments of the present thesis.

9.4.4 Relation between process parameters and product characteristics

A relation between process parameters and product characteristics has been derived from partial mass balances (nuclei and coating material) within the ideal particle growth model in Sections 3.1.3 to 3.2.2. Therein, the solids spray rate $\dot{M}_{spr,s}$, the nuclei feed rate $\dot{M}_f$, the nuclei loss fraction $\Phi_{f,loss}$, and the spray solids loss fraction $\Phi_{spr,loss}$ belong to the process parameters; while the product characteristics comprise the core (nucleus) diameter d_f, the (desired) total particle diameter $d_{pr,set}$, the effective core density ρ_f, and the effective coating density ρ_c. The ICLG-model is based on strong simplifications such as the assumption of mono-sized and spherical nuclei and product granules, uniform densities of cores and coatings, ideal separation performance, and stationary conditions. In the continuous granulation experiments, material losses occur, nucleation takes place, nuclei are polydisperse, and product properties are distributed multi-dimensionally. It is therefore difficult, or perhaps impossible, to analytically derive a relationship between the nuclei feed rate, the solids spray rate, and a proper desired average particle size characteristic, even for steady-state conditions. Assuming the latter and considering material losses to be constant, the production rate $\dot{M}_{pr}$ can also be described by process parameters via $\dot{M}_{pr} = \dot{M}_f(1-\Phi_{f,loss}) + \dot{M}_{spr,s}(1-\Phi_{spr,loss})$ for the experiments, as in the ICLG-model in Eq. 3.22. In order to relate the product mass flow rate $\dot{M}_{pr}$ to product characteristics, partial mass balances have to be combined with number-based population balances and a geometric single particle model such as the spherical two-compartment model of Figure 3.1. The complexity of this issue, shall be briefly explained in the following. For example, the nuclei and the product are polydisperse, which means that $q_{0,f} = q_{0,f}(d_f)$ with $\sigma_f > 0$ and $q_{0,pr} = q_{0,pr}(d_{pr})$ with $\sigma_{pr} > 0$. Further, the coating density is not uniform in real layerwise granulation processes, as it depends on layer thickness, which is shown for instance by product analyses within the discontinuous granulation study of Section 10.1.6. The effective coating density of the product is consequently a function of the core diameter and the total particle diameter: $\rho_c = \mathrm{f}(s_c) = \mathrm{f}(d_f, d_{pr})$. The effective particle density of an individual product granule, which conforms with the spherical two-compartment model, results according to Eq. 3.5 from its core diameter, its total particle diameter, the effective core density, and the effective coating density: $\rho_{pr} = \mathrm{f}\big(d_f, d_{pr}, \rho_f, \rho_c(d_f, d_{pr})\big)$. Hence, the effective product density ρ_{pr} is two-dimensionally distributed over the d_f- and the d_{pr}-coordinate. A formal relation between the production rate $\dot{M}_{pr}$ and distributed particle

properties of the product is possible through the following semi-complete double integral (negative domain of coordinates excluded) of the two-dimensional number density distribution $q_{0,2D,pr} = q_{0,2D,pr}(d_f, d_{pr})$, with the core diameter and the total particle diameter as property coordinates, and with the total number flow rate of the product $\dot{N}_{pr}$, the individual effective particle density ρ_{pr}, and the variable particle volume $\pi d_{pr}^3/6$ as pre-factors of the 2D-distribution function:

$$\dot{M}_{pr} = \int_0^\infty \int_0^\infty \dot{N}_{pr}\rho_{pr}\big(d_f, d_{pr}, \rho_f, \rho_c(d_f, d_{pr})\big)\frac{\pi}{6}d_{pr}^3 q_{0,2D,pr}(d_f, d_{pr})\mathrm{d}d_f\mathrm{d}d_{pr}. \tag{9.20}$$

Even with the assumptions that no breakage and no material loss of cores occur, where

$$\dot{N}_{pr}(\Phi_{f,loss} = 0) = \dot{N}_f = \frac{\dot{M}_f}{\rho_f \int_0^\infty \frac{\pi}{6} d_f^3 q_{0,f}(d_f)\mathrm{d}d_f} = \frac{\dot{M}_f}{\rho_f \frac{\pi}{6} m_{3,0,f}}, \tag{9.21}$$

and that the effective coating density is uniform and homogeneous (ρ_c =const.), the product properties would still be distributed in two dimensions (e.g., $q_{0,2D,pr} = q_{0,2D,pr}(d_f, d_{pr})$), but Eq. 9.20 simplifies then with Eqs. 3.2, 3.4, and 9.21 to:

$$\dot{M}_{pr}(\Phi_{f,loss} = 0) = \dot{M}_f \int_0^\infty \int_0^\infty \left(\frac{d_f^3}{m_{3,0,f}} + \frac{\rho_c}{\rho_f}\frac{(d_{pr}^3 - d_f^3)}{m_{3,0,f}}\right) q_{0,2D,pr}(d_f, d_{pr})\mathrm{d}d_f\mathrm{d}d_{pr}. \tag{9.22}$$

If, in addition, the effective material densities of the cores and coatings are the same ($\Phi_\rho = 1$, see Eq. 3.3), the product is only distributed in terms of total particle diameter. The production rate is then defined by a simple integral of the one-dimensional particle size distribution:

$$\dot{M}_{pr}(\Phi_{f,loss} = 0, \Phi_\rho = 1) = \dot{M}_f \frac{\int_0^\infty d_{pr}^3 q_{0,pr}(d_{pr})\mathrm{d}d_{pr}}{m_{3,0,f}} = \dot{M}_f \frac{m_{3,0,pr}}{m_{3,0,f}} = \dot{M}_f \left(\frac{d_{3,0,pr}^*}{d_{3,0,f}^*}\right)^3. \tag{9.23}$$

However, the integrals of Eqs. 9.20, 9.22, and 9.23 can neither be solved analytically nor numerically, as none of their density distribution functions is given a priori. Latter can also not be approached due to missing size distributions of cores and coating layers of the bed granules and unknown separation functions. The separation curve of Molerus a. Hoffmann [103], for example, is also just a solution for strongly idealized conditions (recapitulated in Section 2.2.7). Furthermore, formation of granules from pure coating material (nucleation) is not considered in Eq. 9.20, but it plays a role in real granulation processes. It is not clear yet, if nucleation processes had a significant influence on product size development in the investigated continuous granulation experiments of the present thesis.

As shown later in the continuous granulation study (Section 10.4), several desired particle growth ratios $\Phi_{d,set}$ are predefined for the experiments. In order to calculate corresponding target values of product diameter $d_{pr,set}$, a suitable statistical moment of the polydisperse nuclei has to be used:

$$d_{pr,set} \stackrel{?}{=} (\text{average of } q_{0,pr}) \stackrel{?}{=} (\text{average of } q_{0,f}) \cdot \Phi_{d,set} \tag{9.24}$$

In the present thesis, the first moment of number-based particle size distributions according to Eq. 2.32 was chosen, which is here the arithmetic mean of nuclei $d_{m,f}$. It shall represent the average diameter of cores of coated products in the experiments, too. This type of mean was also employed in the parameter setting of the population balance simulation study in Section 6. The results of it have promised a reliable control of product mean size via processing strategy CM3, wherein the required spray-to-feed rate ratio $\Phi_{m,set}$ is adapted to the desired growth ratio $\Phi_{d,set}$ and the set separation gas velocity $u_{g,set}$ to the desired product diameter $d_{pr,set}$. Other average size characteristics are also conceivable for defining the desired product diameter $d_{pr,set}$ in Eq. 9.24. Different variants are presented in Section 2.1.2. For example, the mean-volume-equivalent particle diameter $d_{3,0}^*$ according to Eq. 2.36 would agree with the third initial moment of the number-based nuclei size distribution $m_{3,0,f}$, which occurs in Eqs. 9.21 to 9.23.

9.4.5 Adaption of spray rate and nuclei feed rate to desired particle growth ratio

The solids spray rates and nuclei feed rates of the continuous granulation experiments presented in Section 10.4 shall be adapted to the desired particle growth ratio $\Phi_{d,set}$ on basis of the spray-to-feed rate setting

method SFM2 (see Table 3.1), which is derived from the ideal granulation model (Chapter 3). It is recommended to employ the SFM2 method, as spray rates can be freely chosen in this variant with values that are appropriate for given drying conditions and process stability. However, desired spray rates $\dot{M}_{spr,set}$ cannot be generated precisely in practice, when a peristaltic pump is used, since conveying fluctuations occur. In addition, the rotation speed of the pump (symbolized by n_{pum}) can only be set within a discretized range of values, depending on the pump type. For this reason, the following empirical function

$$\dot{M}_{spr,set}[\mathrm{g/h}] = 114.2 \cdot n_{pum}[\mathrm{rpm}]. \tag{9.25}$$

has been determined from weight measurements of spray solution consumed in certain time periods, by which the spray rates shall be predicted from predefined pump rotation speeds for the continuous granulation experiments. Such a correlation depends on experimental conditions, as for instance the position (height) and filling level of the spray solution beaker, material type, length and inner diameter of the conveying hoses, the solids concentration of spray liquid, the orifice diameter of the liquid channel nozzle, and the nozzle air excess pressure. The predicted solids spray rate $\dot{M}_{spr,s,set}$ ensues from multiplication of the calculated set spray rate with the solids fraction of solution:

$$\dot{M}_{spr,s,set} = \dot{M}_{spr,set} x_s. \tag{9.26}$$

It is further derived from the ideal granulation model (see Eqs. 3.3, 3.11, and 3.24) that the required spray-to-feed rate ratio $\Phi_{m,set}$ is fixed by the mass losses and the effective densities ($\Phi_{f,loss}$, $\Phi_{spr,loss}$, ρ_f, and ρ_c) of the core and coating material, and the target-growth ratio $\Phi_{d,set}$. The required spray-to-feed rate ratio $\Phi_{m,set}$ is here defined to be the ratio of the predicted solids spray rate $\dot{M}_{spr,s,set}$ to the adapted set feed rate: $\Phi_{m,set} = \dot{M}_{spr,s,set}/\dot{M}_{f,set}$. It shall be calculated analogously to the ICLG-model by

$$\Phi_{m,set} = \frac{1-\Phi_{f,loss}}{1-\Phi_{spr,loss}} \frac{\rho_c}{\rho_f} (\Phi_{d,set}^3 - 1) \tag{9.27}$$

for the experiments. The effective density of the coating layer ρ_c must be either assumed or estimated from measurement techniques such as X-ray micro-computed tomography (as done by Hampel [2]) or the estimation method in Section 9.3. But, the results of these methods don't agree with each other, as shown later. Hence, a reliable estimation method has not been found yet. On the contrary, the effective density of the nuclei material ρ_f can be measured more precisely, as for example by bulk density measurements for spherical particles with small particle size variance, by water displacement for non-soluble particles, gas pycnometry for particles with no open pores, or by geo-pycnometry for larger nuclei with very small pore openings. The required feed rate ensues from:

$$\dot{M}_{f,set} = \frac{\dot{M}_{spr,s,set}}{\Phi_{m,set}}. \tag{9.28}$$

9.4.6 Adaption of set separation gas velocity to desired particle growth ratio

As in the processing strategy CM3 of the presented PB-simulation study (Section 6.1.1), the set separation gas velocity $u_{g,set}$ of the experimental bed mass controller (given below in Eq. 9.34) shall also be adapted to the desired particle growth ratio $\Phi_{d,set}$, via a terminal product sinking velocity $u_{s,pr}$ that is related to the effective product density ρ_{pr} of Eq. 3.5 and the desired product diameter $d_{pr,set}$:

$$u_{g,set} \coloneqq u_{s,pr} = \sqrt{\frac{4}{3c_d(Re_{s,pr})} \frac{\rho_{pr}-\rho_{fl}}{\rho_{fl}} d_{pr,set} g}. \tag{9.29}$$

The desired product diameter $d_{pr,set}$ is calculated here by multiplying the mean diameter of the nuclei material from Eq. 2.32 and $q_{0,f}$ with the desired particle growth ratio of Eq. 3.1: $d_{pr,set} = d_{m,f}\Phi_{d,set}$. The difference to the PB-model is that the material densities of the cores and coatings are not assumed to be equal here; hence, the granules are represented by a spherical two-compartment model, accordingly to the ideal particle growth model of Chapter 3. The drag coefficient c_d inside Eq. 9.29 was determined by Eq. 2.80 (Kürten et al. [30]) and with $Re_{s,pr} = d_{pr,set}u_{s,pr}/\nu_g$ as definition for the terminal Reynolds numbers. For future investigations, various approaches of the terminal sinking velocity can be suggested too. Diverse theoretical, semi-empirical, and empirical correlations for the drag coefficient c_d, the terminal sinking velocity u_s, and/or the terminal Reynolds number Re_s can be found in Section 2.2.1, that are suitable for different flow regimes (Re_s-ranges). Equation 9.29 shall only be used for the automatic mode of the experimental bed mass controller of this thesis, as explained in Section 9.4.8 in more detail.

9.4.7 Inline detection of fluidized bed mass from pressure drop

An inline detection method of the fluidized bed mass M_{bed} is required for continuous granulation experiments with bed mass control. Hampel [2] has already retrofitted a bed mass detection system to the experimental setup used for this work (ProCell LabSystem, see Section 9.2.2), which is based on pressure drop measurements. At this, a total pressure difference of the process gas across the process chamber (symbolized by Δp_{app}) is measured inline from one pressure sensor located below the distributor plate for p_{in} and another one above the process chamber for p_{out}. A semi-empirical calculation method for converting the inline pressure loss Δp_{app} into the current bed mass M_{bed} was also developed in [2] and implemented into the monitoring and control system (Section 9.4.9) via DASYLab-Software. This method is briefly reproduced here, but with a different notation. Energy losses of fluid element interactions cause the total pressure difference. They arise from laminar friction and turbulences inside the bulk flow of the process gas, across moving particles, especially in the fluidized bed region, and around chamber assemblies such as the gas distributor plate, inner chamber walls, nozzle components, and the Wurster tube. Therefore, the pressure drop can be divided into two fractions: one that is related to instrumental elements of the process chamber (symbolized by Δp_{emp}), and one that is referred to the fluidized bed (symbolized by Δp_{bed}). Both sum up to the total pressure difference:

$$\Delta p_{app} = p_{in} - p_{out} = \Delta p_{emp} + \Delta p_{bed}. \tag{9.30}$$

A relationship between the pressure losses of the mechanical elements Δp_{emp} and gas velocities of the chamber inlet u_{in} and outlet u_{out} has been acquired by pressure drop measurements, where the plant was operated with an empty process chamber and different inlet gas mass flow rates. It was given with

$$\Delta p_{emp} = \frac{\rho_{g,in}}{2}\left(u_{out}^2(1 + c_{d,app}) - u_{in}^2\right), \tag{9.31}$$

where $\rho_{g,in}$ represents the inlet gas density and $c_{d,app}$ a flow coefficient that is correlated to the inlet gas volume flow rate $\dot{V}_{in}$ according to:

$$c_{d,app}[-] = 5 \cdot 10^{-7}\dot{V}_{in}^4 - 10^{-4}\dot{V}_{in}^3 + 1.22 \cdot 10^{-4}\dot{V}_{in}^2 - 0.5638\dot{V}_{in} + 13.839 \quad \text{, with } \dot{V}_{in} \text{ in } [\mathrm{m^3/h}]. \tag{9.32}$$

Due to Eq. 9.30, the pressure drop fraction of the holdup Δp_{bed} follows from the difference of the measured total pressure drop Δp_{app} to the empty-chamber pressure drop Δp_{emp}. Finally, an average cross-section area of process chamber $\bar{A}_{app}$ was introduced, with the help of which the bed mass shall be calculated from the pressure losses of the bed material:

$$M_{bed} = \frac{\Delta p_{bed}\bar{A}_{app}}{g} = \frac{(\Delta p_{app} - \Delta p_{emp})\bar{A}_{app}}{g}, \tag{9.33}$$

The bed mass could be stably regulated with the method described in several granulation experiments [2], each lasting over 8 hours. The continuous granulation experiments were conducted with inlet gas conditions of mass flow rates in the range of 70 and 100 kg/h and temperatures between 70 and 110 °C. Moreover, measurement deviations of the bed mass have been investigated in Hampel's work by a non-spraying batch fluidization experiment, where the fluidized bed mass was increased by a precisely prepared amount of bed material (0.2 kg) in defined time steps from a holdup of 0.2 to 2 kg. The material was added by the feed-related double-pinch valve. The results showed a good agreement with bed masses from 0.2 and 1.2 kg, but their errors became greater with larger holdups. The inlet gas mass flow rate and temperatures of these measurements are not stated in [2]. But, the inlet gas conditions have a strong effect on the total pressure drop, especially the inlet gas mass flow rate. Later in Section 10.1.3, several bed mass curves, which have been detected in discontinuous granulation experiments for different inlet gas conditions, are analyzed in order to choose appropriate inlet gas parameters for the continuous granulation experiments of this thesis.

9.4.8 Monitoring and control system

As mentioned before, the monitoring and control system installed by Hampel [1, 2] was used for the experimental investigations of this work (see Figures 9.1, 9.4, and 9.5). However, the bed mass controller designed in it was modified and supplemented by some features for the continuous granulation experiments of this thesis, as explained in the following. The structure of the new monitoring and control system is illustrated in Figure 9.9. It offers the options of controlling the bed mass in automatic mode (operation) by a feed-back loop and/or in manual mode (operation) by the plant operator.

Feed-back control structure for automatic operation

The feed-back controller of the automatic mode consists of a cascade structure of second order, that includes an inner feed-back loop manipulating the classifier gas flow (actual velocity $u_{g,act}$) and an outer feed-back loop controlling the holdup of the granulator (actual fluidized bed mass $M_{bed,act}$), such as in [1, 2]. The real bed mass $M_{bed,act}$ is to be determined during operation via inline measurements of the total pressure drop of the process chamber Δp_{app}, as described in Section 9.4.7. The measured pressure difference is transmitted to a data acquisition program (here DASYLab®-file), and therein, converted to a current bed mass signal $M_{bed}(t)$ (errors included) on basis of Eqs. 9.30 to 9.33. The calculated bed mass signal goes to a DASYLab®-unit in which the following P-control function

$$u_g(t) = \begin{cases} u_{g,set} - K_m\big(M_{bed}(t) - M_{set}\big) & \text{, if } u_{g,set} - K_m\big(M_{bed}(t) - M_{set}\big) > 0 \\ 0 & \text{, if } u_{g,set} - K_m\big(M_{bed}(t) - M_{set}\big) \leq 0 \end{cases} \tag{9.34}$$

was implemented. In this control function, $u_g(t)$ represents the calculated current separation gas velocity to be generated inside the classifier, $u_{g,set}$ the set separation gas velocity, K_m the gain factor, and M_{set} the set bed mass. The experimental P-control unit conforms with the control function of the PB-model in Eq. 5.18, that has been used in the presented PB-simulation study (Chapters 5 and 6). The difference here is that the separation gas velocity u_g can be set to zero in the experiments for large bed mass values, whereas the employed separation function of the PB-model stringently requires the separation gas velocity to be larger than zero. The parameters of the experimental bed mass controller ($u_{g,set}$, K_m, and M_{set}) must be adjusted before starting the automatic operation mode and are then kept constant. However, they can also be changed during operation using an input field in the DASYLab®-program, which enables manual bed mass control, as detailed below. The calculated separation gas velocity $u_g(t)$ serves as current set value for the mass flow controller (MFC) of the classifier gas. Therefore, a scaling unit integrated in the DASYLab®-program linearly converts the $u_g(t)$-signal into a suitable input-property of the MFC that is realized here by an electric current signal I_{MFC}. The whole MFC-device constitutes the inner loop of the cascade controller. The actual separation gas velocity $u_{g,act}(t)$ created by the MFC is seen as the output signal. It shall be as close as possible to the $u_g(t)$-value with the aim to control the fluidized bed mass according to the outer control loop. It is noted at this point that the adaption of the set separation gas velocity $u_{g,set}$ to desired product characteristics according to Eq. 9.29 is optional. Other values of $u_{g,set}$, and so different processing strategies (see for instance Section 9.4.11), might be possible too. Basically, the process objectives should be achieved. The PB-simulations of Section 6.2, for example, have shown that the set separation gas velocity hardly affects the obtained stationary product characteristics, but has a significant influence on bed mass control deviations, even at steady states. The outer feed-back loop of Hampel's work was realized by a PD-control function of the DASYLab®-software. The disadvantage of it, is that it cannot be coupled to the desired particle growth ratio $\Phi_{d,set}$.

Feature for manual bed mass control

Operation with manual bed mass control can be realized by changing one, two, or all three parameters of the control function ($u_{g,set}$, K_m, and M_{set} from Eq. 9.34) via the input field of the DASYLab®-program. In doing so, the entire linear $u_g(M_{bed})$-curve of the bed mass controller can, for instance, be shifted upwards by higher set separation gas velocities $u_{g,set}$, more strongly inclined by larger gain factors K_m, and moved to the right by greater set bed masses M_{set}. In manual control mode, it is important that the separation gas velocity is set comparatively high when the bed mass is very low, and that the separation gas velocity is set comparatively low when the bed mass is excessively high. The simplest method would be to just increase the gain factor, so that the controller reacts more strongly to bed mass control deviations. In the case of large negative control deviations in bed mass with $(M_{bed} - M_{set})/M_{set} \ll 0$, it is also advisable to increase the set separation gas velocity and the set bed mass, respectively. In the opposite case with $(M_{bed} - M_{set})/M_{set} \gg 0$, the set separation gas velocity and the set bed mass would then have to be reduced. The following range of values can be entered into the inline input field of the present monitoring and control systems: 0 - 5 m/s for $u_{g,set}$, 0 - 12 m/s/kg for K_m, and 0 - 2 kg for M_{bed}. Based on this concept, different operation modes of the classifier are defined in the next Section 9.4.9, according to which manual control periods shall be carried out for some of the continuous granulation experiments in Section 10.4. Further, the inline feature for manual shifting of the P-control function turns out to be advantageous for particular startup strategies, as explained later in Section 9.4.10. But it also allows the plant operator to intervene an automatically controlled continuous granulation process for the case that the bed mass leaves an adequate range of values and endangers process stability.

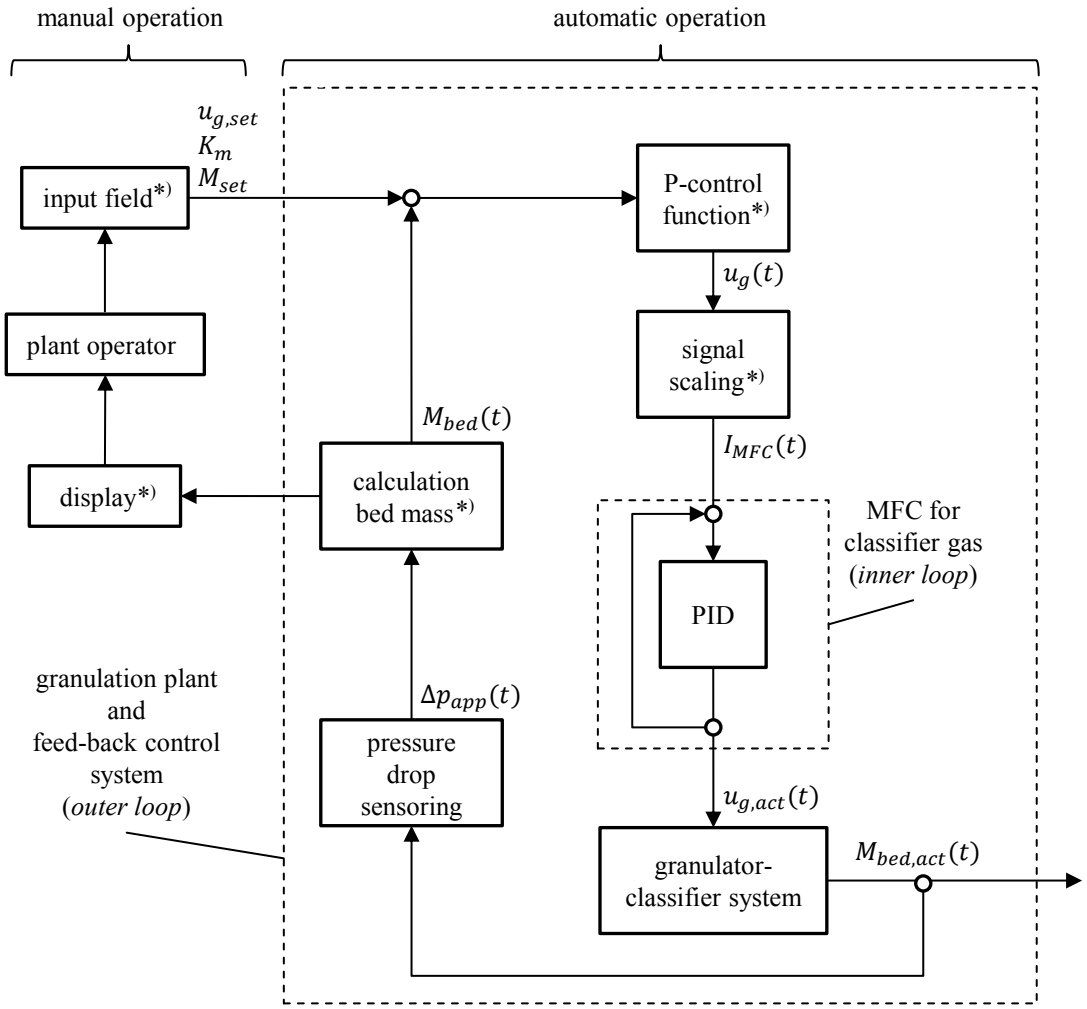

Figure 9.9: Illustration of the 2nd-order-cascade structure of fluidized bed mass controller employed in automatic mode of continuous granulation experiments; *) implemented by DASYLab®-units.

9.4.9 Operation modes of the classifier

Three different operation modes of the classifier shall be formulated here in order to later define and distinguish diverse process strategies in Sections 9.4.10 and 9.4.11 for the continuous granulation experiments of this thesis. These are the

- total product discharge mode (short: discharge mode),
- classification mode (also: separation mode), and
- total product reflux mode (short: reflux mode).

The main characteristics of them are given in Table 9.4.

Conditions of material flows

The discharge mode represents simply the offset of the classifier gas flow, in which the separation gas velocity u_g is set to zero. Thereby, none of the particles entering the classifier can be recycled back to the granulator ($\dot{M}_{rec} = 0$), but all of them are discharged at the product outlet. The production rate equals then the bed discharge rate: $\dot{M}_{pr} = \dot{M}_{sep}$. The classification mode applies when the separation gas velocity u_g has values in the range the terminal sinking velocities from those of nuclei and the product with desired characteristics ($u_{s,f} \lesssim u_g \lesssim u_{s,pr}$). Under these conditions, it comes to a distinct separation of particle flow of the classifier inlet into a recycle flow and product discharge flow, so that both are clearly larger than zero: $\dot{M}_{rec} > 0$ and $\dot{M}_{pr} > 0$. In the reflux mode of the classifier, it is pursued to feed all particles from the classifier back to the granulator. For this purpose, the separation gas velocity must have excessively large values, which is restricted by maximal possible flow rates of the classifier-related MFC: $u_g = u_{g,max}$. This maximum should be at least far greater than terminal product sinking velocity: $u_g \gg u_{s,pr}$ (Eq. 9.29). However, a marginal amount of particles can be mal-discharged at the product outlet due to imperfections of the gas flow and lower local gas velocities in vicinity of the wall. But, this effect was negligibly small in the experiments. According to the described conditions, classification of discharged bed material does not take place within the discharge mode and reflux mode of the classifier.

Setting by control function parameters

The classifier operation modes can be arbitrarily switched over during the granulation experiments by changing the P-control function parameters ($u_{g,set}$, K_m, and M_{set}, see Table 9.4) via the input field of the monitoring and control system of Section 9.4.8 and Figure 9.9. The discharge mode can be generated by setting both the set separation gas velocity and the set bed mass to zero ($u_{g,set} = M_{set} = 0$), whereby the implemented control function of Eq. 9.34 outputs a zero-gas-velocity: $u_g = 0$. At this, the gain factor K_m can be either zero or larger: $K_m \geq 0$. To operate in classification mode, the separation gas velocity u_g should have values in the range of terminal sinking velocities of the bed material and the desired product, as mentioned before. This is achieved in the present work by adapting the set separation gas velocity $u_{g,set}$ to desired product characteristics (e.g., $d_{pr,set}$) with Eq. 9.29. The gain factor can be zero in the classification mode; but, the classifier operates then only with the offset $u_g = u_{g,set}$. At this, manipulation of the separation gas velocity and active feed-back control of the bed mass are refrained, which is not recommendable for the continuous granulation experiments. Instead, the value of the gain factor should be adapted to the overall process conditions, as shown later in Section 10.4.2. The set bed mass of the classification mode is preferred to be in a range of stable Wurster fluidization, where spray droplets can be properly distributed on particle surface. A set bed mass of 1 kg is a reliable value, when Cellets®200 are coated with sodium benzoate within the experimental equipment of Section 9.2, as it has already been proven by Hampel's experiments [2], and as it is concluded from the results of the two-zone continuum model in Section 8.2. The reflux mode can be obtained by setting all three parameters of the P-controller as large as possible, which is given for the implemented monitoring system with: $u_{g,set} = 5\,\mathrm{m/s}$, $K_m = 12\,\mathrm{m/s/kg}$, and $M_{set} = 2\,\mathrm{kg}$. The outputs of the P-controller u_g will then be excessively large, and with the present equipment even above the upper flow limit that the classifier-related MFC can provide. Therefore, an if-function is implemented into the DASYLab®-program (not illustrated in Figure 9.9), which sets the MFC-input signal I_{MFC} to its maximal permissible value for the case that $u_g > u_{g,max}$.

	discharge mode	classification mode	reflux mode
separation gas velocity u_g	$u_g = 0$	$u_{s,f} \lesssim u_g \lesssim u_{s,pr}$	$u_g = u_{g,max}$ $u_{g,max} \gg u_{s,pr}$
recycle particle flow rate $\dot{M}_{rec}$	$\dot{M}_{rec} = 0$	$0 < \dot{M}_{rec} < \dot{M}_{sep}$	$\dot{M}_{rec} \to \dot{M}_{sep}$
product discharge rate $\dot{M}_{pr}$	$\dot{M}_{pr} = \dot{M}_{sep}$	$0 < \dot{M}_{pr} < \dot{M}_{sep}$	$\dot{M}_{pr} \to 0$
setting of the P-controller (Eq. 9.34):			
set separation gas velocity $u_{g,set}$	$u_{g,set} = 0$	$u_{g,set} = u_{s,pr}$, see Eq. 9.29	$u_{g,set} \gg u_{s,pr}$, max. possible
gain factor K_m	$K_m \geq 0$	$K_m \geq 0$*)	$K_m > 0$, max. possible
set bed mass M_{set}	$M_{set} = 0$	optimal fluidization conditions, here 1 kg	$M_{set} \gg M_{bed}$, max. possible

Table 9.4: Characteristics of the classifier operation modes and related configurations of the P-controller unit; *) value of optimal gain factor is ascertained by experimental results in Section 10.4.2.

9.4.10 Growth acceleration strategies for startup periods

Faster startups are favored for continuous processes in general, which means for granulation applications that shorter growing-up periods of time are desired. As described by the ideal granulation model in Section 4.1.4, lower growth times $\tau_{gr,set}$ can be achieved by lower desired product diameters $d_{pr,set}$, lower bed mass values M_{bed}, higher solids spray rates $\dot{M}_{spr,s}$, and larger coating layer porosities ε_c. But, the setting of these parameters has limits. The desired product diameter is an objective-parameter defined by product quality requirements. The bed mass has to be hold in a certain range of values to ensure process stability. Further, higher solids spray rates are accompanied by larger solvent spray rates (here water). But, the latter is restricted by process-gas saturation (drying power, see also Section 7.10.2), drying kinetics, and critical conditions of excessive agglomeration. The coating layer porosity is fixed by drying conditions and type of materials being employed. For these reasons, two different substrategies for gaining growth kinetics in startup phases are conceptualized here: a slow increase of the feed rate in steps (indicated by GAS1) and a manual two-phase bed mass control method (indicated by GAS2). Both of them shall be used together in some of the continuous granulation experiments of this thesis. The abbreviation GAS stands for growth acceleration strategy.

GAS1: step-wise increase of feed rate to its required set value

The first substrategy GAS1 proceeds with lowered feed rates for a certain time period $\tau_{f,step}$ in the process beginning, which is referred to as duration of the feed-rate-reduction phase. Smaller feed rates lessen the bed mass increase, and lead thereby to faster growth rates. When employing this strategy, it is distinguished between the current set feed rate $\dot{M}_{f,set,k}$ and the required set feed rate $\dot{M}_{f,set}$, ensuing from the spray-to-feed rate setting method SFM2. Within the feed-rate-reduction phase ($0 \leq t_{exp} > \tau_{f,step}$), the current feed rate is supposed to be smaller than the required feed rate, whereas both should be equal at the end of this period ($t_{exp} = \tau_{f,step}$) and afterwards:

$$\dot{M}_{f,set,k}(t_{exp}) \begin{cases} < \dot{M}_{f,set} & \text{, for } 0 \leq t_{exp} < \tau_{f,step} \\ = \dot{M}_{f,set} & \text{, for } t_{exp} \geq \tau_{f,step} \end{cases} . \tag{9.35}$$

In order to avoid strong parameter changes during operation, the feed rate shall be evenly increased in small steps until the required feed rate is reached at $t_{exp} = \tau_{f,step}$. The feed rate enlargement steps are described by a time-dependent normalized feed rate step function $\Phi_{f,step}(t_{exp})$. The values of this function ($0 \leq \Phi_{f,step} \leq 1$) are seen as a feed rate reduction factor. It is formulated in the following way. At first, the duration of the feed-rate-reduction phase $\tau_{f,step}$ and the number of feed rate steps $N_{f,step}$ are chosen. From this, the step time $\Delta t_{f,step}$ (time period after which the feed rate shall be raised) and the normalized step

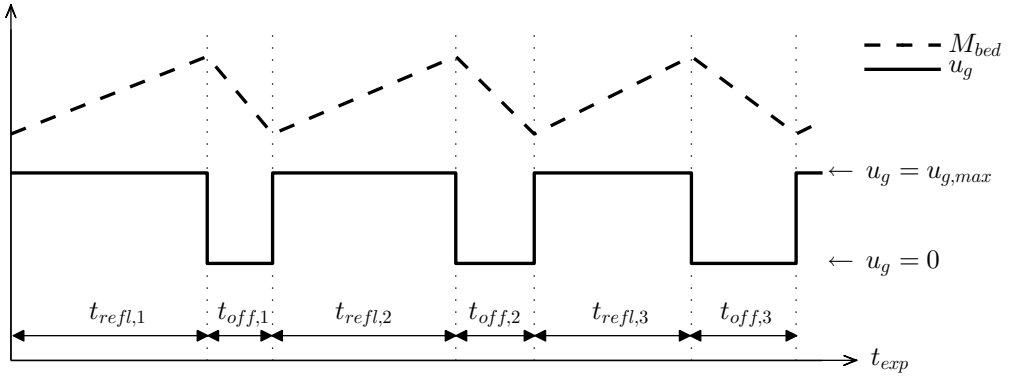

Figure 9.10: Scheme of the growth acceleration strategy GAS2: manual two-phase bed mass control by alternating operation modes of the classifier: total reflux ($u_g = u_{g,max}$) and total product discharge ($u_g = 0$).

width $\phi_{f,step}$ (increment of normalized step function) are derived with:

$$\Delta t_{f,step} = \frac{\tau_{f,step}}{N_{f,step}}, \tag{9.36}$$

$$\phi_{f,step} = \frac{1}{N_{f,step}}. \tag{9.37}$$

After this, the experimental time coordinate t_{exp} is divided into several equidistant intervals with a length of the step time $\Delta t_{f,step}$. The intervals are indicated by a counter variable $k_{f,step}$. It can be calculated from the experiment time using the floor-function according to:

$$k_{f,step}(t_{exp}) = \begin{cases} 1 + \mathrm{floor}\left(\frac{t_{exp}}{\Delta t_{f,step}}\right) & \text{, for } 0 \leq t_{exp} < t_{exp,tot} \\ \frac{t_{exp}}{\Delta t_{f,step}} & \text{, for } t_{exp} = t_{exp,tot} \end{cases}. \tag{9.38}$$

This counter variable can also be seen as a discretized dimensionless coordinate of the experiment time. It is helpful to express the time-dependency of a normalized feed rate step function (symbolized by $\Phi_{f,step}$) with:

$$\Phi_{f,step}(t_{exp}) = \begin{cases} \phi_{f,step}\big(k_{f,step}(t_{exp}) - 1\big) & \text{, for } 0 \leq t_{exp} < \tau_{f,step} \\ 1 & \text{, for } \tau_{f,step} \leq t_{exp} \leq t_{exp,tot} \end{cases}. \tag{9.39}$$

The current set feed rate follows from multiplying the normalized feed rate step function $\Phi_{f,step}$ with the required set feed rate $\dot{M}_{f,set}$ of Eq. 9.28 for stationary conditions:

$$\dot{M}_{f,set,k}(t_{exp}) = \Phi_{f,step}(t_{exp})\dot{M}_{f,set}. \tag{9.40}$$

GAS2: manual two-phase control of bed mass

In the second substrategy GAS2, the fluidized bed mass is controlled by two operation phases of the classifier alternating between reflux mode ($u_g = u_{g,max}$) and discharge mode ($u_g = 0$), described before in Section 9.4.9. Meanwhile, the bed material grows constantly through continuous spraying. Product classification is refrained in the reflux and discharge mode, whereby the growing bed particle size distribution cannot be manipulated by the separator. The entire period of time in which the two-phase bed mass control method should be applied is symbolized by τ_{man}. It is not strictly necessary to conduct both substrategies (GAS1 and GAS2) for the same time duration ($\tau_{f,step} = \tau_{man}$), but it is recommended to do so for an easier experimental procedure. Figure 9.10 shows the scheme of the working principle of GAS2. The total bed mass increases during the reflux mode, as almost all particles from the classifier are fed back to the granulator. The bed mass shall be reduced by the discharge mode for large overstepping of set values. Therefore, the mass flow rate of particles entering the classifier $\dot{M}_{sep}$ must be significantly higher than the total mass flow rate of

index of processing strategy	PS1	PS2-a	PS2-b
application of GAS1 (step-wise feed rate increase)	no	yes	yes
duration of reduced feed rates $\tau_{f,step}$ [h]	0	5	5
number of steps $N_{f,step}$ [−]	0	5	10
step time $\Delta t_{f,step}$ [min]	-	60	30
normalized step width $\phi_{f,step}$ [−]	-	1/5	1/10
application of GAS2 (two-phase bed mass control)	no	yes	yes
duration of manual bed mass control τ_{man} [h]	0	5	5
total number of reflux-discharge cycles N_{man} [−]	0	10	10
duration of a single reflux-discharge cycle Δt_{man} [min]	-	30	30
application of automatic mode (feed-back control of bed mass)	yes	yes	yes
beginning of automatic mode	$t_{exp} \geq 0$	$t_{exp} > 5\,\mathrm{h}$	$t_{exp} > 5\,\mathrm{h}$
duration in a single experiment τ_{auto} [h]	9	4	4
spray-to-feed rate setting method*)	SFM2	SFM2	SFM2
set separation gas velocity $u_{g,set}$**)	$u_{s,pr}$	$u_{s,pr}$	$u_{s,pr}$

Table 9.5: Criteria and parameters of processing strategies applied in the continuous granulation experiments of the present thesis; *) for the solids spray rate and the nuclei feed rate according to Table 3.1; **) calculated according to Section 9.4.6.

inserted solids (nuclei and coating material) minus bed mass losses through dust discharge in exhaust gas and wall adhesion:

$$\dot{M}_{sep} \gg \dot{M}_f(1 - \Phi_{f,loss}) + \dot{M}_{spr,s}(1 - \Phi_{spr,loss}). \tag{9.41}$$

The particle flow rate of the classifier inlet $\dot{M}_{sep}$ (bed discharge rate of Section 9.4.2) is affected by many aspects such as fluidization conditions (e.g., bed mass, inlet gas temperature, and inlet gas mass flow rate), position of the outlet tube leading to the classifier-related double-pinch valve, and open-state times of latter; wherefore, this flow rate is accompanied by large fluctuations as shown later in the results of Section 10.3. Consequently, the time intervals of the reflux mode $t_{refl,i}$ and discharge mode $t_{off,i}$ necessary to achieve low bed mass control deviations can differ during operation. In the experiments of this thesis, with manual two-phase bed mass control, the plant operator assesses how long the classifier operation modes shall be conducted depending on the current state of bed mass. The sum of both time intervals $t_{refl,i}$ and $t_{off,i}$ defines the duration of a single *reflux-discharge cycle*, which is denoted by Δt_{man}:

$$\Delta t_{man} = t_{refl,i} + t_{off,i}. \tag{9.42}$$

This incremental time step is supposed to be constant during the entire manual bed mass control period τ_{man} for ease of use; and thereby, related to a predefined number of manual control cycles N_{man} being applied within the growth acceleration period:

$$\Delta t_{man} = \frac{\tau_{man}}{N_{man}}. \tag{9.43}$$

Setting Δt_{man} properly, depends on bed mass increase and discharge dynamics, and therefore, on process conditions. Lower cycle times improve control accuracy, however, with the disadvantage of more effort. But, the value of Δt_{man} is also important for manageable time schedules, which should be as easy as possible to avoid mistakes by plant operators. Regarding this aspect, it is better to chose round cycle times such as 15, 20, or 30 min, that are coarse divisors of 60 min. This enables a better orientation on time displays of both clocks and stop watches.

9.4.11 Definition of processing strategies

Two processing strategies with different startup concepts, denoted by PS1 and PS2, shall be investigated in the continuous granulation experiments of Section 10.4. At this, two variants of the processing strategy PS2, which are distinguished by PS2-a and PS2-b, are applied. They are generally the same strategies, but they differ in their parameter specifications. The main criteria and parameters of the strategies PS1, PS2-a, and PS2-b are summarized in Table 9.5. The first processing strategy PS1 does not pursue any of the growth acceleration strategies GAS1 and GAS2 suggested in Section 9.4.10; instead, PS1 processes are started in automatic mode of the feed-back bed mass control system of Section 9.4.8 from the beginning on

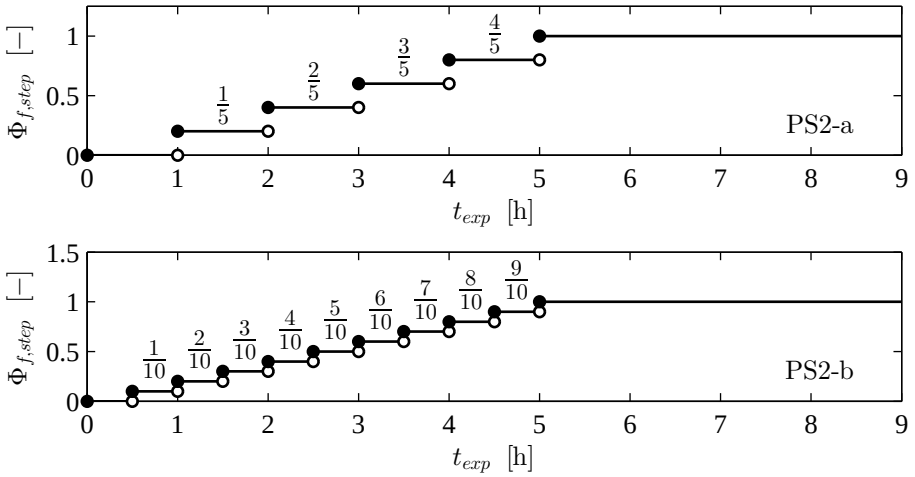

Figure 9.11: Specification of the feed rate step functions $\Phi_{f,step}(t_{exp})$ used in processing strategy variants PS2-a and PS2-b.

($t_{exp} \geq 0\,\text{h}$). The set feed rate is constant for the entire experiment for processes of PS1: $\dot{M}_{f,set,k} = \dot{M}_{f,set}$ for $0 \leq t_{exp} \leq t_{exp,tot}$. The processing strategy PS2 includes both substrategies GAS1 and GAS2, which are to be conducted for 5 h ($\tau_{f,step} = \tau_{man}$), respectively. Thereafter, automatic bed mass control is activated ($t_{exp} > 5\,\text{h}$). The momentaneous set feed rate $\dot{M}_{f,set,k}$ is reduced during the GAS1-phase according to the normalized feed rate step function $\Phi_{f,step}$, as pictured in Figure 9.11. The processing strategy variants PS2-a and PS2-b have quantitative differences in the normalized feed rate step function $\Phi_{f,step}$ of Eqs. 9.38 and 9.39. The $\Phi_{f,step}$-function of the PS2-a variant consists of five steps ($N_{f,step} = 5$), whereas the step function of PS2-b is more finely discretized with ten incremental feed rate enlargements ($N_{f,step} = 10$). As a conclusion of Eq. 9.36, the current feed rate is enhanced every sixty minutes in PS2-a startups ($\Delta t_{f,step} = 60\,\text{min}$) and every thirty minutes in PS2-b startups ($\Delta t_{f,step} = 30\,\text{min}$). After Eq. 9.37, the normalized feed rate step width of PS2-a is with $\phi_{f,step} = 1/5$ twice as large as for PS2-b with $\phi_{f,step} = 1/10$. The partial growth acceleration strategy GAS2 is identical for the variants PS2-a and PS2-b. The number of reflux-discharge cycles is set to $N_{man} = 10$, so that with a total duration of manual operation of $\tau_{man} = 5\,\text{h}$, each cycle must be carried out in thirty minutes: $\Delta t_{man} = 30\,\text{min}$. The relations of Sections 9.4.5 and 9.4.6 for adapting process and control parameters to the desired particle growth ratio $\Phi_{d,set}$ are used within the automatic bed mass control phases ($t_{exp} > \tau_{man}$) of all three processing strategy variants PS1, PS2-a, and PS2-b. For this, the calculation of the set spray rate $\dot{M}_{spr,set}$ and set feed rate $\dot{M}_{f,set}$ bases on the spray-to-feed rate setting method SFM2 of Table 3.1, and the set separation gas velocity $u_{g,set}$ of the employed P-controller (Eq. 9.34) is fixed by the terminal sinking velocity of product granules with desired product characteristics $u_{s,pr}$ according to Section 9.4.6.

9.4.12 Adjustment of set feed rates

Different set feed rates $\dot{M}_{f,set,k}$ from Eq. 9.40 shall be generated by the feed rate control methods F1 and F4 of Section 9.4.3 within the continuous granulation experiments. In order to obtain desired feed rates (controlled variable) by method F1 in the experiments, the cycle time of the feed-related double-pinch valve $t_{dpv,f,k}$ is used as control variable. It needs to be calculated before the experiments for all required feed rate values via Eq. 9.15. Therefore, this equation is solved for the double-switch time $t_{dpv,f}$, the cycle feed rate $\dot{M}_{f,i}$ is replaced by the current required feed rate value $\dot{M}_{f,set,k}$, and the single dosage mass $M_{dos,f,i}$ is given by an empirically averaged estimate value (symbolized by $M_{dos,f,est}$), which follows to:

$$t_{dpv,f,k} = \frac{M_{dos,f,est}}{\dot{M}_{f,set,k}} \qquad \text{, for F1.} \tag{9.44}$$

The estimated single dosage mass was determined with $M_{dos,f,est} = 11.3\,\text{g}$ from dosing behavior analyses of Section 10.2. The corresponding open-state times of the single valves are defined to be both half as large as

the total sluicing time:

$$t_{V1,f,k} = t_{V2,f,k} = \frac{t_{dpv,f,k}}{2} \qquad \text{, for F1.} \tag{9.45}$$

Adjusting the desired feed rates $\dot{M}_{f,set,k}$ in the continuous granulation experiments with method F4 is based on Eq. 9.19. The time gap of dosing $\Delta t_{dos,f}$ has to be pregiven in the F4 experiments. It is recommended to chose simple time intervals such as 15, 20, or 30 min to keep the experimental schedule as easy as possible. In this work, thirty minutes are applied as dosing time gap ($\Delta t_{dos,f} = 30\,\text{min}$), which conforms with Δt_{man} of GAS2. The single dosage masses to be prepared (symbolized here by $M_{dos,f,k}$) ensue then from the actual set feed rate $\dot{M}_{f,set,k}$ and the dosing time difference $\Delta t_{dos,f}$ via:

$$M_{dos,f,k} = \dot{M}_{f,set,k} \Delta t_{dos,f} \qquad \text{, for F4.} \tag{9.46}$$

The index k refers to the counter variable k_{step} of Eq. 9.38, which is introduced in the context of the growth acceleration substrategy GAS1 (Section 9.4.10), and which is suitable for sectioning the total experimental duration and designing lucid process plans.

10 Experimental results

10.1 Discontinuous multi-stage granulation

Several discontinuous multi-stage fluidized bed coating experiments have been conducted in the scope of the present thesis. At this, core materials listed in Tables 9.1 and 9.2 were covered with a sodium benzoate coating within series of experiments with successive coating stages. The products of each stage were used as initial material for the next stage (consecutive experiments). The single batch processes have been repeated multiple times, unless Wurster fluidization was destabilized by excessive agglomeration or even by blockage of the Wurster tube gap through solidified particle bridges. The multi-stage tests were performed for various nozzle gas excess pressures, types of core materials (Cellets® and glass beads), inlet gas mass flow rates, and inlet gas temperatures. The following aspects shall be hereby investigated:

- process conditions with better stability of Wurster granulation (Section 10.1.2),
- destabilization frequency (Section 10.1.2),
- temporal pressure drop evolution (Section 10.1.3),
- accuracy of the inline bed mass detection system from Section 9.4.7 (Section 10.1.3),
- variance in spray rate and spray losses (Section 10.1.4),
- diverse size-related particle growth characteristics (Section 10.1.5),
- density and porosity of the coating layer (Section 10.1.6), and
- terminal product sinking velocity (Section 10.1.7).

10.1.1 Experimental procedure

The multi-stage granulation experiments were carried out with the experimental setup of Figure 9.1 including the ProCell LabSystem of Glatt GmbH and some ancillary equipment, as described in Section 9.2. Each coating stage was performed in the following manner.

Process operation

At first, the granulation plant was put into operation without any particulate material inside the process chamber. The mass flow rate and temperature of the inlet gas were set to the desired values (given below in Table 10.2), and the plant was heated up for nearly twenty minutes. Meanwhile, the pump of the spray solution was set off, and no liquid was sprayed into the granulation chamber; but, the nozzle air injection was already activated. In doing so, the particles to be filled into the process chamber are prevented from falling into the orifice of the two-substance nozzle (bottom configuration with Wurster equipment) and clogging it. The nuclei feeding equipment of continuous granulation experiments (see Figures 9.4 and C.2) was used to insert 800 g of initial bed material into the preheated process chamber within the discontinuous experiments (not illustrated in Figure 9.1) until a stable Wurster fluidization had built up. Subsequently, the nuclei feeder was disconnected, the feed connection was closed by a sealing plug, the pump was switched on, and the chamber holdup was sprayed with a sodium benzoate solution for ninety minutes ($t_{exp,tot} = 90\,\text{min}$), after which pumping and spraying were deactivated again, and the process was shut down in several steps. A hot inlet gas flow was still provided and nozzle gas was still injected during the shutdown phase, so that the bed material could not cover the moist nozzle tip. In order to discharge the batch product, the power of the vacuum fan was increased to create negative pressure inside the process chamber, the sealing plug of the bed outlet channel (see lower left * in Figure 9.1) was opened, and the granulator content was slowly unloaded into a bucket by successively lowering the power of the downstream ventilator and generating slight excess pressures of the process gas.

Post-processing

A small portion of the stage product consists of pure coating material, which arises from premature drying of the spray droplets. This fine fraction, also referred to as dust fraction, has been removed from the stage products by sieving. The applied sieve mesh width was smaller than the lowest diameter of the employed core materials (IM-2, IM-4, or IM-7, see Table 10.2). Most of the dust material was attached to chamber walls, so that pneumatically discharged products were almost dust-free. The final bed mass $M_{bed,end}$ and the bulk density of the granulation product ρ_b have been measured after sieving. From the coated bulk material, 800 g has been taken and prepared as initial bed mass for the next consecutive granulation stage. The rest mass of the stage products ($M_{bed,end} - 800\,\mathrm{g}$) was used to measure its particle size distribution through dynamic image analyses. The multi-stage experiments could not be continued when complete bed agglomeration or Wurster tube blockage appeared. In this case, another multi-stage batch series was started with 800 g of non-coated core materials. The average spray rate of the single stages has been measured by the amount of spray solution consumed in the granulation period of ninety minutes.

10.1.2 Overview on experimental settings and process success statistic

In the following, the materials and process parameters used for the different discontinuous granulation experiments are summarized, their choice is explained, and the occurrence of process breakdowns is briefly discussed. The parameters to be constant for all batch experiments are listed in Table 10.1. Table 10.2 gives an overview on the varied parameters of the experimental settings to be examined and their successful or failed attempts.

Constant parameters

The constant parameters are the initial bed mass of each granulation stage $M_{bed,0}$, the pump rotation speed n_{pum}, the mass fraction of solids in the spray solution x_s, the spraying duration $t_{exp,tot}$, the gap height between distributor plate and Wurster tube H_{wt}, the Wurster tube length L_{wt}, and the inner Wurster tube diameter D_{wt}. The initial bed mass is selected to be 800 g, as this increases a little over 1000 g with proceeding granulation, and thus, proper fluidization conditions are achieved. A pump rotation speed of $n_{pum} = 7\,\mathrm{rpm}$ is employed, as this matches with some continuous granulation experiments of the present thesis. Such a pump setting provides spray rates $\dot{M}_{spr}$ of between 750 and 850 g/h, which is discussed later in Section 10.1.4. The solids concentration in the solution x_s and the Wurster tube dimensions are identical to that in the continuous granulation experiments.

Variation of core materials and process parameters

The conducted multi-stage granulation experiments are labeled by a parameter setting index that consists of the two letters "EB" plus two numbers. The first number is related to employed core material from Table 9.1, with "1" standing for the IM-2 material (Cellets®200), "2" for the IM-4 material (Cellets®350), and "3" for the IM-7 material (glass beads). The particle size distributions of the non-coated initial materials are depicted in Figure C.1, and their main average characteristics are listed in Table C.1. In contrast to Cellets®200, Cellets®350 are not taken as nuclei material in the continuous granulation experiments of this thesis; but, the application of larger core materials has the advantage that dust fractions (here pure sodium benzoate particles) can be better sieved off the stage products. The second number of the parameter setting index indicates a certain combination of three varied process parameters: the nozzle gas overpressure $p_{g,noz}$, the inlet gas mass flow rate $\dot{M}_{in}$, and the inlet gas temperatures T_{in}. The batch granulation series EB-11 and EB-21 are conducted more than one time, which is denoted by another number (of repetition) at the end of the parameter setting index. The discontinuous granulation experiments of EB-11 to EB-14 have been conducted for four different nozzle air excess pressures $p_{g,noz}$ (1 bar, 1.5 bar, 2 bar, and 2.25 bar), an inlet gas mass flow rate of $\dot{M}_{in} = 70\,\mathrm{kg/h}$, and an inlet gas temperature of $T_{in} = 90\,^{\circ}\mathrm{C}$. The multi-stage experiments of EB-21 to EB-34 have been operated with a nozzle gas excess pressure of 1.75 bar, as explained below. In the batch granulation series EB-21 to EB-24, the inlet gas mass flow rate has been varied between four values (70 kg/h, 85 kg/h, 100 kg/h, and 115 kg/h), whereas the inlet gas temperature was set constantly to 70°C. The granulation experiments with glass beads as core material (EB-31 to EB-34) had to be conducted with much higher inlet gas mass flow rates, since glass beads are much heavier than Cellets® (see ρ_p in Table C.1). The multi-stage batch experiments of EB-31 to EB-33 have been operated with an inlet gas mass flow rate of 175 kg/h, respectively, but with different inlet gas temperatures (70°C, 90°C, and 110°C). The inlet

$M_{bed,0}$ [g]	n_{pum} [rpm]	x_s [%]	$t_{exp,tot}$ [min]	H_{wt} [m]	L_{wt} [m]	D_{wt} [m]
800	7	32.25	90	0.02	0.20	0.07

Table 10.1: Constant parameters of the multi-stage batch experiments.

gas temperature of the last setting EB-34 was given with 70℃, while its inlet gas mass flow rate was set to the highest value in this study with 190 kg/h.

Process stability

The results of the two-zone continuum model of Section 8.4 show that the inlet gas parameters of the first four settings EB-11 to EB-14 provide stable operation conditions. However, the batch granulation experiments with the two lower values of nozzle air overpressure (1 bar and 1.5 bar) were destabilized by complete bed agglomeration. On the contrary, six stable stages could be conducted with higher nozzle gas overpressures (2 bar and 2.25 bar) in the multi-stage batch experiments EB-13 and EB-14. At this point it is mentioned that stable continuous granulation experiments up to 9 h could be conducted with a nozzle gas excess pressure of 1.5 bar in the reference case of Hampel [2], but the inner diameter of the liquid opening of the nozzle is not stated therein. In the granulation experiments of the present work (discontinuous and continuous), a two-substance nozzle with an inner diameter of 0.8 mm for the liquid orifice was used. It was concluded from the EB-11 and EB-12 experiments, that the nozzle gas excess pressure should be larger than 1.5 bar for the installed nozzle equipment. It was further expected that higher nozzle gas overpressures might lead to more dust formation (nuclei of pure coating material) in the stage products; because spray liquids are atomized to smaller droplets under those conditions, which favors premature drying of them. For this reason, a nozzle gas excess pressure of 1.75 bar was chosen for the subsequent experiments, which has proven itself adequate through an increase in successful experiments. The experimental setting of EB-21 gets closest to the process-gas-saturation limit among all the batch experiments, as it possesses the lowest drying power of the inlet gas and spraying conditions are uniform in the present discontinuous granulation study. Therefore, it had been repeated five times to demonstrate the frequency of process destabilization due to complete bed agglomeration. In total, 21 single granulation stages had been run for EB-21 setting, from which four (EB-21-1 stage 2, EB-21-2 stage 3, EB-21-4 stage 2, and EB-21-5 stage 4) broke down by excessive agglomeration with the result of a blocked Wurster tube. This complies with a *breakdown probability* of around 19 %. At this, the strong agglomeration in the second stage of EB-21-1 occurred only at the end of the experiment, so that enough free flowing material was produced to continue the multi-stage batch series, more on this later. The batch granulation experiments of EB-22 could only be operated with three stable stages in series. An instability appeared at the end of stage 4, as shown later on. In contrast to this, eight stable granulation stages have been realized for the experimental settings EB-23 and EB-24, where the drying power of the inlet gas is larger than in EB-21 and EB-22. All of the discontinuous experiments with glass beads as core material (EB-31 to EB-34) could be operated with stable Wurster fluidization conditions and steady particle growth. Only, the sixth stage of EB-31 has been disturbed by formation of a large amount of solid bridges, which emerged around the nozzle casing. The orifice of the nozzle has not been covered though until the end of spraying; so that Wurster fluidization was not completely destabilized. However, the product characteristics are influenced by those undesired effects, which is why the experimental series EB-31 was not continued. The multi-stage batch experiments of EB-32 and EB-33 could be conducted for 8 stages, respectively, without any disturbances; and even 16 stable batch granulation processes could be realized in series for the parameter setting of EB-34.

10.1.3 Inline measurements

Process stability of the discontinuous granulation experiments can be recognized by temporal curves of the pressure drop measured across the process chamber Δp_{app} and the gas temperatures of fluidized bed region T_{bed} (drying zone) and the chamber outlet T_{out}. The fluidized bed mass M_{bed} increases almost linearly by constant spraying and the pressure drop grows proportionally with bed mass. Hence, the pressure drop of the process chamber rises with nearly constant slope for stable granulation processes. The nearly constantly injected water content of the spray solution reduces the process gas temperature in the fluidized bed region and at the chamber outlet to a constant level by evaporation cooling. The occurrence of instabilities such

index of experimental setting	index of initial material	type of core material	$p_{g,noz}$ [bar]	$\dot{M}_{in}$ [kg/h]	T_{in} [°C]	number of stages	destabilization in the last stage
EB-11-1	IM-2	Cellets®200	**1**	70	90	**1**	yes
EB-11-2	IM-2	Cellets®200	**1**	70	90	**1**	yes
EB-12	IM-2	Cellets®200	**1.5**	70	90	**1**	yes
EB-13	IM-2	Cellets®200	**2**	70	90	**6**	no
EB-14	IM-2	Cellets®200	**2.25**	70	90	**6**	no
EB-21-1	IM-4	Cellets®350	1.75	70	70	**4**	no
EB-21-2	IM-4	Cellets®350	1.75	70	70	**3**	yes
EB-21-3	IM-4	Cellets®350	1.75	70	70	**8**	no
EB-21-4	IM-4	Cellets®350	1.75	70	70	**2**	yes
EB-21-5	IM-4	Cellets®350	1.75	70	70	**4**	yes
EB-22	IM-4	Cellets®350	1.75	**85**	70	**4**	yes
EB-23	IM-4	Cellets®350	1.75	**100**	70	**8**	no
EB-24	IM-4	Cellets®350	1.75	**115**	70	**8**	no
EB-31	IM-7	glass beads	1.75	175	**70**	**6**	no
EB-32	IM-7	glass beads	1.75	175	**90**	**8**	no
EB-33	IM-7	glass beads	1.75	175	**110**	**8**	no
EB-34	IM-7	glass beads	1.75	**190**	70	**16**	no

Table 10.2: Main differences of the multi-stage batch experiments of the present thesis in terms of employed core materials, process parameters, number of stages conducted in series, and process stability.

as large amounts of agglomerates, Wurster blockage by solidified particle bridges, or even the collapse of the entire fluidized bed by agglomeration lead to strong changes in the detected pressure drop and temperature curves for the following reasons. On the one hand, a smaller surface area of fluidized particles is in direct contact with the gas flow, which results in a decrease in pressure loss due to less friction and turbulence. On the other hand, the sprayed water can no longer be finely distributed onto particle surface of the entire bed, which lessens the overall evaporation rate in the drying zone, and thus, the evaporation cooling effect. Thereby, process gas temperatures of the drying zone and chamber outlet are raised.

Presentation by means of the normalized cumulative granulation time

Figures 10.1, 10.2, and 10.3 show the detected pressure drop and process gas temperatures at different measurement points of the multi-stage batch granulation experiments of Table 10.2. The measured quantities are illustrated against the *normalized cumulative granulation time*, which is defined by

$$t_{norm} = \frac{\sum_{j=1} t_{exp,j}}{t_{exp,tot}}, \tag{10.1}$$

where $t_{exp,j}$ represents the current experimental granulation time of stage j and $t_{exp,tot}$ the entire spraying time period of a single batch experiment (Table 10.1). The measurements for an entire batch series can be presented in one diagram, in which the first stage is plotted over normalized time values between zero and unity, the second stage between unity and two, and so on. The positive integers of the t_{norm}-coordinate, including zero too, corresponds then to the order of the stage number index $j \in \{0, 1, 2, ...\}$.

Signal transfer error of the process gas temperature in the fluidized bed region

The temperatures of the inlet gas T_{in}, process gas inside the fluidized bed T_{bed}, and the outlet gas T_{out} were measured for each experiment. But, in some experiments (all stages from EB-11-1 to EB-14, seventh and eighth stage of EB-21-3, fifth and sixth stage of EB-31, and all stages of EB-32 and EB-33) only the inlet and outlet gas temperatures of the process chamber are shown in the results for reasons of large signal transfer errors of the fluidized bed temperature measurement system. However, process destabilization by complete bed agglomeration can be recognized from the increase of either the fluidized bed or the outlet gas temperature.

Detection of process instabilities

Almost linearly increasing curves of the pressure drop and nearly constant process gas temperatures are observed for the stable granulation processes. Destabilization of the failed experiments (EB-11-1 stage 1, EB-11-2 stage 1, EB-12 stage 2, EB-21-2 stage 3, EB-21-4 stage 2, EB-21-5 stage 4, and EB-22 stage 4) can be clearly seen in the pressure drop and gas temperature measurements. At this, the changes in pressure drop progression and gas temperature begin at the same time.

It is ascertained for the failed granulation batches EB-11-1 to and EB-12 (with lower nozzle gas excess pressures: 1 and 1.5 bar) that the pressure drop does not grow up from the beginning on. Hence, it is assumed that over-wetting and agglomeration started directly after activation of spraying, even though the inlet gas parameters with 70 kg/h and 90℃ provide enough drying power according to results of the two-zone continuum model in Section 8.4. The sprayed droplets are perhaps not small enough or distributed properly on particle surface in EB-11-1 to EB-12, so that the solvent could not be completely evaporated under the given drying conditions. The outlet temperature can be used to compare the instable and stable processes of the granulation experiments with Cellets®200 (EB-11-1 to EB-14), as their inlet gas parameters are equal. The influence of nozzle gas overpressure on the outlet gas temperature can be neglected, as the nozzle gas rate is much smaller than the inlet gas mass flow rate. The outlet temperature of the destabilized experiments EB-11-1, EB-11-2, and EB-12 raises up to around 58 to 61℃, whereas it remains on a constant level within the range of nearly 43 and 46℃ in the succeeded experiments EB-13 and EB-14.

Most of the granulation processes with Cellets®350, shown in Figure 10.2, have been operated without any disturbances. Hereby, a nozzle gas excess pressure of 1.75 bar has proved to be better in terms of process stability than 1 or 1.5 bar. But, the inlet gas temperature of the experiments EB-21-1 to EB-24 was set to 70℃. Such a temperature is in a critical range of values, wherewith many experiments proceeded error-freely, but a few of them broke down at random time points. Especially the combination of a low inlet gas mass flow rate (70 kg/h) and a low inlet gas temperature (here 70℃) lead to critical drying conditions. A better process stability is observed for the experiments EB-23 and EB-24, where the inlet gas mass flow rates are larger with 100 and 115 kg/h, and thus, drying is enhanced.

The batch granulation experiments with glass bead cores, presented in Figure 10.3, could be operated under stable conditions, except for EB-31 stage 6. As mentioned before, in the sixth stage of the EB-31 series, the nozzle casing was almost completely covered by a large amount of aggregated particles; but, the Wurster tube gap had not been blocked, so that stable Wurster fluidization and spraying were still possible up to the end of this experiment. For this reason, no conspicuous changes in the pressure drop evolution and the outlet gas temperature are seen in the upper diagram of Figure 10.3 for $5 \leq t_{norm} \leq 6$. The aggregated particles on the nozzle casing were discovered after process shutdown. This stage was therefore considered to be stable for the total experimental duration of ninety minutes. However, it can be assumed that the amount of aggregated solids would become more in a longer batch experiment, so that the Wurster tube gap would be firstly partially blocked, and less bed granules would be sucked from the drying zone; and secondly, the spray droplets would no longer be distributed on the particles properly, whereby the Wurster granulation would be destabilized.

Influences on inline pressure drop

Within the multi-stage pressure drop curves $\Delta p_{app}(t_{norm})$, the measuring points at the beginning of the individual stages are the most comparable, because the initial bed mass was always precisely prepared with $M_{bed,0} = 800\,\mathrm{g}$ and the process parameters $p_{p,noz}$, $\dot{M}_{in}$, and T_{in} are equal. Only the particle size distributions were very different. As described with Eq. 9.30, the total pressure drop subsumes one fraction from instrumental elements Δp_{emp} and one fraction from the fluidized granules Δp_{bed}. The pressure drop of the instrumental elements should be constant within an entire multi-stage granulation series: $\Delta p_{emp} \neq \mathrm{f}(t_{norm})$. Small variation in the chamber installation when preparing the single stages can be neglected. The pressure drop of the fluidized bed Δp_{bed}, on the contrary, grows during the stages due to bed mass increase; but, it is expected to be nearly the same for the process starts, since the holdups are equal too. According to Eq. 9.30, the total pressure drops of the stage beginnings (Δp_{app} for $t_{norm} \in \{0, 1, 2, ...\}$) are presumably in a narrow range of values. Such results can be seen in the granulation experiments with Cellets®200 (Figure 10.1) and with Cellets®350 (Figure 10.2).

It is further ascertained that the pressure drop curves of successful granulation stages with an inlet gas mass flow rate of 70 kg/h (in EB-13, EB-14, and EB-21-1 to EB-21-5) lie mostly in the same range of values

from around 3 to 4 mbar, although the nozzle gas excess pressures $p_{g,noz}$ and inlet gas temperatures T_{in} are different. Hence, a significant influence of the nozzle gas excess pressure $p_{g,noz}$ and the inlet gas temperature T_{in} on the total pressure drop Δp_{app} cannot be discerned for those conditions. Only the pressure drop curves of stages 7 and 8 in EB-21-3 deviate from the regular behavior with flatter slopes. The particle size distributions of these stage products are very broad compared to these of stage 1 to 6, which is depicted in Figure 10.6. In addition, the Δp_{app}-curves of EB-21-3 stage 7 and 8 differ from other granulation series with 8 stages: see EB-23 and EB-24 in Figure 10.4 and EB-32 and EB-33 in Figure 10.3. Process instabilities by agglomeration and Wurster gap blockage were not observed in stage 7 and 8 of EB-21-3. The discharged bed material had been free flowing, did not contain agglomerates, and its final bed mass $M_{bed,end}$ was similar to the preceding stages, as shown later in Figure 10.4 by upside down triangles. It cannot be clearly stated whether the large variance of the product size distribution has caused the reduced slope of the pressure drop curves in EB-21-3 stage 7 and 8, or simply a measurement error occurred.

The results of the multi-stage batch experiments EB-22 to EB-24 (Figure 10.2) and EB-31 to EB-34 (Figure 10.3) show that the pressure drop curves $\Delta p_{app}(t_{norm})$ are on average the higher, the larger the inlet gas mass flow rate $\dot{M}_{in}$ was set, which conforms with the empirical correlation from Hampel given in Eqs. 9.31 and 9.32. It turns out that the inlet gas mass flow rate is the dominating process parameter affecting the overall pressure drop. Especially in the experiments with glass beads as core material (EB-31 to EB-34), where the inlet gas mass flow rate is required to be far greater with 175 and 190 kg/h, the pressure drop curves are clearly at higher values than those of the Cellets®-experiments. But, the pressure drop curves of batch processes with glass bead cores differ also more strongly between the single stages within a multi-stage series, even when the inlet gas mass flow rate is the same. At this, the multi-stage batch experiment EB-34 with the highest inlet gas mass flow rate of 190 kg/h possesses the strongest shifts of pressure drop curves. Those displacements in the pressure drop might be due to the following the reason. The plant was operated with two ventilators, one located before (pressure fan) and one behind the process chamber (vacuum fan), as illustrated in Figure 9.1. This arrangement provides the option to create negative pressure or overpressure inside the granulator. But, it has the disadvantage that larger control deviations of the inlet gas mass flow rate can occur. Those control errors had fluctuated more strongly for higher inlet gas mass flow rates in the present experimental study, which had to be manually adjusted by regulating the power of the vacuum fan. Therefore, the pressure drop of the instrumental elements Δp_{emp} is probably subject to large fluctuations between individual experiments.

Most of the succeeded granulation experiments with the core materials Cellets®200 and Cellets®350 yielded repeatable measurement results of the pressure drop for inlet gas mass flow rates between 70 and 115 kg/h, even for changing fluidization bed masses by spray granulation. Hence, the presented batch experiments confirm the pressure drop, again, to be a qualified inline detection quantity for bed mass control in continuous Wurster granulation processes, as it has already been proven by Hampel's continuous experiments [2]. However, the present study shows that the process parameters should not deviate too much from Hampel's reference experiments, at least not with the employed equipment of Section 9.2.

Choice of experiments for evaluation of the inline bed mass detection method

As described in Section 9.4.7, the employed data acquisition system also calculates bed mass values from the measured total pressure drop. The inline detection method of the bed mass had been created by Hampel [2] for continuous experiments with inlet gas mass flow rates of $\dot{M}_{in} \in \{70, 85, 100\}$ kg/h. Especially the correlation for the pressure drop of the instrumental elements Δp_{emp} of Eqs. 9.31 and 9.32 was fitted to rather low inlet gas mass flow rates in the range of 70 to 100 kg/h. The installed inline bed mass determination method shows very large errors in the discontinuous coating experiments with glass bead cores (EB-31 to EB-34) due to the much higher inlet gas mass flow rates, and is therefore not considered further. Instead, the bed mass curves of multi-stage batch experiments where Cellets® were coated with inlet gas mass flow rates from 70 and 115 kg/h (EB-13, EB-14, EB-21-3, EB-22, EB-23, and EB-24) are evaluated here. They are depicted in Figure 10.4. From this is ascertained that the stage-wise bed mass evolution grows proportionally to the detected pressure drop. The initial bed mass of each stage was prepared with 800 g. Further, the final bed mass $M_{bed,end}$ of the stages, which were discharged after the spraying period of the experiments, has been weighed offline. These $M_{bed,end}$-points are plotted as upside down triangles in Figure 10.4. The initial values of the inline bed mass curves in Figure 10.4 are summarized in Table 10.3.

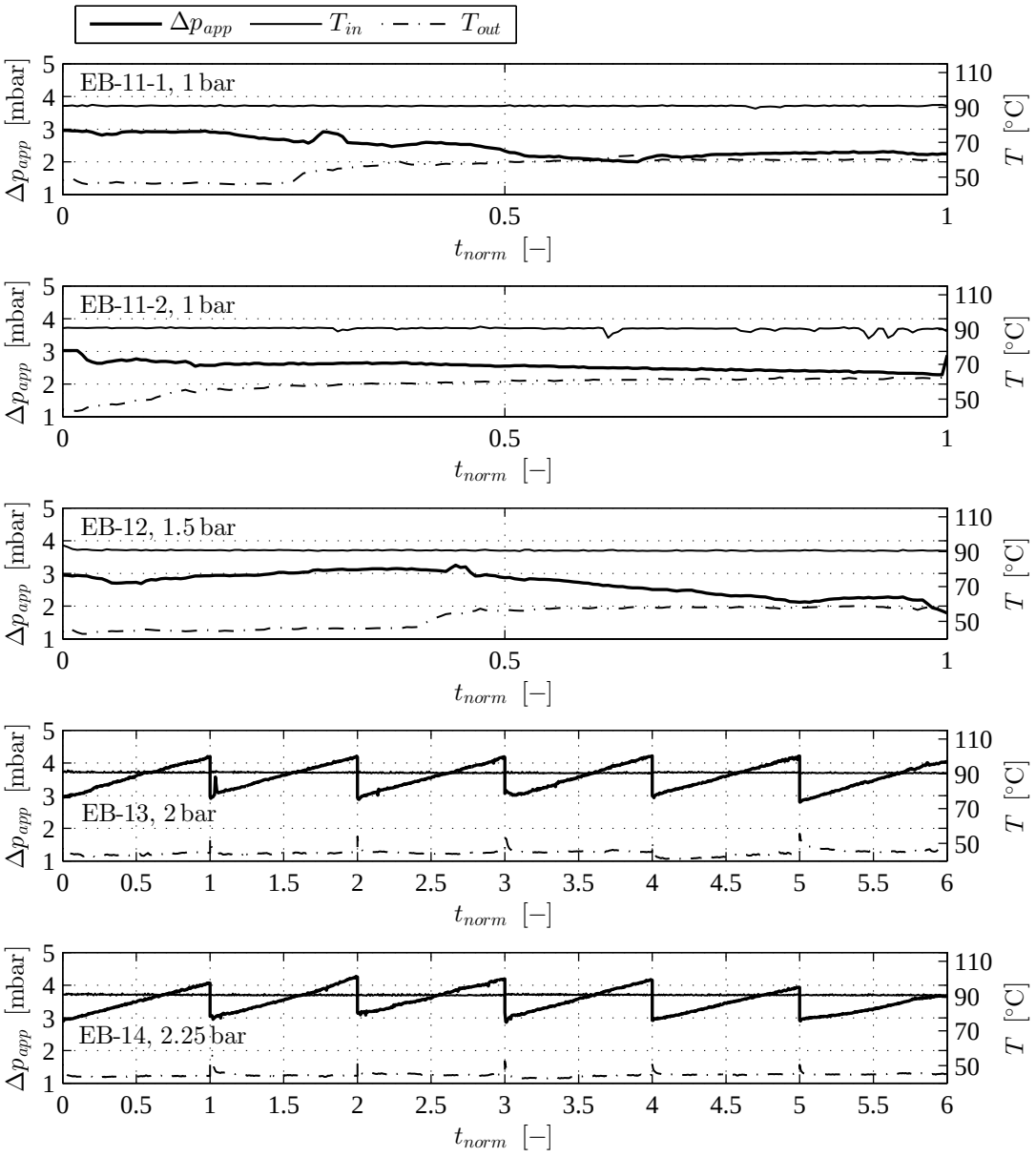

Figure 10.1: Pressure drop across the process chamber Δp_{app} and inlet and outlet gas temperatures versus the normalized process time t_{norm} of Eq. 10.1 for the experiments EB-11-1 to EB-14 from Table 10.2: Cellets®200 as core material, variation of nozzle air excess pressure $p_{g,noz}$; EB-11-1, EB-11-2, and EB-12 have failed and EB-13 and EB-14 were stable.

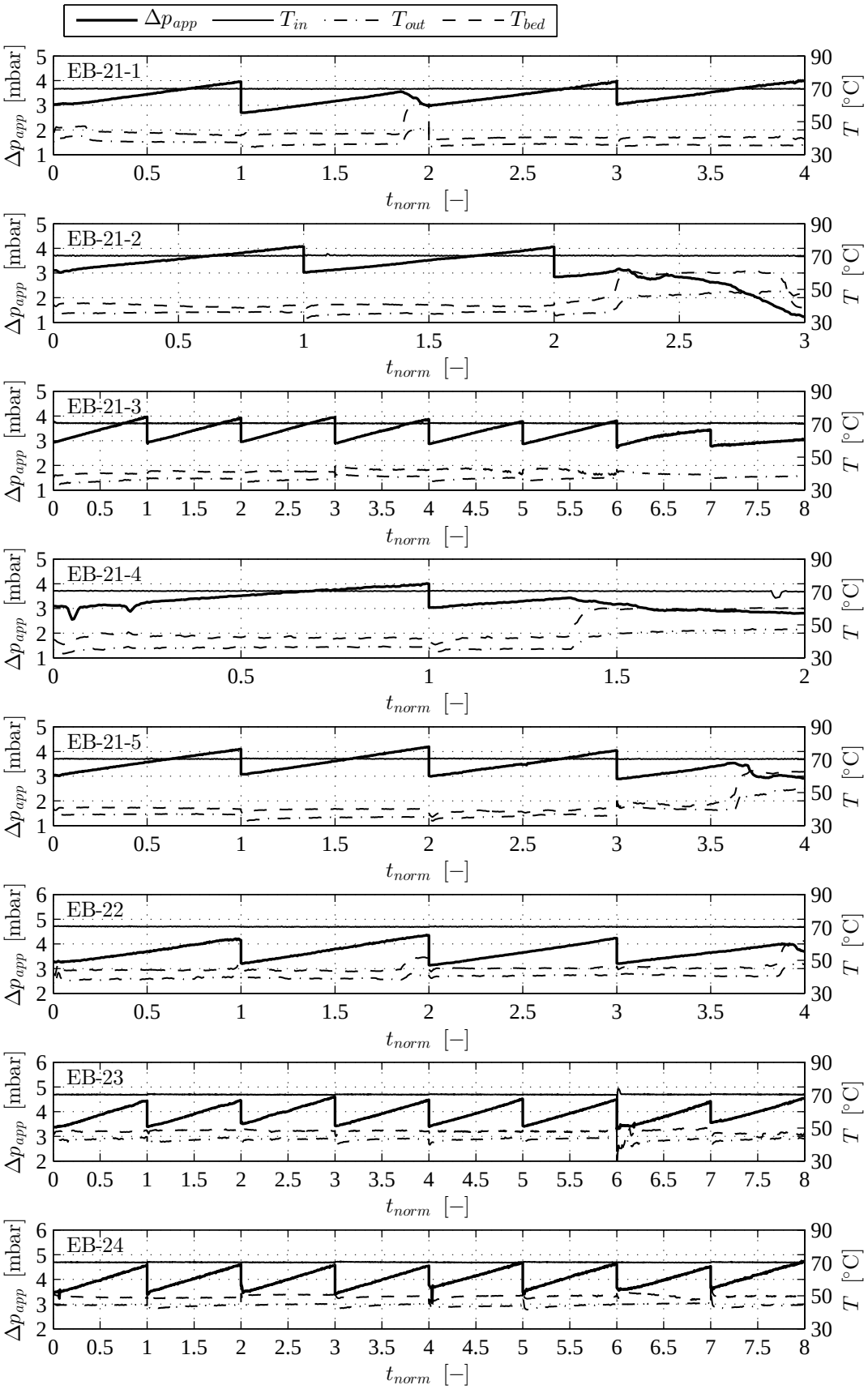

Figure 10.2: Pressure drop across the process chamber Δp_{app} and gas temperatures at different measuring points (inlet, outlet, and bed) versus the normalized process time t_{norm} of Eq. 10.1 for the experiments EB-21-1 to EB-24 from Table 10.2: Cellets®350 as core material, variation of inlet gas mass flow rate $\dot{M}_{in}$.

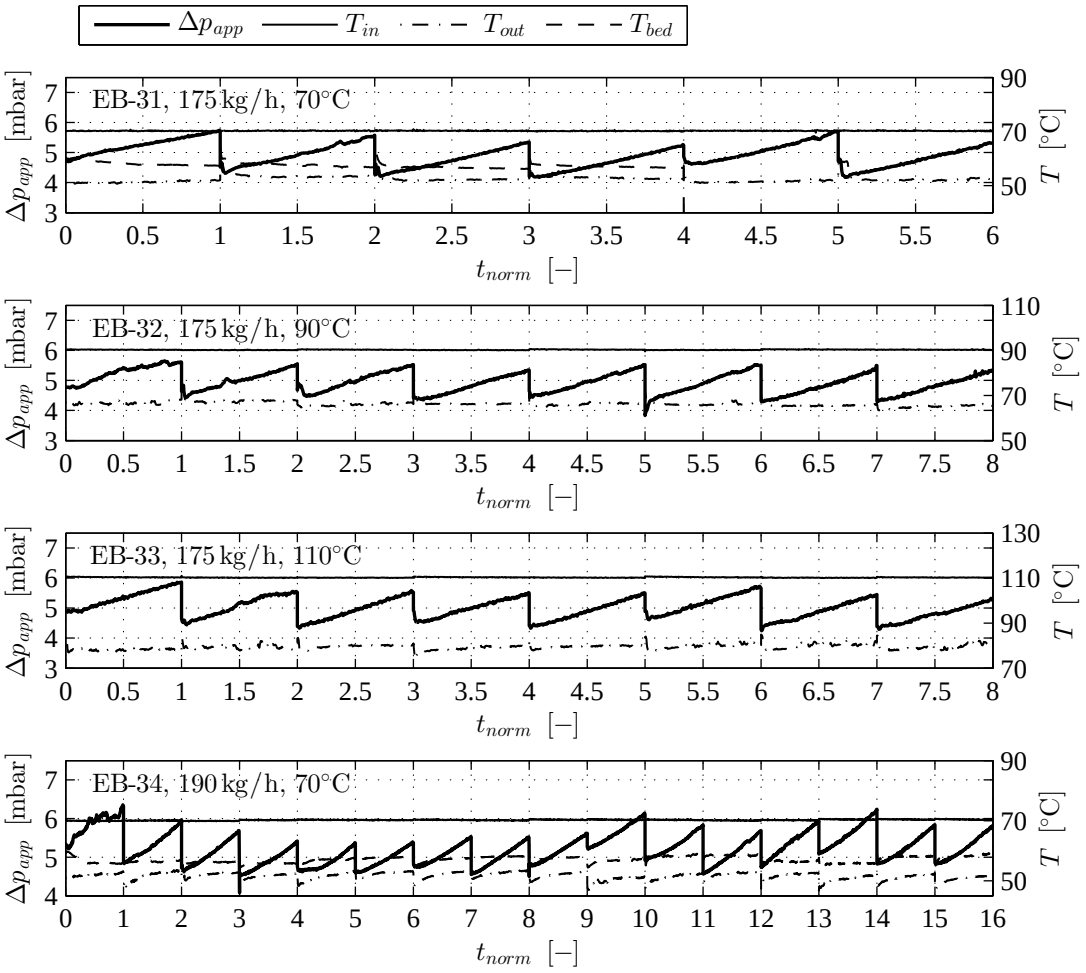

Figure 10.3: Pressure drop across the process chamber Δp_{app} and gas temperatures at different measuring points (inlet, outlet, and bed) versus the normalized process time t_{norm} of Eq. 10.1 for the experiments EB-31 to EB-34 from Table 10.2: glass beads as core material, variation of inlet gas mass flow rate $\dot{M}_{in}$ and inlet gas temperature T_{in}.

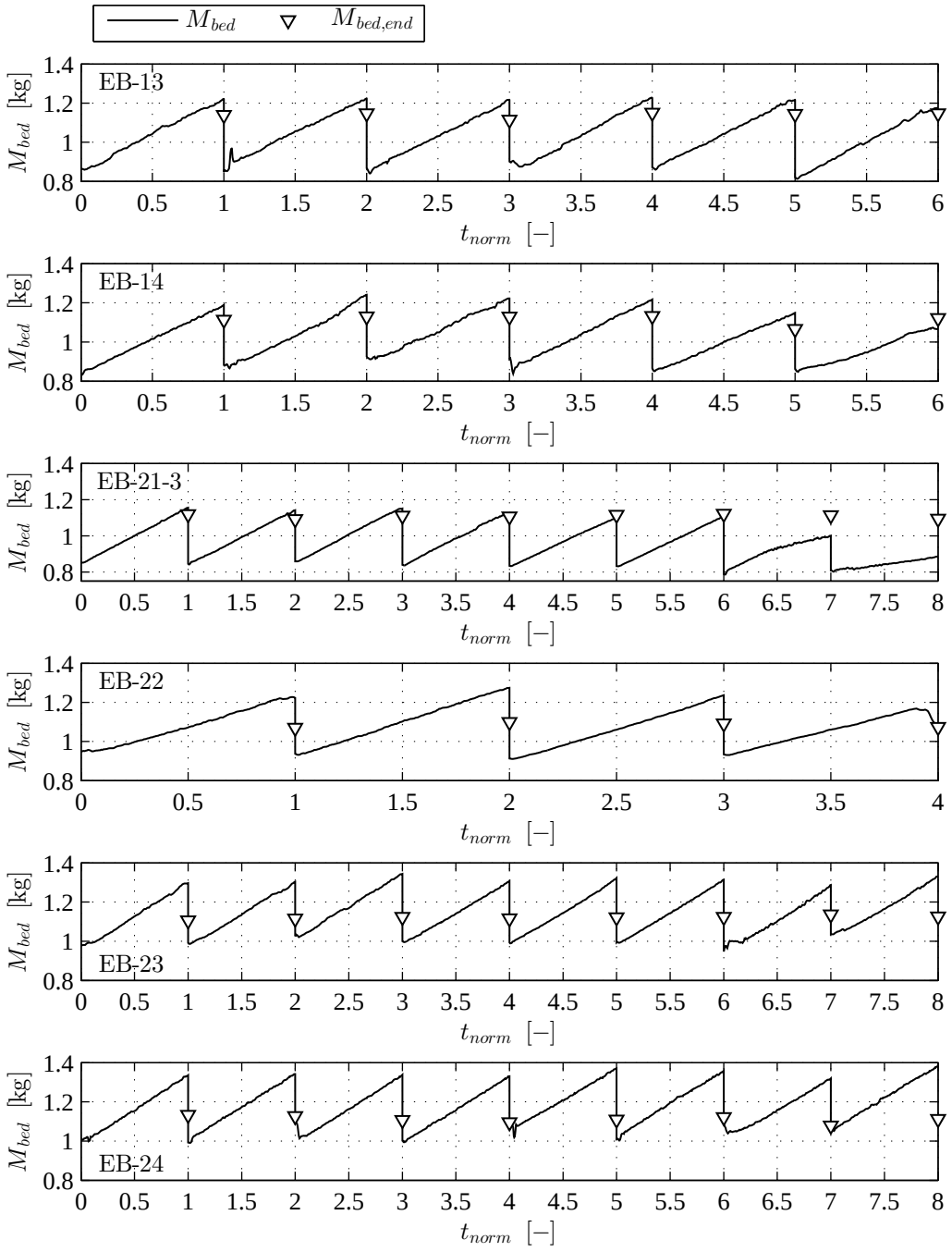

Figure 10.4: Temporal bed mass M_{bed} and final stage bed mass $M_{bed,end}$ (discharged after spraying) versus the normalized process time t_{norm} for several discontinuous multi-stage granulation trials with Cellets®200-cores in EB-13 to EB-14 and Cellets®350-cores in EB-21-3 to EB-24.

batch series:	EB-13	EB-14	EB-21-3	EB-22	EB-23	EB-24
$p_{g,noz}$ [bar]:	2	2.25	1.75	1.75	1.75	1.75
$\dot{M}_{in}$ [kg/h]:	70	70	70	85	100	115
T_{in} [℃]:	90	90	70	70	70	70
stage:	$M_{bed,0}$:					
1	859	832	851	950	980	999
2	849	866	842	932	986	990
3	840	912	859	911	1021	1013
4	875	838	836	931	996	995
5	859	851	832	-	989	1019
6	813	848	831	-	992	1003
7	-	-	786	-	947	1039
8	-	-	802	-	1034	1051
mean	849.2	857.8	829.9	931	993.1	1013.6

Table 10.3: Initial bed mass from the inline detection system ($M_{bed,0}$ in g) for several discontinuous multi-stage granulation experiments; calculated from the detected inline pressure drop across the process chamber Δp_{app}.

Evaluation of the inline detection method for the fluidized bed mass

The initial and final stage bed mass can be compared with the inline bed mass curves at the integers of the normalized time coordinate ($t_{norm} \in \{0, 1, 2, ...\}$). It is evident that the inline bed masses are higher than the respective offline values for almost all illustrated stages. The smallest errors are obtained for the first six stages of the batch series EB-21-3, where the inlet gas mass flow rate was set with 70 kg/h and the inlet gas temperature with 70℃. Increasing inlet gas mass flow rates lead to higher deviations, as it can be seen from the results of EB-22, EB-23, and EB-24. The batch series EB-13 and EB-14 were conducted with the same inlet gas mass flow rate as in EB-21-3, but the nozzle gas excess pressure (2 and 2.25 bar) and the inlet gas temperature (90℃) were higher. An influence of the nozzle gas overpressure on the bed mass detection error cannot be clearly identified in the curves of EB-13 (with $p_{g,noz} = 2$ bar) and EB-14 (with $p_{g,noz} = 2.25$ bar). Assuming nozzle gas excess pressure to have a marginal effect on pressure losses, the multi-stage batch experiments EB-13, EB-14, and EB-21-3 can be compared with each other. In this case, the higher inlet gas temperature of 90℃ would be the prevailing factor for the larger difference between the inline and offline bed mass values of EB-13 and EB-14. The data acquisition program uses the measured outlet temperature to calculate the outlet gas velocity u_{out}, and hereby, the empty-chamber pressure drop Δp_{emp} according to Eq. 9.31. Via this, the translation of the detected pressure drop to the calculated bed mass is affected by the inlet gas temperature. However, the bed mass errors of EB-13 and EB-14 are still lower than in the experiments, EB-22, EB-23, and EB-24, where inlet gas mass flow rates are higher. The inlet gas parameters of EB-21-3 would be the best choice for the continuous granulation experiments regarding accuracy of bed mass control. But, these inlet gas conditions are vulnerable to sporadic bed agglomeration, especially because of the relatively low inlet gas temperature with 90℃. For this reason, the inlet gas conditions of EB-13 and EB-14 (70 kg/h and $T_{in} = 90$℃) are taken for the continuous granulation study of this thesis, as process stability can be better guaranteed for higher inlet gas temperatures.

10.1.4 Variance of spray rate and spray losses

In the presented discontinuous granulation experiments, average spray rates (symbolized here by $\dot{M}_{spr,j}$) have been determined from the consumed amount of sprayed solution divided by the time period of spraying (90 min). They were supposed to be constant, but underlie some fluctuations between the experiments. In the entire batch granulation study, the same pump (Watson-Marlow, type 323-S-314D2/400) was utilized, and the pump rotation speed was given with 7 rpm. According to the empirical function in Eq. 9.25, which was created for the spraying equipment used, the total spray rate to be expected for 7 rpm measures nearly 800 g/h.

Means and variances of measure spray rates

Table C.4 gives an overview on the actual average spray rates of the single stages $\dot{M}_{spr,j}$ of most of the conducted discontinuous granulation series (EB-13, EB-14, EB-21-3, EB-22, EB-23, EB-24, EB-31, EB-32, and EB-33) as well as corresponding mean values and coefficients of variations (CV) of the whole multi-stage series. The average spray rates of single stages $\dot{M}_{spr,j}$ lie between round 750 and 850 g/h, the related mean values vary in a narrower range of 785.1 and 825.8 g/h, and the CV's differ between 1 and 4.2 %.

Possible causes of the deviation from the desired spray rates

An influence of the varied process parameters (nozzle gas excess pressure, inlet gas mass flow rate, and inlet gas temperature) on the spray rates is not ascertained. The deviations are presumably caused by two main aspects: filling level of the spray liquid container and preparation of the peristaltic pump. The filling level of the container was not precisely the same between the experiments because different beakers have been used to supply the spray solution. A small silicone pad had to be put into the pump casing to ensure a better pinching of the silicone tube and improve pumping stability. This pad could slip a little during the process, which might have an influence on the spray rate too.

Conclusion for spraying in continuous granulation experiments

It turned out from the ideal particle growth model (Chapter 3) that the desired product size of continuous layerwise granulation processes in fluidized beds depends on the spray-to-feed rate ratio. According to this, spray rate accuracy is important for a precise product size control. This can be enhanced by operating with a constant filling level of the spray liquid container in the continuous granulation experiments. For this purpose, it is recommended to refill the consumed solution regularly in short time steps.

Spray losses

Furthermore, values of spray losses (coating material discharged in the exhaust gas and adhesion to chamber walls) are required for the parameter setting of continuous granulation experiments, see also Section 9.4.5. These shall be estimated from measurements of some of the presented batch granulation series: EB-13, EB-14, EB-21-3, and EB-22 to EB-34. The part of lost core materials through attachment to walls is neglected at this. The spray losses of single coating stages (symbolized here by $\Phi_{spr,loss,j}$) have been calculated from the end bed mass $M_{bed,end,j}$ and the total amount of sprayed solids ($\dot{M}_{spr,s,j} t_{exp,tot}$) via:

$$\Phi_{spr,loss,j} = 1 - \frac{M_{bed,end,j} - M_{bed,0}}{\dot{M}_{spr,s,j} t_{exp,tot}}. \tag{10.2}$$

The results of the spray losses are given in Table 10.4 for batch granulation series with less or equal than 8 stages and in Table C.5 for the multi-stage experiment EB-34 (16 stages). The detected spray losses vary relatively strongly between the stages. Therefore, the mean values of the single stage spray losses are calculated for each multi-batch series, which are also listed in Table 10.4 and Table C.5. An influence of the nozzle gas excess pressure and the inlet gas temperature on the average spray losses cannot be seen from the multi-stage granulation experiments with Cellets®200 and Cellets®350 as core material, see EB-13 to EB-24. It is apparent in the experiments EB-21-3 to EB-24 (with Cellets®350) that the average spray losses resemble one another between 19 and 21.14 %. In contrast to this, the spray loss mean values are more different for changing inlet gas temperatures in the experiments EB-31 to EB-33, where glass beads are coated at much higher inlet gas mass flow rates. A declining tendency of spray losses with particle size can be recognized in the batch granulation experiments EB-34 with 16 stage in series, see Table C.5. Nevertheless, this measurement method delivers vague results so that dependencies on process parameters cannot be surely stated. A certain amount of spray dust (nuclei of pure coating material) was discharged with product. This fine fraction is not included in the final bed mass, as it had been sieved off the stage products. But, large errors can occur by bed mass losses during a pneumatic bed mass discharge procedure. However, an estimated value of the spray loss fraction $\Phi_{spr,loss}$ is required for the parameter setting of the continuous granulation experiments of this thesis. Therefore, a rough value of 20 % is estimated from the results of the batch experiments.

batch series:	EB-13	EB-14	EB-21-3	EB-22	EB-23	EB-24	EB-31	EB-32	EB-33
$p_{g,noz}$ [bar]:	2	2.25	1.75	1.75	1.75	1.75	1.75	1.75	1.75
M_{in} [kg/h]:	70	70	70	85	100	115	175	175	175
T_{in} [℃]:	90	90	70	70	70	70	70	90	110
stage:	$\Phi_{spr,loss,j}$:								
1	16.05	20.28	18.40	26.53	21.09	15.02	17.99	31.67	25.83
2	11.02	14.02	23.50	21.83	19.06	15.47	10.20	23.80	23.78
3	18.64	15.52	19.01	25.26	20.14	15.21	19.17	27.80	23.64
4	8.83	16.13	19.09	-	20.25	21.82	15.66	29.96	29.63
5	16.26	32.64	17.58	-	9.10	18.23	14.29	17.72	24.91
6	15.81	17.43	18.23	-	19.54	18.63	-	17.26	20.87
7	-	-	17.55	-	18.22	27.44	-	22.97	26.04
8	-	-	20.35	-	17.78	20.15	-	17.73	27.96
mean	14.43	19.34	19.21	21.14	18.15	19	15.46	23.61	25.33

Table 10.4: Spray losses $\Phi_{spr,loss}$ (in %) of different multi-stage batch experiments.

10.1.5 Characteristics of particle growth

For most of the stage products of the present discontinuous granulation study, the particle size distribution has been measured by dynamic image analysis with a CAMSIZER® device from the company Retsch Technology (today: Microtrac MRB).

Cumulative particle size distribution

The measured PSDs of the core materials and stage products are illustrated in form of number-based cumulative size distributions Q_0 in Figure 10.5 for coated Cellets®200 from the experiments of EB-13 and EB-14, in Figure 10.6 for coated Cellets®350 from the experiments of EB-21-1, EB-21-3, and EB-21-5 to EB-24, and in Figure 10.7 for coated glass beads from the experiments of EB-31 to EB-34. The single stages are not denoted in the Q_0-diagrams, but they can be identified from the position of the cumulative curves. The first curve on the left of each diagram is related to the non-coated core material (stage 0); and the Q_0-curves of the coated products (stage 1, 2, ...) are plotted from left to right in the order of consecutive stages. It can be seen that most of the PSD-curves shift stronger to larger particle sizes for higher stages, which speaks for a faster particle growth in consecutive batch experiments. The reason for this is that the excess bed mass ($M_{bed,end} - 800\,\mathrm{g}$) had been taken off the product before a next stage was started. The total number of bed particles was thereby reduced in subsequent stages, which enhances the single particle growth rate (see also Eq. B.1). Further, the product size distributions become wider (with only a few exceptions) by proceeding granulation, presumably for two main reasons. Firstly, bigger granules can catch more spray droplets. Secondly, particle suction through the Wurster tube gap might have a classifying effect due to (vertically oriented) *size-dependent segregation* inside the fluidized bed, so that larger granules pass the spray zone more often than smaller ones.

Average characteristics

Diverse average characteristics have been calculated from the particle size distributions depicted in Figures 10.5, 10.6, and 10.7, which shall also be illustrated and discussed in this section. The first three of them are the number-based mean diameter $d_{m,q_0,j}$ (short: $d_{m,j}$) from

$$d_{m,j} = d_{m,q_0,j} = \int_0^\infty dq_{0,j}(d)\mathrm{d}d = m_{1,0,j} \qquad \text{, for } j \in \{0,1,2,3,...\}, \tag{10.3}$$

the length-based mean diameter $d_{m,q_1,j}$ from

$$d_{m,q_1,j} = \int_0^\infty dq_{1,j}(d)\mathrm{d}d = m_{1,1,j} \qquad \text{, for } j \in \{0,1,2,3,...\}, \tag{10.4}$$

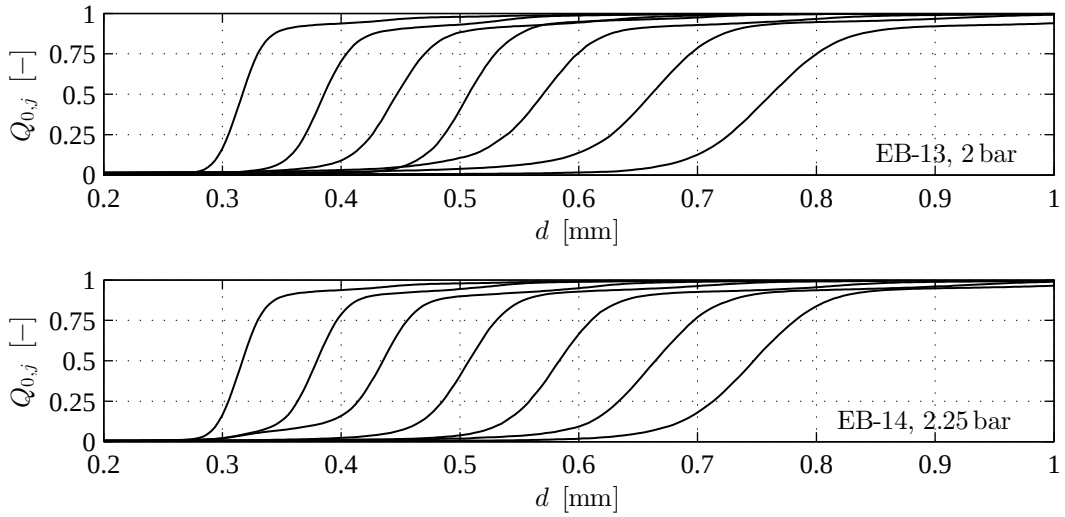

Figure 10.5: Cumulative number-based particle size distribution $Q_{0,j}$ of the core material IM-2 (Cellets®200, first curve on the left) and the stage products (curves rightwards) for two discontinuous multi-stage granulation experiments with different nozzle air excess pressure.

and the diameter of mean particle volume $d^*_{3,0,j}$ from

$$d^*_{3,0,j} = \left(\int_0^\infty d^3 q_{0,j}(d) \mathrm{d}d \right)^{1/3} = (m_{3,0,j})^{1/3} \qquad \text{, for } j \in \{0,1,2,3,...\}. \tag{10.5}$$

The numerical computation steps of cumulative size distribution and density distribution functions ($Q_r(d)$ and $q_r(d)$) are given in Eqs. 2.18 to 2.26. With the quantities from Eqs. 10.3 to 10.5, three different types of particle size enlargement ratio (symbolized here by $\Phi_{d,j}(d_m)$, $\Phi_{d,j}(d_{m,q_1})$, and $\Phi_{d,j}(d^*_{3,0})$) are formulated with reference to the non-coated core materials ($j = 0$) according to

$$\Phi_{d,j}(d_m) = \frac{d_{m,j}}{d_{m,0}} \qquad \text{, for } j \in \{0,1,2,3,...\}, \tag{10.6}$$

$$\Phi_{d,j}(d_{m,q_1}) = \frac{d_{m,q_1,j}}{d_{m,q_1,0}} \qquad \text{, for } j \in \{0,1,2,3,...\}, \tag{10.7}$$

$$\Phi_{d,j}(d^*_{3,0}) = \frac{d^*_{3,0,j}}{d^*_{3,0,0}} \qquad \text{, for } j \in \{0,1,2,3,...\}. \tag{10.8}$$

The values of the reference characteristics of these equations ($d_{m,0}$, $d_{m,q_1,0}$, and $d^*_{3,0,0}$) are listed in Table 10.5. Furthermore, the relative standard deviations of the number-based and length-based particle size distributions ($\zeta_{q_0,j}$ and $\zeta_{q_1,j}$) are determined by:

$$\zeta_{q_0,j} = \frac{\sigma_{q_0,j}}{d_{m,q_0,j}} = \left(\int_0^\infty \left(\frac{d}{d_{m,q_0,j}} - 1 \right)^2 q_{0,j}(d) \mathrm{d}d \right)^{1/2} \qquad \text{, for } j \in \{0,1,2,3,...\}, \tag{10.9}$$

$$\zeta_{q_1,j} = \frac{\sigma_{q_1,j}}{d_{m,q_1,j}} = \left(\int_0^\infty \left(\frac{d}{d_{m,q_1,j}} - 1 \right)^2 q_{1,j}(d) \mathrm{d}d \right)^{1/2} \qquad \text{, for } j \in \{0,1,2,3,...\}. \tag{10.10}$$

The particle growth ratio $\Phi_{d,j}(d^*_{3,0})$ of Eq. 10.8 and the relative standard deviation of the length-based particle size distribution $\zeta_{q_1,j}$ of Eq. 10.10 are used later on for estimating the effective density and porosity of the coating layer by the method from Section 9.3.

Measured particle growth ratios

The average particle size characteristics from Eqs. 10.6 to 10.8 are illustrated on the left hand side of Figures 10.8 and 10.9 for the experiments EB-13, EB-14, EB-21-3, EB-22, EB-23, EB-24, EB-31, EB-32,

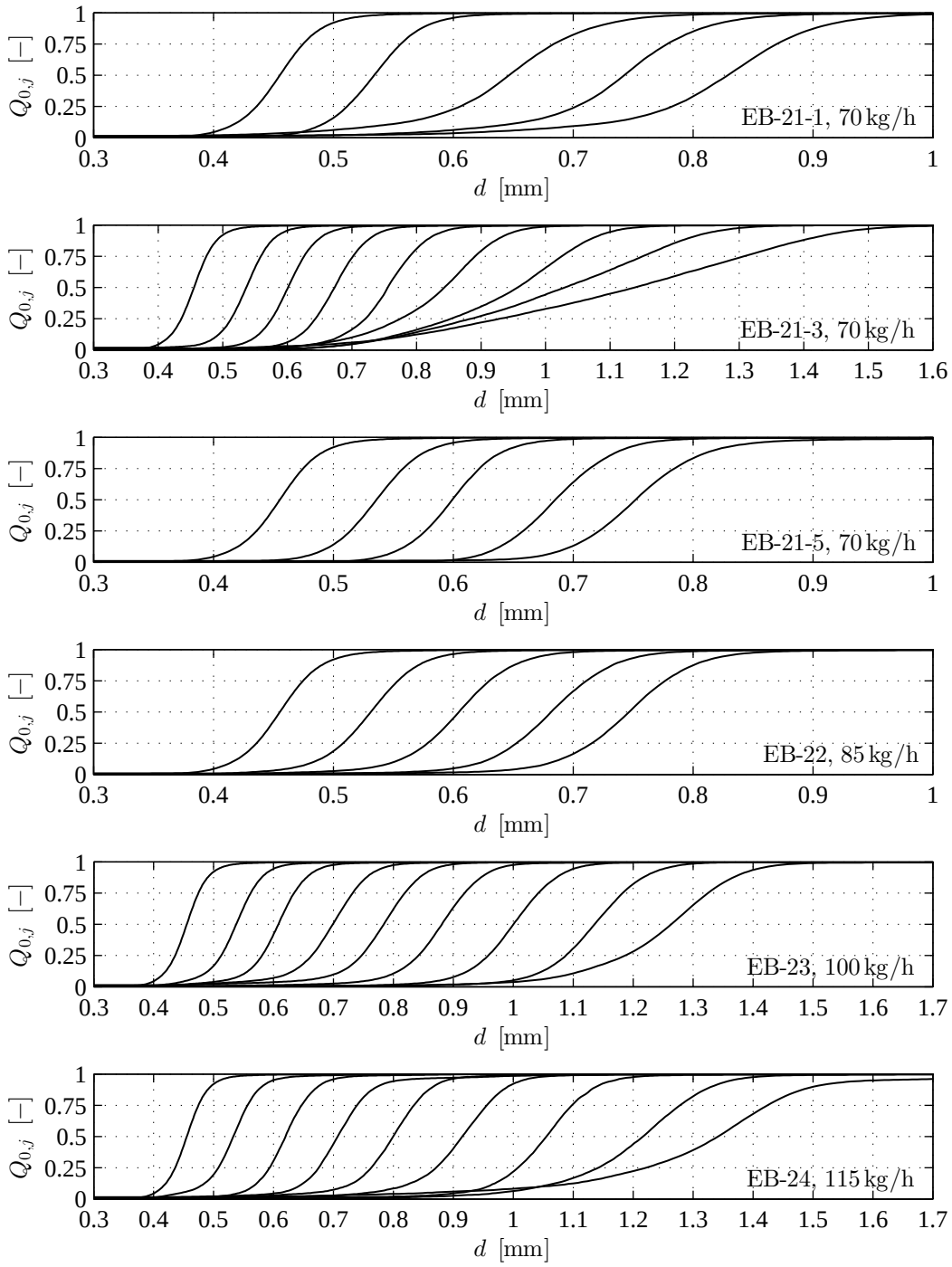

Figure 10.6: Cumulative number-based particle size distribution $Q_{0,j}$ of the core material IM-4 (Cellets®350, first curve on the left) and the stage products (curves rightwards) for several discontinuous multi-stage granulation experiments with different inlet gas mass flow rates.

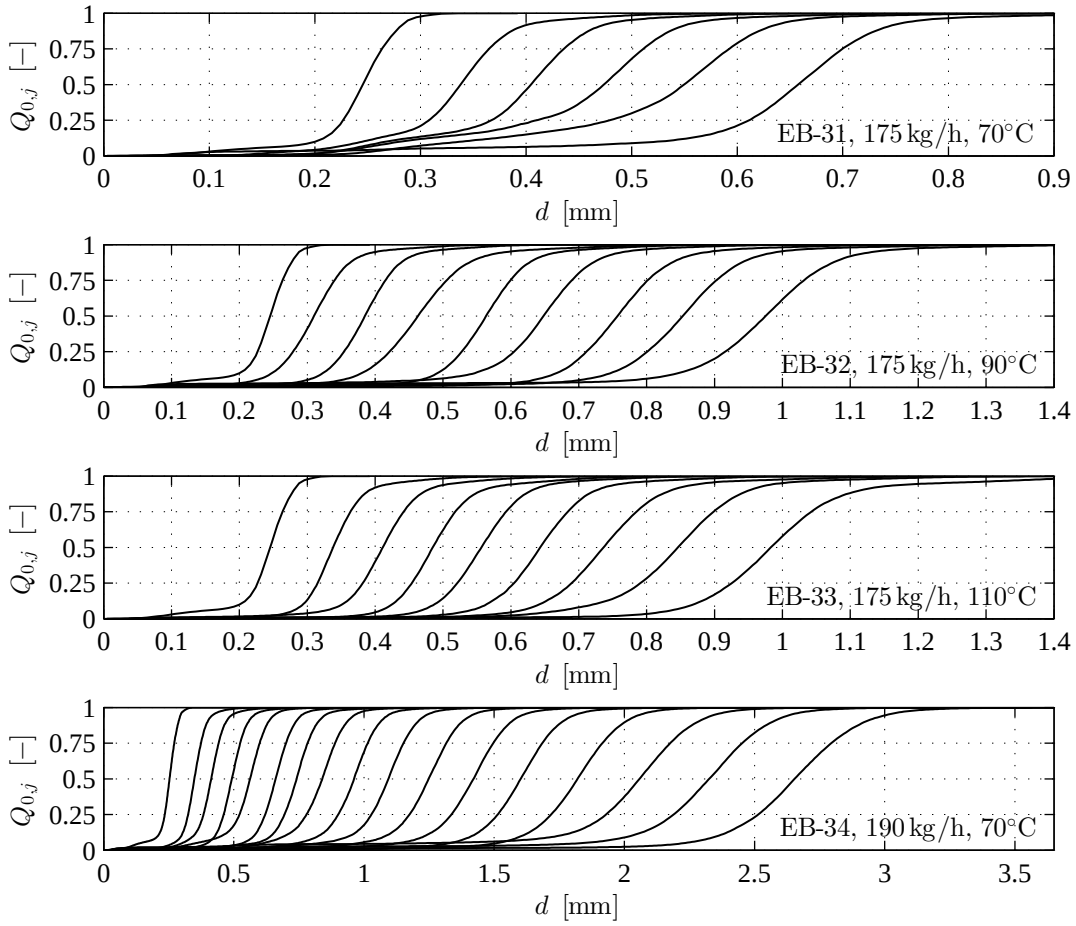

Figure 10.7: Cumulative number-based particle size distribution $Q_{0,j}$ of the core material IM-7 (glass beads, first curve on the left) and the stage products (curves rightwards) for several discontinuous multi-stage granulation experiments with different inlet gas mass flow rates.

index	$d_{m,0}$ [µm]	$d_{m,q_1,0}$ [µm]	$d^*_{3,0,0}$ [µm]
IM-2	327.5	337.8	340.5
IM-4	453.3	459.1	458.4
IM-7	235	254.4	253.3

Table 10.5: Diverse average particle diameters for core materials of the discontinuous granulation experiments: IM-2 (Cellets®200), IM-4 (Cellets®350), and IM-7 (glass beads).

EB-33, and EB-34. It is obvious that the different types of particle growth ratio $\Phi_{d,j}(d_m)$, $\Phi_{d,j}(d_{m,q_1})$, and $\Phi_{d,j}(d^*_{3,0})$ have almost the same progression for all depicted examples. In the granulation series EB-31 to EB-34, they increase linearly in the first 4 stages, except for the stage 1. At these experiments, the particle size enlargement was a bit higher. This effect can also be seen in the cumulative curves of the particle size distribution in Figure 10.7. Therein, the Q_0-distribution of the non-coated glass beads (left curve) possesses a significant fine fraction below diameters of 0.2 mm, which reduces average particle size characteristics. The size distribution of the initial core particles has only been measured from one sample of the employed initial bulk materials. But, it can vary a little by segregation effects that occur during transport, storage, and preparation of the core materials. This might have an influence (more or less) on average particle diameters, and thus, on the defined size enlargement ratios. Another reason could be that the fine fraction of the non-coated glass beads got lost during the batch experiments for example by wall adhesion or through inaccurate discharging of the final bed mass. As mentioned before, the particle growth becomes faster in higher granulation stages, which is also visible by the slopes of the particle growth ratio curves that increase between stages 1 and 8, but only slightly. The longest stage series (EB-34 of Figure 10.9) depicts this effect the clearest.

Relative standard deviations

The relative standard deviations $\zeta_{q_0,j}$ and $\zeta_{q_1,j}$ are illustrated on the right hand sides of Figures 10.8 and Figure 10.9. The values of the calculated relative standard deviations of all depicted multi-batch experiments lie between 5 and 25 %, whereat dissimilar courses of the dispersion parameters are observed along successive stages. Two of the curves (see EB-22 and EB-23) are nearly horizontal. A slight decreasing tendency of the relative standard deviations with particle growth is visible for the batch series: EB-13, EB-14, and EB-32 to EB-34; whereas the examples EB-24 and EB-31 possess low increases on average. The strongest changes of particle size variety are detected for the higher stages ($j > 4$) in the granulation series EB-21-3, at which size-selective effects (more droplet deposition on bigger granules and classifying Wurster suction) on particle growth kinetics are particularly visible.

Conclusions for estimating bulk porosity

The plotted dispersion indices $\zeta_{q_0,j}$ and $\zeta_{q_1,j}$ represent poly-dispersity of the initial bulk materials (at $j = 0$) and the stage products (for $j > 0$). Their particle size variety has an influence on product bulk porosity $\varepsilon_{b,j}$, which is required for the determination of effective coating density of the stage products $\rho_{c,j}$. As ascertained before, the particle size distributions of the stage products become wider with ongoing granulation. For very broad product size distributions, smaller granules can fill the gaps between coarse ones, and therefore, reduce the bulk porosity. The relative standard deviations are suitable measurement parameters to describe this effect. It is mentioned at this that different bases of particles size distributions $q_r(d)$ (e.g.: number $r = 0$, length $r = 1$, surface area $r = 2$, and volume $r = 3$) can have deviant values in their corresponding coefficients of variation ζ_{q_r}, as shown in Figures 10.8 and 10.9. However, an empirical approach was suggested by Tsotsas ([25], described in Section 2.1.3), wherewith the interparticle porosity of polydisperse packages can be roughly estimated in dependency of a so-called *dispersion parameter*. This variety index conforms with the length-based relative standard deviation ζ_{q_1}, as proven by the analysis in Appendix B.1.

Particle growth time

A particle growth ratio of $\Phi_{d,set} = 1.9$ and $\Phi_{d,set} = 2.2$ (inter alia) is wanted to be achieved in the continuous granulation experiments of the present thesis. Startup periods of those processes can take several hours, as also ascertained by the results of the ideal particle growth model (Section 4.1.4) and the three-compartment population balance model (Section 6.1.2). The required growth time $t_{gr,set}$ is a characteristic property to roughly estimate startup durations, and thus, important for planning of continuous experiments. It shall be therefore calculated for the size enlargement ratios 1.9 and 2.2 from the Φ_d-curves (Figures 10.8 and 10.9) of three multi-batch series (EB-13, EB-23, and EB-32). At this, the growth times are obtained by interpolation according to the following rules:

$$j \coloneqq \mathrm{find}_j\big(\Phi_{d,j}(d_{m,q_0}) < \Phi_{d,set} \leq \Phi_{d,j+1}(d_{m,q_0})\big), \tag{10.11}$$

$$t_{gr,set} = \left(t_{norm,j} + \frac{\Phi_{d,set} - \Phi_{d,j}(d_{m,q_0})}{\Phi_{d,j+1}(d_{m,q_0}) - \Phi_{d,j}(d_{m,q_0})}\right) t_{exp,tot}. \tag{10.12}$$

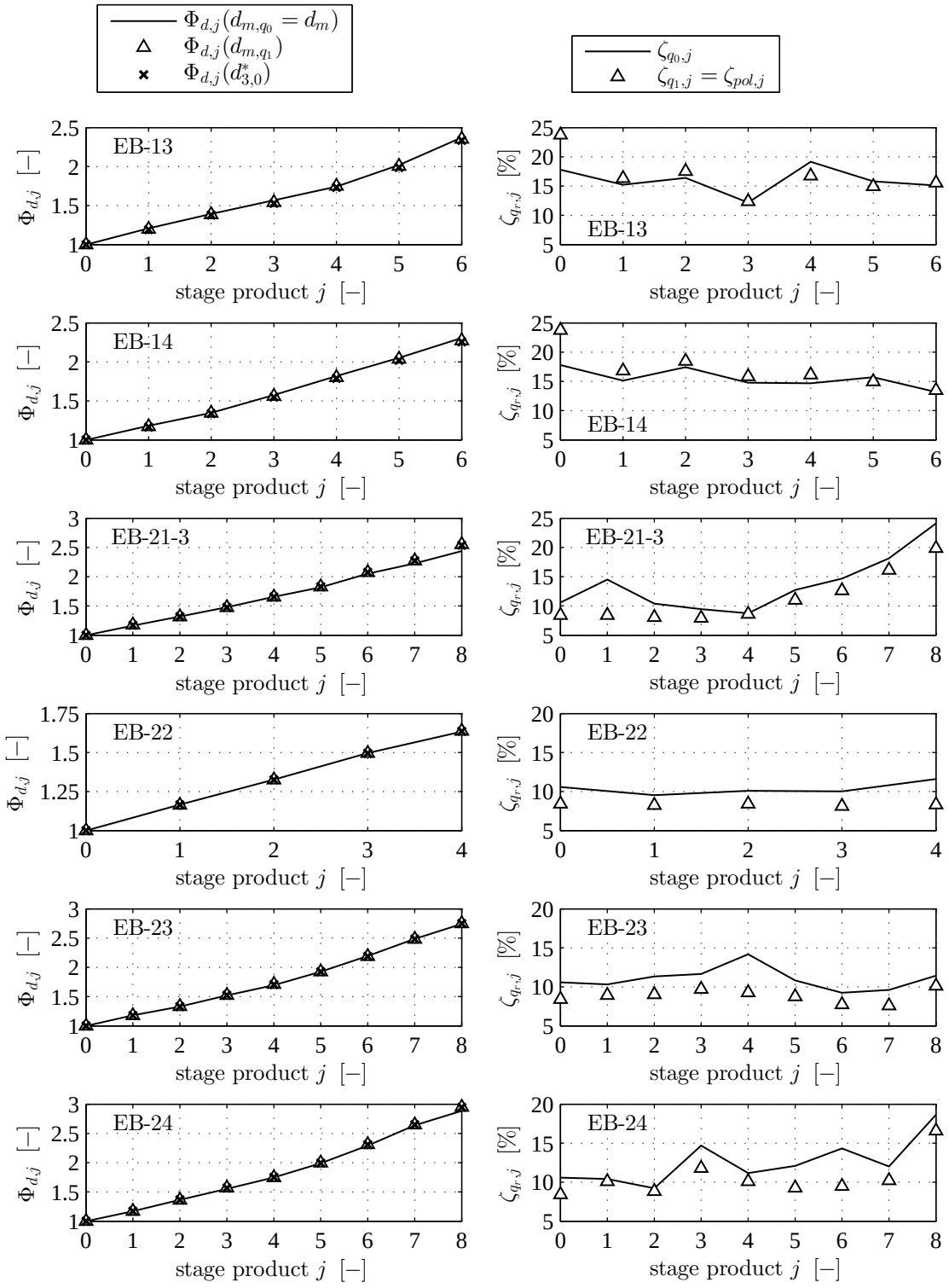

Figure 10.8: Diverse average particle characteristics (left: particle growth ratios, right: relative standard deviations) of the stage products from several discontinuous multi-stage granulation experiments with Cellets®200-cores (EB-13 and EB-14) and Cellets®350-cores (EB-21-3 to EB-24).

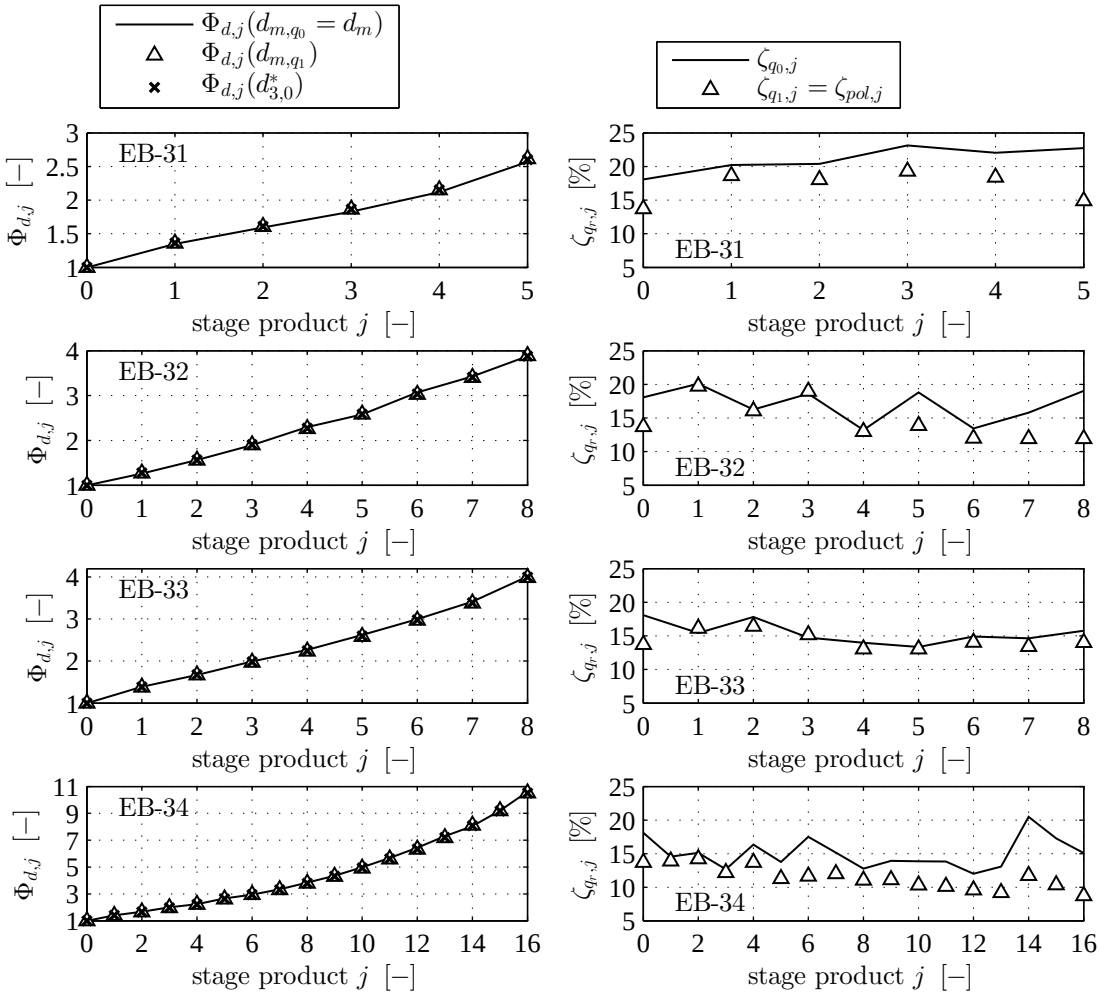

Figure 10.9: Diverse average particle characteristics (left: particle growth ratios, right: relative standard deviations) of the stage products from several discontinuous multi-stage granulation experiments with glass beads as core material in EB-31 to EB-34.

batch series:	EB-32	EB-13	EB-23
core material:	IM-7	IM-2	IM-4
$d_{m,0}$ [µm]:	235	327.5	453.3
$\Phi_{d,set}$:	$t_{gr,set}$:		
1.9	4.52	6.85	7.34
2.2	5.65	8.27	9.04

Table 10.6: Required growth time $t_{gr,set}$ (in h) of desired particle size enlargement ratios of $\Phi_{d,set} \in \{1.9, 2.2\}$ for three multi-batch experiments with different core materials; estimated by interpolation of measured growth ratios $\Phi_{d,j}(d_{m,q_0})$.

The results of them are listed in Table 10.6 in order of the mean diameter $d_{m,0}$ of the employed core materials IM-2, IM-4, and IM-7. It can be seen that bigger initial materials take longer to obtain the desired granule size enlargement for constant spraying conditions. The continuous granulation experiments of the present thesis were planned to be conducted with Cellets®200 (IM-2 and IM-3). To give an example, growing-up times of more than eight hours ($\tau_{gr,set} > 8\,\text{h}$) would be necessary to reach a particle growth ratio of 2.2 in the multi-stage batch experiment EB-13 with Cellets®200. But, the continuous experiments shall be conducted for 9 h, wherefore stationary conditions might not be reached within this time period.

10.1.6 Density-related product characteristics

The bulk densities $\rho_{b,j}$, the bulk porosities $\varepsilon_{b,j}$, the effective coating densities $\rho_{c,j}$, and the layer porosities $\varepsilon_{c,j}$ of the stage products ($j > 0$) from the multi-stage batch experiments EB-13, EB-14, EB-21-3, EB-22 to EB-24, and EB-31 to EB-34 shall be illustrated and discussed in this section. For this purpose, the bulk density of the core material $\rho_{b,0}$ and the stage products $\rho_{b,j>0}$ has been gravimetrically measured by filling a cylinder of known volume. The other three quantities $\varepsilon_{b,j}$, $\rho_{c,j}$, and $\varepsilon_{c,j}$ are determined with the suggested equations of Section 9.3. The bulk porosities of initial materials $\varepsilon_{b,0}$ follow from Eq. 9.1 with the measured effective particle densities $\rho_{p,0}$ from Table C.1 (see for IM-2, IM-4, and IM-7). The interparticle porosity of the stage products $\varepsilon_{b,j>0}$ were obtained by Eqs. 9.2 to 9.4 with help of the length-based relative standard deviations of the core-PSDs ($\zeta_{q_1,0}$) and the product-PSDs ($\zeta_{q_1,j>0}$) from Figures 10.8 and 10.9. The effective coating densities $\rho_{c,j}$ are estimated by Eqs. 9.5 and 9.9 using the measured bulk densities $\rho_{b,j>0}$, the calculated bulk porosities $\varepsilon_{b,j>0}$, and the *average core-to-particle volume fractions* $\Phi^{-3}_{d,j>0}(d^*_{3,0})$, which are obtained by the inverse third power of the particle growth ratios of the mean-volume-equivalent diameter $\Phi_{d,j>0}(d^*_{3,0})$ from Figures 10.8 and 10.9. The coating layer porosities $\varepsilon_{c,j>0}$ ensue from the effective densities and compact solid density of the coatings via Eq. 9.10. According to this equation, the effective coating density and the corresponding porosity are inversely related to each other, so that the effective coating density increases, when the porosity is decreased, and vice versa. The results of said characteristics are depicted in Figure 10.10 for coated Cellets® (IM-2 and IM-4) and in Figure 10.11 for coated glass beads (IM-7), and are described in the following.

Bulk density

The bulk density $\rho_{b,j}$ of each depicted experiment declines within the first stage for the reason that formed coating layer of sodium benzoate is lighter than the carrier materials. This effect is stronger for coated glass beads than for products with Cellets®-cores, since glass beads are much heavier. For the coated Cellets®-products from the experiments of EB-14 and EB-24, the bulk density curves are almost steadily decreasing, but less strongly at higher stages. The products from EB-13, EB-21-3, EB-22, and EB-23 reach relatively constant bulk density values already after a few stages ($j > 1$). In contrast to this, a continuous decrease of bulk density measurements can be clearly ascertained for the coated glass beads in the series EB-31 to EB-34.

Errors of bulk density measurement

The employed bulk density determination method is associated with measurement fluctuations, which are caused, for instance, by random placement of particles during filling. But, these are small here, as the relative standard deviations of the measurement points varied only between 0.06 and 3.02 % with an average

of 0.45 %. A systematic error appears by higher local porosities in the vicinity of container walls (*wall effect*). This error is not considered in the applied estimation method of the coating layer density. It can be neglected for small particles. However, the granules of the longest multi-stage experiment EB-34 are enlarged to a maximal mean diameter d_m of nearly 2.5 mm in the last stage. The used filling cylinder had an inner diameter of 27 mm. It is also visible in the $\rho_{b,j}$-curve of EB-34 that the bulk density decreases within the entire series, which is presumably caused by an enhanced wall effect of the products of higher stages. The employed estimation method of coating layer density should be therefore improved by a model which takes also wall porosities into account; or, bulk density measurements could be repeated. But in this case, the products have to be recreated by the same granulation processes and bulk density should be determined directly after the batch experiments, because it is not guaranteed that the coatings maintain their morphological structure during long-term storage (*stability of morphology*).

Bulk porosity

The bulk porosities of the initial materials $\rho_{b,0}$ and the stage products $\rho_{b,j>0}$ are almost equal. They lie between 43.1 and 45.9 % for the coated Cellets® with an average of 44.6 % and a little lower between 41.8 and 43.1 % for the coated glass beads with an average of 42.5 %. An influence of changing product size distributions by granulation on bulk porosity cannot be ascertained here. Only a slight decrease can be recognized for the last three stages (6, 7, and 8) of the outlier multi-batch experiment EB-21-3. Therein, particle size variety was excessively larger that those of the other granulation series, see Figure 10.8. However, its effect on interparticle porosity is still marginal.

Coating properties on Cellets®

Most of the multi-stage experiments with Cellets®-cores in Figure 10.10 (except of EB-24) show a clear dependency of the effective coating density $\rho_{c,j}$ and layer porosity $\varepsilon_{c,j}$ on the granulation time (here represented by stage number). At this, the effective coating density increases in the first stages (second to fourth) and converges to constant values for the higher stages. The coating layer porosity evolves in an inverse way due to Eq. 9.10. The layer porosities $\varepsilon_{c,j}$ are particularly high up to around 40 % in the first stages and then shrink down to values between 10 and 21 %. The coating characteristics $\rho_{c,j}$ and $\varepsilon_{c,j}$ of the stage products of EB-24 fluctuate in the described ranges of values already from the first stage on. The inlet gas mass flow rates $\dot{M}_{in}$ of the EB-24 setting was the highest with 115 kg/h among the examples of Figure 10.10. Slower *drying kinetics* in these experiments are assumed to be the reason for larger porosities in incipient particle growth. Further enlargement of the coating layers leads also to heavier particles in the granulator, by which stronger impact forces occur during *particle-particle* and *particle-wall collisions*. Layers with higher porosities are perhaps mechanically unstable for fluidization under the adopted process conditions. In this case, particle collisions would have a *compressing effect* on coatings during longer periods of fluidization.

Coating properties on glass beads

The effective coating density and the layer porosity of multi-stage batch experiments EB-31 to EB-34 in Figure 10.11, where glass beads were coated, show a different evolution with ongoing stages than those of the coated Cellets®. The inlet gas mass flow rates are much higher here, wherefore drying is faster. Especially the effective coating density of the coated glass beads from the first three stages is clearly larger than for the lower-stage products from the settings EB-13 to EB-23 in Figure 10.10. But the glass bead coating densities are also somewhat higher across all stages on average. A slight decrease of the coating density is recognizable in the batch series EB-31 and EB-33, whereas the coating densities of EB-32 lie in a narrow range of values for all stages. The coating density curve of EB-34 appears to be more deviant. But, when regarding only the results of stages 2 to 8 of it, a similarity to the batch series EB-31 to EB-33 can be identified. The coating density of the first stage of EB-34 is considered to contain large errors. Especially, its corresponding layer porosity is very low: 2.3 %. As explained in Section 9.3, stronger errors of the employed estimation method can occur for thinner coatings. Moreover, a continuous decrease of the calculated effective density - and therefore an increasing porosity - is visible at the higher stages of EB-34. This effect comes from the error of higher wall porosities in the bulk density measurement for larger granules, as it is mentioned above.

Average coating density and porosity of higher-stage products

It is evident that the effective coating densities and layer porosities between stages 4 and 8, which are referred to as *thick-coating porosities and densities*, have more or less similar values. For this reason, mean

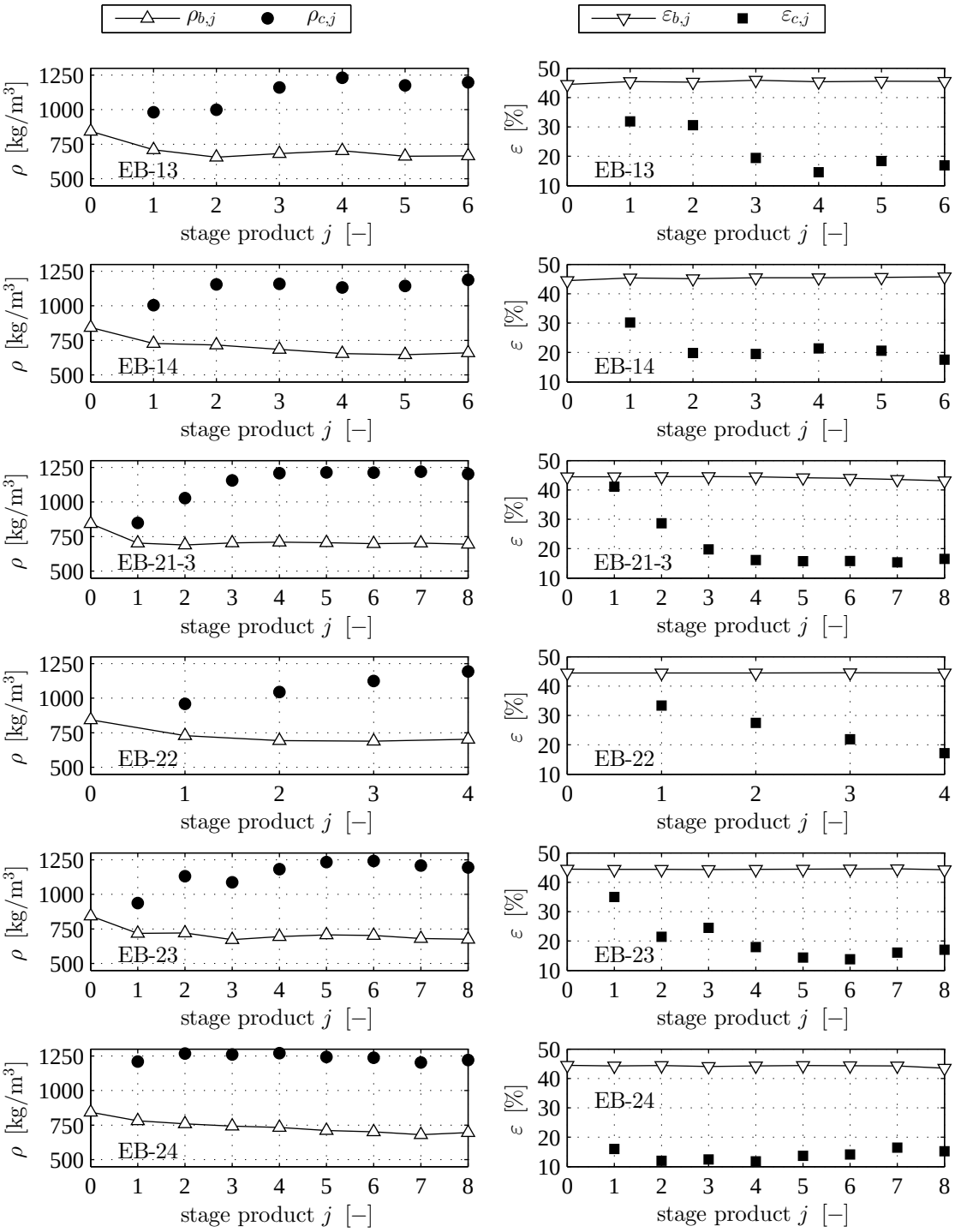

Figure 10.10: Bulk density $\rho_{b,j}$, effective coating density $\rho_{c,j}$, interparticle porosity $\varepsilon_{b,j}$, and coating layer porosity $\varepsilon_{c,j}$ of the stage products of several discontinuous multi-stage granulation experiments with Cellets®200-cores (EB-13 and EB-14) and Cellets®350-cores (EB-21-3 to EB-24).

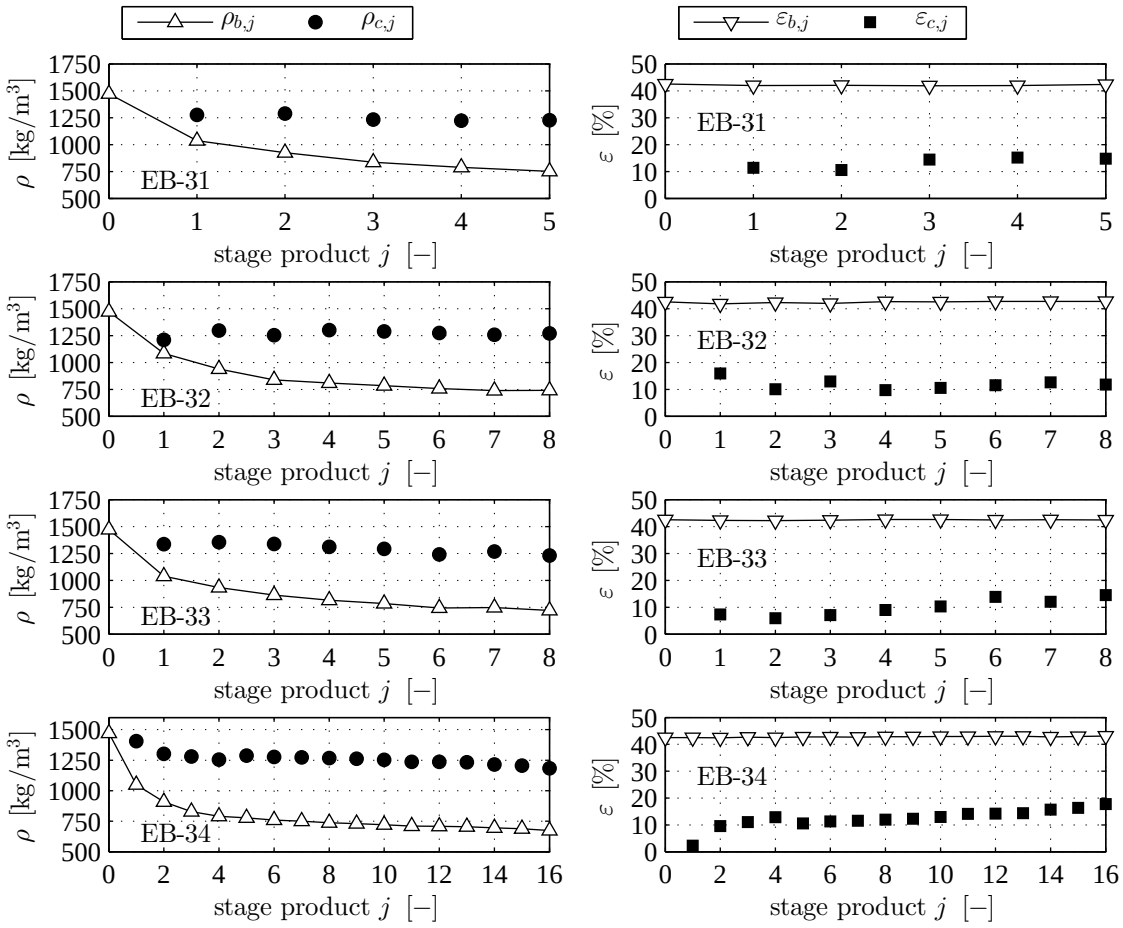

Figure 10.11: Bulk density $\rho_{b,j}$, effective coating density $\rho_{c,j}$, interparticle porosity $\varepsilon_{b,j}$, and coating layer porosity $\varepsilon_{c,j}$ of the stage products of several discontinuous multi-stage granulation experiments with glass beads as core material (EB-31 to EB-34).

batch series:	EB-21-3	EB-23	EB-24	EB-32	EB-33	EB-34
$p_{g,noz}$ [bar]:	1.75	1.75	1.75	1.75	1.75	1.75
M_{in} [kg/h]:	70	100	115	175	175	190
T_{in} [℃]:	70	70	70	90	110	70
mean($\rho_{c,j}$) [kg/m^3]:	1211.1	1212.2	1234.9	1278.1	1268.1	1272.2
SD($\rho_{c,j}$) [kg/m^3]:	5.6	22.6	22.5	14.5	30	10.9
mean($\varepsilon_{c,j}$) [%]:	15.9	15.9	14.3	11.3	11.9	11.7
SD($\varepsilon_{c,j}$) [%]:	0.4	1.6	1.6	1	2.1	0.8

Table 10.7: Mean value and standard deviation (SD) of effective coating density and layer porosity of the products from stages 4 to 8 of different discontinuous multi-stage granulation experiments.

values and standard deviations were determined between these stages for some of the conducted multi-batch experiments. The results are listed in Table 10.7. It can be seen again that the mean effective layer densities of the coated Cellets® (EB-21-3, EB-23, and EB-24) are lower than these of the coated glass beads (EB-32, EB-33, and EB34), even if only a little. In opposite manner, the mean porosity of the Cellets®-coatings has higher values between 14.3 and 15.9 %, whereas the mean porosity on glass beads lie between 11.3 and 11.9 %. The relative standard deviation of the coating densities is less than 2.36 %. It should be mentioned that these results are only valid for thicker coating layers of the stage products. The coating layer thickness can be estimated by the mean-volume-equivalent diameter of the stage products and the core material via:

$$\bar{s}_c = \frac{1}{2}(d^*_{3,0,j} - d^*_{3,0,0}). \tag{10.13}$$

It lies between approximately 150 and 450 µm for the products from stages 4 to 8 of the experiments in Table 10.7. Thinner coatings can have higher porosities for slower drying kinetics.

Comparison to Hampel's measurements

The presented coating characteristics of Figure 10.10 stand in contrast to Hampel's findings [2]. Therein, layer porosities of 43 % (on average) are stated for some 4-hour batch coating processes with inlet gas conditions ($\dot{M}_{in}$ = 70 kg/h and T_{in} = 70℃) that match to the here presented experiment series EB-21-3. But, the spray rate in Hampel's experiment were higher with $\dot{M}_{spr}$ = 1100 g/h, whereby more liquid solvent had to be evaporated, and lower processes gas temperatures were obtained (gas cooling). In this case, the drying rate is even lower than in the example EB-21-3, which might lead to more porous coatings. The detected porosities of Hampel based on scanning electron microscopy and X-ray computed tomography scanning. Four product samples had been taken from the bed during granulation at different time points: 50, 130, 210, and 240 min. The obtained porosity mean values of these measurement points were approximately equal. A change in coating layer porosity with proceeding process time, as it is the case in the present work, could not be ascertained in Hampel's study. The granulation processes of EB-24 were conducted with the highest inlet gas mass flow rate (115 kg/h) among the depicted examples in Figure 10.10. At this, larger values of the effective coating densities are measured already for the first two stages in comparison to the examples EB-13 to EB-14. A reason for this could be that higher inlet gas velocities result in faster drying kinetics, which could lead to more compact coating layers.

10.1.7 Terminal product sinking velocity

The terminal product sinking velocity $u_{s,pr}$ of the last stages of the experimental series EB-21-3 and EB-34 shall be compared with superficial gas velocities inside the Wurster tube (spray zone) in the following. Therefore, an approximate superficial gas velocity inside the spray zone u^*_α is defined with

$$u^*_\alpha := \frac{\dot{M}_{in}\Omega_{2,in} + \dot{M}_{g,noz}}{\rho_g(T^*_{\alpha,bot}, Y_{in})\frac{\pi}{4}D^2_{wt}}, \tag{10.14}$$

which bases on the two-zone continuum model (see Eqs. 7.59 and 7.70 to 7.83) of the present thesis. Heat losses through walls, solvent evaporation in the spray zone, and temperature dependency of process gas heat capacity are neglected in this. The approximate gas temperature of the spray zone inlet $T^*_{\alpha,bot}$ is obtained by

experimental series	stage [−]	$d^*_{3,0,j}$ [mm]	$u_{s,pr,j}$ [m/s]	u^*_α [m/s]
EB-21-3	8	1.164	4.92	2.48
EB-34	16	2.662	8.81	6.3

Table 10.8: Mean-volume-equivalent diameter $d^*_{3,0,j}$ of the largest stage product, its corresponding terminal sinking velocity $u_{s,pr,j} = u_s(d^*_{3,0,j})$, and an approximate superficial gas velocity u^*_α of Eq. 10.14 for the discontinuous granulation series EB-21-3 and EB-34.

Eq. 7.72. The drying power bypass fraction $\Omega_{2,in} = \dot{M}_{dis,2}/\dot{M}_{in}$, the inlet gas moisture content Y_{in}, and the Wurster tube diameter are adopted from Tables 8.1 and 8.2, as these parameters of the TZC-model match with the conducted batch experiments. The nozzle gas mass flow rate can be estimated with nearly 4 kg/h for a nozzle gas excess pressure as in the considered batch experiments (1.75 bar) and the utilized two-substance nozzle type (model 970 S4 from Düsen-Schlick GmbH, [124]), as also stated in Section 8.2.1 and in Appendix C.2.3. The terminal sinking velocities of the largest stage products are determined by Eq. 2.87 for the mean-volume-equivalent particle diameter: $u_{s,pr,j} = u_s(d^*_{3,0,j})$. The results of the mean-volume-equivalent particle diameter $d^*_{3,0,j}$, the terminal product sinking velocities $u_{s,pr,j}$, and the approximate superficial gas velocities u^*_α are listed in Table 10.8. This shows that the terminal sinking velocities (single particle settlement) of the last-stage products are clearly larger than the superficial spray zone gas velocity: $u_{s,pr,j} > u^*_\alpha$. Though, *stable pneumatic conveying* through the Wurster tube and thus Wurster fluidization could still be achieved in these experiments. This is presumably reasoned by the *swarm effects* described in Section 2.2.2, whereby higher particle concentrations reduce the actual sinking velocity of granule swarms, the so called swarm sinking velocity u_{sw}. It has already been ascertained by means of the two-zone continuum model in Section 8.2.3 that the swarm effect stabilizes the circulating Wurster fluidization even at lower gas velocities. The results of the multi-stage experiments show that Wurster granulation can be implemented for a very large range of particle sizes. A *particle growth limit* of stable pneumatic transport through the Wurster tube is not found from the results of the multi-batch experiments.

10.1.8 Conclusions for continuous granulation experiments

The main conclusions of the discontinuous granulation study are summarized in the following with regard to aspects that are important for the continuous granulation experiments of Section 10.4. These include preciseness of the inline detection method of bed mass, choice of stable process parameters, possible desired particle growth ratio $\Phi_{d,set}$ to be set, and growth kinetic issues for achieving faster startups.

Inline detection of bed mass via measured pressure drop

It has been shown that the pressure drop of the process gas suits as an inline detection quantity to represent changing bed masses in Wurster granulation processes. At this, the inlet gas mass flow rate $\dot{M}_{in}$ has a large effect on the pressure drop curves, while the inlet gas temperature T_{in} changes the pressure drop less, and the influence of nozzle gas excess pressure $p_{g,noz}$ is negligibly small. Moreover, Hampel's installed inline detection method for the fluidized bed mass ([2], see Section 9.4.7) provided the best results (lowest deviations) for process conditions with $p_{g,noz} = 1.75\,\text{bar}$, $\dot{M}_{in} = 70\,\text{kg/h}$, and $T_{in} = 70°\text{C}$. It bases on the inline measurement of the total pressure drop of the process chamber Δp_{app} and includes model-based and empirical equations. In order to use this method for different process conditions, adaptions of empirical correlation to the mass flow rate and temperature of the inlet gas have to be acquired. The described bed mass detection method can be improved by some modifications, as described later in Section 11.3.2.

Choice of stable process parameters

It ensues from the entire discontinuous granulation study that each of the investigated process parameters - nozzle air excess pressure, inlet gas mass flow rate, and inlet gas temperature - is significant for process stability. Too low nozzle gas excess pressures led to instabilities of the batch experiments. But, too high values of it are assumed to cause smaller spray droplets, which might result in bigger nucleation rates (unwanted dust particles of pure coating material) and larger spray losses. It has been worked out that a nozzle gas overpressure of 1.75 bar proves to be an adequate value to guarantee process success for an inner diameter of 0.8 mm for the liquid channel of the nozzle. Nevertheless, the drying power of the inlet gas must

be also large enough to evaporate the spray solvent efficiently, avoid high wetting degrees of the fluidized bed material, and prevent process destabilization through excessive agglomeration. This can be achieved either by larger mass flow rates or by higher temperatures of the inlet gas. At this, a mass flow rate of 70 kg/h is favored for the planned continuous experiments, as it is accompanied by the smallest detection error of the bed mass. The inlet gas temperature should be then higher to reduce the risk of instabilities, which is set to 90°C. The presented batch experiments have shown that an inlet gas temperature of 90°C is sufficient to ensure process stability, but only when the nozzle gas overpressure was at least 1.75 bar. However, the first continuous experiments have been conducted with a nozzle gas excess pressure of 1.5 bar, as shown later, and sporadic instabilities occurred therein as well. For this reason, the process parameters of subsequent continuous granulation experiments were chosen with $p_{g,noz} = 1.75\,\text{bar}$, $\dot{M}_{in} = 70\,\text{kg/h}$, and $T_{in} = 90°\text{C}$.

Possible values of the desired particle growth ratio

A particle growth ratio Φ_d up to round 3 could be realized in the experiments with Cellets® as core material and up to 10.5 with glass beads. It has also been shown that large granules can be raised through the Wurster tube although their single particle sinking velocity exceeds the superficial gas velocity inside the Wurster tube. The reason for this is presumed in the swarm effect, which reduces settlement velocities. As a conclusion, stable Wurster fluidization can also be achieved for large-growth granulation. A particle growth limit of stable Wurster passage cannot be ascertained from the presented discontinuous granulation study. However, such a limit is reached at the latest when the particles are so large or the inlet gas mass flow is so small that the superficial gas velocity inside the Wurster falls below the minimal fluidization point u_{mf} of Section 2.2.4. Such operating points are of no interest anyway, since they are below the minimal-Wurster-fluidization limit of Section 7.10.1. The planned continuous experiments of this thesis should be conducted with process parameters ($p_{g,noz} = 1.75\,\text{bar}$, $\dot{M}_{in} = 70\,\text{kg/h}$, and $T_{in} = 90°\text{C}$) similar to that of the multi-batch experiment EB-21-3 ($p_{g,noz} = 1.75\,\text{bar}$, $\dot{M}_{in} = 70\,\text{kg/h}$, and $T_{in} = 70°\text{C}$). The average product size of this batch series could be increased to nearly 2.5, wherefore the continuous experiments were conducted with a desired growth ratio $\Phi_{d,set}$ up to this value.

Fast startup

The experimental setting of EB-13 is most similar to process conditions of the planned continuous granulation experiments. Only the nozzle gas excess pressure $p_{g,noz}$ is a little different: 1.75 bar in continuous experiments and 2 bar in EB-13. The growth times of EB-13 lie between around 6.9 and 8.3 h to reach a particle growth of 1.9 and 2.2, respectively, as shown in Table 10.6. But, the continuous experiments shall be conducted for nine hours without interruption. It is assumed that stationary product size distributions can hardly be arrived under these process conditions. The growing-up period can be shortened by higher spray rates and lower bed masses. However, these parameters are restricted, as larger spray rates and smaller holdups increase the risk of process instabilities. For this reason, the particular startup strategies of Section 9.4.10 are conceptualized for the continuous granulation experiments, which base (among other aspects) on the discerned growth behavior of the multi-stage granulation experiments. It was shown that the removal of the excess bed masses ($M_{bed,end} - 800\,\text{g}$) between the stages led to higher particle growth rates. But, this was done only every ninety minutes. It is assumed that the growth kinetics could be even more enhanced, if the stages were conducted shorter, e.g., every thirty minutes, where the bed mass surplus would more frequently be taken off. Such a procedure can also be applied within the startup phase of the continuous experiments in the following way. Product classification is omitted by *total reflux* (maximal separation gas velocity, Table 9.4) of the particles entering the classifier. In the meanwhile, the holdup and its granule size distribution grow up through continuous spraying. Those conditions conform with single batch granulation processes. But, the bed mass must be then decreased in regular time steps to prevent worse circulating Wurster fluidization conditions due to high holdups and to improve growth kinetics. This can be realized by purging granules out of the process chamber through a classifier, whose gas flow is inactivated for a short time period: *discharge mode*, Table 9.4. The bed particle size distribution is thereby hardly manipulated by classification.

10.2 Dosing analysis of the feed-in double-pinch valve

Four different feed rate control methods are suggest and explained in Section 9.4.3. The characteristic features of them are summarized in Table 9.3. In the scope of this thesis, the first and third method (indicated by

F1 and F3) have been investigated with the experimental setup of Figure 9.2 for different nuclei materials, as listed in Tables 9.1 and 9.2, and diverse parameter conditions given below in Section 10.2.1. The method F1 was applied only in *short-term experiments*, while F3 was examined in short and *long-term experiments*. The latter were conducted for up to 31 h in one case. During the experiments, single dosages of nuclei were fed into a beaker by the continuously operating double-pinch valve. The corresponding feed rate of the single dosages was calculated by Eq. 9.15. A more detailed description of the experimental procedure can be found in Section 9.2.2.

10.2.1 Experimental settings

In the present substudy, six different groups of experimental setting, indicated by EF-1 to EF-6, are defined for the short-term experiments, and another three experimental settings, indicated by EF-7 to EF-9, were realized as long-term experiments. Their parameter conditions are summarized in Tables 10.9 and 10.10. The absolute pressure of the pneumatic control air (see $p_{g,dpv}$ in Figure 9.6) was set to 4 bar for all experiments of this nuclei dosing study.

Short-term experiments

In each short-term experiment, 40 single doses have been measured for continuous operation of the feeding equipment. The difference between the first six groups of experimental settings is that diverse container filling materials (IM-1, IM-2, IM-4, IM-5, IM-6, and IM-7) were used. The feed container was always filled with 6 kg at the beginning of each experiment, and no further nuclei material was added to the feed container during the measurements. The open-state time of the upper pinch valve $t_{V1,f}$ was set uniformly with a value of 10 s, by which a complete filling of the sluice volume could be guaranteed. For each of the groups EF-1 to EF-6, the open-state time of the lower pinch valve $t_{V2,f}$ has been varied between 0.01 and 10 s with the values of Table 10.10. By this, the dosing behavior of feed rate control method F1 is investigated through the experiments with higher flushing-out times ($t_{V2,f} \gg 1\,\mathrm{s}$) and the behavior of method F3 by those with lower flushing-out times ($t_{V2,f} \ll 1\,\mathrm{s}$).

Long-term experiments

The long-term dosing behavior of the feeding equipment has been studied with the last three experimental setting examples EF-7, EF-8, and EF-9 from Table 10.9. All of them were realized with the same type of nuclei material (IM-2, Cellets®200) and uniform open-state times of the pinch valves: $t_{V1,f} = 40\,\mathrm{s}$ and $t_{V2,f} = 0.1\,\mathrm{s}$. The initial filling level of the feeding container was prepared with 6 kg of nuclei for the experiments of EF-7 and EF-9, respectively; whereas, that of EF-8 was much higher with 17 kg. Refilling of nuclei during operation of the double-pinch valve was still refrained in the EF-7 and EF-8 measurements, while in last setting EF-9, the filling level was kept constant by regularly refilling a certain amount of nuclei into the container. All three long-term experiments were conducted for various periods of time, so that different numbers of doses were obtained. At this, the EF-7 measurements lasted around 18.5 h, whereafter the feed material container was emptied completely. The experiment of EF-8 could have been carried out longer due to the higher filling level. However, it was interrupted after around 31 h by a signal error of the data acquisition system, so that further measurement values had to be discarded. The last experiment EF-9 was the shortest with a total duration of 6 h. It has been stopped after 5 h and restarted for another hour on the next day in order to demonstrate a recuperative effect of the pinch valves, which is referred to as memory effect in Section 9.4.1, and which is presumed to be caused by *fatiqued back-reformation* of the rubber material.

10.2.2 Short-term and long-term behavior

The results of all experiments of Table 10.9 are presented in the following. In the short-term dosing experiments of EF-1 to EF-6, the focus lies on the influence of the open-state time of the lower pinch valve $t_{V2,f}$ and of nuclei size and density on the dosing masses, accuracy, and average feed rates of the feeding equipment for both control methods F1 and F3; whereas, influence of *long-term operation* and *filling conditions* on dosing accuracy shall be investigated in the experiments EF-7 to EF-9 for the method F3.

index of experimental setting	short- or long-term analysis	number of doses	index of initial material*)	type of material	$M_{fill,0}$ [kg]	with refilling	$t_{V1,f}$ [s]	$t_{V2,f}$ [s]
EF-1	short	40	IM-1	Cellets®100	6	no	10	0.01 - 10**)
EF-2	short	40	IM-2	Cellets®200	6	no	10	0.01 - 10**)
EF-3	short	40	IM-4	Cellets®350	6	no	10	0.01 - 10**)
EF-4	short	40	IM-5	Cellets®500	6	no	10	0.01 - 10**)
EF-5	short	40	IM-6	Cellets®700	6	no	10	0.01 - 10**)
EF-6	short	40	IM-7	glass beads	6	no	10	0.01 - 10**)
EF-7	long	1661	IM-2	Cellets®200	6	no	40	0.1
EF-8	long	2784	IM-2	Cellets®200	17	no	40	0.1
EF-9	long	539	IM-2	Cellets®200	6	yes	40	0.1

Table 10.9: Parameter settings of the experimental analysis of the feed-related double-pinch valve behavior; *) specified in Table 9.1 and Appendix C.1.1; **) specified in Table 10.10.

$t_{V2,f}$	0.01	0.02	0.03	0.04	0.05	0.06	0.07	0.08	0.09	0.1
[s]	0.11	0.12	0.13	0.14	0.15	0.2	0.25	0.3	0.35	0.4
	0.45	0.5	0.55	0.6	0.65	0.7	0.75	0.8	0.85	0.9
	1	2	3	4	5	6	7	8	9	10

Table 10.10: Open-state times of the lower pinch valve (flushing-out time) investigated in the short-term experiments of EF-1 to EF-6.

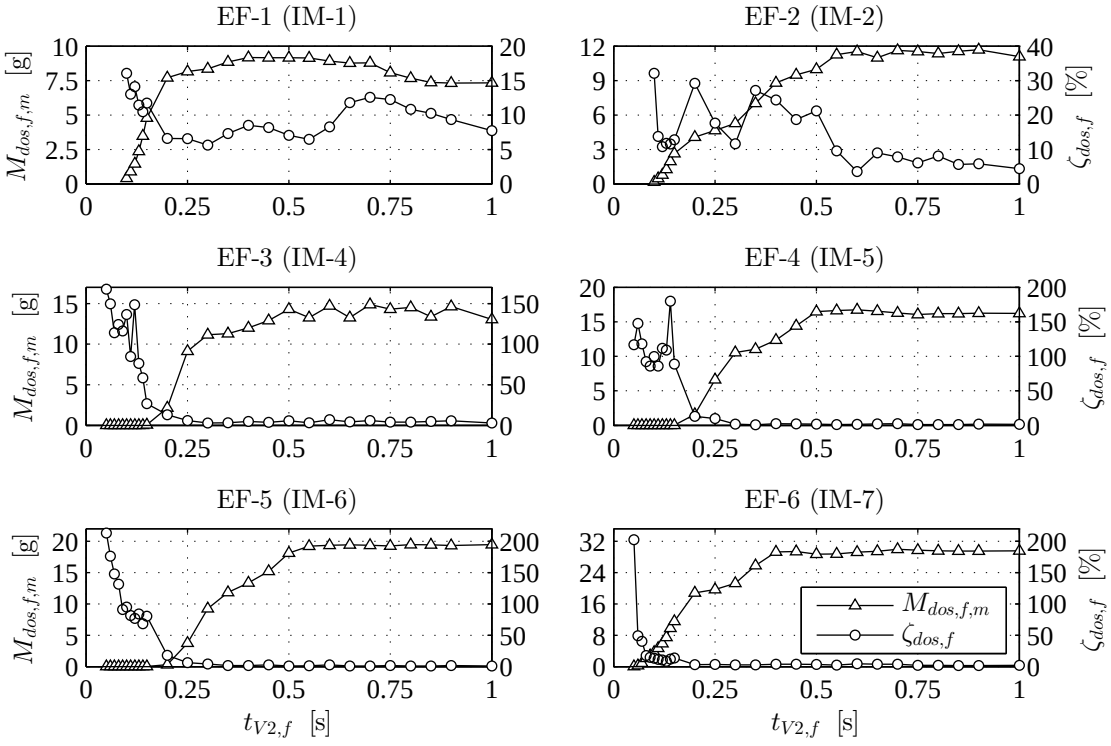

Figure 10.12: Mean value $M_{dos,f,m}$ (left axis) and relative standard deviation $\zeta_{dos,f}$ (right axis) of the dosage mass of the nuclei feeding equipment for different opening times of the lower pinch valve $t_{V2,f}$ shorter than 1 s and for different initial materials, each with $t_{V1,f} = 10\,\mathrm{s}$.

Definition of mean value and relative standard deviation of single dosage masses

The detected single dosage masses $M_{dos,f,i}$ are shown in Figure C.5 for eight open-state time examples of all short-term experimental settings (EF-1 to EF-6). Some of these dosage sequences have large fluctuations, and some show a decreasing tendency of the single dosage mass. In order to get a better comparison between the experiments, the mean value of the single dosage masses $M_{dos,f,m}$ and the relative standard deviation $\zeta_{dos,f}$ (coefficient of variation) are determined according to

$$M_{dos,f,m} = \frac{1}{40} \sum_{i=1}^{40} M_{dos,f,i} \tag{10.15}$$

and

$$\zeta_{dos,f} = \sqrt{\frac{1}{39} \sum_{i=1}^{40} \left(\frac{M_{dos,f,i}}{M_{dos,f,m}} - 1 \right)^2}. \tag{10.16}$$

Average dosage masses and corresponding relative standard deviations for shorter flushing-out times

The mean value of the single dosage masses $M_{dos,f,m}$ and the relative standard deviation $\zeta_{dos,f}$ of the short-term experiments from EF-1 to EF-6 are illustrated in Figure 10.12 as functions of the flushing-out times $t_{V2,f}$ up to values of 1 s. It is obvious that the average dosage mass $M_{dos,f,m}$ can be reduced by low flushing-out times for each of the used materials. Even zero-dosages (not plotted in Figure 10.12) have been observed in the EF-1 and EF-2 experiments with $t_{V2,f} < 0.1\,\text{s}$ (see Table 10.10) and in the EF-3 to EF-6 experiments with $t_{V2,f} < 0.05\,\text{s}$. The average dosage mass starts to increase strongly with higher flushing-out times up to a value of around 0.25 s for the smallest nuclei (IM-1 - Cellets®100) in the setting EF-1 and of around 0.5 s for the other materials in the experimental series EF-2 to EF-6. In this range, the feed rate control method F3 can be applied, where the average dosage mass is manipulated by the flushing-out time $t_{V2,f}$. However, the average dosage mass remains in a constant value range for still higher open-state times of the lower pinch valve. Under those conditions, the average dosage mass cannot be controlled, since the lower pinch valve is opened long enough to discharge all freely movable particles (not fixed to wall by adhesion) from the sluice volume. Those open-state times are rather suitable for the feed rate control method F1. It is further ascertained from Figure 10.12 that the relative standard deviation tends to be higher for low flushing-out times, and smaller when the lower pinch is opened long enough to remove the dosage unit. From this point of view, it is recommended to prefer the feed rate control method F1, instead of F3, to achieve a better dosing accuracy.

Average dosage masses for larger flushing-out times

The average dosage masses of flushing-out times $t_{V2,f}$ from 1 to 10 s are depicted in Figure 10.13 for each of the short-term experimental setting groups. It can be seen that the average dosage mass of settings EF-3, EF-4, and EF-5 changes hardly with the open-state time of the lower pinch valve. The average dosage mass of first and sixth experimental setting (EF-1 and EF-6) grows slightly with prolonged open-state times of the lower pinch valve. On the contrary, this of the second setting (EF-2) declines with $t_{V2,f}$ to a low extent. Such opposite results speak for an unreliable dosing behavior of the double-pinch valve, even when both, filling and flushing of the sluice volume, are unrestricted. At this, it is mentioned that the scavenging air of the used pneumatic system is injected into the sluice volume only by a short impulse right after the lower pinch valve opens; which means that the open-state time of this valve is larger than the required time to discharge the nuclei dose from the sluice volume. Hence, the *flushing-out procedure* can be improved by injecting the scavenging air several times within a single dosing cycle, whereby more attached particles would be removed, reducing dosage mass fluctuations.

Flush-back effect - influence of nuclei size and density

Moreover, the flush-back effect can be recognized in Figures 10.12 and 10.13 at open-state times of the lower pinch valve larger than 0.5 s. It turns out that average dosage mass of most experiments (except of EF-1 and EF-2 at $t_{V2,f} > 7\,\text{s}$) is the larger, the bigger and denser the nuclei materials are. It is assumed that heavier particles in the feeding container are harder to be pushed upwards due to its higher weight pressure. According to this, a larger filling level of the nuclei container would lessen the flush-back effect and better

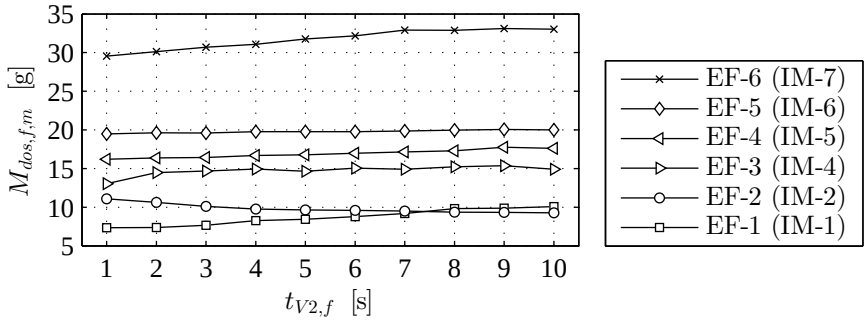

Figure 10.13: Mean value of the dosage mass $M_{dos,f,m}$ of the nuclei feeding equipment for different opening times of the lower pinch valve $t_{V2,f}$ longer than 1 s and for different initial materials, each with $t_{V1,f} = 10\,\mathrm{s}$.

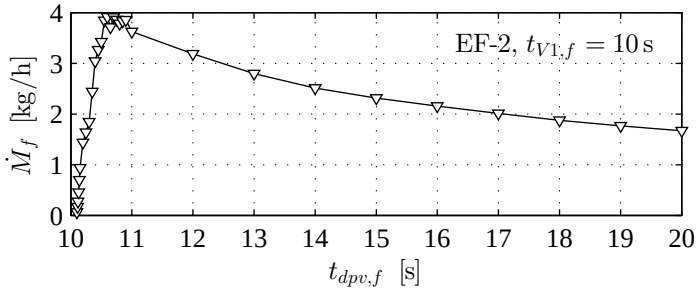

Figure 10.14: Feed rate $\dot{M}_{f,m}$ versus double-switch time $t_{dpv,f}$ of the continuously operating double-pinch valve of the feeding equipment for the experimental series EF-2.

the dosing accuracy of the present feeding equipment. For this reason and to check this conclusion, the long-term experiment EF-8 has been conducted with a far greater container filling level.

Average feed rate

The *momentaneous feed rate* can be high when nuclei are discharged from the sluice volume of the double-pinch valve; but, the average feed rate may still be low in a long-term perspective in terms of a few dosing cycles for the reason that large open-state times of either pinch valve lead to time lags. The average feed rate to be considered in the following is related to the average dosage mass and the double-switch time according to:

$$\dot{M}_{f,m} = \frac{M_{dos,f,m}}{t_{dpv,f}}. \tag{10.17}$$

Figure 10.14 shows the average feed rate $\dot{M}_{f,m}$ versus the double-switch time $t_{dpv,f}$ of Eq. 9.11 for the experimental series EF-2. It is evident that the average feed rate increases sharply between a double-switch time of 10.06 and 10.5 s due to a strong enlargement of the average dosage mass as shown before in Figure 10.12. Maximal feed rates are observed between 10.5 and 10.9 s with a low variance. Double-switch times higher than 10.9 s lead to a *delay effect*, by which the *long-term feed rate* is reduced.

Long-term behavior - memory effect

The single dosage masses $M_{dos,f,i}$ of the long-term dosing measurements (EF-7, EF-8, and EF-9) are depicted versus the experiment time in Figure 10.15. Each of the experiments shows a decreasing evolution of the average dosage mass and large dosing fluctuations. The decline of the dosage mass is the biggest in the beginning of the experiment and becomes smaller with proceeding time. It can also be seen from EF-9 that the initial dosage masses were higher after a break of nearly half a day, but reached the former values at round half an hour after the restart. It is assumed that this decreasing effect is caused by weakened

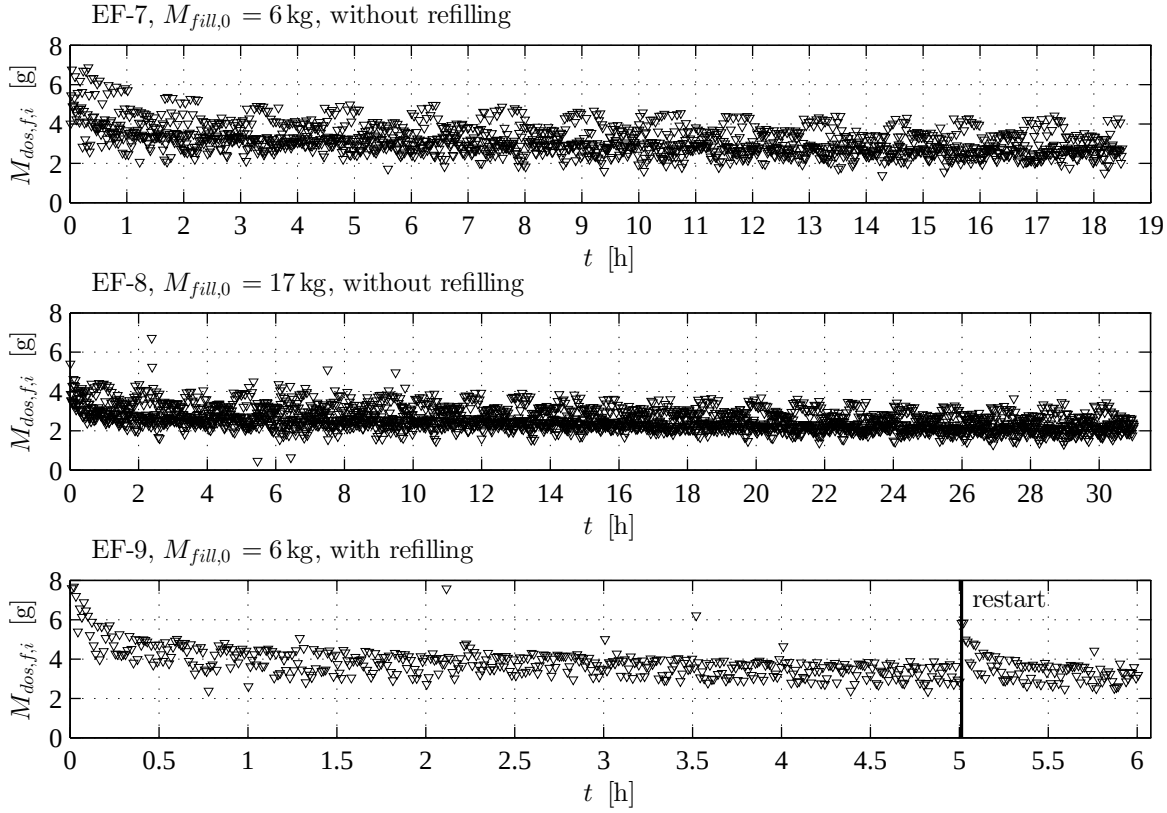

Figure 10.15: Single dosage mass $M_{dos,f,i}$ with operating time of the double-pinch valve of the nuclei feeding equipment for different experimental conditions: initial filling levels $M_{fill,0}$, without refilling of nuclei, and with refilling; each for $t_{V1,f} = 40\,\mathrm{s}$ and $t_{V2,f} = 0.1\,\mathrm{s}$.

back-reformation of the pinch valve rubber material (memory effect) with ongoing operation time. It can be further ascertained that the fluctuations are a little smaller for higher and constant filling level. The dosage masses of EF-8 are, on average, slightly lower than these of EF-7. Hence, the flush-back effect could not be decreased by a higher filling level. The results of the dosing experiments must be carefully evaluated. Beside the described effects (memory effect, back-reformation, and adhesion to wall), other parameters also influence the dosing mass. But also slight changes in the inclination angle of the double-pinch valve channel can occur when reinstalling the nuclei feeding equipment, which might significantly affect the dosing behavior too.

10.2.3 Conclusions for continuous granulation experiments

Pursued to the ideal particle growth model of Chapter 3, lower average feed rates are required to obtain higher desired product diameters ($d_{pr,set}$, see Eq. 9.24) in continuous layerwise granulation processes. In the present thesis, feed rates between nearly 30 and 76 g/h are required in the continuous large-growth granulation experiments. To achieve such values, two options ensue from the feed rate curve in Figure 10.14. On the one hand, very low flushing-out times can be applied, here with $0.1\,\mathrm{s} < t_{V2,f} < 0.15\,\mathrm{s}$ ($\Leftrightarrow 10.1\,\mathrm{s} < t_{dpv,f} = t_{V1,f} + t_{V2,f} < 10.15\,\mathrm{s}$), which corresponds to the feed rate control method F3. But as ascertained before, those parameter values are accompanied by large dosing fluctuations to the detriment of continuous dosing accuracy. On the other hand, the feed rate control method F1 can be used; at which, the open-state time of the lower pinch valve is set to very large values to generate a big time delay, and thus, to reduce the long-term feed rate. The dosing fluctuations would be smaller in this case, but long time periods without nuclei supply would occur. Such a discontinuous feeding behavior impedes the granulation process from reaching stationary conditions. As a conclusion, the feed-related double-pinch valve is over-sized for the granulation plant employed in the present thesis. It is more suitable for granulators of larger scale, where higher spray rates, and hence, bigger feed rates are applicable. But, to adapt the dosing behavior to the granulation chamber dimensions of the present work, a double-pinch valve with small sluice volume is recommended. Furthermore, the double-pinch valve could be combined with other types of conveying devices with a better dosing controllability (e.g., vibrating feeder unit). At this, the nuclei material could be inserted into an empty feeding container by the additional conveyor, from where it would be sluiced into the granulator by a double-pinch valve.

10.3 Analysis of bed discharge dynamics with the feed-out double-pinch valve

An analysis of bed discharge dynamics of the granulator system used in the continuous granulation experiments is presented in this section. The experimental setup of this investigation is illustrated in Figure 9.3, and the procedure is described in Section 9.2.2.

10.3.1 Parameter setting

Three experimental series with different parameters, given in Table 10.11, were conducted in the scope of the bed discharge analysis. The single experiments are indicated by a reference code that begins with the three letters "EBD" and two subsequent digits, where E stands for experiment, B for bed, and D for discharge. The first digit of the alphanumeric codes represents the kind of parameters varied, while the second digit refers to how these parameters have been changed. The entire code is then related to a certain set of parameters, wherewith the experiments should be carried out. The entire parameter variation series is expressed by the reference code leaving out the last digit, as follows: EBD-1, EBD-2, and EBD-3. In the first two experimental series EBD-1 and EBD-2, the feed-out double-pinch valve was operated with *even switching rhythm* ($t_{V1,sep} = t_{V2,sep}$), and in the last series EBD-3 with *uneven switching rhythm* ($t_{V1,sep} \neq t_{V2,sep}$). In the first experimental series EBD-1, the inlet gas conditions were varied with mass flow rates $\dot{M}_{in}$ of 70, 85, and 100 kg/h, and with temperatures T_{in} of 70, 80, and 90°C. At this, an initial bed mass of $M_{bed,0} = 2\,\mathrm{kg}$ was prepared constantly, and the open-state times of both pinch valves $t_{V1,sep}$ and $t_{V2,sep}$ were set to 0.14 s, respectively, before each of the experiments. In the second and third experimental series EBD-2 and EBD-3, the inlet gas mass flow rate, inlet gas temperature, and initial bed mass were uniform with 70 kg/h, 70°C, and 3 kg. The difference between these two series was that, in the EBD-2 experiments, the open-state times of both double-pinch valves $t_{V1,sep}$ and $t_{V2,sep}$ had been equally varied between five different values; whereas,

the EBD-3 series contains five experiments with different opening times of the upper pinch valve $t_{V1,sep}$, where the opening time of the lower pinch valve $t_{V2,sep}$ was kept constant at 0.14 s. The pneumatic air pressure was set with $p_{g,dpv} = 2$ bar in the EBD-1 experiments and with $p_{g,dpv} = 4$ bar in the EBD-2 and EBD-3 experiments. As described in Section 9.2.2, the bed material being discharged from the granulator was collected in sample containers within so-called *sampling units* of thirty seconds ($\Delta t_{sam} = 30$ s). After this period of sampling time, the filled containers were replaced by new empty ones. The mass of the sampling units was measured and recorded. They are the basis of the present analysis of bed discharge dynamics. The process chamber was configurated with Wurster equipment (dimensions given in Figure C.2) in same way as in the discontinuous and continuous granulation experiments (Sections 10.1 and 10.4) of this thesis. The nozzle air excess pressure was set with $p_{g,noz} = 1.75$ bar in each of the bed discharge experiments.

10.3.2 Bed discharge characteristics

Bed mass curves

Time-dependent bed mass curves were calculated from the conducted experiments of Table 10.11 in the following way. The sampling units shall be represented here by the counting variable $k \in \{1, 2, ..., j\}$ with $j \in \{1, 2, ...\}$. The time coordinate of the bed discharge curves is discretized according to $t \in \{0, j\Delta t_{sam}\}$ with $\Delta t_{sam} = 30$ min. The total numbers of units sampled during the entire experiment were different depending on the initial bed mass and the conveying rates obtained. The mass of sampling units is symbolized by $\Delta M_{sam,k}$. The bed mass curves are reconstructed by sequential subtraction from the initial bed mass of the sample masses collected:

$$M_{bed,j} = M_{bed,0} - \sum_{k=1}^{j} \Delta M_{sam,k}. \tag{10.18}$$

The bed mass curves of all experiments from Table 10.11 are depicted in four diagrams of Figure 10.16. The first and second diagram contain the results of EBD-1 experiments, the third diagram these of EBD-2 experiments, and the fourth diagram these of EBD-3 experiments.

Overall bed discharge dynamics

It can be seen from the EBD-1 diagrams that the bed material was discharged the faster, the higher the inlet gas mass flow rate and inlet gas temperature had been. The influence of the open-state times of the pinch valves $t_{V1,sep}$ and $t_{V2,sep}$ on bed discharge dynamics is much stronger than that of the inlet gas parameters, which is visible in the EBD-2 and EBD-3 diagram. At this, a maximum of bed discharge kinetics is ascertained in the middle of the parameter variation ranges of both the EBD-2 and the EBD-3 series. In the EBD-2 series, where the particle sluice is operated in even switching rhythm mode ($t_{V1,sep} = t_{V2,sep}$), emptying the granulator took by far the longest for the experiment with the lowest open-state times ($t_{V1,sep} = t_{V2,sep} = 0.1$ s in EBD-21). The bed unloading experiments with the second smallest even switching times ($t_{V1,sep} = t_{V2,sep} = 0.14$ s in EBD-22) and the largest even switching times ($t_{V1,sep} = t_{V2,sep} = 0.5$ s in EBD-25) of the EBD-2 series were clearly quicker. Even higher bed discharge rates have been obtained for the experiment with opening times of $t_{V1,sep} = t_{V2,sep} = 0.2$ s (EBD-23) and $t_{V1,sep} = t_{V2,sep} = 0.25$ s (EBD-24). The bed mass curves of these examples are close together. In the EBD-3 series with uneven switching rhythm, where $t_{V2,sep} = 0.14$ s, the bed discharge dynamics were the slowest for the smallest open-state time of the upper pinch valve with $t_{V1,sep} = 0.1$ s in EBD-31 and the largest one with $t_{V1,sep} = 5$ s in EBD-35. The other experiments of this series, EBD-32 to EBD-34, are many times faster. At this, the experiments with open-state times of 0.5 s (EBD-32) and 1 s (EBD-33) were the fastest. The bed outlet dynamics of the example with $t_{V1,sep} = 2$ s was a little bit slower.

Fluctuations and non-linearities

It is obvious that the bed mass decreases more linearly and with lower fluctuations in the experiments with the higher pneumatic air pressure of 4 bar (EBD-2 and EBD-3) than in the experiments with 2 bar (EBD-1), except for the EBD-25 experiment ($t_{V1,sep} = t_{V2,sep} = 0.5$ s), as discussed below in Section 10.3.3. Furthermore, it is ascertained from the EBD-2 and EBD-3 results of Figure 10.16 that the feed-out rates strongly decreased after the bed masses had fallen to values below approximate 0.2 kg. The solids concentration in the fluidization region of the process chamber got diluted in this range of holdup due to the lack of bed particles. Consequently, the particle flow rate through the outlet orifice of the chamber ($\dot{M}_{p,out}$, see also Figure 9.8) became lower.

index of experimental setting	$\dot{M}_{in}$ [kg/h]	T_{in} [℃]	$M_{bed,0}$ [kg]	$t_{V1,sep}$ [s]	$t_{V2,sep}$ [s]	$p_{g,dpv}$ [bar]
EBD-11	**70**	70	2	0.14	0.14	2
EBD-12	**85**	70	2	0.14	0.14	2
EBD-13	**100**	70	2	0.14	0.14	2
EBD-14	70	**80**	2	0.14	0.14	2
EBD-15	70	**90**	2	0.14	0.14	2
EBD-21	70	70	3	**0.1**	**0.1**	4
EBD-22	70	70	3	**0.14**	**0.14**	4
EBD-23	70	70	3	**0.2**	**0.2**	4
EBD-24	70	70	3	**0.25**	**0.25**	4
EBD-25	70	70	3	**0.5**	**0.5**	4
EBD-31	70	70	3	**0.1**	0.14	4
EBD-32	70	70	3	**0.5**	0.14	4
EBD-33	70	70	3	**1**	0.14	4
EBD-34	70	70	3	**2**	0.14	4
EBD-35	70	70	3	**5**	0.14	4

Table 10.11: Parameter settings of the experimental analysis of bed discharge dynamics with a double-pinch valve.

Average conveying rates of sampling units

Conveying rates of the feed-out double-pinch valve can be defined by averages with different time intervals of particle sluicing. The smallest time interval is the cycle time of the double-pinch valve $t_{dpv,sep}$ of Eq. 9.12 (double-switch time). The conveying rate of a single dosage ensues from the ratio of the dosage mass to the double-switch time. Such a type of average mass flow rate is used in the dosing behavior study of the feed-in double-pinch valve in Section 10.2. In the study of bed discharge dynamics, however, masses of single dosages had not been measured, but the masses of the sampling units of thirty seconds. Therefore, the average conveying rates to be investigated here are related to the sampling units and calculated according to:

$$\dot{M}_{sep,j} = \frac{\Delta M_{sam,j}}{\Delta t_{sam}}. \tag{10.19}$$

Calculation of mean values and relative standard deviations of the bed outlet conveying rate

The bed discharge rates fluctuated during the experiments. Therefore, a mean value and a relative standard deviation of the feed-out conveying rates $\dot{M}_{sep,j}$ obtained from Eq. 10.19 within a range of certain bed mass values are calculated. These statistical quantities are used to compare the bed discharging behavior of the experiments with different process conditions (parameters of Table 10.11). The limits of this bed mass range, also called here as averaging limits, are chosen with 1.5 and 1 kg, for the reason that such a domain of bed mass values matches to the later presented continuous granulation experiments (Section 10.4), where the same granulator equipment (Section 9.2) and nuclei material (Cellets®200) were employed. The time points at which the bed mass crosses the bounds of 1.5 and 1 kg are approximated by those sampling units (periods) after which the value of the reconstructed bed mass $M_{bed,j}$ is closest to the given averaging limits. The sampling units of these bed mass limits are indicated by $j_{1.5\mathrm{kg}}$ and $j_{1\mathrm{kg}}$, and read out of the bed mass curves according to the following rules:

$$j_{1.5\mathrm{kg}} \coloneqq \mathrm{find}_{\min,j}\big(|M_{bed,j} - 1.5\,\mathrm{kg}|\big), \tag{10.20}$$

$$j_{1\mathrm{kg}} \coloneqq \mathrm{find}_{\min,j}\big(|M_{bed,j} - 1\,\mathrm{kg}|\big). \tag{10.21}$$

The mean value and relative standard deviation of the conveying rates within this averaging range ($j_{1.5\mathrm{kg}}$ and $j_{1\mathrm{kg}}$) ensue then to:

$$\dot{M}_{sep,m}\big|_{j_{1\mathrm{kg}}}^{j_{1.5\mathrm{kg}}} = \frac{1}{j_{1\mathrm{kg}} + 1 - j_{1.5\mathrm{kg}}} \sum_{k=j_{1.5\mathrm{kg}}}^{j_{1\mathrm{kg}}} \dot{M}_{sep,k} \tag{10.22}$$

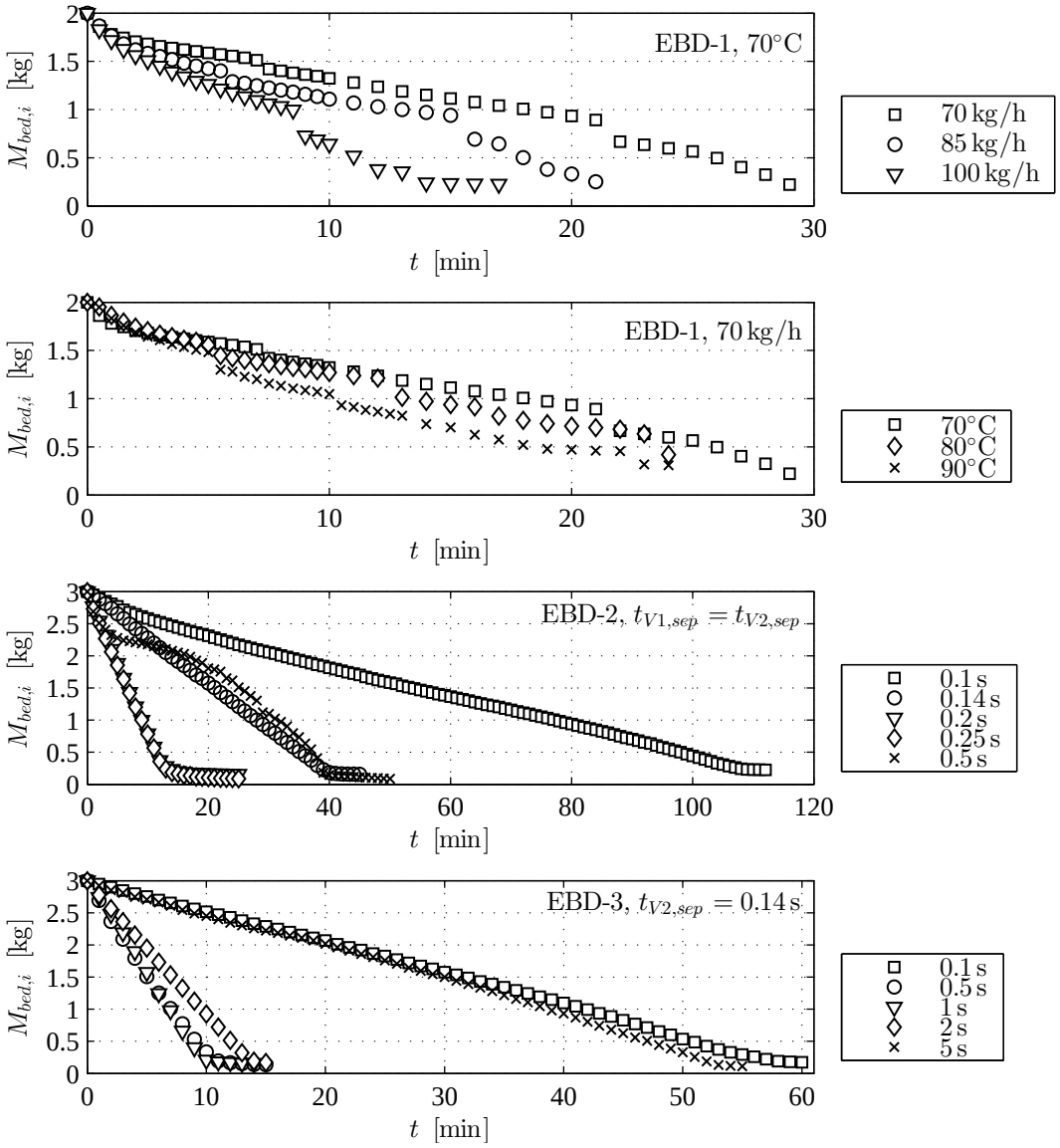

Figure 10.16: Bed mass discharge curves $M_{bed}(t)$ for three experimental series: EBD-1*) - variation of inlet gas conditions ($\dot{M}_{in}$ and T_{in}), EBD-2*) - variation of open-state times ($t_{V1,sep}$ and $t_{V2,sep}$), and EBD-3**) - variation of filling time $t_{V1,sep}$ at a low flushing time $t_{V2,sep}$; *) with even switching rhythm ($t_{V1,sep} = t_{V2,sep}$); **) with uneven switching rhythm ($t_{V1,sep} \neq t_{V2,sep}$).

and

$$\zeta_{\dot{M}_{sep}}\Big|_{j_{1kg}}^{j_{1.5kg}} = \sqrt{\frac{1}{j_{1kg} - j_{1.5kg}} \sum_{k=j_{1.5kg}}^{j_{1kg}} \left(\frac{\dot{M}_{sep,k}}{\dot{M}_{sep,m}\Big|_{j_{1kg}}^{j_{1.5kg}}} - 1 \right)^2}. \tag{10.23}$$

In Figure 10.17, the results of these mean conveying rates and their associated relative standard deviations are plotted versus the varied parameters of the experimental series EBD-1, EBD-2, and EBD-3.

Influence of varied parameters on mean conveying rates

The smallest discharge rate of the first experimental series is detected with round 2.9 kg/h for the EBD-11 experiment with an inlet mass flow rate of 70 kg/h, an inlet gas temperature of 70℃, and a pneumatic air pressure of 2 bar. The average conveying rate has increased to 5.2 kg/h for enlarged inlet gas mass flow rates, and to 5.6 kg/h for raised inlet gas temperatures. As ascertained before by the bed mass curves, the bed discharge dynamics of the EBD-2 and EBD-3 experiments were faster for middle open-state times in the investigated parameter ranges. This effect can also be seen in the average conveying rates of the EBD-2 and EBD-3 diagrams of Figure 10.17. The discharge rates grow at low open-state times, reach a maximum, and fall then again at large opening times of the pinch valve. The maximal average conveying rate of even switching rhythm is observed in the EBD-2 results with 13.1 kg/h at an even switching time of $t_{V1,sep} = t_{V2,sep} = 0.2$ s; while the maximum with uneven switching rhythm is found with 18.4 kg/h for open-state times of $t_{V1,sep} = 1$ s and $t_{V2,sep} = 0.14$ s.

Influence of varied parameters on relative standard deviation of conveying rates

The relative standard deviations of the conveying rates of the EBD-1 series are large with values above 75 %, except for the EBD-13 experiment (100 kg/h and 70℃), where the discharge rates fluctuated with only round 22 %. However, it can be assumed from the bed mass curves that the variance in dosing rates of experiment EBD-13 would be larger if the averaging range ($j_{1.5kg}$ and j_{1kg}) were more broadly defined. The $M_{bed,j}$-curve of EBD-13 shows stronger changes of bed discharge dynamics outside the range of 1.5 and 1 kg. The relative standard deviations of conveying rates of the EBD-2 experiments, where the pneumatic air pressure was given with 4 bar and even switching rhythm of the pinch valves was applied, are much lower than in the EBD-1 experiments. Only, the discharge rates at switching times of 0.5 s had a large variation ($\zeta_{\dot{M}_{sep}} = 80.5$ %). The $\zeta_{\dot{M}_{sep}}$-values of other opening times (from 0.1 to 0.25 s) of the EBD-2 experiments are below 13 %. In the last experimental series EBD-3, where the pneumatic air pressure was also defined with 4 bar, all of the relative control deviations of conveying rates were smaller than 16.5 %.

Estimated average single dosage mass

An estimated average single dosage mass of the discharge periods between bed masses of 1.5 and 1 kg can be further defined by the product of the average conveying rate of Eq. 10.22 and the cycle time of Eq. 9.12:

$$M_{dos,sep,m}\Big|_{j_{1kg}}^{j_{1.5kg}} = \dot{M}_{sep,m}\Big|_{j_{1kg}}^{j_{1.5kg}} t_{dpv,sep}. \tag{10.24}$$

This average dosage mass was calculated for all presented discharge experiments. They can be found in Table 10.12 and shall be briefly described here. The average dosage mass of the EBD-1 experiments is comparatively low with values between 227 and 434 mg, which is a result of the low switching times of both double-pinch valves (0.14 s). It can be seen from the EBD-2 and EBD-3 experiments that the single dosage mass tends to be larger for higher open-state times. But, a steady increase of the dosing masses is not ascertained. In the EBD-2 results, dosage mass values are between 1456 and 1741 mg for even switching rhythms of 0.2, 0.25, and 0.5 s. The largest dosage masses are detected for the experiments EBD-32 to EBD-35 with values between 2627 and 7243 mg, although the opening time of the lower pinch valve $t_{V2,sep}$ was quite low with 0.14 s in the EBD-3 series. The open-state times of the upper pinch valve $t_{V1,sep}$ were larger, so that more bed particles could fill the sluice volume of the double-pinch valve, which is probably the reason for the higher average single dosage masses.

Theoretical mean residence time of bed particles

A theoretical mean residence time of bed particles (symbolized by τ_{bed}) can be formulated for idealized continuous granulation conditions with a stationary bed mass and constant bed discharge rates. Such a

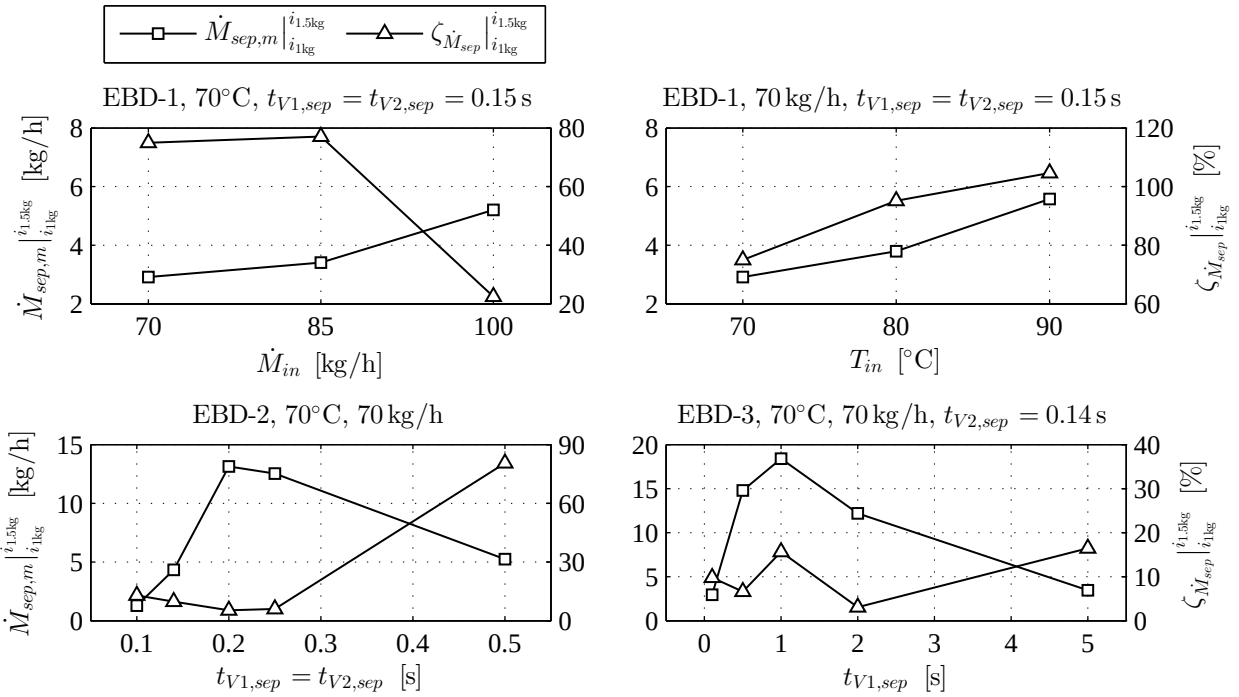

Figure 10.17: Mean values (left axis) and relative standard deviation (right axis) of conveying rates of the feed-out double-pinch valve (defined in Eq. 10.22 and 10.23) versus varied parameters of different experimental series: inlet gas mass flow rate $\dot{M}_{in}$ and inlet gas temperature T_{in} in EBD-1*), open-state times of both valves $t_{V1,sep}$ and $t_{V2,sep}$ in EBD-2*), and filling time $t_{V1,sep}$ in EBD-3**); *) with even switching rhythm ($t_{V1,sep} = t_{V2,sep}$); **) with uneven switching rhythm ($t_{V1,sep} \neq t_{V2,sep}$).

index of experimental setting	$\dot{M}_{sep,m}\big\vert_{j_{1\mathrm{kg}}}^{j_{1.5\mathrm{kg}}}$ [kg/h]	$\zeta_{\dot{M}_{sep}}\big\vert_{j_{1\mathrm{kg}}}^{j_{1.5\mathrm{kg}}}$ [%]	$t_{dpv,sep}$ [s]	$M_{dos,sep,m}\big\vert_{j_{1\mathrm{kg}}}^{j_{1.5\mathrm{kg}}}$ [mg]	$\tau_{bed,1\mathrm{kg}}$ [s]	$\tau_{bed,1.5\mathrm{kg}}$ [s]
EBD-11	2.92	74.9	0.28	227	1234	1851
EBD-12	3.40	77.1	0.28	265	1058	1587
EBD-13	5.21	22.5	0.28	405	691	1037
EBD-14	3.79	95.1	0.28	295	949	1424
EBD-15	5.58	104.7	0.28	434	646	969
EBD-21	1.27	12.9	0.2	71	2836	4253
EBD-22	4.33	9.7	0.28	337	832	1248
EBD-23	13.13	5.3	0.4	1459	274	411
EBD-24	12.54	6.0	0.5	1741	287	431
EBD-25	5.24	80.5	1	1456	687	1031
EBD-31	2.95	9.8	0.24	197	1219	1828
EBD-32	14.78	6.6	0.64	2627	244	365
EBD-33	18.41	15.6	1.14	5829	196	293
EBD-34	12.18	3.1	2.14	7243	295	443
EBD-35	3.43	16.4	5.14	4904	1048	1572

Table 10.12: Characteristics of bed discharge dynamics with feed-out double-pinch valve: average conveying rate $\dot{M}_{sep,m}$, relative standard deviation of conveying rates $\zeta_{\dot{M}_{sep}}$, cycle time of the double-pinch valve $t_{dpv,sep}$, average single dosage mass $M_{dos,sep,m}$, and theoretical mean residence times of particles in the granulator $\tau_{bed,1\mathrm{kg}}$ and $\tau_{bed,1.5\mathrm{kg}}$ for stationary conditions of bed mass and discharge rates; $j_{1\mathrm{kg}}$ and $j_{1.5\mathrm{kg}}$ denote the sampling units between which discharge characteristics were calculated; experimental setup described in Section 9.2.2; basis of calculation given in Section 10.3.2.

residence time shall be estimated here from the bed mass values of 1 and 1.5 kg and the average conveying rates of Eq. 10.22 according to:

$$\tau_{bed,1\mathrm{kg}} = \frac{1\,\mathrm{kg}}{\dot{M}_{sep,m}\big\vert_{j_{1\mathrm{kg}}}^{j_{1.5\mathrm{kg}}}}, \tag{10.25}$$

$$\tau_{bed,1.5\mathrm{kg}} = \frac{1.5\,\mathrm{kg}}{\dot{M}_{sep,m}\big\vert_{j_{1\mathrm{kg}}}^{j_{1.5\mathrm{kg}}}}. \tag{10.26}$$

The results of both residence times are also listed in Table 10.12. They are hyperbolic functions of the average conveying rate. The mean residence time is not examined in great detail here. But, the theoretical mean residence time of the experiment EBD-22 is of matter for continuous granulations experiments. On the one hand, the granulation experiments of the present thesis have been conducted with the double-pinch valve setting of EBD-22 ($t_{V1,sep} = t_{V2,sep} = 0.14\,\mathrm{s}$ and $p_{g,dpv} = 4\,\mathrm{bar}$), wherein the bed mass could be controlled between 1 and 1.5 kg. On the other hand, the mean residence time of granules in the fluidized bed (time needed to enter the classifier on average) is one of the model parameters of the presented three-compartment population balance models of Chapter 5. This residence time factor (symbolized by τ_{sep}) was assumed with 1800 s in the PB-simulations of Section 6.1, where model parameter values were adopted from Hampel's first validated simulation study [1]. The theoretical mean residence times of Eqs. 10.25 and 10.26 obtained for experiment EBD-22 lie between $\tau_{bed,1\mathrm{kg}} = 832\,\mathrm{s}$ and $\tau_{bed,1.5\mathrm{kg}} = 1248\,\mathrm{s}$. This range of residence time is significantly lower than the value τ_{sep} used in Section 6.1; however, it matches with the residence time factor of later PB-simulations of Hampel shown in [2], where τ_{sep} is symbolized with "τ_3" and is defined with 1000 s.

10.3.3 Discussion and conclusions

Comparison of experiments EBD-11 and EBD-22

The experiments of EBD-11 and EBD-22, have been conducted with equal process parameters (see Table 10.11), except for the pneumatic air pressure $p_{g,dpv}$. Their average conveying rates obtained between holdups

of 1.5 and 1 kg differ by the factor of round 1.5. It is not clear whether this difference is caused by the change in pneumatic air pressure or by other factors such as internal gas pressure (fluidized bed), changes in ambient pressure and temperature, or slight shifts in the installation. Therefore, it is recommended for subsequent researches to repeat the bed discharge experiments of a certain parameter setting several times and to measure pressure gradients. But, also experiments with same open-state times of the pinch valves could be conducted for various pneumatic air pressures.

Accidental drop of conveying rates in the EBD-25 experiment

In the EBD-25 experiment, the conveying rates have been reduced significantly in the middle of the experiments between bed mass values of round 2.25 and 2 kg. During this experiment, the connections of the double-pinch valve and the bed outlet orifice had loosened, so that a small gas leak emerged. It was probably the reason for short drop of discharge kinetics. The leaky connection might have changed the internal gas pressure and lowered the dosing rates of the particle sluice. After this, the connections were readjusted by hand, and the subsequent mass flow rates had then been higher again.

Limitation type of bed discharge dynamics - mechanism dominating the overall bed discharge rate

In Section 9.4.2, two serially-connected mechanisms of bed discharge dynamics are described, of which the slower one dominates the overall bed discharge rate. These are the *drop-out mechanism* (Figure 9.8a) and the *particle sluice mechanism* (Figure 9.8b). Already during the experiments, some indications were observed that the latter mechanism is the predominant one of the overall discharge kinetics, but also the subsequent analyses of the results support this assumption. For example, it was seen in the experiments EBD-33 to EBD-35 of Table 10.11 that the transparent sluice volume cylinder had been completely filled before lower pinch valve was opened. At this, the open-state times of the upper pinch valve (filling time) were large enough with $t_{V1,sep} \geq 1\,\mathrm{s}$. That means that there must have been a *particle congestion* in the conveying channel of the feed-out double-pinch valve. In this case, the *potential bed outlet hit rate* $\dot{M}_{p,hit}$ is greater than the the *potential conveyor rate* $\dot{M}_{p,dpv}$, which is the maximal conveying rate that the double-pinch valve can provide under the present experimental conditions, so that the overall bed discharge rate $\dot{M}_{sep}$ was generated by the particle sluice: $\dot{M}_{sep} = \dot{M}_{p,dpv} < \dot{M}_{p,hit}$. Complete filling of the sluice and short stagnation of particles could not be observed by eye in the other experiments, EB-31 and EB-32, due to the very low filling times with $t_{V1,sep} \ll 1\,\mathrm{s}$, which does not rule out the presence of particle congestion in the metallic bed outlet channel. However, it is very likely that particle congestion also appeared in the experiments EB-31 and EB-32 for the following reasons. The granulator-related process parameters (e.g., $\dot{M}_{in}$, T_{in}), and hence, the fluidization conditions were equal among the five EB-3 experiments. Consequently, their potential bed outlet hit rates $\dot{M}_{p,hit}$ are also comparable. Furthermore, the experimentally determined average bed discharge rates $\dot{M}_{sep,m}$ of the EBD-31 and EBD-32 experiments from Figure 10.17 are lower than that of EBD-33 (maximum of this study), in which particle congestion could still be observed visually. In order for the drop-out mechanism to dominate the overall discharge kinetics, particle congestion should have been absent, and to achieve this, the average bed discharge rates of EBD-31 and EBD-32 would have to be at least greater than that of EBD-33, which is not the case. Moreover, it turned out through the experimental series of EBD-2 and EBD-3, where fluidization conditions and pneumatic control air pressure were the same, that the feed-out rates $\dot{M}_{sep}$ can be clearly manipulated by the opening times of the pinch valves. A *distinct controllability* of middle-term average bed discharge rates, in the scale of minutes, would not be possible with a dominating drop-out mechanism, where $\dot{M}_{sep} = \dot{M}_{p,hit} < \dot{M}_{dpv,sep}$. However, a flush-back effect, as observed in the feed-in experiments, is disregarded in this discussion. Such an effect would influence the discharge behavior for both mechanisms. A further differentiation between a convective and a dispersive part of the drop-out mechanism was not made here.

Comparison of EBD-1 results with approaches of fluid-particle transport dynamics

The depicted bed discharge characteristics of the EBD-1 experiments with different inlet gas conditions can be compared to findings of the two-zone continuum model of Wurster fluidization of Chapter 7. In the experimental series of EBD-1, firstly the inlet gas mass flow rate has been increased and secondly the inlet gas temperature. The process gas velocities inside the chamber are both higher for larger mass flow rates and temperatures of the inlet gas. According to Eq. 2.130, the fluidized bed expansion equation after Brötz [83] and Richardson a. Zaki [50], higher gas velocities lead to stronger expansion of the fluidized bed

and to lower particle concentrations, on average. Further, it follows from the approach of Burgschweiger a. Tsotsas ([90,91], see also Section 2.2.6) that both the average bed particle concentration in the drying zone and the bed height ($1-\varepsilon_{1-\alpha}$ and $H_{1-\alpha}$ within the TZC-model) have an influence on particle flows through orifices in fluidized beds. This approach was implemented into the two-zone continuum model (Section 7.7) to determine mass flow rate of particles entering the Wurster tube. The results of it show in Figure 8.2 that the Wurster suction rate $\dot{M}_{wt,tor}$ increases at low inlet gas velocities in vicinity of the minimal-Wurster-fluidization limit, reaches a maximum, and decreases then at greater inlet gas velocities. The inlet gas velocity of the bed discharge experiments is clearly above the minimal-Wurster-fluidization point, in a range where reduced particle concentration lowers the Wurster suction rate. Likewise to this, the potential bed outlet hit rate $\dot{M}_{p,hit}$ would decrease with higher inlet gas mass flow rates and temperatures due to smaller particle concentration. The bed discharge curves of the EBD-1 experiments, however, show the opposite trend. The bed particle discharge rates $\dot{M}_{sep}$ are the greater, the higher the inlet gas mass flow rates and temperatures are, even if only to a little extent. Considering this experimental tendency and the findings from the TZC-model to be true, a conclusion would be that the discharge kinetics of the EBD-1 experiments are not dominated by fluidization conditions (drop-out mechanism), but by the conveying behavior of the feed-out double-pinch valve. Nevertheless, as mentioned before, the presented dependency of bed discharge dynamics on inlet gas parameters ascertained within the EBD-1 experiments is not proven yet because of the lack of information about the absolute pressures inside the fluidized bed and the classifier (p_{bed} and $p_{g,sep}$, see Figure 9.8), and because of the small number of experiments.

Parameter setting of the feed-out double-pinch valve for optimal conveying and classification

The bed discharge rates should be a few times higher than the total input of solids (sum of the nuclei feed rate and the solids spray rate) in continuous granulation. Otherwise, it would come to steady bed mass accumulation, which ends in process destabilization. The results of this substudy show that the conveying rates of the feed-out double-pinch valve can be roughly controlled by open-state times of the pinch valves; but, feed-out rates are limited upwards. The largest bed discharge rates were obtained for open-state times of 0.5 to 1 s of the upper pinch valve ($t_{V1,sep}$) with an open-state time of 0.14 s of the lower pinch valve ($t_{V2,sep}$). Operation with larger conveying rates would increase the separation frequency of bed granules in continuous granulation process. However, bigger discharge rates of a single particle sluice lead to higher particles concentrations inside the classifier, and therefore, to more turbulences in the separation gas, which finally worsens the classification performance. This effect has already been shown by experiments of Hampel [2], where separation sharpnesses had been determined for classification processes with different switching times of the double-pinch valve. The double-pinch valve setting of the experiment EBD-21 had the lowest feed-out rates in the entire study with $t_{V1,sep} = t_{V2,sep} = 0.1\,\text{s}$. This would be the best choice in terms of separation performance. The average conveying rate between bed mass values of 1.5 and 1 kg is ascertained with round 1.27 kg/h for the parameter setting of EBD-21. This value is still larger than the total inputs of solids planned for the continuous granulation experiments of Section 10.4 (see Table 10.15), but not very much. The double-pinch valve setting with $t_{V1,sep} = t_{V2,sep} = 0.14\,\text{s}$ provides clearly higher mass flow rates, as shown with EBD-1 experiments and the EBD-22 experiment. The average conveying rates of Table 10.12 lie between 2.92 and 5.58 kg/h, which is several times larger than the total input rates of solids in the continuous granulation experiments, and which is sufficient to avoid overcharging of the fluidized bed, generates a better control dynamic of the bed mass, and ensures process stability. An even switching rhythm of the classifier-related double-pinch valve with 0.14 s had already been used in stable continuous granulation experiments of Hampel [1,2]. The present analysis of the bed discharge dynamics underpins the choice of these switching times. However, the pressure of the pneumatic control air $p_{g,dpv}$ was not specified in [1,2]. It was set at 4 bar here, as the fluctuations in conveying rates were relatively small for this pressure value.

10.4 Continuous granulation with external product classification

Several continuous Wurster granulation experiments with external product classification (here by a straight-duct air classifier) were conducted for this study with the goal to find an overall operation concept that can accomplish the following requirements:

- process stability in terms of fluidization conditions,
- bed mass control,

- achievement of steady state conditions (in a practical sense) with acceptable fluctuations in bed mass and product size characteristics,
- control of product mean size for large-growth granulation conditions, and
- short startup times.

The focus of the present thesis lies on adjustable product size, larger particle growth, and fast startup in contrast to former research of Hampel [1, 2], where continuous granulation had been investigated with the same experimental equipment and setup detailed in Section 9.2. The desired particle growth ratio $\Phi_{d,set}$, which has been introduced within the scope of the ideal continuous layerwise granulation model in Section 3.1.3, is the main objective quantity here. The term, large-growth granulation, implies that the target-growth ratio is much larger than unity: $\Phi_{d,set} \gg 1$. In the continuous granulation experiments, desired particle growth ratios of up to 2.5 are tried to be achieved. In total, eight different overall operation concepts are defined for this purpose, as shown in Section 10.4.1. Hereby, the processing strategies PS1, PS2-a, and PS2-b, which were previously designed in Section 9.4.11, shall be assessed for various desired particle growth ratios. The experiments of the strategy PS1 (see Section 10.4.2) were realized only with the automatic operation mode of the feed-back control system described in Section 9.4.8. The results of them serve to find an optimal gain factor K_m of the employed proportional bed mass control function in Eq. 9.34. The other experiments (see Section 10.4.3) have been operated with the processing strategies PS2-a and PS2-b, where continuous granulation is started up within an initiating manual bed mass control period (short: manual control period), before the control system is set to the automatic mode. Beside this, two process parameters - the spray-to-feed rate ratio $\Phi_{m,set}$ and the set separation gas velocity $u_{g,set}$ - are adapted to the desired growth ratio $\Phi_{d,set}$ for the automatic control period in each processing strategy by the equations of Section 9.4.5 and Section 9.4.6. These relations were derived from the ideal particle growth model in Chapter 3 and proved by PB-simulations in Chapter 6 to be suitable for stable continuous granulation with adjustable product size. At this, the set spray rate $\dot{M}_{spr,set}$ and set feed rate $\dot{M}_{f,set}$ are calculated according to the spray-to-feed rate setting method SFM2 of the ideal granulation model, given in Table 3.1. Most of the presented continuous granulation experiments should be conducted as startup processes of nine hours. A few of them had been continued in follow-up experiments of another nine hours on a later date. By this, long-term stability of the control system - especially of the P-controller - shall be demonstrated. But also *oscillations in bed particle and product size distributions* can be observed better. Further, the manual control periods of PS2-a and PS2-b involve two growth acceleration substrategies, respectively, which were defined in Section 9.4.10. In the first of them (indicated by GAS1), the feed rate is step-wisely increased from zero to the set feed rate, which ensues from SFM2, during the entire manual control period. The second substrategy (indicated by GAS2) pursues the aim to control bed mass by two alternating operation modes of the classifier (total reflux and total discharge mode, see Section 9.4.9). Hereby, size-selective effects on bed granule size distribution shall be suppressed during the manual control period. The influence of the growth acceleration substrategies on oscillating effects and startup times is investigated in addition. The choice of other process parameters is based on previous researches of Hampel [1, 2] and on results of the two-zone continuum model in Chapter 8, discontinuous granulation experiments in Section 10.1, and the dosing analysis of the feeding equipment in Section 10.2. Moreover, the two feed rate control methods F1 and F4, the operation principles of which are explained comprehensively in Section 9.4.3, were applied in this study. The method F1 offers automatic feeding of external nuclei; though, it is accompanied by dosing fluctuations. On the contrary, dosing of nuclei is precisely defined in the method F4, but it must be controlled by hand then. However, the model-based parameter setting method SFM2 can be better evaluated with a more accurate adjustment of the feed rate.

10.4.1 Overall operation concepts and parameter setting

The setup of the utilized equipments for nuclei feeding, spraying, Wurster fluidization, air classification, inline data acquisition, bed mass control, and material sampling (bed granules and product) is described in Section 9.2.2 and illustrated in Figure 9.4. The design of different overall operation concepts, that include processing procedures and the parameter setting, is outlined in the following.

Definition of overall operation concepts, startup, and follow-up experiments

As mentioned before, different processing strategies (PS1, PS2-a, and PS2-b), feed rate control methods (F1 and F4), gain factors (K_m in Eq. 9.34), and desired particle growth ratios ($\Phi_{d,set}$) are employed for the

index of operation concept	process-ing strategy	feed rate control method	K_m [m/s/kg]	$\Phi_{d,set}$ [−]	number of follow-up experiments
EC-11	PS1	F1	1	1.3	-
EC-12	PS1	F1	3	1.3	-
EC-13	PS1	F1	5	1.3	-
EC-21	PS2-a	F1	3	1.6	-
EC-22	PS2-a	F1	3	1.9	1
EC-31	PS2-b	F4	3	1.9	-
EC-32	PS2-b	F4	3	2.2	2
EC-33	PS2-b	F4	3	2.5	-

Table 10.13: Overview on main attributes of operation concepts applied in this continuous granulation study and numbers of follow-up experiments.

parameter setting in this study. Their influence on process behavior and product characteristics shall be primarily investigated here. Several combinations of these attributes define the overall operation concepts of the experiments in essence. They are given in Table 10.13. The diverse operation concepts are denoted by an alphanumeric experimental reference code that contains the two letters "EC" at the beginning, where "E" stands for experiment, "C" for continuous, and two subsequent digits. The first digit is related to the utilized processing strategy, and the second one indicates that either the gain factor K_m or wanted granule size enlargement ratio $\Phi_{d,set}$ is varied. The processing strategy PS1 is applied in the first three startup experiments (EC-11 to EC-13), PS2-a in the next two startups (EC-21 and EC-22), and PS2-b in the last three ones (EC-31 to EC-33). The nuclei feed rate was firstly controlled by the method F1 in the experiments EC-11 to EC-22, and later by F4 in experiments of EC-31 to EC-33. The more precise dosing of F4 promises a more accurate product size control under steady state conditions. The gain factors K_m of the first three startups were changed between 1, 3, and 5 m/s/kg. The focus of this parameter variation lies on the evolution of bed mass M_{bed} and separation gas velocity u_g that ensues from the control system. A gain factor of 3 m/s/kg was chosen for the subsequent experiments, because it had shown the best performance in terms of both bed mass and product size control - more on this later. Large-growth granulation was not the goal in the first three startup experiments, whereat the desired particle growth ratio was set to 1.3, respectively. However, it is one of the goals to find an overall operation concept, wherewith stationary large-growth granulation can be performed. For this reason, the desired particle growth ratios were increased for the subsequent operation concepts to 1.6 in EC-21, 1.9 in EC-22 and EC-31, 2.2 in EC-32, and 2.5 in EC-33. Table 10.13 shows further, which operation concepts were also realized in follow-up experiments. At this, EC-22 was continued in one and EC-32 in two follow-up experiments. In order to distinguish between preceding and subsequent experiments, another number is added to the indices of operation concept according to:

- EC-22-1 for the startup of EC-22,
- EC-22-2 for the follow-up experiment of EC-22,
- EC-32-1 for the startup of EC-32,
- EC-32-2 for the first follow-up experiment of EC-32,
- EC-32-3 for the second follow-up experiment of EC-32.

The follow-up experiments were operated in automatic bed mass control mode from the beginning on and with same parameter setting, with which the preceding experiments had been finished.

Uniform process parameters

Some of the process parameters were equal among all presented continuous granulation experiments including startups and follow-up processes. These are listed in Table 10.14 and described below. The set bed mass of the feed-back control system was defined with $M_{set} = 1$ kg in automatic mode. Further, an initial bed mass of $M_{bed,0} = 1$ kg were prepared for all startup processes. The initial bed masses of the follow-up experiments deviated from this value, as they were taken from the final bed mass of their preceded experiments. As spray

material, an aqueous solution of sodium benzoate with a solids mass fraction of $x_s = 32.25\,\%$ was used. The inlet gas mass flow rate $\dot{M}_{in}$ and temperature T_{in} were chosen with 70 kg/h and 90°C to provide enough drying power for evaporating the injected water content of the spray material. The results of the two-zone continuum model of wet Wurster fluidization with comparable process chamber dimensions have shown in Section 8.4 that these inlet gas conditions deliver more than enough evaporation energy to avoid process gas saturation for an exemplary water spray rate of 677.5 g/h. The largest water spray rate, that was operated within the experiments, measured around 700 g/h. Furthermore, stable Wurster granulation with same process chamber configuration could be generated in the discontinuous experiments (Section 10.1.2) for such inlet gas parameters, but only with sufficiently large nozzle gas overpressures $p_{g,noz}$. The latter had to be corrected to ensure Wurster fluidization stability as shown later in the discussion of varied parameters. The open-state times of the classifier-related double-pinch valve $t_{V1,sep}$ and $t_{V2,sep}$ were both set to 0.14 s. Pure classification experiments of Hampel (without injecting spray solids) have shown that this double-pinch valve setting generates an adequate separation performance. The air pressure of the pneumatic control system $p_{g,dpv}$, wherewith the double-pinch valves of the nuclei feeding and classification equipments were switched, was fixed at 4 bar. The dimensions of the nuclei equipment, process chamber, configuration of Wurster tube, and the classification equipment are specified in Figure C.2. The design of the inlet gas distributor plate (perforated metal plate pictured in Figure C.3) is given in Appendix C.2.2.

Model-based parameters

Appropriate estimates of several model-based parameters are required to adapt spray-to-feed rate ratios $\Phi_{m,set}$ (a part of parameter setting method SFM2, see Eq. 9.27) and set separation gas velocities $u_{g,set}$ (Eqs. 3.5 and 9.29) to desired particle growth ratios $\Phi_{d,set}$. These parameters are the mass loss fractions of nuclei $\Phi_{f,loss}$ (core material) and sprayed solids $\Phi_{spr,loss}$ (coating material), the mean nuclei diameter $d_{m,f}$, the effective nuclei density ρ_f, and the effective coating density ρ_c. The choice of their values is described in the following. Those of them which were set constantly in this study are also listed in Table 10.14.

The mass loss fraction of nuclei $\Phi_{f,loss}$ and sprayed solids $\Phi_{spr,loss}$ had not been considered for the first granulations experiments of processing strategy PS1. The related material loss fractions are given then with zero. Only after first results of the discontinuous experiments (Section 10.1), it was noticed that significant losses of bed mass occur during granulation with the employed equipment. But, the exact proportions of the component losses are difficult to measure. For reasons of simplicity, the losses of coating mass are presumed to be substantially greater than those of core material; wherefore, the nuclei loss fraction was set to zero ($\Phi_{f,loss} = 0$) for all remaining continuous granulation experiments, too. The coating mass loss fraction, however, has to be larger than zero. The estimation of it is explained below in the context of the varied parameters of this study.

Two production batches of Cellets®200 - the particle size distributions of which have significant differences - have been used as initial granulator holdup and as external nuclei to be fed continuously. Their particle size distributions, indicated here by IM-2 and IM-3, are shown in Figure C.1. Other particle characteristics of IM-2 and IM-3 are given in Table C.1. The mean diameters of these materials deviate relatively strongly from each other with circa 328 µm for IM-2 and with round 262 µm for IM-3. But, the effective particle density of both delivery batches was stated with 1380 kg/m^3 in manufacturer's specification sheets, as previously described in Section 9.1. This value has been adopted as effective nuclei density ρ_f in the parameter setting. The effective coating density ρ_c is calculated here on basis of X-ray micro-tomography analysis of Hampel [2], where layer porosities of sodium benzoate coatings on core particles of Cellets®200 were measured. The author stated a coating layer porosity of $\varepsilon_c = 43\,\%$ and a compact coating density of $\rho_{s,c} = 1440\,\mathrm{kg/m^3}$. By this, the effective coating density ensues to 820.8 kg/m^3 via $\rho_c = \rho_{s,c}(1 - \varepsilon_c)$. It is mentioned at this point that, in the present thesis, effective coating densities of products from discontinuous granulation experiments of Section 10.1.6 were analyzed by a different method, which is derived in Section 9.3. Although same material combination and inlet gas conditions were investigated, the layer porosities of the presented measurements are smaller than Hampel's findings. However, they were determined after this continuous granulation study and have therefore not been used here.

Varied parameters

Table 10.15 gives an overview on further process parameters in the order of the operation concepts of Table 10.13. The choice and/or calculation of their values is explained in the following. The nozzle gas excess pressure $p_{g,noz}$ was set presumably too low with 1.5 bar in the first three startups (EC-11 to EC-13),

name	symbol	unit	value
process parameters:			
set bed mass*)	M_{set}	[kg]	1
solids mass fraction of spray liquid	x_s	[%]	32.25
inlet gas mass flow rate	$\dot{M}_{in}$	[kg/h]	70
inlet gas temperature	T_{in}	[°C]	90
open-state time of V1**)	$t_{V1,sep}$	[s]	0.14
open-state time of V2**)	$t_{V2,sep}$	[s]	0.14
pressure of pneumatic control air	$p_{g,dpv}$	[bar]	4
model-based parameters:			
feed material loss fraction	$\Phi_{f,loss}$	[%]	0
effective nuclei density	ρ_f	[kg/m^3]	1380
compact coating density	$\rho_{s,c}$	[kg/m^3]	1440
coating layer porosity	ε_c	[%]	43
effective coating density	ρ_c	[%]	820.8

Table 10.14: Uniform process parameters and model-based parameters of the presented continuous granulation experiments; *) only for automatic bed mass control periods; **) classifier-related double-pinch valve.

whereof two broke down at the end of the experiments. As shown in Section 10.1, the instable discontinuous experiment EB-12 (see Table 10.2) was also conducted with this pressure value. Therefore, the nozzle gas overpressure was set to 1.75 bar in the subsequent continuous granulation experiments (EC-21 to EC-33). These could be then entirely executed under stable process conditions. As stated above, a spray loss fraction had not been considered in the first three granulation experiments, wherefore it is defined with zero in this case. This material loss fraction was introduced for the succeeding continuous experiments EC-21 to EC-33 after first outcomes of the discontinuous granulation study. At this, a rough estimate of 20 % was chosen from calculations of several batch experiments (see Section 10.1.4) for the rest of the continuous granulations study. The nuclei IM-2 had been fully consumed in the experiments of EC-11 to EC-21. The new material IM-3 was therefore procured from the same manufacturer (HARKE GROUP) and used in the remaining operation concepts: EC-22 to EC-33. The aforementioned mean diameters $d_{m,f}$ of the initial materials are also listed in Table 10.15. The corresponding desired product diameters $d_{pr,set}$ are obtained by multiplication of mean diameter and desired particle growth ratio: $d_{m,f}\Phi_{d,set}$. As described above, the parameter setting method SFM2 of Table 3.1 shall be applied in all automatic control periods of the experiments; whereby, spray-to-feed rate ratios $\Phi_{m,set}$ are adapted to the desired growth ratios $\Phi_{d,set}$ of the operation concepts. Therefore, a certain spray rate has to be pregiven for each experiment, as shown in Section 9.4.5. These were adjusted by the rotation speed of the connected pump n_{pum}, with 8 rpm for the experiments EC-11 to EC-13, 7 rpm for EC-21 and EC-22, and 9 rpm for EC-31 to EC-33. It was set the highest in the last three operation concepts in order to increase growing-up kinetics, and therefore, to reach larger particle growth ratios in shorter times. The predicted set spray rates $\dot{M}_{spr,set}$ were determined by the empirical correlation in Eq. 9.25. The required set feed rates $\dot{M}_{f,set}$ of automatic control periods ensue from Eqs. 9.26 to 9.28. The set separation gas velocity $u_{g,set}$ of the P-controller in Eq. 9.34 is coupled to the desired growth ratio $\Phi_{d,set}$ via Eq. 9.29 and $d_{pr,set} = d_{m,f}\Phi_{d,set}$, but only for the automatic mode of bed mass control.

Adjustment of feed rate in automatic control periods

In both control methods F1 and F4, one of two control parameters (see Section 9.4.12) is needed to be fixed, which is here the estimate dosage mass of a single sluiced nuclei package (symbolized by $M_{dos,f,est}$) for F1 and the dosing time gap (symbolized by $\Delta t_{dos,f}$) for F4. The estimate dosage mass was assumed with $M_{dos,f,est} = 11.3$ g for all experiments with method F1 (EC-11 and EC-22). This value was taken from the dosing behavior analysis of Section 10.2. At this, it matches to one result of the experimental series EF-2, where the nuclei material IM-2 was conveyed with open-state times of 10 s for the upper pinch valve ($t_{V1,f}$) and of 1 s for the lower pinch valve ($t_{V2,f}$). The feed container was filled with 6 kg of nuclei in all F1 experiments. By using the estimated dosage mass in Eq. 9.44, dosing cycle times of the double-pinch valve $t_{dpv,f}$ are calculated for the F1-experiments. The opening times of the upper and lower pinch

operation concept	$p_{g,noz}$ [bar]	$\Phi_{spr,loss}$ [%]	nuclei material*)	$d_{m,f}$ [µm]	$d_{pr,set}$ [µm]	n_{pum} [rpm]	$\dot{M}_{spr,set}$ [g/h]	$\dot{M}_{f,set}$ **) [g/h]	$u_{g,set}$ **) [m/s]
EC-11	1.50	0	IM-2	328	426	8	913.6	413.9	1.76
EC-12	1.50	0	IM-2	328	426	8	913.6	413.9	1.76
EC-13	1.50	0	IM-2	328	426	8	913.6	413.9	1.76
EC-21	1.75	20	IM-2	328	524	7	799.4	112.0	2.02
EC-22	1.75	20	IM-3	262	498	7	799.4	59.2	2.30
EC-31	1.75	20	IM-3	262	498	9	1027.8	76.1	2.30
EC-32	1.75	20	IM-3	262	576	9	1027.8	46.2	2.59
EC-33	1.75	20	IM-3	262	655	9	1027.8	30.5	2.88

Table 10.15: Varied parameters and employed nuclei materials of the presented continuous granulation experiments in the order of applied operation concepts; *) specified in Tables 9.1 and C.1; **) only in automatic bed mass control periods.

valves of method F1 follow from Eq. 9.45. The respective values are given on the left hand side of Table 10.16. It should be noted that these double-pinch valve settings are only used in automatic control periods, which is the case for the entire startup experiments with strategy PS1 (EC-11 to EC-13), for the last four hours of the startups with PS2-a (EC-21 and EC-22-1), and for the entire follow-up process of EC-22-2. In automatic control periods, the actual set feed rate $\dot{M}_{f,set,k}$ of Eq. 9.40 complies with the set feed rate $\dot{M}_{f,set}$ of parameter setting method SFM2, and the value of the feed rate step function $\Phi_{f,step}$ equals unity. In the PS1-experiments of this study (EC-11 to EC-13), the set feed rates are identical; hence, the double-switch time was set uniformly with $t_{dpv,f} = 98.3\,\text{s}$ here. The single dosage time periods are larger for the operation concepts EC-21 and EC-22, as their set feed rates are lower than in previous concepts (EC-11 to EC-13). The single open-state times ($t_{V1,f}$ and $t_{V2,f}$) should be equal for all F1-experiments, actually. But, it can be seen that they differ by 0.1 s in the startup of EC-22 for two reasons. Firstly, only four digits with displaceable decimal point can be configurated on the switch panel of the pneumatic control system (No. 4 in Figure 9.4), and secondly, the summation condition of Eq. 9.11 shall be fulfilled. The dosing time gap of method F4 was defined with thirty minutes ($\Delta t_{dos,f} = 30\,\text{min}$) for automatic control periods of the PS2-b-experiments (EC-31 to EC-33). The single dosage masses $M_{dos,f,k}$, which had to be prepared with the F4-method, ensue from Eq. 9.46. Their values are shown on the right hand side of Table 10.16, where the single open-state times are also listed. They were defined constantly with $t_{V1,f} = t_{V2,f} = 1\,\text{s}$ in all PS2-b-experiments in order to insert single doses quickly. The single dosage masses are small with values up to 38.05 g. However, it took quite a lot dosing cycles (up to 15 double-switches) to completely feed it into the process chamber - because the filling level of the feed container is practically zero in method F4, so that strong flush-back effects (explained in Section 9.4.3) emerged in these experiments.

Adjustment of feed rate in manual control periods (GAS1)

As mentioned before, successively increased feed rates of the growth acceleration substrategy GAS1 are wanted to be achieved within manual control periods. These had to be adjusted too in the startup experiments with method F1 (EC-21 and EC-22) and F4 (EC-31 to EC-33). The reduced feed rates of the F1-experiments should be generated for time steps of one hour according to the feed rate step function of PS2-a in Figure 9.11. The required double-switch times can be obtained via division of the dosing cycle time of the automatic bed mass control periods (Table 10.16) by the feed rate step function: $t_{dpv,f}/\Phi_{step,f}$. According to this, relatively high values of dosing cycle time arise especially in the second experimental hour with 1816 s for EC-21 and 3436.5 s for EC-22. Automatic operation of the double-pinch valve becomes impractical under those conditions. Therefore, the desired feed rates were approximated by feeding single nuclei doses manually after evenly distributed time intervals. At this, the number of dosages was adapted to actual set feed rates $\dot{M}_{f,set,k}$ (Eq. 9.40). These numbers are listed in Table 10.17. Lowered feed rates (in long-term perspective) of the F4-experiments can still be realized precisely. For this purpose, the dosing time gap $\Delta t_{dos,f}$ of method F4 was also fixed to thirty minutes, and smaller nuclei dosages ($M_{dos,f}$) were prepared pursuant to Eq. 9.46.

control method F1				control method F4			
operation concept	$t_{dpv,f}$ [s]	$t_{V1,f}$ [s]	$t_{V2,f}$ [s]	operation concept	$M_{dos,f}$ [g]	$t_{V1,f}$ [s]	$t_{V2,f}$ [s]
EC-11 to EC-13	98.3	49.15	49.15	EC-31	38.05	1	1
EC-21	363.2	180.6	180.6	EC-32	23.11	1	1
EC-22	687.3	343.7	343.6	EC-33	15.24	1	1

Table 10.16: Control parameters of the feed rate control methods (F1 and F4) for the employed overall operation concepts (EC-11 to EC-33) of the present study.

experimental time period [h]:	0 - 1	1 - 2	2 - 3	3 - 4	4 - 5
number of dosages for EC-21 [−]:	0	2	4	6	8
number of dosages for EC-22 [−]:	0	1	2	3	4

Table 10.17: Number of dosages of nuclei for different experimental time periods of the growth acceleration substrategy GAS1 in experiments with processing strategy PS2-a (EC-21 and EC-22).

Manual bed mass control (GAS2)

The growth acceleration substrategy GAS2 (manual bed mass control) was realized in the same manner for startup experiments of processing strategy PS2-a (EC-21 and EC-22) and PS2-b (EC-31 to EC-33). The main constants have already been specified in Table 9.5. Accordingly, the manual control periods are conducted for five hours with ten *reflux-discharge cycles*, that end every thirty minutes. The necessary operation modes of the classifier - total reflux and total discharge - are generated by setting the hand control panel (illustrated by the input field in Figure 9.9) of the monitoring system with different combinations of the set separation gas velocity $u_{g,set}$, the gain factor K_m, and the set bed mass M_{set}. The values of them are given in Table 10.18. At this, each of these parameters is set to maximum of the adjustment range for the total reflux and to zero for the total discharge periods.

Sampling of bed material and product - experimental subsections

The time coordinate of continuous granulation experiments is divided into several subsections of thirty minutes, in which a sample of the bed material and of the product are withdrawn. Bed particle samples are taken from the granulator always in the middle of an experimental subsection, which means around the 15th, 45th, and 75th minute of the experiment, and so on. This procedure takes circa one minute. The sampling orifice for bed material is located on the process chamber wall in height of the fluidization region, as illustrated with No. 14 in Figure 9.4. Product samples, on the contrary, are collected during the entire *experimental subsections* by a small container at the classifier bottom outlet, see No. 11 in Figure 9.4. These sample bottles are exchanged every thirty minutes, which means at the 30th, 60th, and 90th minute of the experiment, and so on. However, product characteristics are related to the mean time point of their sampling periods, and therefore, to almost the same time points as the bed particle samples.

10.4.2 Optimization of the gain factor

The results of the PS1-experiments (EC-11, EC-12, and EC-13) are presented in this section. The gain factor K_m of the P-control function has been varied between 1 m/s/kg for the EC-11-, 3 m/s/kg for the EC-12-, and 5 m/s/kg for the EC-13-experiment. Out of these experiments, an optimal gain factor was chosen, which had

classifier operation mode	$u_{g,set}$ [m/s]	K_m [m/s/kg]	M_{set} [kg]
total reflux	5	12	2
total discharge	0	0	0

Table 10.18: Parameter combinations of P-control function Eq. 9.34 for two classifier operation modes (Section 9.4.9): total reflux and total discharge mode; used in manual bed mass control periods.

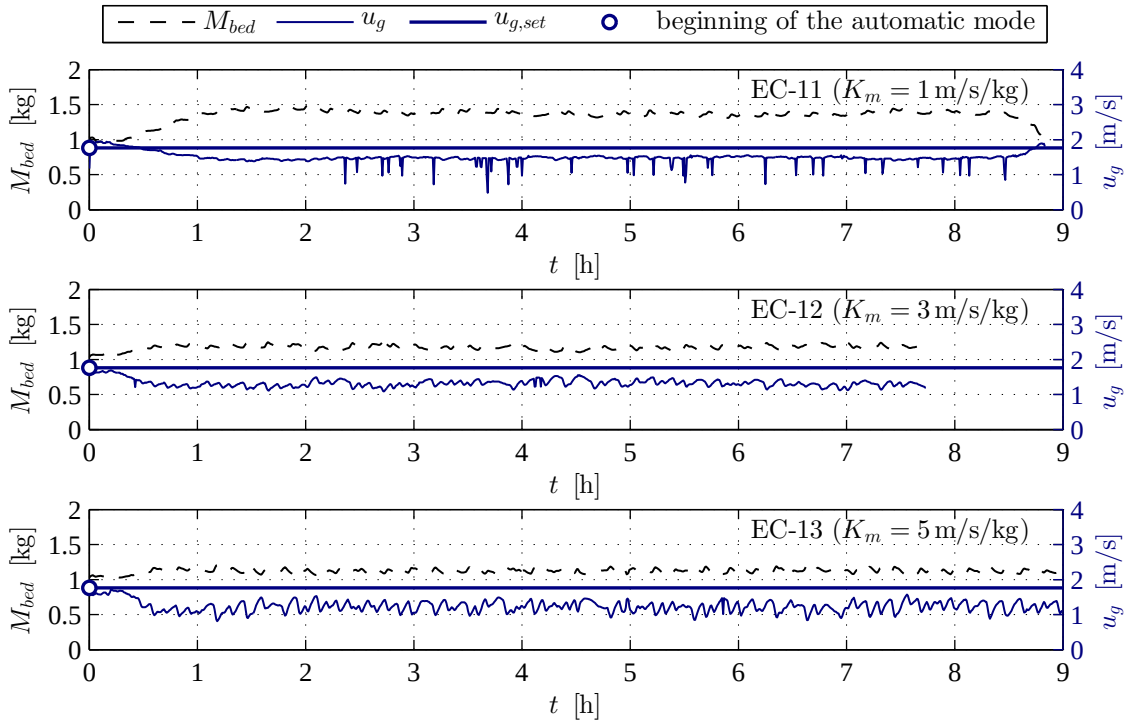

Figure 10.18: Bed mass M_{bed} and separation gas velocity u_g with process time for three startup experiments*) of continuous granulation with different gain factors K_m and a desired particle growth ratio $\Phi_{d,set}$ of 1.3; *) operation concepts EC-11, EC-12, and EC-13 specified in Tables 10.13 and 10.15.

shown the best *overall process behavior* of the employed control system of Section 9.4.8. The focus here lies on bed mass control, manipulation of separation gas velocity, and *signal transduction* to the classifier-related mass flow controller.

Temporal curves of bed mass and separation gas velocity

In order to evaluate process behavior, two measurement quantities are analyzed. The first is the detected bed mass M_{bed}, which is calculated from inline measurements of the chamber pressure drop Δp_{app} as described in Section 9.4.7. The second is the separation gas velocity u_g, which comes from an output signal of the classifier-MFC. Figure 10.18 contrasts the temporal curves of bed mass M_{bed} (dashed lines) and separation gas velocity u_g (solid lines) for each experiment. The bed mass control deviation is oriented to the set point of $M_{set} = 1\,\mathrm{kg}$ in each experiment from the beginning on. The set separation gas velocity was fixed uniformly with $u_{g,set} = 1.76\,\mathrm{m/s}$, which is also plotted in the diagrams by horizontal solid bold lines. The circles in the set separation gas velocity mark the starting time point of automatic feed-back control of bed mass. These are located here at $t = 0$ and at $t = 5\,\mathrm{h}$ in the other startup experiments of EC-21 to EC-33, shown below. It can be seen that the bed mass increases at the beginning of each process and converges into a *constant fluctuation range*. Furthermore, the separation gas velocity curves evolve inversely to the bed mass. But also clearly visible fluctuations are ascertained in the separation gas velocity measurements for each experiment, whereat the u_g-line of EC-11 has considerable outliers. These are perhaps caused by *errors in signal processing*. Disregarding the outliers, it becomes obvious that the fluctuations of separation gas velocity are enhanced by higher gain factors. The first two experiments could not be conducted for entire nine hours due to strong agglomerations, which blocked the Wurster tube and destabilized Wurster fluidization. These breakdowns emerged after around 8.5 h in the experiment EC-11 and after around 7.5 h in the experiment EC-12. However, the granulation experiments were operated long enough to make meaningful statements about process evolution with the implemented control system.

index of startup	$\bar{M}_{bed}$ [kg]	$\bar{u}_g$ [m/s]	$\bar{\zeta}_m$ [%]	$\bar{\zeta}_u$ [%]	$\sigma_{M_{bed}}$ [g]	σ_{u_g} [m/s]
EC-11	1.38	1.45*)	38.1	17.4*)	35.2	0.05*)
EC-12	1.18	1.31	17.8	25.5	28.9	0.09
EC-13	1.13	1.21	12.7	31.1	26.8	0.14

Table 10.19: Mean value, average relative control deviation, and standard deviation in bed mass and separation gas velocity of the time period $1 \leq t \leq 7\,\mathrm{h}$ in the continuous granulation experiments EC-11, EC-12, and EC-13; *) outliers excluded.

Evaluation of control errors and degrees of fluctuation

Several statistical quantities have been determined between the first and seventh hour ($1 \leq t \leq 7\,\mathrm{h}$) of the bed mass and separation gas velocity curves to evaluate their control errors and degrees of fluctuation. These are mean values ($\bar{M}_{bed}$ and $\bar{u}_g$), relative control deviations ($\bar{\zeta}_m$ and $\bar{\zeta}_u$), and standard deviations ($\sigma_{M_{bed}}$ and σ_{u_g}). The results of them are listed in Table 10.19 for each PS1 experiment. The relative control deviations are formally the same process success indices as defined in Section 5.4 and used in the PB-simulation study of Section 6.1. But, the relative control errors of the experiments are determined from the mean values according to:

$$\bar{\zeta}_m = \frac{|\bar{M}_{bed} - M_{set}|}{M_{set}}, \tag{10.27}$$

$$\bar{\zeta}_u = \frac{|\bar{u}_g - u_{g,set}|}{u_{g,set}}. \tag{10.28}$$

By this, it becomes evident that higher gain factors lead to lower bed mass control errors, but also to higher control deviations in separation gas velocity. Hence, *control accuracy* cannot be improved for both, bed mass and separation gas velocity, at the same time by gain factor variation. At this, the smallest relative control deviation in bed mass is observed with 12.7 % and the lowest in separation gas velocity with 17.4 %. However, the main objective of the utilized bed mass controller (Section 9.4.8) is to maintain stable Wurster fluidization, wherefore the current bed mass is only needed to be hold within a certain range of values. Such conditions are guaranteed between around 0.7 and 1.5 kg for the employed granulator (ProCell LabSystem, see Section 9.2.1), external nuclei material (Cellets®200, see Table 10.15), and spray solution (sodium benzoate in water). Thus, large relative control deviations in bed mass up to 50 % can be accepted. Thereby, desired separation gas velocities can be achieved better for the benefit of a more reliable product size control. From this point of view, the lowest gain factor would be favored. Another aspect is the degree of fluctuation in the bed mass and separation gas velocity curves, which shall be quantified by the respective standard deviations $\sigma_{M_{bed}}$ and σ_{u_g} of Table 10.19. At this point, it is mentioned that the u_g-outliers were excluded from the determination of statistical quantities of Table 10.19. The standard deviations of the M_{bed}- and u_g-curves have the same tendency with increasing gain factors as the corresponding mean values; which means that higher gain factors result in lower fluctuations of the bed mass and larger variations of the separation gas velocity. But the magnitude of bed mass fluctuations hardly influences process stability even when maximal, as in EC-11. By contrast, increasing fluctuations of the separations gas velocity with higher gain factors can have a significant effect on the product classification. Considering these arguments, lower gain factors should be preferred too. However, the aforementioned outliers of separation gas velocity are also taken into account for the choice of an optimal gain factor, as described below.

Decision for optimal gain factor - compromise

The main conclusions of the bed mass and separation gas velocity evolution are recapitulated briefly here. The *permissible bed mass control range* is large in terms of process stability, whereas acceptable margin of separation gas velocity is low in terms of product size control. When considering these aspects, it would be favorable to operate continuous granulation by proportional bed mass control with the lowest gain factor K_m. But in order to avoid a repeated occurrence of strong outliers in separation gas velocity, it was decided to use a gain factor of 3 m/s/kg as a compromise for the subsequently conducted granulation experiments.

Particle size evolution of bed and product

The number-based particle size distributions of the bed and product samples (symbolized by $q_{0,bed}$ and $q_{0,pr}$) are shown in Appendix C.5 (Figures C.6 to C.8). Beside $q_{0,bed}$- and $q_{0,pr}$-curves, all PSD-diagrams contain three process characteristics that indicate boundary conditions of particle growth in continuous granulation. These are the nuclei size distribution ($q_{0,f}$ - thin solid black line), the mean nuclei diameter ($d_{m,f}$ - vertical bold dashed black line), and the desired product diameter ($d_{pr,set}$ - vertical bold solid black line). As mentioned before, particle size evolution of the bed and product material was not the main focus of these startup experiments. Nevertheless, the results should be discussed briefly at this point. It is obvious that the PSD-curves of the bed and the product particles lie closely together for all samples in each of the depicted experiments. Particle growth in direction of the objective-grain size can be recognized. But both the bed and the product have wide particle size distributions, whereat the product granules are only slightly larger. The desired particle growth ratio of 1.3 is relatively low in these experiments, for which a sufficient size-selective product discharge cannot be realized with the employed classifier setting. The separation performance can be improved by, for instance, longer classifier tubes or other types of separators (e.g., zig-zag classifier or vibrating sieve), when such a granule size enlargement is aimed to be achieved. However, usage of a different separation technique was omitted. Instead of this, it was the goal to show that the installed experimental setting is suitable for continuous granulation processes with larger particle growth ratios, which can also be attained with a simple straight-duct air classifier despite of its imperfect separation behavior (low separation sharpness). This target is part of the subsequent section.

10.4.3 Continuous granulation with introductory manual control of bed mass and granule size

This section shows the continuous granulation experiments of the overall operation concepts from Table 10.13 with the processing strategy variants PS2-a (concepts: EC-21 and EC-22) in the first part and PS2-b (concepts: EC-11 to EC-33) in the second part. The PS2 experiments were started with an introductory manual control period of five hours, which included the two growth acceleration strategies GAS1 and GAS2. The automatic mode of the feed-back control system was then activated for the last four hours of the startups (EC-21, EC-22-1, EC-31, EC-32-1, and EC-33) and permanently retained in the follow-up experiments (EC-22-2, EC-32-2, and EC-32-3). The difference between the two PS2 variants is that the feed rate step function of the growth acceleration strategy GAS1 is less finely discretized in PS2-a than in PS2-b. Independently of this, feed rates are regulated according to the control method F1 in the PS2-a experiments and according to the control method F4 in the PS2-b experiments. The measurement properties, which are described in the previous Section 10.4.2, are also examined here. These comprise the inline measurement of fluidized bed mass M_{bed} and separation gas velocity u_g, but also offline measurements of the (number-based) particle size distributions of the bed $q_{0,bed}$ and the product $q_{0,pr}$. They are the most important properties to reflect process stability, performance in bed mass control, and product size development. The measurement results of the PS2-a experiments are shown in Figures 10.19 to 10.22, and these of the PS2-b experiments in Figures 10.23 to 10.28. In contrast to the PS1 experiments of Section 10.4.2, granule size evolution of the bed and product is considered in more detail for the PS2 experiments; whereat large-growth granulation, startup times, oscillation effects, and control accuracy make up the focus. Nuclei size distributions $q_{0,f}$, mean nuclei diameters $d_{m,f}$, and desired product diameters $d_{pr,set}$ are drawn in the PSD-charts of the PS2 experiments (as in the PS1 experiments) as orientation points, whereby the applied operating concepts can be better assessed. The effectiveness of the growth acceleration strategies GAS1 and GAS2 as well as possible reasons for inaccuracies in the product size control are discussed in Sections 10.4.4 and 10.4.5, in which the results of both variants PS2-a and PS2-b are summarized and contrasted with each other.

Manual control periods of PS2-a startups

The manual two-phase control of bed mass in the first five hours of the PS2-a startups (EC-21 and EC-22-1) can be clearly discerned in Figure 10.19 by means of the separation gas velocity curves ($u_g(t)$ - solid lines). Most of the time within the manual control periods, the classifier gas velocity is at the maximum value (around 8.5 m/s with neglected fluctuations) that could be created by the associated mass flow controller. At this, total reflux of particles entering the separation tube was generated, so that the bed mass enlarged. Small amounts of the bed material were discharged in regular time steps (round every half hour) by switching off the classifier gas supply, as can be seen in the diagrams too. The duration of these total discharge modes ($t_{off,i}$, described in Section 9.4.9) was varied by the system operators at their own discretion, depending on the

current bed mass value. The bed mass increased more in the manual control period of the EC-22-1 experiment than in EC-21. Therefore, longer total discharge periods of up to four minutes ($t_{off,i} \in \{1, 2, 3, 4\}$ min) were performed in EC-22-1, whereas these were only between one and two minutes in EC-21. It is presumed that large temporal changes in the particle mass flow through the feed-out double-pinch valve are the reason for the different bed mass development. The growth in fluidized bed mass within manual control periods of the EC-21 and EC-22-1 experiments is clearly visible in the first ten PSD-charts of Figures 10.20 and 10.21. Therein, the bed particle size distribution moves steadily in the direction of the target-product diameter $d_{pr,set}$ (vertical solid black line) and becomes wider. But the formation of bimodal $q_{0,bed}$-curves with a growing modal peak on the left and a shrinking modal peak on the right is also observed for somewhat advanced process times, after around three hours in the EC-21 and four hours in the EC-22-1 experiment. The largest part of the left modal peak consisted of nuclei which had been added to the granulator with a time delay in accordance with the GAS1 strategy. They increased with further process time, since the feed rate had been raised successively. The majority of the right modal peak represents the coated initial bed material (from $M_{bed,0}$). The number of these granules decreased during the manual control period through the total discharge modes. The product size distributions depicted for the first five hours ($q_{0,pr}$-curves) represent particles which had left the granulator-separator system during the total discharge modes. As part of the growth acceleration strategy, the aim was to prevent size-selective separation effects during the bed discharge modes. However, the $q_{0,pr}$- and $q_{0,bed}$-curves are not entirely identical in the respective experimental subsections (of half an hour). Instead, the product-PSDs are slightly shifted to larger diameters. This suggests an *internal classification effect* that can arise from size-dependent segregation in the fluidization area of the Wurster chamber and the low position of the outlet pipe on the chamber wall. The right peak of the bed-PSD of the EC-21 experiment with a smaller desired particle growth ratio (1.6) slightly exceeded the target-product size at the end of the manual control period ($4.5 - 5$ h); whereas an even lower percentage of the bed-PSD had reached the desired product diameter in the EC-22-1 experiment with a higher desired particle growth ratio (1.9) after the same time.

Automatic control periods of PS2-a startups

The beginning of the automatic control periods (five hours after start of process) of the EC-21 and EC-22 experiments is indicated in Figure 10.19 by circles on the $u_{g,set}$-lines. The bed mass recorded during the entire automatic control period is close to the setpoint ($M_{set} = 1$ kg) in the EC-21 experiment, while it grows steadily in EC-22-1. But in both cases, stable Wurster fluidization could be guaranteed. The solids spray rates to be set ($\dot{M}_{spr,s,set}$, Eq. 9.26) were the same in the two startups at around 258 g/h. Though, the total input of solids ($\dot{M}_{spr,s,set} + \dot{M}_{f,set}$) was greater in EC-21 ($\Phi_{d,set} = 1.6$), as the set feed rate was decreased to gain a higher desired particle growth ratio in EC-22-1 ($\Phi_{d,set} = 1.9$), see also Eqs. 9.27 and 9.28. Nevertheless, in the EC-21 example, more bed material could be unloaded. The reason for the different bed mass curves can be deduced from the granule size development of the fluidized bed depicted in Figures 10.20 and 10.21. The right modal peaks of the bed particle size distributions, which had developed in the manual control periods of the two startups, continued to move along the particle size coordinate and flattened out in the automatic control periods. Thus, the coarse fraction of the bed was gradually discharged. In contrast to EC-22-1, a significant proportion of the right modal peak of the EC-21 experiment grew above the target value, which also defines the desired separation diameter of the classifier. Therefore, the larger bed granules of the EC-21 experiment were able to exit the process through the product outlet more efficiently, resulting in lower bed mass values than in EC-22-1. After the seventh hour in the EC-21 and the eighth hour in the EC-22-1 experiment, the right modal peaks had disappeared, leaving monomodal bed-PSDs, the majority of which were much smaller than the desired product diameters. The *formation of a bimodality* of the $q_{0,bed}$-curves and the subsequent reformation to monomodal shapes lead to oscillations in the product size distributions. Such an oscillation is distinctly visible in the EC-21 results, but hardly for EC-22-1. However, the follow-up experiment EC-22-2 (Figure 10.22) shows that a PSD-oscillation of the product takes also place for the EC-22 concept, more on this below. The detected oscillations are characterized by an *overgrowth* beyond the target value and a subsequent *back-shift* towards smaller diameters, which can be seen very clearly in the automatic control period of the EC-21 startup. In the product-PSDs of EC-22-1, only a target-exceedance of the coarse fraction and a slight increase of fines (left tail) can be observed. In addition, the mean-value-based particle growth ratio ($\Phi_{d_m} = d_{m,f}^{-1} \int_0^\infty dq_{0,pr} \mathrm{d}d$) and the associated relative control deviation ($\zeta_d = \Phi_{d_m}/\Phi_{d,set} - 1$) have been determined for the last three hours of both startup experiments, which are listed in Table C.7. They reflect the PSD-oscillations on average. For example, in the seventh hour of the EC-21 process, relative deviations in product size control between 6 and 6.5 % (target exceeded) are

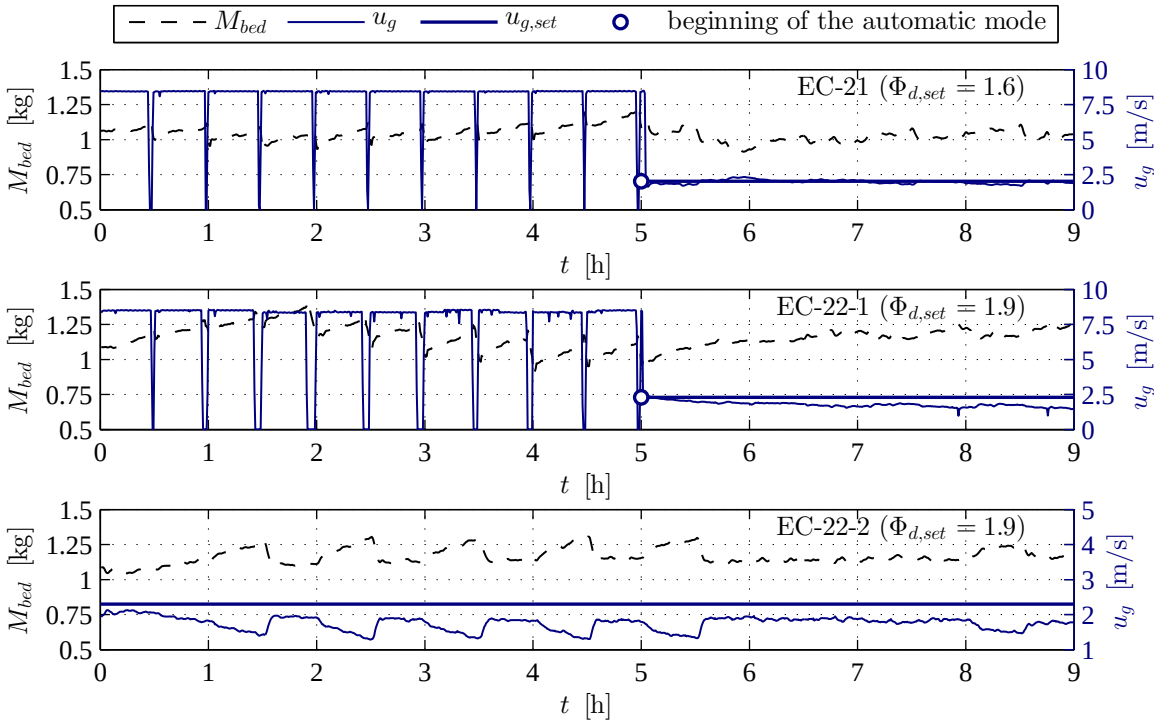

Figure 10.19: Bed mass M_{bed} and separation gas velocity u_g with process time for continuous experiments with different operation concepts: EC-21 and EC-22*) of Tables 10.13 and 10.15; *) employed in one startup EC-22-1 and one follow-up experiment EC-22-2.

ascertained, which afterwards decreased to negative values of up to −30 %. The relative control deviations of the EC-22-1 experiment were smaller than in EC-21 with absolute values of maximally 3.6 %. But at the end of this experiment, they tended to decline, which indicates the beginning of the PSD-oscillation found in the associated follow-up experiment EC-22-2. Finally, it can be said that the PSDs were still changing in the last hours of the automatic control periods, whereat this was quite strong in the EC-21 example and somewhat weaker in the case of EC-22-1. Hence, steady-state conditions of bed particle and product size distributions had not been reached in any of the PS2-a startups.

Follow-up experiment of processing strategy PS2-a

As mentioned before, the startup EC-22-1 was continued in one follow-up granulation experiment EC-22-2 on a later day, whose results are described in the following. The bed mass and separation gas velocity curves of EC-22-2 are illustrated in the lowest diagram of Figure 10.19, and the related granule size evolution of the bed and product in Figure 10.22. It is evident that the detected bed mass ended at around 1.25 kg in EC-22-1 and began with circa 1.09 kg in EC-22-2. The bed mass difference was mainly caused by material losses, that occurred when the granulator was emptied after the shut-down of the EC-22-1 process. The real initial bed mass of the EC-22-2-experiment weighed 1091.1 g, which is very close to the inline measurement. On a side note, the measurement error of the implemented inline detection method (Section 9.4.7) is small for bed mass values around 1 kg, as stated by Hampel [2]. Nonetheless, such a strong change in the initial condition can have a significant influence on subsequent development of bed mass, and thereby, on separation gas velocity and product size. In the present case, the bed mass control deviation was lowered at the process restart, whereby the separation gas velocity rose from round 1.5 m/s at $t = 9$ h in EC-21-1 to round 1.9 m/s at $t = 0$ h in EC-21-2. Due to the higher classifier gas velocity, less product particles could be discharged. Consequently, the bed mass grew up back to a value of 1.25 kg within the first 1.5 hours of the follow-up experiment. After this, a bed mass oscillation with five waves of similar shape took place, which lasted until the sixth hour of the follow-up experiment. Therein, the bed mass dropped rapidly by values of up to 180 g every sixty minutes. Among these periods, it remained at a constant level for almost thirty minutes

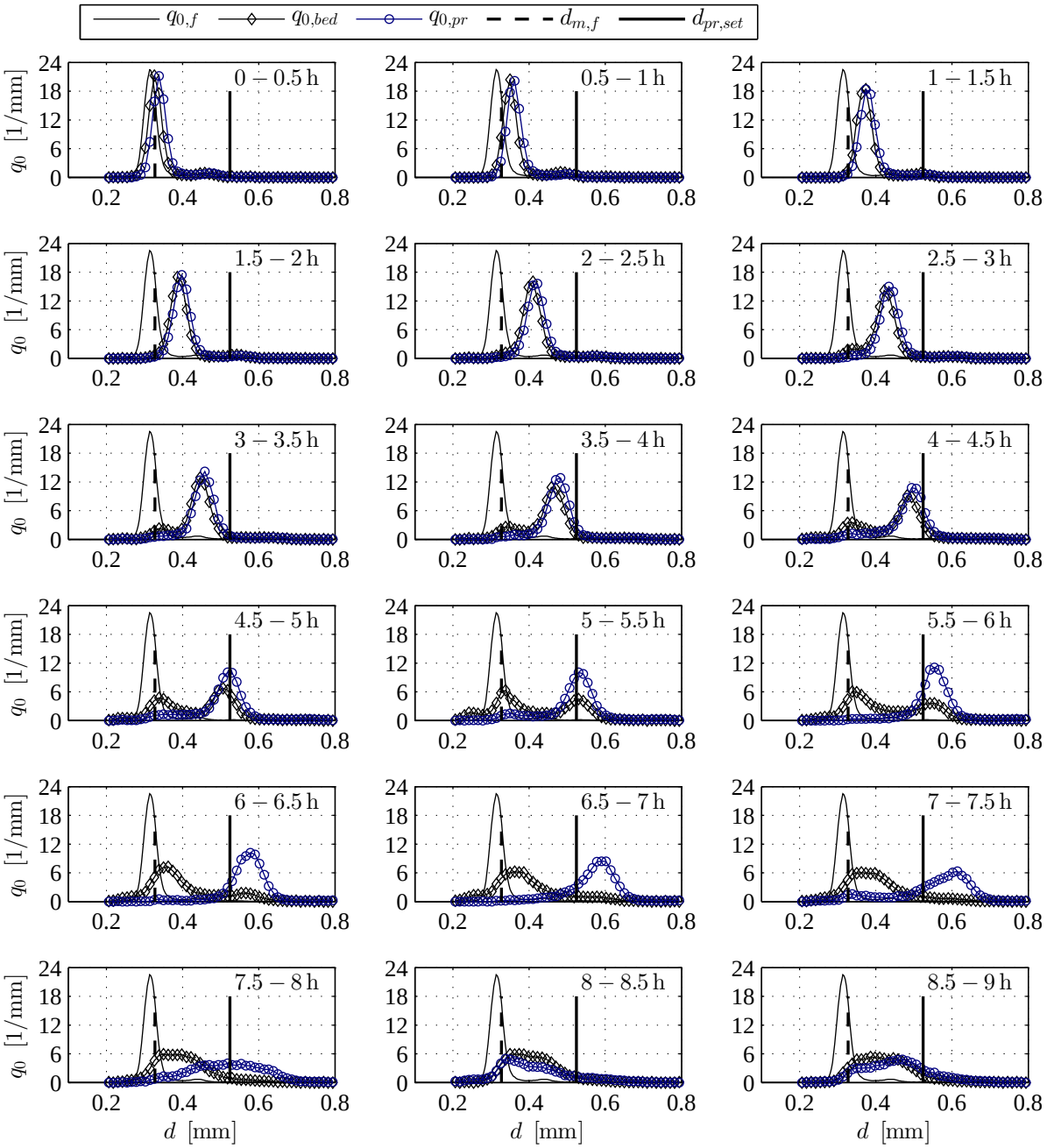

Figure 10.20: Number-based particle size distribution of the feed $q_{0,f}$, the bed $q_{0,bed}$, and the product $q_{0,pr}$ for the half-hour time sections of the startup experiment EC-21*) ($\Phi_{d,set} = 1.6$); *) operation concept for continuous granulation specified in Tables 10.13 and 10.15.

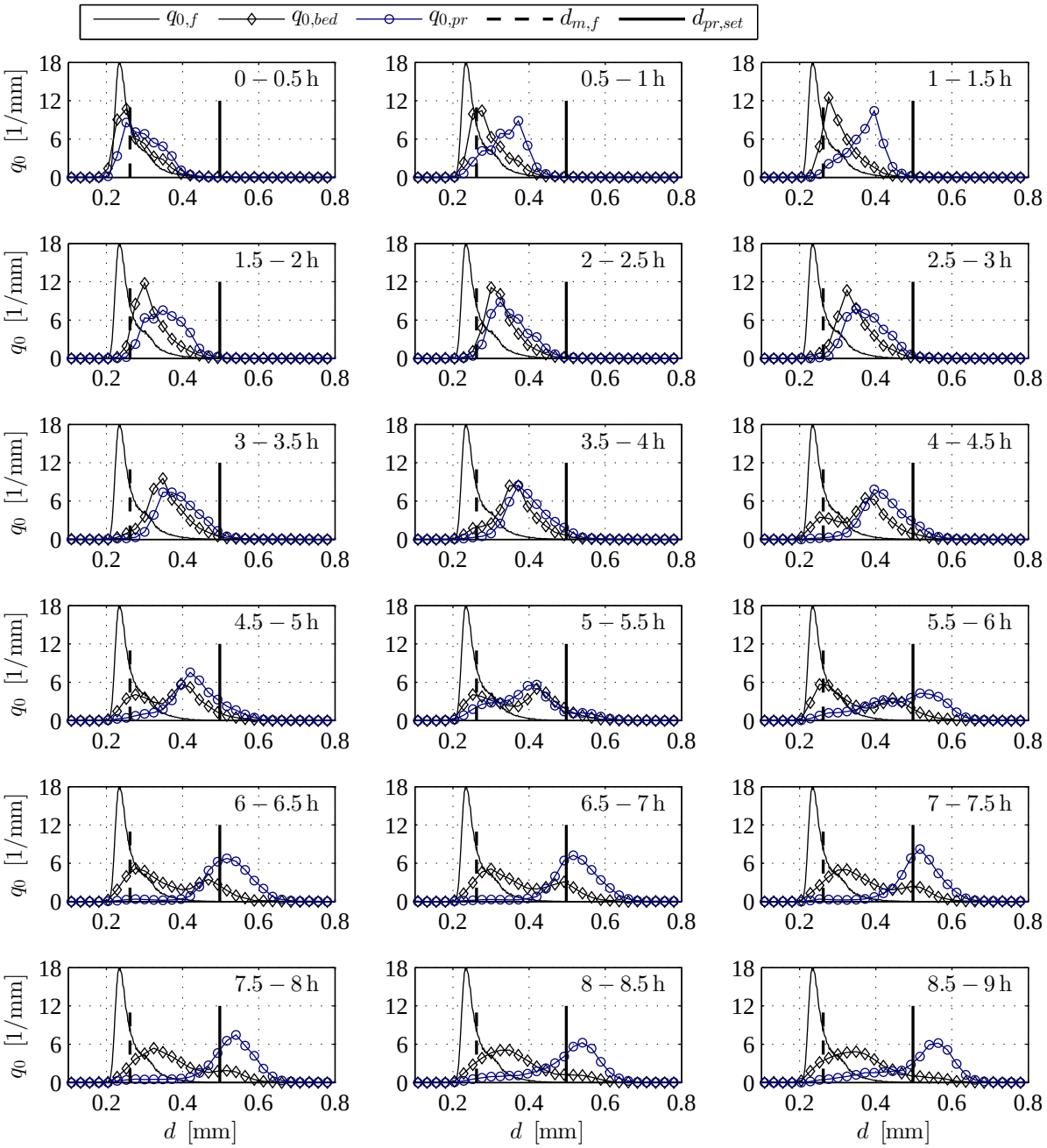

Figure 10.21: Number-based particle size distribution of the feed $q_{0,f}$, the bed $q_{0,bed}$, and the product $q_{0,pr}$ for the half-hour time sections of the startup experiment EC-22-1*) ($\Phi_{d,set} = 1.9$); *operation concept for continuous granulation specified in Tables 10.13 and 10.15.

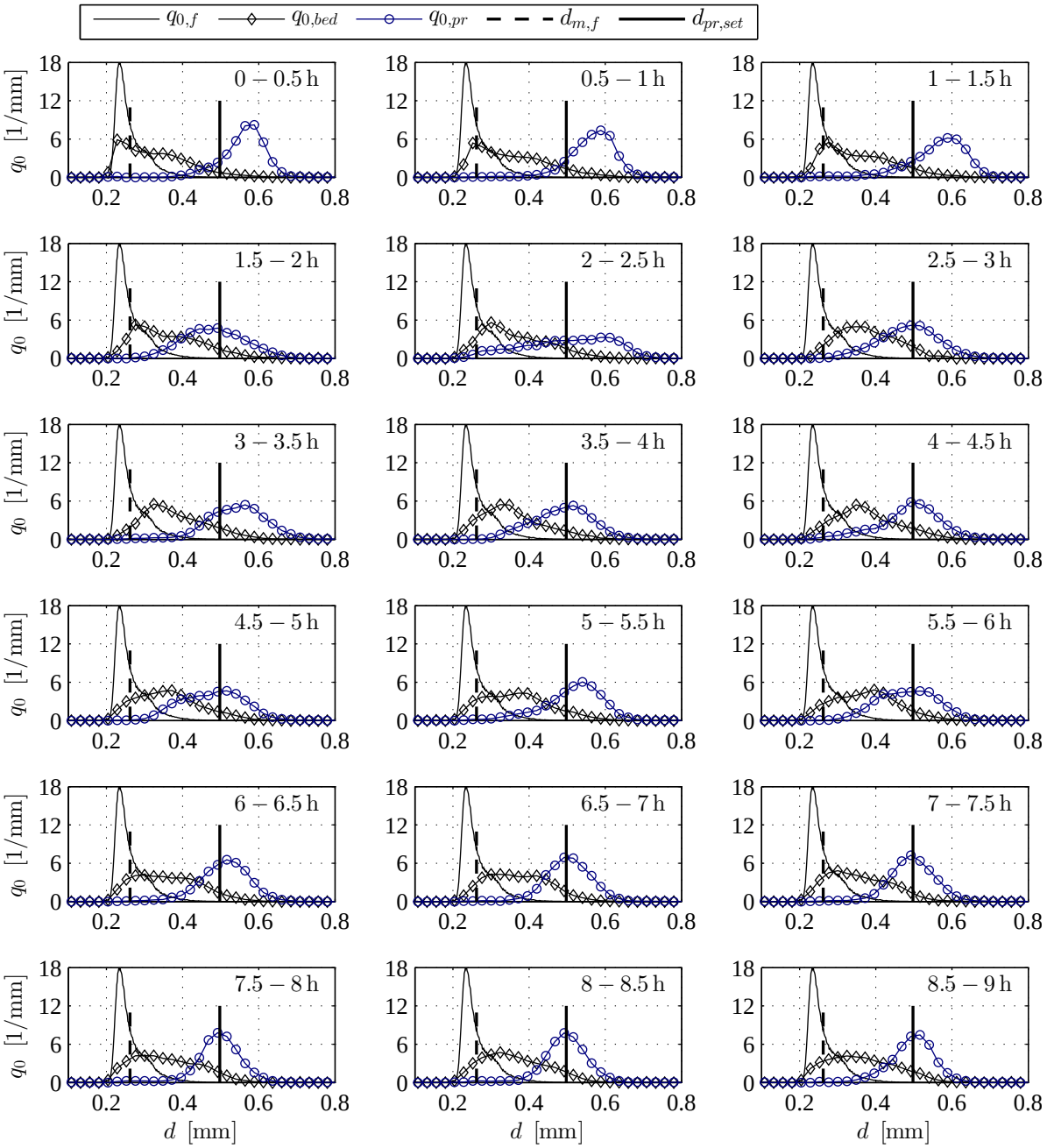

Figure 10.22: Number-based particle size distribution of the feed $q_{0,f}$, the bed $q_{0,bed}$, and the product $q_{0,pr}$ for the half-hour time sections of the follow-up experiment EC-22-2*) ($\Phi_{d,set} = 1.9$); *) operation concept for continuous granulation specified in Tables 10.13 and 10.15.

after each drop in bed mass, and then increased again to holdups of approximate 1.3 kg in another thirty minutes. The cause of this oscillating behavior cannot be determined exactly. Some possible reasons are elucidated later (in Section 10.4.4), along with observed oscillation effects of the PS2-b experiments. As a consequence of the implemented proportional control function of Eq. 9.34, the separation gas velocity is symmetrical to the bed mass curve, wherefore it has similar oscillations. The horizontally mirrored courses of the recorded bed mass and manipulated separation gas velocity can be seen particularly well in this example. In the further course of the process, up to the eighth hour, the bed mass remained constant within a small fluctuation range; subsequently, it began to oscillate again, but less. The product size oscillations were strong in the first six experimental hours. Changes in product size variety stick out from the PSD-diagrams. It is not evident whether the PSD-oscillations are mainly caused by evolution of the bed granule size distribution (as in EC-21) or by the large fluctuations in the separation gas velocity. However, the $q_{0,pr}$-oscillations became much smaller in the remaining part of this experiment. The mean-value-based particle growth ratio Φ_{d_m} and the corresponding relative product size control deviation ζ_d have also been determined for the entire follow-up experiment EC-22-2 (stated in Table C.8). These results make it even clearer that the product's PSD-oscillations are dampened throughout the follow-up process. In the first six hours of the EC-22-2 experiment, the relative control deviation fluctuated between -4.5 and $+12.9\,\%$, whereas it varied only between -1.9 and $+1.6\,\%$ in last three hours. The bed granule size distributions were also only slightly changing. Therefore, it is assumed that stationarity in terms of product characteristics was reached in a practical sense in the last three process hours. It can be speculated that steady-state conditions could have been reached earlier, if continuous granulation of the EC-22 concept was conducted without *process interruption*. The stationary control deviation in terms of product mean diameter is ascertained with absolute values of less than 2 %. It can also be seen in the PSD-charts that the stationary product size distributions of EC-22-2 lie around the objective-granule size of 0.5 mm. The average relative deviation of the product size control of the entire follow-up experiment was calculated with a value of just $+1.3\,\%$, which is a remarkable result. Beside this, the skewness of each product-PSD of EC-22-2 was determined. All of them were below zero, which means that the product-PSD tail left from the product mean diameter was always bigger than the right one. The performance in controlling product size by processing strategy PS2 is evaluated in conjunction with the results of PS2-b-experiments, later in Section 10.4.5. At this, the focus is on potential errors of the spray-to-feed rate setting method SFM2 and adaption of the set separation gas velocity $u_{g,set}$ to the desired product diameter $d_{pr,set}$.

Manual control periods of PS2-b startups

The detected bed mass and separation gas velocity of the entire startup experiments (EC-31, EC-32-1, and EC-33) with processing strategy PS2-b, including manual and automatic control periods, are shown in Figure 10.23. The respective bed particle and product size distributions are given in Figures 10.24, 10.25 and 10.28. Within the manual control periods, the M_{bed}- and u_g-curves are similar to these of the PS2-a startups. The classifier gas flow was alternately switched between maximum and minimum according to the growth acceleration substrategy GAS2 in order to control bed mass through total reflux and discharge modes of the classifier and to suppress classification of the bed material. The GAS2 strategy could also be performed here without great difficulties in terms of process stability. Only a slight drop of the separation gas velocity appeared within the second and fourth hour of the example EC-32-1. But, it had no significant influence on total reflux of particles in the separator. The granule size distributions of the bed $q_{0,bed}$ and product samples $q_{0,pr}$, which were collected during manual control periods, are depicted in the first ten PSD-diagrams, respectively. Again the plotted product-PSD-curves of the first five hours belong to total discharge modes. The following similarities with the PS2-a results can be noted for the growth acceleration periods: the bed particle size distribution also became bimodal, both PSD-curves $q_{0,bed}$ and $q_{0,pr}$ are close together in the same experimental subsections, and the product granules are on average slightly larger than these from the bed. Hence, an *internal classification effect* of the chamber outlet tube is demonstrated once again by the PS2-b measurements. This effect can be recognized particularly well from the lower $q_{0,pr}$-values in the range of the left modal peaks of the bed-PSDs, whereat latter represents the fine fraction of granules inside the bed. The variation of desired particle growth ratio $\Phi_{d,set}$ of the PS2-b startups is different from PS2-a experiments with 1.9 in EC-31, 2.2 in EC-32-1, and 2.5 in EC-33. The lowest of them could be reached within a manual control period of five hours in the startup experiment EC-31, whereas it could not in the other startups EC-32-1 and EC-33.

Automatic control periods of PS2-b startups

The transition from manual to automatic control mode (at $t = 5\,\mathrm{h}$) could be realized faultlessly in the startups EC-31 and EC-33. The bed mass control deviation of the EC-31 experiment was very low in the entire automatic control period. It can be compared to PS2-a result of the concept EC-22, where the same desired growth ratios ($\Phi_{d,set} = 1.9$) and required spray-to-feed rate ratio ($\Phi_{m,set} = 4.356$, from Eq. 9.27) were predefined. But, the set spray rate $\dot{M}_{spr,set}$ was higher in EC-31, so that bed particles grew faster and fell out in the product outlet already after shorter total residence times, on average. This might be a logical explanation for lower bed mass values of EC-31, as the total residence time is proportionally related to the fluidized bed mass. Such a relationship is also given in Eq. 3.46, that is derived from the ideal granulation model of Chapter 3. In the fifth to seventh hour of the EC-33 experiment, bed mass control deviations are small, such as in the EC-31's automatic phase. The bed mass values of the last two hours of experiment EC-33 were lower than in EC-31, even below the setpoint, although the set spray rate of EC-33 was equal to EC-31's. But, the set feed rate $\dot{M}_{f,set}$ was less than half as large as the set feed rate of the EC-31 concept, which is probably the reason for the decreasing bed mass in the last experiment EC-33. The transition from manual to automatic bed mass control period in the EC-32-1 experiment was not problem-free. Immediately after the changeover, an error in signal transmission to the classifier-MFC occurred. As a consequence, undesirably large separation gas velocities appeared in the sixth hour of experiment EC-32-1. This reduced the product mass flow, so that the bed mass increased sharply. The misadjustment was noticed shortly after the sixth hour, at which it could be remedied by resetting all parameters of the implemented P-control function ($u_{g,set}$, K_m, and M_{set}). The faulty separation gas velocities led to incapable product classification, what can also be seen from corresponding PSD-curves of the bed and product in Figure 10.25 (diagrams of $5 \leq t \leq 6\,\mathrm{h}$). Therein, $q_{0,bed}$ and $q_{0,pr}$ are highly superimposed. The last eight PSD-charts of Figures 10.24, 10.25, and 10.28 show that the right modal peaks of bed granule size distributions were gradually vanishing in the automatic control periods of each PS2-b startup, as also recognized in the PS2-a results. During these time periods, convection of the product-PSDs to the right along the particle size coordinate is clearly visible. The relative product size control deviations ζ_d, listed in Table C.7, indicate that the product mean diameter did not increase steadily throughout the automatic control periods. The tendency towards growing product size can, though, be discerned in each of the PS2-b startups. Significant *product overgrowth* is recorded for the EC-31 process, in which the desired particle growth ratio was the lowest among the PS2-b experiments. The target exceedance began as early as the twelfth experimental subsection ($5.5 - 6\,\mathrm{h}$) and reached its maximum in the sixteenth experimental subsection ($7.5 - 8\,\mathrm{h}$). In between ($6.5 - 7.5\,\mathrm{h}$), there was a decrease in the product mean diameter. It is assumed that this decline in average product size is caused by a bigger *mal-discharge of fines* in the product and not by an oscillating effect of the bed granule size distribution, because the fraction of the $q_{0,pr}$-distribution below the target size (left tail) is larger. On the other hand, it appears that in the last hour of the EC-31 experiment, a back-oscillation of the product-PSD was triggered. In this time section, product size distribution became significantly wider, just like with the beginning $q_{0,pr}$-oscillation of the EC-21 experiment. Strong product overgrowth emerged in the EC-32-1 startup too, but only in the last half hour of the experiment due to the higher target-growth ratio ($\Phi_{d,set} = 2.2$), and to less extent than obtained in the EC-31 process. A subsequent increase in product size, followed by PSD-oscillations, can be observed in the corresponding follow-up experiment EC-32-2, more on this later. The desired increase in granule size of the EC-33 experiment was the largest with $\Phi_{d,set} = 2.5$. Therefore, the product size distribution had only arrived at the target value at the end of the EC-33 process, with only a smaller part of it being larger than the desired granule size. From the mean-value-based particle growth ratio Φ_{d_m} and the associated relative control deviation ζ_d, in Table C.7, it follows that the product mean size did not reach the target diameter during the entire EC-33 startup. Product size oscillations with periods of a few hours are not detected in EC-33. However, it cannot be excluded that this would not have happened for longer process times, because the product size distribution had still been changing quite noticeably towards the end of the experiment. In summary, it must be said that a manual control period of five hours is definitely too long for the growth conditions of the operation concept EC-31. The manual control period of the EC-32-1 experiment could have been a little shorter to avoid exceeding the target of product size, perhaps an hour less. But, five hours of manual bed mass control seems to be appropriate for the EC-33 example. Stationarity in terms of product size cannot be identified for any of the PS2-b startups. For this purpose, hardly variable product-PSDs have to be measured for several hours (at least three, four would be better), which was not the case here. The experiments EC-31 and EC-33 should have been conducted for a longer period in order to study oscillation effects and product characteristics under steady-state conditions. Aspects like these, however, are examined below for the entire experimental series of the EC-32 concept.

Follow-up experiments of processing strategy PS2-b

The EC-32-1 startup process was continued in two follow-up experiments, EC-32-2 and EC-32-3, as stated before. The results of them shall be described in the following. The temporal curves of bed mass and separation gas velocity are depicted in the third and fourth diagram of Figure 10.23. Figures 10.26 and 10.27 show the corresponding bed particle and product size distributions of the experimental subsections. In addition, four scalar quantities related to product characteristics have been calculated for all eighteen experimental subsections of both follow-up experiments, which are the mean-value-based particle growth ratio Φ_{d_m} and its corresponding relative product size control deviation ζ_d, the standard deviation σ_{pr}, and the skewness γ_{pr}. The results of them are given in Table C.8. First of all, it should be noticed that the bed mass was consistently hold within a range of stable Wurster fluidization for both follow-up experiments. In this way, process stability could be guaranteed by the proportional feed-back control system used for a total of twenty-one hours, even with two *operational interruptions*. At this, the detected bed mass was always above the set point (1 kg), whereat relatively strong fluctuations are observed. The fluctuations and control deviations in bed mass were greater in EC-32-2 than in EC-32-3. It is further visible that high bed mass values of up to 1.29 kg were measured in the first minute of the first follow-up experiment EC-32-2. The real initial bed mass of EC-32-2, which was taken from the final bed material of the previous EC-32-1 experiment, was also quite large at 1152.6 g compared to other experiments. The masses of final bed materials measured after process shut-downs are listed in Table C.6. As already mentioned in the discontinuous granulation study (Section 10.1), the more the masses deviate from 1 kg, the higher the inline detection error in the bed mass is. Due to inverse behavior of the control system, the separation gas velocity was low in the beginning of the EC-32-2 process, so that smaller bed granules could be discharged. Hence, the bed mass decreased rapidly over the next eighteen minutes, causing the classifier gas velocities to increase again. The short period of low separation gas velocity can also be clearly discerned from a wider product size distribution in the first PSD-diagram of Figure 10.26 ($0 - 0.5$ h). Subsequently, the bed mass grew to a value of just above 1.2 kg by the point in time of about $t = 2.5$ h after process beginning, followed by a series of increases and declines (disregarding small fluctuations) in the rest of experiment EC-32-2. It is conspicuous that most turning points in this oscillation appear almost every half hour. A more detailed discussion of such oscillation effects is given later in Section 10.4.4. In the first four hours of the second follow-up experiment EC-32-3, a similar bed mass evolution is ascertained, with it rising and falling nearly every half hour in three cycles. Except for the latter, no further distinct oscillation pattern - in a scale of hours - can be deduced from the bed mass curve in the remaining part of this experiment. The PSD-curves of bed particles still change a little with process time in the EC-32-2 experiment, while they remain more constant in the subsequent experiment EC-32-3. The evolution of bed particle size distribution was affected by the first process stop of the experimental granulation series EC-33. This can be seen from a slight shift in the $q_{0,bed}$-curves towards smaller granules in the first sample PSD-measurement ($0 - 0.5$ h). An exact reason for this has not been found. The bed particle size distribution then fluctuated slightly within the first seven hours of the EC-32-2 experiment. Therein, the formation of a bimodality, even if only weakly, can be recognized in the PSD-charts of $5 - 6.5$ h. After the seventh hour, the bed particle size distributions became more constant. The second experimental interruption barely influenced the granule size development of the fluidized bed at the beginning of the EC-33-3 experiment; and the subsequent bed-PSDs remained in their form similar to the last two hours of the previous experiment. Thus, constant conditions (in the practical sense) in bed granule size distribution lasting for a total of around ten hours can be ascertained. Changes in the product size distribution also occurred. Some fluctuations in the product-PSDs are visible for both follow-up experiments, although they were still quite large in the EC-32-2 experiment and clearly smaller in the EC-33-3 experiment. The $q_{0,pr}$-curves oscillated particularly quickly in the first two hours of EC-33-2, which was very likely due to the first process interruption. The aforementioned initial drop in separation gas velocity at the beginning of the EC-32-2 process led to a lower mean diameter and a greater size variety of the product granules collected in the first experimental half hour. This can be also be seen from the comparatively high standard deviation in Table C.8. The relative product size control deviation rose rapidly from -8.4 to $+8.4$ % within the first experimental hour, which is a result of u_g-drop after the process start. Faster growth as a reason for this can be ruled out for such a short period of time. Subsequently, the product-PSDs stayed around the desired diameter within the 1.5th and seventh hour. Meanwhile, the relative control deviation lay in an acceptable range of values between -2.7 and $+2.9$ %. In the last two hours of the EC-32-2 experiment, the product grew slightly above the target value. Relative control deviations in product size of up to $+7.9$ % have been obtained during this time period. The (overall) average relative product size control deviation of the entire EC-32-2 experiment is quite small with a value of only $+1.6$ %, which is almost as good as the average control error ($+1.3$ %) of the EC-22-2 process. Another PSD-oscillation of the product

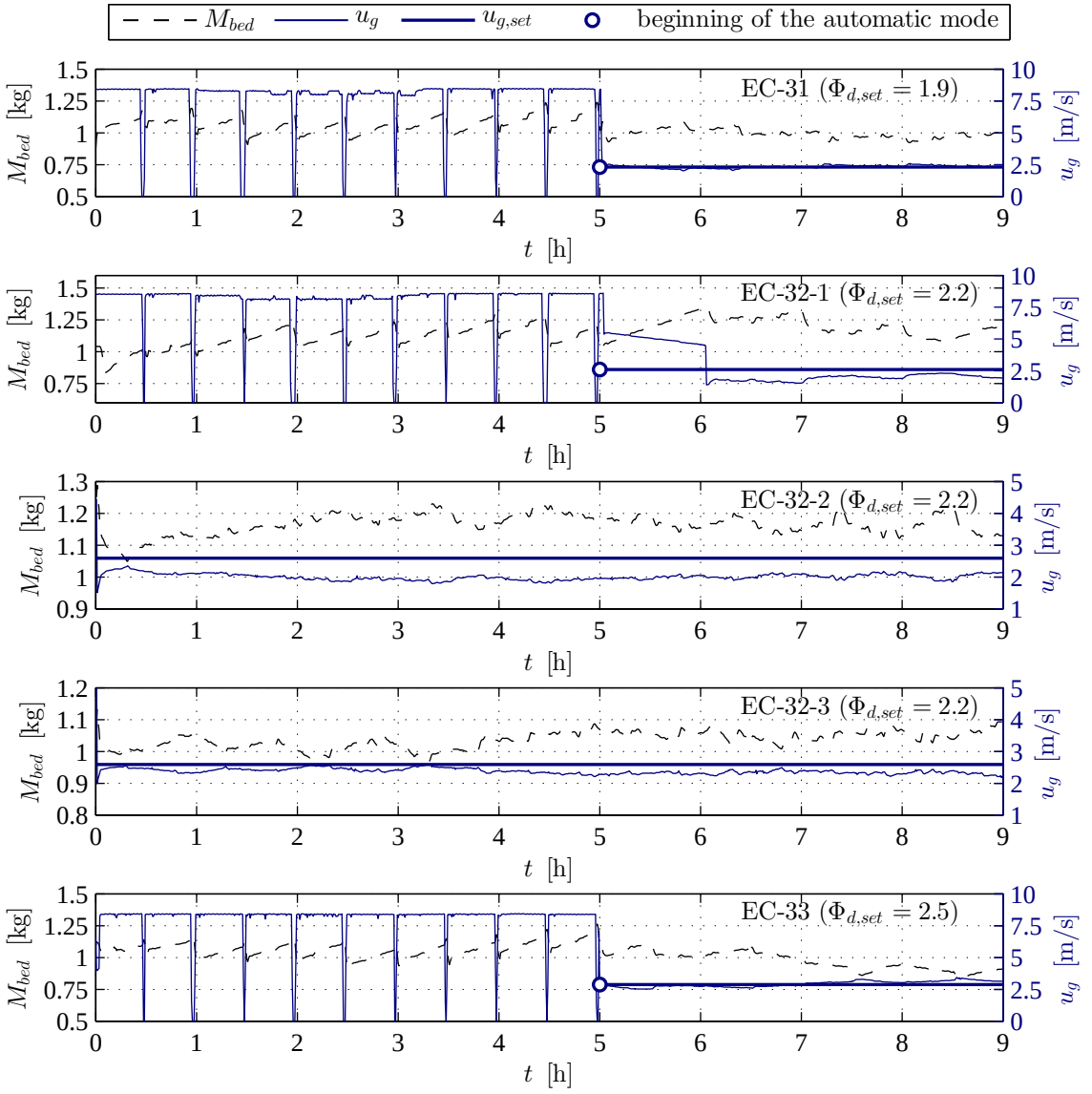

Figure 10.23: Bed mass M_{bed} and separation gas velocity u_g with process time for continuous experiments with different operation concepts: EC-31, EC-32*) and EC-33 of Tables 10.13 and 10.15; *) employed in one startup EC-32-1 and two follow-up experiments EC-33-2 and EC-33-3.

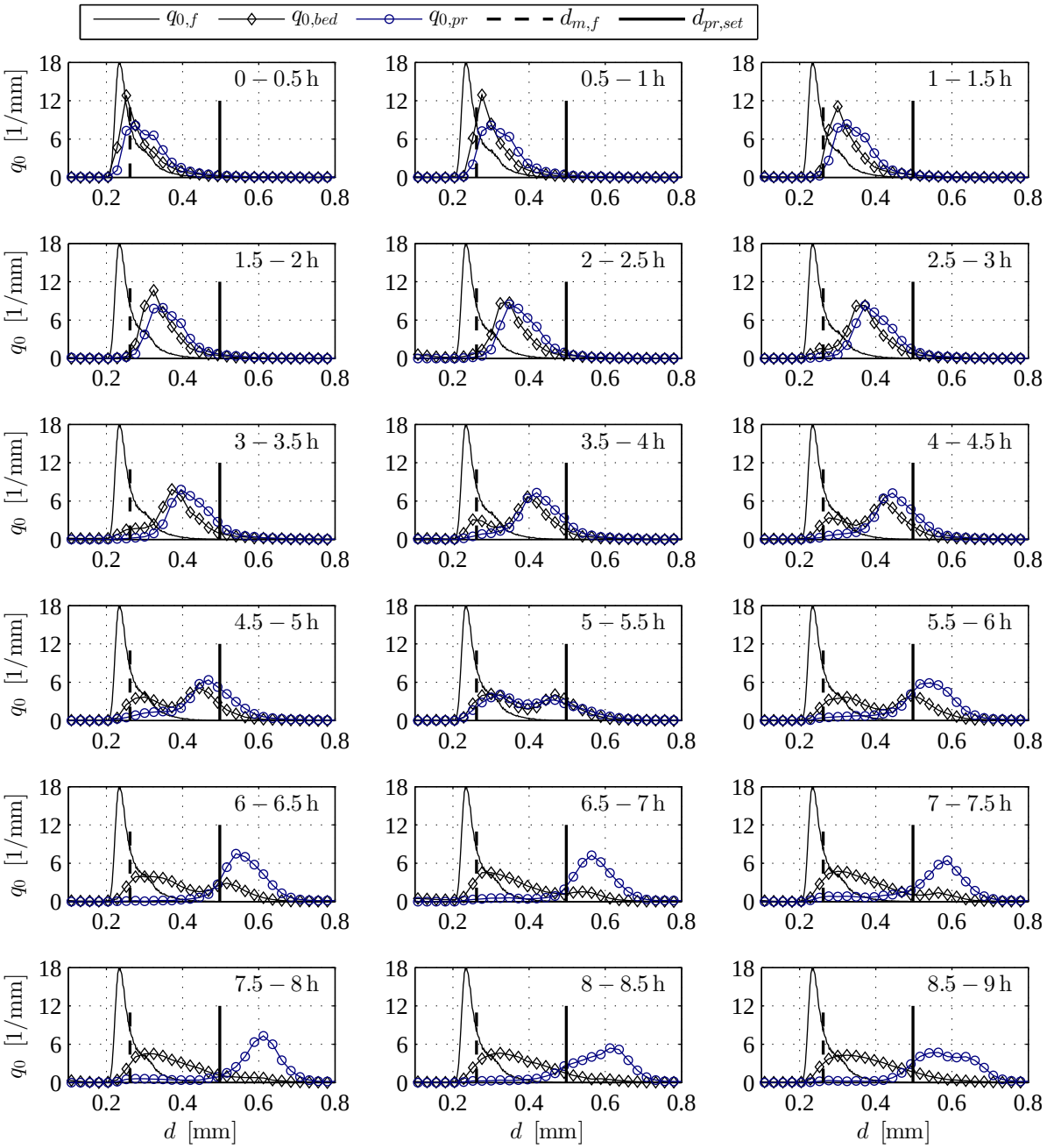

Figure 10.24: Number-based particle size distribution of the feed $q_{0,f}$, the bed $q_{0,bed}$, and the product $q_{0,pr}$ for the half-hour time sections of the startup experiment EC-31*) ($\Phi_{d,set} = 1.9$); *) operation concept for continuous granulation specified in Tables 10.13 and 10.15.

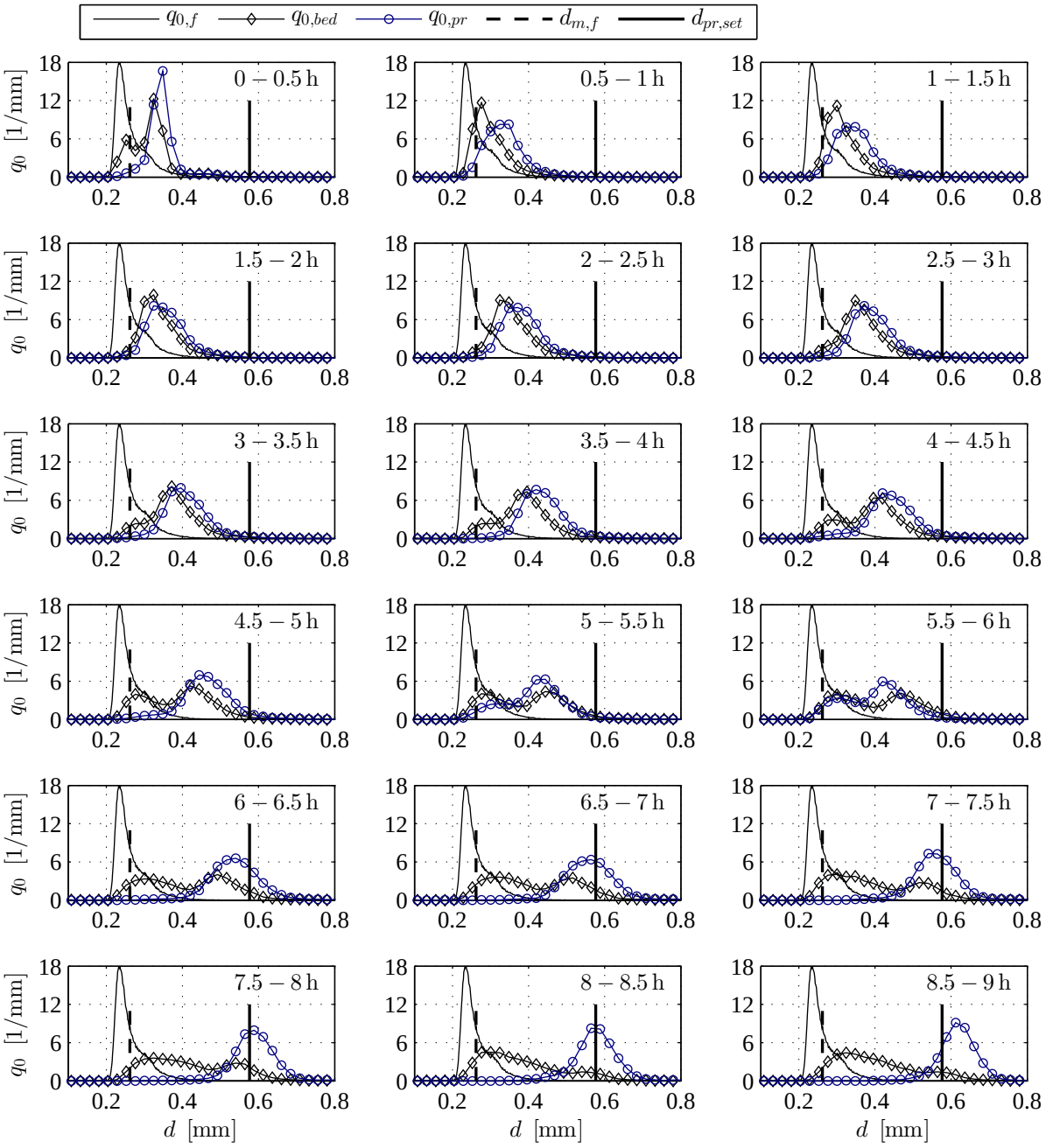

Figure 10.25: Number-based particle size distribution of the feed $q_{0,f}$, the bed $q_{0,bed}$, and the product $q_{0,pr}$ for the half-hour time sections of the startup experiment EC-32-1*) ($\Phi_{d,set} = 2.2$); *) operation concept for continuous granulation specified in Tables 10.13 and 10.15.

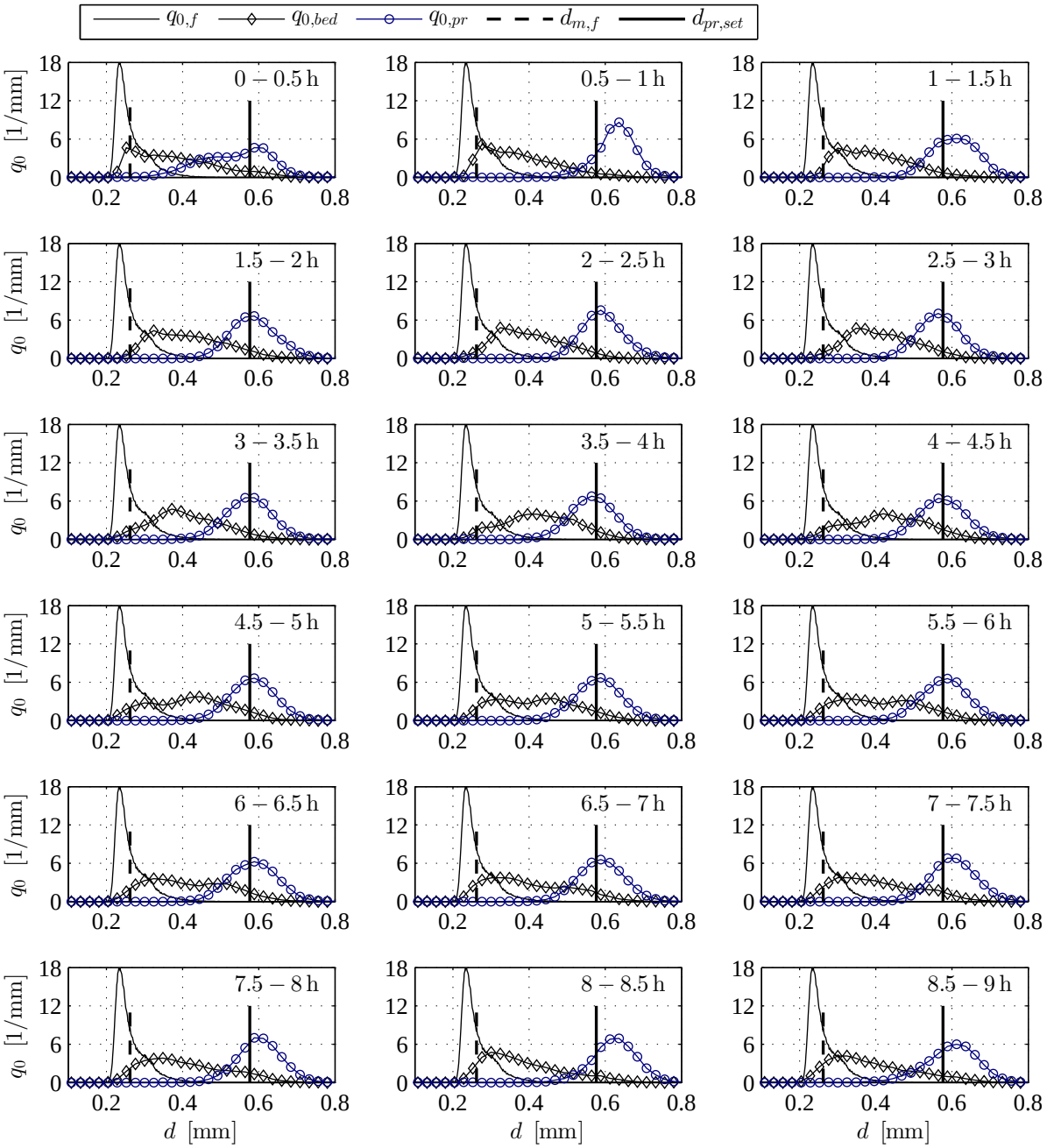

Figure 10.26: Number-based particle size distribution of the feed $q_{0,f}$, the bed $q_{0,bed}$, and the product $q_{0,pr}$ of the half-hour time sections of the follow-up experiment EC-32-2*) ($\Phi_{d,set} = 2.2$); *) operation concept for continuous granulation specified in Tables 10.13 and 10.15.

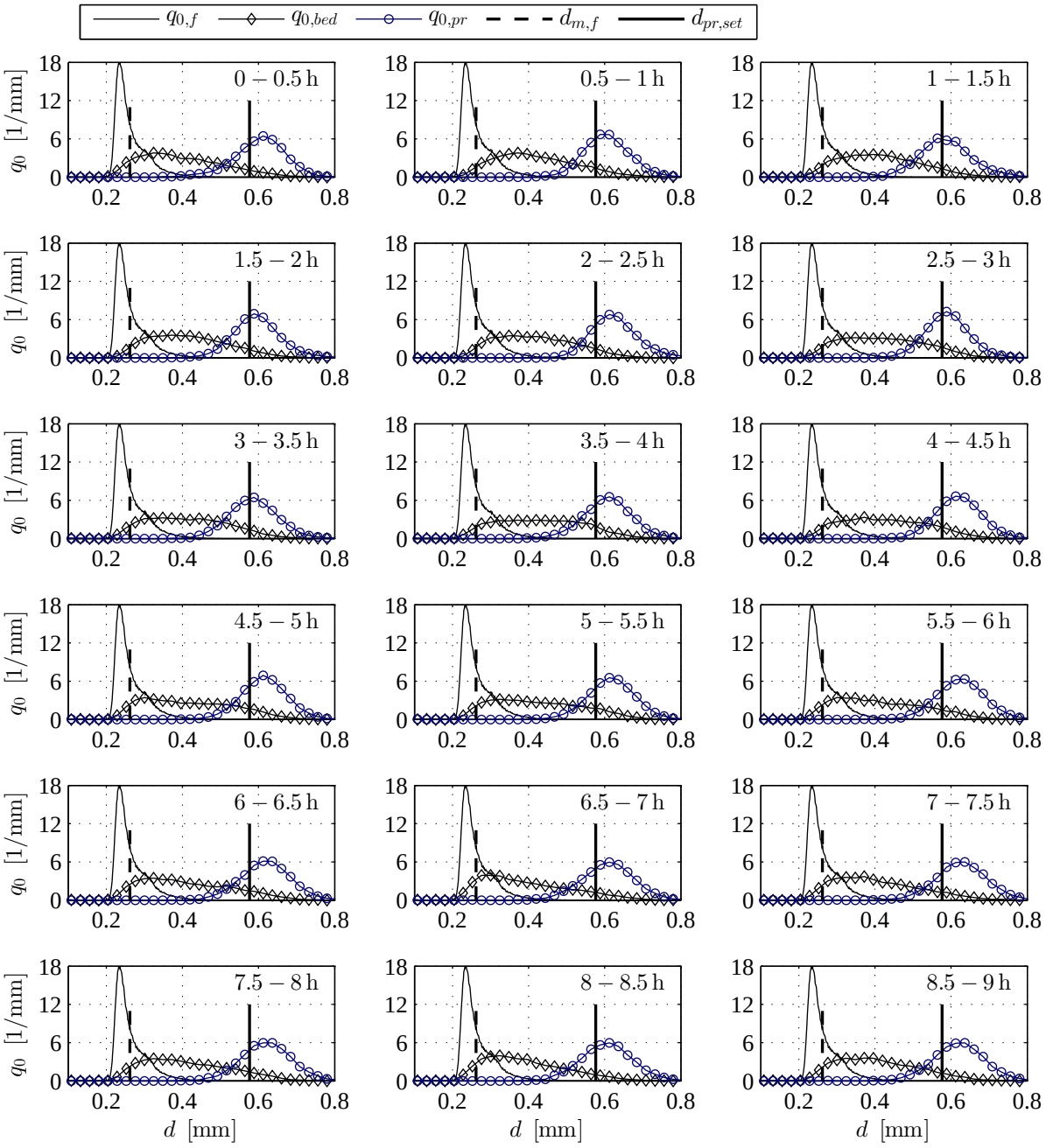

Figure 10.27: Number-based particle size distribution of the feed $q_{0,f}$, the bed $q_{0,bed}$, and the product $q_{0,pr}$ for the half-hour time sections of the follow-up experiment EC-32-3*) ($\Phi_{d,set} = 2.2$); *) operation concept for continuous granulation specified in Tables 10.13 and 10.15.

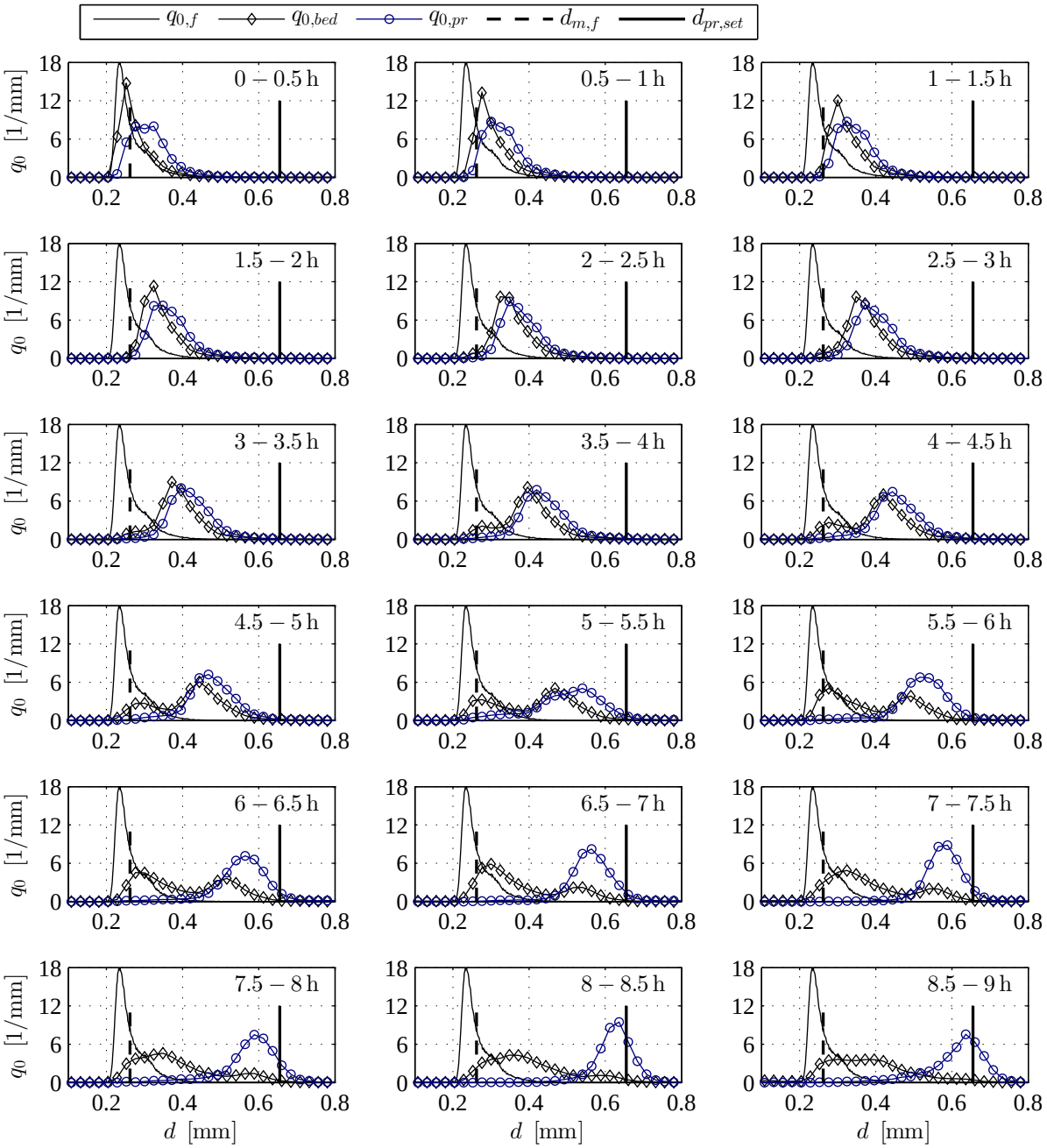

Figure 10.28: Number-based particle size distribution of the feed $q_{0,f}$, the bed $q_{0,bed}$, and the product $q_{0,pr}$ for the half-hour time periods in the startup experiment EC-33*) ($\Phi_{d,set} = 2.5$); *) operation concept for continuous granulation specified in Tables 10.13 and 10.15.

emerged in the first four hours of experiment EC-32-3, but to less extent than in the process beginning of EC-32-2. It cannot be exactly determined whether the second process interruption caused these oscillations. However, they appeared in the same time period, in which definite bed mass oscillations (EC-32-3 of Figure 10.23) were recorded. Subsequent PSD-curves of the product ($4 - 9\,\mathrm{h}$) varied only slightly. In contrast to the first follow-up experiment EC-32-2, the relative product size control deviation shows positive values for the entire duration of the second follow-up experiment EC-32-3. The (overall) average relative product size control deviation of the EC-32-3 experiment was greater than in the previous follow-up experiment EC-32-2 with a value of $+5.6\,\%$. On the other hand, the fluctuations in product size control deviation were smaller in EC-32-3 than in EC-32-2, what is evident from the standard deviation of the relative product size control deviation: see $\mathrm{SD}(\zeta_d)$ in Table C.8. This speaks for a damped oscillation in product size distribution over time. It is obvious that the results of PSD-skewness (γ_{pr}) have negative values for all product samples of both follow-up experiments of the concept EC-32, which was also the case in the EC-22-2 experiment. Neglecting small oscillations, it is assumed that at the end of the first follow-up experiment (last two hours of EC-32-2) stationary conditions (in a practical sense) exist in regard of bed particle and product size distributions; while the bed- and product-PSDs in the second follow-up experiment (EC-32-3) are considered to be completely stationary. Potential error sources in product size control are discussed later in Section 10.4.5 together with the results of the PS2-a experiments.

10.4.4 Discussion of unwanted effects of the PS2 experiments

Different types of oscillation in bed mass and particle characteristics are obtained in the PS2 experiments. At this, a distinction is made between *short-term*, *middle-term*, and *long-term oscillations* of measured process variables, whereat short-term refers to oscillations in the scale of seconds (e.g., fluidization-related pressure fluctuations), middle-term to the scale of minutes, and long-term to hours. Short-term bed mass fluctuations can be seen in each experiment, but are of no interest here, as they neither affect process stability nor desired product size development. Middle-term oscillations in bed mass emerged in a few experiments and long-term bed mass oscillation were not ascertained in any of the experiments. On the contrary, oscillations of the measured particle size distributions are only visible over periods of hours, but not of minutes. In this section, possible reasons of the observed oscillations are discussed, the partial growth acceleration strategies GAS1 and GAS2 are evaluated, and suggestions for faster startup strategies are described.

Middle-term bed mass oscillations in the EC-22-2 and EC-32 experiments

Middle-term oscillations in bed mass were detected in the experiments EC-22-2 (with PS2-a and F1, see third diagram of Figure 10.19) and EC-32 (with PS2-b and F4, see second to fourth diagram of Figure 10.23). The bed mass oscillation in the EC-22-2 experiment has a very clearly repeating pattern. Strong changes in the curves appear at half and full hours of the experiment, at which filled product sample containers connected to the classifier bottom were replaced by a new empty one. When doing this, the ball valve below the classifier gas inlet should be closed, see also Figure 9.4 between No. 10 and 11. This replacement was perhaps not carried out properly, so that the internal gas pressure in the process chamber would be affected, resulting in an inline detection error of bed mass. The bed mass oscillation in the EC-32 experiments has relatively sharp turning points. But these reversions do not always lie exactly on time points where the product sample containers were exchanged (t: 0.5 h, 1 h, 1.5 h, etc.), as EC-22-2. In addition, the bed mass oscillations of EC-22-2 and EC-32-2 do not resemble one another in their shape; which is why they can have different causes. For example, *temporal changes in bed discharge dynamics* (see also Section 10.3) have an influence on bed mass evolution. However, such an effect seems implausible for cyclical bed mass variations. Another influencing factor could be a *fouling effect inside the classifier*. As was discovered after the experiments, a certain amount of granules and dusty coating material had adhered to the inner wall of the classifier tube. At this, thin layers of material with a thickness of up to 3 mm were found. Cohesive material layers on inner classifier walls reduce the free cross-section, whereby effective separation gas velocities are enlarged locally. The fouling effect could have a significant influence on product mass flow rate, and therefore, on bed mass evolution. During operation, the aim was to remove the adhering material from time to time by tapping the classifier tube to re-establish desired separation conditions. It could explain the ups and downs in bed mass; though, it has not been proven. The effectiveness of detachment could not be checked during the experiments due to opacity of the metal tube. Precise regularity and recording were also not taken into account. The masses of adhered materials (listed in Table C.6) were measured after all experiments of the concepts from EC-21 to EC-33. Local changes in effective separation gas velocity can also not be read from the shown results, because the illustrated u_g-curves represent average classifier inlet gas velocities that

are determined from the MFC-back-signals. Particle growth kinetics as reason for the described bed mass fluctuations can be precluded, as it is too slow. For instance, the PSD-curves of bed granules in the EC-22-2 experiment (Figure 10.22) oscillate only slightly within the first six hours. It is also unlikely that formation and subsequent breakage of agglomerates emerge with the regularity of the depicted bed mass oscillations. The $q_{0,bed}$-curves do not suggest that either. Additionally, almost no agglomerates were found in both the bed and the product samples.

Middle-term oscillations in product size distribution

Middle-term oscillations in product size distribution cannot be ascertained by the present PSD-measurements due to the sampling procedure within the experiments. The shown product-PSDs are averages of thirty-minute sampling periods, wherefore PSD-oscillations can only be detected in the long-term scale (here between one and five hours). However, that does not mean that small-scale fluctuations (here less than thirty minutes) in $q_{0,pr}$ did not emerge in the experiments. It is possible that brief increases and declines in bed mass and separation gas velocity, as observed in the experiments, can lead to middle-term PSD-oscillations of the product, which would be subsumed in long-term results.

Bimodal bed-PSDs and long-term oscillations in product size distribution

Development of temporary bimodal bed-PSDs and long-term product PSD-oscillations was observed in all PS2 experiments, except for EC-33, where the conducted process time was not long enough to detect *product overgrowth and back-oscillation of* $q_{0,pr}$. In the EC-21 experiment ($\Phi_{d,set} = 1.6$), the product size distributions most closely had reached the target diameter $d_{pr,set}$ already at the end of the manual control period ($t_{exp} = \tau_{man}$). At this, the target overgrowth and back-oscillation were the strongest among all PS2-experiments. The oscillation effects were smaller in the experiments of EC-22 and EC-31 with $\Phi_{d,set} = 1.9$, and even weaker in the EC-32 experiment with $\Phi_{d,set} = 2.2$, while it could not be observed in the last granulation experiment EC-33 with $\Phi_{d,set} = 2.5$. It is not proven that such effects would not emerge if the latter experiment were continued for longer, because steady-state conditions in product characteristics had not been achieved in EC-33. Nevertheless, it is assumed that product overgrowth and oscillation would possibly appear to even less extent than in EC-32, as the desired particle growth ratio of EC-33 is larger. The damping of the oscillations can be particularly well recognized in the startup and follow-up experiments of the concepts EC-22 (with PS2-a) and EC-32 (with PS2-b). The results show that bimodal shape of bed-PSDs strongly influences product PSD-oscillation. A correlation between the gradual disappearance of $q_{0,bed}$*-bimodality* and *damping of* $q_{0,pr}$*-oscillation* can also be ascertained. In the last hours of the startup experiments (EC-22-1 and EC-32-1), the right modal peaks of the $q_{0,bed}$-curves reached the target diameter $d_{pr,set}$ and flatted out. Meanwhile, product-target overshoots ($d_{pr} > d_{pr,set}$) appeared. In the beginning of the follow-up experiments (EC-22-2 and EC-32-2), the right peaks of $q_{0,bed}$ had disappeared and the product-PSDs migrated back to lower particle diameters. It is assumed that evolution of distinct bimodal shapes in bed granule size distribution is due to lower initial feed rates ($\dot{M}_{f,set,k}$) from strategy GAS1 within the manual control period. At this point is mentioned that the feed rate step function (Figure 9.11) of processing strategy variant PS2-a was more coarsely discretized than in PS2-b; but, bimodal shapes of the bed-PSDs were more or less equally remarkable in both variants PS2-a and PS2-b. It is moreover presumed that a dampened PSD-oscillation of the product (overshoot and back-oscillation) can also occur without development of significantly bimodal bed-PSDs, and that the latter only has an *amplifying effect* on product PSD-oscillation. Nonetheless, $q_{0,bed}$-bimodality and damped $q_{0,pr}$-oscillation prolong the startup periods.

Evaluation of the growth acceleration substrategies GAS1 and GAS2

Realization of the strategy GAS1 (reduced initial feed rates) is rather laborious for the feed rate control methods F1 and F4. For both methods, the adjustment of different feed rate values requires extensive calculations in the experimental preparation according to Section 10.4.1. As mentioned before, temporary bimodal shapes of bed particle size distribution are presumably caused by strategy GAS1 and enhance product PSD-oscillations, resulting in longer startup periods. It is also assumed that the simultaneous use of GAS1 and GAS2 leads to a more distinct bimodality of the $q_{0,bed}$-distributions. The second partial growth acceleration strategy GAS2 (manual two-phase bed mass control) was easy to realize by contrast. The application period of GAS2 (five hours) was probably too long for the PS2 operation concepts, except for EC-33; which is seen as another influencing factor of the observed product overgrowth and long-term PSD-oscillations. Product size oscillations could possibly be avoided, or would take place to less extent, if

only GAS2 were implemented into the processing strategy. In doing so, the *duration of manual bed mass control phase* (τ_{man}, GAS2, Table 9.5) should be adapted to process conditions.

Improvements of startup strategies - Optimal duration of manual control period

Due to the mentioned difficulties, it is recommended to forego the first partial growth acceleration strategy GAS1 in future studies, which means that the processing strategy PS2 is operated with set feed rates from beginning on. In addition, the duration of GAS2 (τ_{man} manual control period) could be optimized. Finding this optimum for reducing startup periods and avoiding target-diameter exceedance and PSD-oscillations of the product depends on many aspects, such as the desired particle growth ratio $\Phi_{d,set}$, initial bed mass $M_{bed,0}$, effective solids spray rate $\dot{M}_{spr,s,eff} = \dot{M}_{spr,s}(1-\Phi_{spr,loss})$, and effective coating density ρ_c. However, experiment EC-33 might be a good reference case for the choice of appropriate durations of manual control periods, since it would probably has the lowest PSD-oscillation among the shown examples. It can be seen in the tenth diagram of Figure 10.28 that the bed- and product-PSDs (except for the left modal peak of $q_{0,bed}$) are nearly in the middle of the $d_{m,f}$ and $d_{pr,set}$ marker lines. As a conclusion, the unweighted mean diameter of Eq. 2.42 could be an orientation point for the duration of manual bed mass control, which would have to be calculated here by

$$d_{p,mid} = \frac{d_{m,f} + d_{pr,set}}{2} = \frac{d_{m,f}(1 + \Phi_{d,set})}{2}. \tag{10.29}$$

Those mean diameters can be derived approximately from PDS-diagrams of the other operation concepts EC-21 to EC-32. It follows that around two hours seems to be a reasonable manual control time for the EC-21, EC-22, and EC-31 concepts, while three hours might be more suitable for EC-32. In future granulation studies, *pure manual control experiments*, where only GAS2 is applied, could be performed prior to planned continuous experiments to determine required growth times of sufficient $d_{p,mid}$-overshoot. Furthermore, granule size evolution during the manual mode of controlling the bed mass can also be examined by means of PB-simulations. The three-compartment PB-model of Chapter 5 would have to be modified in this case. Moreover, startup times can be shortened by lowering bed mass values in the manual control mode, whereby particle growth kinetics are increased. It is shown by the discontinuous granulation substudy (Section 10.1) that process stability was still ensured at an initial holdup of 0.8 kg. Such low values can be generated by longer time periods of total discharge mode of the classifier (see $t_{off,i}$ in Figure 9.10).

10.4.5 Discussion of accuracy of product size control

As part of the processing strategy PS2, the aim was to control product size under stationary conditions by two parameter setting methods. The first comprises an adaption of spray-to-feed rate ratio $\Phi_{m,set}$ to the desired particle growth ratio $\Phi_{d,set}$ (indicated by SFM2), which is described in Section 9.4.5. The second involves adjusting the set separation gas velocity $u_{g,set}$ of the P-control function to the desired product diameter $d_{pr,set}$, as defined in Section 9.4.6. The method for setting the spray-to-feed rate ratio SFM2 was derived from the ideal continuous layerwise granulation model, see also Table 3.1. The effectiveness of the control of product size shall be discussed here using the stationary results (in a practical sense) of the EC-22 and EC-32 operation concepts. *Practical stationarity* in size distributions of the bed and product granules (short- and middle-term fluctuations neglected) could be identified with small changes in the last three hours of the EC-22-2 experiment ($\Phi_{d,set} = 1.9$) and with very small fluctuations in the last five hours of the EC-32-3 experiment ($\Phi_{d,set} = 2.2$). The product-PSDs of EC-22-2 hit the objective-grain diameter $d_{pr,set}$ very precisely, although the less accurate feed rate control method F1 has been employed. By contrast, the EC-32-3 experiment, which was conducted with the more accurate feed rate control method F4, shows $q_{0,pr}$-curves that lie a little above the target value. Such an opposing process evolution conflicts with the prediction of product size by the applied parameter setting method SFM2 in the first moment. But, there could be several other reasons for an inaccurate product size control, as explained in the following.

Influence of model parameters of method SFM2

For instance, several unknown values of the model parameters of method SFM2 had to be assumed for the present continuous granulation study, which are the material losses of spray solids $\Phi_{spr,loss}$ (coating) and nuclei $\Phi_{f,loss}$ and the effective coating density ρ_c. They were set constantly in the PS2 experiments (EC-21 to EC-33) with $\Phi_{spr,loss} = 20\,\%$, $\Phi_{f,loss} = 0$, and $\rho_c = 820.8\,\mathrm{kg/m^3}$. At this, mass losses that had been measured in the discontinuous granulation study (see Section 10.1.4) were entirely attributed to coating

material by neglecting core losses. In the batch experiments, only the pump rotation speed of 7 rpm was used, which corresponds to spray rates of around 800 g/h. Such spray rates were only adjusted in the EC-21 and EC-22 experiments as part of the continuous granulation study. With values above 1000 g/h they were higher in the experiments EC-31 to EC-33, in which the impeller of the pump rotated at 9 rpm. The spray loss fraction could possibly be lower in this case, but this is only a purely hypothetical consideration. It was also found that material losses varied widely between discontinuous experiments with the same inlet gas and spraying conditions. Hence, a randomness factor cannot be completely excluded in this context. On the other hand, larger pump rotation speeds are accompanied by higher water spray rates; whereby more wetting of the fluidized bed occurs. Thus, wet surfaces of bed particles collide more frequently to chamber walls under those conditions, so that adhesion of granules to the process chamber (fouling) is amplified. The nuclei mass loss fraction $\Phi_{f,loss}$ would be then higher in the EC-32 experiments than in EC-22, and the associated error would be bigger. Such an error propagates in the parameter setting variant SFM2 as follows. According to Eqs. 9.27 and 9.28, values of the core loss fraction that are estimated too low lead to excessive ratios in the spray-to-feed rate $\Phi_{m,set}$ and to insufficiently large set feed rates $\dot{M}_{f,set}$. Consequently, the steady-state particle growth ratio obtained (in an average sense, e.g., $\Phi_{d_m} = d_{m,pr}/d_{m,f}$) would lie above the predefined desired particle growth ratio; or in other words: the obtained product mean size would exceed the target diameter, as observed in the EC-32-2 experiment. As already mentioned, the effective coating density ρ_c was calculated from Hampel's porosity measurements [2], and its value was presumably underestimated. The macroscopic coating analysis method of the present work (Section 9.3), which was carried out after the continuous granulation experiments, provides an effective coating density of around 1200 kg/m^3 for thick sodium benzoate layers on Cellets®-cores. If the latter value were more truthful for the process conditions of the continuous experiments, then the error in ρ_c would be quite large in all experiments. The analyses of coated Cellets® have also shown that effective coating density changes greatly when low particle growth ratios are generated (represented by Φ_d), but only slightly at particle growth ratios above circa 1.7. The desired particle growth ratios of the examples EC-22-2 and EC-32-3 were even greater; wherefore, the variation in granule size enlargement ($\Phi_{d,set} = 1.9$ and $\Phi_{d,set} = 2.2$) and its possible influence on coating properties are not considered to be a significant reason for the ascertained differences in product size control. In contrast, the different drying kinetics in the EC-22 and EC-32 processes could affect the apparent coating density. Such a behavior is also recognized in discontinuous granulation experiments, see for instance Table 10.7. At this, the coatings tend to be less dense with slower drying kinetics. In view of this, the effective coating densities in the EC-32 experiments would be lower than in EC-22. A decrease in the effective coating density would lead to higher growth rates and thus to larger product grains than is expected from the parameter setting variant SFM2. However, the influence of different drying kinetics is not regarded as a dominant cause of the control deviations in product size, since the change in effective coating density between batch products of different drying conditions was not very large. Aside from that the sensitivity of product size development could be examined in future investigations by means of a two-dimensional population balance model, which contains an ideal two-component single particle model (such as in Chapter 3) and in which particle size and layer thickness are distributed properties.

Influence of definition of target-product diameter

Another aspect of imprecise parameter setting concerns the determination of the desired product diameter $d_{pr,set}$ of the continuous experiments, which was calculated from the first statistical moment of the number-based nuclei size distribution $d_{m,f}$ (according to Eq. 2.32) and the predefined desired growth ratio $\Phi_{d,set}$. This concept is based on the ideal granulation model, where mono-sized nuclei and product granules, stationarity, and ideal separation conditions are assumed. The nuclei diameter, target-product diameter, and desired particle growth ratio are exactly defined in this model. Further, particle characteristics of nuclei and product granules are unequivocally related to solids spray rate and feed rate in the idealized granulation model. In the experiments on the contrary, employed nuclei have a certain polydisperse particle size distribution, and the product size distribution in steady state is not known a priori. Beside this, a clear relation between nuclei feed rate, solids spray rate, and product average characteristics is missing, as described in Section 9.4.4. For these reasons, the target-grain diameters of product had to be estimated by a statistical moment of the polydisperse nuclei size distribution. In the present experimental granulation study, the arithmetic mean $d_{m,f}$ was chosen, because the use of such a mean value for *target-product formulation* in PB-simulations with the process control strategy CM3 (Section 6.1) has delivered promising results. The desired product diameter then ensues from: $d_{pr,set} = d_{m,f}\Phi_{d,set}$. Unlike in the experimental processes, however, the core size distribution was symmetric and component densities (core and coating) were uniform

in this PB-study. Therefore, it has not been proven whether the used type of target-product diameter represents an exact objective or just a rough guide for the experiments. Nevertheless, a scalar target value in product size indicates the direction for continuous granulation processes and creates comparability between them. To name another variant, the mean-volume-equivalent diameter (according to Eq. 2.36) of the nuclei size distribution could be tried out in order to define the target-product size in future studies. Different types of objective-size formulation (based on e.g., arithmetic mean or volume-equivalent mean) could be implemented into a two-dimensional population balance model with granule size and coating thickness as internal property coordinates and compared to stationary product-PSDs. Moreover, the set separation gas velocity of the P-control function $u_{g,set}$ was adapted to the desired product diameter (according to Section 9.4.6) in the experiment. The possible error of $d_{pr,set}$ affects product classification too. This effect is presumably stronger if the selectivity of the classifier is very precise ($\kappa_{sep} \to 1$); and it is possibly relativized for flatter separation curves. The separation performance in the present experiments was not very high, but only sufficient. A separation sharpness of approximately 85 % was measured by Hampel [2] with the same classification equipment, parameter setting of the feed-out pinch valves, and type of particulate materials (Cellets® coated with sodium benzoate). Furthermore, in most cases, the manipulated separation gas velocity u_g deviates from the set value anyway due to control deviations. Therefore, the error in the adjustment of the set separation gas velocity due to an imprecise definition of the target diameter is not regarded as a decisive reason for control deviations in product size.

Influence of unwanted particle formation effects

Other types of particle formation can occur in the granulation chamber that might influence product size development. This includes aggregation of coated Cellets® (agglomeration) and formation of sodium benzoate cores by either premature drying of spray liquids (nucleation) or fragments of coating layers (attrition). The agglomeration tendency in Wurster granulation is low due to the high shear forces in the Wurster tube, but only as long as the drying capacity of the inlet gas is sufficiently greater than the amount of water sprayed in. Such drying conditions were guaranteed in the PS2 experiments. In addition, the product samples of the presented continuous granulation experiments hardly contained any agglomerates. Only a few agglomerates, consisting of only two to four coated particles, were observed by the eye in some of the samples. Hence, agglomeration cannot be one of the major factors causing control deviations in product size. From this point of view, granulation with Wurster equipment is more suitable for validating the processing strategy PS2 in terms of product size control than processes in top-spray configuration. A fraction of pure sodium benzoate particles (without a Cellets®-core) in the product samples, which arises from nucleation and attrition, was not determined in this study. Such particles are often lighter than the coated Cellets®, since they are smaller - especially immediately after their formation - and have a lower effective density. Therefore, it is assumed that the majority of sodium benzoate particles (NaB) are either emitted as dust in the exhaust gas or adhered to the inner walls of the granulator system. This content is taken into account by the spray loss factor $\Phi_{spr,loss}$ in the spray-to-rate setting method SFM2. However, it is possible that particles of pure coating material remain in the Wurster bed and become larger. In this case, less mass of spray solids would be deposited on the surfaces of coated Cellets® reducing the product size on average. But, negative product size control deviations ($d_{m,pr} \ll d_{pr,set}$) are not detected in the stationary PSD-charts. Instead, most of the product granules were even bigger than the target value in the EC-33-3 experiment. In addition, the spray rate in the EC-33-3 experiment was about 28 % higher than in the EC-22-2 example, so that the gas temperatures and drying kinetics in the process chamber were lower for EC-33-3. The tendency towards premature drying of spray droplets, and thus towards formation of sodium benzoate cores, is reduced under these conditions, which could explain larger control errors in product size of the EC-32-3 experiment. Apart from this, breaking of Cellets® in Wurster fluidization can be ruled out due to their mechanical stability.

Influence of imperfections of the ancillary equipment

There are also other potential sources of error in product size control, which are related to random variations in the ancillary equipment. For example, the two-substance spray nozzle had to be readjusted before each of the continuous granulation experiments. When doing this, small changes in the installation might have a significant impact on the spraying pattern, and thus, on spray losses, coating efficiency, and nucleation tendency. However, there is a lack of data on this aspect to draw further conclusions. Another possible factor is that the estimated single dosage mass $M_{dos,f,est}$ of the feed rate control method F1 can be subject to relatively large errors due to dosing fluctuations. The value thereof was taken from dosing measurements (see EF-2 in Section 9.44) with comparatively low single open-state times of the feed-related pinch valves

($t_{V1,f} = 10\,\mathrm{s}$ and $t_{V2,f} = 1\,\mathrm{s}$). The single opening times in the EC-22 experiment were far greater with a value of respectively 343.7 s. The estimated single dosage mass may vary under those conditions. The experimental series EF-2 (see Figure 10.13) showed lower average dosage masses for larger opening times of the lower pinch valve ($t_{V2,f} > 1\,\mathrm{s}$). However, this needs not be the case in the granulation experiments either. Other factors such as the inclination angle and the rotation angle of the double-pinch valve affect the dosing behavior too. In the dosing study, the single doses were fed into a measuring beaker near the process chamber, whereas the double-pinch valve in the continuous granulation experiment was directly connected to the process chamber. Care was taken in the dosage measurements to ensure that the feeding equipment was oriented with the same angle of inclination as in the continuous experiments; but there was still a slight shift. Because of this, actual feed rates could have been different in the continuous experiments. A concrete statement about the so-called memory effect (mentioned in Section 9.4.1) of the pinch material (here rubber) in continuous experiments cannot be made. The memory effect means that reformation of the pinch material is slowed down in permanent operation of the double-pinch valve with short open-state times, which lowers the feed rate in the long term. The influence of this effect was observed in investigations of the feed rate control method F3 (see Figure 10.15), in which the opening times of the lower pinch valve had been very short: $t_{V2,f} = 0.1\,\mathrm{s}$. Due to the long open-state times in the continuous experiments, it is conceivable that the pinch material had enough time to return to its original shape, so that a long-term reduction in the feed rates probably did not take place. The spray rate error is considered to be small for the continuous granulation. Changes in spray rate were determined in the discontinuous granulation study (Section 10.1.4), which are shown in Table C.4. At this, the pump rotation speed was set to 7 rpm in each of the discontinuous experiments. The spray rates obtained varied with relative standard deviations (CV) of 1 to 3.9 %, whereat the pinch pad was not properly adjusted in the impeller housing of the pump in some batch experiments, which led to significantly reduced spray rates and an increase in the spray-rate-CV.

Influence of PSD-skewness of the product on success indices

The PSD-skewness of the product (γ_{pr}) was determined for all follow-up experiments (EC-22-2, EC-32-2, and EC-32-3) of this continuous granulation study, see Table C.8. The PSD-skewness results show negative values for all product samples in each of these experiments. In a figurative sense, this means that the left tail of product-PSD is always longer than the right one. This effect is most probably due to the broad bed granule size distributions below the target value in combination with separation imperfections. For left-tailed and monomodal product-PSDs, the mean value is smaller than the mode. Therefore, product overgrowth appears visually stronger in the PSD-charts than in the case of mean-value-based success indices such as the presented particle growth ratio Φ_{d_m} and the corresponding relative control deviation ζ_d.

Feasibility for rough product size control

The experiments of this study have proven that product size can be roughly adjusted in continuous granulation with external product classification through a processing strategy with the spray-to-feed rate setting method SFM2 and a set separation gas velocity of a proportional bed mass controller that is adapted to the desired product diameter. At this, the desired particle growth ratio $\Phi_{d,set}$ is the primary target quantity, according to which several process parameters have to be defined. The startup experiments of this continuous granulation study (EC-21, EC-22-1, EC-31, EC-32-1, and EC-33), which were conducted for only nine hours, did not provide any stationary bed granule and product size distributions, wherewith the product size control strategy could be validated. Nevertheless, it is evident that the product mean diameters grew faster in the startups, the higher the desired particle growth ratio is. This can be recognized particularly well from the long-term mean values of the particle growth ratios obtained, which are listed in Table C.7. The product mean diameters determined for stationary conditions in extended granulation by the follow-up experiments (EC-22-2, EC-32-2, and EC-32-3) were close to the target value. The (overall) time-averaged relative product size control deviations of these experiments (see Table C.8) show two remarkably good values of 1.3 and 1.6 %, and one practically acceptable value of 5.6 %. Therefore, the applied product size control strategy within PS2 is considered to be successful.

11 Summary and outlook

The aim of this thesis was to develop operation concepts for continuous fluidized bed spray granulation with external product classification and to investigate process limits in this regard. For this purpose, diverse partial effects of continuous fluidized bed spray granulation were examined with the help of three models and various experimental investigations using the example of a laboratory system with Wurster equipment (Section 9.2). The findings of the presented sub-studies were taken into account in diverse processing strategies including model-based parameter settings and different control methods. These were finally applied in several continuous granulation experiments with very satisfactory results. However, some aspects of the models, the operation concepts, and the experimental equipment can also be further improved. In the following, the most essential findings of this work are compiled in Section 11.1 for the model results and in Section 11.2 for the experimental results.

11.1 Summary of model results

The modeling part of this work includes the ideal continuous layerwise granulation model (ideal granulation model or ICLG-model) in Chapters 3 and 4, the three-compartment population balance model (short PB-model) in Chapters 5 and 6, and the two-zone continuum model of circulating Wurster fluidization in Chapters 7 and 8. A summary of the characteristics, results, and conclusions of the models is given below.

Ideal continuous layerwise granulation model

The ideal continuous layerwise granulation model considers continuous layerwise granulation under very idealized conditions (Section 3.1.1) such as operation in steady state, mono-sized and spherical nuclei and product granules, absence of agglomeration processes and nuclei breakage, and perfect product separation with a uniform residence time of granules in the entire granulator-separator system. A similar, somewhat simpler model has already been presented by Mörl et al. ([110], see Section 3.1.2), in which intraparticle density is assumed to be homogeneous and uniform among all bed particles. The new ideal granulation model, on the other hand, considers both cases: same and different material densities of nuclei and on-sprayed layers. In addition, mass loss terms of the core and coating materials are also taken into account here. The ideal granulation model describes how process parameters have to be set for stationary conditions. However, the conditions of the real process should not deviate too far from the assumptions of the ideal granulation model. The ICLG-model also enables the definition of various process parameters (Sections 3.1.3 and 3.1.4), and with these, the formulation of various processing strategies, as for the PB-simulations (Section 6.1.1) and for the continuous granulation experiments (Section 9.4 and 10.4). These include the desired particle growth ratio $\Phi_{d,set}$, the component density ratio Φ_{ρ}, the nuclei mass loss fraction $\Phi_{f,loss}$, the spray mass loss fraction $\Phi_{spr,loss}$, and the required spray-to-feed rate ratio $\Phi_{m,set}$. The desired growth ratio $\Phi_{d,set}$ is the main target quantity, in dependency of which several other characteristics are described within the ICLG-model. A relationship between the required spray-to-feed rate ratio $\Phi_{m,set}$ and the target-growth ratio $\Phi_{d,set}$ was derived from partial mass balances of the particle components in Section 3.2. It turned out in the course of this thesis that the $\Phi_{m,set}$-$\Phi_{d,set}$-relation is the key element in controlling the product mean size. Three variants of adapting the spray-to-feed rate ratio to the desired particle growth ratio are possible. These are the *spray-to-feed rate setting methods* SFM1, SFM2, and SFM3 (Table 3.1). The second of them is the most reasonable for experimental application, since it is better to predefine the spray rate properly in terms of process stability. From the spherical two-component particle model with different material densities of nuclei and coatings, it follows that the total effective particle density ρ_p changes particularly strongly with initial growth up to twice the core size ($\Phi_{d,set} = 2$) and gradually takes on the value of the coating density with further growth (see normalized particle density ξ_{ρ} in Figure 4.2). The limiting case analysis of a one-dimensional population balance applied on the ICLG-model has shown (Sections 3.3.1 and 3.3.2) that the desired particle growth ratio and/or the target-product diameter are independent of the bed mass: $\{\Phi_{d,set}, d_{pr,set}\} \neq \mathrm{f}(M_{bed})$. This means that the processing strategies that follow from the ideal granulation model can be applied to variable system scale.

Moreover, the *relative product sinking velocity* $\Phi_{u_{s,pr}}$, the *critical coating-to-core density ratio* $\Phi_{\rho,cr}$, and the *minimum required particle growth ratio* $\Phi_{d,min}$ were introduced (Section 3.6), with the help of which the influence of particle growth on the product sinking velocity $u_{s,pr}$ can be characterized. For continuous granulation with product discharge through air classification, it is imperative that the product granules have a higher terminal sinking velocity than the nuclei ($u_{s,pr} > u_{s,f}$). However, when coating layers are much lighter than the cores, the product sinking velocity can be lower than that of the nuclei for initial growth (low $\Phi_{d,set}$). In such conditions, the coating-to-core density ratio is less than the value of the critical coating-to-core density ratio ($\Phi_\rho < \Phi_{\rho,cr}$) and the relative product sinking velocity is less than unity ($\Phi_{u_{s,pr}} < 1$). The continuous granulation with air classification can then only be used for sufficiently large particle growth. The minimum required particle growth ratio sets the point from which on the product sinking velocity exceeds unity ($\Phi_{u_{s,pr}} > 1$) and increases further with ongoing granulation ($\Phi_{d,set} > \Phi_{d,min}$). If buoyancy force is neglected ($F_{bu} = 0$) in calculation of terminal sinking velocity of the cores and products, very simple values for the critical coating-to-core density ratio can be derived for the Stokes and the quadratic flow regime (Eqs. 3.103 and 3.104, Table 2.2). For small particles settling in the Stokes range, the product sinking velocity decreases with initial growth if the coating density is less than around one third of the density of the core ($\Phi_\rho < \Phi_{\rho,cr}(F_{bu} = 0) = 1/3$). For large particles settling in the quadratic regime, undercritical coating states are reached when the coating density is less than around two thirds of the density of the core ($\Phi_\rho < \Phi_{\rho,cr}(F_{bu} = 0) = 2/3$). In the transition regime, the critical coating-to-core density ratio lies between circa one third and circa two third.

Three compartment population balance model

The PB-study in this thesis is based on the experimentally validated two-zone population balance model from Hampel's reference case ([1, 2],see also Section 2.3.2), with which layerwise particle growth of continuous granulation with external air classification of the product was simulated. The model considers a granulator-separator system, in which the granulator consists of a spray zone and a drying zone and is joined to a *straight-duct air classifier* via a bed outlet channel and a fine-fraction recycle connection. In the present thesis, it is spoken of a three-compartment population balance model to also imply the classifying process unit and to differentiate the model from the discontinuous granulation process without classification, which, according to Hampel, can also be simulated well using a two-zone population balance model. The following assumptions were made for the three-compartment PB-model. All particles - external nuclei, bed granules, and the product - are spherical and of uniform effective particle density. The nuclei are polydisperse. Granules of the system can only linger in the spray zone and drying zone. The product classification is considered to be infinitely fast or quasi-stationary, and is described by Heinrich's extended version of the drift-and-dispersion model of Molerus a. Hoffmann ([88, 103], see also Section 2.2.7). The residence time in the spray zone and drying zone is constant for all particles. Only layerwise particle growth takes place, and other PSD-changing phenomena such as agglomeration, breakage, nucleation, and material losses of nuclei and spray solids by wall adhesion and elutriation with exhaust gas are disregarded. The even-growth approach of Mörl et al. was used ([110], see also Appendix B.2). Further, Hampel's model includes an *proportional bed mass controller* (Eq. 2.162), which pursues to hold the bed mass M_{bed} close to a set value by manipulating the separation gas velocity u_g. The three-compartment PB-model of this thesis adopts the described assumptions, but the particle flow structure (Figures 2.7 and 5.1) has been adapted to the real process of the reference case (Figure 2.6), and some supplements were added in terms of bed mass and product size control. The bed mass control function was extended with a *deactivation option*, also referred to as *offset mode*, and a *mathematical securing* for high bed mass values in order to avoid calculated separation gas velocities of or less than zero in the PB-simulations. The controller output of the offset mode and the zero-control-deviation velocity (conforms with u_0 in Eq. 2.162) of the activated mode were defined as the here so-called *set separation gas velocity* $u_{g,set}$, which can be defined arbitrarily or coupled to desired product characteristics.

Besides, the *separation frequency factor* k_{sep} was introduced to describe the number density distribution inflow rate of granules into the separator $\dot{n}_{sep}$. The separation frequency factor is defined by two different approaches (Eqs. 5.6 to 5.8). One, denoted by SFF1, is given with the reciprocal of a constant separation time factor τ_{sep}, and the other, denoted by SFF2, is defined by the ratio of a constant bed discharge rate $\dot{M}_{sep}$ to the current bed mass $M_{bed}(t)$ (both described in [2]). The main advantage of the SFF2-variant is that the classifier entry rate $\dot{M}_{sep}$ can be determined by experimental bed discharge rates (e.g., Section 10.3), and temporal changes in bed mass can be taken into account. In contrast to the previous work, the growth rate G_d (Eq. 5.12) here is related to the surface area of only the spray zone particles, and the effective densities of

the core and coating materials are equal. Thereby, the conservation of mass is maintained. In addition, the separation function was reformulated for the present PB-investigations to parameterize it by two quantities, analogously to the original model of Molerus a. Hoffmann of Eq. 2.146. These are represented here by the *Bodenstein number of the axial gas dispersion* $Bo_{ax,g}$ (Eq. 2.138) and the average separation gas velocity u_g. The separation sharpness κ_{sep} according to Eq. 2.136 for the classifier was created as a function of these two separation parameters, in each case over a process-relevant value range (Figure 6.1). It shows that the performance of the straight-duct air classifier is the better, the higher the Bodenstein number of axial gas dispersion is. This means by the $Bo_{ax,g}$-definition in Eq. 5.13 that longer and thinner classifier tubes lead to sharper separation.

The population dynamics investigation of this thesis is divided into two sub-studies (Sections 6.1 and 6.2). Therein, three different *simulation processing strategies* (Table 6.1: CM1, CM2, and CM3) were examined with the aim of a stable bed mass control and a variable and precise product mean size control. These differ essentially in the activity mode or inactivity mode (offset) of the bed mass controller and the application or omission of the spray-to-feed rate setting method of the ideal granulation models from Section 3.2.2. The set separation gas velocity $u_{g,set}$ is adapted to the desired product size $d_{pr,set}$ ($\Phi_{d,set}$ too) via the terminal sinking velocity (Eq. 5.30) in all three processing strategies. Other parameters are taken from Hampel's study. In strategy CM1, the controller's offset function is applied and bed mass control is omitted with the risk of process destabilization. The ratio of solids spray rate to nuclei feed rate is chosen freely and not adapted to the target diameter $d_{pr,set}$. In strategy CM2, the spray-to-feed rate ratio is set in the same way as in CM1, but the bed mass is actively controlled. Processes of strategy CM3 are operated with both active bed mass control and a spray-to-feed rate setting method of the ICLG-model. From the three variants of setting the required spray-to-feed rate ratio (Table 3.1), method SFM3 was used for the CM3-simulations. For validating process goals by scalar success indices, the *relative control deviations* (see Eq. 5.33) in bed mass ζ_m, separation gas velocity ζ_u, and product mean size ζ_d were introduced.

The three strategies were firstly simulated for a *slight-growth granulation process* with $\Phi_{d,set} = 4/3$ and a *large-growth granulation process* with $\Phi_{d,set} = 8/3$, each of which for a given separation sharpness of 85 %. Here the temporal courses of the product size distribution $q_{0,pr}$, the bed mass M_{bed}, the separation gas velocity u_g, and the product mean diameter d_m were evaluated. All of these simulations have reached a steady state. However, only the third strategy CM3 was able to guarantee accurate control of product mean size under stationary conditions. In addition, the terminal relative control deviations in bed mass $\zeta_{m,end}$ and product size $\zeta_{d,end}$ were determined for each processing strategy and for various desired particle growth ratios between 1.02 and 3.5 and various separation sharpnesses between 0.25 and 0.95 (Figure 6.4). The results of this two-dimensional parameter variation study have shown that CM1-processes can end up in excessive bed mass values far above the granulator capacity for large-growth granulation goals with $\Phi_{d,set} \gg 4/3$ and with high separation sharpnesses, where process stability is definitely lost. The other two strategies CM2 and CM3 provide bed mass control deviations in an acceptable range. An adjustable and precise product mean size control is not possible with the first two strategies CM1 and CM2, regardless of the separation performance. As ascertained before with the slight-growth and large-growth granulation examples, the $\zeta_{d,end}$-plots of the CM3-strategy have shown again that product mean size can be controlled arbitrarily with high accuracy, but only if separation is sufficiently sharp.

The PB-simulations of Section 6.1 were conducted with the separation frequency factor approach SFF1. In the second PB-study of Section 6.2, simulations for five different gain factors K_m (between 1 and 12 m/s/kg) were created for both separation frequency factor approaches. The results of the two methods SFF1 and SFF2 are almost the same. It is therefore assumed that subsequent simulations can also be carried out using the SFF2-method. The variation of the gain factor has hardly any influence on the time curves of separation gas velocity and product mean size. The development of bed mass over time and its stationary states change significantly for the various gain factor examples. However, instable process conditions in terms of inappropriate bed masses can still be ruled out. Subsequently, five simulations of different desired particle growth ratios between $\Phi_{d,set} = 4/3$ and $\Phi_{d,set} = 8/3$ were investigated with the SFF2-variant and with an experimentally optimized gain factor of $K_m = 3\,\mathrm{m/s/kg}$. The gain factor is significantly smaller than in the previous study and thus leads to greater control deviations in bed mass during the startup. The effect is stronger for large-growth than for slight-growth granulation conditions. Excessively high bed masses could arise in the transient phase with a smaller gain factor for very high desired particle growth ratios. A manual control method, as proposed in Sections 9.4.9 and 9.4.10, would be recommended for startup then. Compared to a bed mass controller with an integrative element, a pure P-controller proves to be advantageous for product size control due to its property of guiding the system to a certain steady

state with remaining control deviation. As a result, such bed mass values are obtained in steady state, the control deviation of which results in such separation gas velocities, for which the classifier discharges just as much core and coating material in the product as supplied by the spray-to-feed rate ratio. This means that the *law of mass conservation* can provide a ratio of coating layer thickness to core diameter on average and, thus, a desired particle growth ratio, when a proportional bed mass controller is used. The integrative part in the control function could generate more precise bed masses, but would be disruptive for product size control accuracy. Further, the PB-simulations also show that the product grain size achieved is independent of the bed mass, as previously predicted by the ideal granulation model.

In summary, the following conditions must be fulfilled in order to achieve stable continuous fluidized bed spray granulation with external product classification, feed-back bed mass control, and controllable product mean size.

- For bed mass control by manipulating the separation gas velocity, a proportional control structure should be used.
- The set separation gas velocity (zero-control-deviation velocity) of the bed mass controller should be calculated from the terminal sinking velocity of a granule with the desired product diameter.
- The spray-to-feed rate ratio should be adapted to the desired particle growth ratio using the ideal continuous layerwise granulation model.
- The separation performance should be sufficiently good, with a separation sharpness of over 80 %.

Two-zone continuum model

The presented two-zone continuum model describes the following main aspects of Wurster granulation:

- inlet gas flow separation by a perforated bottom plate with sections of different opening ratios for creating a binary distribution of average flow velocity,
- fluid transport dynamics of process gas passing the spray zone (Wurster tube interior) and the process gas expanding the fluidized bed within the drying zone (Wurster tube exterior),
- humidification and cooling of the drying zone process gas by evaporation,
- fluid-particle transport dynamics of circulating Wurster fluidization,
- dimensionless process parameters, and
- process limits in terms of minimal Wurster fluidization, process-gas saturation, and Wurster-tube exceedance.

Heat losses, injection of process gas from the nozzle into the spray zone, and spray zone evaporation are formally contained in the TZC-model too, but they play only a side role in this thesis. The *binary velocity distribution* of the flow passing the gas distributor plate could be derived analytically from an isothermal flow separation model (Section 7.4.2), where two distributor plate sections of different perforation degrees are seen as flow resistances connected in parallel, and where the empirical pressure drop equations of Hunt et al. [70] and McAllister et al. [71] are included. The fluid transport dynamics of the process gas (e.g., average superficial velocities) are determined analytically for all the model compartments (Sections 7.3 to 7.5) without regarding the movement of particles. Sucking of process gas from the drying to the spray zone is neglected. Otherwise an iterative calculation of the process gas proportions in the spray zone and drying zone would be necessary. Circulating Wurster fluidization of the bed material has to be calculated iteratively with the equation sequence (Section 7.7), which involves the following effects: pneumatic transport of particles and swarm sinking within the spray zone, fluidized bed expansion in the drying zone, and Wurster suction of particles from the drying zone into the spray zone. The main idea behind calculating Wurster fluidization through a continuum model lies in the combination of the approaches of terminal sinking velocity (Section 2.2.1), the swarm correction factor of Richardson a. Zaki ([50], here Eqs. 2.91 and 2.93), the expansion equation according to Brötz and Richardson a. Zaki ([50, 83], here Section 2.2.5), and the *modified Torricelli outflow equation* of Burgschweiger a. Tsotsas ([90, 91], here Section 2.2.6). In the present thesis, Martin's terminal sinking velocity approach ([40], here Eqs. 2.83 and 2.87) and Kraume's suggestion for the Richardson-Zaki exponent ([28], here Eq. 2.98) were used. Other approaches are conceivable, whereby

attention should be paid to the existing flow regime (Table 2.2). For calculating process gas cooling and increase of mass flow rate by evaporation, a concept based on the here so-called *isenthalpic saturation point* (T_{sat}, Y_{sat}, Eqs. 7.13 to 7.28) and on a *lever principle* (Eq. 7.30) was developed. The isenthalpic saturation point is based on the assumption that the dry-air-specific enthalpy of humid air h_{1+Y} remains constant during moisture absorption in drying processes. A logarithmic transformation of empirical, physical data of saturated air (Figure 7.3) enabled to derive a simple polynomial relationship (Eq. 7.26) between saturation states (T_{sat}, Y_{sat}) and possible initial states (T, Y) that lie on the same h_{1+Y}-line in a Mollier-diagram (Figure 7.1 b). This correlation provides a quick estimation method for the saturation and cooling limit of a certain initial state with a given air temperature and humidity; but, it deviates a little from the more precise *adiabatic saturation point* (temperature and moisture content). The height of the conical fluidized bed was estimated by a quadratic approximation of the bed volume (Eq. 7.12). This calculation method is only suitable for steep conical apparatus walls, which is the case in the experimental system (Section 9.2.1), employed in this work.

Furthermore, different *dimensionless process parameters* are defined in the scope the two-zone continuum model in Section 7.9, which are the dimensionless inlet gas velocity ξ_{in} (Eq. 7.129), the dimensionless water spray rate $\dot{\mu}_w$ (Eq. 7.130), the dimensionless nozzle air rate $\dot{\mu}_{g,noz}$ (Eq. 7.131), the dimensionless bed mass μ_{bed} (Eq. 7.132), and the normalized bed height $\Phi_{h,1-\alpha}$ (Eq. 7.133). With them, circulating Wurster granulation can be characterized for different process conditions, plant scales, and bed materials. General definitions of the process limits, in terms of *minimal Wurster fluidization*, *process-gas saturation*, and *Wurster-tube exceedance*, as well as the critical water spray rate are formulated (Section 7.10). The different process limits are expressed by means of the inlet gas velocity (u) and its dimensionless equivalent (ξ). The minimal-Wurster-fluidization limit (u_{mwf} and ξ_{mwf}) determines that inlet gas velocity from which on the bed material begins to fluidize in the drying zone. The process-gas-saturation limit (u_{sat} and ξ_{sat}) indicates the minimum inlet gas velocity or the maximum water spray rate at which the process gas in the drying zone is saturated. The Wurster-tube-exceedance limit (u_{exc} and ξ_{exc}) is characterized by that inlet gas velocity that lets the homogeneous fluidized bed expand to the upper edge of the Wurster tube. The critical water spray rate $\dot{M}_{w,cr}$ marks the point where the limits of minimal Wurster fluidization and process-gas saturation intersect. This point is alternatively described by the corresponding critical dimensionless water spray rate $\dot{\mu}_{w,cr}$. The minimal-Wurster-fluidization limit needs to be considered for undercritical water spray rates ($\dot{M}_w < \dot{M}_{w,cr}$ and $\dot{\mu}_w < \dot{\mu}_{w,cr}$) and the process-gas-saturation limit for overcritical water spray rates ($\dot{M}_w > \dot{M}_{w,cr}$ and $\dot{\mu}_w > \dot{\mu}_{w,cr}$). *Approximate, analytical solutions* for these process limits and the critical water spray rate have been derived in Section 7.11 with different simplifications, such as isothermal system, adiabatic walls, no evaporation in the spray zone, and/or presence of the entire bed mass in the drying zone.

The results of the two-zone continuum model include a derivation of characteristics related to distributor plate perforation design and isothermal flow separation (Section 8.1), a sensitivity analysis of fluid-particle transport dynamics (Section 8.2), a sensitivity analysis of process limits (Section 8.3), and a characterization of process conditions in Hampel's reference case (Section 8.4).

The main characteristics of the distributor plate sections (Section 8.1) are the area fraction $\varphi_{dis,i}$ and the perforation degree $\Psi_{dis,i}$; those of isothermal flow separation are the binary velocity split ratio $\omega_{2,3}$, the inlet gas velocity acceleration factor $\omega_{2,in}$, the inlet gas velocity throttling factor $\omega_{3,in}$, the drying power bypass fraction $\Omega_{2,in}$, and the drying gas mass fraction $\Omega_{3,in}$. The gas velocities passing the distributor plate section below the Wurster tube are much higher than the flow entering the drying zone, by the distribution factor of $\omega_{2,3} = 5.58$. Such a velocity ratio is recommended for a stable Wurster granulation process. The process gas velocity of the drying zone inlet is lower than the inlet gas velocity (here by the throttling factor of $\omega_{3,in} = 0.65$) due to the low perforation degree of the third distributor plate section. Hence, the inlet gas velocity of the minimal-Wurster-fluidization limit u_{mwf} is always larger than the characteristic minimal fluidization velocity of the bed material u_{mf}. Moreover, most of the injected water evaporates in the drying zone. Although the area in the gas inlet below the drying zone is around 85 % ($\varphi_{dis,3}$) of the total cross-section, just 55 % (drying gas mass fraction $\Omega_{3,in}$) of the inlet gas flows through this distributor plate section due to its low degree of perforation of 4.75 % ($\Psi_{dis,3}$). As a result, round 45 % (drying power bypass fraction $\Omega_{2,in}$) of the inlet gas drying capacity goes through the spray zone, where significantly less water is evaporated. This reduces the overall drying performance of the system significantly.

Within the first sensitivity analysis (Section 8.2), the dimensionless inlet gas velocity ξ_{in}, the bed mass M_{bed}, the water spray rate $\dot{M}_w$, and the inlet gas temperature T_{in} are varied, and their influence on characteristics of the spray zone and the drying zone is investigated, which are the bed mass fraction of the spray zone α_m, interparticle porosities ε_α and $\varepsilon_{1-\alpha}$, particle residence times τ_α and $\tau_{1-\alpha}$, the pneumatic conveying velocity

$u_{pn,\alpha}$, fluidized bed height $H_{1-\alpha}$, and the *Wurster suction rate* $\dot{M}_{wt,tor}$. These characteristics of fluid-particle transport dynamics change only slightly with the water spray rate and the inlet gas temperature, since they are almost independent of thermodynamic states of the process gas; but, they are primarily affected by the (dimensionless) inlet gas velocity and also by bed mass. Solutions of the two-zone continuum model have been obtained for the entire (dimensionless) inlet gas velocity domain from the minimal-Wurster-fluidization limit for a non-sprayed isothermal system or from the process-gas-saturation limit for a sprayed adiabatic system up to the Wurster-tube-exceedance limit. Even at low inlet gas velocities close to the point of minimal Wurster fluidization, particles can still be conveyed through the Wurster tube due to the swarm effect, which lowers sinking velocity and enhances interstitial gas velocity. From the results it is concluded that circulating Wurster fluidization possesses the property of a *swarm-effect-based self-stabilization*.

The second sensitivity analysis (Section 8.3) focuses on the influence of inlet gas temperature, heat losses, and evaporation on correction factors of process gas velocity and drying capacity (Section 8.3.1) and of the influence of inlet gas temperature, spraying and evaporation conditions, and particle diameter on limits of minimal Wurster fluidization and process-gas saturation (Section 8.3.2). The dimensionless inlet gas velocity of the minimal-Wurster-fluidization limit $\xi_{mwf,ad}$ increases almost linearly with the dimensionless water spray rate $\dot{\mu}_w$, but flatter than the process-gas-saturation line. Process gas velocity is greatly reduced by evaporation cooling. The adverse influence of the released water vapor is much lower, so that spraying has an overall lowering effect on process gas velocity. This results in higher gas inlet velocities of the minimal-Wurster-fluidization limit and the Wurster-tube-exceedance limit at larger water spray rates. The intersection of the minimal-Wurster-fluidization limit and the process-gas-saturation limit, and thus, the critical water spray rate remains approximately constant for different inlet gas temperatures. An increase in the particle diameter significantly shifts this point of intersection to higher water spray rates. Undercritical dimensionless water spray rates are more likely to be obtained at lower water spray rates, larger cross-sectional areas of the inlet gas, higher inlet gas temperatures, and for bigger and denser particles. The approximate adiabatic process-gas-saturation limit ($u^*_{sat,ad}$ and $\xi^*_{sat,ad}$) is an exact linear function of the dimensionless water spray rate $\dot{\mu}_w$ by definition. It grows therefore proportionally to the water spray rate $\dot{M}_w$ and inversely proportionally to the cross-sectional area of the gas inlet $A_{app,0}$ and maximal specific drying capacity of the inlet gas $Y_{sat,ref} - Y_{in}$. Thus, higher inlet gas velocities are needed to avoid saturated-process-gas conditions at constant water spray rates, when either the process chamber cross-section or inlet gas temperature is reduced, or both. The functional relationship between the dimensionless inlet gas velocity of the approximate adiabatic process-gas-saturation limit $\xi^*_{sat,ad}$ and the dimensionless water spray rate $\dot{\mu}_w$ is quasi-independent from the inlet gas temperature T_{in}, whereas the inlet gas velocity of process-gas saturation $u^*_{sat,ad}$ changes significantly with the inlet gas temperature. On the opposite manner, the dimensionless inlet gas velocity of the process-gas-saturation limit does and the corresponding inlet gas velocity of process-gas saturation does not depend on particle size. For this reason, the dimensional spray-rate-dependent limit curve of process-gas saturation ($u^*_{sat,ad}$-$\dot{M}_w$-diagram) is recommended as a general limit curve for sprayed Wurster fluidization for different particle characteristics, but only at constant inlet gas temperature. The corresponding dimensionless limit curve of process-gas saturation ($\xi^*_{sat,ad}$-$\dot{\mu}_w$-diagram) serves, on the other hand, as a general limit curve for different inlet gas temperatures, but only for particles having the same terminal sinking velocity (size and apparent density).

Lastly, twelve different operation points, which match with process conditions of the reference case of Hampel, were characterized by the TZC-model (Section 8.4). They differ in inlet gas temperature T_{in}, inlet gas mass flow rate $\dot{M}_{in}$, and water spray rate $\dot{\mu}_w$. Model characteristics to be determined are the dimensionless water spray rate $\dot{\mu}_w$, the dimensionless inlet gas velocity ξ_{in}, the dimensionless inlet gas velocity of the approximate adiabatic process-gas-saturation limit $\xi^*_{sat,ad}$, the dimensionless inlet gas velocity of the approximate adiabatic Wurster-tube-exceedance limit $\xi^*_{exc,ad}$, the bed mass fraction of the spray zone α_m, and the residence times of the spray zone τ_α and drying zone $\tau_{1-\alpha}$. All operation points are above the process-gas-saturation limit and far below the Wurster-tube-exceedance limit ($\xi^*_{sat,ad} < \xi_{in} \ll \xi^*_{exc,ad}$). The operation points with an inlet gas temperature of 90℃ should be preferred, as drying conditions are further away from the saturation line than at 70℃. The dimensionless water spray rates of operation points with 90℃ are between 18 and 23 %. These values are much greater than the critical water spray rates, wherefore the minimal-Wurster-fluidization limit is not relevant for the process conditions, but the process-gas-saturation limit is. The point of minimal Wurster fluidization could be the lower process limit if the bed particles were much bigger and heavier. Moreover, two operation maps $\xi_{in}(\dot{\mu}_{in})$ are designed for different inlet gas temperatures in Section 8.4.2. Therein the described process limits ($\xi^*_{mwf,ad}$, $\xi^*_{sat,ad}$, and $\xi^*_{exc,ad}$) enclose a permissible parameter regime for Wurster granulation. At this, dimensionless inlet gas velocity must be between the

lower process limit, which is either by minimal Wurster fluidization or by process-gas saturation, and the Wurster-tube exceedance: $\max\big(\xi_{mwf}(\dot{\mu}_w), \xi_{sat}(\dot{\mu}_w)\big) < \xi_{in} < \xi_{exc}(\dot{\mu}_w)$. At higher dimensionless water spray rates, the permissible range of inlet gas velocities becomes smaller, until the limits of process-gas-saturation and Wurster-tube-exceedance coincide at very high water spray rates (here around 80 %). The dimensionless water spray rate should be far below the point of interception, because in its vicinity the drying potential would be too low and the bed would be too high. In order to avoid this, the spray rate can be reduced or the inlet gas temperature increased. For the continuous granulation experiments with the system from Section 9.2.1, according to the TZC-model, an inlet gas mass flow rate of at least 70 kg/h and an inlet gas temperature of at least 90°C are to be used, if water spray rates of up to 700 g/h are injected. Besides, the zone-related parameters α_m, τ_α, and $\tau_{1-\alpha}$ were calculated for the twelve operation point examples of Hampel. They are close to values used in the PB-study of this thesis and in [2], which underpins the use of the TZC-model for further research.

11.2 Summary of experimental results

Diverse partial effects of continuous granulation with external classification, which occur with the experimental equipment used here, were investigated in this work. For this purpose, several discontinuous multi-stage granulation series (Section 10.1), a dosing behavior analysis of the nuclei feeding equipment (Section 10.2), an analysis of the bed discharge dynamics through the feed-out double-pinch valve (Section 10.3), heat loss measurements (Appendix C.6.1), and measurements of evaporation cooling across the Wurster tube (Appendix C.6.2) were carried out. The results of experimental sub-studies and these of modeling part (Chapters 3 to 8) were taken into account in the design of operation concepts for the continuous granulation experiments (Section 10.4).

Discontinuous multi-stage granulation

The discontinuous multi-stage granulation experiments were conducted for twelve different process conditions (Table 10.2), which differ in nozzle gas excess pressure $p_{g,noz}$, the type of core material (Cellets®200, Cellets®350, and glass beads), inlet gas mass flow rate $\dot{M}_{in}$, and inlet gas temperature T_{in}. The following aspects were examined: susceptibility to process destabilization, optimal setting of the inlet gas parameters (T_{in} and $\dot{M}_{in}$) and nozzle gas excess pressure $p_{g,noz}$, detection of process instabilities by pressure drop and temperature measurements, influence of process parameters and growth in bed mass on inline measurement of the pressure drop $\Delta p_{app,0}$ and inline bed mass detection M_{bed}, extent and variance of spray rates $\dot{M}_{spr}$ and spray losses $\Phi_{spr,loss}$, evolution of particle size characteristics, size-selectivity of particle growth in Wurster granulation, average particle growth kinetics and time required for certain growth, density and porosity of coating layers, and growth limit of pneumatic conveyability through the Wurster tube.

A *nozzle gas excess pressure* of at least 1.75 bar should be set for the utilized spraying equipment (Section 9.2.1) to ensure process stability. For the inlet gas parameters, the same recommendation ensues from the batch granulation experiments as from the two-zone continuum model. The inlet gas temperature should be at least $T_{in} = 90$°C, if the inlet gas mass flow rate is given with $\dot{M}_{in} = 70$ kg/h and spray rates $\dot{M}_{spr}$ match the conditions of continuous granulation experiments (here around 800 g/h). Trials with an inlet gas temperature of 70°C and an inlet gas mass flow rate of 70 kg/h often collapse. It is presumed that, in these experiments, process gas conditions of the drying region (Wurster tube exterior) are very close to saturation, where relative humidity is high and drying potential is low, as in the TZC-model results. Particle surfaces are very wet, and thus, rates of agglomeration are very high under those conditions, which ends in collapse of Wurster fluidized bed.

Pressure drop across the process chamber $\Delta p_{app,0}$, bed temperature T_{bed}, and outlet gas temperature T_{out} are good *indicators of disruptions to fluidization*. The measured pressure drop increases linearly with spraying time within the individual error-free granulation stages. In process breakdowns, the pressure drop decreases irregularly, as the holdup is greatly reduced. Bed and outlet gas temperatures increase in the case of strong bed agglomeration, since less liquid evaporates and the process gas is cooled less. The pressure drop measurements of granulation stages with Cellets® as core material and low inlet gas mass flows from 70 to 115 kg/h are more reproducible, while stages with glass bead cores and higher inlet gas mass flow rates of 175 and 190 kg/h fluctuate more. This is probably due to larger fluctuations in the control deviations of inlet gas flow between individual stages. Therefore, the continuous granulation experiments of thesis were conducted with Cellets®.

The *inline bed mass detection method* of Section 9.4.7 was examined by series of batch experiments with Cellets® for various inlet gas mass flow rates (Figure 10.4). The curves increase linearly with spraying time, as expected. Final states of the individual stages were compared with gravimetric bed mass measurements. Deviations are smallest at 70 kg/h and become larger with higher inlet gas mass flow rates. The inline detection method was implemented by Hampel [2] and adapted to 70 kg/h of inlet gas flow and a bed weight of 1 kg of Cellets®200. For experiments with larger inlet gas mass flow rates, such as for bigger and/or denser nuclei, the inline measurement method should be either fitted to those conditions or improved by a model that covers a broader range of inlet gas parameters (see Section 11.3.2). For the continuous granulation experiments, however, the present method is sufficient. From the model studies of this work, it emerged that the bed mass only has to be kept in an acceptable range for process stability (e.g., between 0.7 and 1.5 kg for Cellets®200), and that control of product mean size is independent of bed mass. For bed mass control, it is more important that changes (decrease and increase) in bed mass are detected inline, than an exact measurement. The discontinuous granulation experiments have shown that the bed mass can be recorded sufficiently well.

In the discontinuous experiments, it has been shown that adjusted spray rates fluctuate only with a small relative standard deviation of up to 4 %. Variance in spray rates can be further reduced by maintaining the filling level of the solution container and carefully installing the spraying equipment (pump, container position, nozzle installation, silicone tubes). In addition, the proportion of mass losses of sprayed solids $\Phi_{spr,loss}$ was determined. These vary considerably within the discontinuous granulation series and also between single stages. No tendency with process parameters could be identified. A mean spray loss fraction of around 20 % was selected from the batch granulation results for the parameter setting of the continuous granulation experiments. Loss of nuclei material was assumed to be negligible.

The mean particle growth (Φ_d with t) is almost constant in the beginning of a granulation series and is accelerated after around the fourth stage. The reason is reduced initial bed mass (800 g) for the next granulation stage. In the experiments with Cellets® as core material, particle growth ratios Φ_d of up to 3 were achieved. It is assumed that the products could have been enlarged further. An extreme example is the granulation series EB-34, in which the mean core diameter (here glass beads) is increased more than tenfold by sodium benzoate layers. From this point of view, the large-growth granulation goals in the continuous experiments are not expected to fail by instable circulating Wurster fluidization. Product size distributions get wider from stage to stage. This speaks for a classifying effect of the Wurster suction gap, which is probably caused by vertically-oriented particle-size-dependent segregation inside the fluidized bed. The standard deviation increases with ongoing granulation, whereas the relative standard deviation remains almost constant. Growth times for a particle size ratio of $\Phi_{d,set} = 1.9$ and $\Phi_{d,set} = 2.2$ were estimated to lie between 4.5 and 9 h (Table 10.6). It can be assumed that the startup times in continuous granulation experiments will be even larger. This brings with it a need for the development of *startup strategies to accelerate growth.*

The effective coating density ρ_c of the stage products was derived from the bulk density and the relative standard deviation of the length-based particle size distribution using a spherical two-component particle model (Section 9.3). In the experiments with *slower drying kinetics* (lower mass flow rates, Cellets®, Figure 10.10), the average effective coating densities are lower at the beginning of growth. With further granulation (higher stages) they go over into a constant range of values. The coating density depends significantly on the layer thickness. In experiments with *fast drying* (higher gas mass flow rates, glass beads, Figure 10.11), the coating densities are very high even at the beginning of growth. The coating densities here are, on average, somewhat greater than for more slowly dried coatings on Cellets®. In case of very large particles, when measuring the bulk density, the effect of *higher local interparticle porosities in the vicinity of walls* should be taken into account, or wider measuring cylinders should be used. This leads to measurement errors with lower coating densities, as can be seen in the longest granulation series EB-34 from the decreasing coating density curves. Porosities of the coating layers were determined from compact solid density and the measured effective coating densities (Eq. 9.10). These are significantly smaller for thicker layers (higher stage products, $10 - 20$ %) with slower drying than by micro-CT analysis from Hampel ([2], around 40 %).

With the help of the two-zone continuum model, superficial gas velocity of the spray zone was calculated in Section 10.1.7 for the two process examples EB-21-3 and EB-34 and compared with the mean terminal sinking velocities of their last stage products (Table 10.8). The comparison shows that the estimated superficial gas velocities are significantly smaller than the sinking velocities. Nevertheless, the *pneumatic conveyability* through the Wurster tube was given, so that stable Wurster granulation was generated. According to this, a swarm effect that reduces actual sinking velocities in the spray zone stabilizes the circulating Wurster granulation.

Dosing analysis of the feed-in double-pinch valve

The nuclei feeding equipment of the continuous granulation experiments consists of a storage container with a hopper welded to the bottom, which is connected to a double-pinch valve (Figure C.2). In the analysis of the nuclei feeding equipment (Figure 9.2), the short-term dosing behavior for several types of materials of different sizes and densities and various opening times of the lower pinch valve $t_{V2,f}$ was studied (Tables 10.9 and 10.10). The long-term dosing behavior over several hours was investigated for three different filling level conditions and a very short *flushing-out time* ($t_{V2,f} = 0.1\,\mathrm{s}$). This substudy should help to define a suitable control method for the feed rate. According to the spray-to-feed rate setting method of the ideal granulation model (Table 3.1), feed rate must be adjusted exactly in order to obtain a targeted product mean size. Three practical phenomena, which affect the average dosage units and their fluctuations, have been observed in the experimental preparation and execution. One is the *memory effect* that comes from the increase in inertia of re-opening of the pinch valves in permanent operation, which reduces the free cross-sectional area between the pinches, and thus, the mean dosing rate. The second is the *fouling effect* that is due to adherence of particles in the sluice volume. This fluctuated visibly between the dosing units. The third one is called the *flush-back effect*, in which the upper pinch valve does not close quickly and tightly enough, so that a part of the air injected into the sluice volume shoots back with a certain amount of particles through it.

The dependence of feed rate on flushing-out time is characterized by a maximum. Feed rate is zero for very short opening times, and above a critical flushing-out time, it begins to rise rapidly up to a feed rate maximum, from which it decreases again and gradually turns into a *hyperbolic curve*. For the realization of continuous large-growth granulation processes with high desired particle growth ratios, the spray rate should be adjusted to proper value and low feed rates have to be used after the spray-to-feed rate setting method SFM2. According to the nuclei dosing analysis, such low feed rates can be achieved either by throttling the single dosages with very short flushing-out times, or by very large flushing-out times, in which the feed rate is essentially *regulated by time delays*. Operation with short flushing-out times, however, is accompanied by very large dosing fluctuations. The dosing accuracy at large opening times is much better, which is why a time delay strategy for feed rate control is to be preferred. Furthermore, the individual dosage fluctuations are lower for larger and heavier particles, since fouling is presumably less. Moreover, it was detected that average single dosage masses increase with size and density of particles at high flushing-out times. Here, a weaker flush-back effect on the larger and heavier nuclei is assumed to be the cause. The memory effect can be especially well seen in the beginning (first 10 dosages) of some of the short-term dosing experiments, but also over hours in the long-term investigation. Besides, aspects such as the angle of inclination of the nuclei feeding channel, vertical arrangement of the double-pinch valve, and the pressure of pneumatic flush-air play a role for the control of feed rate too. A purely model-based feed rate control strategy cannot be formulated for the present equipment due to the multiple factors influencing the dosing behavior. Instead, the feed rates have to be determined separately before the continuous granulation experiments and adapted to nuclei material properties.

Analysis of bed discharge dynamics with the feed-out double-pinch valve

The analysis of bed discharge dynamics through the feed-out double-pinch valve contains fifteen experiments (Figure 9.3), which differ in the inlet gas mass flow rate $\dot{M}_{in}$, inlet gas temperature T_{in}, initial bed mass $M_{bed,0}$, opening times of both pinch valves $t_{V1,sep}$ and $t_{V2,sep}$, and pressure of the pneumatic control air $p_{g,dpv}$ for pressing the pinch valves together and flushing particles off the sluice volume (Table 10.11). During the experiments, the bed mass discharged was measured every thirty seconds in so-called sampling units. The temporal course of bed mass was reconstructed from the initial mass and the sampling units. In the first five experiments, it was ascertained that bed mass decreased faster at larger inlet gas mass flow rates and temperatures. Fluctuations in the sampling units were significantly lower with higher pressure of the pneumatic control air. Bed discharge dynamics was influenced to a great extent by the opening times. A distinction was made between two switching types of the particle sluice: *even switching rhythm*, in which the open-state times of both valves are the same, and *uneven switching rhythm* with unequal opening times. The next five bed discharge experiments were carried out with even switching rhythm for varied open-state times. Uneven switching rhythms were applied in the last five experiments. At this, only the opening time of the upper pinch valve was changed. For both switching types, a maximum of bed discharge dynamics over the time parameters was detected. Average conveying rates and relative standard deviations of the sampling units were derived from the sections of the bed mass curves between 1.5 kg and 1 kg. The average conveying rates showed once again that bed discharge rates have a maximum in a certain value range of the open-state times, which is in analogy to the dosing behavior of the nuclei feeding equipment.

As described in Section 9.4.2, two bed discharging processes connected in series are considered: the *drop-out mechanism* and the *particle sluice mechanism*. The slower step of both determines the overall bed discharge dynamics. The bed outlet channel is not full when discharge is limited by the drop-out mechanism, but fills when the particle sluice mechanism dominates. In some experiments, particle congestion could be recognized visually through the sluice volume (transparent plastic cylinder). Bed discharge rates could be manipulated very clearly using the switching times, which would not be the case with prevailing drop-out processes. In the continuous granulation experiments, the bed discharge rates should be sufficiently larger than the supply rate of external nuclei and spray solids; but, they must also not be too high, as separation in the overloaded classifier would suffer. The results show that these two requirements are well met by an even switching rhythm of 0.14 s for both pinch valves, as also suggested by Hampel [2]. A simultaneous switching time of 0.1 s would improve product classification; however, the average bed discharge rates measured for 0.1 s (EBD-21, Table 10.12) are close to the total input rates of solids. Such critical conditions can lead to slow bed mass control dynamics and excessive bed mass development in continuous granulation, endangering process stability.

Continuous granulation with external product classification

The processing strategy CM3 (Table 6.1), conceptualized for the PB-simulation study (Chapter 6), should be used in the continuous granulation experiments, as it can ensure bed mass stability and enable variable control of product mean size. It works with an *proportional bed mass controller* (Eqs. 5.18 and 5.17), which manipulates the separation gas velocity u_g. In it, set separation gas velocity $u_{g,set}$ is defined by the terminal sinking velocity of granules with desired product characteristics. In addition, in the CM3 strategy, the spray-to-feed rate ratio $\Phi_{m,set}$ is adapted to the desired particle growth ratio $\Phi_{d,set}$ according to the ICLG-model (Section 3.2.2). This aspect of the strategy had emerged as the key element for product size control throughout the entire PB-study. In the experimental study, the methods of adapting the spray-to-feed rate ratio (Section 9.4.5) and the set separation gas velocity (Section 9.4.6) to the desired product characteristics ($\Phi_{d,set}$ and $d_{pr,set}$) and the bed mass controller (Sections 9.4.7 and 9.4.8) had to be modified for practical reasons. Compared to the PB-study, the following aspects have been added in the experimental parameter setting and processing strategies. The mass losses of the spray solids were taken into account after the first three continuous granulation experiments. The effective densities of the coating and the core material are not considered to be the same. Both were defined according to Hampel's results [2]. Instead of SFM3 (used for the PB-study), the spray-to-feed rate setting method SFM2 (Table 3.1) was used to predefine spray rates with adequate drying conditions and faster particle growth kinetics via adjustable pump rotation speeds (discrete values of n_{pum}). The effective particle density of the set separation gas velocity $u_{g,set}$ depends here on the desired growth ratio $\Phi_{d,set}$, since component densities are different. The current bed mass is determined via the pressure loss in the process chamber with the help of Hampel's inline detection implementation (Section 9.4.7). Large parts of the control and monitoring system (DASYLab-sheet) built-up by Hampel were taken over for this thesis. Some features were exchanged, and others were added. The former bed mass controller was replaced by the P-control structure of Eq. 9.34. In contrast to the PB-simulations, the separation gas velocity (output signal of the controller) is set to zero, and not to a minimum sink rate, when a critical bed mass is exceeded.

In addition, an input field was installed, with which the set separation gas velocity $u_{g,set}$, the gain factor K_m, and the set bed mass M_{set} can be adjusted before and changed during operation. By suitably selecting these three control parameters, the separation gas velocity can be set to zero, to a maximum, or to normal operation values. Based on this, three operation modes of the classifier (Table 9.4.9) have been defined, which are the

- *total discharge mode* at $u_g = 0$,
- *classification mode* with $u_{s,f} \lesssim u_g \lesssim u_{s,pr}(\Phi_\rho, \Phi_{d,set}) \ll u_{g,max}$ (from active bed mass control), and
- *total reflux mode* at $u_g = u_{g,max} \gg u_{s,pr}(\Phi_\rho, \Phi_{d,set})$.

The discharge and reflux modes enable manual bed mass control in case of critical bed mass developments. Furthermore, two *growth acceleration strategies*, denoted by GAS1 and GAS2, were developed to shorten startup periods. The first one GAS1 pursues a *step-wise increase of feed rate* $\dot{M}_f$ from zero to the value of the SFM3 setting method ($\dot{M}_{f,set}$) to avoid a rapid increase in bed mass and to generate larger initial spray-to-feed rate ratios in the process beginning. Strategy GAS2 is a concept with *two-phase manual bed mass control*, where the holdup is kept low by alternating between the total discharge and the total reflux

mode of the classifier. The advantage here is that the bed material is discharged unclassified, so that the coarse fraction does not leave the granulator-separator system too quickly. However, the time schedule of the reflux-discharge cycles has to be adapted inline by plant operators.

To realize the calculated feed rates in the experiments with the nuclei feeding equipment, four possible *feed rate control methods* were designed (Section 9.4.3), which are designated with F1, F2, F3, and F4. The first three feed rate control methods are intended for *automatic operation* of the double-pinch valve with a sufficient nuclei filling level in the storage container. F1 works on the principle of a pure time delay of a certain dosage unit, F2 by limiting the filling time of the sluice volume, and F3 by limiting the flushing-out time. In F4, precisely weighed amounts of nuclei are poured into the empty hopper and fed into the granulator at predefined time intervals (dosing time gaps). Due to the *manual mode of operation*, F4 is not recommended for industrial use, but it is very well suited for the experimental validation of model-based processing strategies, as the long-term averaged feed rate is precisely defined. Methods F1 and F4 are used in the continuous granulation experiments. The other two were not chosen due to their dosing inaccuracy.

Subsequently, two *experimental processing strategies* with the names PS1 and PS2 were designed for the continuous granulation experiments (Table 9.5), which are made up of combinations of the substrategies described above. Both include the spray-to-feed rate setting method SFM2 and the proportional bed mass control strategy where the set separation gas velocity is related to the terminal sinking velocity with desired product characteristics. PS1 does not contain any of the two growth acceleration strategies GAS1 and GAS2, whereas PS2 acts with both of them in two variants PS2-a and PS2-b. PS1 experiments were run in automatic mode of the bed mass control system from the beginning on. PS2 experiments started with both GAS strategies in the first five hours and then continued in automatic mode.

The composition of the chosen processing strategy/variant (PS1, PS2-a, or PS2-b), feed rate control method (F1 or F4), target-growth ratio $\Phi_{d,set}$, and product-size-independent parameters of the automatic bed mass controller (K_m and M_{set}) are referred to as *overall operation concepts* here. Eight such concepts were formulated (Tables 10.13 and 10.14), and carried out in at least one startup experiment. One of them (EC-22) was continued in one follow-up experiment on a later day and another (EC-32) in two. The first three operation concepts (EC-11, EC-12, and EC-13) were based on the processing strategy PS1, the feed rate control method F1, and a small desired particle growth ratio of 1.3. From three different gain factors used, $K_m = 3\,\mathrm{m/s/kg}$ showed a good compromise between *signal transmission difficulties* and the classifier, control deviation of bed mass and separation gas velocity, and bed mass control dynamics. The next two operation concepts (EC-21 and EC-22) contain the PS2-a strategy and the feed rate control method F1. Here the desired particle growth ratio was increased to 1.6 for EC-21 and 1.9 for EC-22. In the last three operation concepts (EC-31, EC-32, and EC-33), the PS2-b strategy and the more precise F4 method were employed. The desired size enlargement ratio $\Phi_{d,set}$ was increased to 1.9, 2.2, and 2.5.

Two of the PS1 experiments broke down after 7.5 h and 8.5 h, because the nozzle gas excess pressure was too low with 1.5 bar. Further, their measured product mean sizes were far below target, for the reason that mass losses of spray solids was neglected in the calculation of the required spray-to-feed rate ratio $\Phi_{m,set}$. Thus, the results of these experiments cannot be used to evaluate the processing strategy aspects involved in PS1, but only to optimize the gain factor K_m.

The PS2 experiments were entirely stable. Bed mass could be kept in ranges of stable Wurster granulation with the manual two-phase growth acceleration strategy GAS2, and with the automatic mode of the bed mass control system including a proportional feed-back structure. Even without reaching steady states in product size, it can be seen from the experiments that higher spray-to-feed rate ratios $\Phi_{m,set}$ lead to faster growth and larger product mean diameters. This shows that product size can be manipulated by the spray-to-feed rate ratio. The follow-up experiments with the PS2 strategy achieved stationarity in product size distribution, close to the predicted mean size ($d_{pr,set}$). Their overall relative control deviations in product mean size (ξ_{d_m}, average over nine hours) were 1.3 %, 1.6 %, and 5.6 % above target. The *strategy aspects of PS2*, based on the CM3 strategy of the PB-simulation study (Table 6.1), *were thus successful*. These include the usage of a proportional bed mass control structure with manipulation of separation gas velocity, and adaption of the controller's set separation gas velocity $u_{g,set}$ and the required spray-to-feed rate ratio $\Phi_{m,set}$ to the target diameter of the product $d_{pr,set}$ or the desired particle growth ratio $\Phi_{d,set}$.

During the PS2-experiments, *oscillations in bed mass and product size distributions* were observed; those of bed mass occur in a *short- and middle-term scale* (seconds and minutes), and those of product-PSDs in *long-term scale* (hours). Short-term oscillations of bed mass result from pressure drop fluctuations of bubbling fluidization. It is assumed that middle-term bed mass oscillations and long-term product size oscillations

are essentially uncorrelated. Theoretically, bed mass and product size mutually affect each other by the law of conservation of mass, so that their oscillations are correlating, but only in the same scale of time. The middle-term bed mass fluctuations of the experiments are likely due to practical effects such as wall deposits in the classifier, which were regularly knocked off. Middle-term fluctuations of the product-PSDs, which might be superimposed on the long-term oscillation, cannot be ruled out. They would not be recognizable in the measurement results anyway, because of the rough half-hour procedure of sampling bed and product materials.

The growth acceleration aspects of the PS2 strategy were rather impractical and disadvantageous. For example, the startup times of experiments EC-22 and EC-32 could not be shortened with the growth acceleration strategies GAS1 and GAS2; instead, they became even longer. The first growth acceleration strategy GAS1 is not recommended at all. It is hard to implement, and it contributed to the development of a strongly bimodal bed particle size distribution in the transient phase of the experiments, and thus, to a product target overshoot with subsequent, damped back-oscillation. The use of both strategies GAS1 and GAS2 intensifies the oscillation effects. However, GAS2 is not viewed as entirely inappropriate. It is very well suited to keep the bed mass low in the initial phase of continuous granulation, generate higher growth rates, and possibly also fasten startup periods. The use of only GAS2 might though lead to a significant exceedance of the target-product size, if it is carried out for too long. Adequate duration of GAS2 depends, for instance, on the desired particle growth ratio $\Phi_{d,set}$, the bed mass M_{bed}, the solids spray rate $\dot{M}_{spr,s}$, and the PSD of the nuclei $q_{0,f}$.

Processes with a desired particle growth ratio of up to $\Phi_{d,set} = 2.2$ tended to have a positive bed mass deviation ($M_{bed} > M_{set}$). Factors such as the solids spray rate, the separation function of the classifier, and bed discharge rates $\dot{M}_{sep}$ play a role, here. Presumably, because of mal-discharges of the classifier, bed mass values below the set point are more likely to be obtained if the desired size enlargement ratios $\Phi_{d,set}$ are even higher. In such a case, the set bed mass could be raised a little to end up with bed masses in a range of adequate Wurster fluidization and spraying.

11.3 Outlook

11.3.1 Recommendations for modeling

In this section, various aspects for development of the presented models as well as further model-based investigations are recommended.

Ideal continuous layerwise granulation model

The critical coating-to-core density ratio ($\Phi_{\rho,cr}$, e.g., Eqs. 3.103 and 3.104) and the minimum required particle growth ratio ($\Phi_{d,min}$, e.g., Eqs. 3.109 and 3.110) could also be determined analytically or numerically by other approaches of terminal sinking velocity than those of the Stokes' and the quadratic approximation solution. Many applications of fluidized bed spray granulation, however, are situated in the *transition flow regime*. The suggestions by Goroshko et al. (Eq. 2.74) and Haider a. Levenspiel (Eq. 2.89) are suitable for the holistic description of all three flow regimes of sinking objects (Table 2.2 for spheres). The superposition approach by Goroshko et al. has quite large deviations from a sinking sphere in the transition regime. Haider a. Levenspiel's approach is very precise across all three regimes, but requires iterative calculations. Martin's solution in Eqs. 2.83 and 2.87 can also be used for all three regimes, but only for terminal Reynolds numbers up to ten thousand ($Re_s \leq 10^4$).

Furthermore, influence of width of bed particle size distribution in continuous granulation on operation range of fluidization can be investigated using the ideal particle growth model (Chapter 3) and the equations for fluid-particle transport dynamics from Section 2.2. In monodisperse fluidized beds with uniform particle density, terminal sinking velocities are always greater than those of minimal fluidization. In polydisperse beds, however, minimal fluidization velocity and terminal sinking velocity are distributed. For the theoretical process (neglecting turbulence and swarm effects), the smallest terminal sinking velocity should not be below the greatest minimum fluidization velocity in order to generate a complete fluidization of the bed without elutriation. First, the minimal fluidization point (Re_{mf} or u_{mf}) could be represented as a function of the desired particle growth ratio $\Phi_{d,set}$, the Archimedes number of nuclei $Ar_f = \frac{\rho_f - \rho_g}{\rho_g} \frac{d_f^3 g}{\nu_g^2}$, and the component density ratio Φ_ρ. The *smallest possible fluidization range number* $f_{rp,smp}$ (after Eq. 2.125) could then be

examined according to the following definition:

$$f_{rn,smp} = \mathrm{find}_{\min,f_{rn}}\big(f_{rn}(\Phi_{d,set}, d_f, \rho_f, \Phi_\rho)\big) = \frac{\mathrm{find}_{\min,u_s}\big(u_s(1 \le \Phi_d \le \Phi_{d,set}, d_f, \rho_f, \Phi_\rho)\big)}{\mathrm{find}_{\max,u_{mf}}\big(u_{mf}(1 \le \Phi_d \le \Phi_{d,set}, d_f, \rho_f, \Phi_\rho)\big)}. \quad (11.1)$$

With the help of this equation, process parameters can be determined for which the smallest possible fluidization range number of the bed becomes unity: $f_{rn,smp}(\Phi_{d,set} = \Phi_{d,max}, Ar_f, \Phi_\rho) = 1$. Such conditions only occur at high desired particle growth ratios. They characterize an *upper growth limit for processable layerwise granulation* ($\Phi_{d,max}$) in spray fluidized beds, where the entire polydisperse bed can still be hold up.

Three-compartment population balance model

The processing strategy CM3 could be assessed with other parameter conditions using the presented three-compartment population balance model of Chapter 5. For example, mean size and variance of nuclei can be varied. Granulation processes of different system scales can be simulated through various set bed masses M_{set} and initial bed masses $M_{bed,0}$ to check scale-up feasibility of the CM3 strategy. At this, it is better to adapt solids spray rate to plant scale for quick transient particle growth. The mass-specific solids spray rate of the present experiments (Table 10.14 and 10.15) with respect to the set bed mass ($\dot{M}_{spr,set}x_s/M_{set}$) could be a good orientation. They lie between 0.25 and 0.33 h^{-1}. A two-dimensional parameter variation analysis of the set bed mass M_{set} and the gain factor K_m would be useful in order to study dynamics and control accuracy of the bed mass controller of CM3. It is also of interest what influence the separator entry rate $\dot{M}_{sep}$ (bed discharge rate) has on process stability, control accuracy of product mean size, and product size variety. The ratio of the separator entry rate to the mass flow rate of total solids input ($\dot{M}_{sep}/(\dot{M}_f + \dot{M}_{spr,s})$) represents a measure of *average separation frequency* (number of separation events) of bed granules until their discharge in the product outlet under stationary conditions. The CM3 strategy could be additionally combined with the growth acceleration strategy GAS2 of Section 9.4.10, or possibly others, and applied in PB-simulations. Various scenarios, such as different durations of the GAS2-phase, could be tested. The goal here would be the development of an overall processing strategy for fast startups without significant product overgrowth and PSD-oscillations. With the help of the ideal particle growth model of Chapter 3, the three-compartment population balance model of this thesis could be converted into a two-dimensional PB-model, which has the same structure of material flows, but different effective densities of cores and coating layers, and where the particle growth ratio of the individual granules Φ_d of Eq. 3.2 or the normalized particle density ξ_ρ of Eq. 3.6 could form the second internal property coordinate. This allows to examine the influence of different component density ratios Φ_ρ from Eq. 3.3 on continuous granulation with external product classification and processing strategy CM3. However, solving partial differential equations of such a 2D-PB-model numerically is challenging, especially for the process start, where nuclei are non-coated, the bed material is uniformly distributed over the second coordinate ($\Phi_d = 1$ or $\xi_\rho = 0$), and the two-dimensional number density distribution is indefinable. Instead, simulations could be started with *slightly precoated nuclei* with a thin distribution of the layer thickness or the particle growth ratios among the particle collective.

Two-zone continuum model of Wurster fluidization

The Wurster suction rate $\dot{M}_{wt,tor}$ of the two-zone continuum model study was approached by the modified Torricelli outflow equation from Burgschweiger a. Tsotsas ([90, 91], here in Section 2.2.6), which contains two empirical correction factors: the outflow coefficient (here: $\lambda_{tor} = 0.0316$) and the exponent of a pulsation factor (here: $m_{pul} = 0.2605$). The values of these constants have been fitted to discharge experiments [90,91] from fluidized beds through an internal classifier tube. The opening of the tube was positioned in the upper area of the fluidized beds, so that pulsation processes had an influence on the discharge rate. When particles are sucked from a fluidized bed into a Wurster tube, the opening (Wurster tube gap) is at the bottom of the bed. Fluidized bed pulsation probably does not play a major role for the Wurster suction rate then. In the further development of the two-zone continuum model, it is recommended to set the pulsation factor of Eq. 2.133 to unity ($k_{pul} = 1$) or the associated exponent to zero ($m_{pul} = 0$). The outflow coefficient λ_{tor} must be adapted to experimental measurements or to CFD-DEM simulation results. If only the bed mass, and thereby, the bed height are changed in such investigations, the *validity of the modified Torricelli law* in circulating Wurster fluidization can be checked. The outflow coefficient would be constant in this case.

The influence of different particle diameters or densities on fluid-particle transport characteristics of the spray zone and drying zone could be investigated in future work. For this, it is recommended to describe

the *Richardson-Zaki exponent* m_{sw} from Eq. 2.93 by holistic approaches from Rowe ([64], here Eq. 2.100) or Khan a. Richardson ([65], here Eq. 2.101), as these have steady transitions from laminar (Stokes) to fully turbulent (quadratic) flow conditions. For example, Figure 2.4 shows the good agreement between Rowe's approach and the experimental fit equations of Richardson a. Zaki [50]. Rowe's suggestion for the Richardson-Zaki exponent should be combined with an analytical approach of the terminal sinking velocity u_s or terminal Reynolds number Re_s, e.g., with Eq. 2.74 (Goroshko et al. [35]) or with Eq. 2.83 (Martin [40]), in order to avoid further iterations and to simplify the calculation. The determination of the Richardson-Zaki exponent by Khan a. Richardson has the advantage of being directly dependent on the Archimedes number Ar. Knowledge of terminal sinking velocity or terminal Reynolds number is then no longer necessary.

11.3.2 Recommendations for experimental investigations

Suggestions for improvement of the experimental setup of this thesis and further experimental investigations are given in the following.

Improvement of the classifier equipment

Classification is more efficient in longer tubes. The entire granulator system could be set up higher to extend the classifier tube downwards. Due to wall effects, it is not recommended to operate with thinner classifiers in practice, even if the model of Molerus a. Hoffmann ([103], here Section2.2.7) promises a sharper selectivity. *Multiple parallel classifier tubes* might reduce particle concentration, and thus, improve the separation performance. Internal classification should not be applied, as pressure fluctuations from fluidization would disturb the flow inside the classifier and worsen separation. The use of a broad single *zig-zag classifier* could also sharpen the product classification. The standing laboratory system does not have to be elevated then, and the granules would be more diluted in the classifier gas. Connection to the granulator chamber may still be via a double-pinch valve.

Dosing analysis of the nuclei feeding equipment

A memory effect was observed in the dosing experiments with the feed rate control method F3 of Section 9.4.3. The switching times of the individual pinch valves were quite short in these experiments, especially the flushing-out time. In the continuous granulation experiments with control method F1, however, the open-state times of both valves were very long. Further long-term dosing experiments might help to test if the memory effect is less strong, and the pinch material can recover, when both opening times are very high.

Improvement of the nuclei feeding equipment

More precise automatic feed rate control can be achieved by combinations of the feed-in double-pinch valve, the nuclei feed container, and another conveying device such as a vibrating chute. The flush-back effect of the double-pinch valve could be avoided by setting the pinch pressure higher than the flushing-out pressure, and by flushing the scavenging air into the sluice volume with a short delay, so that the upper pinch valve has sufficient time to close.

Pure growing-up experiments with manual two-phase control of bed mass

Pure growing-up experiments could be carried out, in which the bed mass is kept close to a target value by the manual discharge-recycle principle of the GAS2 strategy of Section 9.4.10, and where feed rates are at a certain constant value from the beginning on. From such experiments, average particle growth ratios can be determined from PSD-analyses of the discharged products, and from this, *growth time curves* can be created in form of a $\Phi_d(t)$-diagram. Using those curves, the necessary startup time to reach the desired growth ratio $\Phi_{d,set}$ of planned continuous granulation experiments can be estimated, and the duration of the GAS2-phase (τ_{man}) can be adapted accordingly. A suggestion for this is the growth time of the unweighted mean diameter of Eq. 10.29. If the feed is omitted and the pump is switched off during the total discharge periods, the discontinuous multi-stage granulation experiments can be carried out without shutting down the labsystem. This allows a more precise PSD-analysis of particle growth in shorter time intervals with much less experimental effort and the investigation of the maximum growth limits of granules.

Inline detection of fluidized bed mass

Hampel's method for inline bed mass detection bases on pressure drop measurements ([2], Section 9.4.7) and model-based and empirical equations. In order to use this method for different inlet gas conditions, the following improvements are suggested. It is recommended to discard the dependency of the empty-chamber pressure drop Δp_{emp} of Eq. 9.31 on superficial gas velocity at the chamber outlet u_{out}. It should be assumed that cross-sectional expansion of the conical process chamber leads to a reduction in kinetic energy (velocity or dynamic pressure) and not in static pressure. The pressure sensors installed in the laboratory granulator system do not measure the dynamic pressure ($\rho_g u^2/2$), but the pressure perpendicular to the flow (p_g). Instead, the empty-chamber pressure drop Δp_{emp} can be approached by the sum of two pressure drop fractions: one for the gas distributor plate Δp_{dis} and one subsuming pressure losses Δp_{int} from chamber walls, nozzle gas injection, and all other inserts of the chamber (e.g., Wurster tube and temperature sensors). The pressure drop of the distributor plate Δp_{dis} can be derived by correlations from Hunt et al. [70] and McAllister et al. [71] (here Eqs. 7.51 to 7.62). The *internal pressure drop* Δp_{int} could be described by

$$\Delta p_{int} = c_{int}(u_{in}, T_{in}) \frac{\rho_g(T_{in})}{2} u_{in}^2, \tag{11.2}$$

where the drag coefficient c_{int} is a function of inlet gas velocity u_{in} and inlet gas temperature T_{in}. The drag coefficient c_{int} must be adapted from pressure drop measurements at different inlet gas conditions without fluidized beds, where $c_{int} = 2(\Delta p_{app} - \Delta p_{dis})/\rho_g(T_{in})/u_{in}^2$. In the granulation process, the total pressure drop is defined as the sum of three pressure losses:

$$\Delta p_{app} = \Delta p_{dis} + \Delta p_{int} + \Delta p_{bed}. \tag{11.3}$$

It must also be checked if the water spray rate and evaporation cooling have an influence on the entire pressure drop across the process chamber.

Application of the spray-to-feed rate setting method SFM2 to horizontal sprayed fluidized beds

The spray-to-feed rate setting method SFM2 of Table 3.1 could be applied in continuous coating or layering in horizontal beds. This plant type offers large cross-sections, which enables greater drying capacities, and thus, higher overall spray rates. The challenge here is regulating the bed mass and avoiding agglomeration. Discharge at the end of elongated beds could be realized through a gap between an *integrated weir* and the gas inflow plate. The granulator output could also be combined with external product classification and fine-fraction recycle. The use of a proportional bed mass controller by manipulating the classifier gas velocity would probably be unsuitable in such processes because of the large ratio of bed mass to bed discharge rate. Instead, the bed discharge rate could be manipulated by readjusting the weir position at the end of the column in order to vary the height of the gap. The weir would have to be raised if the holdup is too high, or lowered if it is too small.

A Natural constants and material properties

property	symbol	unit	value
ideal gas constant	$\tilde{R}$	[J/mol/K]	8.314
acceleration constant of earth gravity	g	[m/s^2]	9.81

Table A.1: Natural constants employed in this thesis.

property	symbol	unit	value
molar fraction of oxygen in dry air	$\tilde{y}_{O_2}$	[mol-%]	78.12
molar fraction of nitrogen in dry air	$\tilde{y}_{N_2}$	[mol-%]	20.96
molar fraction of argon in dry air	$\tilde{y}_{Ar}$	[mol-%]	0.92
molar mass of oxygen	$\tilde{M}_{O_2}$	[g/mol]	28.013
molar mass of nitrogen	$\tilde{M}_{N_2}$	[g/mol]	31.999
molar mass of argon	$\tilde{M}_{Ar}$	[g/mol]	39.948
molar mass of dry air	$\tilde{M}_{air}$	[g/mol]	28.958
molar mass of water vapor	$\tilde{M}_{vap}$	[g/mol]	18.015

Table A.2: Specific properties of humid air.

B Methods for modeling

B.1 Transformation of length-based relative particle size variance

The following shows a detailed transformation from the relative standard deviation of the length-based particle size distribution ζ_{q_1} of Eq. 2.44 to the dispersion parameter ζ_{pol} of Eqs. 2.54 and 2.55, which is suggested by Tsotsas in [20, 25] for calculations of polydisperse bulk porosities.

$$
\begin{aligned}
\zeta_{q_1}^2 &= \frac{\sigma_{q_1}^2}{d_{m,q_1}^2} \\
&= \frac{\int_0^\infty (d - d_{m,q_1})^2 q_1(d)\mathrm{d}d}{d_{m,q_1}^2} \\
&= \frac{\int_0^\infty d^2 q_1(d) - 2d d_{m,q_1} q_1(d) + d_{m,q_1}^2 q_1(d)\mathrm{d}d}{d_{m,q_1}^2} \\
&= \frac{\int_0^\infty d^2 q_1(d)\mathrm{d}d}{d_{m,q_1}^2} - 2\frac{\int_0^\infty d q_1(d)\mathrm{d}d}{d_{m,q_1}} + \int_0^\infty q_1(d)\mathrm{d}d \qquad \text{, with } d_{m,q_1} = \int_0^\infty d q_1(d)\mathrm{d}d \\
&= \frac{\int_0^\infty d^2 q_1(d)\mathrm{d}d}{\left(\int_0^\infty d q_1(d)\mathrm{d}d\right)^2} - 2 + 1 \qquad \text{, with } q_1(d) = \frac{d q_0(d)}{\int_0^\infty d q_0(d)\mathrm{d}d} = \frac{d q_0(d)}{m_{1,0}} \\
&= \frac{\int_0^\infty d^3 q_0(d)\frac{1}{m_{1,0}}\mathrm{d}d}{\left(\int_0^\infty d^2 q_0(d)\frac{1}{m_{1,0}}\mathrm{d}d\right)^2} - 1 = \frac{\int_0^\infty d^3 q_0(d)\mathrm{d}d \cdot m_{1,0}}{\left(\int_0^\infty d^2 q_0(d)\mathrm{d}d\right)^2} - 1 \\
&= \frac{m_{3,0} m_{1,0}}{m_{2,0}^2} - 1 = \frac{\frac{m_{1,0}}{m_{3,0}}}{\left(\frac{m_{2,0}}{m_{3,0}}\right)^2} - 1 \\
&= \frac{\frac{\int_0^\infty d q_0(d)\mathrm{d}d}{m_{3,0}}}{\left(\frac{\int_0^\infty d^2 q_0(d)\mathrm{d}d}{m_{3,0}}\right)^2} - 1 = \frac{\int_0^\infty d\frac{q_0(d)}{m_{3,0}}\mathrm{d}d}{\left(\int_0^\infty d^2 \frac{q_0(d)}{m_{3,0}}\mathrm{d}d\right)^2} - 1 \qquad \text{, with } q_3(d) = \frac{d^3 q_0(d)}{\int_0^\infty d^3 q_0(d)\mathrm{d}d} = \frac{d^3 q_0(d)}{m_{3,0}} \\
&= \frac{\int_0^\infty d^{-2} q_3(d)\mathrm{d}d}{\left(\int_0^\infty d^{-1} q_3(d)\mathrm{d}d\right)^2} - 1 = \zeta_{pol}^2
\end{aligned}
$$

B.2 Size-independent growth rate of Mörl

Mörl ([128], see equation "39") has suggested a size-independent growth rate approach with

$$
G_d = \frac{\mathrm{d}d}{\mathrm{d}t} = \frac{2\dot{M}_{spr} x_s}{\rho_c A_{bed}} = \frac{2\dot{M}_{spr} x_s}{\rho_c N_{bed} \int_0^\infty \pi d^2 q_{0,bed}(d)\mathrm{d}d}, \tag{B.1}
$$

according to which the temporal change of bed granule size d is calculated from the spray rate $\dot{M}_{spr}$, the mass fraction of solids in the spray solution x_s, the effective coating layer density ρ_c, and the total surface area of sprayed particles $A_{bed} = \int_0^\infty \pi d^2 n_{bed}(d)\mathrm{d}d$. It is used for some derivations within the ideal continuous layerwise granulation model of Chapter 3 (e.g., estimation of required growth time) and within the three-compartment population balance model of Chapter 5. Due to its simple structure, the G_d-approach of Mörl was also recommended later in [29, 73], and it found use in plenty of investigations, as for instance in [2, 88, 89, 126, 129–131]. The notation of Eq. B.1 is adapted to the present work and deviates from that of the named references.

C Experimental basics and results

C.1 Characteristics of raw materials

C.1.1 Bulk raw materials

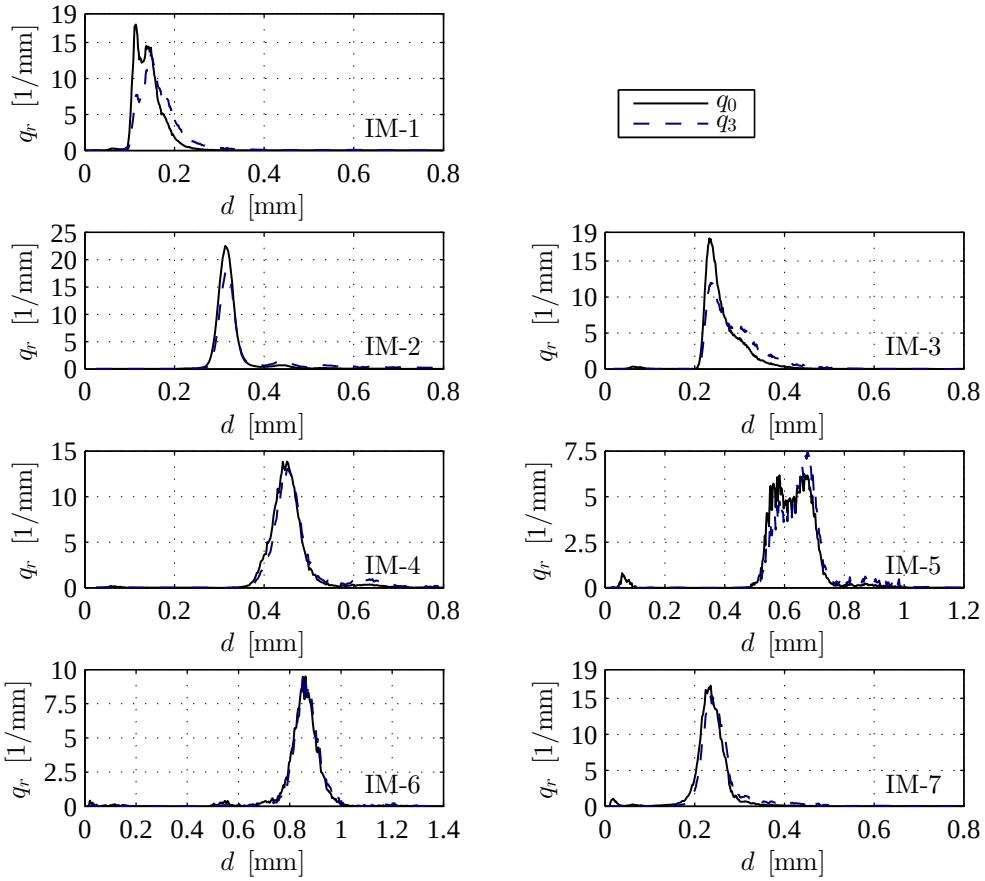

Figure C.1: Number- and volume-based particle size distributions (q_0 and q_3) of the initial bulk materials (IM-1 to IM-7) employed in the present thesis.

property	unit	IM-1	IM-2	IM-3	IM-4	IM-5	IM-6	IM-7
d_{50,q_0}	[µm]	137.7	316.8	250	449.8	628.1	856.5	235.5
d_{mod,q_0}	[µm]	113.6	313.4	232.8	451.0	676.2	861.6	235.8
d_{m,q_0}	[µm]	141.8	327.5	262.0	453.3	621.2	844.3	235.0
σ_{q_0}	[µm]	32.1	58.2	46.2	56.1	105.0	111.2	45.8
ζ_{q_0}	[%]	22.64	17.78	17.63	12.37	16.91	13.17	19.49
d_{50,q_3}	[µm]	157.8	325.4	273.6	458.1	654.5	866.2	246.6
d_{mod,q_3}	[µm]	147.4	316.4	235.8	453.3	678.7	861.6	235.8
d_{m,q_3}	[µm]	182.8	395	289	476.1	658.4	871.3	260.7
σ_{q_3}	[µm]	121.7	173	60.5	76.7	86.2	72.8	62.4
ζ_{q_3}	[%]	66.6	43.8	20.9	16.1	13.1	8.4	23.9
d_{32}	[µm]	159.7	356.9	278.8	467.2	648.6	865.4	251.1
ζ_{q_1}	[%]	26.6	23.75	17.85	12.27	12.28	8.69	17.12
Ψ_{sph}	[%]	90.2	87.2	93	93.5	94.2	95.1	74.4
ρ_b	[kg/m^3]	772.1	842.8	808.3	847.3	839.6	856.5	1467.7
ρ_p	[kg/m^3]	1482.9	1517.6	1452.7	1475.9	1449.3	1445.1	2561
ε_b	[%]	47.9	44.5	44.4	42.6	42.1	40.7	42.7
$u_{mf}(d_{m,q_0}, 20℃)$	[mm/s]	13.6	66.3	41.1	109.7	193.9	300.1	60.1
$u_s(d_{m,q_0}, 20℃)$	[m/s]	0.63	1.73	1.30	2.29	3.12	4.01	1.77

Table C.1: Diverse characteristics of the raw bulk materials (non-coated core particles) used in the present thesis.

C.2 Equipment

C.2.1 Dimensions of classifier, granulator, and nuclei feeding equipment

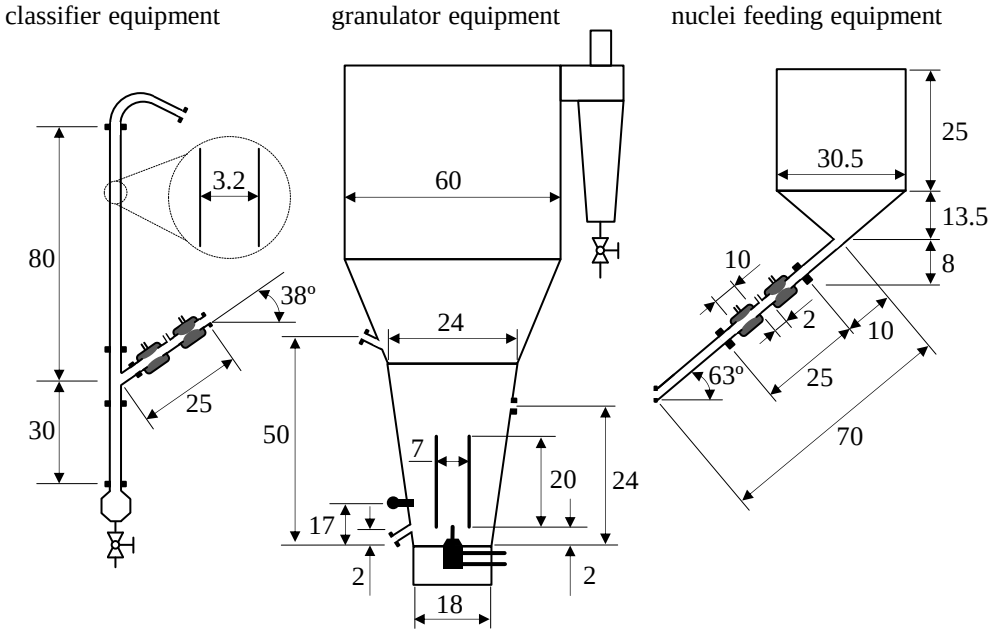

Figure C.2: Dimensions of the classifier, granulator, and nuclei feeding equipment used in the experimental investigations of the present thesis, further description given in Section 9.2.2; measures in cm.

C.2.2 Specification of the utilized gas distributor plate

Figure C.3 shows the gas distributor plate (perforated metal plate) of the experiments of the present thesis, for the entire cross-section in a), and for a zoomed quarter in b), in which a subdivision into five sections of different perforation degree (indicated by $j \in \{\mathrm{A}, \mathrm{B}, \mathrm{C}, \mathrm{D}, \mathrm{E}\}$) is marked. The entire perforation design of the real distributor plate shall be precisely described by means of five sectional characteristics including the sectional outer diameter $D_{dis,j}$, the sectional area fraction $\varphi_{dis,j}$, the sectional number of holes $N_{dis,j}$, the hole diameter $d_{dis,j}$, and the sectional opening ratio $\Psi_{dis,j}$. The values of these characteristics are listed in Table C.2. They are employed for specifying a model distributor plate of only three sections (Section 8.1) for the sensitivity analysis of the two-zone continuum model (Chapter 7). The first section ($j = \mathrm{A}$) is for installing a spray nozzle. Hence, it does not contain any perforation holes for the process gas ($N_{dis,\mathrm{A}} = 0$). The second and third section ($j = \mathrm{B}$ and $j = \mathrm{C}$) are located in the area below the Wurster tube, which is also called as *up-bed-zone* in [132]. The fourth section ($j = \mathrm{D}$) lies in the area around the Wurster, which is also referred to as *down-bed-zone* [132]. The holes below the Wurster tube ($d_{dis,\mathrm{B}}$ and $d_{dis,\mathrm{C}}$) are bigger than the holes below the down-bed-zone ($d_{dis,\mathrm{D}}$). Thereby higher gas velocities are generated in the interior of the Wurster tube than in its exterior. The fifth section ($j = \mathrm{E}$) is directly at the chamber wall. The holes of the fifth section ($d_{dis,\mathrm{E}}$) are as large as these of the second section ($d_{dis,\mathrm{B}} = d_{dis,\mathrm{E}}$). It is intended to create high local gas velocities in wall proximity to prevent the adherence of granules. The sectional area fractions and the sectional opening ratio $\Psi_{dis,j}$ are calculated by analogy to Eqs. 7.40 and 7.42. The thickness of the gas distributor plate is given with $s_{dis} = 3\,\mathrm{mm}$.

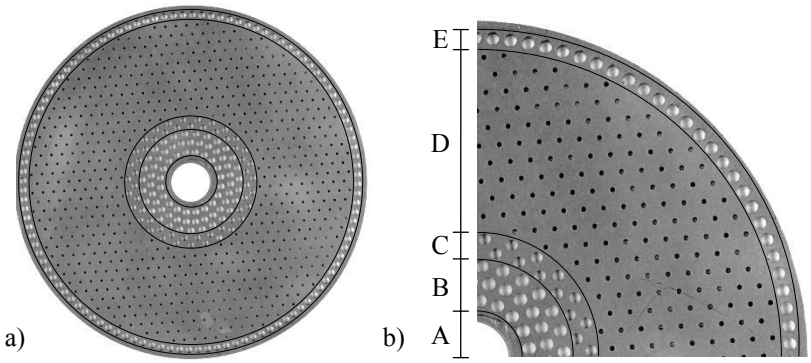

Figure C.3: Top view of the complete distributor plate in a) and subdivision into distributor plate sections in b).

section number j:			A	B	C	D	E
property	symbol	unit					
outer diameter of section j	$D_{dis,j}$	[m]	0.03	0.055	0.07	0.17	0.18
area fraction of section j	$\varphi_{dis,j}$	[%]	2.778	6.559	5.787	74.074	10.802
number of holes in section j	$N_{dis,j}$	[−]	0	74	54	684	112
hole diameter of section j	$d_{dis,j}$	[mm]	-	3	2.5	1	3
opening ratio of section j	$\Psi_{dis,j}$	[%]	0	31.34	18	2.85	28.80

Table C.2: Specifications of perforation sections of the gas distributor plate employed in the experimental investigations of the present thesis.

C.2.3 Nozzle air flow rate

The nozzle gas injection rate $\dot{M}_{g,noz}$ is one of the predefined parameters of the two-zone continuum model of Wurster fluidization of Chapter 7. It depends on nozzle design and nozzle gas excess pressure $p_{g,noz}$ to be set. In the experimental part of this thesis, a two-substance nozzle of the type "model 970 S4" from the company Düsen-Schlick GmbH was employed. The manufacturer provides a data sheet in [124], in which the normal volume flow rate $\dot{V}_{g,noz,0}$ (at 0℃) is given for six different nozzle air excess pressures $p_{g,noz}$, as shown in Figure C.4. From these points, a linear fit equation was created for the normal volume flow rate with

$$\dot{V}_{g,noz,0}\left[\frac{\mathrm{m}^3}{\mathrm{h}}\right] = 0.9067\left[\frac{\mathrm{m}^3}{\mathrm{h}}\right] + 1.2457\left[\frac{\mathrm{m}^3}{\mathrm{h}\cdot\mathrm{bar}}\right]\cdot p_{g,noz}[\mathrm{bar}] \tag{C.1}$$

in the context of this thesis. In order to estimate corresponding mass flow rates from the normal volume flow rate of Eq. C.1, an adequate value of the gas density is required. This gas density was calculated by Eq. 7.31 for process-like conditions of the present thesis, whereat the system pressure of 1 bar was assumed to be substantial, and the moisture content of utilized air delivery system is given by $Y_{in} = 1.03\,\mathrm{g/kg}$. In doing so, the mass flow rate of the nozzle air follows from

$$\dot{M}_{g,noz} \coloneqq \rho_g(0℃, Y_{in}, p_{sys})\dot{V}_{g,noz,0}. \tag{C.2}$$

Table C.3 shows some $\dot{M}_{g,noz}$-values for six examples of different nozzle gas excess pressure.

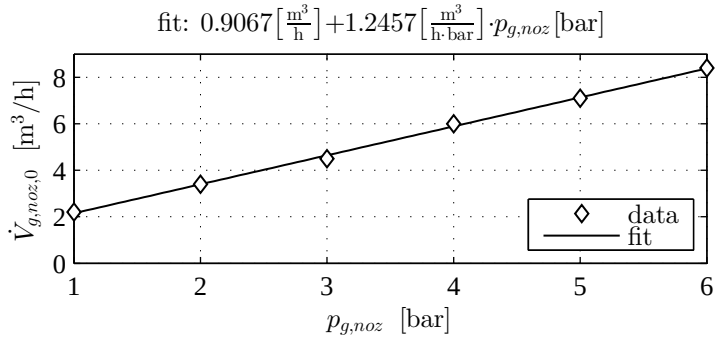

Figure C.4: Linear regression of the normal volume flow rate of nozzle air consumption with nozzle air pressure (overpressure), based on manufacturer's specification of the nozzle type "model 970 S4", see [124].

$p_{g,noz}$ [bar]	$\dot{M}_{g,noz}$ [kg/h]
1	2.75
1.25	3.14
1.5	3.54
1.75	3.94
2	4.33
2.25	4.73

Table C.3: Mass flow rates of atomization air for different nozzle air pressures $p_{g,noz}$, calculated for the nozzle gas temperature of $T_{in} = 0℃$ and an inlet gas moisture content of $Y_{in} = 1.03\,\mathrm{g/kg}$.

C.3 Discontinuous multi-stage granulation

batch series:	EB-13	EB-14	EB-21-3	EB-22	EB-23	EB-24	EB-31	EB-32	EB-33
$p_{g,noz}$ [bar]:	2	2.25	1.75	1.75	1.75	1.75	1.75	1.75	1.75
$\dot{M}_{in}$ [kg/h]:	70	70	70	85	100	115	175	175	175
T_{in} [°C]:	90	90	70	70	70	70	70	90	110
stage:	$\dot{M}_{spr}$:								
1	839.9	816.8	806.8	757.3	800.9	809.4	826	803	822.9
2	811.5	797.7	786.3	791.6	805.5	798	747.4	816.1	771.3
3	803.9	808.9	793.7	806.4	838.3	746.8	832.6	828.8	831.1
4	798.6	822.7	783.1	634.3*)	818.7	781	818.1	827.9	817.2
5	849.1	820.7	790.2	-	730.9	781.8	824.0	820.9	829.6
6	851.5	808.9	812.7	-	831.3	817.6	-	847.3	823.9
7	-	-	784.0	-	849.0	792.1	-	817.8	811.1
8	-	-	761.9	-	818.7	809.1	-	801.4	829.6
mean:	825.8	812.6	789.8	785.1	811.6	792	809.6	820.4	817.1
CV [%]:	2.6	1	1.8	2.6	4.2	2.7	3.9	1.7	2.3

Table C.4: Time-averaged spray rate $\dot{M}_{spr}$ (in g/h) of different multi-stage batch experiments; *) failure in spraying, this value is excluded from the calculation of the mean and the CV of the spray rates (see bottom).

stage	$\Phi_{spr,loss}$ [%]	stage	$\Phi_{spr,loss}$ [%]
1	20.83	9	14.29
2	17.20	10	7.70
3	19.32	11	13.62
4	24.64	12	12.00
5	32.89	13	16.20
6	18.72	14	11.78
7	14.89	15	12.55
8	14.12	16	10.42

Table C.5: Spray losses $\Phi_{spr,loss}$ (in %) of the discontinuous multi-stage batch experiment EB-34.

C.4 Single dosage mass of the feed-in double-pinch valve

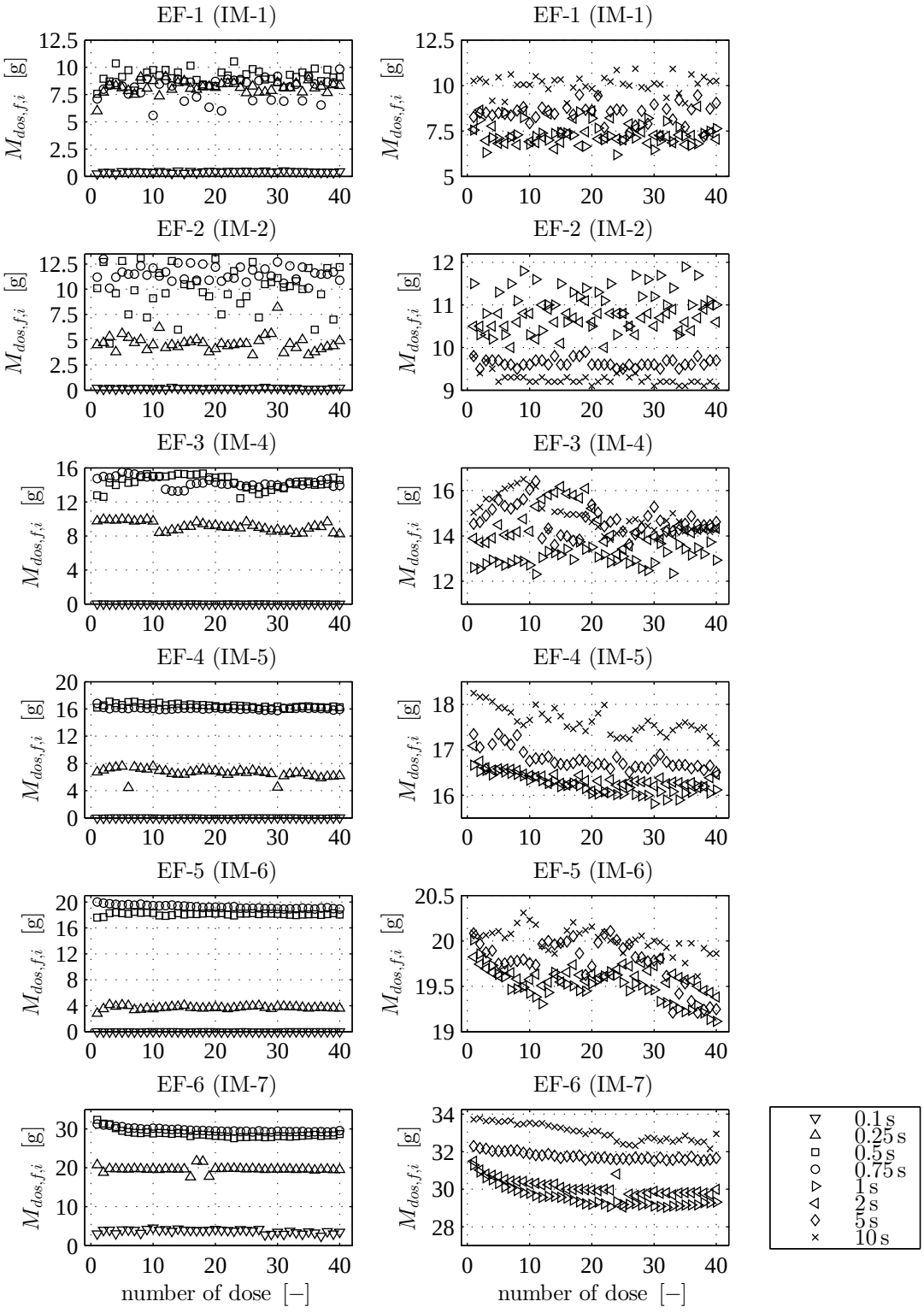

Figure C.5: Dosage mass $M_{f,i}$ with the sequence number of single doses conveyed by the continuously operating double-pinch valve of the feeding equipment for different initial materials (IM) and several opening times of the lower pinch valve $t_{V2,f}$.

C.5 Continuous granulation experiments

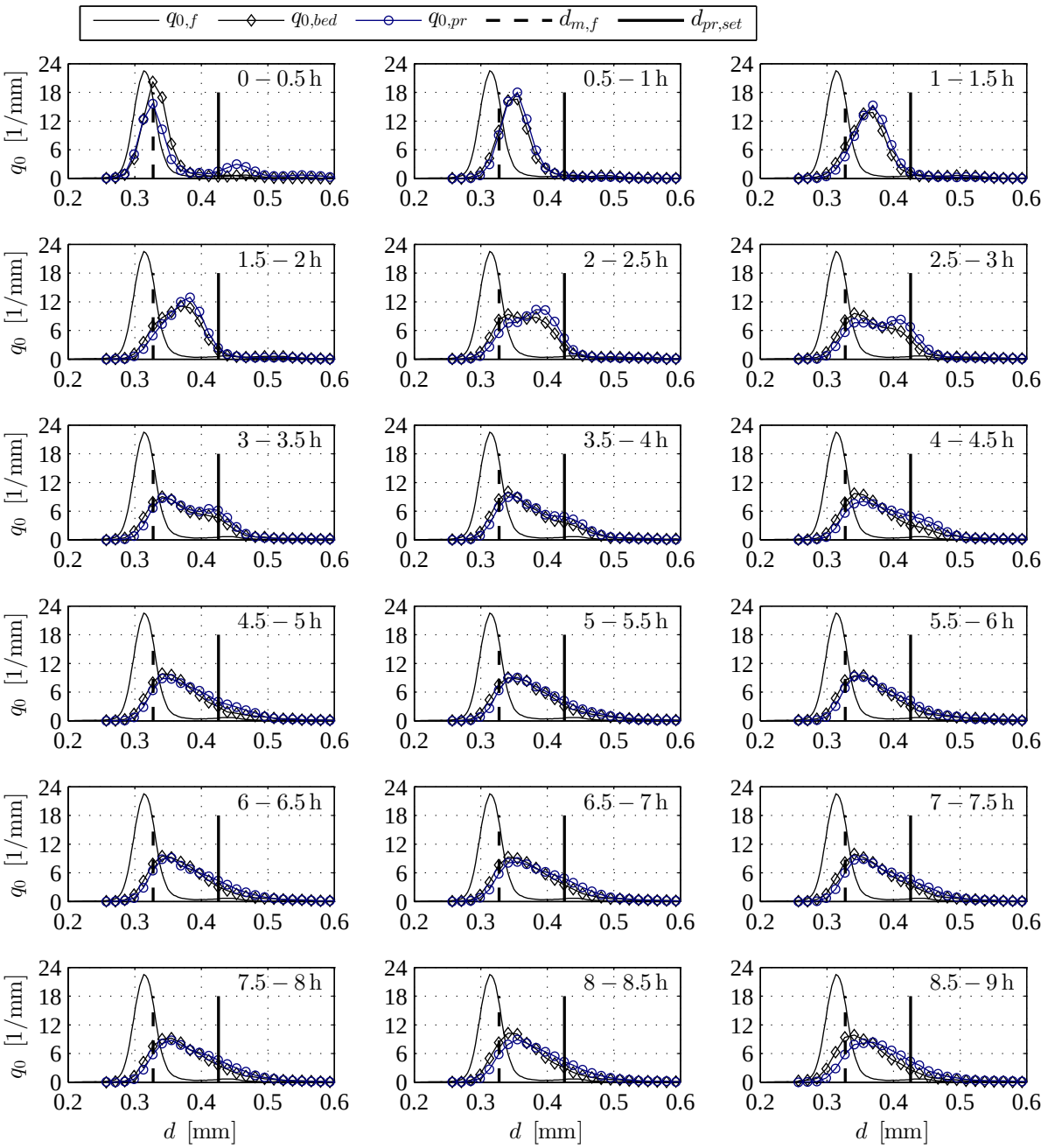

Figure C.6: Number-based particle size distribution of the feed $q_{0,f}$, the bed $q_{0,bed}$, and the product $q_{0,pr}$ for the half-hour time sections of the startup experiment EC-11* ($\Phi_{d,set} = 1.3$, $K_m = 1\,\mathrm{m/s/kg}$); *operation concept for continuous granulation specified in Tables 10.13 and 10.15; destabilization after round 8.7 h.

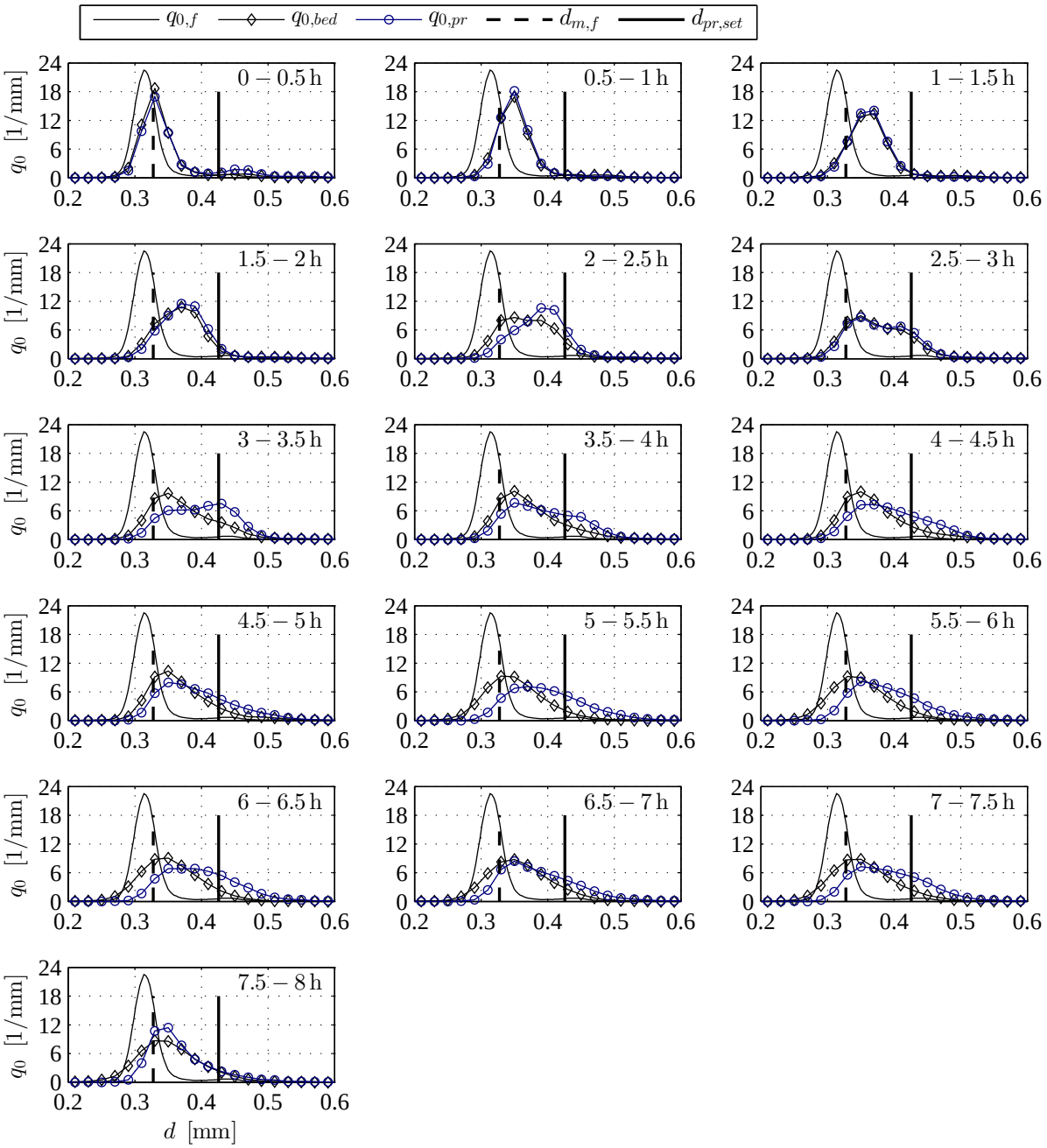

Figure C.7: Number-based particle size distribution of the feed $q_{0,f}$, the bed $q_{0,bed}$, and the product $q_{0,pr}$ for the half-hour time sections of the startup experiment EC-12*) ($\Phi_{d,set} = 1.3$, $K_m = 3\,\mathrm{m/s/kg}$); *) operation concept for continuous granulation specified in Tables 10.13 and 10.15; destabilization after round 7.6 h.

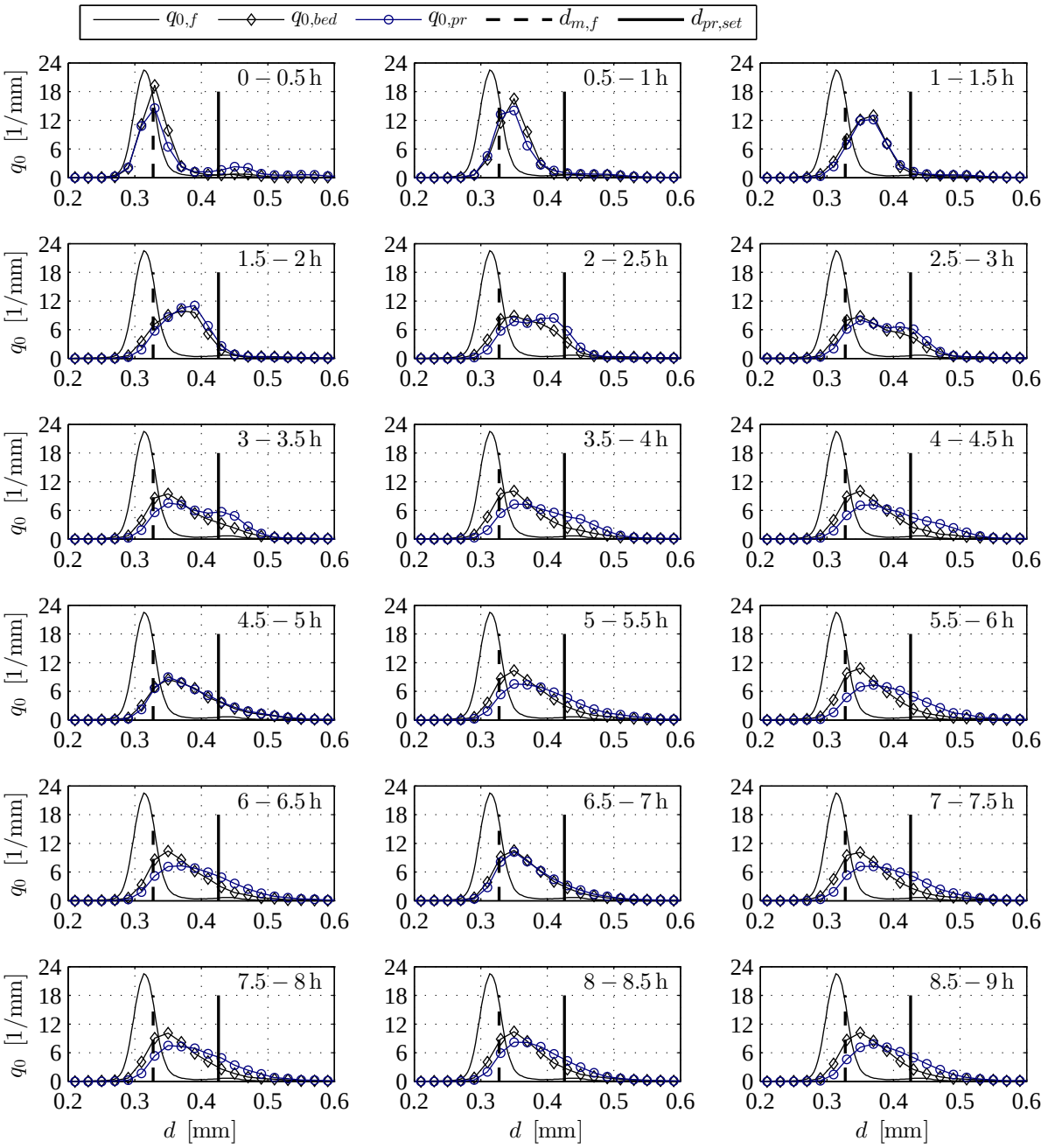

Figure C.8: Number-based particle size distribution of the feed $q_{0,f}$, the bed $q_{0,bed}$, and the product $q_{0,pr}$ for the half-hour time sections of the startup experiment EC-13*) ($\Phi_{d,set} = 1.3$, $K_m = 5\,\mathrm{m/s/kg}$); *) operation concept for continuous granulation specified in Tables 10.13 and 10.15.

operation concept	$M_{bed,end}$ [g]	$M_{c,sep}$ [g]
EC-21	1146.2	44.6
EC-22-1	1091.1	127.4
EC-22-2	1067.7	74.7
EC-31	958.2	82.5
EC-32-1	1152.6	36.7
EC-32-2	1000.6	71.6
EC-32-3	1015.9	88.0
EC-33	878.6	33.3

Table C.6: Further quantities measured after process stop of several continuous granulation experiments: final bed mass (symbolized by $M_{bed,end}$) and mass of dusty coating material that was attached to the inner classifier wall (symbolized by $M_{c,sep}$).

exp. index:	EC-21		EC-22-1		EC-31		EC-32-1		EC-33	
$\Phi_{d,set}$:	1.6		1.9		1.9		2.2		2.5	
$d_{m,f}$:	328 µm		262 µm		262 µm		262 µm		262 µm	
$d_{pr,set}$:	524 µm		498 µm		498 µm		576 µm		655 µm	
time section	Φ_{d_m} [–]	ζ_d [%]	Φ_{d_m} [–]	ζ_d [%]	Φ_{d_m} [–]	ζ_d [%]	Φ_{d_m} [–]	ζ_d [%]	Φ_{d_m} [–]	ζ_d [%]
$6-6.5$ h	1.704	+6.5	1.950	+2.6	2.139	+12.6	2.056	−6.6	2.128	−14.9
$6.5-7$ h	1.696	+6.0	1.968	+3.6	2.114	+11.3	2.136	−2.9	2.144	−14.3
$7-7.5$ h	1.643	+2.7	1.927	+1.4	2.067	+8.8	2.143	−2.6	2.217	−11.3
$7.5-8$ h	1.550	−3.1	1.960	+3.2	2.225	+17.1	2.210	+0.5	2.208	−11.7
$8-8.5$ h	1.086	−32.1	1.876	−1.2	2.195	+15.5	2.206	+0.3	2.377	−4.9
$8.5-9$ h	1.342	−16.1	1.930	+1.6	2.194	+15.5	2.367	+7.6	2.311	−7.6
mean:	1.504	−6.0	1.935	1.9	2.156	13.4	2.186	−0.6	2.231	−10.8
SD:	0.223	13.9	0.030	1.6	0.054	2.9	0.096	4.4	0.088	3.5

Table C.7: Process success indices*) for the last three hours of different startup experiments; *) mean-value-based particle growth ratio Φ_{d_m} and corresponding relative control deviation in product size ζ_d; each quantity calculated from the number-based product size distribution $q_{0,pr}$ according to: $\Phi_{d_m} = (\int_0^\infty dq_{0,pr}\mathrm{d}d)/d_{m,f}$ and $\zeta_d = \Phi_{d_m}/\Phi_{d,set} - 1$.

exp. index:	EC-22-2		EC-32-2		EC-32-3	
$\Phi_{d,set}$:	1.9		2.2		2.2	
$d_{m,f}$:	262 µm		262 µm		262 µm	
$d_{pr,set}$:	498 µm		576 µm		576 µm	
time section	Φ_{d_m} [−]	ζ_d [%]	Φ_{d_m} [−]	ζ_d [%]	Φ_{d_m} [−]	ζ_d [%]
0 − 0.5 h	2.125	+11.9	2.015	−8.4	2.295	+4.3
0.5 − 1 h	2.144	+12.9	2.385	+8.4	2.311	+5.0
1 − 1.5 h	2.131	+12.1	2.311	+5.0	2.242	+1.9
1.5 − 2 h	1.835	−3.4	2.235	+1.6	2.273	+3.3
2 − 2.5 h	1.892	−0.4	2.263	+2.9	2.386	+8.4
2.5 − 3 h	1.849	−2.7	2.140	−2.7	2.249	+2.2
3 − 3.5 h	2.058	+8.3	2.186	−0.6	2.241	+1.9
3.5 − 4 h	1.848	−2.7	2.157	−1.9	2.320	+5.4
4 − 4.5 h	1.854	−2.4	2.191	−0.4	2.360	+7.3
4.5 − 5 h	1.815	−4.5	2.204	+0.2	2.340	+6.4
5 − 5.5 h	1.946	+2.4	2.220	+0.9	2.350	+6.8
5.5 − 6 h	1.834	−3.5	2.215	+0.7	2.384	+8.4
6 − 6.5 h	1.930	+1.6	2.228	+1.3	2.355	+7.0
6.5 − 7 h	1.908	+0.4	2.247	+2.1	2.310	+5.0
7 − 7.5 h	1.878	−1.2	2.308	+4.9	2.371	+7.8
7.5 − 8 h	1.864	−1.9	2.296	+4.4	2.368	+7.6
8 − 8.5 h	1.872	−1.5	2.373	+7.9	2.308	+4.9
8.5 − 9 h	1.873	−1.4	2.269	+3.1	2.358	+7.2
mean:	1.925	+1.3	2.236	+1.6	2.323	+5.6
SD:	0.11	+5.6	0.08	+3.8	0.05	+2.1
time section	σ_{pr} [µm]	γ_{pr} [−]	σ_{pr} [µm]	γ_{pr} [−]	σ_{pr} [µm]	γ_{pr} [−]
0 − 0.5 h	72	−1.88	107	−1.28	79	−1.38
0.5 − 1 h	74	−1.94	69	−2.89	71	−1.09
1 − 1.5 h	88	−1.46	67	−0.85	73	−0.01
1.5 − 2 h	85	−0.29	69	−1.04	70	−0.52
2 − 2.5 h	122	−0.46	62	−0.47	76	−1.23
2.5 − 3 h	81	−0.30	82	−2.78	68	−1.16
3 − 3.5 h	84	−0.67	69	−1.13	69	−0.01
3.5 − 4 h	84	−0.62	68	−1.17	70	−0.28
4 − 4.5 h	89	−0.72	68	−0.66	77	−2.08
4.5 − 5 h	86	−0.52	85	−2.69	75	−1.66
5 − 5.5 h	90	−1.37	65	−0.28	79	−1.83
5.5 − 6 h	83	−0.62	67	−0.74	74	−1.17
6 − 6.5 h	80	−1.70	74	−1.55	80	−1.57
6.5 − 7 h	73	−1.70	69	−1.19	84	−1.61
7 − 7.5 h	72	−1.60	66	−0.75	92	−2.39
7.5 − 8 h	82	−2.28	66	−0.99	78	−1.23
8 − 8.5 h	75	−1.95	74	−1.81	79	−1.08
8.5 − 9 h	75	−2.02	86	−1.81	83	−1.70

Table C.8: Process success indices*) and product characteristics**) for each time section of three follow-up experiments; *) mean-value-based particle growth ratio Φ_{d_m} and corresponding relative control deviation in product size ζ_d; **) standard deviation σ_{pr} and skewness γ_{pr}; each quantity calculated from the number-based product size distribution $q_{0,pr}$ according to: $\Phi_{d_m} = (\int_0^\infty dq_{0,pr}\mathrm{d}d)/d_{m,f}$, $\zeta_d = \Phi_{d_m}/\Phi_{d,set} - 1$, $\sigma_{pr} = \int_0^\infty (d - d_{m,pr})^2 q_{0,pr}\mathrm{d}d$, and $\gamma_{pr} = (\int_0^\infty (d - d_{m,pr})^3 q_{0,pr}\mathrm{d}d)/\sigma_{pr}^3$.

C.6 Process gas temperature measurements

In the scope of thesis, the effects of heat losses and process gas cooling by evaporation within the spray zone are investigated by temperature measurements. The utilized equipment of these experiments is described in Section 9.2.1, the procedure in Section 9.2.2, and the setup is illustrated in Figure 9.5. The results of the heat loss measurements are shown in Appendix C.6.1 and that of spray zone evaporation cooling in Appendix C.6.2.

C.6.1 Characteristics of heat losses of the inlet gas through walls

The heat loss of the inlet gas when flowing through the distributor plate should be quantified here by the effective inlet gas temperature $T_{in,eff}$ and the dimensionless temperature drop Θ_{loss}. The effective inlet gas temperature was measured a few centimeters above the inflow plate for various inlet gas mass flow rates $\dot{M}_{in}$ between 60 and 120 kg/h and inlet gas temperatures T_{in} between 60 and 120℃ using the thermocouple of the drying zone. The results are shown in Figure C.9. It can be seen that the inlet gas temperature decreases less with higher inlet gas mass flow rates. The dimensionless temperature drop, which describes the relative decrease in inlet gas temperature, was calculated by Eq. 7.65 with the $T_{in,eff}$-values given in Figure C.9 and with measured values of the surroundings temperature T_{sur}. The Θ_{loss}-results are shown in Figure C.10, over the inlet gas temperature T_{in} with the inlet gas mass flow rate $\dot{M}_{in}$ as a curve parameter. In the experiments, the plant was heated up until nearly constant temperature conditions were obtained, which took around half an hour. The surroundings temperature of the experimental hall differed between 18 and 24℃ depending on seasonal and daily weather conditions. This leads to some fluctuations in the depicted curves. The relative temperature drop Θ_{loss} tends to grow more strongly with inlet gas temperature T_{in} for larger inlet gas mass flow rate $\dot{M}_{in}$. It is clear, however, that the dimensionless temperature drop is greater at higher mass flow rates. Since the influence of $\dot{M}_{in}$ on Θ_{loss} is clearly stronger than that of T_{in}, a one-dimensional function of the relative temperature drop on the inlet gas mass flow rate shall be derived here from the measurements of Figure C.9 according to

$$\bar{\Theta}_{loss,exp}(\dot{M}_{in,i}) = \frac{1}{13}\sum_{i=1}^{13}\Theta_{loss,i,j} = \frac{1}{13}\sum_{i=1}^{13}\Theta_{loss}(\dot{M}_{in,i}, T_{in,j}), \tag{C.3}$$

for $\dot{M}_{in,i} \in \{60, 70, ..., 120\}$ kg/h and $T_{in,j} \in \{60, 65, ..., 120\}$℃. The averaged relative temperature drop of measurements is illustrated in Figure C.11 as function of inlet gas velocity at standard temperature and pressure conditions of dry air, which follows from the employed mass flow rates via:

$$u_{in,stp,i} = \frac{\dot{M}_{in,i}}{\frac{\pi}{4}D_{app,0}^2\rho_{g,stp}}. \tag{C.4}$$

The gas density is calculated by Eq. 7.31 with $T = 0$℃, $p_{sys} = 1$ bar, and $Y = Y_{in} = 1$ g/kg. The averaged relative temperature drop $\bar{\Theta}_{loss,exp}$ declines significantly with the inlet gas velocity. Although it looks like it, a linear dependency can be excluded. Instead, it is more likely to assume a hyperbolic curve, since it can be expected that ambient temperature prevails above the distributor plate at inlet gas velocities approaching zero ($T_{in,eff}(u_{in} \to 0) = T_{sur}$ and $\Theta_{loss}(u_{in} \to 0) = 1$) and that the inlet gas temperature is maintained at infinite inflow velocities ($T_{in,eff}(u_{in} \to \infty) = T_{in}$ and $\Theta_{loss}(u_{in} \to \infty) = 0$). With these two limiting cases, an empirical hyperbolic fit can be applied, as shown in Figure C.11.

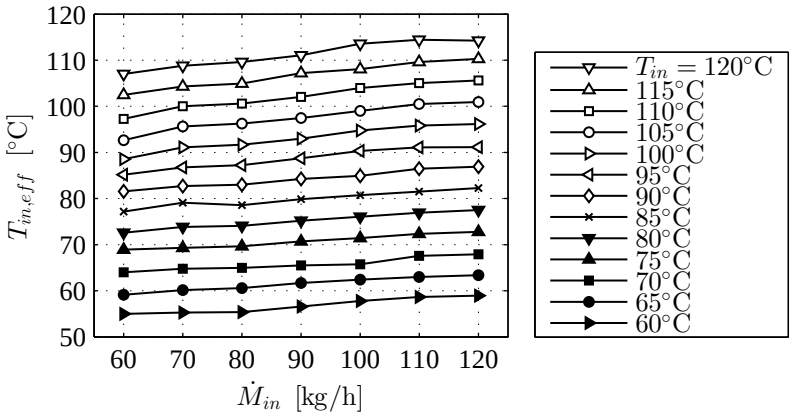

Figure C.9: Effective inlet gas temperature $T_{in,eff}$ versus the inlet gas mass flow rate $\dot{M}_{in}$ for different inlet gas temperatures T_{in}.

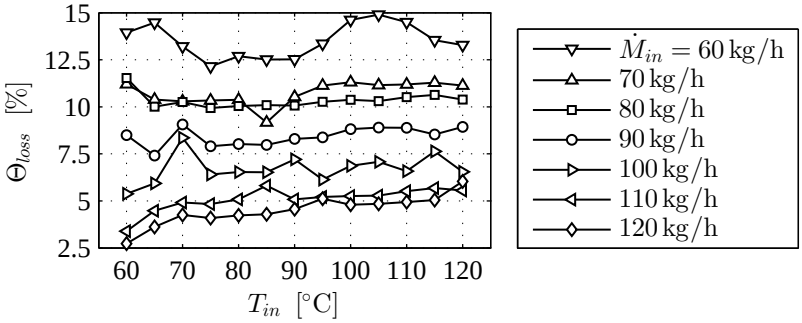

Figure C.10: Dimensionless temperature drop Θ_{loss} versus inlet gas temperature T_{in} for different inlet gas mass flow rates $\dot{M}_{in}$.

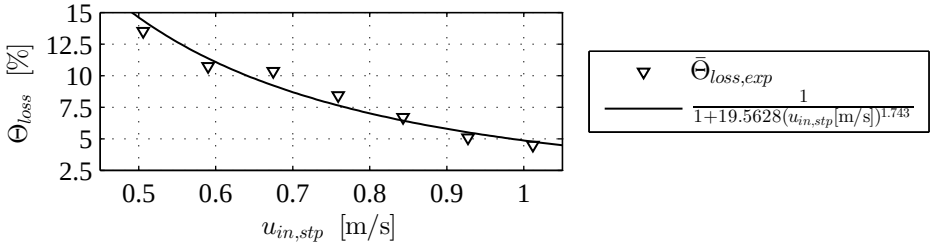

Figure C.11: Fit of the average dimensionless temperature drop $\Theta_{loss,exp}$*) versus inlet gas velocity referred to STP-conditions $u_{in,stp}$, *) averaged along the inlet gas temperature coordinate T_{in}.

C.6.2 Characteristics of evaporation in the spray zone

The effect of spray zone gas cooling by evaporation shall be quantified here by the drying potential of the spray zone outlet gas $\eta_{dry,\alpha,top}$ of Eq. 7.74. It was calculated by temperatures of the Wurster tube inlet gas $T_{wt,in}$ and the Wurster tube outlet gas $T_{wt,out}$ using equations of the two-zone continuum model of Chapter 7. Both temperatures were measured for seven different inlet gas mass flow rates $\dot{M}_{in,i} \in \{60, 70, ..., 120\}$ kg/h, seven different inlet gas temperatures $T_{in,j} \in \{60, 70, ..., 120\}$℃, and three different pump rotation speeds $n_{pum,k} \in \{5, 7, 9\}$ rpm. The water spray rates of the n_{pum}-variation are given with $\dot{M}_w = \{504, 705.6, 907.2\}$ g/h and the corresponding area-specific water spray rates ($\dot{m}_w = \dot{M}_w / A_{app,0}$) with

$\dot{m}_w = \{2.18, 3.06, 3.93\}\,\mathrm{kg/min/m^2}$. The mass flow rates of the Wurster tube inlet gas $\dot{M}_{dis,2}$ and the nozzle gas $\dot{M}_{g,noz}$ were determined with the $\dot{M}_{in}$-values employed, $\Omega_{2,in}$ of Eq. 7.59 (from Table 8.1), and Eqs. 7.31, C.1, and C.2. The two mass flow rates $\dot{M}_{dis,2}$ and $\dot{M}_{g,noz}$ ensue to the total mass flow rate going into the spray zone $\dot{M}_{g,\alpha,bot}$, as given in Eq. 7.70. The spray zone inlet gas temperature $T^*_{\alpha,bot}$ was estimated by Eq. 7.72. The drying potential of the spray zone outlet gas $\eta_{dry,\alpha,top}$ is approximated here by

$$\eta_{dry,\alpha,top}(\dot{M}_{in,i}, T_{in,j}, n_{pum,k}) = \frac{T_{wt,out}(\dot{M}_{in,i}, T_{in,j}, n_{pum,k}) - T_{sat}\big(T^*_{\alpha,bot}(\dot{M}_{in,i}, T_{in,j}, n_{pum,k}), Y_{in}\big)}{T^*_{\alpha,bot}(\dot{M}_{in,i}, T_{in,j}, n_{pum,k}) - T_{sat}\big(T^*_{\alpha,bot}(\dot{M}_{in,i}, T_{in,j}, n_{pum,k}), Y_{in}\big)}, \quad \text{(C.5)}$$

where T_{sat} is the isenthalpic saturation temperature from Eqs. 7.23 to 7.26 with $T = T^*_{\alpha,bot}$ and $Y = Y_{in}$ as input variables. The inlet gas moisture load is adopted from Table 8.1 with $Y_{in} = 1$ g/kg. Furthermore, two different average quantities are derived from the drying potential of the spray zone outlet gas $\eta_{dry,\alpha,top}$ of Eq. C.5 with:

$$\bar{\eta}_{dry,\alpha,top}(T_{in,j}, n_{pum,k}) = \frac{1}{7}\sum_{i=1}^{7} \eta_{dry,\alpha,top}(\dot{M}_{in,i}, T_{in,j}, n_{pum,k}), \quad \text{(C.6)}$$

$$\bar{\bar{\eta}}_{dry,\alpha,top}(n_{pum,k}) = \frac{1}{49}\sum_{i=1}^{7}\sum_{j=1}^{7} \eta_{dry,\alpha,top}(\dot{M}_{in,i}, T_{in,j}, n_{pum,k}). \quad \text{(C.7)}$$

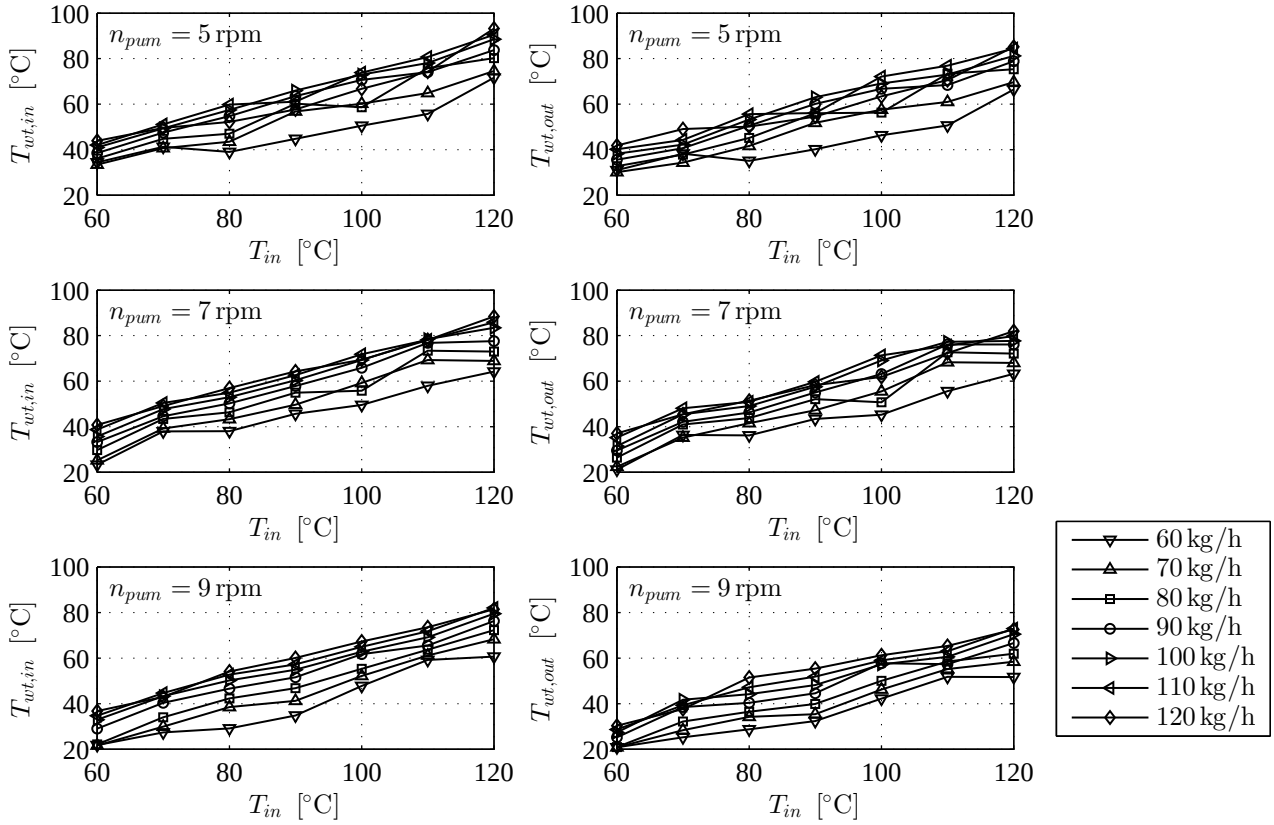

Figure C.12: Gas temperature of the Wurster tube inlet $T_{wt,in}$ and the Wurster tube outlet $T_{wt,out}$ versus the inlet gas temperature of the process chamber T_{in} for different inlet gas mass flow rates $\dot{M}_{in}$ (legend) and different pump rotation speeds $n_{pum} \in \{5, 7, 9\}\,\mathrm{rpm}$.

The measured gas temperatures of the Wurster tube inlet and outlet are shown in Figure C.12, their difference $\Delta T_{wt} = T_{wt,in} - T_{wt,out}$ in Figure C.13, and the average drying potentials of the spray zone outlet gas of Eqs. C.6 and C.7 in Figure C.14. In addition, a linear fit of $\eta_{dry,\alpha,top}$ versus the area-specific water spray rate $\dot{m}_w$ and an exponential fit of $\eta_{dry,\alpha,top}$ versus the inlet gas temperature T_{in} are illustrated in Figure C.14. The fits of Figure C.14 represent the decreasing tendency of $\eta_{dry,\alpha,top}$ with $\dot{m}_w$ on average and the increasing tendency of $\eta_{dry,\alpha,top}$ with T_{in} on average.

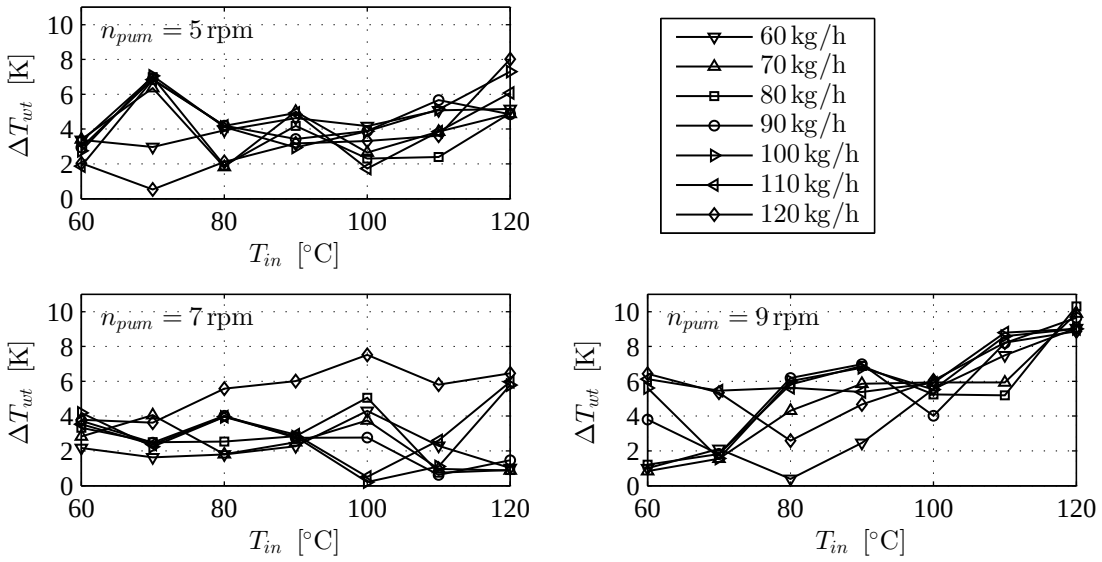

Figure C.13: Gas temperature difference of the Wurster tube inlet to outlet ΔT_{wt} versus the inlet gas temperature T_{in} for different inlet gas mass flow rates $\dot{M}_{in}$ and different pump rotation speeds $n_{pum} \in \{5, 7, 9\}\,\mathrm{rpm}$.

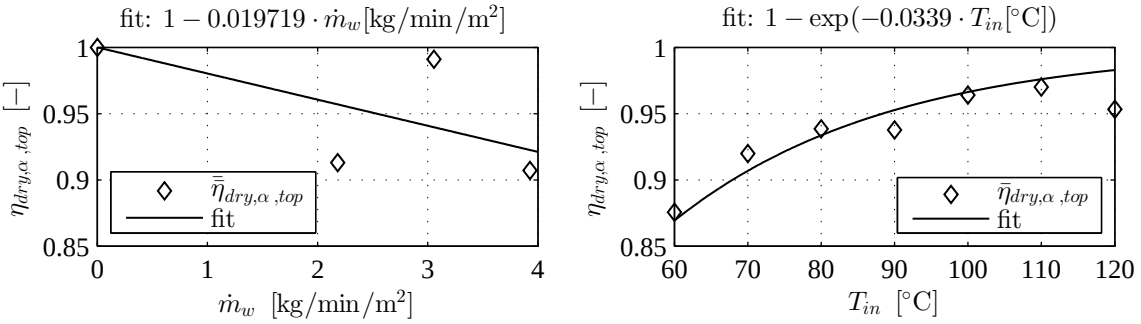

Figure C.14: Fit of averaged drying potential at the top of the spray rate $\eta_{dry,\alpha,top}$ versus the cross-section area-specific water spray rate $\dot{m}_w$ and the inlet gas temperature T_{in}, respectively.

Bibliography

[1] Hampel, N. A. ; Bück, A. ; Peglow, M. ; Tsotsas, E.: Continuous pellet coating in a Wurster fluidized bed process. In: *Chemical Engineering Science* 86 (2013), 87–98. https://doi.org/10.1016/j.ces.2012.05.034

[2] Hampel, N. A.: *Diskontinuierliches und kontinuierliches Pelletcoating im Wurster-Wirbelschichtprozess*, Doctoral thesis, Otto von Guericke University Magdeburg, Germany, 2015. https://doi.org/10.25673/4340

[3] Wadell, H.: Sphericity and roundness of rock particles. In: *The Journal of Geology* 41 (1933), Nr. 3, S. 310–331

[4] Geldart, D.: Single particles, fixed and quiescent beds. In: Geldart, D. (Hrsg.): *Gas Fluidization Technology*. Chichester : Wiley, 1986. – ISBN 0–471–90806–1, S. 11–32

[5] Allen, T.: *Particle Size Measurement*. 3. ed. Boston, MA and s.l. : Springer US, 1981 (Powder Technology Series). – ISBN 978–0–412–15410–2

[6] Allen, T.: *Powder Sampling and Particle Size Determination*. Amsterdam : Elsevier, 2003. – ISBN 978–0–444–51564–3

[7] Kaye, B. H.: Particle size characterization. In: Fayed, M. E. (Hrsg.) ; Otten, L. (Hrsg.): *Handbook of Powder Science & Technology*. Boston, MA : Springer US, 1997. – ISBN 978–0–412–99621–4, S. 1–34

[8] Yang, W.-C.: Particle characterization and dynamics. In: Yang, W.-C. (Hrsg.): *Handbook of Fluidization and Fluid-Particle Systems*. New York : Marcel Dekker, 2003 (Chemical industries). – ISBN 0–8247–0259–X, S. 1–27

[9] Rhodes, M.: *Introduction to Particle Technology*. 2. ed. Chichester : Wiley, 2008. – ISBN 978–0–470–01427–1

[10] Zogg, M.: *Einführung in die mechanische Verfahrenstechnik*. 3. ed. Stuttgart : Teubner, 1993. – ISBN 3–519–16319–5

[11] Stiess, M.: *Mechanische Verfahrenstechnik - Partikeltechnologie 1*. 3. ed. Berlin, Heidelberg : Springer, 2009. – ISBN 978–3–540–32551–2

[12] Polke, R. ; Schäfer, M. ; Scholz, N.: Charakterisierung disperser Systeme. In: Schubert, H. (Hrsg.): *Handbuch der Mechanischen Verfahrenstechnik*. Wiley, 2003. – ISBN 978–3–527–30577–7, S. 7–100

[13] Bullen, P. S.: *Handbook of Means and Their Inequalities*. Dordrecht : Springer, 2003 (Mathematics and Its Applications). – ISBN 978–94–017–0399–4

[14] Schmidt, M. ; Bück, A. ; Tsotsas, E.: Experimental investigation of the influence of drying conditions on process stability of continuous spray fluidized bed layering granulation with external product separation. In: *Powder Technology* 320 (2017), 474–482. https://doi.org/10.1016/j.powtec.2017.07.012

[15] Schmidt, M.: *Process dynamics and structure formation in continuous spray fluidized bed processes*, Doctoral thesis, Otto von Guericke University Magdeburg, Germany, 2018. http://dx.doi.org/10.25673/13438

[16] Rumpf, H. C. H. ; Gupte, A. R.: Einflüsse der Porosität und Korngrößenverteilung im Widerstandsgesetz der Porenströmung. In: *Chemie Ingenieur Technik - CIT* 43 (1971), Nr. 6, 367–375. https://doi.org/10.1002/cite.330430610

[17] Sauter, J.: Die Grössenbestimmung der in Gemischnebeln von Verbrennungskraftmaschinen vorhandenen Brennstoffteilchen. In: *VDI-Forschungsheft* (1926), Nr. 279

[18] DIN ISO 9276-2:2018-09: *Darstellung der Ergebnisse von Partikelgrößenanalysen - Teil 2: Berechnung von mittleren Partikelgrößen/-durchmessern und Momenten aus Partikelgrößenverteilungen.* https://doi.org/10.31030/2867011. Version: 2018-09

[19] Wirth, K.-E.: Druckverlust bei der Strömung durch Schüttungen. In: *VDI-Wärmeatlas.* 10. ed. Berlin, Heidelberg : Springer, 2006. – ISBN 3–540–25504–4, S. Laf1–Laf5

[20] Tsotsas, E.: Wärmeleitung und Dispersion in durchströmten Schüttungen. In: *VDI-Wärmeatlas.* 10. ed. Berlin, Heidelberg : Springer, 2006. – ISBN 3–540–25504–4, S. Mh1–Mh15

[21] Grace, J. R. ; Ebneyamini, A.: Connecting particle sphericity and circularity. In: *Particuology* 54 (2021), 1–4. https://doi.org/10.1016/j.partic.2020.09.006

[22] Brown, G. G. ; Foust, A. S. ; Katz, D. L. ; Schneidewind, R. ; White, R. R. ; Wood, W. P. ; Brown, G. M. ; Brownell, L. E. ; Martin, J. J. ; Williams, G. B. ; Banchero, J. T. ; York, J. L.: *Unit Operations.* CBS Publishers and Distributors, 1950

[23] Partridge, B. A. ; Lyall, E.: Minimum fluidisation velocities for spherical and irregular particles fluidized by air. In: *Atomic Energy Research Establishment - Report (AERE-R)* (1969), Nr. M.2152

[24] Geldart, D.: Particle entrainment and carryover. In: Geldart, D. (Hrsg.): *Gas Fluidization Technology.* Chichester : Wiley, 1986. – ISBN 0–471–90806–1, S. 123–153

[25] Tsotsas, E.: Eine einfache empirische Gleichung zur Vorausberechnung der Porosität polydisperser Kugelschüttungen. In: *Chemie Ingenieur Technik - CIT* 63 (1991), Nr. 5, 495–496. https://doi.org/10.1002/cite.330630513

[26] Tsotsas, E.: Wärmeleitfähigkeit von Schüttschichten. In: *VDI-Wärmeatlas.* 10. ed. Berlin, Heidelberg : Springer, 2006. – ISBN 3–540–25504–4, S. Dee1–Dee9

[27] Bauer, R.: *Effective radiale Wärmeleitfähigkeit gasdurchströmter Schüttungen mit Partikeln unterschiedlicher Form und Größenverteilung*, Doctoral thesis, University Karlsruhe, Germany, 1976

[28] Kraume, M.: *Transportvorgänge in der Verfahrenstechnik: Grundlagen und apparative Umsetzungen.* Berlin, Heidelberg : Springer, 2004. – ISBN 3–540–40105–9

[29] Mörl, L. ; Heinrich, S. ; Peglow, M.: Fluidized bed spray granulation. In: Salman, A. D. (Hrsg.) ; Hounslow, M. J. (Hrsg.) ; Seville, J.P.K. (Hrsg.): *Granulation.* 11. ed. Amsterdam : Elsevier, 2007 (Handbook of powder technology). – ISBN 978–0–444–51871–2, S. 21–188

[30] Kürten, H. ; Raasch, J. ; Rumpf, H.: Beschleunigung eines kugelförmigen Feststoffteilchens im Strömungsfeld konstanter Geschwindigkeit. In: *Chemie Ingenieur Technik - CIT* 38 (1966), Nr. 9, 941–948. https://doi.org/10.1002/cite.330380905

[31] Clift, R. ; Grace, J. R. ; Weber, M. E.: *Bubbles, Drops, and Particles.* Reprint. der Ausg. New York, NY Acad. Press, 1978. Mineola, NY : Dover Publ, 2013. – ISBN 0–486–44580–1

[32] Taneda, S.: Experimental investigation of the wake behind a sphere at low Reynolds numbers. In: *Journal of the Physical Society of Japan* 11 (1956), Nr. 10, 1104–1108. https://doi.org/10.1143/JPSJ.11.1104

[33] Brauer, H. ; Mewes, D.: Strömungswiderstand sowie stationärer und instationärer Stoff- und Wärmeübergang an Kugeln. In: *Chemie Ingenieur Technik - CIT* 44 (1972), Nr. 13, 865–868. https://doi.org/10.1002/cite.330441314

[34] Stokes, G. G.: On the effect of internal friction of fluids on the motion of pendulums. In: *Transactions of the Cambridge Philosophical Society* (1851), Nr. 9, S. Part II, 8–106

[35] Goroshko, V. D. ; Rozenbaum, R. B. ; Todes, O. M.: Izv. Vysshykh Uchebn. Zavedenii (Russian: Approximate laws of suspended bed hydraulics and constrained fall). In: *Neftyanaga i Gazovaya* (1958), Nr. 1, S. 125

[36] Sergeev, Y. A.: Propagation of waves and dispersed-phase concentration discontinuities in a gas-fluidized bed of weakly interacting particles. In: *Fluid Dynamics* 23 (1988), Nr. 5, 706–713. https://doi.org/10.1007/BF02614146

[37] Zabrodsky, S. S.: *Hydrodynamics and Heat Transfer in Fluidized Beds.* Cambridge : The MIT Press, 1966 ("Translation of Gidrodinamika i Teploperenos v Kipyaschem Sloye by Fizmatgiz, Moscow-Leningrad, 1963")

[38] Mushtejev, W. I. ; Uljanov, W. M.: *Suschka dispersnich materialov (Russian: Drying of disperse materials).* Moskwa : isd. Chimija, 1988

[39] Kaskas, A. A.: *Schwarmsinkgeschwindigkeit in Mehrkornsuspensionen am Beispiel der Sedimentation*, Doctoral thesis, Technical University of Berlin, Germany, 1970

[40] Martin, H.: Wärme- und Stoffübertragung in der Wirbelschicht. In: *Chemie Ingenieur Technik - CIT* 52 (1980), Nr. 3, 199–209. https://doi.org/10.1002/cite.330520303

[41] Martin, H.: Wärmeübergang in Wirbelschichten. In: *VDI-Wärmeatlas.* 10. ed. Berlin, Heidelberg : Springer, 2006. – ISBN 3–540–25504–4, S. Mf1–Mf9

[42] Haider, A. ; Levenspiel, O.: Drag coefficient and terminal velocity of spherical and nonspherical particles. In: *Powder Technology* 58 (1989), Nr. 1, 63–70. https://doi.org/10.1016/0032-5910(89)80008-7

[43] Chhabra, R. P. ; Agarwal, L. ; Sinha, N. K.: Drag on non-spherical particles: an evaluation of available methods. In: *Powder Technology* 101 (1999), Nr. 3, 288–295. https://doi.org/10.1016/S0032-5910(98)00178-8

[44] Decker, S.: *Zur Berechnung von gerührten Suspensionen mit dem Euler-Lagrange-Verfahren*, Doctoral thesis, Martin Luther University Halle-Wittenberg, Germany, 2005

[45] Rajesh S. ; Adhikari, R.: Generalized Stokes laws for active colloids and their applications. In: *Journal of Physics Communications* 2 (2018), Nr. 2, 025025. https://doi.org/10.1088/2399-6528/aaab0d

[46] Zehner, P.: Flüssigkeits/Feststoff-Strömungen in verfahrenstechnischen Apparaten. In: *Fortschritt-Berichte VDI-Reihe* 3 (1988), Nr. 160

[47] Kim, I. ; Elghobashi, S. ; Sirignano, W. A.: Three-dimensional flow over two spheres placed side by side. In: *Journal of Fluid Mechanics* 246 (1993), 465–488. https://doi.org/10.1017/S0022112093000229

[48] Ramachandran, R. S. ; Wang, T.-Y. ; Kleinstreuer, C. ; Chiang, H.: Laminar flow past three closely spaced monodisperse spheres or nonevaporating drops. In: *AIAA Journal* 29 (1991), Nr. 1, 43–51. https://doi.org/10.2514/3.10543

[49] Chen, W. ; Scott, K. J.: Sedimentation. In: Fayed, M. E. (Hrsg.) ; Otten, L. (Hrsg.): *Handbook of Powder Science & Technology.* Boston, MA : Springer US, 1997. – ISBN 978–0–412–99621–4, S. 635–682

[50] Richardson, J. F. ; Zaki, W. N.: Sedimentation and fluidisation. In: *Transactions of the Institution of Chemical Engineers* (1954), Nr. 32, S. 35–53

[51] Hawksley, P. G. W.: Survey of the relative motion of particles and fluids. In: *British Journal of Applied Physics* 5 (1954), Nr. S3, S1–S5. https://doi.org/10.1088/0508-3443/5/s3/302

[52] Maude, A. D. ; Whitmore, R. L.: A generalized theory of sedimentation. In: *British Journal of Applied Physics* 9 (1958), Nr. 12, 477–482. https://doi.org/10.1088/0508-3443/9/12/304

[53] Thacker, W. C. ; Lavelle, J. W.: Stability of settling of suspended sediments. In: *Physics of Fluids* 21 (1978), Nr. 2, 291–292. https://doi.org/10.1063/1.862205

[54] Di Felice, R. ; Kehlenbeck, R.: Sedimentation velocity of solids in finite size vessels. In: *Chemical Engineering & Technology* 23 (2000), Nr. 12, 1123–1126. https://doi.org/10.1002/1521-4125(200012)23:12<1123::AID-CEAT1123>3.0.CO;2-2

[55] Lewis, E.W. ; Bowerman, E. W.: Fluidization of solid particles in liquids. In: *Chemical Engineering Progress* 1952 (48), S. 603–611

[56] Zehner, P.: Beschreibung der Fluiddynamik von gleichmässig fluidisierten Kugelschwärmen. In: *Chemical Engineering and Processing: Process Intensification* 19 (1985), Nr. 1, 57–65. https://doi.org/10.1016/0255-2701(85)80005-2

[57] Mier, P.: *Experimentelle Untersuchung und numerische Simulation der Flüssigkeits-Feststoff-Strömung im Strahlschlaufenapparat*, Doctoral thesis, Technical University of Berlin, Germany, 2006

[58] Watanabe, H.: Voidage function in particular fluid systems. In: *Powder Technology* 19 (1978), Nr. 2, 217–225. https://doi.org/10.1016/0032-5910(78)80030-8

[59] Brauer, H. ; Kriegel, E.: Kornbewegung bei der Sedimentation. In: *Chemie Ingenieur Technik - CIT* 38 (1966), Nr. 3, 321–330. https://doi.org/10.1002/cite.330380326

[60] Brauer, H.: *Grundlagen der Einphasen- und Mehrphasenströmungen.* Aarau, Frankfurt a.M. : Verlag Sauerländer, 1971

[61] Molerus, O.: *Fluid-Feststoff-Strömungen.* Berlin, Heidelberg : Springer, 1982. – ISBN 978–3–642–50215–6

[62] Brauer, H.: Particle/Fluid Transport Processes. In: *Fortschritte der Verfahrenstechnik.* 1979 (17)

[63] Wilhelm, R. H. ; Kwauk, M.: Fluidization of solid particles. In: *Chemical Engineering Progress* (1948), Nr. 44, S. 201–218

[64] Rowe, P. N.: A convenient empirical equation for estimation of the Richardson-Zaki exponent. In: *Chemical Engineering Science* 42 (1987), Nr. 11, 2795–2796. https://doi.org/10.1016/0009-2509(87)87035-5

[65] KHAN, A. R. ; Richardson, J. F.: Fluid-particle interactions and flow characteristics of fluidized beds and settling suspensions of spherical particles. In: *Chemical Engineering Communications* 78 (1989), Nr. 1, 111–130. https://doi.org/10.1080/00986448908940189

[66] Bertil Andersson, K. E.: Pressure drop in ideal fluidization. In: *Chemical Engineering Science* 15 (1961), Nr. 3-4, 276–297. https://doi.org/10.1016/0009-2509(61)85032-X

[67] Hanratty, T. J. ; Bandukwala, A.: Fluidization and sedimentation of spherical particles. In: *AIChE Journal* 3 (1957), Nr. 2, 293–296. https://doi.org/10.1002/aic.690030230

[68] Lewis, W. K. ; Gilliland, E. R. ; Bauer, W. C.: Characteristics of fluidized particles. In: *Industrial & Engineering Chemistry* 41 (1949), Nr. 6, 1104–1117. https://doi.org/10.1021/ie50474a004

[69] Leu, R.-J. ; Ghosh, i. M.: Polyelectrolyte characteristics and flocculation. In: *Journal - American Water Works Association* 80 (1988), Nr. 4, 159–167. https://doi.org/10.1002/j.1551-8833.1988.tb03021.x

[70] Hunt, C. D. ; Hanson, D. N. ; Wilke, C. R.: Capacity factors in the performance of perforated-plate columns. In: *AIChE Journal* 1 (1955), Nr. 4, 441–451. https://doi.org/10.1002/aic.690010410

[71] McAllister, R. A. ; McGinnis, P. H. ; Plank, C. A.: Perforated-plate performance. In: *Chemical Engineering Science* 9 (1958), Nr. 1, 25–35. https://doi.org/10.1016/0009-2509(58)87004-9

[72] Hoppe, K. ; Mittelstrass, M.: *Grundlagen der Dimensionierung von Kolonnenböden.* Dresden : Theodor Steinkopff, 1967

[73] Uhlemann, H. ; Mörl, L.: *Wirbelschicht-Sprühgranulation.* Berlin and Heidelberg : Springer, 2000. – ISBN 978–3–642–57004–9

[74] Kunii, D. ; Levenspiel, O.: *Fluidization Engineering*. 2. ed. Butterworth-Heinemann, 1991. – ISBN 978–0–409–90233–4

[75] Schubert, H.: Durchströmung von Partikelschichten. In: Schubert, H. (Hrsg.): *Handbuch der Mechanischen Verfahrenstechnik*. Wiley, 2003. – ISBN 978–3–527–30577–3, S. 139–153

[76] Ergun, S.: Fluid flow through packed columns. In: *Chemical Engineering Progress* 48 (1952), Nr. 2, S. 89–94

[77] Specht, E.: *Heat and Mass Transfer in Thermoprocessing: Fundamentals, Calculations, Processes*. 1. ed. Essen : Vulkan-Verlag, 2017. – ISBN 978–3–8027–2991–1

[78] Glicksman, L. R.: Fluidized bed scale-up. In: Yang, W.-C. (Hrsg.): *Fluidization, Solids Handling and Processing*. Westwood, New Jersey : Noyes Publications, 1998 (Particle Technology Series). – ISBN 978–0–8155–1427–5, S. 1–110

[79] Botterill, J.S.M. ; Teoman, Y. ; Yüregir, K. R.: The effect of operating temperature on the velocity of minimum fluidization, bed voidage and general behaviour. In: *Powder Technology* 31 (1982), Nr. 1, 101–110. https://doi.org/10.1016/0032-5910(82)80009-0

[80] Wirth, K.-E.: Strömungszustände und Druckverlust in Wirbelschichten. In: *VDI-Wärmeatlas*. 10. ed. Berlin, Heidelberg : Springer, 2006. – ISBN 3–540–25504–4, S. Lcb1–Lcb11

[81] Tsotsas, E. ; Schlünder, E. U.: Some remarks on channelling and on radial dispersion in packed beds. In: *Chemical Engineering Science* 43 (1988), Nr. 5, 1200–1203. https://doi.org/10.1016/0009-2509(88)85081-4

[82] Wen, C. Y. ; Yu, Y. H.: A generalized method for predicting the minimum fluidization velocity. In: *AIChE Journal* 12 (1966), Nr. 3, 610–612. https://doi.org/10.1002/aic.690120343

[83] Brötz, W.: Grundlagen der Wirbelschichtverfahren. In: *Chemie Ingenieur Technik - CIT* 24 (1952), Nr. 2, 60–81. https://doi.org/10.1002/cite.330240204

[84] Brötz, W.: *Grundriß der chemischen Reaktionstechnik für Chemiker und Ingenieure, Apparatebauer und Studenten der chemischen Technologie und Verfahrenstechnik*. Weinheim : Verlag Chemie, 1958

[85] Sathiyamoorthy, D. ; Sridhar Rao, C.: Gas distributor in fluidized beds. In: *Powder Technology* (1978), Nr. 20, 47–52. https://doi.org/10.1016/0032-5910(78)80007-2

[86] Sathiyamoorthy, D. ; Sridhar Rao, C.: The choice of distributor to bed pressure drop ratio in gas fluidised beds. In: *Powder Technology* 30 (1981), Nr. 2, 139–143. https://doi.org/10.1016/0032-5910(81)80006-X

[87] Mörl, L. ; Mittelstrass, M. ; Sachse, J.: Berechnung der Verteilungsspektren von Feststoffgranulatteilchen in Wirbelschichtapparaten mit klassierendem Abzug. In: *Chem. Technol.* 30 (1978), Nr. 5, S. 242–245

[88] Heinrich, S.: *Modellierung des Wärme- und Stoffübergangs sowie der Partikelpopulationen bei der Wirbelschicht-Sprühgranulation*, Doctoral thesis, Otto von Guericke University Magdeburg, Germany, 2000

[89] Heinrich, S. ; Peglow, M. ; Ihlow, M. ; Henneberg, M. ; Mörl, L.: Analysis of the start-up process in continuous fluidized bed spray granulation by population balance modelling. In: *Chemical Engineering Science* 57 (2002), Nr. 20, 4369–4390. https://doi.org/10.1016/S0009-2509(02)00352-4

[90] Burgschweiger, J.: *Modellierung des statischen und dynamischen Verhaltens von kontinuierlich betriebenen Wirbelschichttrocknern*, Doctoral thesis, Otto von Guericke University Magdeburg, Germany, 2000

[91] Burgschweiger, J. ; Tsotsas, E.: Experimental investigation and modelling of continuous fluidized bed drying under steady-state and dynamic conditions. In: *Chemical Engineering Science* 57 (2002), Nr. 24, 5021–5038. https://doi.org/10.1016/S0009-2509(02)00424-4

[92] Rumpf, H. ; Leschonski, K.: Prinzipien und neuere Verfahren der Windsichtung. In: *Chemie Ingenieur Technik - CIT* 39 (1967), Nr. 21, 1231–1241. https://doi.org/10.1002/cite.330392105

[93] Levenspiel, O.: *Tracer Technology: Modeling the Flow of Fluids*. New York : Springer, 2012. – ISBN 978–1–4419–8074–8

[94] Tomas, J. ; Gröger, T.: *Verfahrenstechnische Bewertung einer mehrstufigen Querstrom-Aerosortierung mineralischer Stoffe*, Preprint Fakultät für Verfahrens- und Systemtechnik 1, Otto von Guericke University Magdeburg, Germany, 2000

[95] Bohnet, M.: *Mechanische Verfahrenstechnik*. Hoboken : John Wiley & Sons, 2012. – ISBN 978–3–527–31099–1

[96] Shadpoor, S. ; Pirouzi, A. ; Hamze, H. ; Mazaheri, D.: Determination of Bodenstein number and axial dispersion of a triangular external loop airlift reactor. In: *Chemical Engineering Research and Design* 165 (2021), 61–68. https://doi.org/10.1016/j.cherd.2020.10.018

[97] Molerus, O.: Stochastisches Modell der Gleichgewichtssichtung. In: *Chemie Ingenieur Technik - CIT* 39 (1967), Nr. 13, 792–796. https://doi.org/10.1002/cite.330391304

[98] Fokker, A. D.: Die mittlere Energie rotierender elektrischer Dipole im Strahlungsfeld. In: *Annalen der Physik* 348 (1914), Nr. 5, 810–820. https://doi.org/10.1002/andp.19143480507

[99] Planck, M.: Über einen Satz der statistischen Dynamik und seine Erweiterung in der Quantentheorie. In: *Sitzungsberichte der Preussischen Akademie der Wissenschaften zu Berlin* 24 (1917), S. 324–341

[100] Kolmogorov, A.: Über die analytischen Methoden in der Wahrscheinlichkeitsrechnung. In: *Mathematische Annalen* 104 (1931), Nr. 1, 415–458. https://doi.org/10.1007/BF01457949

[101] Einstein, A.: Über die von der molekularkinetischen Theorie der Wärme geforderte Bewegung von in ruhenden Flüssigkeiten suspendierten Teilchen. In: *Annalen der Physik* 322 (1905), Nr. 8, 549–560. https://doi.org/10.1002/andp.19053220806

[102] Molerus, O.: Über die Axialvermischung bei Transportprozessen in kontinuierlich betriebenen Apparaturen. In: *Chemie Ingenieur Technik - CIT* 38 (1966), Nr. 2, 137–145. https://doi.org/10.1002/cite.330380208

[103] Molerus, O. ; Hoffmann, H.: Darstellung von Windsichtertrennkurven durch ein stochastisches Modell. In: *Chemie Ingenieur Technik - CIT* 41 (1969), Nr. 5-6, 340–344. https://doi.org/10.1002/cite.330410523

[104] Heinrich, S.: Unsteady and steady-state particle size distributions in batch and continuous fluidized bed granulation systems. In: *Chemical Engineering Journal* 86 (2002), Nr. 1-2, 223–231. https://doi.org/10.1016/S1385-8947(01)00293-5

[105] Müller, D. ; Bück, A. ; Tsotsas, E.: Influence of separation properties and processing strategies on product characteristics in continuous fluidized bed spray granulation. In: *Powder Technology* 342 (2019), 572–584. https://doi.org/10.1016/j.powtec.2018.10.024

[106] Börner, M. ; Peglow, M. ; Tsotsas, E.: Derivation of parameters for a two compartment population balance model of Wurster fluidised bed granulation. In: *Powder Technology* 238 (2013), 122–131. https://doi.org/10.1016/j.powtec.2012.04.014

[107] Ramkrishna, D.: *Population Balances: Theory and Applications to Particulate Systems in Engineering*. New York : Acad. Press, 2000. – ISBN 978–0–125–76970–9

[108] Hulburt, H. M. ; Katz, S.: Some problems in particle technology. In: *Chemical Engineering Science* 19 (1964), Nr. 8, 555–574. https://doi.org/10.1016/0009-2509(64)85047-8

[109] Randolph, A. D. ; Larson, M. A.: *Theory of Particulate Processes: Analysis and Techniques of Continuous Crystallization: Academic Press*. New York : Academic Press, 1988. – ISBN 0–12–579652–8

[110] Mörl, L. ; Mittelstrass, M. ; Sachse, J.: Zum Kugelwachstum bei der Wirbelschichttrocknung von Suspensionen oder Lösungen. In: *Chem. Technol.* 29 (1977), Nr. 10, S. 540–542

[111] Hoffmann, T. ; Rieck, C. ; Schmidt, M. ; Bück, A. ; Peglow, M. ; Tsotsas, E.: Prediction of shell porosities in continuous fluidized bed spray layering. In: *Drying Technology* 33 (2015), Nr. 13, 1662–1670. https://doi.org/10.1080/07373937.2015.1064943

[112] Li, J. ; Freireich, B. ; Wassgren, C. ; Litster, J. D.: A general compartment-based population balance model for particle coating and layered granulation. In: *AIChE Journal* 58 (2012), Nr. 5, 1397–1408. https://doi.org/10.1002/aic.12678

[113] Rieck, C. ; Hoffmann, T. ; Bück, A. ; Peglow, M. ; Tsotsas, E.: Influence of drying conditions on layer porosity in fluidized bed spray granulation. In: *Powder Technology* 272 (2015), 120–131. https://doi.org/10.1016/j.powtec.2014.11.019

[114] Bück, A. ; Neugebauer, C. ; Meyer, K. ; Palis, S. ; Diez, E. ; Kienle, A. ; Heinrich, S. ; Tsotsas, E.: Influence of operation parameters on process stability in continuous fluidised bed layering with external product classification. In: *Powder Technology* 300 (2016), 37–45. https://doi.org/10.1016/j.powtec.2016.03.019

[115] Maronga, S. J. ; Wnukowski, P.: Modelling of the three-domain fluidized-bed particulate coating process. In: *Chemical Engineering Science* 52 (1997), Nr. 17, 2915–2925. https://doi.org/10.1016/S0009-2509(97)00112-7

[116] Mörl, L.: Granulatwachstum bei der Wirbelschichtgranulationstrocknung unter Berücksichtigung sich neu bildender Granulatkeime. In: *Wissenschaftliche Zeitschrift der Technischen Hochschule Otto von Guericke Magdeburg* 24 (1980), Nr. 6, S. 13–19

[117] Hounslow, M. J. ; Ryall, R. L. ; Marshall, V. R.: A discretized population balance for nucleation, growth, and aggregation. In: *AIChE Journal* 34 (1988), Nr. 11, 1821–1832. https://doi.org/10.1002/aic.690341108

[118] Abberger, T.: Population balance modelling of granulation. In: Salman, A. D. (Hrsg.) ; Hounslow, M. J. (Hrsg.) ; Seville, J.P.K. (Hrsg.): *Granulation* Bd. 11. Amsterdam : Elsevier, 2007. – ISBN 978–0–444–51871–2, S. 1109–1186

[119] Salman, A. D. ; Reynolds, G. K. ; Tan, H. S. ; Gabbott, I. ; Hounslow, M. J.: Breakage in granulation. In: Salman, A. D. (Hrsg.) ; Hounslow, M. J. (Hrsg.) ; Seville, J.P.K. (Hrsg.): *Granulation* Bd. 11. Amsterdam : Elsevier, 2007. – ISBN 978–0–444–51871–2, S. 979–1140

[120] Mörl, L. ; Sachse, J. ; Schuart, L. ; Mittelstrass, M.: Zur Berechnung und Optimierung von Wirbelschichtgranuliertrocknungsanlagen. In: *Chem. Technol.* 31 (1979), Nr. 6, S. 296–297

[121] Sigloch, H.: *Technische Fluidmechanik*. Berlin, Heidelberg : Springer, 2017. – ISBN 978–3–662–54467–9

[122] Span, R.: Stoffwerte von Luft. In: *VDI-Wärmeatlas*. 10. ed. Berlin, Heidelberg : Springer, 2006. – ISBN 3–540–25504–4, S. Dbb1–Dbb16

[123] Wagner, W.: Stoffwerte von Wasser. In: *VDI-Wärmeatlas*. 10. ed. Berlin, Heidelberg : Springer, 2006. – ISBN 3–540–25504–4, S. Dba1–Dba15

[124] Düsen-Schlick GmbH: *Module System Range 970*. https://www.myschlick.com/fileadmin//user_upload/Downloads/SCHLICK-Downloads/Catalogue-excerpts/de-gb/ca-two-substance-nozzles-model-970-de-gb.pdf. Version: 24.03.2022

[125] Rieck, C. ; Bück, A. ; Tsotsas, E.: Estimation of the dominant size enlargement mechanism in spray fluidized bed processes. In: *AIChE Journal* 66 (2020), Nr. 5. https://doi.org/10.1002/aic.16920

[126] Rieck, C.: *Microscopic and macroscopic modeling of particle formation processes in spray fluidized beds*, Doctoral thesis, Otto von Guericke University Magdeburg, Germany, 2020. https://doi.org/10.25673/35295

[127] Sondej, F. S.: *Morphologische Charakterisierung beschichteter Partikel und feststoffhaltiger Mikrotropfen*, Doctoral thesis, Otto von Guericke University Magdeburg, Germany, 2019. http://dx.doi.org/10.25673/25927

[128] Mörl, L.: *Anwendungsmöglichkeiten und Berechnung von Wirbelschichtgranulationstrocknungsanlagen*, Doctoral thesis B, Technical University Magdeburg, Germany, 1980

[129] Dosta, M. ; Heinrich, S. ; Werther, J.: Fluidized bed spray granulation: Analysis of the system behaviour by means of dynamic flowsheet simulation. In: *Powder Technology* 204 (2010), Nr. 1, 71–82. https://doi.org/10.1016/j.powtec.2010.07.018

[130] Priese, F. ; Wolf, B.: Development of high drug loaded pellets by Design of Experiment and population balance model calculation. In: *Powder Technology* 241 (2013), 149–157. https://doi.org/10.1016/j.powtec.2013.03.026

[131] Hoffmann, T.: *Experimentelle Untersuchungen des Einflusses von verschiedenen Prozessparametern auf das Partikelwachstum bei der Wirbelschicht-Sprühgranulation*, Doctoral thesis, Otto von Guericke University Magdeburg, Germany, 2017. http://dx.doi.org/10.25673/4625

[132] Grave, A. ; Pöllinger, N.: GLATT Wirbelschichttechnologie zum Coating von Pulvern, Pellets und Mikropellets. In: Kumpugdee Vollrath, Mont (Hrsg.) ; Krause, Jens-Peter (Hrsg.): *Easy Coating*. Wiebaden : Vieweg + Teubner, 2011 (Studium). – ISBN 978–3–8348–9896–8

Scientific contributions

Publications

Daniel Müller, Andreas Bück, Evangelos Tsotsas: *Influence of separation properties and processing strategies on product characteristics in continuous fluidized bed spray granulation*, Powder Technology 342, 2019, 572-584, Elsevier Science, Amsterdam. https://doi.org/10.1016/j.powtec.2018.10.024. – ISNN 00325910

Conference proceedings

Christian Rieck, **Daniel Müller**, Andreas Bück, Evangelos Tsotsas: *Modelling of continuous spray-coating in fluidized bed with a vertical tube air classifier* (No 5), 9th International Granulation Workshop (GWS), June 26th-27th, 2019, Lausanne, Switzerland.

Daniel Müller, Andreas Bück, Evangelos Tsotsas: *Heat and mass transfer modelling of continuous Wurster spray granulation with external product classification* (Contribution No. 7269), 21st International Drying Symposium, September 11th -14th, 2018, Valencia, Spain. http://dx.doi.org/10.4995/IDS2018.2018.8877

Daniel Müller, Andreas Bück, Evangelos Tsotsas: *Optimization of continuous Wurster fluidized bed spray granulation based on population balance analysis*, 6th International Conference on Population Balance Modeling, May 7th – 9th, 2018, Ghent, Belgium.

Daniel Müller, Christian Rieck, Andreas Bück, Evangelos Tsotsas: *Modelling of continuous fluidized bed spray-granulation* (Paper-No 71), 8th International Granulation Workshop (GWS), June 28th - 30th, 2017, Sheffield, United Kingdom.

Daniel Müller, Christian Rieck, Andreas Bück, Evangelos Tsotsas: *Modelling of continuous spray-coating in fluidized bed with a vertical tube air classifier*, 20th International Drying Symposium (IDS), August 7th-10th, 2016, Gifu, Japan.

Conference oral presentations

Daniel Müller, Andreas Bück, Evangelos Tsotsas: *Continuous fluidized bed spray granulation with controlled product size through model-based parameter setting and external product classification*, Jahrestreffen der ProcessNet-Fachgruppen: Mechanische Flüssigkeitsabtrennung, Zerkleinern und Klassieren sowie Agglomerations- und Schüttguttechnik, March 15th – 16th, 2021, Online-Conference, Germany.

Christian Rieck, Daniel Müller, Andreas Bück, Evangelos Tsotsas: *Modelling of continuous spray-coating in fluidized bed with a vertical tube air classifier*, 9th International Granulation Workshop (GWS), June 26th-27th, 2019, Lausanne, Switzerland.

Gerd Strenzke, Daniel Müller, Andreas Bück, Evangelos Tsotsas: *Experimental investigation of dynamic process stability of continuous fluidized bed spray agglomeration with internal classification*, PARTEC International Congress on Particle Technology, April 9th -11th, 2019, Nuremberg, Germany.

Daniel Müller, Christian Rieck, Andreas Bück, Evangelos Tsotsas: *Modelling of continuous spray-coating in fluidized bed with a vertical tube air classifier*, 20th International Drying Symposium (IDS), August 7th-10th, 2016, Gifu, Japan.

Conference posters

Rongyi Zhang, **Daniel Müller**, Evangelos Tsotsas: *Coating of fine particles in fluidized bed* (Poster No. AGG06), Jahrestreffen der ProcessNet-Fachgruppen: Mechanische Flüssigkeitsabtrennung, Zerkleinern und Klassieren sowie Agglomerations- und Schüttguttechnik, March 15th – 16th, 2021, Online-Conference, Germany.

Daniel Müller, Andreas Bück, Evangelos Tsotsas: *Investigation of continuous Wurster granulation with external product classification* (Poster No. 8), 9th International Granulation Workshop, June 26th – 28th, 2019, Lausanne, Switzerland.

Daniel Müller, Andreas Bück, Evangelos Tsotsas: *Variable control of product size in continuous fluidized bed spray granulation with external classification* (Poster No. 64), April 9th-11th, 2019, PARTEC International Congress on Particle Technology, Nuremberg, Germany.

Daniel Müller, Lisa Mielke, Andreas Bück, Evangelos Tsotsas: *A two-zone continuum model of heat, mass and momentum transfer in Wurster fluidized bed* (Poster No. P 2.03), Jahrestreffen der ProcessNet-Fachgruppen: Mischvorgänge, Trocknungstechnik und Wärme- und Stoffübertragung, March 18th-20th, 2019, Essen, Germany.

Daniel Müller, Andreas Bück , Evangelos Tsotsas: *Heat and mass transfer modelling of continuous Wurster-spray-granulation with external product classification* (Contribution No. 7269), 21st International Drying Symposium, September 11th -14th, 2018, Valencia, Spain.

Daniel Müller, Andreas Bück, Evangelos Tsotsas: *Optimization of continuous Wurster fluidized bed spray granulation based on population balance analysis*, 6th International Conference on Population Balance Modeling, May 7th – 9th, 2018, Ghent, Belgium.

Daniel Müller, Andreas Bück, Evangelos Tsotsas: *Multi-modelling of continuous Wurster-fluidized-bed spray granulation with interconnected product classification* (Poster No. TRO P07), Jahrestreffen der ProcessNet-Fachgruppen: Mechanische Flüssigkeitsabtrennung, Trocknung und Grenzflächenbestimmte Systeme und Prozesse, February 26th – 28th, 2018, Halle-Merseburg, Germany.

Daniel Müller, Andreas Bück , Evangelos Tsotsas: *Modeling of one-stage continuous fluidized bed spray-coating* (Poster-No. 13, Abstract-No. 25, Paper-No. 71), 8th International Granulation Workshop, June 28th - 30th, 2017, Sheffield, United Kingdom.

Daniel Müller, Andreas Bück, Evangelos Tsotsas, *Modellierung der einstufigen und kontinuierlichen Wirbelschicht-Sprühgranulation mit integrierter Produktklassierung* (Poster No. P 3.04), Jahrestreffen der ProcessNet-Fachgruppen: Agglomerations- und Schüttguttechnik, Grenzflächenbestimmte Systeme und Prozesse, Trocknungstechnik, Lebensmittelverfahrenstechnik und Wärme- und Stoffübertragung, February 13th – 17th, 2017, Bruchsal, Germany.

Supervised student theses

- **Arne Wurzer** (Master thesis)
  Untersuchung des Arbeitsbereichs und der erforderlichen Prozessparameter der kontinuierlichen Wurster-Sprühgranulation, December 2019, Otto von Guericke University, Magdeburg, Germany.

- **Pridivi Raj Kumar Kumareshan** (Master thesis)
  Determination of particle growth limits, spray losses and further process parameters for discontinuous and continuous fluidized bed spray granulation, May 2019, Otto von Guericke University, Magdeburg, Germany.

- **Madlen Muminow** (Master thesis)
  Untersuchung des Klassierrohreintragsmassenstroms und des Partikelwachstums für die kontinuierliche Wurster-Sprühgranulation. April 2019, Otto von Guericke University, Magdeburg, Germany.

- **Chethana Manjunatha** (Master thesis)
  Determination of particle size limits and required process parameters for continuous Wurster spray granulation, December 2018, Otto von Guericke University Magdeburg, Germany.

- **Leonard Messing** (Bachelor thesis)
  Experimentelle Untersuchung einer Regelungsstrategie für die kontinuierliche Wurster-Sprühgranulation mit externer Klassierung, May 2018, Otto von Guericke University Magdeburg, Germany.

- **Madlen Muminow** (Bachelor thesis)
  Experimentelle Untersuchung prozessbeeinflussender Parameter einer kontinuierlich betriebenen Wurster-Sprühwirbelschichtanlage, May 2017, Otto von Guericke University Magdeburg, Germany.